ISSN 0911-5730
UVSOR-25
April 1998

UVSOR

ACTIVITY REPORT

1997

Ultraviolet Synchrotron Orbital Radiation Facility
Institute for Molecular Science

CONTENTS

Solid State Spectroscopy I (IR – VUV)

UVSOR
ACTIVITY REPORT
1997

edited by
H. Hama, S. Tanaka, T. Gejo

Preface

This is the new Activity Report reporting the research activities which were done at the UVSOR facility in 1997. This is the fourth volume in the red-covered Activity Report series. For these four years, major part of beamline improvement and upgrade projects for the second 10 years of UVSOR are going well, where the first SR was emitted in November 1983. I would like to acknowledge various kinds of supports to the projects by the government and the outside users, and efforts of the UVSOR staff. We hope breakthroughs in science will soon be brought by users of the improved and upgraded beamlines. We are now trying to develop new fields in molecular science towards the next century, by combining various detection systems and light sources, such as synchrotron radiation, laboratory laser and FEL (free electron laser). In April 1997 two research facilities, the Laser Research Center for Molecular Science and the Research Center for Molecular Materials, have been established in the Institute for Molecular Science (IMS). Strong collaboration with these facilities will be important for the future of UVSOR in IMS, although most users within IMS belong to the Department of Vacuum UV Photoscience since 1991.

I am attaching herewith two letters from foreign scientists, Dr. Ian Munro and Dr. Adam P. Hitchcock. Dr. Munro retired from Director of SRS, Daresbury Laboratory, last year and now is a visiting professor of the Department of Vacuum UV Photoscience, IMS. Daresbury Laboratory and IMS are key institutions in the areas of "Application of Synchrotron Radiation to Molecular Spectroscopy and Photochemistry" and "Scientific Application of Synchrotron Radiation" in the UK-Japan Scientific Cooperation Program. Dr. Hitchcock spent a few days in IMS to discuss collaboration in molecular science with us. He is one of the key persons of the Canadian Light Source (CLS) project. We are very grateful to them for valuable letters to evaluate the UVSOR facility. We will further elaborate our future programs by taking into account their comments.

February, 1998

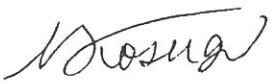

Nobuhiro Kosugi
Director of UVSOR

Status of UVSOR

Status of the UVSOR Accelerator Complex in 1997

Hiroyuki HAMA, Masahito HOSAKA, Toshio KINOSHITA, Jun-Ichiro YAMAZAKI

UVSOR Facility, Institute for Molecular Science, Okazaki 444 Japan

1. General

The UVSOR storage ring has been operated without serious hardware troubles in 1997. Because of continuous efforts for replacement of old devices, particularly power supplies for pulse magnets, in these years, malfunction of devices has become fewer. In addition, troubles on the control circuite for the booster synchrotron is now able to be fixed smoothly because spare parts for most of core circuites have been secured. Operation time in each month is shown in Fig. 1. Because there ware 4 shut-off terms in seasons, large flutcuation is apparently seen. However the most of scheduled machine time was consumed properly.

Beam injection is performed twice per day at 9 am and 1 pm. On the third day in a week, an additional injection is at 5 pm. The maximum beam current is limited to be 240 mA by optical elements of SR beam lines, then approximately 120 mA remains at the time of next injection. However after the last injection, the machine time is often extended, so that the averaged beam current in the machine time is about 100 mA as shown in Fig. 2.

Troubles concerened in the booster synchrotron are still large portion in the time lost. As mentioned above, there was no serious situation because most of troubles were fixed rapidly. Although we lost 10-hour machine time because of a trouble of a computor software, this was also not serious trouble. Among additional equipments a couple of major problems were occured on the superconducting wiggler. In January, a trouble happened in a compressor for the 4 K refrigerator, which was fixed perfectly in May. However another trouble occured on a control system of an old power supply fro the magnets. Because ICs in the system were old commercial ones, it took a long time to obtain a substitution and the system came back after the summer. The superconducting system of the wiggler had been apparently working well for a while, a failure to keep the liquid He in

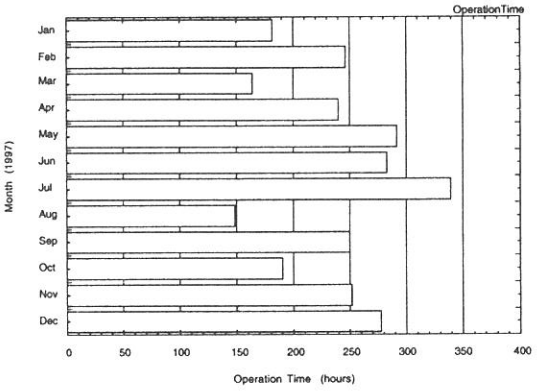

Fig. 1 Integrated operation time per month in 1997.

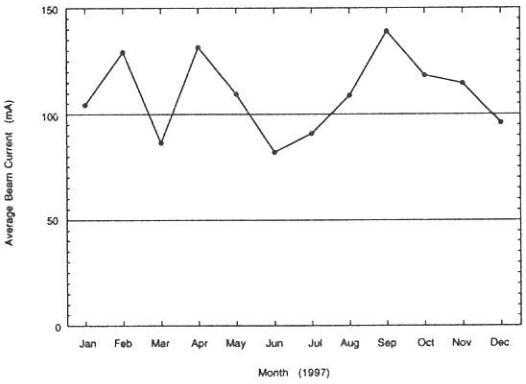

Fig. 2 Averaged beam current in each month.

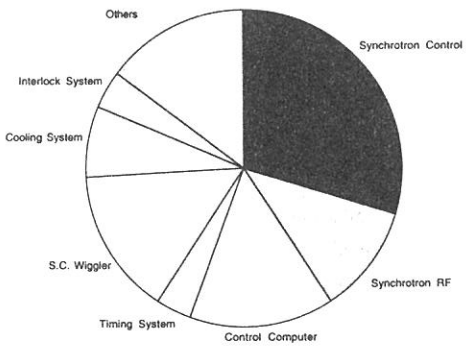

Fig. 3 Time lost per devices

the system occured again. At the moment the wiggler is in shut-off to be investigated. Because the system seems to have no malfunction, capability of the refrigerator may become below a heat intrusion. A basic measure will be implemented.

2. Lifetime and Ring Vacuum

In the spring shut-off term, a part of the ring beam chamber was replaced. The vacuum was recovered quickly, and the lifetime of the beam became a same level as the last year by the summer. However frequent leakage of the vacuum from a beam line occured in the fall, so that the lifetime became less again. Moreover an effect of the ion trap was seen very much, and then the vertical beam size had been not stabilized for a long time. Although the effect still remains, the partial filling of the bunches and an RF clearing against the ions are working effectively at the moment.

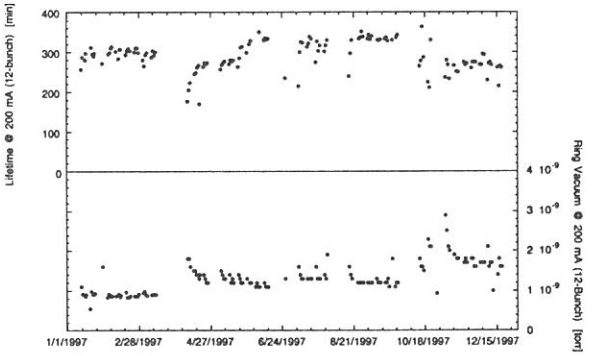

Fig. 4 Lifetime and average ring vacuum at 200 mA with the 12-bunch mode.

3. Transverse Resonance Kicker

To improve the beam handling on the storage ring, a transverse resonance kicker (TRK) system has been developed. In the normal multi-bunch operation, 3/4 filling mode is used to reduce an effect of the ion-trapping. Electron bunch filling was controlled by selecting the RF bucket using a timing control system for the fast kicker extraction of the booster synchrotron so far. However it was difficult to erase specific bunches so that the transverse beam instability due to ion-trapping has been not completely damped and the purity of single-bunch mode has been not very well. The TRK system generates electromagnetic field with a very short duration less than 3 ps. To avoid distortion of the pulse due to reflection, whole system including electrodes and a vacuum chamber was designed to be matched to the intrinsic impedance of 50 Ω. The short pulse is synchronized with the revolution of a specific bunch, which is, moreover, modulated by the betatron oscillation frequency. Because the electron momentum on the ring is high, a huge power is required to kick out the bunch at once. Meanwhile, using the TRK system the electron bunch is transversely kicked at each turn, and the amplitude of betatron oscillation grows rapidly even with a relatively low kick power. The electrons finally may touch the wall of vacuum chambers or go out of the dynamic aperture. As a result, for example, the impurity ratio of the single bunch became less than $10^{-4\text{-}5}$ by sweeping the satellite bunches using the TRK.

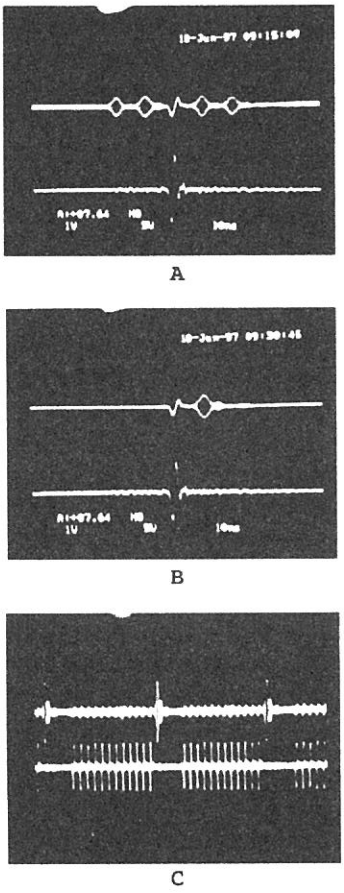

Fig. 5 RF signals in TRK and the bunches. During the single bunch injection (A), in the single bunch operation (B) and in the 14 bunches mode.

4. Conclusion

The 15-year old machine is still working well. Nevertheless our goal is not only to maintain the machines but also to improve them to have competitive performance. In the forthcoming year, parts of the beam chamber of the ring will be modified for issues of both the vacuum and the coupling impedance. These continuous improvements may be the motive power to survive in the world.

ACCELERATOR COMPLEX

Injection Linac

Energy	15 MeV
Energy Spread	~ 1.6 MeV
Frequency	S-band 2.856 Hz
Acceleration	$2\pi/3$ Traveling Wave
Length	2.5 m
Klystron Power	~ 1.8MW

Booster Synchrotron

Lattice Type	FODO
Energy	600 MeV
Beam Current	32 mA (8-bunch filled)
Circumference	26.6 m
Super Cell	6
Bending Radius	1.8m
Betatron Number	2.25 (horizontal)
	1.25 (vertical)
Momentum Compaction α	0.138
Harmonics	8
RF Frequency	90.115 MHz
Repetition Rate	2.6Hz

Storage Ring

Lattice Type	Chasman-Green
Energy	750 MeV
Critical Energy	425 eV
Circumference	53.2 m
Super Cell	4
Bending Radius	2.2 m
Betatron Tune	3.16 (horizontal)
	2.64 (vertical)
Momentum Compaction α	0.032
Harmonics	16
Emittance	$1.15\ 10^{-7}$ m rad (horizontal)
	1.15×10^{-8} m rad (vertical)
Beam Size	0.39 mm (horizontal)
	0.26 mm (vertical)
Bunch Length	170 ps (at zero current)
Beam Current	Multi-Bunch 200 mA
	Single-Bunch 50 mA
Lifetime	4 h at 200mA
	9 h at 100mA

Additional Equipment

Higher - Harmonic Cavity	3 × 90.115 Mhz
Superconducting Wiggler	4 T (maximum)
Undulator	for SR
Optical Klystron	for FEL

Control System

Preface: Based on Dual-Host system with CAMAC loop and friendly man-machine interface

Architecture

CPU	VAX4000 (× 2)
OS	VMS
Connection	DECNET & Local Cluster
Operator Console	X - Servers (VXT200 × 3)
Status Monitors	VT286s + Macintosh
Interfaces	CAMAC serial loop
	GPIB for Beam Monitors
	RS232C for Host CPU of Wiggler
Languages	FORTRAN, C, Pascal

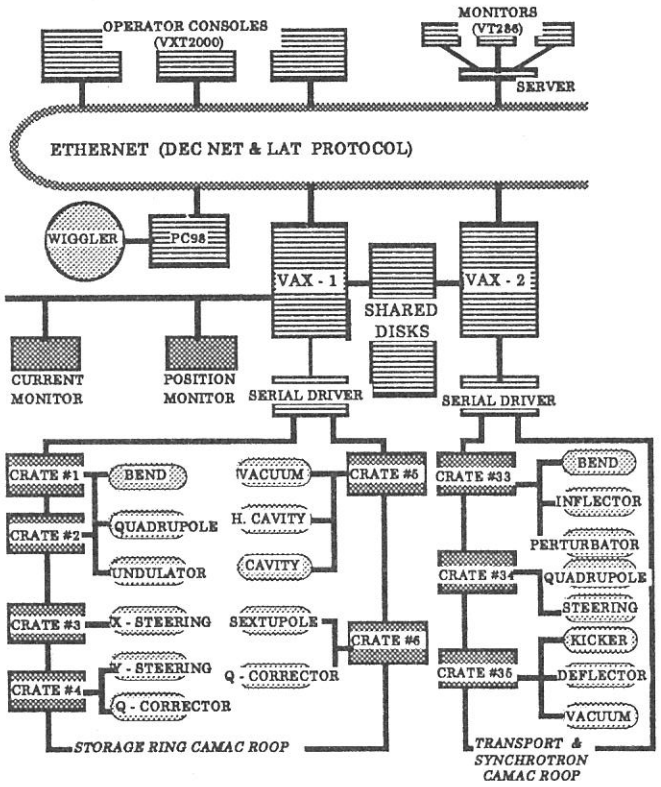

Scheme of Accelerator Control System "UCOSS"

Beam Lines in 1997

Masao KAMADA
UVSOR Facility, Institute for Molecular Science

In recent years, improvements and trials have been carried out in order to obtain better performance and new scientific achievements. The UVSOR have organized workshops and discussed the improvements and upgrade of beam lines with users. About one third of beam lines has been upgraded in a couple of years. A Seya-Namioka monochromator at beam line 7B was replaced by a 3-m normal-incidence monochromator to improve a resolving power and spectral range for solid state spectroscopy. Another one at beam line 2B2 was also replaced by a Dragon-type monochromator for gaseous experiments in VUV and EUV ranges. A multi-layer monochromator was installed to beam line 4A for photochemical reaction experiments. These monochromators are now under commissioning. A glancing-incidence monochromator (a 15-m SGM monochromator) at BL8B1 was operational mainly for gaseous experiments in EUV region with a TOF-Mass spectrometer, besides the use for solid-state spectroscopy. A Bruker FT-IR interferometer and an old FT-FIR of a Martin-Puplett type at beam line 6A1 were used for solid-state experiments in the wide wavelength range from near infrared to millimeter wave. A new monochromator (SGM-TRAIN) at beam line 5A, which has been constructed for the use of circularly polarized light from the helical undulator, was opened in 1997 for photoemission experiments in EUV range.

Therefore, seventeen experimental stations were operational in 1997, while three stations are under commissioning. The UVSOR facility will soon have twenty stations operational; two soft-x-ray stations equipped with a double-crystal monochromator, eight extreme ultraviolet stations with a glancing incidence or a plane-grating monochromator, four vacuum-ultraviolet stations with a Seya-Namioka-type or a normal incidence-type monochromator, two (far) infrared stations equipped with a FT interferometer, a multi-layer monochromator, and three white-light stations without any monochromator.

Several trials with lots of efforts have been carried out to achieve new scientific and experimental findings. In 1997, the two-photon excitation experiment was successfully carried out at BL1B with the combination of YAG laser and VUV photons. New spectroscopy taking advantage of synchronization of photon pulses between undulator radiation and laser was also succeeded in gaseous phase at BL3A2. New experiments with an electron-ion coincidence (EICO) method to investigate SR-induced desorption on solid surfaces were actively conducted at beam line 2B1. Photochemical reaction experiments on semiconductors and Diamond were carried out at BL3A1, 4B, and 8A. Infared reflection at high pressure and magnetic circular dichroism in high magnetic field were successfully studied with FT-IR and FT-FIR at BL6A1. Several photoemission experiments were actively conducted to investigate electronic structures: Two-dimensional photoemission experiments for solid and gaseous molecules at BL1A and BL3B, respectively, Angle-resolved spectroscopy on molecular films at BL8B2, Photoelectron microscopy on magnetic specimens at BL5B or BL7A, and Spin- and angle-resolved photoelectron spectroscopy at BL5A. A YB66 crystal was used for soft x-ray experiments at BL7A, where focussing mirror system is under installation.

There were lots of troubles, especially water-related troubles, in 1997. Since the concrete wall in the basement had many old cracks, the water leakage in the room for electricity happened often in rainy and typhoon seasons. A water pump in the second cooling-circulation system was broken. The pressure in the pre-mirror

chamber at BL8B1 became worse suddenly due to a water leakage from the cooling pipe for the pre-mirror. These are common problems to old facilities in the world. On the other hand, we had several troubles due to careless actions by users in 1997. Water from the loosely connected hoses was splashed at BL2A and BL8B2. The air was introduced in the monochromator chamber at BL7A during exchanging specimens. Similar air-leak trouble happened at BL6A1. The viton o-ring in the gate valve was melt during baking procedures at BL8A.

These accidents pushed us to confirm the alarm/emergency call system and also the education/safety system for beginner users. The second version of the UVSOR guidebook was published for this purpose. The UVSOR facility strongly asks all users to conduct their experimental procedures according to the beam line manuals and the guidebook.

The persons who want to use the open and the in-house beam lines are recommended to contact with the following station master or supervisor and the representative, respectively. The persons who want to know updated informations of the UVSOR facility are recommended to open http://www.uvsor.ims.ac.jp/.

Table I. Station masters and supervisors of open beam lines

Beam Line	Station Master	Sub Master	Supervisor
1B	M. Hasumoto	S. Tanaka	M. Kamada
2B1	S. Tanaka	M. Kamada	M. Kamada
3A1	M. Kamada	K. Hayashi	M. Kamada
3A2	N. Kondo	T. Gejo	T. Kinoshita
5A	S. Tanaka	M. Hasumoto	M. Kamada
5B	S. Kimura	M. Hasumoto	T. Kinoshita
6A1	S. Kimura	O. Matsudo	M. Kamada
7A	T. Kinoshita	O. Matsudo	T. Kinoshita
7B	T. Kinoshita	M. Hasumoto	T. Kinoshita
8A	T. Gejo	N. Kondo	T. Kinoshita
8B1	T. Gejo	N. Kondo	T. Kinoshita

Table II. Representatives of in-house beam lines.

Beam Line	Representative	Department/Facility
1A	N. Kosugi	VUV Photo Science
2A	N. Kosugi	UVSOR
2B2	K. Mitsuke	VUV Photo Science
3B	K. Mitsuke	VUV Photo Science
4A	T. Urisu	VUV Photo Science
4B	T. Urisu	VUV Photo Science
6A2	M. Kamada	UVSOR
6B	K. Yakushi	Molecular Assemblies
8B2	N. Ueno	VUV Photo Science

BL1A

Soft X-Ray Beamline for Photoelectron-Photoabsorption Spectroscopy

BL1A is a soft x-ray beamline for photoelectron-photoabsorption spectroscopy. The beamline is equipped with a focusing premirror and a double crystal monochromator[1]. The monochromator serves soft x-rays in the energy range from 585 to 4000 eV by using several kind of crystals such as β-alumina, beryl, quartz, InSb and Si crystals. The throughput spectra of the beryl ($10\bar{1}0$) and InSb (111) crystals are shown in Fig.1. Typical energy resolution ($E/\Delta E_{h\nu}$) of the monochromator is about 1500 when we use a pair of beryl or InSb crystals.

For photoelectron-photoabsorption spectroscopy, an ultra-high-vacuum (UHV) apparatus is connected. The top view of the apparatus is shown in Fig. 2. It is equipped with a high-performance electron analyzer (SES-200, SCIENTA Co.). The pass energy (E_P) can be varied between 1 and 500 eV and typical resolving power ($E_P/\Delta E_{elec.}$) is more than 1000. Using the apparatus, resonant photoelectron spectra for solid samples can be obtained with the total energy resolution (ΔE_{total}) of ~0.7 eV around hν=1000 eV.

Reference

[1] A.Hiraya et al., Rev. Sci. Instrum.,**63** (1992) 1264.

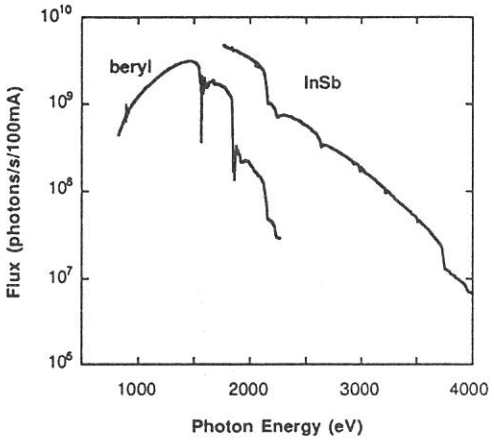

Figure 1. Throughput spectra of the double crystal monochromator at the BL1A.

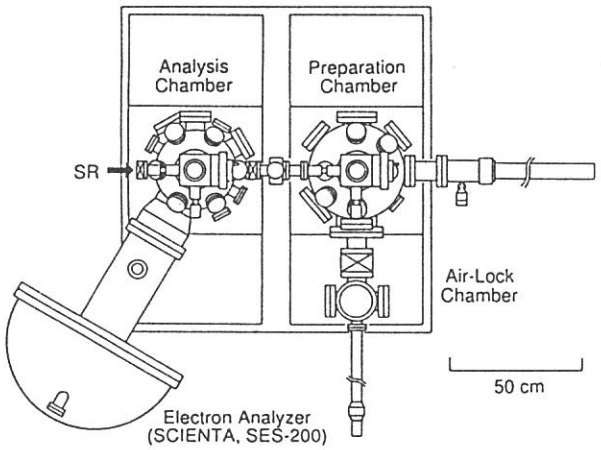

Figure 2. Top view of the UHV apparatus for photoemission-photoabsorption spectroscopy.

Specification

Monochromator	: double crystal monochromator (θ_B=70-20°)
Monochromator crystals (2d value, energy range)	: β-alumina (22.53Å, 585-1609eV), beryl (15.965Å, 826-2271eV), quartz (8.512Å, 1550-4000eV), InSb (7.481Å, 1764-4000eV), Si (6.271Å, 2104-4000eV)
Resolution	: E/ΔE=1500 for beryl and InSb
Experiment	: photoelectron-photoabsorption spectroscopy for solid

BL1B

Seya-Namioka Monochromator for General Purpose in VUV Region

The beam line 1B has been used for many experiments such as absorption, reflectivity, photo-ionization, and luminescence in condensed phase. The system consists of a pre-mirror, a 1-m Seya-Namioka type monochromator, and a post-mirror. Three gratings with 600, 1200, and 2400 gr/mm can cover the wavelength range from 40 nm to 650 nm, and two post mirror make it possible to change the focus point. A long-focus mirror is usually used with a LiF window to separate a main chamber for spectroscopy in liquids and biospecimens, while a short-focus mirror is suited to solid-state spectroscopy. The output flux from this monochromator is about 10^{10} phs/s around 200 nm with 0.1 mm slits. The spectral distributions obtained with three gratings are shown in the figure, although they are not the best data because of the contamination of the mirrors and gratings due to the recent careless accident.

A second monochromator (Spex 270M) and a LN-cooled CCD detector (Princeton Inc.) are available for luminescence experiments, together with a liquid helium-flow type cryostat. A time-resolved system to observe luminescence and excitation spectra with three time-gates is also possible. The decay measurement is one of the highlights of this station. A couple of weeks are supplied for the decay measurements under single bunch operation. A TAC system is therefore one of the standard instruments at this beam line.

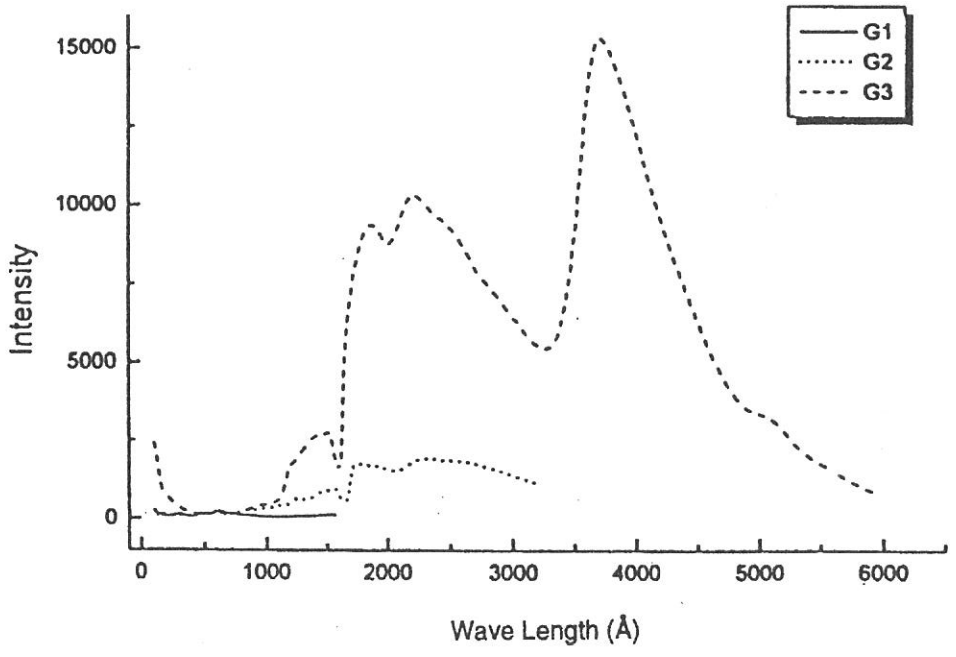

BL2A

Gas Phase Photoabsorption and Fluorescence Spectroscopy

Photoabsorption cross section and fluorescence excitation spectra of gaseous sample are simultaneously measured in a vacuum cell or effusive jet condition. The primary photons in the 30-400 nm region are dispersed by a 1-m Seya monochromator. Higher order light in the 80-120 nm range is suppressed by using a long channel with a cross section 2.5 × 5.0 × 170 mm long filled with argon gas at a pressure ≅0.3 Torr as shown in fig. 1. No filter is used between 30 and 80 nm since the photon flux at $\lambda<40$ nm is very weak (see fig. 1). The gas filter and cell are placed in a main chamber which is evacuated by a 5000 *l*/s diffusion pump (Varian, Model VHS10). A LiF window is used for the measurement at the $105<\lambda<210$ nm range as usual. Thus, the total photoabsorption cross section and fluorescence excitation spectra are available in the wide wavelength region 30-210 nm without or with little contamination by the higher order light.

Dispersed fluorescence and polarity of emission from the excited fragment are also measurable in addition to the total photoabsorption and emission cross sections. In the single bunch operation of synchrotron radiation with the period of 178 ns, a radiative life time can be measured.

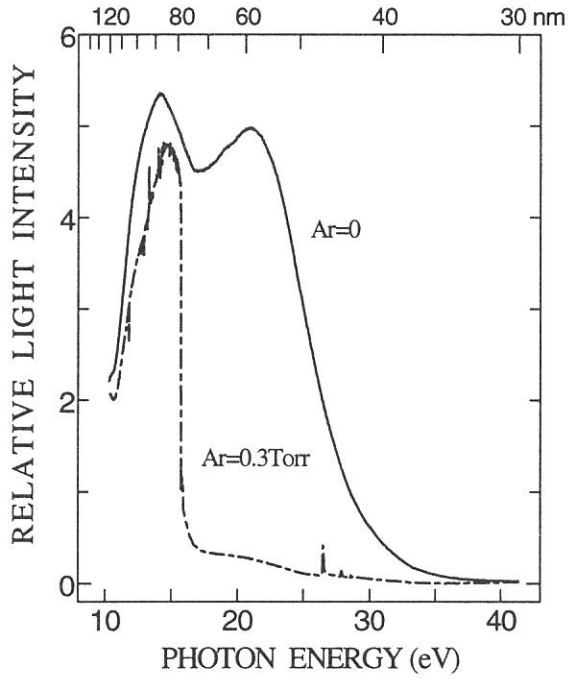

Fig. 1. Transmitted I_0 intensity with and without an Ar gas filter.

Specification

Monochromator : 1-m Seya
Wavelength range : 30-400 nm
Resolution : $\Delta E/E \cong 10^{-3}$ at 100 nm
Grating : 1200 *l*/mm blazed at 96 nm
Experiments :
- Vacuum cell or effusive jet
- Total photoabsorption cross section
- Fluorescence cross section
- Dispersed fluorescence
- Radiative lifetime
- Emission polarity

BL2B1

Soft-X ray beamline for solids and solid surfaces

BL2B1 is a beamline in order to study solids and solid surfaces by the use of photoabsorption and photoelectron spectroscopy. A 2-meter grazing incidence monochromator ('Grasshopper' type, Mark XV; Baker Manufacturing Co.) is installed. A 2400 l/mm grating has been installed since April 1994, and was replaced by a 1800 l/mm grating at March 1997. The resolving power is better than 600 at C-K edge (about 290 eV). Figure 1 shows the photoelectron yield from the Au mesh (10%-transmission) located near the position of a sample by the use of the 1800/mm grating. The dip around 300 eV is due to carbon contamination of optical elements.

The analyzing chamber is installed at the focusing point of the monochromized light. The pressure is less than $1x10^{-10}$ Torr. A double-pass CMA, a LEED optics, an ion-gun for sputtering, and a sample holder which can be cooled with liquid nitrogen and heated, etc. are equipped for the 'in-situ' measurements. The photoelectron spectroscopy including CIS (Constant initial state spectroscopy), CFS (Constant final state spectroscopy) can be measured using CMA, which is controlled by a personal computer. Samples can be transferred to the analyzing chamber from the air, through the preparation chamber in which sample treatments (e.g. cleaving, filing, and deposition) can be made.

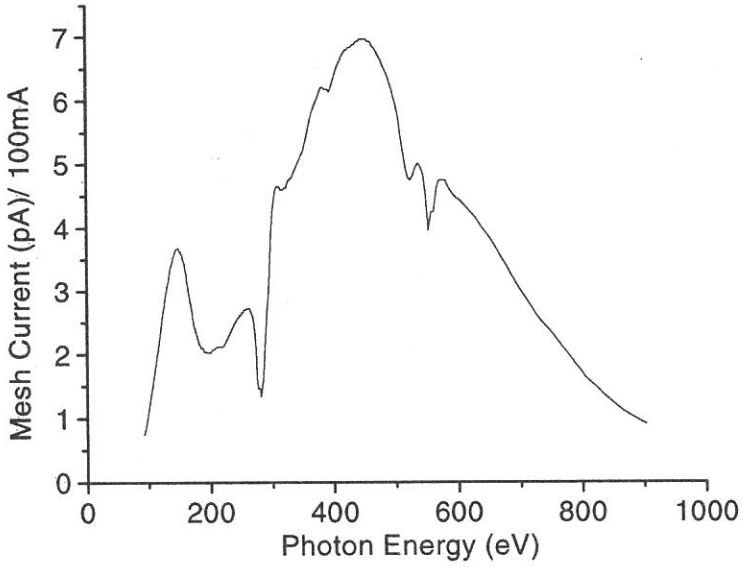

Figure 1. Photoelectron yield measured by the use of the Au mesh

Specification

Monochromator	:2m grasshopper type
Energy range	:95-1000 eV (1800 l/mm)
Resolution of photon	:<0.4eV at 300eV (1800 l/mm)
Resolution of photoelectron	:<0.3eV (hv=150eV)

Experiment : Photoelectron spectroscopy, X-ray absorption spectroscopy,

BL3A1

Irradiation Port with Undulator Radiation

The beam line 3A1 has been used for various kinds of experiments need intense undulator radiation. In recent years, photo-desorption, photo-chemical reaction, SR-CVD, photo-etching, irradiation damage effects in condensed phase, light amplification induced by core-level excitation, and so on have been carried out at this beam line. The luminescence from High-Tc superconductors and fullerens, the fluorescence yield of which is not high enough at beam lines for bending radiation, has been observed. A combination experiment with undulator radiation and a diode laser has been successfully conducted for time-response measurement of SR-induced desoprtion.

A planar-type undulator installed in a long straight section of the UVSOR storage ring provides an intense quasi-monochromatic radiation to beam lines 3A1 or 3A2. The undulator consists of 24 sets of magnets, a period length of which is 80 mm. The photon-energy range from 8 to 52 eV can be covered by the fundamentals with a K-value from 0.62 to 3.6, although higher harmonics are mixed into the spectral distribution in case of high K-values.

The beam line 3A1 has no monochromator between the undulator and a sample chamber. The radiation is introduced by a toroidal focusing mirror into sample chamber through a pinhole of 1 mm in diameter and metallic filter (Al, Sn, and In). A gold mesh is always installed in the sample chamber to monitor the incident photons. A typical spectrum distribution measured by the monochromator at BL 3A2 is shown in the figure, where the undulator gap is 60 mm and the photon flux is estimated to be about 10^{14}-10^{15} phs/s on the samples.

A differential pumping system can be provided for the users who want to use gaseous materials. A second monochromator (Jobin-Yvon HR-320), another VUV monochromator (home-made one of normal-incident type), and a helium storage-type cryostat are available for luminescence experiments. A TAC system is also one of the standard instruments of this beam line. For liquid- or gaseous-phase experiments, MgF_2 windows can be installed to separate the sample chamber from the beam line.

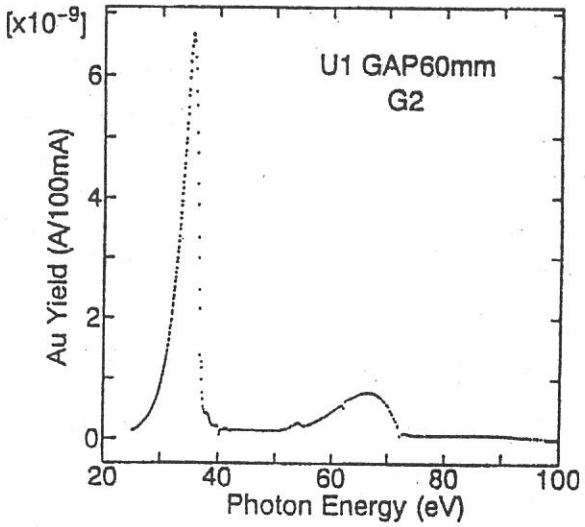

Fig. 2 Typical spectrum of undulator

BL3A2

Gas-Phase Dissociative Photoionization Apparatus

This machine has been constructed to study the formation of multiply-charged ions and their dissociation processes. The monochromator is constant-deviation grazing-incidence type with 2.2m focal length and covers wide wavelength region(10-100nm) where many kinds of molecules and multiply-charged ions are effectively measured. High intensity photon beam is available by introducing the radiation emitted from the undulator to the monochromator. The apparatus contains an angle-resolved time-of-flight mass spectrometer (TOFM) equipped with automatic data acquisition system for photoion-photoion coincidence measurements. For full understanding of dissociative multiple photoionization, we detect the coincidence signals of two fragment ions produced from a parent ion, evaluate the kinetic energy release in "Coulomb explosion", and measure the angular distributions for the fragment ions. The sensitivity with respect to high-speed ions (several tens of electron volts) is much improved in comparison with commercial TOFMS.

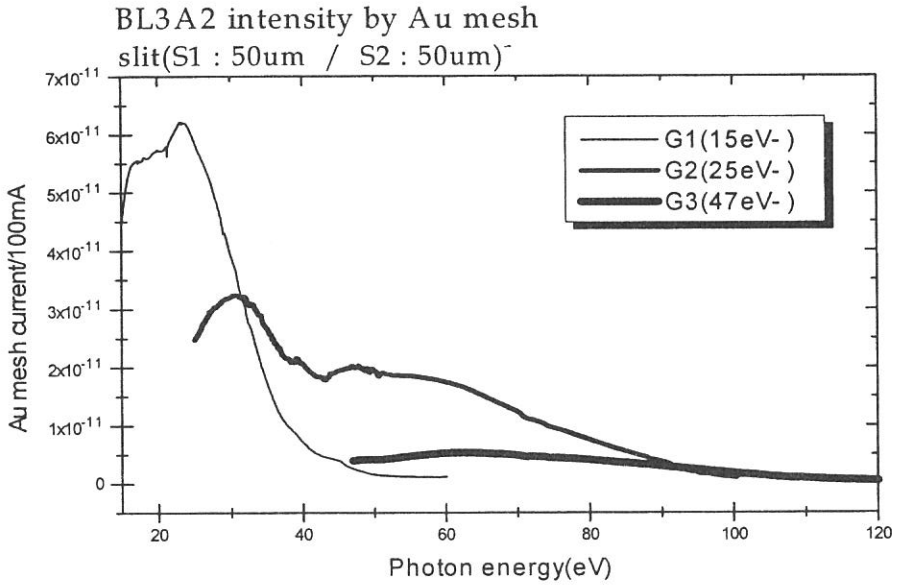

Specifications

monochromator	:	2.2m Constant-Deviation Grazing-incidence
Spectral range	:	10 - 100nm (15eV - 120eV)
Resolution	:	550 - 800 (0.03eV - 0.18eV)
Mass spectrometer	:	300
Length of the drift tube	:	0.2 - 1m
Rotatable angle	:	0 - 90° with respect to the photon beam

BL3B

Beam Line for Gas Phase Two-Dimensional Photoelectron Spectroscopy

This beam line is devoted to studies of elementary atomic and molecular processes induced by excitation of valence electrons. A monochromator is a vertically dispersed normal incidence type with 3m focal length and 10° angle between the incident and diffracted photon beams. The maximum wavelength resolution of 0.007nm is narrow enough to separate vibrational levels of excited states for various molecules. A main component in an experimental chamber is a spherical sector electrostatic energy analyzer which has been designed and setup for photoelectron spectroscopy. One can perform two-dimensional photoelectron spectroscopy with good resolution (≤ 30meV) in which the photoelectron yield is measured as a function of both photon energy and electron kinetic energy (binding energy). A two-dimensional spectrum, usually represented as a contour plot (*e.g.* Fig. 1), contains rich information on photoionization dynamics and properties of superexcited states. A great variety of interesting high-lying states involved in autoionization have been studied as follows: (1) a bound valence state of nitric oxide whose autoionization gives rise to a number of irregularly spaced peaks in its photoionization efficiency curve,[1] (2) the $(3\sigma_g)^{-1}(3\sigma_u)^1$ valence state of acetylene which dominates photoionization cross section and leads to strong vibrational excitation,[2] (3) Rydberg states of nitric oxide which undergo dissociation into N** + O($^1D^e$, $^3P^e$) followed by autoionizing transitions of the superexcited nitrogen atoms,[3] and (4) multiple-electron-excited Rydberg states of carbonyl sulfide which are primarily produced by conversion from the Rydberg states converging to $OCS^+(B^2\Sigma^+)$ and subsequently dissociate into S** + CO($X^1\Sigma^+$) giving rise to autoionizing transitions of the superexcited sulfur atoms.[4]

1) K. Mitsuke *et al.*, *J. Electron Spectrosc. Rel. Phenom.* **79**, 395 (1996).
2) H. Hattori and K. Mitsuke, *ibid.* **80**, 1 (1996); H. Hattori *et al.*, *J. Chem. Phys.* **106**, 4902 (1997).
3) Y. Hikosaka *et al.*, *ibid.* **105**, 6367 (1996).
4) Y. Hikosaka *et al.*, *ibid.* **107**, 2950 (1997).

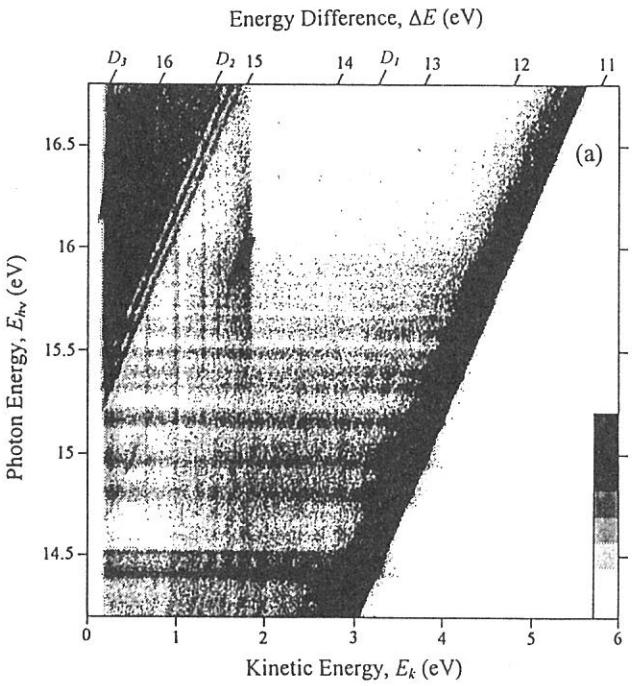

Figure 1. Two-dimensional photoelectron spectrum of OCS taken at the photon energy range from 14.2 to 16.8eV. The electron yield is presented by the plots with eight tones from light to dark on a linear scale.[4]

Specification

Monochromator : 3 m normal incidence
Wavelength range : 30 - 200 nm
Resolution : 0.007 nm at 100 nm

BL4A

Multi-Layered Mirror Monochromator Beam Line for Synchrotron Radiation Stimulated Processing Study

This beam line is now under construction. Synchrotron radiation stimulated reaction has been studied actively during the last decade. The excitation energy dependence of the reaction, however, is a difficult data to obtain, due to that it requires a large number of monochromatised photons which is not supplied by the conventional monochromator beam lines. This beam line is designed to supply 10^{13} to 10^{14} monochromatised tunable photons/s with 3–5 % resolutions, by using a double crystal type multi-layered mirror monochromator. The multi-layered mirrors now considered are Mo/Si for 50–90 eV and Mo/C or Mo/B_4C for 90–150 eV ranges. The calculated reflectivities for a Mo/Si mirror is shown in Fig. 1. The background photons of the lower energy region can be removed by a metal thin film filter.The beam spot size at the focussed point (sample surface in the reaction chamber) is about 2x3 mm^2. For the energy range of 200–500 eV which is covered by this beam line, however, the reflectivity of the multi-layered mirror is generally low, and development of the high efficiency mirror is required.

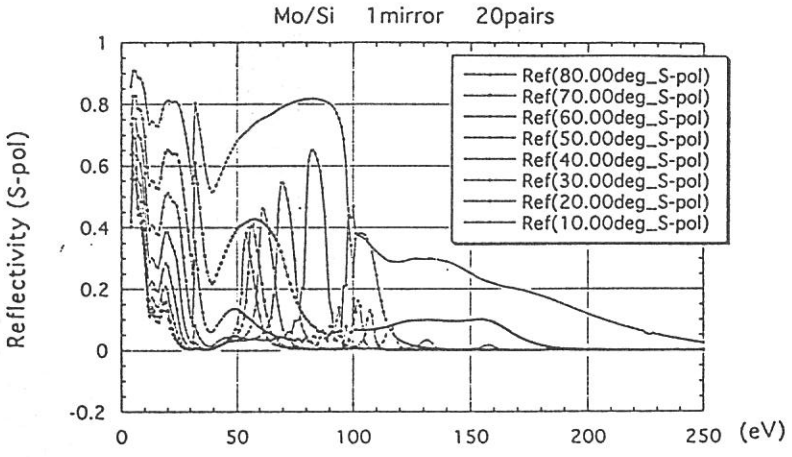

Fig. 1 Calculated reflectivities of the Mo/C multi-layered mirror.

Specifications

Monochromator	:Multi-layered mirror monochromator
Wavelength range	:50–150 eV
Resolution	:3–5 %
Experiments	:Excitation energy dependence of the SR processing

BL4B

Synchrotron Radiation Stimulated Processing Beam Line

Several kinds of synchrotron radiation stimulated processing experiments can be conducted using this beam line. The reaction gases up to about 0.1 torr can be used by the differential vacuum pumping. Reaction apparatus shown in Fig. 1 is consisted of four ultra high vacuum chambers, which is used for etching and chemical vapor deposition (CVD) experiments, Si gas source molecular beam epitaxy (MBE) experiments, sample storage, and air-locked sample introduction. The infrared reflection absorption spectrum measurement system is equipped to the reaction chambers to monitor the surface reaction *in situ*. The SR stimulated chemical reaction of surface submonolayer hydrogen on Si(100) have been successfully monitored recently [1].

[1] A.Yoshigoe, K.Mase, Y Tsusaka, T.Urisu, Y.Kobayashi, and T.Ogino, Appl. Phys. Lett. 67 (1995) 2364.

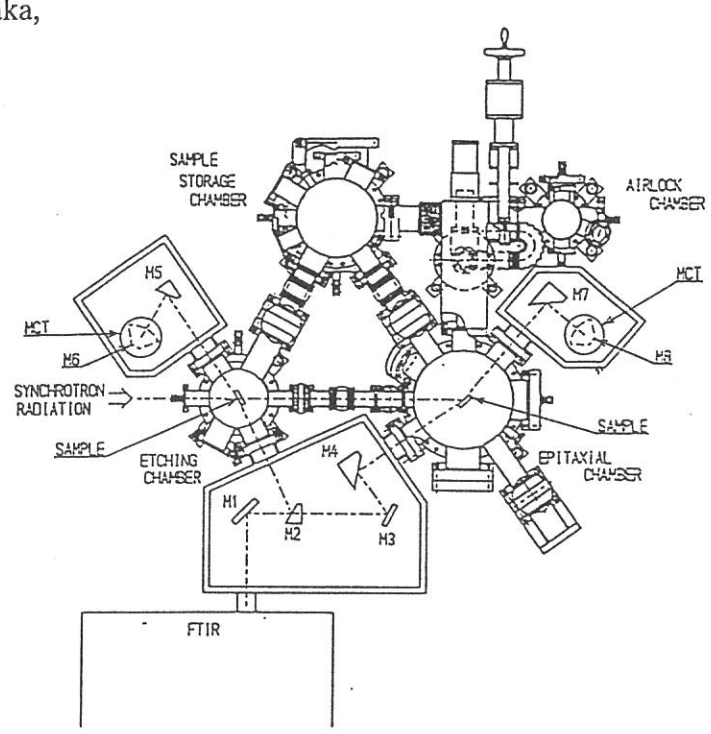

Figure 1. Reaction apparatus

Specification

Monochromater	: white beam reflected by bent-cylindrical mirror with grazing incidence angle of 2 degrees.
Wavelength range	: 1-100nm
Experiments	: SR-stimulated processing

BL 5A

Photoelectron Spectrometer for Solids and Surfaces

The beamline 5A is designed for spin- and angle-resolved photoelectron experiments for solids and surfaces with the circularly polarized synchrotron radiation from a helical undulator and for high-resolution photoelectron experiments with bending magnet radiation. The beamline consists of a Spherical Grating Monochromator with Translational and Rotational Assembly Including a Normal incidence mount (SGM-TRAIN), a spin- and angle-resolved photoelectron spectrometer, and a high-resolution photoelectron spectrometer.

The SGM-TRAIN is an improved version of a constant-length SGM to aim the following points; (1) wide energy range of 5-250 eV, (2) high resolving power, (3) use of linear and circular polarization, (4) reduction of second-order light, and (5) two driving modes by a computer control. The second-order light is well suppressed by using laminar-profile gratings and combinations of mirrors and gratings.

Specifications

1)Monochromator

Type:SGM-TRAIN
(two glancing-incidence and one normal-incidence)
Energy Range: 5-250 eV
Resolution: 0.5-80 meV with slits of 0.01mm
Flux: $3x10^{10}$ phs/sec at 120 eV with slits of 0.1 mm
(for bending manget radiation)

2) Main Instruments

Two-levels UHV chamber ($1x10^{-10}$ Torr)
Hemi-spherical electron-energy analyzer
(OMICRON HR-125)
Spin- and Angle-resolved spectrometer
(low-energy diffused scattering type)
LEED of reverse type (OMICRON)
Ion-gun (ULVAC-Phi)
He-lamp for UPS
Low-temperature cryostat (>30 K)

3)Helical Undulator (Optical Klystron)

Number of periods	18
Period length, □u	110 mm
Length of dispersive part	302.5 mm
Total length	2351.2 mm
Deflection parameter, Kx,y	0.07-4.6 (helical mode)
Deflection parameter, K	0.15-8.5 (planar mode)
Fundamentals	2-45 eV (Circular polarization)

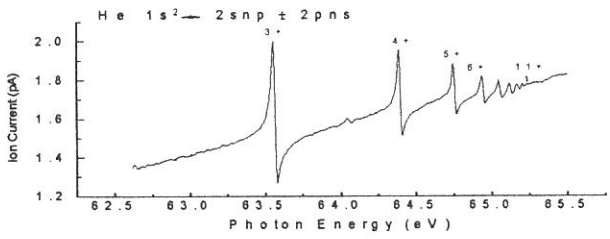

Fig. 1 He ionization spectrum

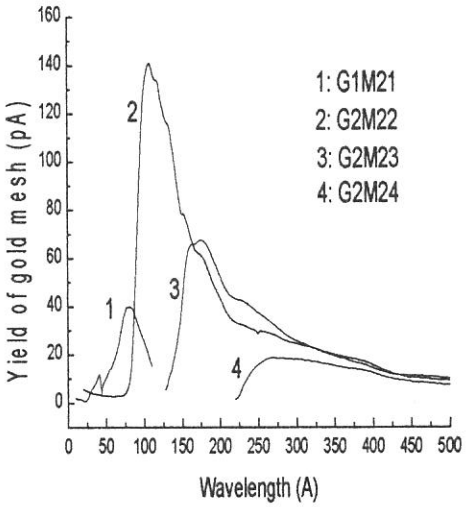

Fig. 2 Typical spectral distribution

Refs: M. Kamada et al., Rev. Sci. Instrum. 66, 1537 (1995), N. Takahashi et al., Jpn. J. Appl. Phys. 35, 6314 (1996).

BL5B

Calibration Apparatus of Optical Elements

BL5B has been constructed to calibrate optical elements. The beam line consists of a plane grating monochromator (PGM) and three chambers (Fig. 1). The chamber A is used for calibration of optical elements, the camber B for optical measurements of solids and the chamber C for photo-stimulated desorption (PSD) experiments. The chamber C is sometimes changed to a chamber for photoemission microscopy.

The calibration chamber is equipped with a goniometer. The goniometer, which was installed for the characterization of optical components, has six degrees for freedom; X-Y translation of a sample, and interchange of samples and filters. They are driven by vacuum pulse motors. Since the polarization of SR is essential for such measurement, axis of the rotation can be made in either horizontal or vertical direction (s- or p-polarization).

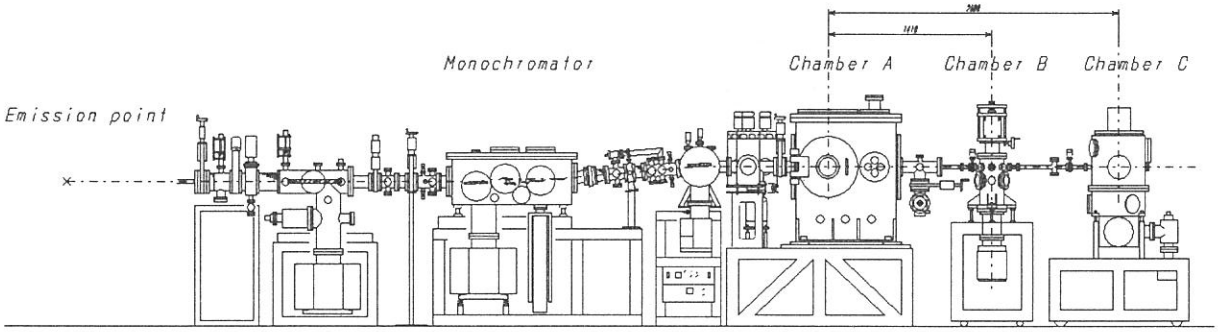

Figure 1. Schematic figure of BL5B spectrometer system.

Specification

Monochromator: Plane grating

Wavelength range: 2 - 200 nm (Fig. 2)

Resolution: $\lambda / \Delta\lambda = 300 \sim 500$

Experiments: Calibration of optical elements, absorption of solids, photo-stimulated desorption from rare gase solids, photoelectron microscopy.

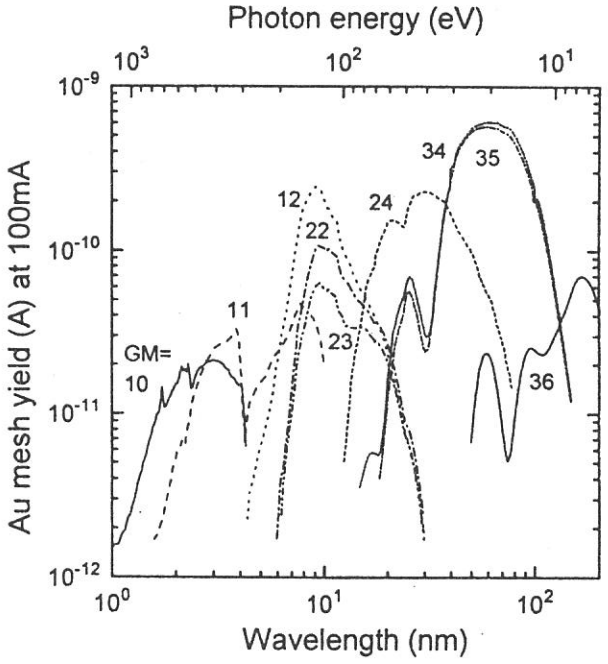

Figure 2. Throughput spectra of BL5B detected by a gold mesh (84% transmission).

BL6A1

Fourier-Transform Middle- and Far-Infrared spectrometers for Solids

UVSOR covers very wide energy range from soft x-ray to millimeter wave. BL6A1 was constructed in order to cover a long wavelength part in the spectral distribution of UVSOR from near-infrared to millimeter wave. Beam line is composed of two kinds of interferometers, a Martin-Puplett type (SPECAC) and a rapid-scan type (Bruker).

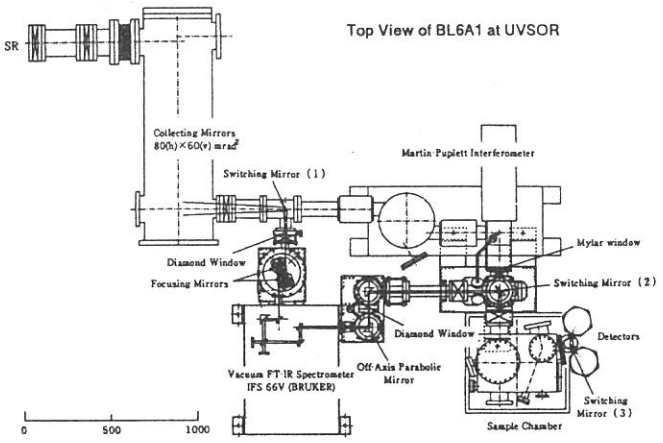

Figure 1. Top view of BL6A1.

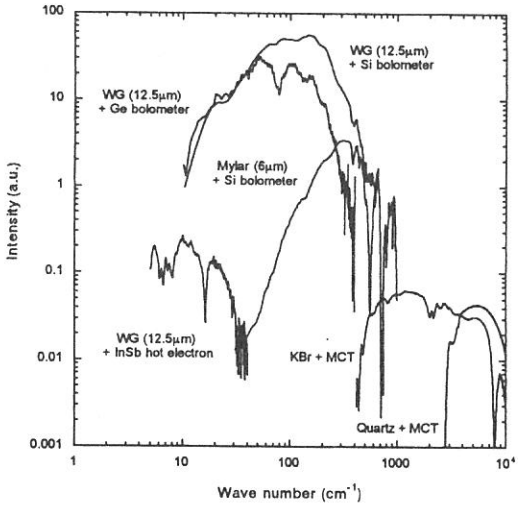

Figure 2. Throughput spectra of BL6A1.

Specification

Monochromator: Martin-Puplett type and rapid-scan type interferometers

Detectors: Si bolometer (20 - 1000 cm^{-1})

Ge bolometer (with polyethylene window, 30 - 300 cm^{-1})

Ge bolometer (with quartz window,10 - 200 cm^{-1})

InSb hotelectron bolometer (2 set, 5 - 50 cm^{-1})

MCT (400 - 10000 cm^{-1})

Photovoltaic type MCT (400 - 4000 cm^{-1}, time response: 10 nsec)

Wavelength range: 0.5 mm - 33 μm (5 - 300 cm^{-1}) by Martin-Puplett interferometer

20 - 1 μm (50 - 10000 cm^{-1}) by rapid-scan interferometer

Resolution: $\lambda / \Delta\lambda$ = 500 - 20000

Experiments: Temperature dependence of reflectivity and transmission spectra, absorption under high pressure (up to 20 GPa), reflectivity under magnetic field (up to 8 T), time-resolved spectroscopy.

BL6A2

Photoelectron Spectrometer for Solids and Surfaces

A Plane Grating Monochromator (PGM) consists of pre-mirrors, a plane grating, focusing mirror, and a post-mirror, with an exit slit only. It covers the wide spectral range from 2 to 130 eV with exchanging two gratings and 5 focusing mirrors. A typical spectral distribution is shown in the figure, where the numbering indicates the combination of the grating and the mirror. A typical photon flux is about 10^{11} phs/s/100 mA at 90 eV with a resolving power of 700. Angle-integrated and angle-resolved photoelectron spectrometers are available. The overall resolution of the integrated type analyzer is about 0.3 eV, while the angle-resolved hemispherical analyzer has a resolving power of 100 with an angular resolution of 1.1° in two axes. The optical system including an ICCD detector can be installed. The standard instruments for surface analysis such as Auger, LEED, Ion gun, and gas doser are installed in the analyzing chamber, the base pressure of which is 1.2×10^{-10} Torr. The samples are transferred from an air-lock chamber to the analyzing chamber through a preparation chamber.

Specifications

1) Monochromator

Type: Plane Grating Monochromator (no entrance slit)

Range: 2-130 eV

Resolution: 0.015-0.3 eV with slit of 0.3 mm

Flux: 10^{11} phs/s/100 mA at 90 eV with 0.1mm slit

2) Main Instruments

Angle-integrated Cylindrical Analyzer
(home made, ΔE=0.3 eV)

Angle-Resolved Hemi-Spherical Analyzer
(home made, $E/\Delta E$=100 $\Delta\theta$=1.1° Two-axes)

Second Monochromator (Jobin-Yvon HR-320)

ICCD (Princeton Instrum.)

Preparation Chamber

Air-lock chamber for quick insertion

LEED of Reverse type (OMICRON)

Ion-gun of Differential type (ULVAC-Phi)

Auger (ULVAC-Phi)

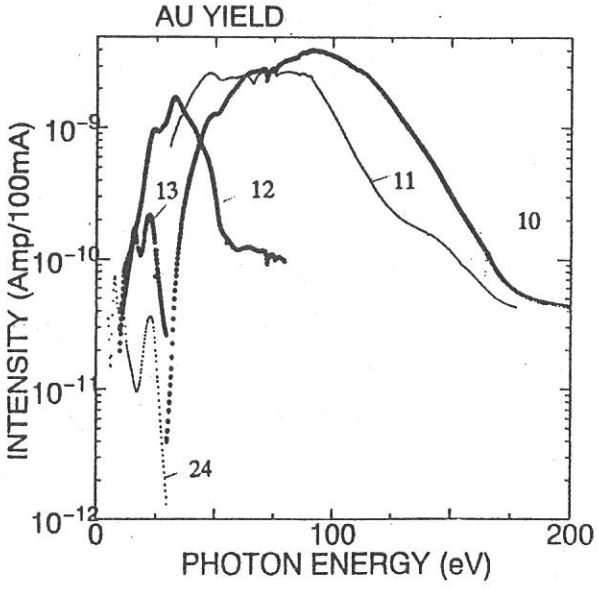

Fig. 1 Typical spectral distribution

BL6B

Fourier-Transformed Far-Infrared Spectrometer

BL6B has been designed to measure reflectance on small samples with high precision over FIR-IR regions. The optical system of BL6B consists of the following three parts: (1) beamline optics in ultrahigh vacuum (1×10^{-9} Torr), equipped with interchangeable four kinds of exit-window without breaking the vacuum, (2) adjusting optics between the beamline and a spectrometer, (3) a Bruker IFS-113v spectrometer, which offers automatic change of six beam-splitters under vacuum (~5 Torr). A reflectance unit is placed into a sample compartment of the spectrometer, also in the vacuum atmosphere. Temperature dependence can be traced with a LHe flow-type cryostat from room temperature down to 4 K. An infrared microscope is applied, if necessary, to obtain accurate reflectivity on samples smaller than millimeter size.

BL6B is specially suitable for the study of optical properties of organic conductors because available size of the crystals is usually very small. We are now investigating the electronic structure of organic conductors that have a single-particle gap appeared in far-infrared region, caused by SDW, CDW, or superconducting transition. The superconducting character is also discussed through the change of reflectivity versus the temperature around the T_c.

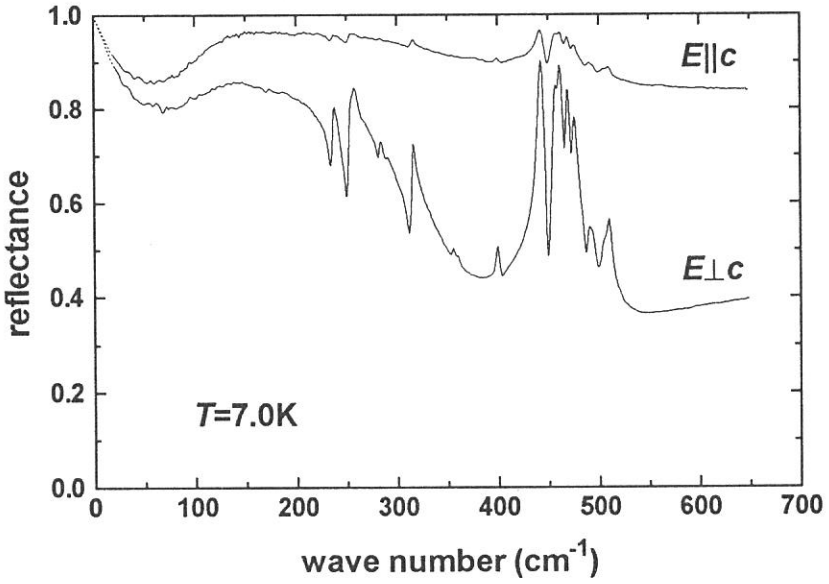

Figure 1. Polarized reflectance of β"-(BEDT-TTF)$_2$AuBr$_2$ measured at 7.0 K.

Specification

Interferometer	:	Michelson type
Spectral range	:	6 - 10,000 cm^{-1}
Resolution	:	better than 0.1 cm^{-1}
Experiment	:	reflectance and transmittance of solid state

BL7A

Soft X-ray Spectrometer for Solids

The beam line BL7A equipped with a double crystal monochromator (DXM) was constructed for the spectroscopic research of solids in the soft X-ray region, where both the bending magnet and the 4T wiggler radiations are provided. The schematic drawings of the beam line and scanning mechanism of the double crystal monochromator are shown in Figure 1. When we use the relatively lower photon energy light (less than 1.7keV), we use the bending magnet line whereas the wiggler line is used for higher energy experiments. Recently, we have succeeded to measure soft X-ray spectra by using YB66 monochromator crystal, which is known to be one of the best monochromator crystals covering soft X-ray region from 1.1 to 2keV with higher performance. Further improvements of the beam line, for example, installation of the focusing mirror system and the new software etc., are in progress.

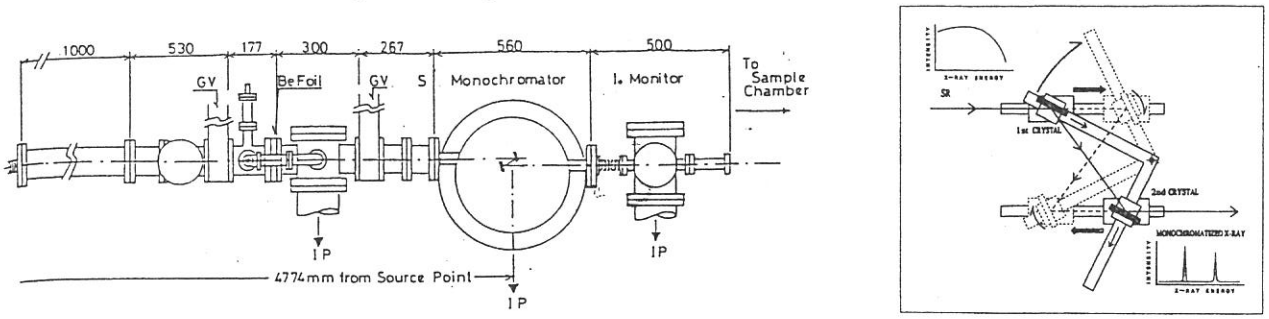

Figure 1. The schematic drawings of the beam line and scanning mechanism of the double crystal monochromator at the BL7A.

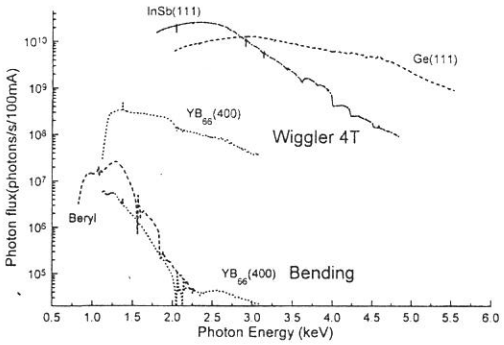

Figure 2. Throughput from the double crystal monochromator with typical monochromator crystal.

Specification

Monochromator : Double Crystal Monochromator

Monochromator crystals and covered photon energy:

β-Al_2O_3 (0.58-1.74keV), Beryl (0.82-2.27keV), YB66(400) (1.12-3.08keV), Quartz-Y(1010) (1.53-4.26keV), InSb(111) (1.74-4.85keV), Ge(111) (2.00-5.55keV).

Typical resolution : 0.46eV (Beryl Crystal, E=860eV)

Experiments : X-ray absorption spectroscopy (by photoelectron total yield and/or fluorescence)

BL7B

3m Normal Incidence Monochromator for UV, VIS and IR Spectroscopy of Solids

The beamline BL7B is now under reconstruction. The 1m Seya-Namioka type monochromator is replaced to the 3m normal incidence monochromator (3m NIM; McPherson upgrade model of 2253) for the extended researches of the highest level with the higher resolution and intensity, the wider wave-length region available and so on. It will be also possible to utilize the linear and circular polarization inherent in synchrotron radiation (SR) and to realize some combined experimental systems, for example, with the synchronized laser to SR pulse or with the extended field. The outline of the new beamline is shown in Figure 1. The main parts of the system are a pre-mirror focusing system, a 3-m NIM and a post-mirror focusing system. The light from 50 to 1000 nm wavelength region is covered by changing three gratings *in situ*. Each spherical grating is original laminar type fabricated on SiO_2 and has effective grooved area of 120x40mm^2. The 2 focusing positions are available for the experiments. At the position between 2 positions, LiF or MgF2 window valve is installed. Therefore, the measurements for the organic materials, liquid and biochemical ones are possible at the 2nd focal position.

After the final adjustment and test run, this beamline will be used for absorption, reflection and fluorescence measurements on various materials with higher performance (high energy resolution, high intensity, well-polarized light, short repetitive pulse light) not only in the VUV region but also in the near UV, VIS and near IR region.

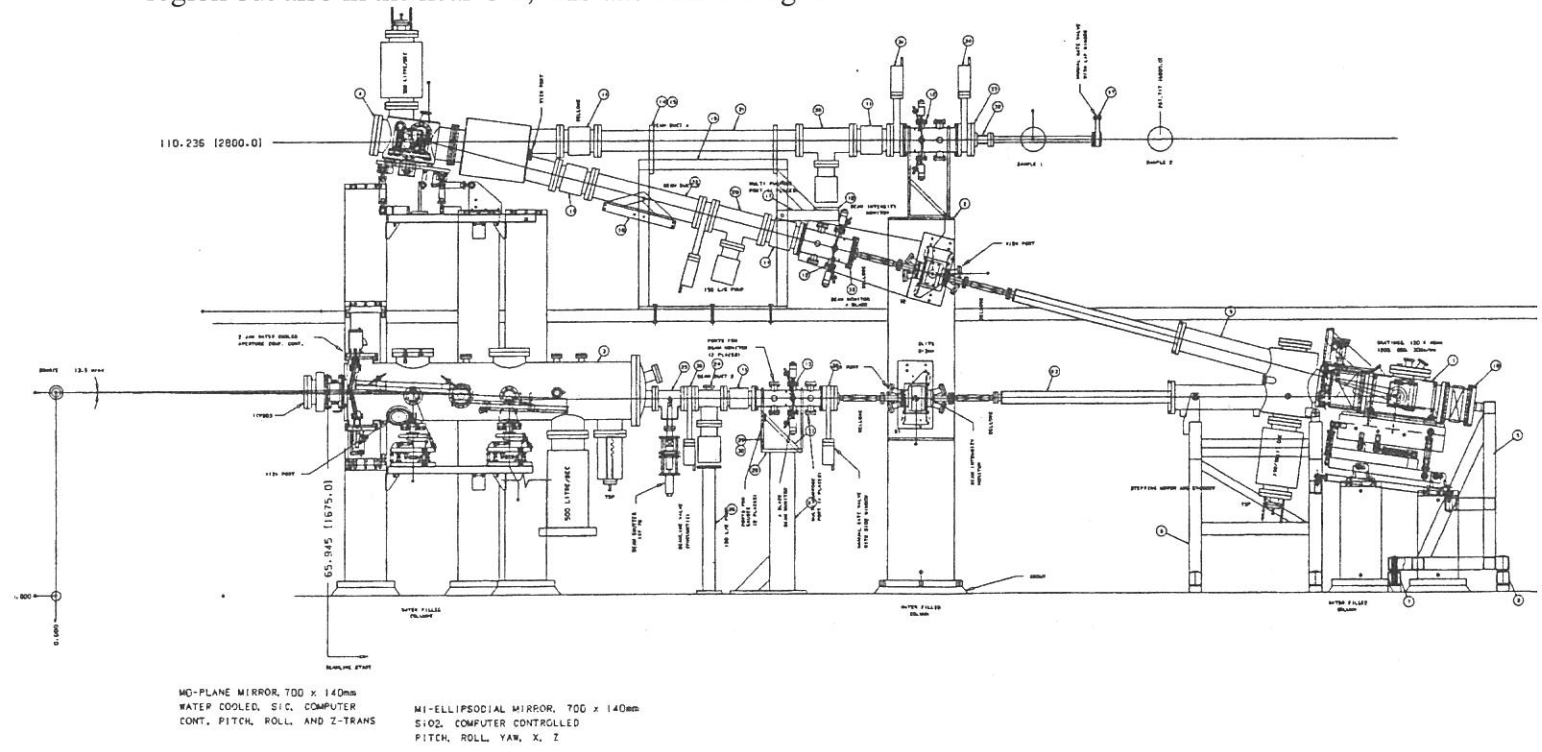

Figure 1. The outline of the side view of the new beamline BL7B.

Specification

Monochromator	: 3m Normal Incidence Monochromator
Wavelength range	: 50nm-1000nm
Typical resolution	: E/ΔE=4000-23000 for 0.01mm slit
Experiments	: Absorption, reflection, fluorescence spectroscopy mainly for solids

BL8A

Free Port

This beamline was constructed as a free port to which user can connect their own instruments. The beamline consists of a front end, a focusing premirror chamber and a separation chamber. Both focused and unfocussed beam can be used. A general purpose reaction chamber and a two (or three) stage differential pumping system are available for the experiments that use gas samples without window. With using three stage differential pumping system, gas pressure at the reaction chamber upto 0.5 torr can be used while keeping ultra high vacuum at the premirror chamber.

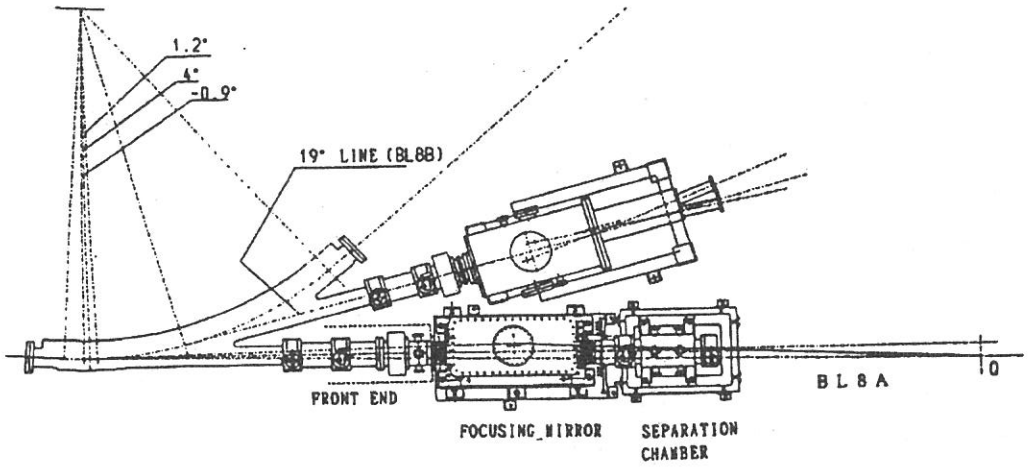

UP VEW OF BL8A

Specification

Spectral range : whole range of synchrotron radiation from UVSOR

Acceptance angle

Unfocused beam : 25 mrad (horizontal) × 8 mrad (vertical)
0.6 mrad (horizontal) × 0.6 mrad (vertical)
(with ϕ 3 mm aperture before sample)

Focused beam : 7.7 mrad (horizontal) × 8 mrad (vertical)
Beam spot size at focu : 3 mm (horizontal) × 2 mm (vertical)
Source - mirror distance : 2500 mm
Mirror - focus distance : 2807 mm

BL8B1

Photoabsorption and Photoionization Spectrometer

Last year a new beam line BL8B1 was constructed for observation of high resolution photoabsorption and photoionization experiments in the photon energy range from 30 to 800 eV, which includes the 1s core excitation energy of C, N and O atoms. For high resolution measurement among these energy, a constant-deviation constant-length spherical grating monochromator (CDCL-SGM) with three gratings (G1: R = 15 m; 1080 l/mm, G2: R = 15 m 540 l/mm, G3: R = 7.5 m; 360 l/mm) has been employed, whose entrance and exit slit positions and directions of incident and exit photon beams do not change during its scan. Consequently, it provides us with an resolution (E/ΔE) of 4000 at 400 eV and of 3000 at 245 eV. A drain current of gold foil reveals the absolute photon flux normalized by an ring current when two slit widths are 10 μm (Fig. 1).

Being Equipped at the downstream of the mono - chrometer, an chamber with a time-of-flight ion detector and a photoelectron detector allows us to measure photoelectron - photoion coincidence (PEPICO) and photoion - photoion coincidence (PIPICO) spectra. Measurements of absorption, electron yield and emission spectra of solid samples are also available.

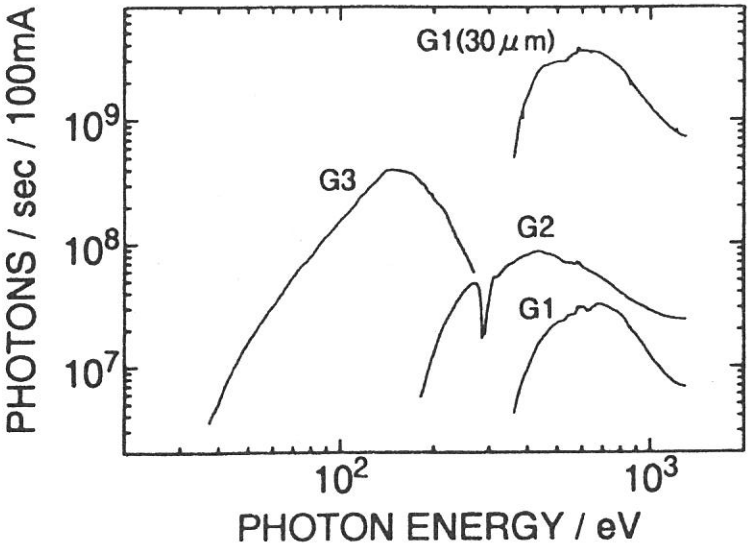

Figure 1. Absolute photon fluxes measured by a drain current of gold foil

Specification

Monochrometer	: 2.2 m constant-deviation grazing incidence
Wavelength range	: 30 to 800 eV
Resolution	: E/ΔE = 4000 at 400 eV and 3000 at 245 eV
Available Experiments	: Measurement of photoabsorption and photoionization spectra for gas and solid sample

BL8B2

Angle-Resolved Ultraviolet Photoelectron Spectrometer for solids

BL8B2 is a beamline for angle-resolved ultraviolet photoemission spectroscopy (ARUPS) system which is designed for measuring various organic solid such as molecular crystals, organic semiconductor, and conducting polymers. The beamline consists of a plane-grating monochromator (PGM), a sample preparation chamber with a fast entry Load-Lock chamber, a measurement chamber with an accurate manipulator for temperature dependence (base pressure 3×10^{-10} Torr), a cleaning chamber (base pressure 2×10^{-10} Torr), and a sample evaporation chamber (base pressure 3×10^{-10} Torr). The cleaning chamber is equipped with back-view LEED/AUGER, Ar^{+} gun and an infrared heating units. The PGM consists of pre-mirrors, a plane grating, focusing mirror, and a post-mirror, with an exit slit. It covers the wide range from 2 to 150 eV with exchanging two gratings (G1; 1200 l/mm, G2; 450 l/mm) and five cylindrical mirrors. The toroidal mirror focuses the divergent radiation onto the sample in the measurement chamber. The spot size of the zeroth-order visible light at the sample surface is about $1\times1mm^2$. The energy resolution at a slit width of 100 μm was found to be 0.004 - 0.3 eV in the wavelength range from 2 to 130 eV. A hemispherical electron energy analyzer of 25 mm mean radius with an angular resolution of 2° can be rotated around vertical and horizontal axes. The sample mounted on a manipulator can be also rotated around two axes.

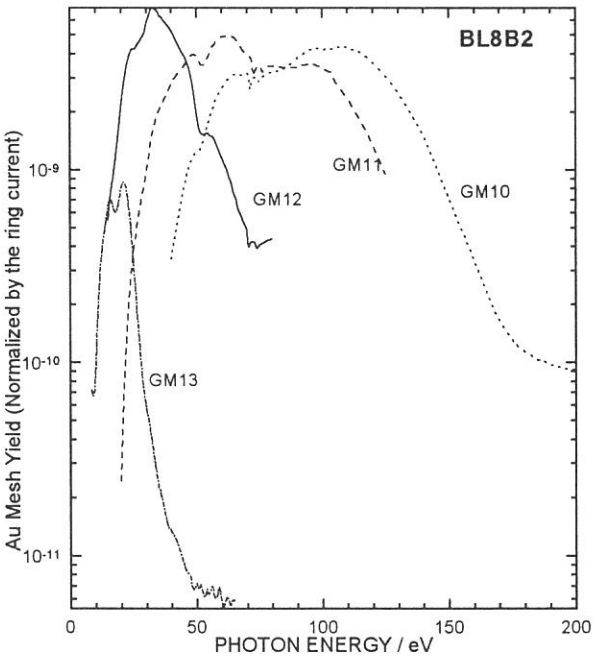

Figure Throughput spectra of plane-grating monochromator at BL8B2 with 100 μm exit slit.

Specification

Monochromator : plane grating monochromator
Spectral range : 2 - 130 eV
Resolution : 0.25 eV at 40 eV, as determined by the Fermi edge of gold.
Experiment : Ultraviolet Photoelectron Spectroscopy for various organic solids
Polarization : 85~91 % at 5000 Å

In-house beam lines

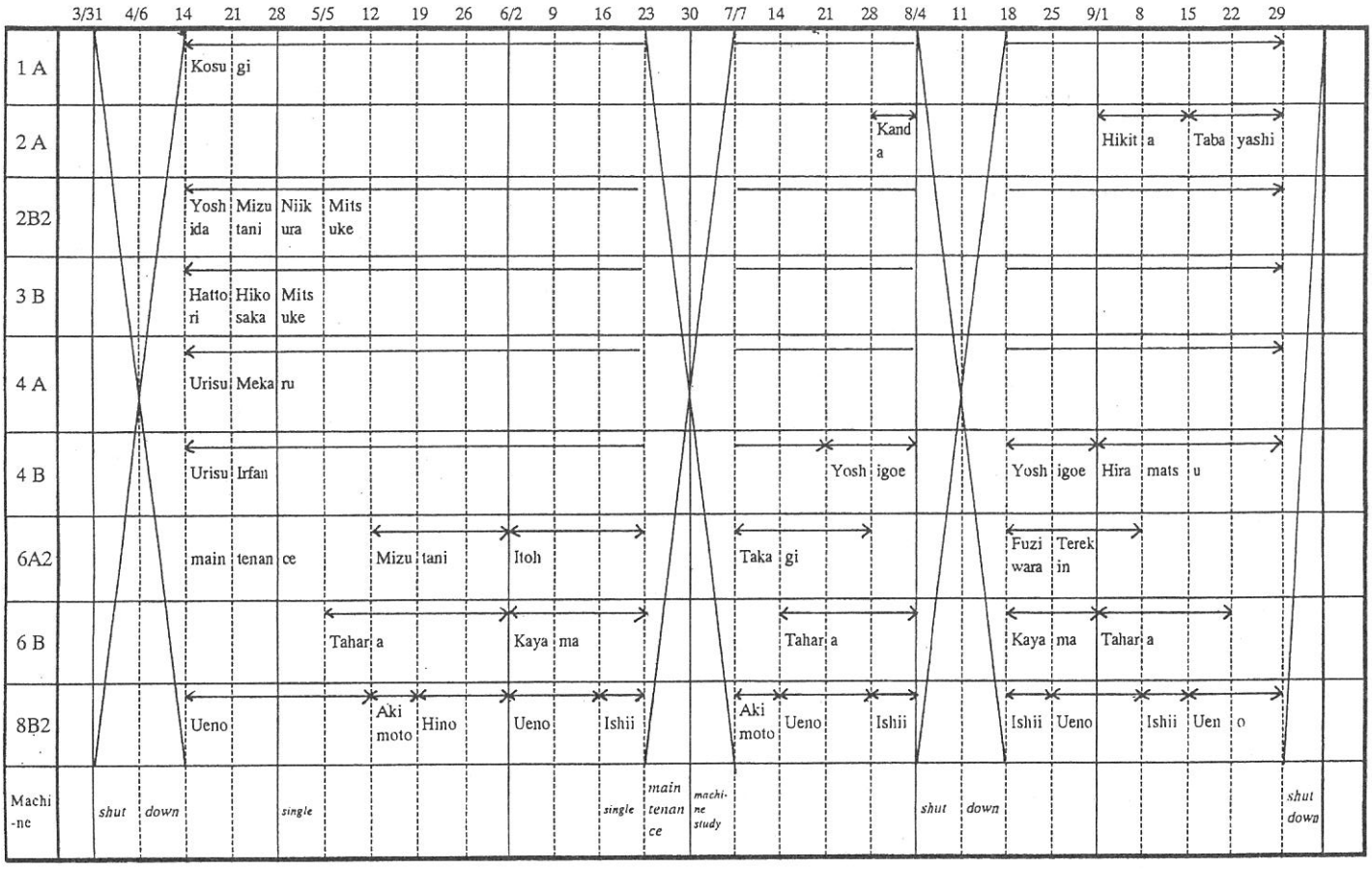

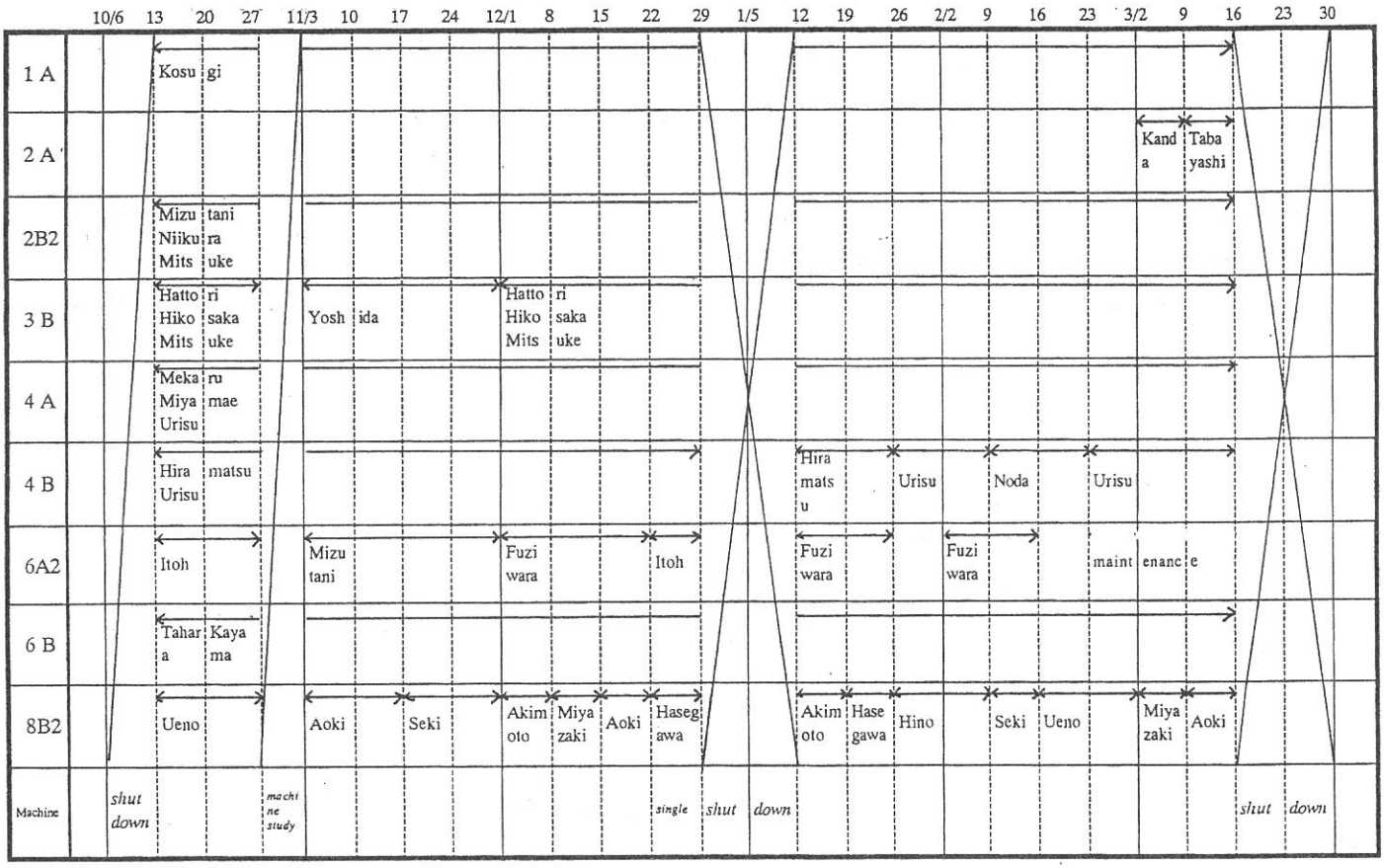

Open beam lines

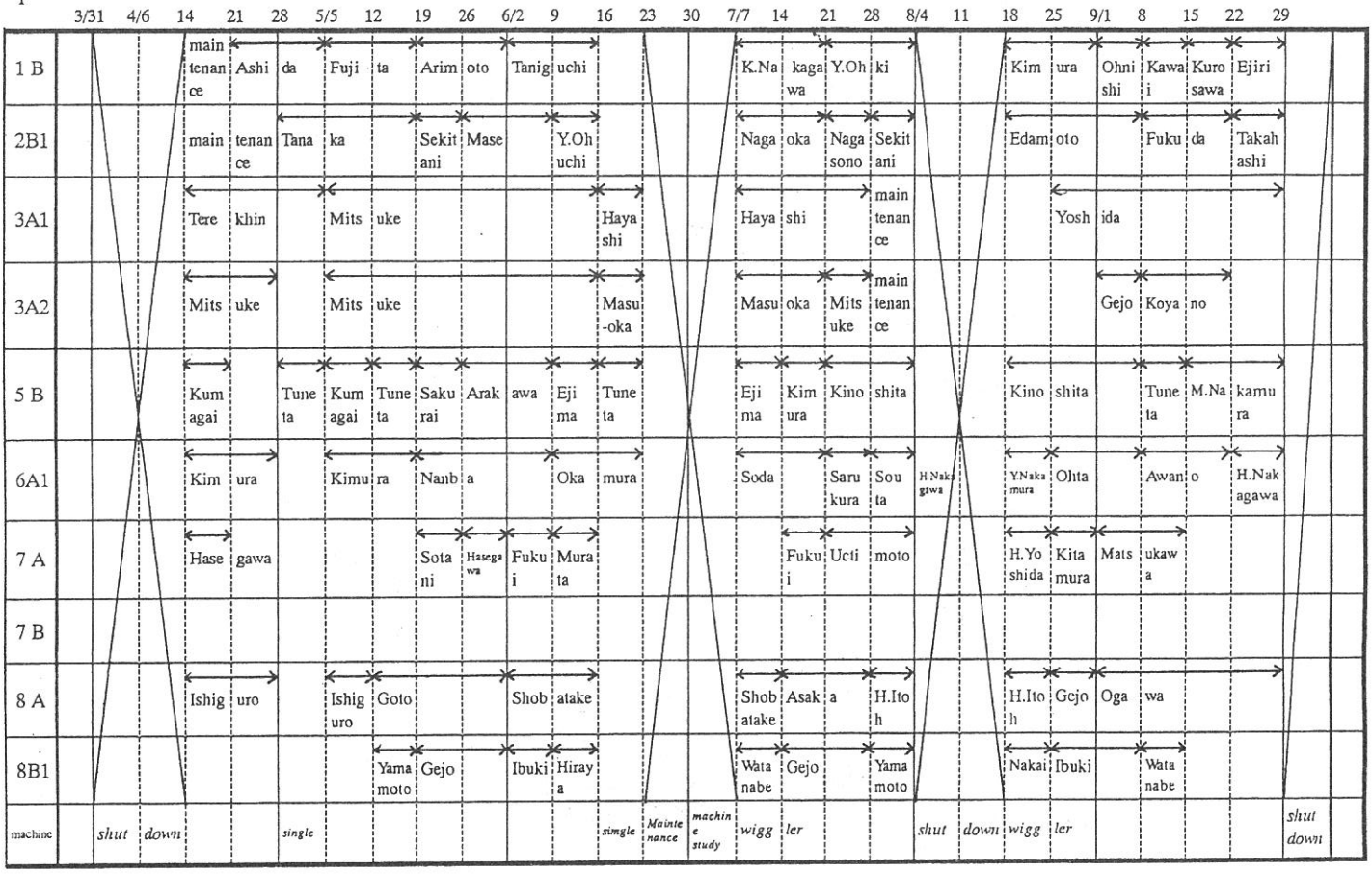

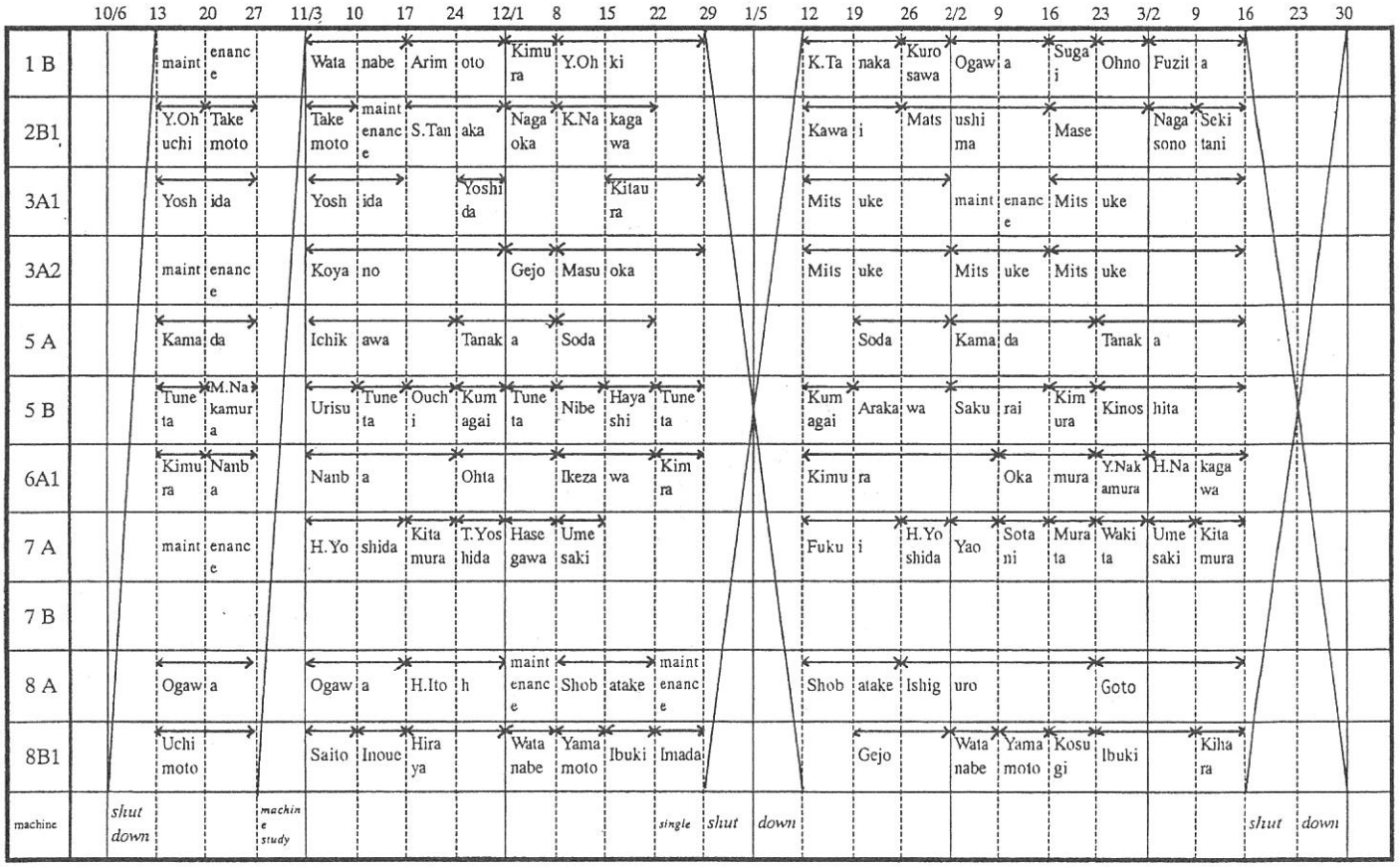

The UVSOR 750 MeV Storage Ring

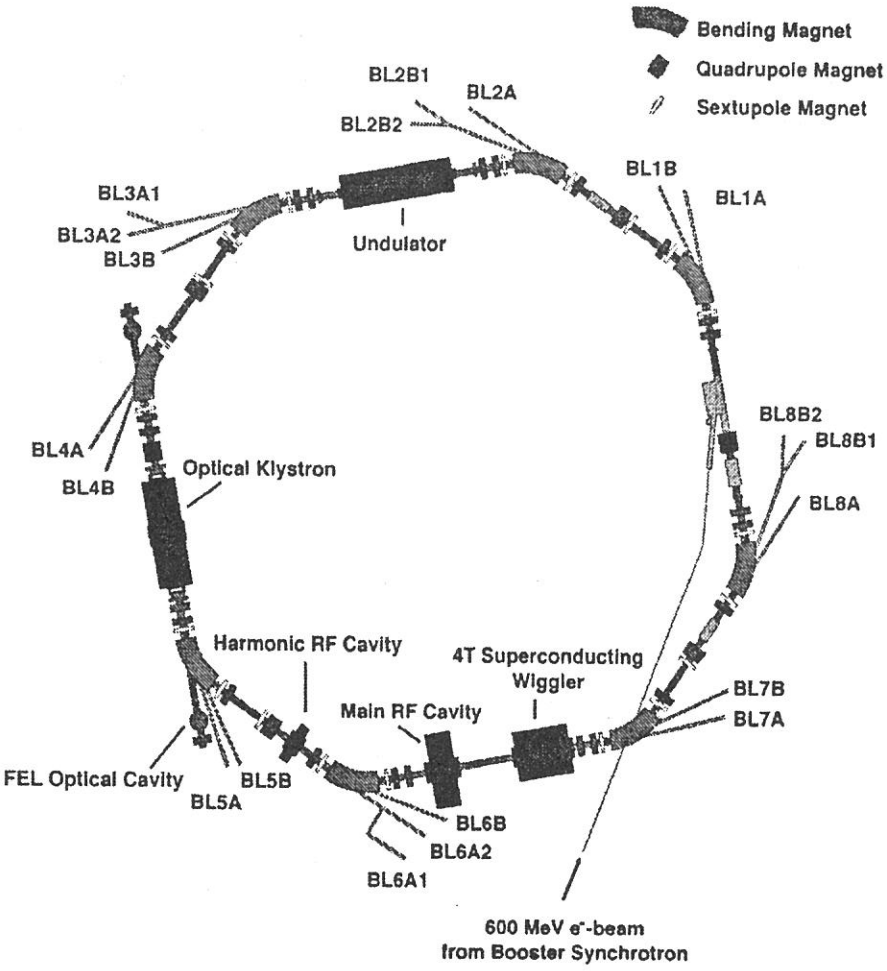

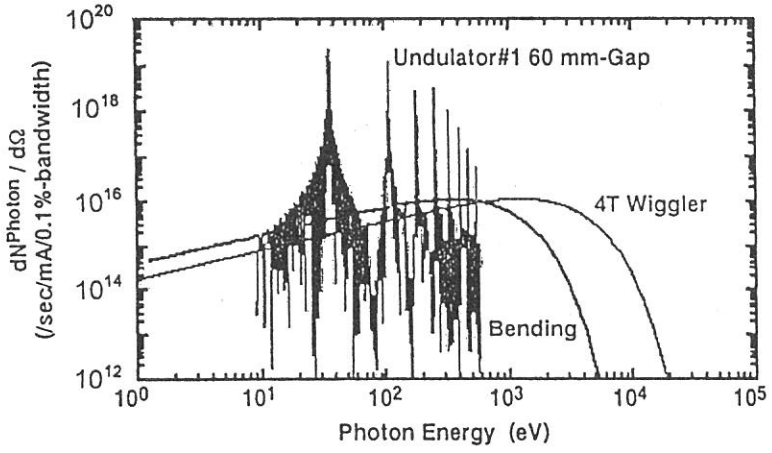

On-Axis Photon Intensity with 750 MeV-Electrons

Longitudinal Beam Dynamics in Operation with Negative Momentum Compaction Factor on the UVSOR Electron Storage Ring

Masahito HOSAKA, Jun-Ichiro YAMAZAKI, Toshio KINOSHITA and Hiroyuki HAMA

UVSOR Facility, Institute for Molecular Science, Okazaki 444, Japan

To investigate variations of the bunch length and the energy spread of the electron beam on a storage ring, we have measured longitudinal electron distributions and spectra of spontaneous radiation from an optical klystron on the UVSOR storage ring operated with both signs of negative and positive momentum compaction factors. In general, the single bunch dynamic behavior such as lengthening of the bunched beam circulating in a storage ring is governed by the electromagnetic interaction between the impedance of the vacuum chamber. A longitudinal single bunch instability including increase of the energy spread of the beam due to high frequency impedance of many parts of the vacuum chamber, i.e., cavity, sudden change of pipes, groove, low Q cavity-like structure, etc., is well known as *microwave instability* [1]. On old machines, which were designed without deep consideration for the impedance, both longitudinal and transverse single bunch instability were often observed. However as far as recent reports on relatively new machines, there have been no clear evidence observed for the onset of microwave instability [2]. On the UVSOR ring, we have also observed no significant single bunch instability up to the maximum beam current can be stored at present. Based on a low Q resonator impedance model, Fang et. al. recently pointed out a possibility of which the threshold current for microwave instability would be high and the bunch lengthening would be not significant when a storage ring is operated with a negative momentum compaction factor [3].

In the nominal operation for users of synchrotron radiation (SR), a bit of a positive dispersion remains in straight sections to minimize the effective emittance, and then the momentum compaction factor α is estimated to be + 0.035. For the experiment with negative α, we developed a new operating point, where α can be tuned smoothly from positive to negative without change of the betatron tunes. This operating point has been also optimized to use of the helical optical klystron with small gaps [4]. Calculated Twiss parameters of the lattice at positive and negative α operations are shown in Fig. 1a and 1b, respectively.

A dual-sweep streak camera is a powerful tool to observe the electron distribution in the bunch and its variation in a certain time range [5]. Since a slow-sweep axis can be expanded up to 100 ms from the one turn period, we can not only observe the corrective longitudinal oscillation with the synchrotron frequency of about 15 kHz but also detect instabilities of which the electron distribution is slowly varied. Current dependent bunch lengthening has been measured up to ~ 100 mA with the single-bunch mode for the almost same absolute values of the positive and the negative momentum compaction factors ($|\alpha|$ = 0.033). RMS bunch lengths were deduced from spectra averaged over many turns in the two-dimensional dual-sweep images of SR from a bending magnet. Figure 2 shows variations of the bunch length at a wide range of the single bunch current. For the case of the positive α, the bunch lengthens monotonously, which is in

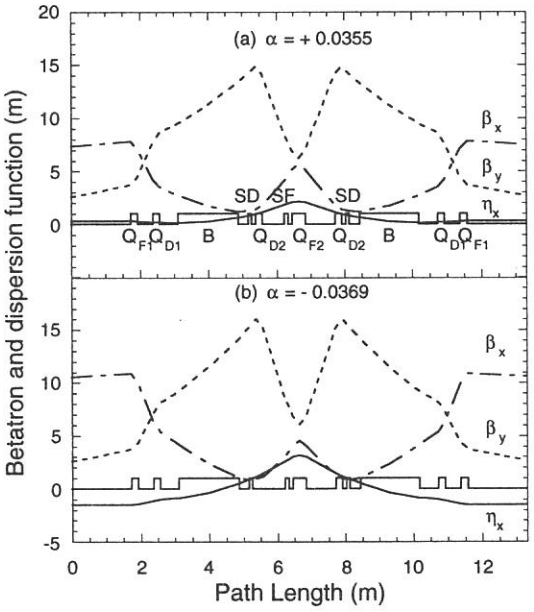

Fig.1 Calculated Twiss parameters for one unit cell at positive a (a) and negative a (b) operations.

agreement with our pervious measurements [6]. Based on potential-well distortion theory with a broad band impedance model [7], the bunch length σ_b at the average beam current I is expressed as

$$\left(\frac{\sigma_b}{\sigma_{b0}}\right)^3 - \left(\frac{\sigma_b}{\sigma_{b0}}\right) = \frac{e\,\alpha\,I\,[Z/n]_{eff}}{\sqrt{2\pi}\,\nu_s^{\,2}\,E}\left(\frac{R}{\sigma_{b0}}\right)^3, \qquad (1)$$

where σ_{b0} is the zero current (natural) bunch length and $[Z/n]_{eff}$ is the effective longitudinal coupling impedance. By fitting the data for the positive α with eq. (1), we obtained the effective impedance of 1.6 Ω, where we assumed no frequency dependence for $[Z/n]_{eff}$. As shown in Fig. 2, the fitting quality is not so bad that there seems to be no significant frequency dependence for $[Z/n]_{eff}$ at the narrow region of which the bunch length observed.

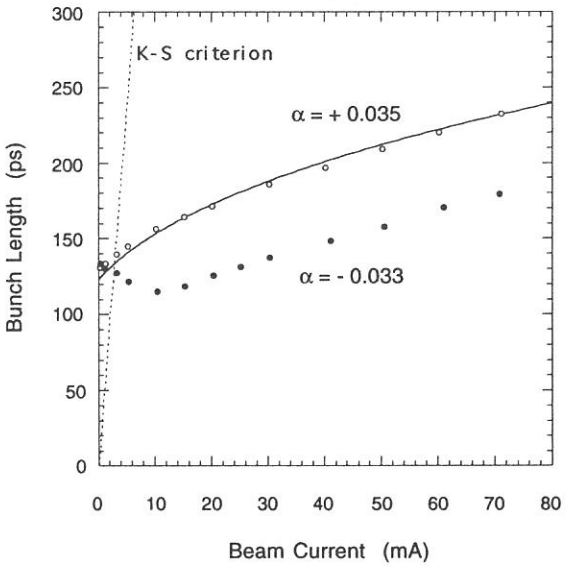

Fig. 2 Measured bunch lengths plotted as a function of the beam current.

Since the bunch lengthening due to potential-well distortion does not accompany increase of the energy spread, the *Keil-Schnell* criterion for the threshold condition of longitudinal microwave instability is able to be modified by replacing the peak current of the lengthened bunch [8].

The peak current for the Gaussian particle distribution is written as $I\,C/\left(\sqrt{2\pi}\,\sigma_b\right)$, the *Keil-Schnell* stability criterion is rewritten as

$$\sigma_b \geq \frac{C\,[Z/n]_{eff}\,I}{F\sqrt{2\pi}\,E\,|\alpha|}\left(\frac{\sigma_E}{E}\right)^{-2}, \qquad (2)$$

where σ_E/E is the relative energy spread of the beam, respectively. A form factor of the particle distribution in the momentum space F is approximately the unity for bell-shape distributions. Using the deduced value of 1.6 Ω for $[Z/n]_{eff}$, a threshold bunch length for microwave instability estimated from eq. (2) is approximately 47 ps/mA. The beam with the bunch length below this line would be longitudinally unstable. However this threshold condition is obviously over estimated, because we have not observed clear evidence of instability even at the higher beam current of 100 mA with the positive α. Since the *Keil-Schnell* stability criterion is for the worst case and the threshold condition should be varied by a combination of actual resistive and reactive impedances.

The bunch lengthening with the negative α was drastically changed. As one can see, the bunch shortening was observed up to ~ 15 mA, and then the bunch lengthened with the current. We confirmed the point of discontinuity around 15 mA as an onset of longitudinal microwave instability by the 2-dimensional streak camera image.

The bunch shortening can be simply explained assuming the wake field generated by an inductive (L) impedance as $V_{wake} = -L\left(dI/dt\right)$. Since the synchronous phase of the beam with the negative α is the opposite side of the slope of the accelerating RF field, a combined field with the RF field and the wake field becomes steep if the other is gently-sloping.

Radiation spectrum from the optical klystron is very sensitive to the beam energy spread. A modulation factor, which indicates degree of interference between two radiations from undulators separated by a dispersive section, defined as $f_{\mathrm{mod}} = (S_+ - S_-)/(S_+ + S_-)$, where S_+ and S_- are the maximum and the minimum intensities of a jagged-structure spectrum, respectively. Complete interference in both spatial and frequency demains makes $f_{\mathrm{mod}} = 1$. An actual modulation factor may be separated into two terms as $f_{\mathrm{mod}} = f_\varepsilon\, f_\gamma$, where f_ε and f_γ are the modulation factors originated from the emittance and the energy spread, respectively. The analytical formula of f_γ is written as

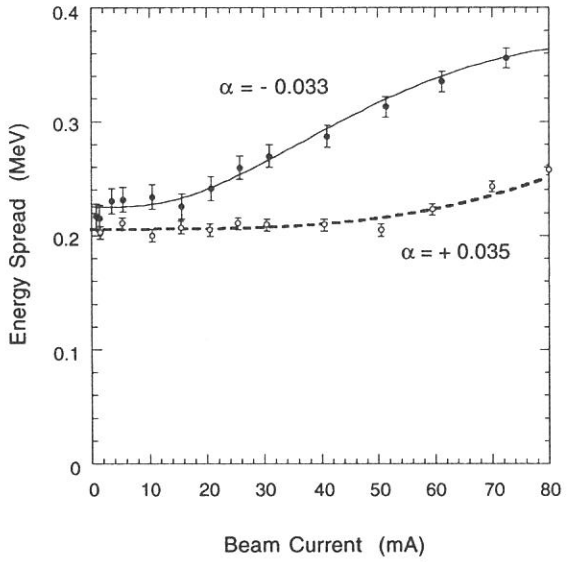

Fig. 3 Deduced energy spread from the modulation factor of the spontaneouse spectra. Lines are drawn by eyes.

$$f_\gamma = \exp\left[-8\pi^2 \left(N_u + N_d\right)^2 \left(\frac{\sigma_E}{E}\right)^2\right], \qquad (3)$$

where N_u and N_d are the period number of one undulator and the interference order of the radiation.

We chose a resonant wavelength of 355 nm to measure the modulation factor, and N_d at the wavelength was 130. Results of the measurement of the energy spread are plotted as a function of the beam current in Fig. 3. One can apparently notice the threshold beam current around 15 mA exists for the increase of the energy spread in the negative α operation, which corresponds with the result of the bunch length measurement. Meanwhile there seems to be no clear indication of the onset of microwave instability in the positive α operation. Although there is a small discontinuity seen around the beam current of 50 mA, the increase rate of the energy spread at the higher beam current is slow. We have not identified whether microwave instability occurred in the positive α operation.

The normalized effective longitudinal impedance of 1.6 Ω was deduced from the bunch lengthening with the positive α. The reason why the instability was occurred only in the negative α operation is that the potential-well distortion due to the impedance acts to shorten the bunch length for the negative α and the peak current reaches the threshold of instability at the lower beam current than the positive α. The averaged bunch length with the negative α is shorter than that with the positive α at the wide range of the beam current. Nevertheless the negative α operation has no advantage because of the lower threshold current of microwave instability. As far as the UVSOR ring, the suggestion of Fang et. al. is not realized. Probably the impedance model of a low Q resonator is not suitable for the UVSOR ring. As mentioned previously, the interaction between the electron bunch and the impedance of the chamber depends upon properties of the impedance, such as the combination of inductive and resistive components and the frequency dependence.

References

[1] for example; A. W. Chao, AIP Proc. No. 105 (American Institute of Physics, New York, 1983) 353.
[2] A. H. Lumpkin et. al., Proc. 18th Int. Free Electron Lasers Conf., Rome, Italy, 1996.
[3] S. X. Fang et. al., KEK Preprint 94-190 (National Laboratory for High Energy Physics, Tsukuba 1995).
[4] H. Hama et. al., Proc. 3rd Aisan Symp. on Free Electron Laser (IONICS Publishing Co. Ltd., Tokyo 1997) 17.
[5] H. Hama et. al., Nucl. Instr. and Meth. A375 (1996) 32.
[6] H. Hama et. al., Proc. 9th Symp. on Accelerator Science and Technology, Japan (1993) 468.
[7] B. Zotter, Proc. CERN Accelerator School, Paris 1984, CERN report 85-19 (CERN, Geneva, 1985) 415; J-L. Laclare, CERN Report 87-03 (CERN, Geneva, 1987) 264.
[8] E. Keil and W. Schnell, CERN report ISR-TH-RF/69-48 (CERN, Geneva, 1969).

A Question on Natural Chromaticity

Hiroyuki HAMA, Masahito HOSAKA, Jun-Ichiro YAMAZAKI, Toshio KINOSHITA

UVSOR Facility, Institute for Molecular Science, Okazaki 444, Japan

Chromaticity represents strength of momentum dependence of the betatron tune in circular accelerators. Natural chromaticity of a separated function storage ring is normally negative, so that the chromaticity is corrected to be zero or slightly positive by using sextupole fields to avoid a head-tail instability because a momentum compaction factor is usually positive. Since there are two families of sextupole magnets on the UVSOR ring, the corrected chromaticity ξ is written in a frame of the linear lattice function as

$$\xi = a\,SF + b\,SD + \xi_0, \qquad (1)$$

where SF and SD are strengths of each sextupole family, and a, b and ξ_0 are coefficients depend on the lattice functions and the natural chromaticity, respectively. The chromaticity is able to be experimentally deduced from the tune shift caused by change of the electron momentum. If one obtain a series of chromaticities as a function of strengths of SF and SD, the natural chromaticity can be deduced. In operations with negative momentum compaction factors, the beam is not killed with no sextupolse fields, so that the natural chromaticity can be directly obtained.

We have measured the natural chromaticities for various operating points, and the experimental ones were compared with the calculated ones. Representative operating points in the experiments are (ν_x, ν_y)= (3.16, 2.64) and (3.16, 1.44), and the momentum compaction factor was varied from + 0.03 to - 0.03 on each operating point. Although the coefficients a and b strongly depend on magnitudes of the beta functions at positions of the sextupoles, it is usually very difficult to change the Twiss parameter so much. According to the calculations, the natural chromaticity was able to be varied from - 3 to- 6 and from - 4.5 to - 6.5 in the horizontal and the vertical planes, respectively. Experimental results are shown in Fig. 1. For the horizontal chromaticity, a good agreement with the calculation can be seen. However a big discrepancy is obvious for the vertical chromaticity.

It is easily imagined that some additional multipole field exists in the ring. Since the horizontal beta function is relatively lower than the vertical beta function around the bending magnets to reduce the emittance in the Chasman-Green lattice, we have assumed a sextupole field is created in the fringe of the bending magnets. By using a thin lens approximation, an identical additional sextupole is added to both edges of the bend and its strength was estimated to reproduce the experimental data. Because there was no solution to simultaneously reproduce both the horizontal and the vertical experimental data, we obtained the strength of additional sextupole independently for each direction and each data, and averaged it. Consequently we

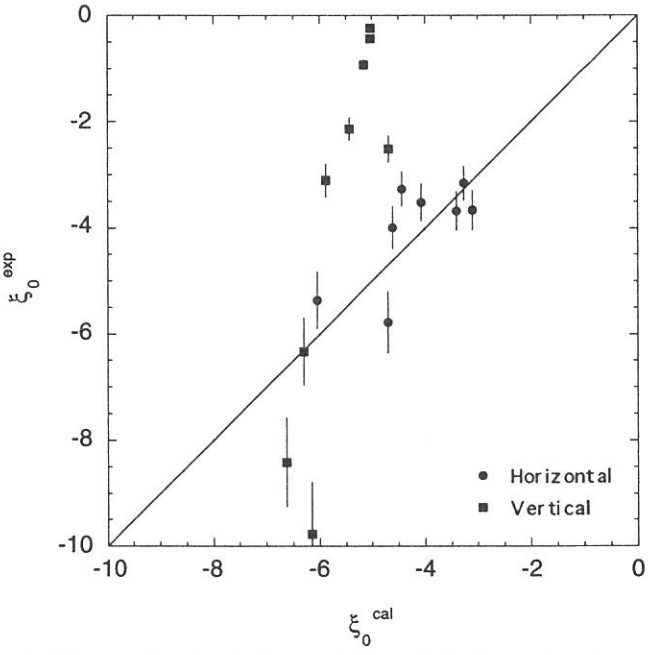

Fig.1 Measured natural chromaticities plotted as a function of the calculated ones.

obtained a strength + 1.43 (± 0.40) $T/m^2\,m$ for a beam rigidity of 2 $T\,m$ (E = 600 MeV). This magnitude of the additional sextupole is unexpectedly strong. Note the strength of the sextupoles is usually ~ 8 $T/m^2\,m$ in the normal operation.

Because we have made the sextupole strength represents the whole additional multipole field in the bend, this is probably not perfectly correct. However the most of experimental data is able to be reasonably reproduced as shown in Fig. 2. Unfortunately there was no precise information on the fringe field of the bending magnet, it is difficult to discuss qualitatively whether the additional sextupole is a proper model. In another experiment, we have measured higher order dispersion functions. Because those quantities are much affected by the sextupole field, this additional field will be examined.

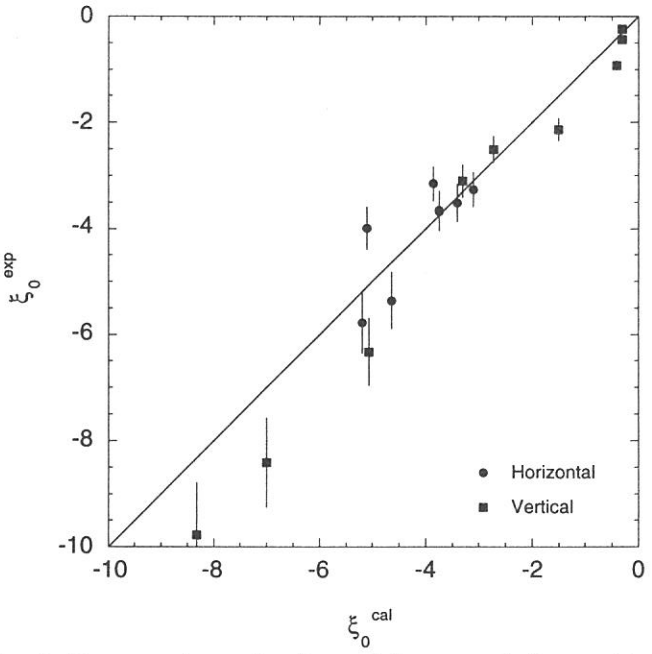

Fig. 2 The experimental values of the natural chromaticity compared with the calculated ones of which the additional sextupole is taken into account.

Anyhow the chromaticity has been practically estimated well by adding the fringe sextupole field in the linear lattice calculation. The strength of the regular sextupole magnets can be, therefore, calibrated by the calculations. We have used identical magnets and power supplies for the sextupole families. The strengths of the sextupole families have been calculated to reproduce the experimental chromaticity at each operating point and excitation current. Since the strength of the sextupole field is proportional to the excitation current, we would obtain an empirical relation between the field strength and the excitation current. The result is shown in Fig. 3. As one can see, the linearity of the strength is fairly good, and a strength parameter of 7.15 $T/m^2/A$ was obtained. Unfortunately we have no measured data of the sextupole magnets. The design value of the field strength parameter is 6.7 $T/m^2/A$, which is not far from the result.

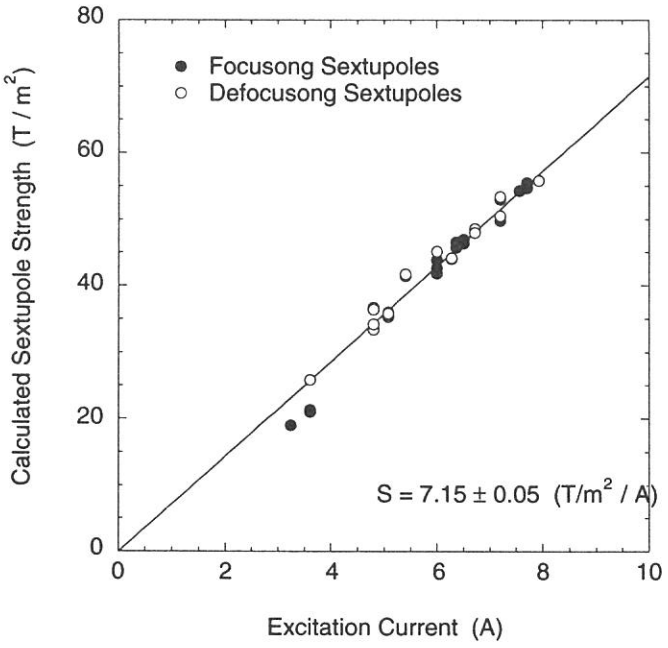

Fig. 3 Calculated field strengths of sextupoles plotted as a function of the excitation current.

Normally there are complicate multipole components exist in the fringe of the dipole magnets whose bending radius is small. In this case the kinetic terms in the orbit calculation may be not negligible. Further investigation will be performed by measuring higher order dispersion function and momentum compaction factor.

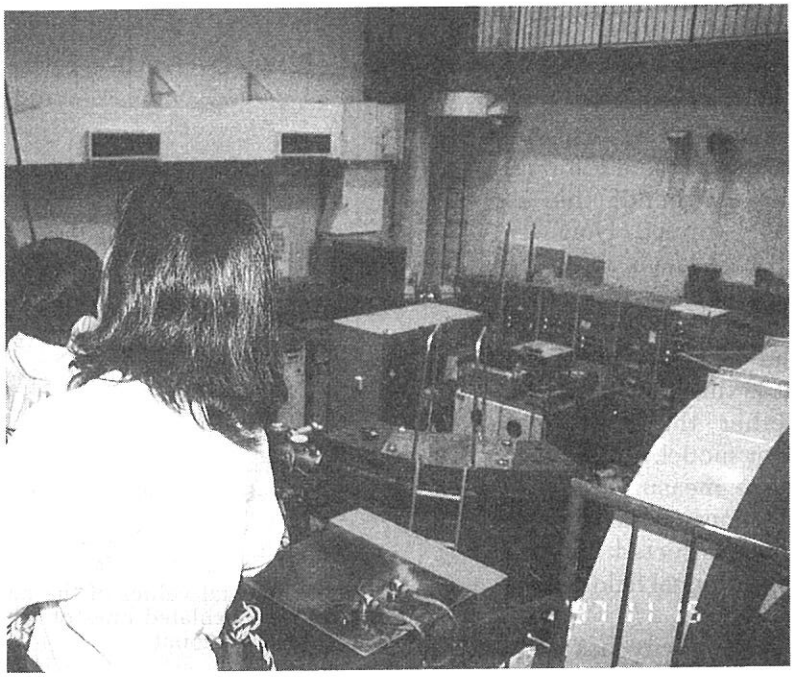

"Mum, how the electron is accelerated at the synchrotron?"

"Open House" on Nov. 15

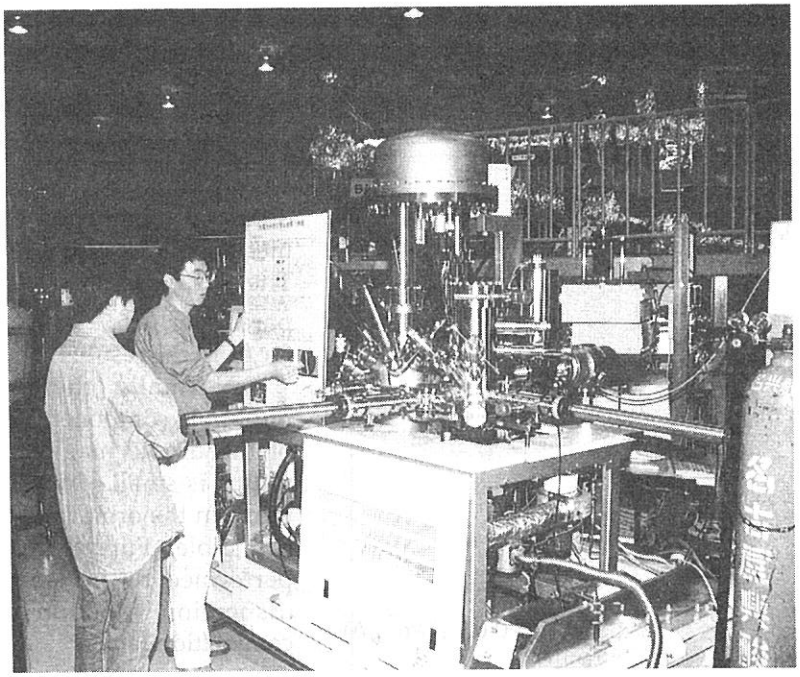

"OK. Let me tell you what is interesting of the photoelectron microscopy."

"Open House" on Nov. 15

(BL2B1)

Development of a New Electron–Ion Coincidence Spectrometer

Kazuhiko Mase, Mitsuru Nagasono, Shin–ichiro Tanaka, and Tsuneo Urisu

Institute for Molecular Science, Okazaki 444–8585, Japan

Energy–selected electron ion coincidence (EICO) spectroscopy is an ideal tool for investigations of the ion desorption induced by electronic transitions, because it provides ion mass spectra for the ion desorption channels related to the selected electron transitions [1]. Recently, we have developed an EICO apparatus combined with synchrotron radiation for the study of surface dynamics at BL2B1 in UVSOR [2]. Auger electron photoion coincidence (AEPICO) spectroscopy demonstrated that the character of the orbitals where holes are created, as well as the effective hole–hole Coulomb repulsion are critical factors which influence ion desorption probability derived from Auger final states [3]. Photoelectron photoion coincidence (PEPICO) spectroscopy, on the other hand, provided direct evidences of site–specific ion fragmentation induced by core–electron excitations [4]. In the present article, we describe details of a remodeled EICO spectrometer developed recently.

The EICO apparatus consists of a cylindrical mirror electron energy analyzer (CMA) and a time–of–flight ion mass spectrometer (TOF–MS) (Figure 1). The solid angle and the resolution of the CMA can be altered by changing the exit slit, that is, $E/\Delta E \geqq 100$ at the solid angle of 0.50 sr, and $E/\Delta E \leqq 80$ at 1.0 sr. The ion collection efficiency of TOF–MS is 40%. The merits of the new apparatus are high resolution, high sensitivity, high signal–to–background ratio, low noise, low cost, and high performance. The data acquisition time is reduced by a factor of 1/5 as compared with that for the first apparatus. The new spectrometer has greatly enhanced the activity of EICO users group at BL2B1 [5].

References

[1] K. Mase *et al.*, *J. Jpn. Soc. Synchrotron Rad. Res.* **10**, 1 (1997) (in Japanese).

[2] K. Mase *et al.*, *Rev. Sci. Inst.* **68**, 1703 (1997).

[3] M. Nagasono *et al.*, *Surf. Sci.* **377–379**, 380 (1997).

[4] S. Nagaoka *et al.*, *J. Chem. Phys.*, **107**, 10751 (1997); Mase *et al.*, *Surf. Sci.* **377–379**, 376 (1997).

[5] K. Mase *et al.*, *Surf. Sci.* **390**, 97 (1997); M. Nagasono *et al.*, *Surf. Sci.* **390**, 102 (1997); T. Sekitani *et al.*, *Surf. Sci.* **390**, 107 (1997); S. Tanaka *et al.*, *Surf. Sci.* **390**, 204 (1997).

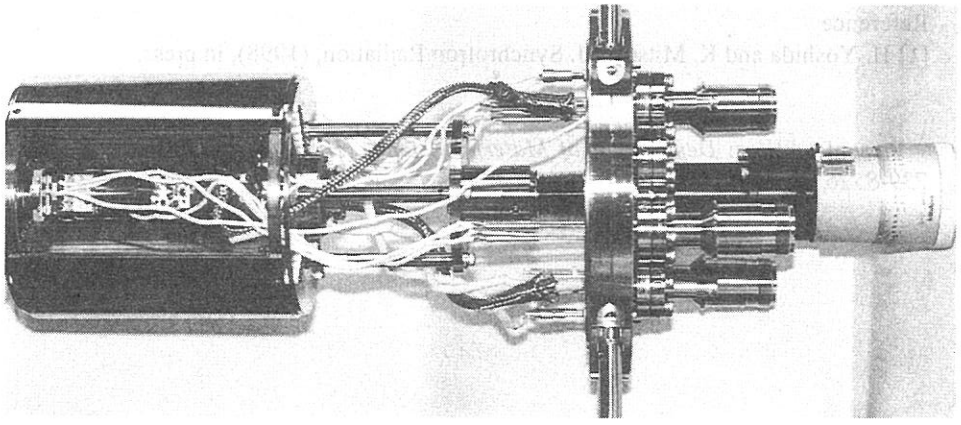

Figure 1. Photograph of the new EICO spectrometer.

(BL2B2) **Construction of an 18m Spherical Grating Monochromator**

Hiroaki YOSHIDA[A] and Koichiro MITSUKE

Department of Vacuum UV Photoscience, Institute for Molecular Science, Myodaiji, Okazaki 444-8585, Japan

An 18 m spherical grating monochromator (18 m SGM) with high resolution and high photon flux has been developed at the bending-magnet beamline BL2B2 of the UVSOR[1]. The monochromator is designed to cover the energy range of 20-200 eV. A resolving power of 5000 and photon flux of more than 10^{10} photons s^{-1} are expected at a 100 mA ring current. A small including angle of 140° is adopted for G3 and two plane mirrors coated with aluminium are located between G3 and the exit slit as optical filters. These geometrical devices may contribute significantly to reduction of the high-order lights.

A schematic layout of the beamline is shown in Fig. 1. The optical system consists of two prefocussing mirrors (M0 and M1), a fixed entrance slit (S1), an aperture (AP), a spherical grating (G1, G2 or G3), two folding mirrors (M2 and M3), a movable exit slit (S2) and a refocussing mirror (M4). The first mirror M0, which is located 2.136 m downstream from the source point in the electron storage ring, deflects the photon beam by 13°. Vertical and horizontal acceptance angles of this mirror are 6 and 15 mrad, respectively. It serves as a horizontal focussing mirror with a focal distance of 7 m. This mirror is installed in the same vacuum chamber as a prefocussing mirror of the neighboring beamline BL2B1. Spatial restriction imposed from the beamline BL2B1 determines the axis of our monochromator. The vertical prefocussing mirror M1 is placed 1.8 m behind M0 with a demagnification of 3:1 and a grazing angle of 5°. To decrease distortion induced by heat load, M0 and M1 are equipped with water-cooling systems.

The monochromator is designed to cover the energy range of 20-200 eV with the three gratings: G1 (2400 lines mm^{-1}, R = 18 m) at 80-200 eV , G2 (1200 lines mm^{-1}, R = 18 m) at 40-100 eV and G3 (2400 lines mm^{-1}, R = 9.25 m) at 20-50 eV. The including angles are 160° for G1 and G2 and 140° for G3. The directions of the incident and exit photon beams are fixed. The arm length of S1 from the grating is fixed at 2 m, while that of S2 varies from 4.18 to 4.58 m. A wavelength scanning mechanism is very simple because movement of the grating is confined only to mechanical rotation. A set of optical filters, i.e., the plane mirrors M2 and M3, are inserted across the photon beam between G3 and S2, which may significantly reduce the high-order lights of G3. These mirrors can be removed from the optical path without breaking vacuum when G1 or G2 is chosen. The coma aberration of spherical gratings is expected to be greatly decreased by AP placed 1 m from S1.

The refocussing mirror M4 is located 1.46 m downstream from the mean position of S2, deflecting the photon beam by 10° to make it horizontal. Demagnifications of vertical and horizontal directions are 1:1 and 2.75:1, respectively. The distance from the source point to the sample point is about 14.7 m.

Parameters of the optical elements are summarized in Table 1. The M0 mirror is fabricated by Hidaka Kougaku Kenkyusyo Inc. (Japan) and the other mirrors by Optron Inc. (Japan). All the optical elements are made of quartz coated with Au except M2 and M3 which are coated with Al to substantially prevent the reflection of the high-order lights. Ion-etched holographic laminar gratings are manufactured by JOBIN-YVON, Div. of INSTRUMENTS S. A. (France). Slope errors of G1, G2 and G3 are 0.28, 0.25 and 0.18 arc sec, respectively.

This monochromator was manufactured by TOYAMA Co., Ltd. (Japan) and assembled at UVSOR in May 1997. At present the optical alignment is being performed.

The authors would like to gratefully acknowledge useful suggestions from Professor Atsunari Hiraya of Hiroshima University, Professor Akira Yagishita of Photon Factory, Dr. Yonglian Yan of BSRL in China and Professor Eiji Ishiguro of Ryukyu University.

Reference

[1] H. Yoshida and K. Mitsuke, J. Synchrotron Radiation, (1998), in press.

[A] Present address: *Department of Material Science, Hiroshima University, Kagamiyama, Higashi-Hiroshima 739-8526, Japan*

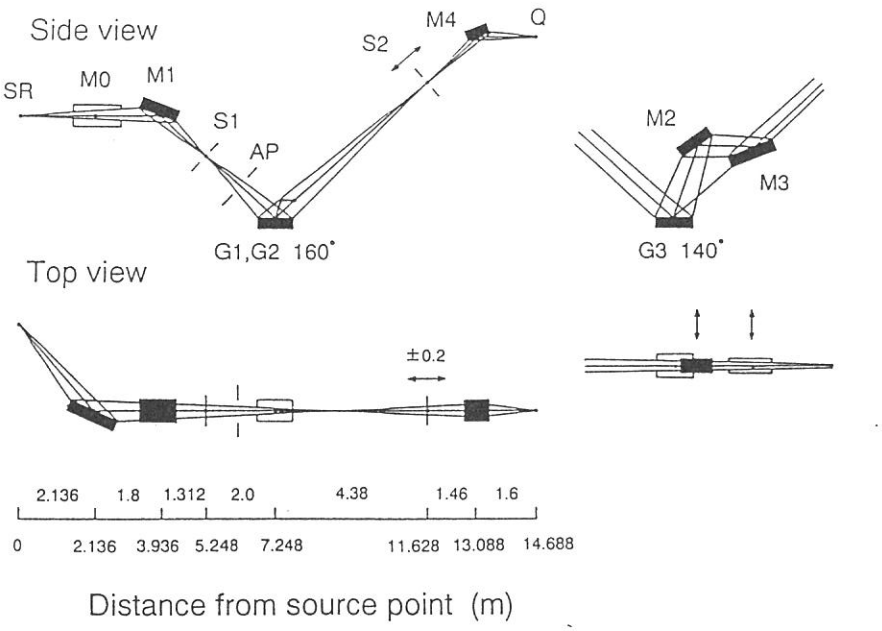

Fig. 1 Schematic layout of renewed BL2B2 equipped with an 18 m SGM. Two optical paths with including angles of 160° for G1 and G2 and 140° for G3 are indicated. SR, synchrotron radiation source point; M0, elliptically bent plane mirror; M1, spherical mirror; S1, entrance slit; AP, aperture; G1, G2 and G3, spherical gratings; M2 and M3, plane mirrors; S2, exit slit; M4, toroidal mirror; Q, sample point.

Table 1 Parameters of mirrors and gratings of 18 m SGM

Mirror	M0	M1	M2	M3	M4
Shape	Elliptical [a]	Spherical	Plane	Plane	Toroidal
Radii R× ρ (mm) [b]	28914 [c]	23405			18341×202.2
Material	quartz	quartz	quartz	quartz	quartz
Coating (nm)	Au 100	Au 100	Al 100	Al 100	Au 100
Reflective area L×W (mm)	500×20	400×34	250×24	600×24	300×50
Micro roughness (Å rms)	—	3.29	3.08	1.42	5.0
Grazing angle (°)	6.5	5.0	15.0	5.0	5.0

Grating	G1	G2	G3
Shape	Spherical	Spherical	Spherical
Radius (mm)	17987±18	17987±18	9246±6
Groove density (lines mm^{-1})	2400	1200	2400
Duty ratio [d]	0.61	0.675	0.62
Groove depth (nm)	11.4	22.6	23.5
Au coating (nm)	40±4	40±4	40±4
Material	quartz	quartz	quartz
Ruled area L×W (mm)	130×20	130×20	130×20
Size L×W×t (mm)	140×30×25	140×30×25	140×30×25
Micro roughness (Å rms)	3.6	< 5	< 5
Slope error (arc sec)	< 0.28	0.25	0.18
Including angle (°)	160	160	140

[a] Elliptically bent plane mirror.
[b] Tangential (R)×sagittal (ρ).
[c] Radius at the center of the mirror.
[d] Groove width / pitch.

(BL2B2, 3A2)

Construction and Apparatus of the Two-Dimensional Photoelectron Spectrometer at Beamlines 2B2 and 3A2

Koichiro Mitsuke[A], Kota Iwasaki[A,B], Hiromichi Niikura[A,C]
Masakazu Mizutani[A], and Yasumasa Hikosaka[A]

[A] *Institute for Molecular Science, Myodaiji, Okazaki 444-8585, Japan*
[B] *Inoue Fellow; Inoue foundation for Science, Sarugaku-cho, Shibuya-ku, Tokyo 150, Japan*
[C] *The Graduate University for Advanced Studies*

Vacuum UV photoexcitation of an electronically-ground-state molecule induces various phenomena, *i.e.* direct ionization, shape resonance, superexcitation, autoionization, direct dissociation, predissociation, fluorescence emission, nonradiative transition (nonadiabatic transition, internal conversion and intersystem crossing, *etc.*), and binary or trinary combinations of these processes. As a rule, electron emission due to direct ionization or autoionization dominates over the other processes, even if the energy transferred to the molecule is not more than few electron volts above its first ionization potential. Hence, photoelectron spectroscopy is considered to be crucially helpful in our understanding the mechanism of VUV photoexcitation and subsequent decay channels of gas-phase molecules as well as condensed matters.

In UVSOR, beamline 3B is devoted to the gas phase two-dimensional photoelectron spectroscopy. Here, the term "two-dimensional" means that photoelectron yield is measured as a function of both photon energy and electron kinetic energy (binding energy). A two-dimensional spectrum, usually represented as a contour plot, contains rich information on photoionization dynamics and properties of superexcited states (see the *Current status of beamline 3B* in this journal). Unfortunately, a wavelength or photon-energy coverage of our normal incidence monochromator connected with BL3B ranges from 35 to 200 nm or from 6 to 35 eV, respectively, so that feasible subjects are limited to elementary atomic and molecular processes caused by outer-valence-electron excitation. To extend our knowledge over the research fields of inner-valence- and inner-shell-electron excitations, we should carry out photoelectron spectroscopy at beamlines equipped with a grazing-incidence monochromator. UVSOR facility has a few beamlines for gaseous experiments which can supply photons of higher energies than BL3B. In the present report, description is made on construction of a new apparatus of two-dimensional photoelectron spectroscopy which is now set downstream of a constant-deviation grazing-incidence monochromator at the undulator beamline 3A2. Furthermore, this apparatus is scheduled to be incorporated into a performance test system for a new Dragon-type monochromator which is under construction at the bending-magnet beamline 2B2. The former monochromator is designed to cover the energy range from 13 to 120 eV, while the latter from 20 to 200 eV.

Figure 1 shows a schematic diagram of a measurement chamber which contains an electron energy analyzer of 166° spherical electrostatic deflection type, a quadrupole mass spectrometer, a detector of photon pulses, and a gold-mesh current monitor. The energy dispersed electrons are detected with a position sensitive detector (PSD) composed of dual microchannel plate (MCP) multipliers and a two-dimensional resistive-anode encoder. Detection efficiency of PSD is expected to be about 50 times as high as that of a single channel MCP detector, as far as other conditions are the same, since PSD can collect all of the energy-dispersed electrons simultaneously that can pass through between the two spherical sector surfaces. The kinetic energy can be precisely determined from a displacement of the location of the incident electron along the

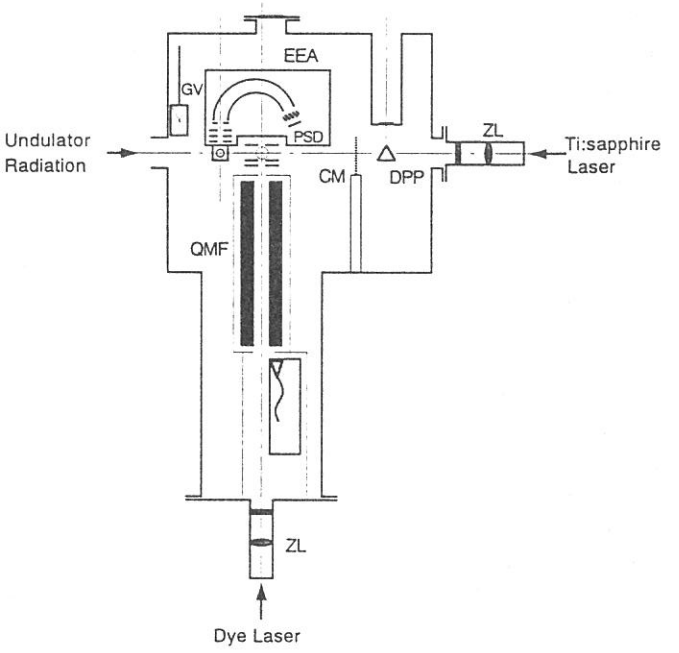

Figure 1. Schematic diagram of the apparatus. GV, gate valve; QMF, quadrupole mass filter; EEA, electron energy analyzer; PSD, position sensitive detector; CM, gold-mesh current monitor; DPP, detector of photon pulses; ZL, zoom lens.

coordinate of energy dispersion. Measuring two-dimensional photoelectron spectra are controlled by the CAMAC and NIM systems. Figure 2 shows a dependence of the energy resolution ΔE (FWHM) on the transmission energy T_E of electrons traveling inside the analyzer. Open circles represent experimental peak widths determined from the $Ar^+(^2P_{3/2}, {}^2P_{1/2})$ bands in photoelectron spectra of Ar taken by using the He I resonance line (photon energy of 21.218 eV) furnished from a supplementary helium discharge lamp. The solid line shows a plot of theoretical band widths (FWHM) estimated by assuming both the entrance and exit slits of 4 mm diameter. At T_E higher than 2 eV, every experimental ΔE value is smaller than obtained by theoretically, since the present PSD has a spatial resolution of 250 μm. On the other hand, ΔE values at T_E lower than 1 eV appear to be about twice as large in the experiment as in the theory. This lowering of the resolving power is probably ascribed to a remaining magnetic field in a part of PSD, which will soon be replaced. Figure 3 shows a photoelectron spectrum of O_2 containing a little amount of Ar measured by using the undulator radiation from BL3A2. The photon energy and overall energy resolution are set to 23.934 and 0.07 eV, respectively.

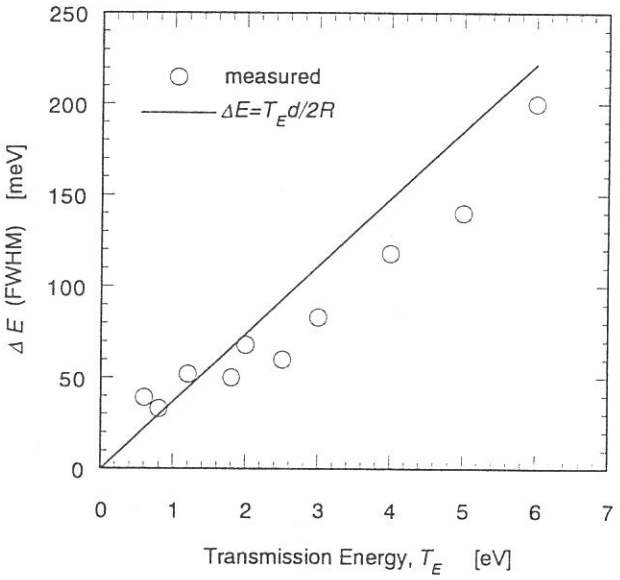

Figure 2. Dependence of the energy resolution ΔE (FWHM) on the transmission energy T_E. In the theoretical equation, d and R denote the width of entrance and exit slits and the mean radius of the electron orbit.

The instrument illustrated in Fig. 1 has been especially designed and fabricated toward another important final goal, that is two-photon ionization photoelectron spectroscopy using time-correlated synchrotron radiation and laser photon pulses. For this purpose, a laser beam can be introduced through a zoom lens unit so as to counterpropagate the synchrotron radiation beam. Synchronization of the laser to synchrotron radiation is performed by use of an electronics module which provides phase-locked stabilization of laser pulses. The temporal overlap of the two photon pulses can be adjusted by monitoring the signal from the detector of photon pulses. In addition, we are planning to fulfill resonance-enhanced-multiphoton ionization (REMPI) spectroscopy of dark neutral fragments produced by competitive (pre)dissociation of superexcited states.

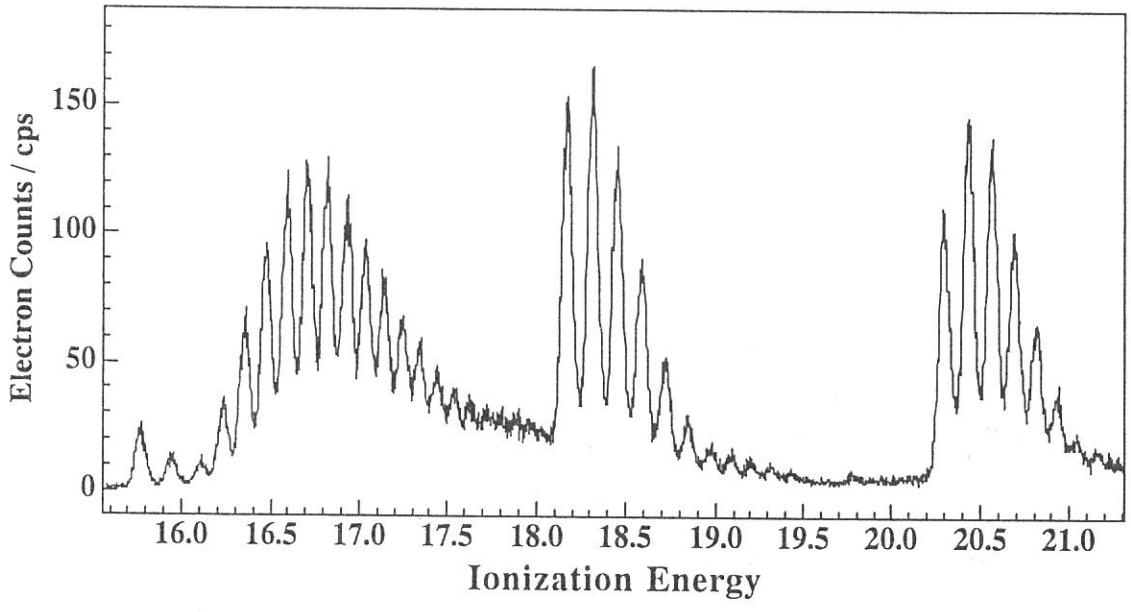

Figure 3. Photoelectron spectrum of O_2 containing a little amount of Ar measured by using the undulator radiation from BL3A2. The photon energy and overall energy resolution are set to 23.934 and 0.07 eV, respectively.

(BL3A2)

Two-dimensional imaging technique for measuring translational energy and angular distribution of ionic photofragments

Tatsuo GEJO and Norio SAITO [A]

Institute for Molecular Science, Myodaiji, Okazaki 444-8585, Japan

[A] *Electrotechnical Laboratory, Umezono, Tsukuba-shi, 305-0045, Japan*

The dynamics of molecular in the valence energy regime can be investigated by preparing to excited state at well-defined energy and analyzing the ionic photofragments. Two dimensional imaging technique is one of the most powerful methods for obtaining this information because calculation on the basis of momentum conservation law provides Newton diagram of photofragments. We have launched the two dimensional imaging technique with using a position sensitive detector (PSD) at BL3A2 in UVSOR.

The machine consists of a beam nozzle, a skimmer, ion lenses, an position sensitive detector with MCP (fig. 1). This configuration is particularly suitable for PIPICO and PIPIPICO technique because symmetric configuration of ion lens and MCP around the molecular beam axis minimize the affect of the initial velocity distribution of the beam. After being skimmed, the molecular beam pass thorough SR region, and less than one molecular per one photon beam on the average undergo ionization and/or dissociation. Accordingly it allows an coincidence technique. After the acceleration by ion lens, ion fragments hit the PSD. The determination of position on the detector is based on the time delay between two signals from each end of an wire behind the MCP: The position is obtained by the subtracting of time when each two signals arrive. Since the direction of polarization of SR is parallel to the axis of TOF tube, the TOF and the position of the ionic fragments on the detector provide its velocity and direction in center-of-mass frame.

At BL3A2 we have successfully measured the image of N^+ and N_2^+ signal from nitrogen at the valence region (20-100 eV). However, significant noise level excluded us from analyzing the data. This noise mainly comes from the fluctuation of the ground level caused by RF signals at the storage ring. The improvement of the detection system will allow us to obtain the data.

We thank Prof. T. Suzuki at IMS for his technical advice.

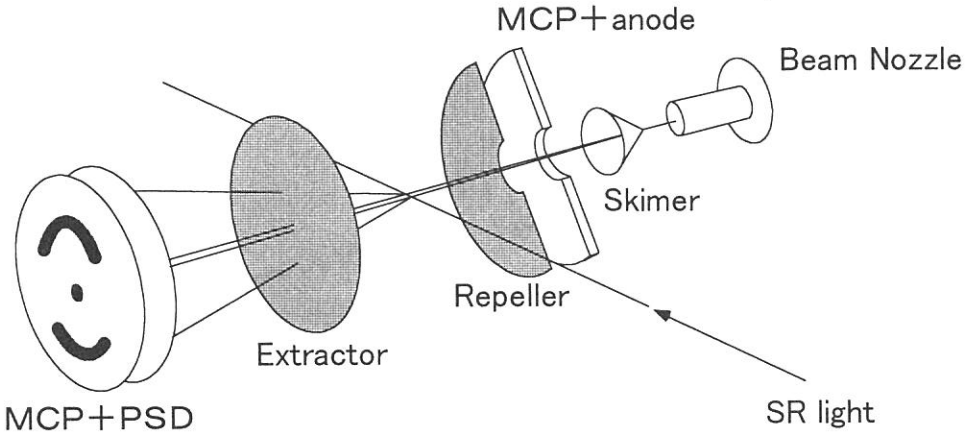

Fig. 1: Schematic view of 2D imaging technique

(BL4A1)

Performance of the Double Multi-Layered-Mirror Monochromator and Beamline BL-4A1

Harutaka Mekaru[A],Takayuki Miyamae[B] and Tsuneo Urisu[B]

[A]The Graduate University for Advanced Studies,
[B]Institute for Molecular Science, Myodaiji, Okazaki 444-8585

The authors developed a double multilayered mirror (MLM) monochromator and constructed the beamline BL-4A1 at the UVSOR for studies of synchrotron radiation (SR) stimulated processes.

The important photon energy region for the experimental investigation of SR stimulated processes, especially of the core electron excitation processes, is from a few tens to hundreds of electron volts. In the present work, our attention was focused on the region between 60 and 120 eV that includes the core electron binding energy of Al (2s : 119eV, 2p : 74eV) and Si (2p : 103eV). In this region a fairly high reflectivity is obtained by using Mo/Si (for 60-120eV) and Mo/C (for 85-120eV) MLMs. Further, a carbon 100nm thick filter was combined to remove the background noise of the low energy region consisting of total reflection components

In this report we present experimental results for the performance of a double MLM monochromator in the energy range 60 to 128eV and compared to calculations. Measurements of the Al $L_{2,3}$ (72eV) absorption edge using Mo/Si MLMs with a C filter and the Be K (111.5eV) absorption edge using Mo/C MLMs with a C filter are also presented and compared with calculations. The photon flux was estimated between 2×10^{13} and 8×10^{15} photons/cm^2. The energy selectivity of the MLM monochromator and Al $L_{2,3}$ edge and Be K edge are clearly seen. The measured maximum transmission of the monochromator using Mo/Si MLMs is 42% with a resolution of ΔE=6.4eV and that using Mo/C MLMs is 13% with a resolution of ΔE=5.6eV. We conclude that the photon flux and the resolution are sufficient performance for studies of SR stimulated processes.

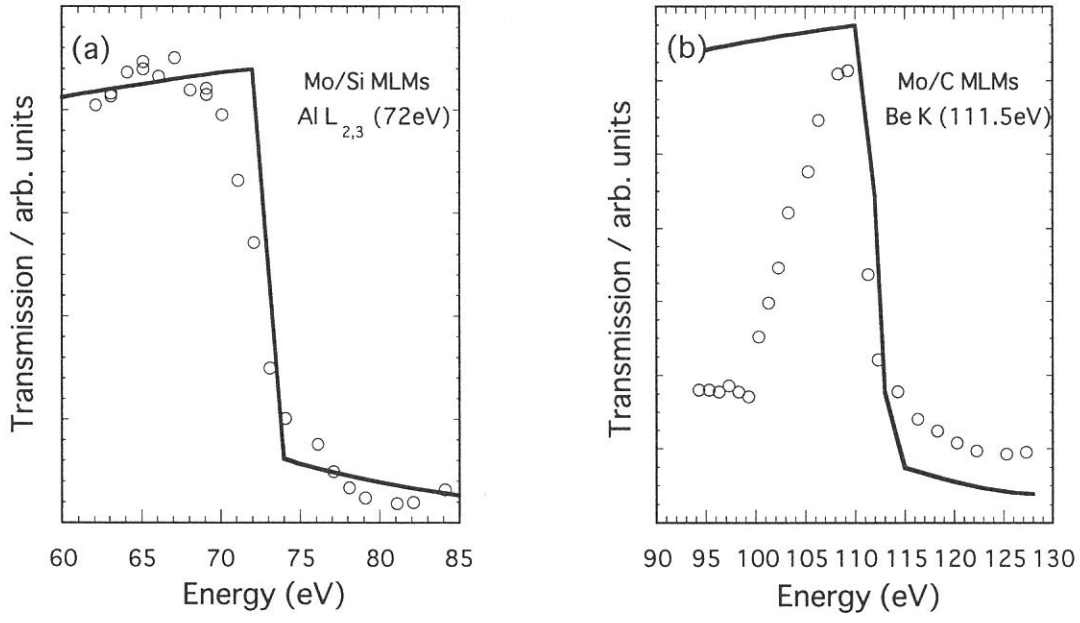

Figure 1 Transmission of the 120 nm thick aluminum filter measured (dots) and calculated (solid line) in the vicinity of the Al $L_{2,3}$ edge using Mo/Si MLMs (a) and the 100nm thick beryllium filter measured and calculated in the vicinity of the Be K edge using Mo/C MLMs (b).

(BL4B)

Development of UHV-STM System for Study of Surface Photochemical Reactions Induced by Synchrotron Radiation.

Takayuki MIYAMAE[a], Shinya HIRANO[b], Hironaga UCHIDA[c], and Tsuneo URISU[a]

[a] *Institute for Molecular Science, Myodaiji, Okazaki 444-8585*

[b] *The Graduate University for Advanced Studies*

[c] *Toyohashi University of Technology, Toyohashi 441*

We have newly developed a scanning tunneling microscopy (STM) system for the study of surface photochemical reactions. The design of our UHV-STM system is schematically shown in Fig. 1. The STM is located in the left-hand side of the main chamber. A back-view LEED, an atomic hydrogen doser, and a heating device are located on the right-hand side of the chamber. The pumping of the system is carried out by ion pump, Ti sublimation pump, and a non-evapolable getter pump for the main chamber and a turbomolecular pump for the sample preparation chamber which is stopped during the STM experiments. A pressure better than 1×10^{-10} Torr can be maintained in the main chamber. The STM body is suspended by three stainless steel springs for vibration isolation. The entire UHV system is mounted on an air-suspended vibration isolation table. STM images of the Si(111)-7×7 clean surface and atomic hydrogen-chemisorbed surface are shown in Fig. 2. Now experiments using STM for the geometrical topography and electronic structure of atomic hydrogen-chemisorbed Si surface and its change by the synchrotron radiation stimulated surface reaction is underway.

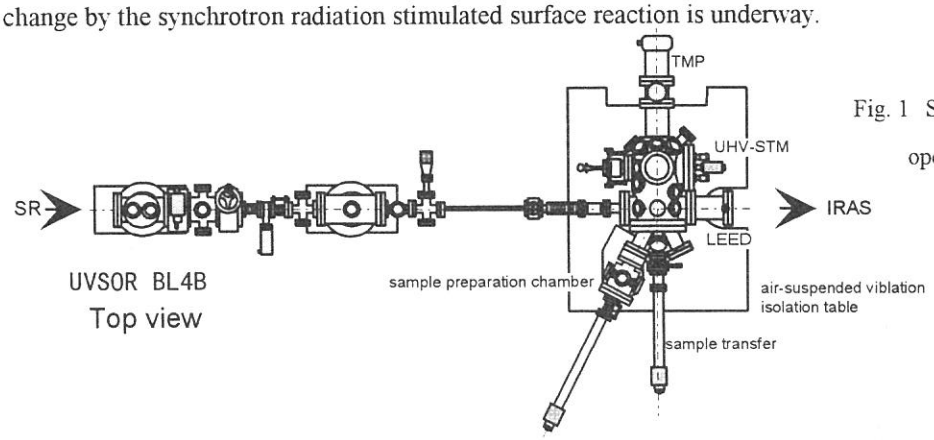

Fig. 1 Schematic of the STM system operated in the UHV condition.

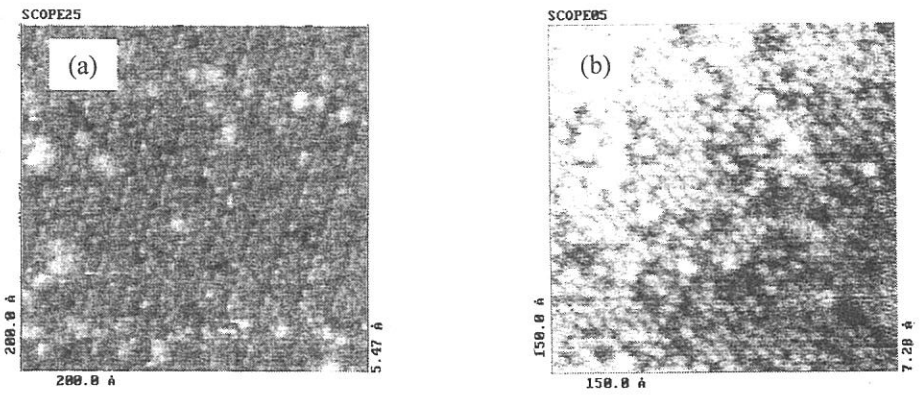

Fig. 2 STM images of the occupied states of the Si(111) clean surface (a) and the surface following a low coverage exposure to H atoms (b).

(BL5A)

Performance of the electron spectrometer for the high-resolution photoelectron spectroscopy at BL5A

Shin-ichiro Tanaka, Jun-ichi Murakami and Masao Kamada

Institute for Molecular Science, Okazaki, 444-8585, Japan

BL5A is consists of a helical undulator, an SGM-Train (Spherical Grating Monochromator with Transnational and Rotational Assemblies Including Normal-incidence mount) monochromator and a UHV chamber which equipped with a LEED optics, a CMA (cylindrical Mirror Analyzer) for the Auger electron spectroscopy, an ion gun, a gas-dose system using a pulse valve, a spin- and angle- resolved electron spectrometer, a hemispherical electron analyzer for high resolution photoelectron spectroscopy and a sample holder with a liquid-He cryostat. In this report, we describe the hemispherical analyzer and the sample holder, and show an achieved performance.

The hemispherical analyzer is "EA-125HR" made by OMICRON, Germany, which consists of the 11-element zoom lens, a 180° hemispherical analyzer of 125 mm mean radius and a detection system with 5 channeltrons. The potential of lens (selectable among 3 magnification modes) is controlled by the PC (Gateway 2000) via the "EAC-300" control unit. The data detected with 5 channeltrons are shifted in energy and added to make one spectrum with high count rate. Unfortunately, the simultaneous control of the SGM-Train monochromator and the electron analyzer can not be made yet.

A sample can be cooled by a home-made liquid-He cryostat of a transfer type. The sample is electrically isolated by a sapphire sheet of 1mm thick, and can be heated to more than 1500 K by resistive heating or electronic bombardment from the rear. The sapphire sheet also works as a thermal switch because its thermal resistance varies drastically depending on the temperature. It has a Chromel-Almel thermocouple, but not precisely calibrated at low temperatures. The lowest temperature was estimated by the adsorption and desorption measurements of gases, e.g., CO, O_2, N_2, Ar on the sample, and was less than 25 K.

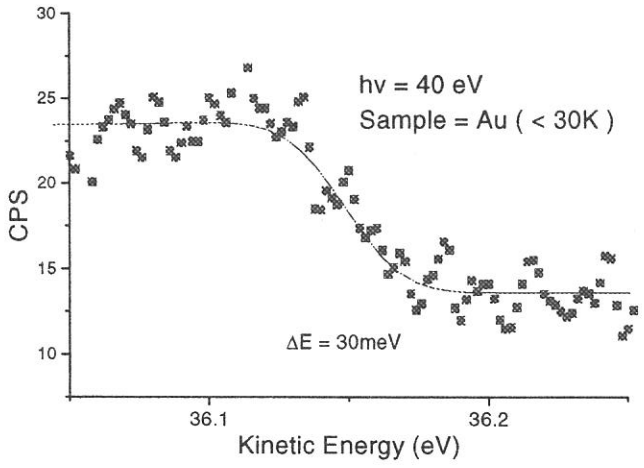

Left figure shows an example of the photoelectron spectrum at the Fermi edge of the Au film measured at BL5A. The photon energy was 40 eV. It is noted that the photon from the bending magnet was used. Solid line is an error function fitted to the data. The ΔE (2σ) in the error function is 30 meV, which includes the Fermi-Dirac distribution, and the instrumental resolution should be better.

(BL5A)

Construction and performance test of SGM-TRAIN at UVSOR

Masao Kamada, Masami Hasumoto, Nobuo Mizutani, Toshio Horigome, Shin-ichi Kimura, Shin-ichiro Tanaka, Kusuo Sakai, and Kazutoshi Fukui*

Institute for Molecular Science, Okazaki 444-8585, Japan
**Fukui University, Fukui 910, Japan*

A new monochromator called SGM-TRAIN (Spherical Grating Monochromator with Translational and Rotational Assembly Including a Normal incidence mount) has been constructed at BL5A. The SGM-TRAIN is designed for experiments where the circularly polarized synchrotron radiation from a helical undulator is used, as well as bending magnet radiation. The SGM-TRAIN has the advantage that the small emittance of a storage ring and the large space for a long beam line are not necessary. The design of the SGM-TRAIN is based on the following requirements: (1) Fundamentals from the helical undulator appear in the photon energy range of 5-43 eV, with the harmonic radiation being emitted up to 250 eV. (2) A floor space limits a distance between the first pre-mirror and a sample position to 8 m. (3) Degree of circular polarization should be kept as high as possible. (4) Higher order light must be suppressed. (5) Bending magnet radiation is used as well as undulator radiation. (6) Beam size and emittance in the vertical direction are 0.52 mm and 11.5 πnm rad, respectively.

The SGM-TRAIN is an advanced version of a constant-length monochromator proposed by Ishiguro et al. (1). The SGM-TRAIN consists of two glancing incidence mounts and a normal incidence mount. The parameters of main optical elements are given in Table I. Pre-mirrors, BM0 and UM0, are used for bending magnet radiation and undulator radiation, respectively. Two post-mirrors, M31 and M32, are exchanged for normal and glancing incidence mounts, and the focus point is about 1.5 m from the post-mirror. Two types of scanning modes, the combination mode of rotation and translation and the rotational mode at fixed translational position, are available in the SGM-TRAIN, since all driving systems are directly controlled by a computer.

Figure 1 shows the doubly ionization spectrum of He at the pressure of 50 mTorr. The spectrum was obtained in the combination scanning mode with 10 μm slits and G2M22. Rydberg lines up to n=11 are clearly observed, indicating a resolving power of about 4,000 at 200 Å. The resolving power of about 3,500 was also obtained from the Ar $L_{2,3}$ spectrum at 50 Å with the combination G1M21. These values are by 20-30 % less than the expected values (2). Figure 2 shows photoelectric yield spectra of a gold mesh for bending magnet radiation. The spectra #1-#4 correspond to the combinations of G1M21, G2M22, G2M23, and G2M24, respectively. Laminar-profiles of the gratings and coating

Table I. Parameters of main optical elements

name	shape	coating	angle(°)	radius(m)	dimension(mm³)
BM0	Toroidal	Au	172	58.540 (ρ = 0.527)	310x25x25
UM0	Spherical	Au	174	181.607	340x25x25
M1	Spherical	Au	175	61.240	420x35x30
M21	Plane	Au	172		110x30x20
M22	Plane	Au	152		60x30x10
M23	Plane	SiC	152		60x30x10
M24	Plane	Al	152		60x30x10
M25	Plane	Pt	7		40x30x10
G1	Spherical	Au	172	25.406	110x30x20
G2	Spherical	Au	152	7.245	60x30x20
G3	Spherical	Au	7	2.549	40x30x20
M31	Toroidal	Au	175	26.090 (ρ = 0.164)	280x30x25
M32	Toroidal	Au	175	28.090 (ρ = 0.079)	280x30x25

materials (Au, SiC, Al, and Pt) on the plane mirrors were chosen in order to suppress the second-order light with less decrease in the degree of circular polarization. Further testing and tuning of the SGM-TRAIN are requested in order to get better performance with circularly polarized light from the helical undulator, which was installed into the one of the straight sections of the UVSOR storage ring .

References

(1) Ishiguro, E, Suzui, M, Yamazaki, J, Nakamura, E, Sakai, K, Matsudo, O, Mizutani, N, Fukui, K, Watanabe, M (1989), Rev. Sci. Instrum. 60, 2105-2110.

(2) Kamada, M, Saka, K, Tanaka, S, Ohara, S, Kimura, S, Hiraya, A, Hasumoto, M, Nakagawa, K, Ichikawa, K, Soda, K, Fukui, K, Fujii, Y, and Ishiguro, E (1995), Rev. Sci. Instrum. 66, 1537-1539.

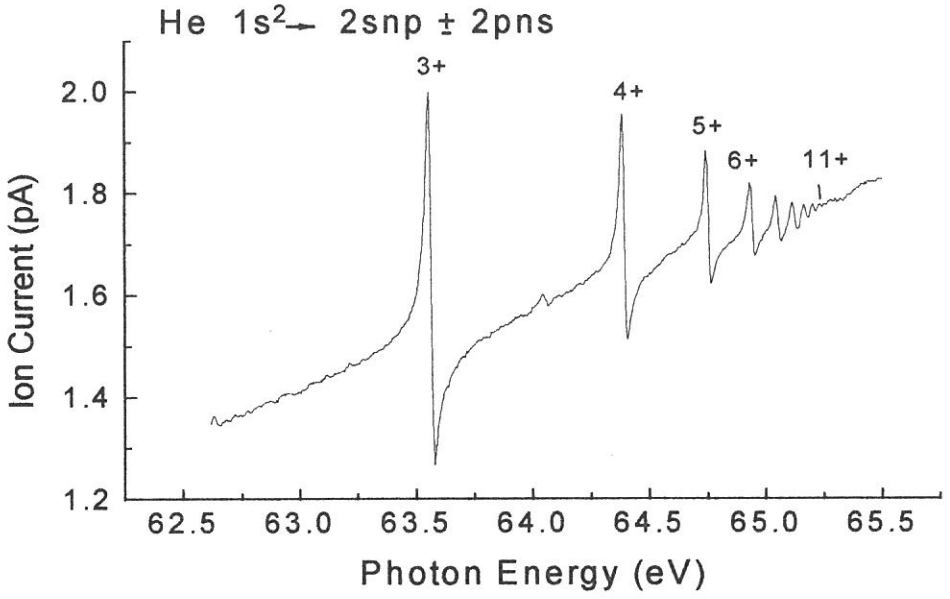

Fig. 1. The doubly ionization spectrum of He at the pressure of 50 mTorr.

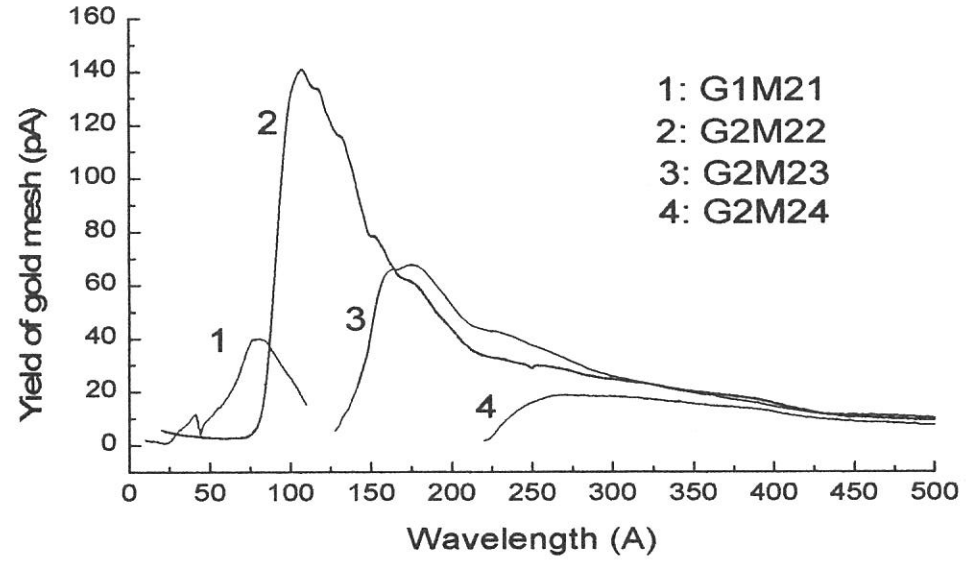

Fig. 2. Photoelectric yield spectra of a gold mesh for bending magnet radiation.

(BL5A)

Performance of The Helical Undulator of BL5A

S. Kimura, M. Kamada, H. Hama, K. Kimura[1], M. Hosaka, J. Yamazaki, X Marechal[2], T. Tanaka[2] and H. Kitamura[2]

UVSOR Facility, Institute for Molecular Science, Okazaki 444-8585
[1]Department of Structural Molecular Science, The Graduate University for Advanced Studies, Okazaki 444-8585
[2]SPring-8, Kamigori, Hyogo 678-12

Optical excitations with circularly polarized light are useful to know magnetic moments of electrons. The difference spectrum between absorption for right and left circularly polarized light is called circular dichroism (CD). The CD method is one of powerful tools for the investigation of electronic structures, not only of magnetic materials but also of non-magnetic materials. On the other hand, a spin-resolved photoelectron spectroscopy can give us information about momentum and spin of electrons. The combination of the circularly polarized light and the spin-resolved photoelectron analyzer allows us to observe the electronic structures of materials with selected magnetic moments.

For the investigation of electronic structures of magnetic and non-magnetic materials by a spin-resolved photoelectron spectroscopy, we have constructed a beam line, BL5A, of UVSOR. The beam line consists of a helical undulator, a high-resolution monochromator and a spin- and angle-resolved photoelectron analyzer. The monochromator, which is named SGM-TRAIN (spherical grating monochromator with translational and rotational assembly including a normal incidence mount), is an improved version of a constant deviation and constant length monochromator [1]. The spin- and angle-resolved photoelectron analyzer is a type of low-energy diffuse scattering [2]. These apparatus have already been completed and reported in elsewhere. Recently, the first spectrum of circularly polarized light in the vacuum-ultraviolet region from the helical undulator was observed. In this paper, the performance of the helical undulator and the observed spectrum are reported.

The UVSOR helical undulator is a modified version of a helical undulator, or an elliptical wiggler [3] and an 8-figure undulator [4] which were designed for the 8-GeV storage ring, SPring-8. Since the energy of UVSOR is about one order less than that of SPring-8, special cares were taken to optimize the magnetic fields. The peak energy of the fundamental radiation can be swept only by changing the undulator gap while keeping the degree of the circular polarization.

The helical undulator has three lanes in the upper and the lower magnet arrays shown in Fig. 1. The undulator looks like a planar one. However, in the helical configuration, the center lane produces the vertical magnetic field and the side lanes make the horizontal field. The vertical and horizontal magnetic fields were set to be almost equal to each other in the undulator gap of 30 – 150 mm. In the range of the undulator gap, the range of the deflection parameter, K, is 4.6 – 0.07. The fundamental emission peak is expected to cover the photon energy range of 2 – 43 eV [5].

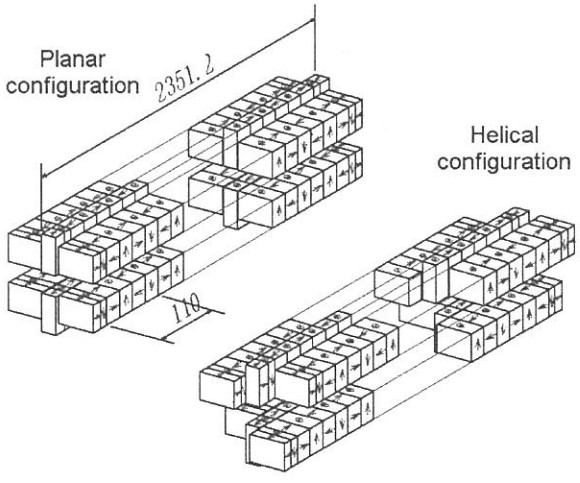

Fig. 1. Schematic figure of the UVSOR helical undulator in the planar and helical configurations.

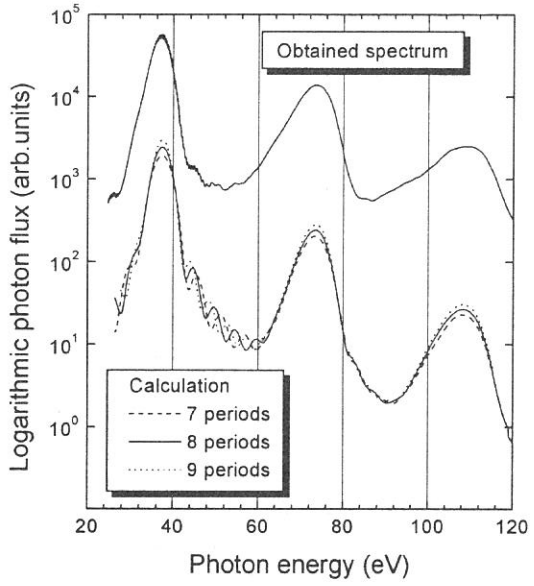

Fig. 2. Obtained (upper curve) and calculated (lower curves) spectra from the undulator at the undulator gap of 100 mm. The analytical calculation was done by using the parameters of the acceptance angle of 0.4 mrad and of 7, 8 and 9 periods of the magnet array. Note that the intensities of calculated spectra are shifted from the measured one for making the figure easier to read.

The observed spectrum at the undulator gap of 100 mm is shown in the upper part of Fig. 2. The fundamental radiation was observed at the photon energy of 37 eV, and the second and the third harmonics were also observed. In the case of the on-axis spectrum from the circularly polarized undulator radiation, the higher order components should not appear. In our experimental set-up for the performance test, however, not only the on-axis component but also the off-axis one of the undulator radiation was detected. Therefore the higher harmonics were observed in the spectrum.

Note that the observed spectrum was obtained by using the rearranged magnet array of the helical optical klystron for a helical free electron laser. In the optical klystron configuration, three periods at the center of the magnet arrays are rearranged [6]. By using the optical klystron, the shortest free electron laser wavelength of 239 nm was achieved [7]. As shown in Fig. 2, the interferogram appears in the fundamental radiation because of the use of the magnet array of the optical klystron. The interferogram is due to the interference of radiation from the former nine periods with that from the latter nine periods.

The analytical calculation results of the undulator spectrum with three different numbers of periods (7, 8 and 9 periods) are plotted in the lower part of Fig. 2. The best-fit spectrum of the analytical calculation was obtained with eight periods of undulator despite the nine periods of the undulator, and the acceptance angle of 0.4 mrad. The result means that the undulator radiation consists of the emissions from each center eight periods of the former and the latter magnet arrays. According to the calculation of the electron beam trajectory, the trajectories at the first and the last periods are far from the on-axis. Therefore the emission from the half of the first and the half of the last periods is not considered to interfere with the emission from the other periods. The value of 0.4 mrad is consistent with the maximum of the angular distribution of the undulator with eight periods.

References

[1] M. Kamada *et al.*, Rev. Sci. Instrum. **66**, 1537 (1995).
[2] N. Takahashi *et al.*, Jpn. J. Appl. Phys. **35**, 6314 (1996).
[3] X. M. Maréchal *et al.*, Rev. Sci. Instrum. **66**, 1937 (1995).
[4] T. Tanaka and H. Kitamura, J. Electron Spectrosc. Rel. Phenom. **80**, 441 (1996).
[5] S. Kimura *et al.*, J. Electron Spectrosc. Rel. Phenom. **80**, 437 (1996).
[6] H. Hama, Nucl. Instr. and Meth. in Phys. Res. A **375**, 57 (1996).
[7] K. Kimura *et al.*, UVSOR Activity Report 1996, 42 (1997).

(BL5B)

Reflectance of Mo/Si and Mo/C Multilayered Mirrors for the Double Multi-Layered-Mirror Monochromator of Beamline BL-4A1

Harutaka Mekaru[A] and Tsuneo Urisu[B]

[A]The Graduate University for Advanced Studies,
[B]Institute for Molecular Science, Myodaiji, Okazaki 444-8585

Multilayer structures of molybdenum/silicon and molybdenum/carbon have been shown to have high reflectivities in the extreme ultraviolet and , therefore, potential for use as monochromator elements. The authors developed a double multilayered mirror (MLM) monochromator and set up it as the part of the beamline BL-4A1 at the UVSOR for studies of synchrotron radiation (SR) stimulated processes.
We had measured the reflectivity of a multilayered mirror using monochromatized SR from the beamline 5B and reported here that we could estimated MLMs for use monochromator elements.

Figure 1(a) shows the experimental and calculated reflectivities of the Mo/Si MLM. A experimental reflectivity of 25.5% at the photon energy of 73eV and a normal incident angle of 40 degree demonstrated in the experimental data (solid curve) and the calculated one (dashed line). Figure 1(b) shows the experimental and calculated reflectivities of the Mo/C MLM. A reflectivities of 11.2% at the photon energy of 101eV and a normal incident angle of 30 degree and the calculated one.

The calculated reflectivity of the Mo/Si MLM showed the same peak energy of around 73eV as experimental one and that of the Mo/C MLM showed almost the same peak energy of around 97eV of the Mo/C MLM. However, the experimental reflectivity of a Mo/Si MLM is about 50.5% of the calculated value (50.5%) and that of a Mo/C MLM is about 85.3% of the calculated one (13.1%). These are because we did not think effects of the interface roughness and diffuseness layers on calculation.

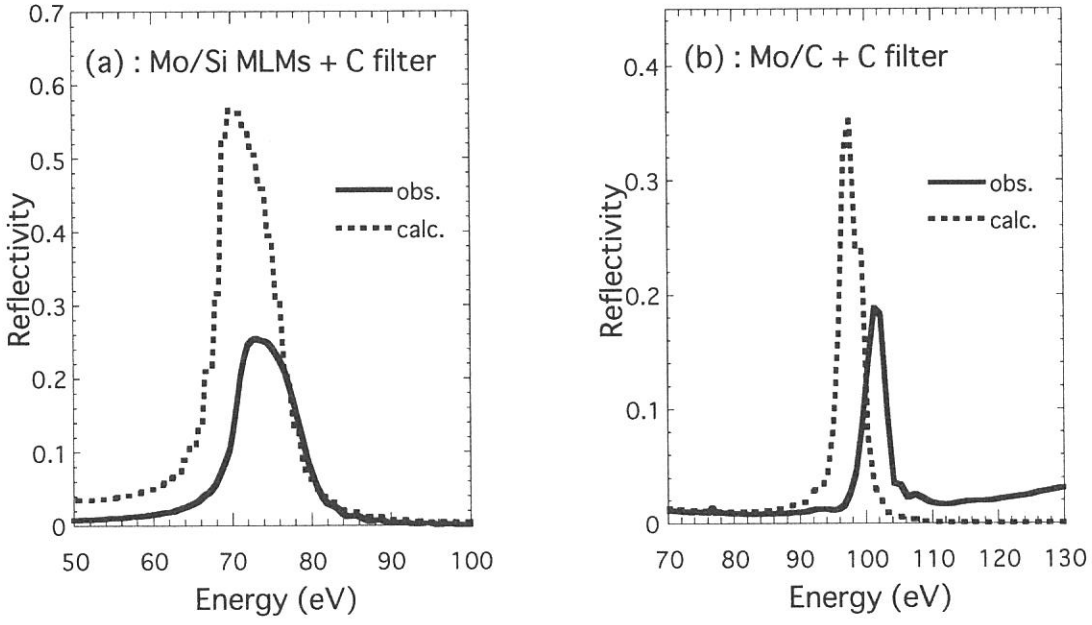

Figure 1 Experimental and calculated reflectivities of the Mo/Si MLM (a) and the Mo/C MLM (b).

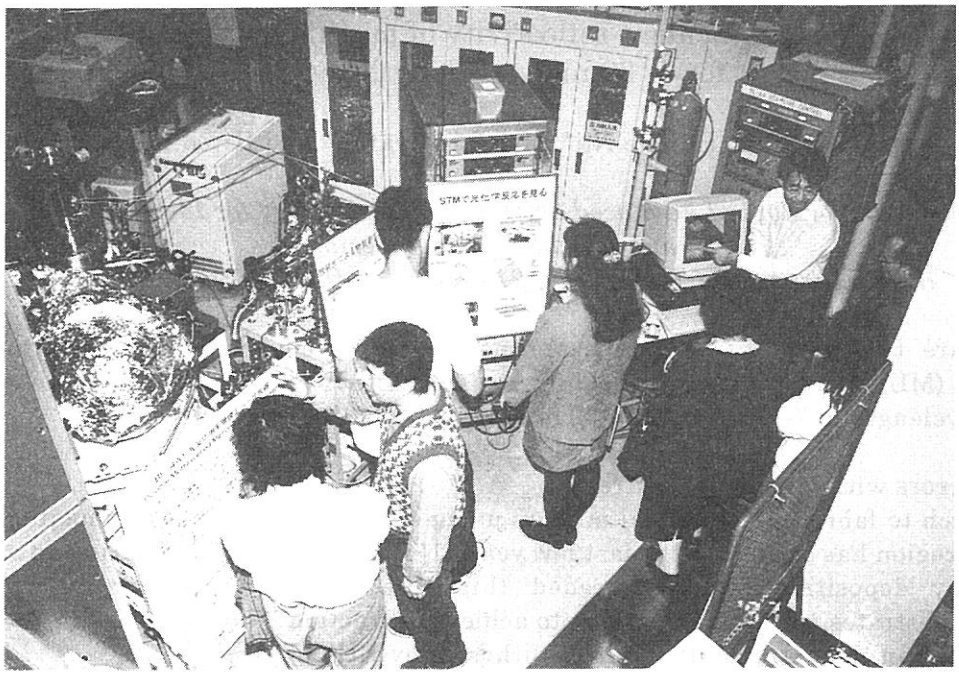

"What's going on BL4A and 4B"

"Open House" on Nov. 15

"Coincidence, that is the question"

"Open House" on Nov. 15

(BL5B)

Normal incident reflectivity of multilayer mirrors for 7- 20 nm wavelength region

Masahito Niibe, Hajime Nii* Atsushi Miyafuji* and Hiroo Kinoshita

Laboratory of Advanced Science and Technology for Industry
*and *Faculty of Engineering,*
Himeji Institute of Technology, 2167 Shosha, Himeji, Hyogo 671-2201

There are two purposes in this experiment. One is measuring reflectivity of Mo/Si multilayer (ML) mirrors with low residual stress. Another is measuring reflectivity of MLs for the wavelength of 7-10 nm and 16-20 nm regions.

I. ML mirrors with low residual stress

A research to fabricate aspherical mirrors using deposition methods for imaging optics in soft X-ray region has started in the last few years[1]. The technology is figuring an aspherical surfaces by depositing laterally graded thin film on a spherical substrates, and it is important to achieve diffraction limit resolution in extreme-ultra-violet lithography(EUVL) optical system. We used ML films instead of single layer films for the deposition films because surface of the ML is very smooth to avoid scattering of X-rays by surface roughness. However the ML typically have a residual stress of 200 MPa (compressive) that is high enough to deform the figure of precision substrates for the imaging optics.

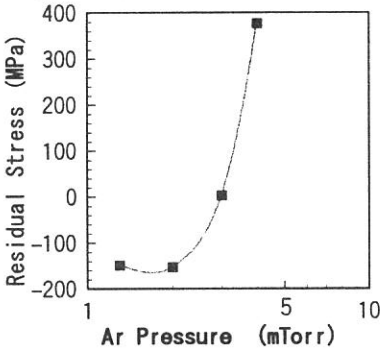

Fig. 1 Stress in Mo/Si MLs

We have been able to reduce the residual stress of the ML films to almost zero by optimizing a deposition condition of rf-enhanced-plasma magnetron sputtering system. Figure 1 shows Ar gas pressure(PAr) dependence of residual stresses in Mo/Si MLs. The residual stress was reduced to zero at PAr=3 mTorr.

We measured normal incidence reflectivity of the MLs prepared under various Ar pressure. The measurement was carried out at BL5B (radiometric calibration beam line) in UVSOR.

The reflectivity spectrum of ML at PAr=3 mTorr is shown in Fig. 2(diamond). The peak reflectivity was over 50% and the value was almost equal to that of the ML with high quality surface deposited at PAr=1.3 mTorr (dotted)[2]. So we concluded that ML in zero stress is not inferior to the ML for high reflectivity.

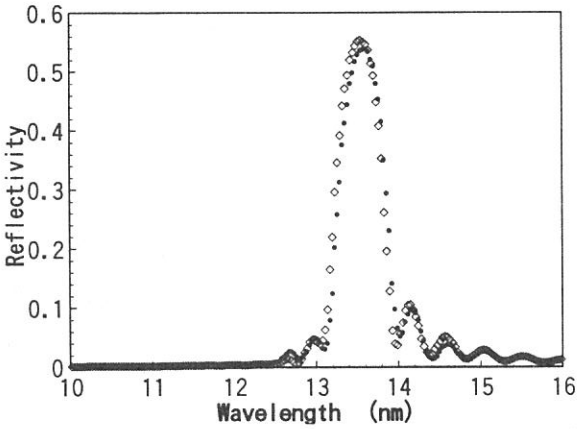

Fig. 2 Reflectivity of Mo/Si MLs deposited at PAr=1.3 mTorr (dotted) and 3 mTorr (diamond).

II. Reflectivities of MLs for the wavelength of 7- 10 nm and 16-20 nm regions.

Mirrors with high reflectivity at normal incidence for the soft X-ray and extreme-ultra-violet(EUV) wavelength regions would be useful for a number of applications, including synchrotron radiation optics. To date, Mo/Si ML mirrors have given the best results in the wavelength region that extends from 12 to 16 nm, and peak reflectivity of 65% at λ =13 nm have been achieved. However, below and above these wavelengths no material pairs have been found that yield comparable results.

Recently, mirrors for the 7-10 nm and 16-20 nm wavelength regions became very important

because of the application in X-ray microscopy and X-ray lasers. A theoretical search has shown that B4C-based MLs, such as Pd/B4C, Rh/B4C and Ru/B4C, and Al-based MLs, such as Mo/Al, could ideally give normal-incidence peak reflectivities ranging from 35% to 52% at λ =7-10 nm and 60% at λ =18.5 nm regions, respectively.

Rh/B4C and Mo/Al ML mirrors were fabricated by rf magnetron sputtering system under different deposition conditions. They were characterized by reflectivity measurements at normal and grazing angle of incidence. Figure 3 shows the reflectivity spectrum of the Rh/B4C ML mirrors measured at 7 - 10 nm wavelength region. Normal-incidence peak reflectivities of 10.5%, 11.2% and 20.2% were obtained at wavelengths of 7.7, 9.2 and 10.3 nm, respectively. Figure 4 shows the reflectivity spectrum of the Mo/Al ML mirror. Normal-incidence peak reflectivities was measured to be 17% at wavelength of 18.5 nm.

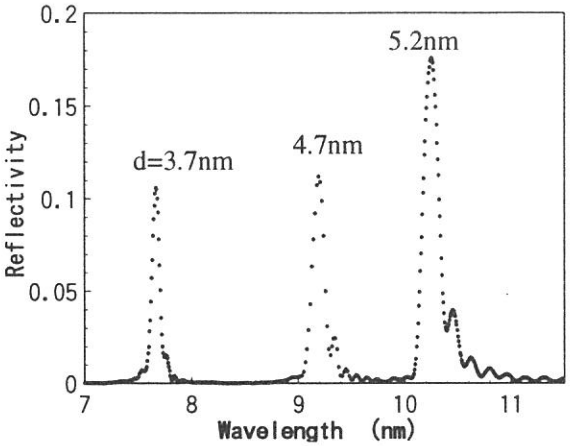

Fig. 3 Reflectivity of Rh/B4C ML mirrors at an angle of incidence of 5 deg.

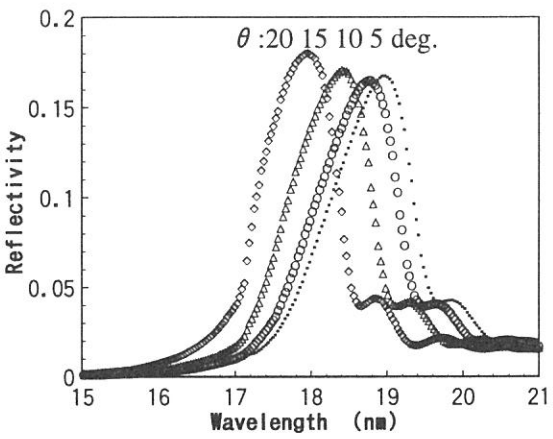

Fig. 4 Reflectivity of a Mo/Al ML mirror at angles of incidence of 5, 10, 15 and 20 deg.

III. Evaluation of higher order lights at BL5B monochromator

X-rays from a grating monochromator contains higher order lights of a grating. Even if suitable filters are used, higher order lights cannot completely be suppressed. In order to evaluate the contributions of higher orders, we measured reflectivity of a ML as function of wavelength.

Figure 5 shows the observed reflectivity of a Rh/B4C ML for wide wavelength range with no filter. Used combination of grating and mirror of the PGM monochromator was G2-M2. Angle of incidence was fixed to 10 deg. The first order Bragg reflection occurs at λ =7.5 nm. Observed reflectivity peaks at longer wavelength are due to the first order Bragg reflection of higher order lights from the grating.

From the result, the ratio of higher order contribution to the first order was estimated to be 0.2 at λ =15 nm.

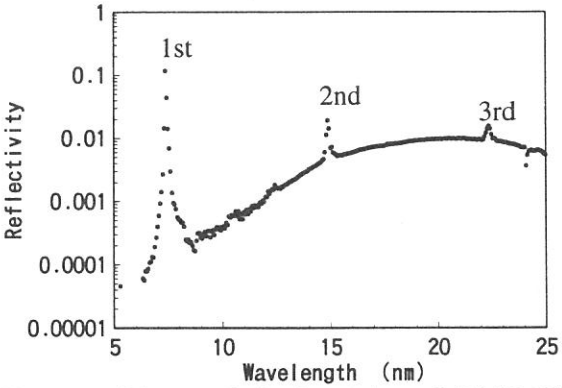

Fig. 5 Observed Reflectivity of Rh/B4C ML for 5-25 nm wavelength region.

[1] M. Niibe et al. : Jpn. J. Appl. Phys., 36 (1997) pp. 7601-7604.
[2] M. Niibe et al. : Rev. Laser Eng., 24 (1996) pp.48-60.

(BL5B)

Development of Novel Soft X-Ray Optics with Oxide Multilayer Structures

Hiroshi Kumagai, Katsumi Midorikawa, Sohachi Iwai[A] and Katsunobu Aoyagi[A]

Laser Technology Laboratory,
The Institute of Physical and Chemical Research (RIKEN),
2-1 Hirosawa, Wako, Saitama 351-0198, Japan
[A] *Semiconductor Laboratory,*
The Institute of Physical and Chemical Research (RIKEN),
2-1 Hirosawa, Wako, Saitama 351-0198, Japan

Development of high-performance normal-incidence multilayer optics for the *water-window* wavelength region between the oxygen and carbon K absorption edges at 2.33 and 4.36 nm, respectively, where water is relatively transmissive and organic materials are absorptive, has been a technical challenge of great interest. The extremely small periods (1.2-2.2 nm) of soft-X-ray reflectors require very rigorous specifications to be met with respect to interface roughness and interlayer mixing, because interface roughness on an atomic scale has a substantial effect on soft-X-ray reflectance. Therefore, the highest reflectance achieved at *water-window* wavelengths has been 3.3%,[1] in spite of the various efforts which have been made in this field. The reason that the reflectances achieved at these wavelengths are so low is that the Fresnel coefficients of materials are so small at these wavelengths that a large number of bilayers must be used, which means that the problems of interface roughness and imperfect interfaces due to interlayer mixing become serious.

The authors have proposed the use of a novel metal oxide multilayer, whose material combination is the same as that used in free electron lasers, for soft-X-ray reflectors at *water-window* wavelengths,[2,3] because an oxide multilayer can prevent the forming of an alloy at the interface, and the absorption of oxygen in oxides is negligible at the *water-window* wavelengths; moreover, the metal oxide multilayer can be fabricated by the atomic layer deposition or atomic layer epitaxy technique. These techniques can be used to control surfaces on an atomic scale by sequentially dosing the surface with appropriate chemical precursors and then promoting surface chemical reactions which are inherently self-limiting. We have found that the self-limiting adsorption mechanism works in the fabrication of oxide thin films such as aluminum oxide and titanium oxide.[4-6]

We report here on reflectance performances of novel metal oxide multilayers of titanium oxide and aluminum oxide using monochromatized synchrotron radiation (SR) from the beamline 5B of the 750-MeV electron storage ring located at the Ultraviolet Synchrotron Radiation Facility (UVSOR).

Figure 1 shows the experimental and calculated results of incidence-angle dependence on reflectances of the aluminum oxide/titanium oxide multilayer fabricated by the atomic layer deposition method of controlled growth with sequential surface chemical reactions. A high reflectance (s-polarization) of 33.4% at the wavelength of 2.734 nm and an incident angle of 71.8° from the normal incidence are

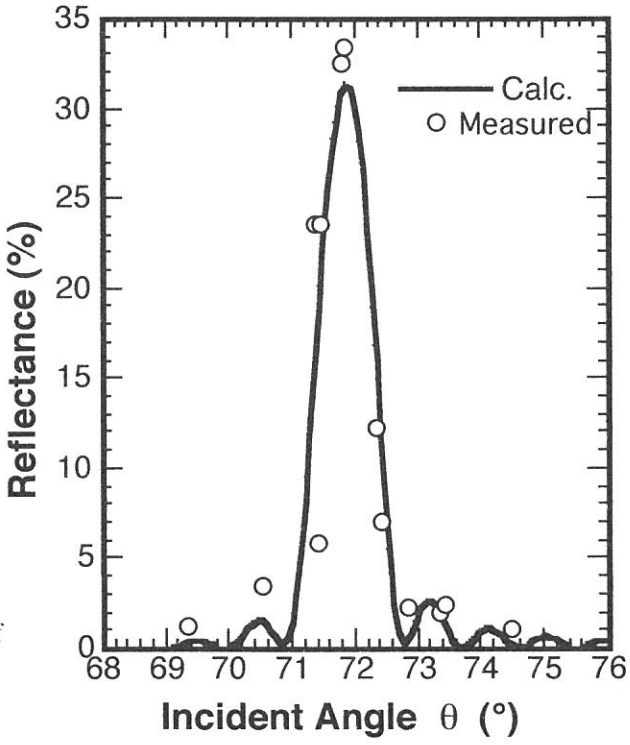

Figure 1 Experimental and calculated results of incidence-angle dependence on reflectances of the aluminum oxide/titanium oxide multilayer.

demonstrated in the experimental plots, which were obtained using the monochromatized SR. The calculated reflectance (solid line) shows almost the same reflectance of around 32% as the experimental one. Full width of the half maximum of the reflectance at 71.8° is about 1.0°.

Figure 2 shows the experimental and calculated profiles of reflectances of the aluminum oxide/titanium oxide multilayer fabricated by the atomic layer deposition method of controlled growth with sequential surface chemical reactions. Although the bilayer thickness is as short as 2.6nm and the period is 40, high reflectance (s-polarization) of 15.8% at the wavelength of 2.734 nm and an incident angle of 58.5° from the normal incidence are demonstrated in the experimental plots. The calculated reflectance (dashed line) shows a reflectance of 20.3%. The descrepency between experimental and calculated reflectances arises from the surface and interface roughnesses.

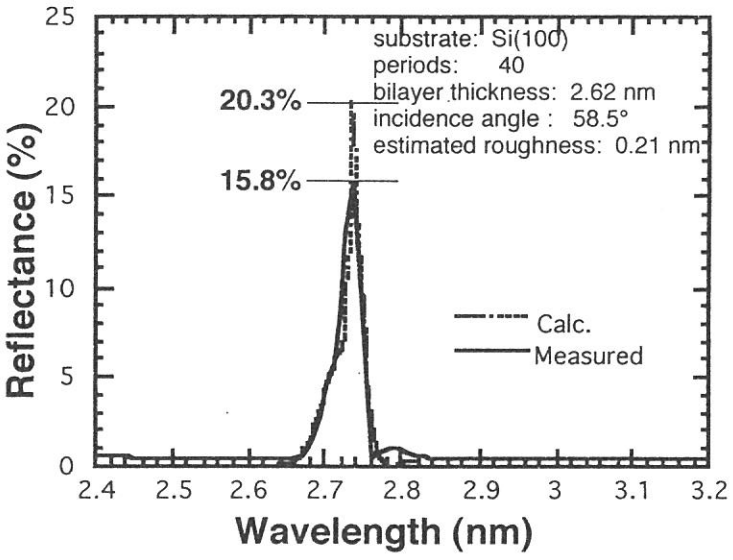

Figure 2 Eexperimental and calculated profiles of reflectances of the aluminum oxide/titanium oxide multilayer.

This work was supported by the Joint Studies Program (1997) of the Institute for Molecular Science.

References

1) I. V. Kozhevnikov, A. I. Fedorenko, V. V. Kondratenko, Yu. P. Pershin, S. A. Yulin, E. N. Zubarev, H. A. Padmore, K. C. Cheung, G. E. van Dorssen, M. Roper, L. L. Balakireva, R. V. Serov and A. V. Vinogradov, Nuclear Instruments and Methods in Physics Research **A 345**, 594 (1994).
2) H. Kumagai, K. Toyoda, K. Kobayashi, M. Obara and Y. Iimura, Appl. Phys. Lett. **70**, 2338 (1997).
3) H. Kumagai, M. Matsumoto, Y. Kawamura, K. Toyoda and M. Obara, Jpn. J. Appl. Phys. **33**, 7086 (1994).
4) H. Kumagai, K. Toyoda, M. Matsumoto and M. Obara, Jpn. J. Appl. Phys. **32**, 6137 (1993).
5) H. Kumagai and K. Toyoda, Appl. Surf. Sci. **82/83**, 481 (1994).
6) H. Kumagai, M. Matsumoto, K. Toyoda, M. Obara and M. Suzuki, Thin Solid Films **263**, 47 (1995).

(BL5B) **X-ray phase compensation in multi-periodic structure; strict reflection-wavelength control method for short periodic multilayer mirrors**

Masashi Ishii, Sohachi Iwai, Tatzuo Ueki and Yoshinobu Aoyagi
The Institute of Physical and Chemical Research (RIKEN), Wako-shi Saitama 351-0198

The shortening of the reflection wavelength of multilayer mirrors, is an important requirement for future X-ray applications.[1-4] Recently, atomic layer epitaxy (ALE) has been adopted to produce X-ray multilayer mirrors[5]. In ALE, since the epitaxial growth is automatically stopped at 1 monolayer (ML) due to a 'self-limiting mechanism',[6-9] ALE has great potential for the realization of the short period multilayer optics with atomically abrupt interfaces. But despite this, the reflection wavelengths of multilayer mirrors fabricated by ALE becomes discrete, since the periodic length is discrete according to the layer-by-layer growth. In this report, we describe a new wavelength control method using a phase compensation in multi-periodic structure[10]. Reflection properties of multi-periodic structure produced by metalorganic vapor phase epitaxy (MOVPE) indicate that this method enables us to design the X-ray mirror with a selectable reflection wavelength by combination of layer-by-layer grown of films with various periodic lengths.

The concept of the multi-periodic structure to control the reflection wavelength shown in Fig. 1 is an example of the multi-periodic mirror with the reflection wavelength halfway between reflection wavelength of $(AlP)_2(GaP)_2$, $\lambda_{2,2}$, and that of $(AlP)_3(GaP)_2$, $\lambda_{3,2}$. Fig. 1 (a) and (c) indicate normal periodic structures of $(AlP)_2(GaP)_2$ and $(AlP)_3(GaP)_2$, with periodic length of $d_{2,2}$ and $d_{3,2}$, respectively. In the case of (a), the X-ray phase is same after passing through $d_{2,2}$ as shown by the closed circles, so that X-rays reflected at interfaces constructively interfere, resulting in an overall reflection at the wavelength, $\lambda_{2,2}$. Similarly, the X-ray with $\lambda_{3,2}$ is reflected in the case (c). In contrast with these structures, Fig. 1 (b) shows the multi-periodic mirror, in which the 1 period is composed of two parts, $d_{2,2}$ and $d_{3,2}$. Although the X-ray with the wavelength of $(\lambda_{2,2} + \lambda_{3,2})/2$, has a phase lag after passing through the period $d_{2,2}$ as shown by the open circle, it reverts to the same phase as initial one at the end of the next $d_{3,2}$ period. Thus the $d_{3,2}$ compensates the phase lag of $d_{2,2}$. This phase compensation results in X-ray diffraction, and an X-ray mirror at $(\lambda_{2,2} + \lambda_{3,2})/2$ may be realized. For the sake of convenience, this multi-periodic structure, $[(AlP)_2(GaP)_2]_1[(AlP)_3(GaP)_2]_1$ is represented by $(2,2)_1(3,2)_1$ in the following discussion. Fig. 2 indicates the calculated reflectivity of $(2,2)_1(3,2)_1$, along with those of $(AlP)_2(GaP)_2$ and $(AlP)_3(GaP)_2$. A sharp reflection peak midway of $\lambda_{2,2}$ and $\lambda_{3,2}$, is clearly seen with no other reflection signal obtained in this wavelength range. Fig. 3 is an amplitude reflectance of $(2,2)_1(3,2)_1$ calculated at $(\lambda_{2,2} + \lambda_{3,2})/2$. As shown in this figure, zigzag interface phase caused by the two periodic lengths is observed. This zigzag phase indicates that the X-ray phase is compensated at the interface, agreeing with the qualitative explanation in Fig. 1 (b). Since this concept does not depend on optical constants, if multilayer mirrors with other more optically favorable materials can be fabricated by ALE, a similar discussion will be applied to new materials.

In order to discuss actual phase compensation properties, the multi-periodic structure is fabricated by using MOVPE system which has a cold-wall-type horizontal quartz reactor with a RF heating system. Tertiarybutylphosphine (TBP) was used as the group-V source gas. Triethylgallium (TEG) and dimethylaluminum hydride (DMAH) were alternatively introduced into the growth chamber for the growth of GaP and AlP, respectively. The periodic length is controlled by variation of the TEG feeding time. The substrates were (100)-oriented nondoped GaP which were chemically treated in $(NH_4)_2S_x$ solution. The X-ray reflectance was measured using monochromatized synchrotron radiation (SR) from the 750 MeV electron storage ring located at the Ultraviolet Synchrotron Radiation Facility (UVSOR).

Fig. 4 (b) indicates the reflection propertiy of the multi-periodic structure in which the 1 period is composed of two AlP/GaP layers with different thickness of 2.3 and 3.0 nm. Note that the difference of these periodic lengths is only a few monolayers. The reflectance of normal AlP/GaP multilayer structures with single periodic lengths of (a) 2.3 nm, (c) 3.0 nm and (d) 5.3 m, is also shown in this figure. These reflectance are normalized by that of the

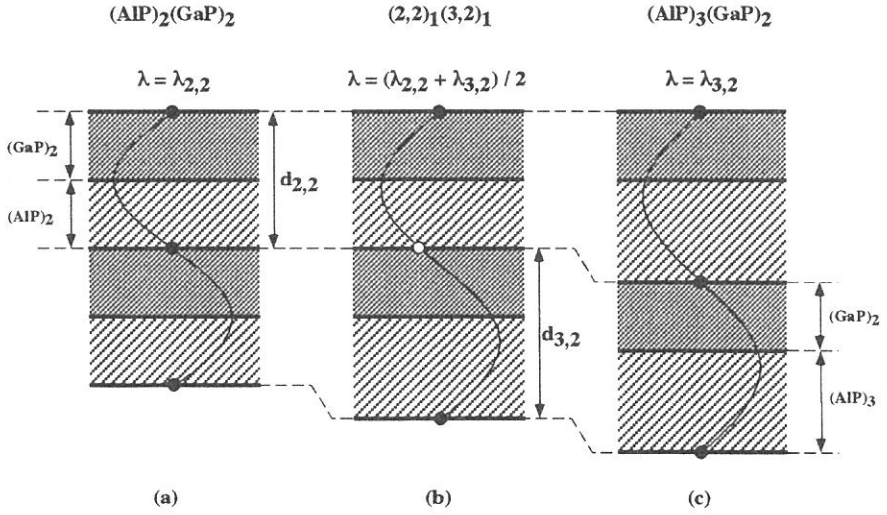

Fig. 1 The concept of the multi-periodic structure to control the reflection wavelength

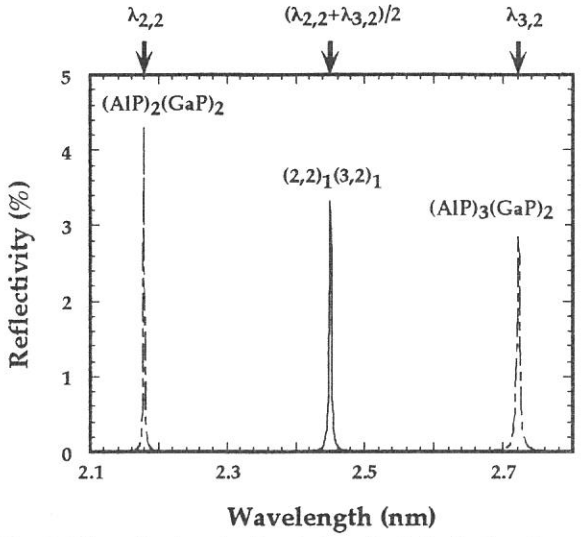

Fig. 2 The calculated reflectivity of $(2,2)_1(3,2)_1$, along with those of $(AlP)_2(GaP)_2$ and $(AlP)_3(GaP)_2$

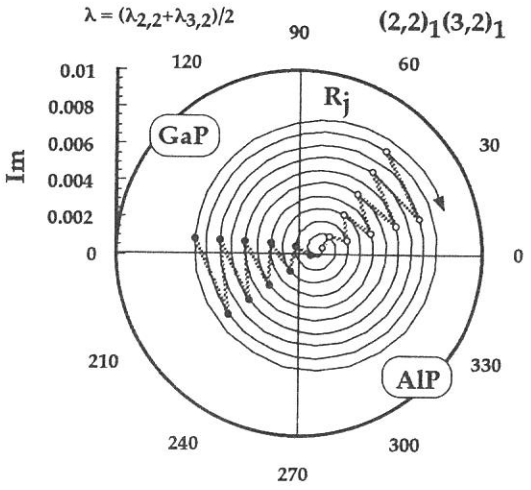

Fig. 3 The amplitude reflectance of $(2,2)_1(3,2)_1$ calculated at $(\lambda_{2,2} + \lambda_{3,2})/2$

multi-periodic structure. The incidence angle is fixed at 27° . A reflection peak midway of (a) and (c) caused by the phase compensation is clearly observed. Moreover, the reflection loss by this compensation is quite low, so that it acts just as a normal multilayer mirror with the middle periodic length of (2.3 + 3.0)/2. On the other hand, the reflectance of (d) caused by $2d \sin\theta = 2\lambda$ is low, indicating that the reflection of the multi-periodic structure is essentially different from the higher order diffraction. The comparison of X-ray phase between the multi-periodic reflection and higher order diffraction was discussed in another paper[10]. The reflection wavelength of the multi-periodic mirror is determined by the combined ratio of the periodic layers. Based on this simple combination rule, a strict reflection wavelength control without the interface roughness is expected to be realized by multi-periodic structures fabricated by ALE.

In summary, an X-ray phase compensation as a new reflection wavelength control method for layer-by-layer controlled multilayer mirrors is proposed. The phase compensation is clearly observed in reflection properties of multi-periodic structure produced by MOVPE. The multi-periodic structures fabricated by ALE are expected to act as short-wavelength x-ray mirrors without interface roughness.

[1] D. G. Stearns, R. S. Rosen and S. P. Vernon: Opt. Lett. 16, 1283 (1991).
[2] J. F. Seely, G. Gutman, J. Wood, G. S. Herman, M. P. Kowalski, J. C. Rife and W. R. Hunter: Appl. Opt. 32, 3541 (1993).
[3] C. Montcalm, B. T. Sullivan, M. Ranger, J. M. Slaughter, A. Kearney, C. M. Falco and M. Chaker: Opt. Lett. 19, 1004 (1994).
[4] I. V. Kozhevnikov, A. I. Fedorenko, V. V. Kondratenko, Y. P. Pershin, S. A. Yulin, E. N. Zubarev, H. A. Padmore, K. C. Cheung, G. E. van Dorssen, M. Roper, L. L. Balakireva, R. V. Serov and A. V. Vinogradov: Nucl. Instr. and Meth. in Phys. Res. A345, 594 (1994).
[5] M. Ishii, S. Iwai, T. Ueki and Y. Aoyagi: J. Cryst. Growth 180, 15 (1997).
[6] J. Nishizawa: J. Electrochem. Soc. 132, 1197 (1985).
[7] Y. Aoyagi: J. Vac. Sci. Technol. B5, 1460 (1987).
[8] M. Ishii, S. Iwai, T. Ueki and Y. Aoyagi: Appl. Phys. Lett. 71, 1044 (1997).
[9] M. Ishii, S. Iwai, T. Ueki and Y. Aoyagi: Thin Solid Films (in press).
[10] M. Ishii, S. Iwai, T. Ueki and Y. Aoyagi: Appl. Opt. 36, 2152 (1997).

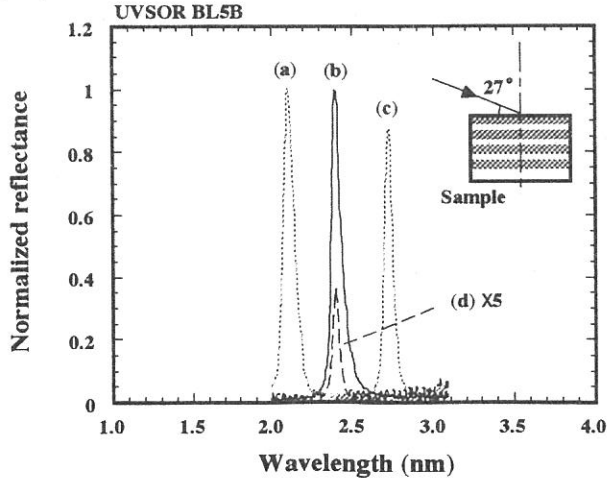

Fig. 4 Reflectance of various samples produced by MOVPE. The periodic lengths are (a) 2.3, (c) 3.0 and (d) 5.3 nm. (b) is the multi-periodic structure in which the 1 period is composed of two AlP/GaP layers with different thickness of 2.3 and 3.0 nm.

(BL5B)

High Quality XUV Multilayer Mirror for XUV Doppler Telescope Aboard Sounding Rocket

Saku TSUNETA, Taro SAKAO, Hirohisa HARA, Toshifumi SHIMIZU,
Ryouhei KANO, Tsuyoshi YOSHIDA[1], Shin'ichi NAGATA[1],
Ken KOBAYASHI[1]

National Astronomical Observatory, 2-21-1 Osawa, Mitaka, Tokyo, 181, Japan
[1] *Department of Astronomy, School of Science, The University of Tokyo, Bunkyo-ku, Tokyo, 113, Japan*

We have been developing the high-quality XUV multilayer mirrors for the XUV telescope aboard the ISAS sounding rocket experiment over 3 years. The telescope consists of a Cassegrain multilayer optics with an X-ray CCD camera. The mission is (1) to obtain single temperature (1.8 MK) X-ray images of the Sun by isolating the specific emission line [Fe XIV line (211.3Å)], and (2) to obtain the Dopplergram of the solar corona with two normal incidence telescopes, whose peak wavelengths are slightly (about 2Å) shifted toward red and blue from the line. (The line moves in between the blue and red windows of the multilayer mirrors due to the motion of the plasma, and the velocity map of the 1.8MK plasma is obtained by subtracting the blue from the red images.)

In order to improve the detection limit of the velocity fields, and to avoid the contamination from the nearby emission lines, we need to develop a high-wavelength resolution mirror ($\lambda/\Delta\lambda \sim 40 - 50$) tuned for the 211Åline. Such a high wavelength resolution is realized by increasing the number of the layer pairs contributing to the reflectance, *ie* by selecting less-absorbing materials for both the reflector and the spacer, and by decreasing the thickness of the reflector. We have successfully developed the MoSi/Si multilayer mirror with system (two mirrors) wavelength resolution as high as 47 (Figure 1).

The multilayer coated on the large-area mirror inherently has large non-uniformity in the wavelength of the reflectivity peak owing to the radius-dependent distance from the sputtering source. This must be corrected with an accuracy of a few times 0.1Åover 15 cm diameter. We have measured the non-uniformity of the large-area sample mirror with UVSOR, and made a more uniform mirror with the correcting mask designed on the basis of the measurement. This iteration was repeated several times. The final uniformity is exceptionally good, and is within 0.1Åover the distance (Figure 2).

We have also developed the anti-reflection layer (light-trap) to the MoSi/Si mirror for the intense (X100) HeII line at 304Å. Fig. 1 also shows the sharp peak at 211Å, and the anti-peak near 304Å. The quantum efficiency of the flight CCD camera is also measured with UVSOR. Figure 3 shows the excellent performance of the Site back-illuminated CCD.

References (published in FY1997):

Hara, H., Kano, R., Nagata, S., Sakao, T., Shimizu, T., Tsuneta, S., Yoshida, T., Kosugi, K., XUV Doppler Telescope with multilayer optics, Proc. SPIE, Grazing incidence and multilayer X-ray optics, 3113, 420–429, 1997.

Ishiyama, W., Murakami, K., Tsuneta,S., Sakao, T., Hara, H., Shimizu, T., Yoshida, T., Nagata, S., Kano, R., Fabrication of multilayer mirrors for the XUV Doppler telescope for solar corona observation, Proc, The 4th International Conference on The Physics of X-Ray Multilayer Structures, in press, 1998.

Nagata, S., Hara, H., Sakao, T., Shimizu, T., Tsuneta, S., Yoshida, T., Ishiyama, W., Murakami, K., Oshino, T., Development of the multilayer mirrors for XUV Doppler telescope, Proc. SPIE, Grazing incidence and multilayer X-ray optics, 3113, 193–201, 1997.

(BL5B)

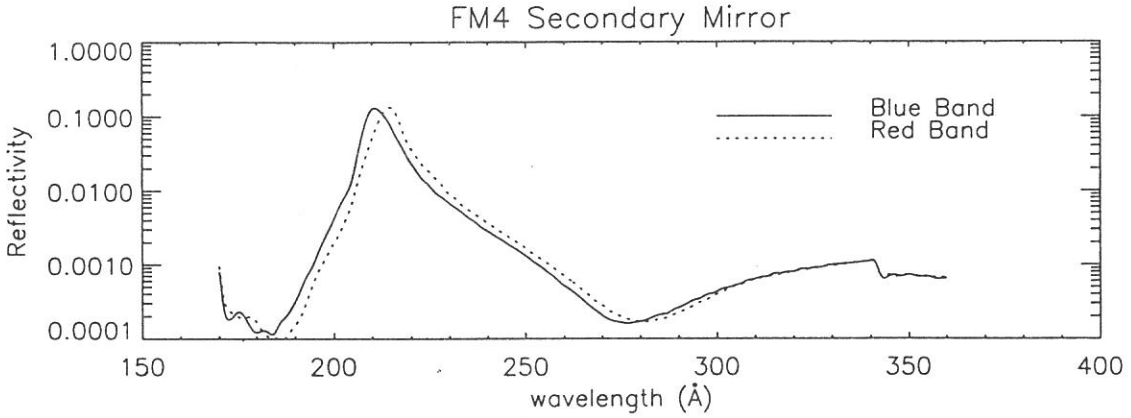

Figure 1: Measured reflectivity profile of the flight MoSi/Si (Γ =0.2) primary mirror. The secondary mirror has similar profile. The anti-peak around 304Åis due to the light-trap (single Si layer) to absorb the intense HeII line at 304Å, which is hazardous for the observation.

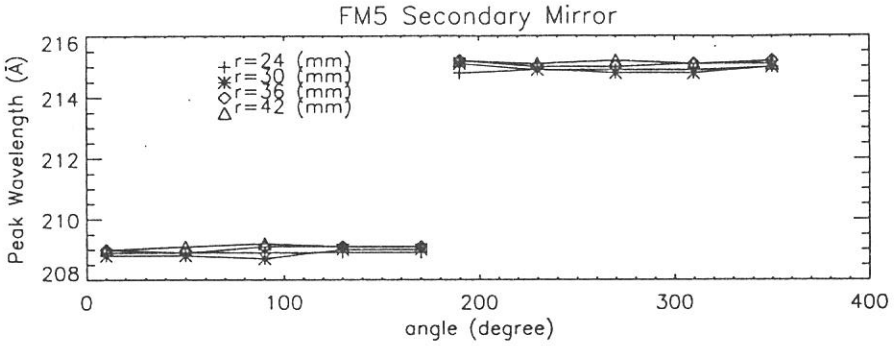

Figure 2: Exceptionally good uniformity of the flight mirror: peak wavelength as a function of the azimuth angle for various radius. The uniformity is within 0.1Å. The half of the mirror corresponds to the red passband, and the other half to the blue passband.

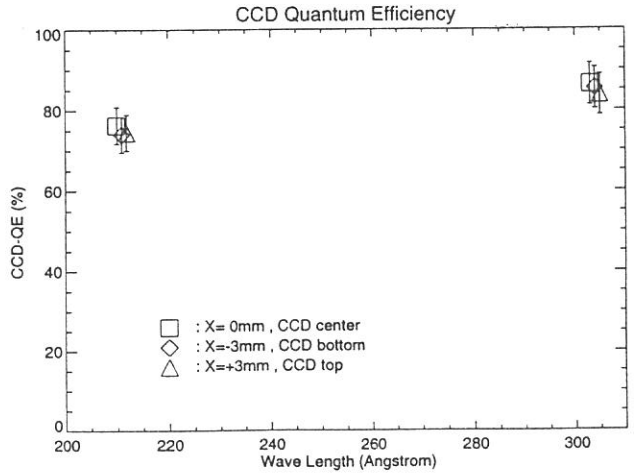

Figure 3: Quantum efficiency of the flight CCD camera measured with UVSOR. The CCD used here is the Site back-illuminated 512X512 CCD. The data shows the excellent performance of the CCD in XUV wavelengths.

(BL5B)

The Calibration of the eXtreme Ultra-Violet Scanner (XUV-S)

Masato Nakamura [A], Yoshiyuki Takizawa [A], Ichiro Yoshikawa [A],
Atsushi Yamazaki [A], Kei Shiomi [A] and Hiroko Hayashi [A]

[A] *Faculty of Earth and Planetary Science, University of Tokyo, Bunkyo-ku, Tokyo 113-0033*

Planet-B will be launched in July 1998 to the Mars and our designed eXtreme Ultra-Violet Scanner (XUV-S) is on board. The scanner will observe the resonantly scattered emissions of He atoms and He ions, HeI (584Å) and HeII (304Å) respectively, and analyze the distribution of He atoms and He ions in the plasmasphere of the Earth and the Martian atmosphere. The scanner consists of a thin metal filter, a multi-layer coated mirror and micro channel plates (MCPs) with CsI coating. The purpose of this our experiment at UVSOR is to measure the transmittance of the filter and the reflectivity of the mirror in the extreme ultra-violet region, especially at HeII (304Å).

From our last experiment result at UVSOR we know that the line of the grating and mirror setting for 304Å considerably contain the higher-order lines, for example the second order of 152Å. Therefore it is the first purpose that a pure 304Å line is guided into the chamber for calibration. For the reduction of the higher-order lines the guided line is transmitted a filter which has a very low transmittance only in the wavelength region of higher-order lines. Materials having the character are Aluminum and Magnesium. Al has very low transmittance below 170Å, and Mg below 250Å. So we use an Al/Mg filter for the purpose. The beam transmitted through an Al/Mg filter is guided into the chamber and grazed by using our grating on the center of the goniometer. Incident angle is 45 degree, and our detector is rotated and observes the grazed lines (Fig.1). The center spot of Fig.1 is the zero-order line, and both side spots are the plus and minus first order 304Å line. If there is a contamination of a higher-order line, a spot between the center and the side spots should be observed. But it is not showed on Fig.1, therefore the beam through an Al/Mg consist of only 304Å and is enough pure for our purpose. We consider this pure 304Å beam as the direct one and measure the transmittance of the filter and the reflectivity of the multi-layer coated mirror.

The filter for XUV divides two parts: the half consists of Al, the other half Al/C. Though the transmittance of Al for 304Å and 584Å are the same order, the transmittance of C for 304Å is much more than for 584Å. Therefore the part of the Al filter measures both HeI and HeII, and the part of the Al/C filter measures HeII. During the measurement of the transmittance, the detector MCPs for experiments is set on the place to detect directly the pure 304Å beam and the filter is set to interrupt the beam or not to. Alternately MCPs detect the transmitted beam and the pure direct beam, and the rate of the counts is the filter transmittance. The transmittance depended on wavelength (200 500Å) by using the GM35 of the goniometer is shown in Fig.2. The solid circle shows the transmittance of the Al/C filter, the open circle shows the Al filter and the solid and dash line shows the simulation value of the Al/C and Al filter respectively. Below 340Å the obtained shape of the transmittance is consistent with the simulation value, but over 340Å the difference between the measurement and the simulation value. It is thought that this is because the higher-order line is contaminated.

The mirror reflectivity is measured by using a photo diode because the MCPs have the dependence of the sensitivity on a incident angle of a beam. Also the reflected beam and the pure direct beam is detected by the photo diode, and the rate of the output current is the reflectivity. The dependence of the reflectivity on the wavelength (150 600Å) is measured by using the GM35, and shown in Fig.3. The

peak of the reflectivity is shown at the wavelength of 304Å, and it is shown that the coated multi-layer of the mirror is very well.

It is the future work to estimate the effect of the higher-order line and to measure the transmittance and the reflectivity at 584Å.

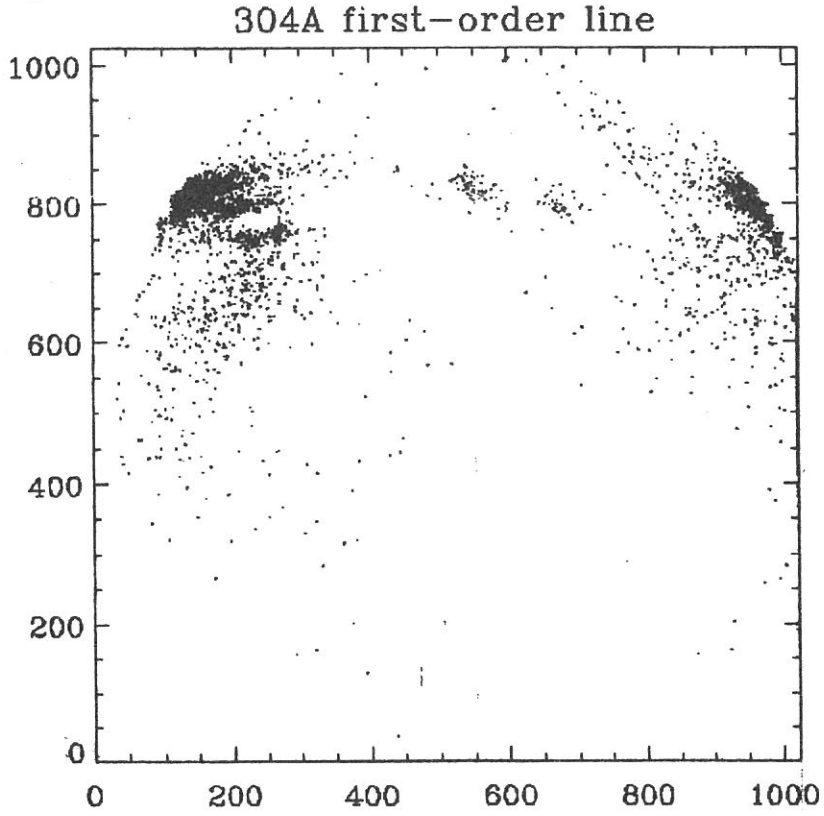

Fig.1 The line transmitting Al/Mg filter. The grazed line by using our grating consist only of 304Å, because no spot appears between the zero-order spot and the plus and minus first-order spot.

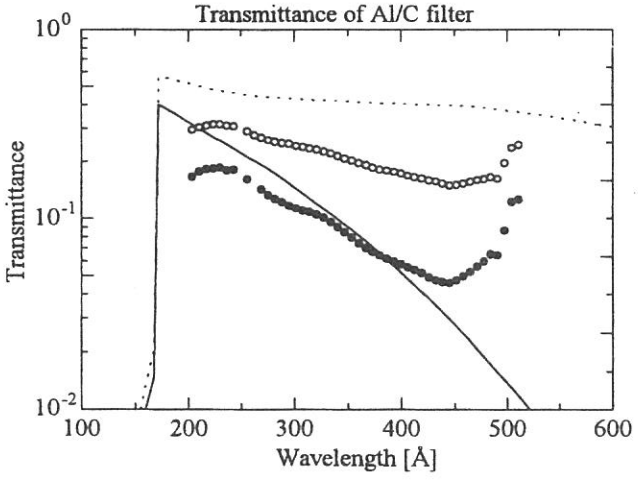

Fig.2 The transmittance of the filter Al and Al/C for XUV-S. The solid and open circle shows the transmittance of the Al and Al/C part of the filter, respectively.

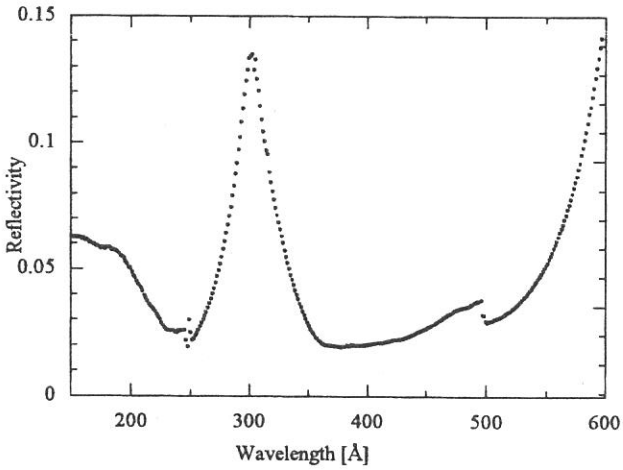

Fig.3 The reflectivity of the multi-layer coated mirror for XUV-S. The peak of the reflectivity is shown at the HeII emission (304Å).

(BL6A1)

Infrared magnetic circular dichroism experiment using synchrotron radiation

Shin-ichi KIMURA

UVSOR Facility, Institute for Molecular Science, Okazaki 444-8585

In vacuum-ultraviolet (VUV) and x-ray regions, synchrotron radiation (SR) is well known to be one of powerful light sources for the investigation of electronic and crystal structures of materials. The main reason is that there had been no continuous light source in their regions before. Recently, not only the high brightness of SR but also the good linear and circular polarizations is conventionally used because polarizations give us new informations.

In the infrared region, on the other hand, there are several continuous light sources using blackbody nature. The intensity is comparatively strong but the brightness is not so high. Since SR is much higher brightness than such ordinary light sources, infrared synchrotron radiation (IRSR) has been used for the investigation of optical properties of small size material and surface vibration. Recently, more than ten beam lines for IRSR are working or under construction. Almost all the beam lines are planned to do experiments of infrared microscopy and imaging [1]. IRSR has become a new field of SR science.

Another features of IRSR are polarization properties. Ordinary light sources have no polarization. Then linear polarizer and 1/4-lambda plate are needed to make linear and circular polarizations. Therefore the available energy range is limited by the optical elements. On the other hand, SR has polarization in itself. Therefore SR with linear or circular polarizations can cover wide energy range without optical elements. This is a useful property for the investigations of electronic structure near the Fermi level and

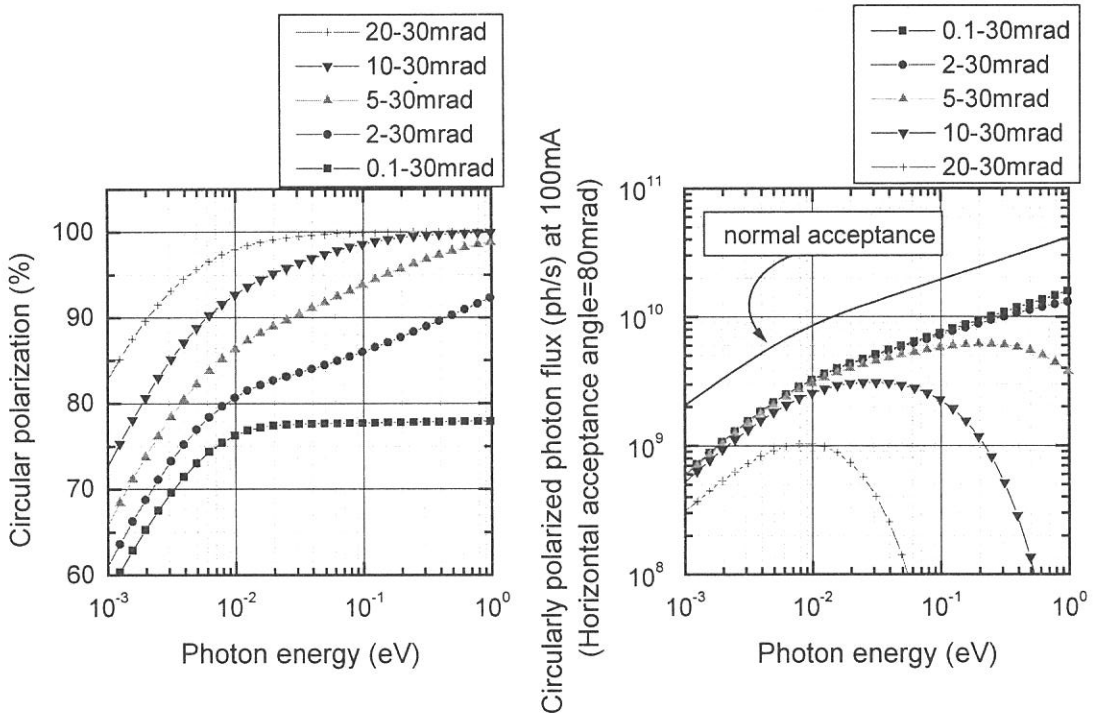

Fig.1. Expected circular polarization and circularly polarized photon flux of BL6A1 in several acceptance angles.

of the TO phonon band with circular dichroism.

According to the consideration, circular polarization and the effective intensity of IRSR from an infrared beam line, BL6A1, of UVSOR were calculated. The results are shown in Fig. 1. The vertical acceptance angle of BL6A1 is ±30 mrad. The acceptance angle is much larger than that of other VUV beam lines in UVSOR (typically ±4 mrad). The large acceptance angle gives us high circular polarization and high intensity in infrared region. The circularly polarized IRSR can be used in the energy range of 7 meV - 2 eV because it is limited by transmittance of beam splitters of a Michelson interferometer as mentioned below. Since the acceptance angle of 5 - 30 mrad is usually taken during circular polarization experiments, the polarization should be higher than 80 % and the intensity should be less than half of the case of normal experiment. Therefore we can use sufficient circular polarization and sufficient intensity in the photon energy range of 7 meV - 2 eV, which is available energy range at BL6A1.

Using the circularly polarized IRSR, the measurement of infrared magnetic circular dichroism (IRMCD) has been started. The main purpose is to investigate the coupling between carriers and magnetic moments of strongly correlated electron systems. The experimental setup is shown in Fig. 2. The optical system using the superconducting magnet is the infrared magneto-optical apparatus, which was constructed in the last fiscal year [2]. A Michelson-type FTIR interferometer (Bruker IFS66v) is used when the IRMCD experiment is done. There is a knife-edge depicted in Fig. 2 on the light pass to the interferometer. The upper or lower part of IRSR from UVSOR is picked up by the knife-edge and is derived to the interferometer. The light is guided to a sample mounted at the center of a superconducting magnet and to a detector by plane and parabolic mirrors. There are a lot of mirrors and one beam splitter. However the circular polarization of light was confirmed to be over 70 % at the detector position.

We measured IRMCD spectra of absorption of magnetic exciton of GdAs for instance. The results are presented in this issue [3].

References

[1] (e.g.) S. L. Hulbert and G. P. Williams, Sync. Rad. News **10**-1 (1997) 16.

[2] S. Kimura, UVSOR Activity Report 1996 (1997) p. 170.

[3] S. Kimura, D. X. Li, Y. Haga and T. Suzuki, in this issue.

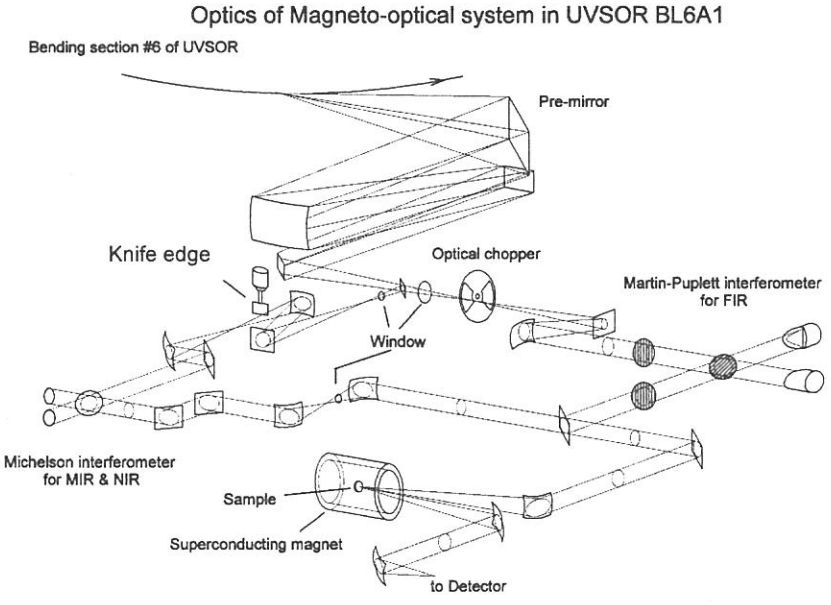

Fig. 2. Optical system of infrared magnetic circular dichroism measurement using SR at BL6A1.

(BL7A)

Focusing mirror system of the double crystal monochromator beamline BL7A

Toyohiko KINOSHITA, Tokuo MATSUKAWA[1] and Hiroaki YOSHIDA[2]

Institute for Molecular Science, Myodaiji, Okazaki 444-8585, Japan

[1]Department of Physics, Naruto University of Education, Naruto 772-8502, Japan

[2]Department of Material Science, Faculty of Science, Hiroshima University, Kagamiyama 1-3-1, Higashi-Hiroshima 739-8526, Japan

Since the first commissioning of the double crystal monochromator (DXM) beamline BL7A[1], the soft x-ray light from this beamline has been widely used by many users and been very invaluable for solid state spectroscopy. However, in recent few years, there exist some requirements concerning to the improvements of the beamline from the users. In order to satisfy the user's requirements and to get higher performance of the beamline, several improvements are now in progress, for example, renewing the computer control system, reconstruction of the big flange of the DXM chamber for easier exchange of the monochromator crystals, the use of YB_{66} monochromator crystal[2], installation of a wire beam monitor for easier alignment of the beamline and so on. The installation of the focusing mirror system is one of the big project among the improvements.

To provide higher photon flux in higher than 1keV photon energy region at BL7A, the superconducting magnet wiggler is installed in the straight section of the upper stream of the bending magnet section B7[3]. The wiggler is a wavelength shifter type and covers relatively higher photon energy range than normal bending magnet radiation. We use both the wiggler radiation and bending magnet radiation. When the higher energy light is used from the wiggler with crystals such as InSb(111) and Ge(111), the beam line is fixed just to the down stream of the straight section (0° line). In the case to use the SR from the bending section, the DXM accepts SR emitted at the point on the electron orbit downstream by 2° from the edge of the bending section. In order to avoid radiation damage to the insulator crystals such as beryl and quartz, we use the bending magnet radiation. The light of the photon energy rage from 1keV to 2keV is provided. Between the user's times of the wiggler radiation and the bending radiation, we have to exchange the beam line set up from 0° line to 2° line. Due to this exchange procedure, much beam time and much performance of the beamline have been lost.

In order to solve above problem, we designed the mirror system. The schematic drawing of the mirror system is shown in Fig. 1. Two pairs of the mirror system (total 4 mirrors) are installed in the chamber. The parameter value of each mirror is described in Table I. The "pair 1" and "pair 2" can be easily exchanged *in situ*. The system is installed in the downstream of the front end and the upper stream of the DXM chamber. The wiggler radiation is directly introduced to the straight line and reflected by one pair of the focusing mirrors to the vertical way. The output light comes out to the same direction as that of the incident light, but the height is 8mm higher. When we use the "pair 1", the higher energy light than 1.8keV will be reduced to less than 10% because of low reflectivity of Si in this condition. To cover the higher energy region, another "pair 2" coated by Cr will be used, which will show no structures in throughput spectrum at 700-5000eV region. The idea to reduce higher energy component of the light is similar to that reported in Ref. 4. The result of the ray tracing at the sample position for the "pair 2" system is shown in Fig. 2. The ray tracing was performed for the light of λ =15 Å. The result for the "pair 1" mirror is almost similar. As an option for the trouble of the wiggler itself, a port for the radiation from the bending magnet is also equipped.

By using this system, we may not need to move the beamline from the 0° line to 2° line . Higher photon flux and smaller spot size than the present ones can also be expected in conjunction with the wiggler radiation. It is expected that the reduction of the high energy component such as the glitches observed in the YB_{66} throughput[2] will become possible, when we use the pair of Si coated mirrors. These will give us a lot of advantages to perform soft x-ray spectroscopy measurements.

Acknowledgements

Authors would like to thank to the staff members of the UVSOR facility for the support.

References

1) T. Murata et al., *Rev. Sci. Instrum.* **63**(1992)1309.
2) T. Kinoshita et al., *J. Synchrotron Radiation*, in press: *UVSOR Activity Report* (1996) p. 198.
3) E. Nakamura et al., *J. Electron Spectrosc. Relat. Phenom.* **80** (1996) 421.
4) G. M. Lamble, *Rev. Sci. Instrum.* **66** (1995) 1422.

Table I. Parameters of the focusing mirror system. The substrate of the mirrors are quartz. M2 mirrors are located at 4900mm down stream from the center of the wiggler. These parameter values are for the focusing the beam to 8900mm down stream from the wiggler.

	coating	size	Incidence angle	Radius of the cylindrical mirror M1 for sagittal focusing	Radius of principle axes of the elliptic mirror M2 for meridional focusing
pair 1	Si	400(l)x35(w)x50(t) mm^3	89°	R=77.4(mm)	a=4450.07 (mm) b=77.27(mm)
pair 2	Cr	700(l)x35(w)x50(t) mm^3	89.5°	R=38.8(mm)	a=4450.03 (mm) b=38.63(mm)

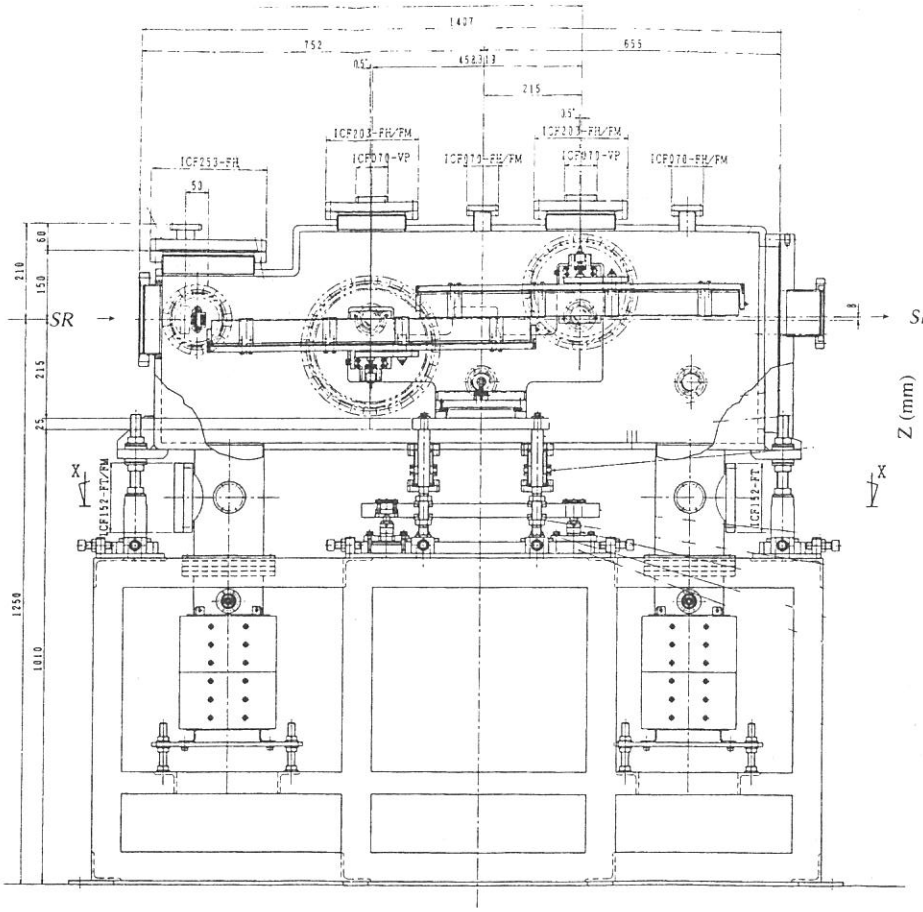

Figure 1. Schematic drawing of the focusing mirror system at BL7A.

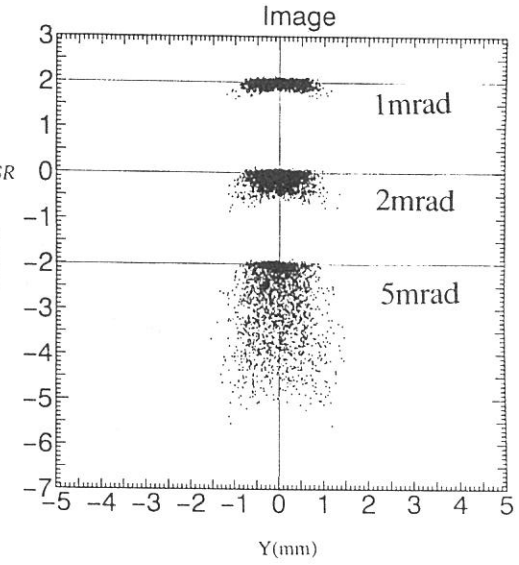

Figure 2. Result of the ray tracing at sample position for the "pair 2" mirror system. Depending on the horizontal acceptance angle of the wiggler radiation, the spot sizes are different.

(BL8B1)

Polarization diagnosis for BL8B1 and characterization of transmission multilayers for use around 65 eV

Tadashi Hatano, Weibing Hu, Masaki Yamamoto and Makoto Watanabe

Research Institute for Scientific Measurements, Tohoku University, Katahira 2-1-1, Aoba-ku, Sendai, 980-77, Japan

Since multilayers proved to be excellent polarizers when they are used at near pseudo-Brewster angle, soft x-ray multilayer polarizers have been rapidly developed. Multilayers work as phase retarders as well when the angle of incidence is readjusted appropriately. Multilayers of transmission type can be put into the optical path and rotated without varying the optical axis, which is remarkably helpful for the optics alignment. We designed and fabricated reflection and transmission multilayer polarizers of Al/YB_6 and Mo/Si for use in the 55~90 eV region to make measurements for magneto-optical effects around $M_{2,3}$ edges of 3*d*-transition metal elements.[1] We have performed diagnosis on the polarization for the beamline BL8B1 and characterization of the transmission multilayers with an elliptometric method.[1,2] This report is narrowed down to the performance of an Al/YB_6 37 layer film for use around 65 eV due to limitations of space. The monochromator was operated with the grating G3 and the mirror M22 used. The experimental setup is illustrated in fig. 1.

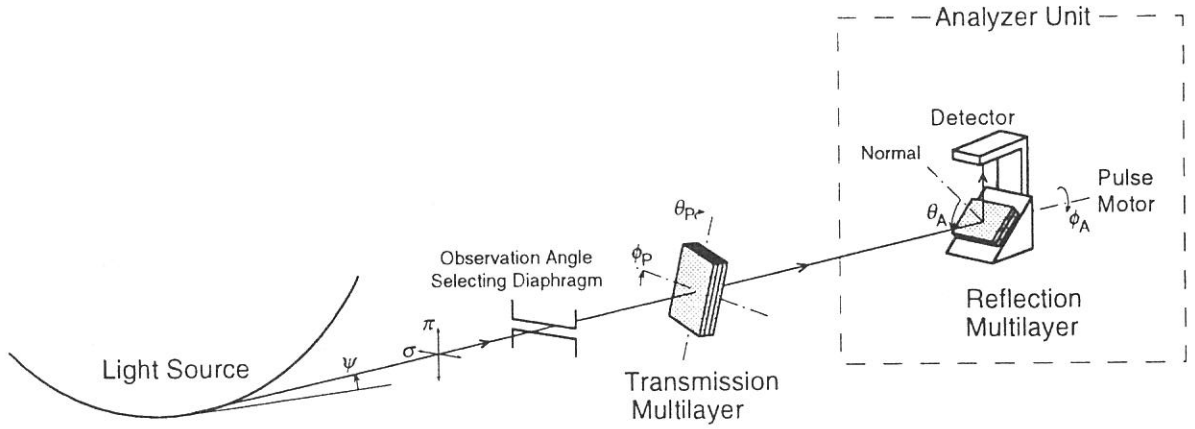

Fig. 1. Experimental setup at BL8B1.

Using an Al/YB_6 reflection multilayer as an analyzer, we made a preliminary investigation of the optics alignment of the beamline BL8B1 by studying the polarization property without a transmission multilayer.[2] The vertical aperture of the diaphragm just before the pre-mirror M1, was fixed at 1.5 mm and its middle level was positioned so that the lower end of M1 was irradiated to select the angle of observation ψ at ψ_1 as shown in fig. 2. In another configuration, the diaphragm was displaced to the position of $\psi = \psi_2$, where the upper end of M1 was irradiated. The displacement was 5.8 mm, which

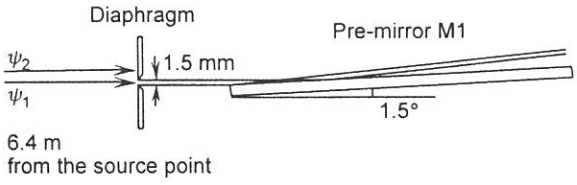

Fig. 2. Schematic of the observation angle selecting diaphragm in front of the pre-mirror M1.

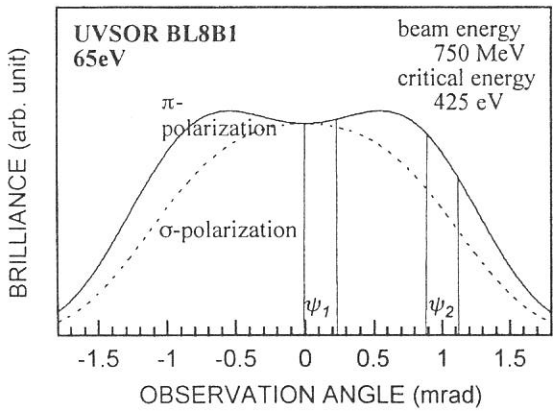

Fig. 3. Calculated intensity of σ- and π-components of BL8B1, UVSOR at the photon energy 65 eV as a function of the observation angle.

corresponds to $\psi_2 - \psi_1 = 0.9$ mrad. The state of polarization of the beam monochromatized at 65 eV was evaluated using so-called rotating analyzer unit, which gives the intensity ratio and the phase difference between σ- and π-components of bending radiation. Here we use $P_{SR} = (I_\sigma - I_\pi) / (I_\sigma + I_\pi)$ as a parameter to represent the degree of horizontal polarization. From the experimental results, P_{SR} was found to be 95% and 43% at $\psi = \psi_1$ and at $\psi = \psi_2$, respectively. Figure 3 illustrates the diaphragm position on the observation angle vs. brilliance curve calculated using the following parameters; the beam energy 750 MeV, the critical energy 425 eV and the photon energy 65 eV. It is noticed at BL8B1 that the angle for maximum intensity was observed between ψ_1 and ψ_2, which was not identical to $\psi = 0$. On the other hand, the phase difference δ_{SR} originally equals $\pm 90°$ depending on the sign of ψ, but will be retarded on the beamline optics by Δ_{BL}. Parameter values of $\delta_{SR} = 78.5°$ and $\Delta_{BL} = 11.5°$ were also obtained from the same measurements.

After the beamline diagnosis on the polarization, the Al/YB_6 transmission multilayer was inserted between the monochromator and the analyzer unit. The azimuthal angle ϕ_P was fixed at 0° and the angle of incidence θ_P was scanned from 38° to 50°. From the polarization measurements of transmitted light, the phase retardation $\Delta_P = \arg(t_s) - \arg(t_p)$ as well as the polarizance $P_P = (|t_p|^2 - |t_s|^2) / (|t_p|^2 + |t_s|^2)$ were analyzed using the values of P_{SR} and δ_{SR} evaluated in the preceding paragraph, where t_p and t_s are the amplitude transmission coefficients for p- and s-components, respectively. The experimental results are presented and compared with calculated ones as functions of the angle of incidence. The maximum polarizance and retardation were found to be 92% at $\theta_P = 42°$ and 68° at $\theta_P = 44°$, respectively.

One of the use of transmission multilayers is improvement of the degree of linear polarization as polarizers. When the source is linearly polarized to 95%, our polarizer of polarizance 92% can increase this to 99.8%, by which one can make precise measurements of optical rotation. Another use of transmission multilayers is generation of circular polarization as phase retarders. In the present case of $\Delta_P = -68°$ at $\theta_P = 44°$, linearly polarized light will be transformed into right- and left-handed 93% circular polarization by the retarder if the principal axis is oriented at $\phi_P = \pm 68°$.

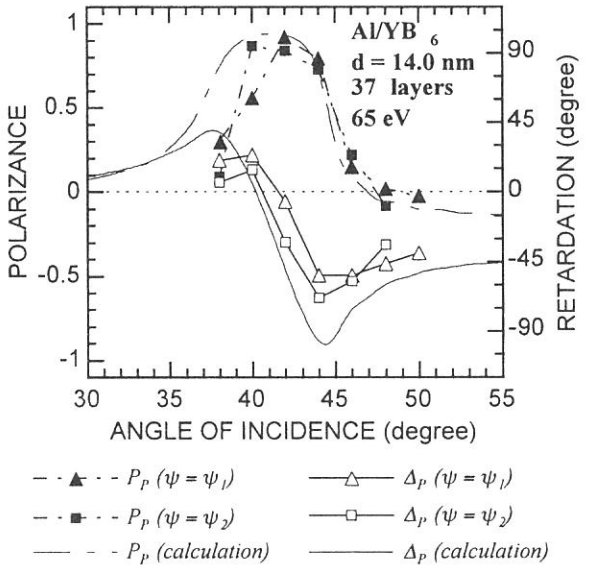

Fig. 4. Measured and calculated polarizances and retardations of the Al/YB_6 transmission multilayer as a function of angle of incidence at 65 eV. Polarizances measured at $\psi = \psi_1$ and $\psi = \psi_2$ are shown by closed triangles and squares, respectively, and retardations, by open triangles and squares.

REFERENCES

[1] W. Hu, T. Hatano, M. Yamamoto and M. Watanabe, J. Synch. Rad., (1998) (to be published).

[2] T. Hatano, W. Hu, M. Yamamoto and M. Watanabe, J. Electron Spectrosc. Relat. Phenom., (1998) (to be published).

(BL2A)

C_6F_5X (X = H, F, Cl, Br, and I) Excited Radical Cation Formation Efficiency in the 10-40 eV Region

T. Hikida[1], T. Ibuki[2], and K. Okada[3]

[1]*Department of Chemistry, Tokyo Institute of Technology, 152-8551*

[2]*Kyoto University of Education, 612-0863*

[3]*Department of Chemistry, Hiroshima University, 739-8526*

The fluorescence from $C_6F_5X^{+\cdot}$ (X=H, F, Cl, Br, and I) cation radicals were observed in the VUV photolysis of C_6F_5X (X=H, F, Cl, Br, and I) . The energy dependence of the excited radical formation were studied by the fluorescence excitation spectra (>400 nm) between 10 eV and 40 eV. Together with the absorption spectra, the fluorescence intensity efficiencies of the excited radical cations were determined as a function of excitation energy. The results are shown in the figure for $C_6F_5X^{+\cdot}$ (X=H, F, Cl, Br, and I).

The absolute emission cross-section was determined to be 17.5 $\pm$ 0.7 Mb for C_6F_5Cl at 21.22 eV. Then, the efficiency was calculated to be 0.10, knowing that the absorption cross-section of C_6F_5Cl at 21.2 eV is 170 Mb. Using this value and relative emission intensities, the absolute efficiencies of $C_6F_5X^{+\cdot}$ (X=H, F, Cl, Br, and I) were obtained. The vertical scales of the figure were thus determined.

All the samples showed clear thresholds at around 12 eV. The efficiencies increased and then remained nearly constant between 13 eV and 16 eV. The dark σ^{-1} excited state is energetically possible at 13.7, 13.9 and 12.4 eV for H, F, and Cl derivatives, but no such formation is indicated. Between 18 eV and 24 eV, another lower plateau appeared, and then gradually decreased to near zero for further increase in the excitation energy. The profiles of efficiency curves were very close for all the samples studied. Only the intensities varied. In table 2 are the summery of the thresholds and the fluorescence efficiencies of five samples.

The emission efficiency is given by the product of the formation efficiency and the emission quantum yield. Knowing the emission quantum yields (1.0), the formation of the excited radicals seem to be fairly effective. For X=H and F, 1.8% and 8% of absorbed photons in 13-16 eV should be converted to the excited radicals, respectively, and it may be very high, 18% or more for X=Cl. Very small efficiencies for $C_6F_5Br^{+\cdot}$ and $C_6F_5I^{+\cdot}$, however, are probably the reflection of small emission quantum yields. The dark σ^{-1} levels are lying below the emissive π^{-1} levels for these molecules. The absence of emission was often explained by the presence of energetically accessible σ^{-1} states near the emissive π^{-1} state.

The fluorescence quantum yields of $C_6F_5H^{+\cdot}$ and $C_6F_6^{+\cdot}$ measured by the photoelectron-photon coincidence experiments are reported to be strongly dependent on the excitation energy. For example, the quantum yield of $C_6F_6^{+\cdot}$ emission decreased from 1.0 at 12.5 eV to 0.25 at 13.3 eV. Further increase in the excitation energy, it decreased drastically to 0.01 at 13.9 eV and to near zero at 14.2 eV. The fluorescence excitation measurements did not show such phenomena.

The photoexcitation reactions should form the excited cation radicals with various vibrational energies. The

vibrational distribution of the photoproducts may be nearly constant for the 13-16 eV, and also for 18-24 eV regions. Excess energy should be removed by electron. It is interesting to note that the first portions of the efficiency curve where the efficiency is high and nearly constant is largely comprised of benzenic π orbital excitation. The second part of the curve is the same energy region as the absorption by the halogen lone pair. The last part where the efficiency is very low is probably the energy region of the inner shell excitation.

Table 1 Ionization energy and intensity threshold, and fluorescence efficiency.

	$C_6F_5X^{+\cdot}$	ionization energy (eV)		efficiency(%)	
		reported	this work	13-16 eV	18-24 eV
C_6F_5H	$\tilde{B}\ ^2B_1\ (\pi^{-1})$	12.50	12.49	1.8	0.85
C_6F_6	$\tilde{B}\ ^2A_{2u}(\pi^{-1})$	12.58	12.51	8.4	3.2
C_6F_5Cl	$\tilde{B}\ ^2B_1\ (\pi^{-1})$	12.20	12.17	18	10
C_6F_5Br	$\tilde{C}\ ^2B_1\ (\pi^{-1})$	11.90	12.12	0.13	0.08
C_6F_5I	$\tilde{C}\ ^2B_1\ (\pi^{-1})$	11.25	11.13	0.03	0.02

Fig.1 Fluorescence efficiency of $C_6F_5X^+$

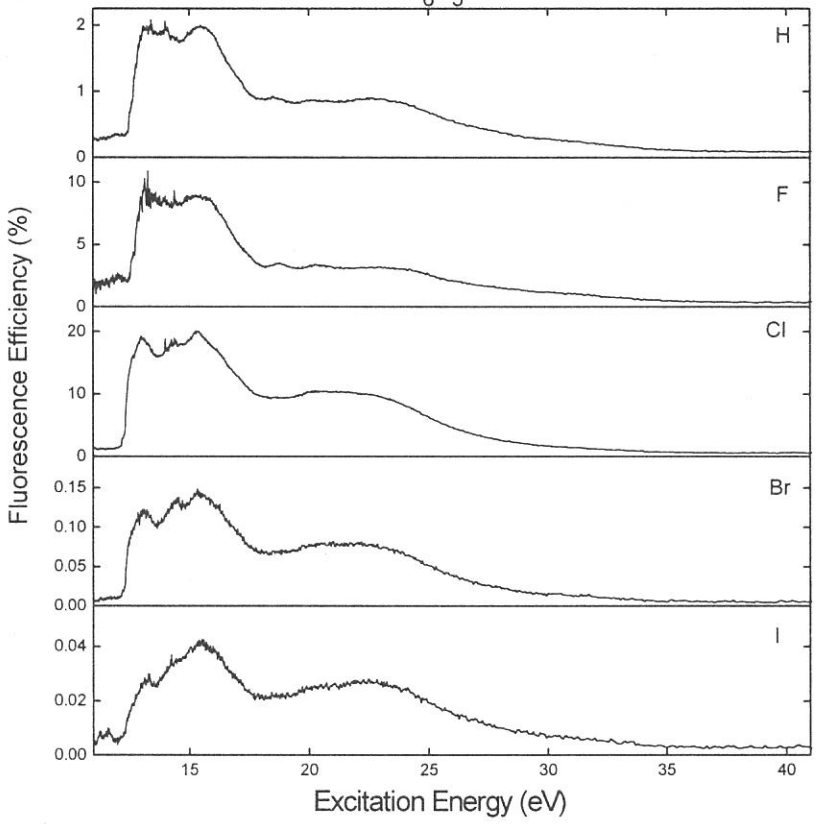

(BL2A)

Photoabsorption and Fluorescence Excitation Cross Sections of Butyl Cyanide and Butyl Isocyanide the VUV Region

Kazuhiro KANDA, Takashi NAGATA[A], and Toshio IBUKI[B]

Department of Fundamental Science, College of Science and Engineering, Iwaki Meisei University, Iwaki 970-8551

[A] Institute for Molecular Science, Myodaiji, Okazaki 444-8585

[B] Kyoto University of Education, Fukakusa. Fushimi-ku Kyoto 612-0863

A considerable amount of studies have been accumulated on the production of the excited CN radicals from cyanides by the VUV photoexcitation, however there have been scare reports on the photodissociative excitation of isocyanides. In the dissociative excitation by rare gas metastable atoms, the internal energy distributions of the produced CN($B^2\Sigma^+$) were reported to be much different in the case of isocyanides compared to the case of cyanides.[1] Deeper insight into the dissociation process requires the knowledge of the highly excited states in the VUV region. In the present study, photodissociation of relevant alkyl cyanides and isocyanides, *n*-C_4H_9CN, *t*-C_4H_9CN, *n*-C_4H_9NC and *t*-C_4H_9NC was investigated by the measurement of the photoabsorption spectrum and the fluorescence excitation spectrum for the CN($B^2\Sigma^+$-$X^2\Sigma^+$) emission in the wavelength range 105-165 nm. The photoabsorption cross section was obtained from the ratio of the vacuum UV photon fluxes measured with the sample gas on and off. The CN($B^2\Sigma^+$-$X^2\Sigma^+$) emission in the UV and visible region was monitored with a combination of a band-pass filter (Toshiba C-39A) and a photomultiplier (Hamamatsu R585). The absolute emission cross section, σ_{em}, was determined by a comparison of the intensity of the CN($B^2\Sigma^+$-$X^2\Sigma^+$) emission produced in the photodissociation of CH_3CN in the 105-150 nm region.[2]

Fig. 1 shows absorption (thin line) and fluorescence excitation (thick line) spectra of *n*-C_4H_9CN, *t*-C_4H_9CN, *n*-C_4H_9NC and *t*-C_4H_9NC. The absorption spectra of *n*-C_4H_9CN and *t*-C_4H_9CN showed only structureless broad bands. The broadening of the absorption band is consistent with our previous study on the photodissociative excitation of small nitriles.[3] On the other hand, numerous sharp peaks were observed in the absorption spectra of *n*-C_4H_9NC and *t*-C_4H_9NC. These peaks are assignable to the Rydberg transitions converging to the first and second ionization potentials. The absorption cross section increases toward shorter wavelength in the 105-165 nm region. In the fluorescence excitation spectra from *n*-C_4H_9CN and *t*-C_4H_9CN, no sharp peak was observed as well as the photoabsorption spectra. The structure in the CN($B^2\Sigma^+$) excitation spectra from *n*-C_4H_9NC and *t*-C_4H_9NC corresponds to the structure in the absorption spectra of these isocyanides. The absolute value of cross section for the CN($B^2\Sigma^+$-$X^2\Sigma^+$) emission is *n*-C_4H_9CN < *t*-C_4H_9CN << *n*-C_4H_9NC < *t*-C_4H_9NC, that is, σ_{em} from isocyanide is larger than that from relevant cyanide and σ_{em} from photodissociation of containing tertiary butyl group is larger than that from containing normal butyl group. Even maximum of Quantum yield for the production of CN($B^2\Sigma^+$) takes maximum, ≈0.1, at 142 nm of *t*-C_4H_9NC. Dissipation of available excess energy to the alkyl group restrains the production of excited CN radical, because the disposed

energy to the R-CN or R-NC bonding decreases. Normal butyl group is more effective heat bath than tertiary butyl group, because of its flexible structure. Relatively large quantum yield from isocyanide and sharp peaks in the absorption and fluorescence excitation indicate that a little excess energy was disposed to alkyl group. These differences between the case in the cyanide and isocyanide is considered to be ascribable to the lifetime in the excited dissociative state. Namely, dissociative time of the excited isocyanide is regarded to be so short that the available energy cannot disposed to the alkyl group sufficiently.

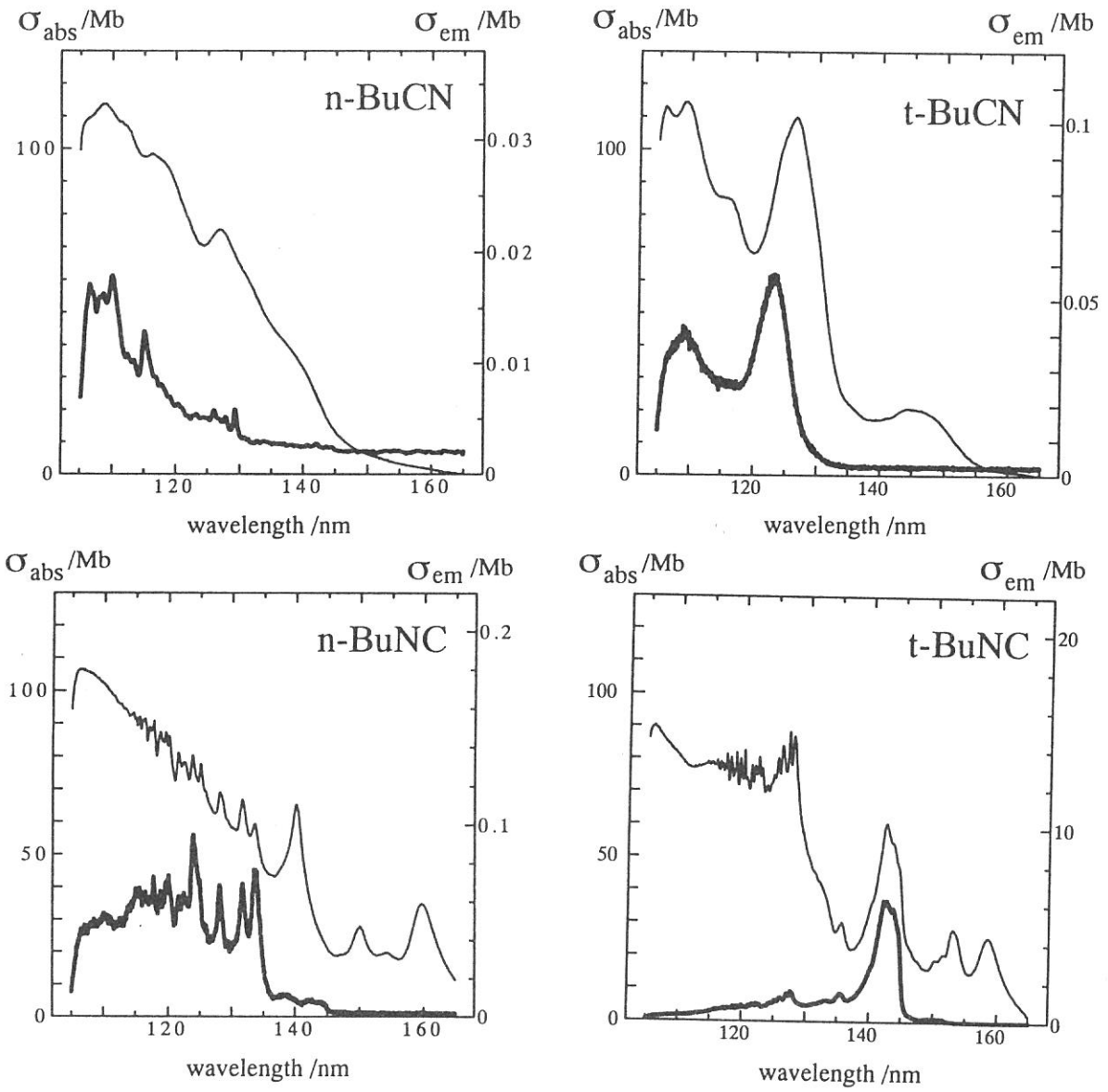

Fig. 1 The absorption and photoexcitation cross sections of n-C_4H_9CN, t-C_4H_9CN, n-C_4H_9NC and t-C_4H_9NC in the 105-165 nm region. The spectral resolution was 0.1 nm.

Reference

[1] K. Suzuki and T. Kondow, Atomic Collision Research in Japan, Progress Report, 16, 56 (1990).

[2] M. Kono, D. Thesis, Grad. Univ. Adv. Stud., (1995).

[3] K. Kanda et al., UVSOR Activity Report 1996, 82.

BL2A

Photoabsorption and Fluorescence Excitation of Formamide in the Vacuum Ultraviolet Region.

T. SUGIHARA, K. TABAYASHI, O. TAKAHASHI, K. SAITO, and T. IBUKI*

Department of Chemistry, Faculty of Science, Hiroshima University, Kagamiyama, Higashi-Hiroshima 739-8526

**Institute for Molecular Science, Myodaiji, Okazaki 444-8585*

Photochemistry of simple acid amides is of fundamental importance in connection with the photochemical properties of biological polymers, since they have the basic chromophoric unit in polypeptides. So far, photoabsorption spectra of the monomeric amides in the UV and VUV region have been accumulated, very little is known about the photochemical reaction initiated by UV and VUV photons. Here, fluorescence excitation cross section of formamide has been measured in the wavelength range 105-210 nm, dissociative excitation processes have been examined. The absorption bands are also reassigned based on the recent PES data and ab initio MO calculations.

The electronic configuration of $HCONH_2$ in the ground state is given by $(6a')^2(7a')^2(8a')^2(9a')^2(1a'')^2(10a')^2(2a'')^2$. The highest occupied 2a" and the next 10a' MOs have the π_{CO} and n_O characters, and are very close together in formamide. The absorption bands(solid line) and our assignments are shown in Fig. 1. The vibrational progressions in the Rydberg transitions have average spacings of ~530 and ~1600 cm^{-1}. They are assigned to NH_2 scissors and CO stretching vibrations from the vibrational analysis of the relevant ions by MO (HF/6-31G(d)) calculations.

Fig. 1 also shows the fluorescence excitation cross section(dotted line) obtained with detection of 370-850 nm radiation. The maximum cross section is found to be 0.044 Mb at λ_{exct} = 120 nm, which corresponds to the total quantum yield of 0.0023. The dispersed fluorescence measurement was not available due to low fluorescence intensity, excitation measurements were repeated with combinations of an optical filter and a PMT to cover different wavelength ranges in the 160–850 nm. From the comparison of these fluorescence excitation intensities, the dissociative excitation process,

$$HCONH_2 + h\nu \rightarrow HCO + NH_2(\tilde{A}\,^2A_1),$$

is concluded to be the most prominent fluorescent channel following the VUV excitation.

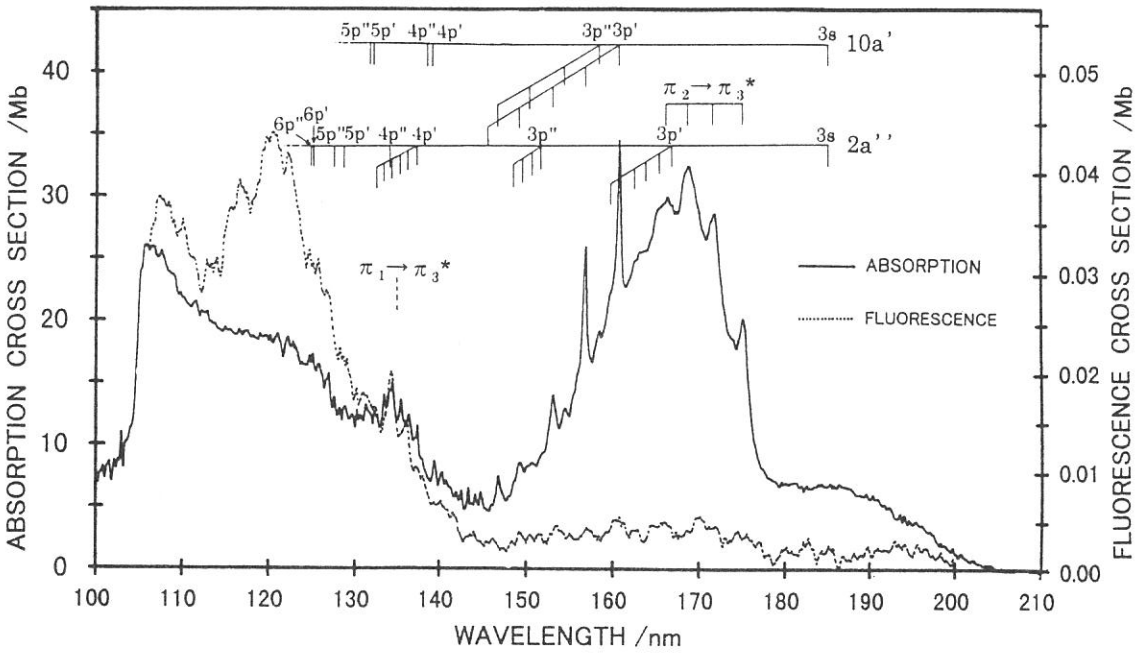

Fig. 1. Photoabsorption and fluorescence excitation cross sections for $HCONH_2$ in the 105-210 nm region. The spectral resolution was 0.2 nm. The sample pressure was 38 mTorr.

(BL3A2)

Anisotropic Angular Distribution of Ionic Fragments in the Dissociation of CO_2^{2+}

Toshio MASUOKA

Department of Applied Physics, Faculty of Engineering, Osaka City University, Sugimoto 3-3-138, Sumiyoshi-ku, Osaka 558-8585

Angular distributions of fragment ions ($O^+ + CO^+$ and $C^+ + O^+$) produced in dissociative double photoionization of carbon dioxide have been studied in the photon energy region 41-100 eV by use of a photoion-photoion coincidence (PIPICO) technique and a source of synchrotron radiation.

The spectral profiles of PIPICO peaks are determined by the kinetic-energy distribution and the angular distribution of the fragment ions, both with respect to the spectrometer axis, and other experimental conditions such as the electric field across the ionization region, the size and the degree of polarization of the photon beam and so on. In order to obtain the angular distribution of fragment ions, the kinetic-energy distribution was determined first by analyzing the PIPICO spectra measured at the so-called "pseudomagic angle," which is equal to about 55° under the assumed condition that the degree of polarization of the light $p = 0.9$ (Ref. 1).

The differential partial cross section of the fragment ions for the partially polarized light is given by

$$\frac{\partial\sigma_i}{\partial\Omega} = \frac{\sigma_i}{4\pi}\left[1 + \frac{\beta}{4}(3p\cos 2\theta + 1)\right]$$

in the frame work of the dipole approximation for randomly oriented molecules with cylindrical symmetry in the gas phase, where β is the asymmetry parameter that characterizes the angular distribution and θ is the angle of the spectrometer axis relative to the electric vector of the light.

The asymmetry β parameter was obtained by the following three steps. (1) Spectral profiles at $\theta = 0°$ and 90° were calculated for a set of various kinetic energies of the fragment ions with an arbitrarily fixed β parameter. (2) The spectral profile of the PIPICO peak at the angle θ was calculated, based on the kinetic-energy distribution already determined and the profiled calculated in step 1. (3) By treating the β value as a running parameter, its most probable value was determined as the one for which the sum of squares of the residuals between the observed and calculated profiles was minimized.

The observed β parameter is shown in Figs. 1 and 2 for $O^+ + CO^+$ and $C^+ + O^+$ channels, respectively, as a function of excitation energy. At low energy side close to the respective thresholds, the uncertainty in the β parameter is relatively large because of the poor counting statistics and the wavy background superposed on the PIPICO peaks. However, a clear trend in the β parameter can be seen as a function of excitation energy. For the $O^+ + CO^+$ channel, the mean value of the β parameter is close to 0.6 in the 47.5-60 eV region and is close to zero in the 70-100 eV region. For the $C^+ + O^+$ channel, the β parameter decreases as a function of excitation energy, which is the similar trend in the $O^+ + CO^+$ channel.

The observation of anisotropy in double photoionization from the valence orbitals of CO_2 will be discussed in relation to the symmetry consideration involved in the transition.

Reference

1) T. Masuoka, I. Koyano, and N. Saito, Phys. Rev. A 44, 4309 (1991).

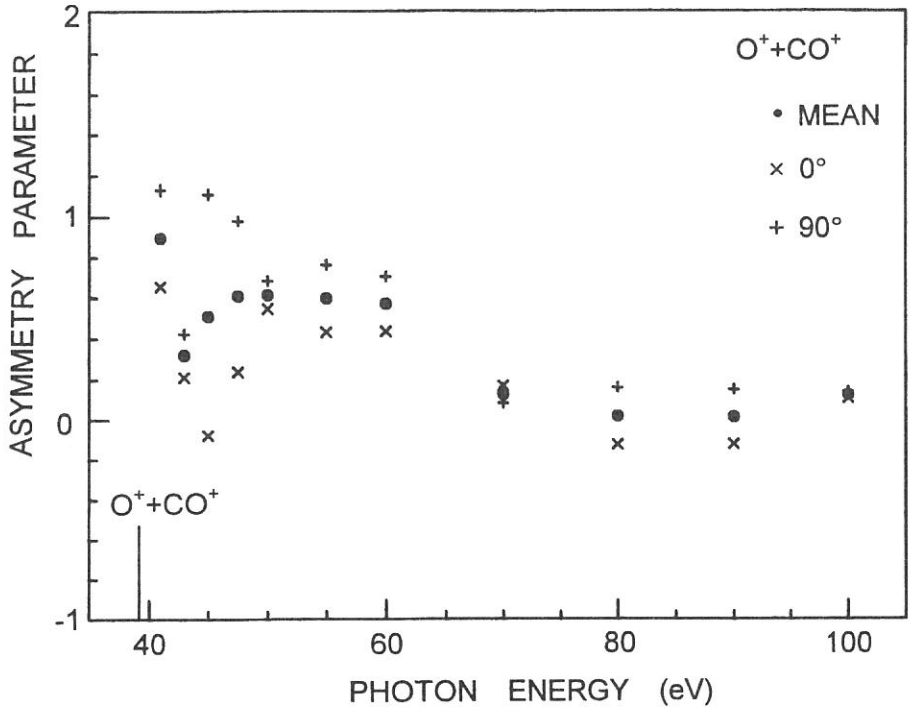

FIG. 1 Asymmetry parameter β for the $O^+ + CO^+$ dissociation channel of CO_2^{2+} measured at θ = 0° (×) and 90° (+).

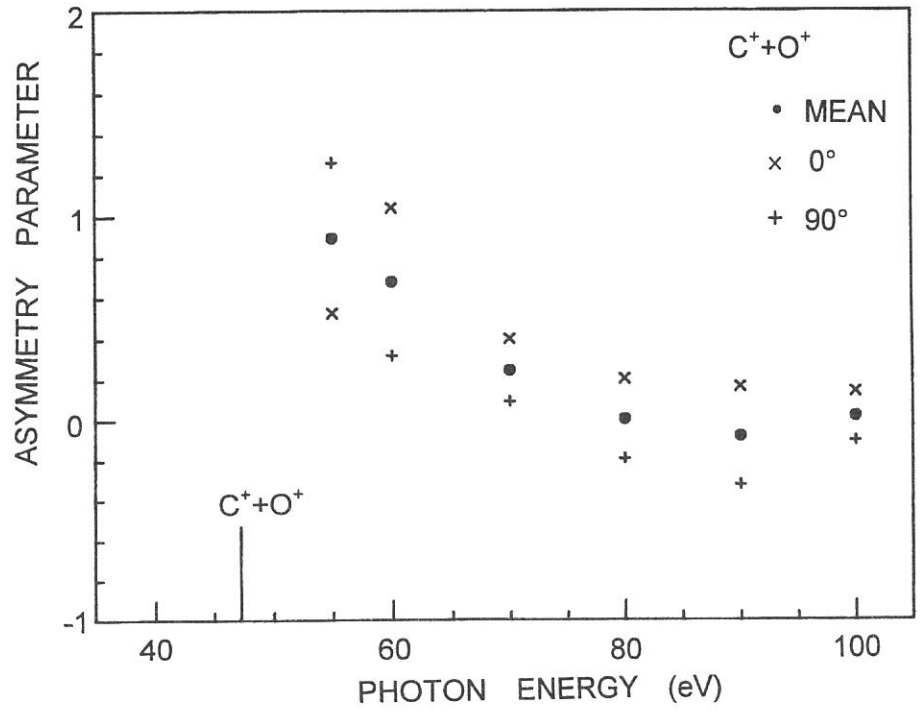

FIG. 2 Asymmetry parameter β for the $C^+ + O^+$ dissociation channel of CO_2^{2+} measured at θ = 0° (×) and 90° (+).

(BL3A2)

Dissociative Photoionization of Ferrocene in the Fe:3p Inner-Valence Region.

Yusuke Tamenori, and Inosuke Koyano
Departmentof MaterialScience, Himeji Institute of Technology, Kamigori, 678-12

In previous X-ray absorption and electron energy loss measurements on various transition metal compounds, it was suggested that the strong photoionization resonance can be found in the vicinity of metal np ionization threshold, which can be attributed to np transition to an unoccupied molecular orbital. However, there has been little information about ion fragmentation following the resonance transition. We are performing a series of detailed studies of dissociative photoionization of transition metal compounds in the inner valence region by use of TOF mass spectrometry and photoion-photoion coincidence technique (PIPICO).[1] In the present work, the dissociative photoionization of ferrocene ($Fe(cp)_2$) is studied in the range 37-100eV placing a special emphasis on the behavior in the vicinity of the Fe:3p ionization threshold (55eV).

Figure 1 shows an example of TOF mass spectrum taken at an incident photon energy of 50eV and a drift tube length of 20cm. The abundant ion is the parent ion ($Fe(cp)_2^+$) with some intensities for cp loss fragments($Fe(cp)^+$, Fe^+). The fragment ions originating from the ligand (C_nH_m n=2-5) are also observed with high abundances. However, owing to the closely spaced mass peaks, we can not distinguish between some different fragment ions. Such overlapped peaks are shown under a single label e.g. $C_3H_m^+$. Only one metastable doubly charged ion was observed at the mass number of 93, which is assigned to $Fe(cp)_2^{2+}$. Figure 2 present a PIPICO spectrum taken at 66eV of incident photons. The most abundant ion-pairs are those corresponding to the formula Fe^+-$C_3H_m^+$. Other ion-pairs involving $C_3H_m^+$ as a partner also give a high abundance. The relative intensity of ions and ion-pairs produced by the cp breakage is very high in contrast to the case of previous studies of metal-carbonyl compounds where simple ligand elimination is the dominant dissociation process.

Shown in Figure 3 are the incident photon energy dependences of the partial photoion yields of main observed ions. It is interesting to note that only the partial photoion yield of $Fe(cp)_2^{2+}/Fe(C_3H_3)^+$ shows the remarkable enhancement in the range from about 55eV to 70eV, which corresponds to the Fe:3p edge, whereas other ions are only slightly enhanced in this energy region. Although the observed variation is relatively small, the present result clearly indicates the occurrence of characteristic fragmentation following the resonance excitation. On the other hand, this result contrasts with the dissociative photoionization of metal-carbonyls in which the yields of almost all observed ions show an increase at the metal np edge. This difference may result from the difference in the mechanisms of intramolecular energy transfer through the metal-carbonyl and metal-cycropentene coordination bonds.

<Reference>

1, Y. Tamenori, K. Inaoka, and I. Koyano, *J. Electron Spectros. Rela. Phenom.* 79 , 503 (1996); Y. Tamenori, and I. Koyano, *J. Phys. Chem.* in press

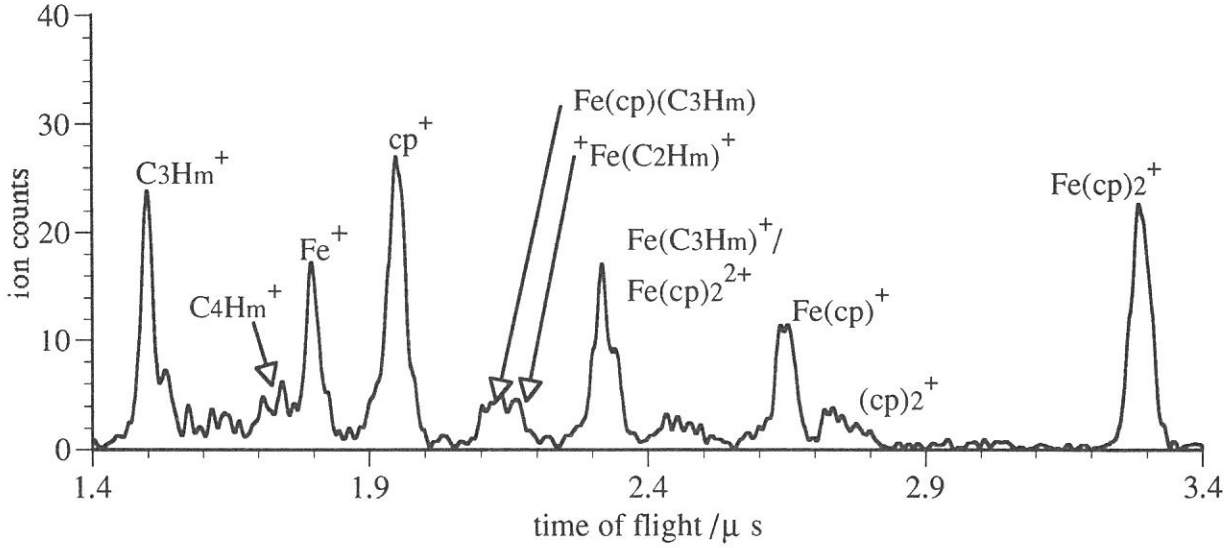

Figure 1, A TOF mass spectrum of ferrocene taken at 50eV of incident photon energy.

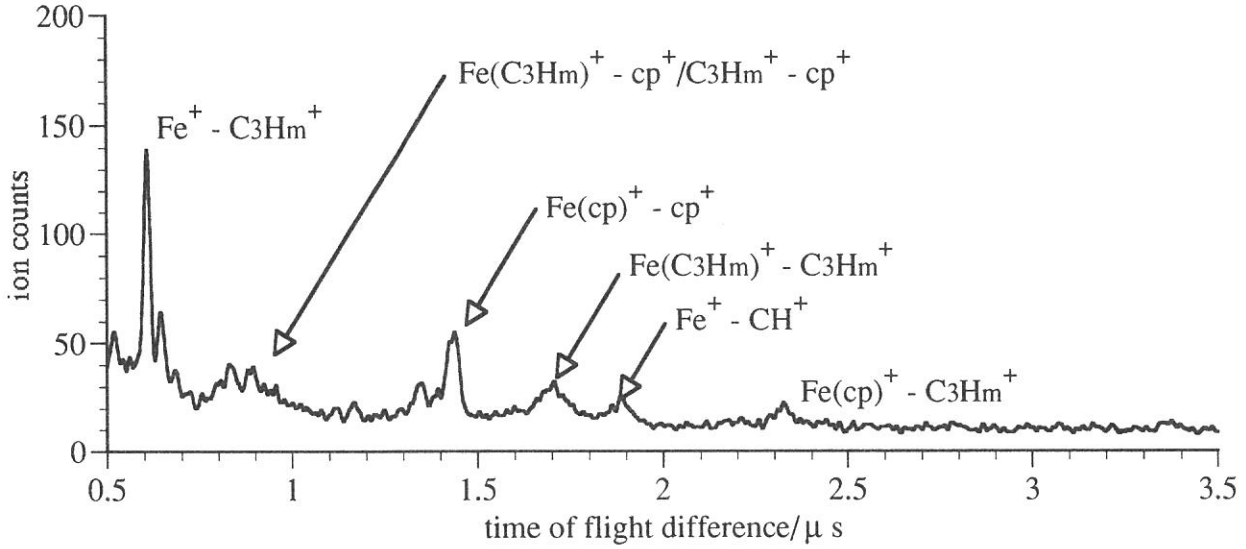

Figure 2, A PIPICO spectrum of ferrocene taken at 66eV of incident photon energy.

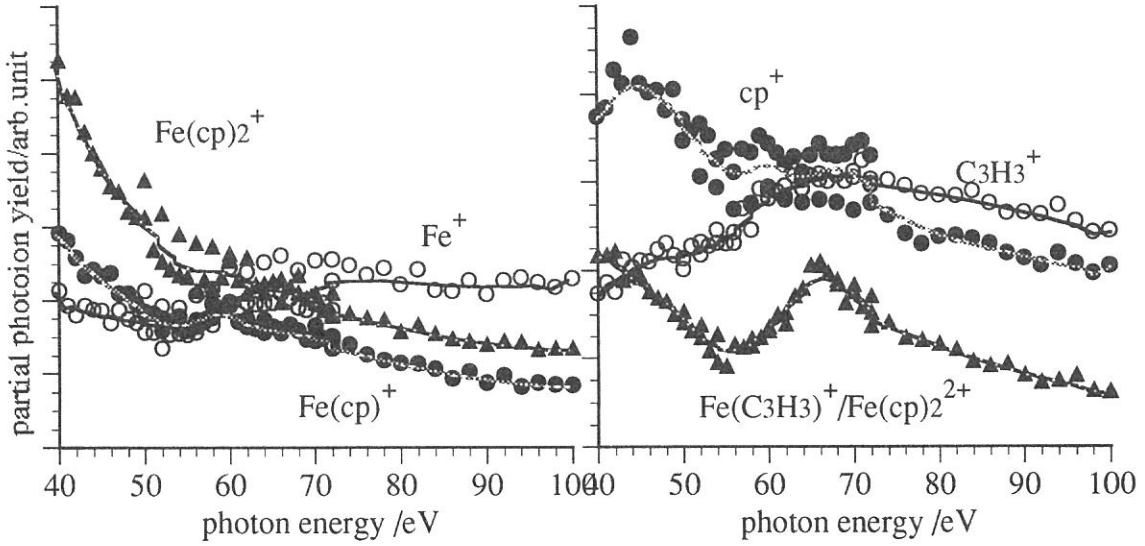

Figure 3, Incident photon energy dependence of the partial photoion yield of ferrocene.

(BL3A2)

Laser Induced Fluorescence Excitation Spectroscopy of N_2^+ Produced by Predissociation of N_2O^+ ($B\ ^2\Pi$).

Hiromichi Niikura*, Masakazu Mizutani**, Kota Iwasaki** and Koichiro Mitsuke**

*The Graduate University for Advanced Studies, **Institute for Molecular Science, Myodaiji, Okazaki, 444 - 8585, Japan.

Laser induced fluorescence (LIF) spectroscopy combined with synchrotron radiation (SR) photoexcitation has been exploited for investigating the internal energy distribution of fragment ions produced by VUV photoexcitation and the detailed mechanism for their formation.[1] In the present work, we measured the LIF yield curve of $N_2^+(X\ ^2\Sigma_g,\ v''=0)$ produced by the dissociative photoionization of N_2O with SR. The second harmonic of a Ti-sapphire laser was used to cause an excitation transition of $N_2^+(B\ ^2\Sigma_u,\ v'=0) \leftarrow N_2^+(X\ ^2\Sigma_g,\ v''=0)$. Then, fluorescence $N_2^+(B\ ^2\Sigma_u,\ v'=0) \rightarrow N_2^+(X\ ^2\Sigma_g,\ v''=1)$ at ~ 427 nm was monochromatized and detected.

Experimental details have been reported elsewhere.[1] The spectral band width $\Delta\lambda$ (FWHM) of SR was made to go up to 4 Å for getting a better signal-to-background ratio. In this resolution, the intensity was typically 3×10^{15} photons $cm^{-2}\ s^{-1}$. The average power of the second harmonic of the Ti-sapphire laser was 150 mW at 389 - 392 nm. Both the entrance and exit slit widths of the monochromator which monitors the fluorescence were reduced to 0.5 mm to eliminate the background emission from other species, dominantly from excited neutral fragments. The spectral resolution (FWHM) of the monochromator was 4 nm.

Figure 1 shows the yield curve of $N_2^+(X\ ^2\Sigma_g, v''=0)$ obtained by plotting the fluorescence intensities as a function of the SR photon energy in the range 18.4 - 19.8 eV. The wavelength of the laser was tuned at 391.5 nm which corresponds to the band head of the *P*-branch for the excitation $N_2^+(B\ ^2\Sigma_u,\ v'=0) \leftarrow N_2^+(X\ ^2\Sigma_g,\ v''=0)$. Several structures are identified to the $nd\pi$ Rydberg series converging to $N_2O^+(C\ ^2\Sigma^+)$ by comparing with the previous assignments,[2] while $nd\sigma$ Rydberg series are indiscernible. The mechanism for production of the fragment ion N_2^+ has been inferred[2] from its photoionization efficiency curve as follows:

$$N_2O + h\nu_{SR} \rightarrow N_2O^{**} \quad \text{(Excitation to a Rydberg State)} \quad (1)$$

$$N_2O^{**} \rightarrow N_2O^+(B\ ^2\Pi) + e^- \quad \text{(Autoionization)} \quad (2)$$

$$N_2O^+(B\ ^2\Pi) \rightarrow N_2^+(X\ ^2\Sigma_g) + O\ (^3P_g) \quad \text{(Predissociation)} \quad (3)$$

On the other hand, the contribution of direct ionization to N_2O^+ ($B\ ^2\Pi$) instead of processes (1) and (2) is considered to be small as actually expected from Fig. 1. The relative peak intensity appears to weakly depend on the principal quantum number of n = 3 - 6, and no marked difference in the intensity distribution is exhibited between the present LIF measurement and the previous mass spectrometric detection[2] of N_2^+.

In the future, this pump-probe technique combining SR excitation with LIF spectroscopy is expected to provide valuable information on vibrational and rotational energy distributions of fragment ions produced by photoexcitation and photoionization in the VUV region.

References

1) M. Mizutani, H. Niikura, A. Hiraya and K. Mitsuke, J. Synchrotron Rad., in press.

2) J. Berkowitz and J. H. D. Eland, J. Chem. Phys., **67** (1977) 2740

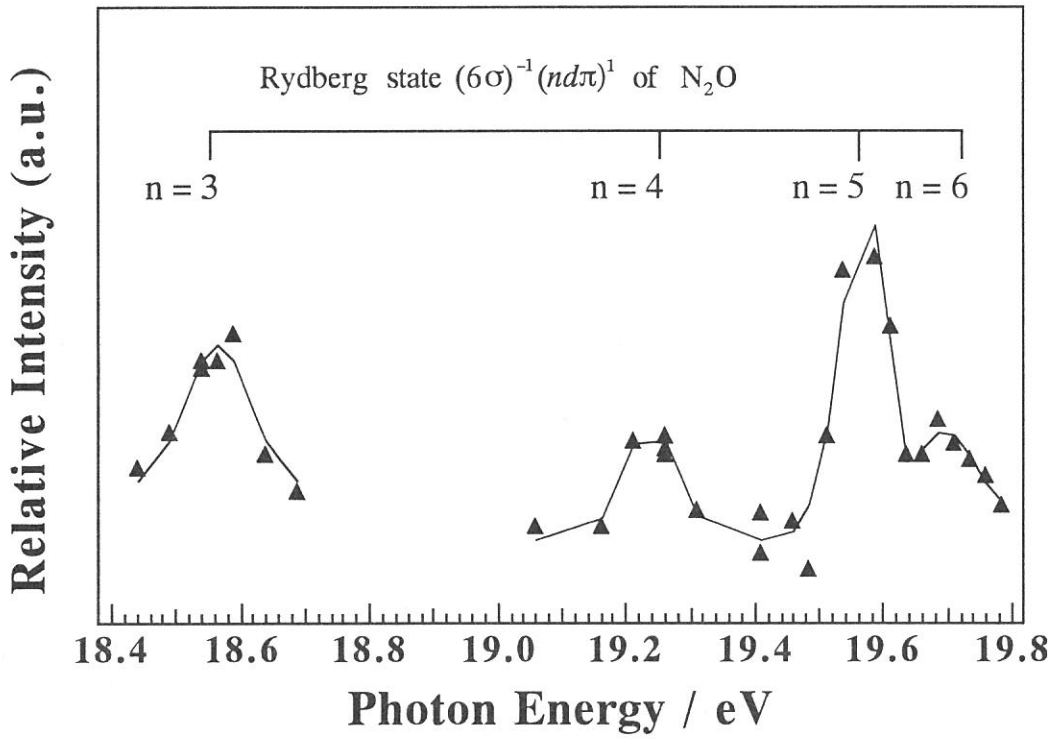

Figure 1. Photodissociation yield curve of $N_2^+(X\,^2\Sigma_g, v'' = 0)$ produced from N_2O obtained by plotting the LIF count rate as a function of the SR photon energy. The assignments of the $nd\pi$ Rydberg states converging to N_2O^+ $(C\,^2\Sigma_g^+)$ are indicated.

(BL3A2)

Laser Induced Fluorescence Excitation Spectroscopy of N_2^+ Produced by VUV Photoionization of N_2

Masakazu MIZUTANI, Hiromichi NIIKURA[A] and Koichiro MITSUKE

Department of Vacuum UV Photoscience, Institute for Molecular Science, Okazaki 444-8585, Japan
[A]The Graduate University for Advanced Studies, Okazaki 444-8585, Japan

In order to study the mechanism of dissociation of state-selected ions or neutral dissociation of superexcited molecules, a pump-probe experimental method combining synchrotron radiation excitation and laser-induced fluorescence (LIF) excitation spectroscopy has been developed. The main subject of this report is observation of the internal distribution of ions produced by VUV excitation by means of the LIF method.

As the most appropriate starting point, we have paid our attention to N_2^+ ions produced from N_2 by VUV photoionization with synchrotron radiation. The schematic diagram of the apparatus and detection system is shown in Figure 1. The fundamental light of the undulator radiation is monochromatized by a grazing-incidence monochromator (photon energy, E_{SR}) and introduced coaxially with the second harmonic of a mode-locked Ti:sapphire laser (Spectra Physics Lasers, Tsunami, 3950-L2S).[1] Sample gases, N_2, are photoionized preferentially into vibronically ground N_2^+ ions by irradiation of synchrotron radiation, and an LIF excitation spectrum of N_2^+ is measured in the laser wavelength region of the ($B\ ^2\Sigma_u^+$, $v' = 0$) ← ($X\ ^2\Sigma_g^+$, $v'' = 0$) transition at 389 - 392 nm. The fluorescence of the ($B\ ^2\Sigma_u^+$, $v' = 0$) → ($X\ ^2\Sigma_g^+$, $v'' = 1$) transition at about 427 nm is dispersed by another monochromator and detected with a photomultiplier (Hamamatsu, R464S).

Figure 2 shows an LIF excitation spectrum of N_2^+ produced by photoionization of N_2 at $E_{SR} = 15.98$ eV. Since this photon energy agrees with the resonance energy for the $4d\sigma_g$, $v = 0$ state converging to N_2^+ ($A\ ^2\Pi_u$), most of N_2^+ ions are produced by autoionization of this Rydberg state. The LIF excitation spectrum exhibits two maxima due to the *P* and *R* branches in which rotational bands are heavily overlapped. The rotational temperature is approximated by simulating the LIF excitation spectrum by using the theoretical intensity distribution of rotation bands convoluted with the present laser spectral width of 9.2 cm^{-1}. In Figure 2 a calculated spectrum at $T = 300$ K is indicated by a solid line. Experimental data points appear to gather around this curve. This suggests that rotational excitation in N_2^+ ($X\ ^2\Sigma_g^+$, $v'' = 0$) is not particularly induced through autoionization of the $4d\sigma_g$ Rydberg state. Similar results have been obtained on direct ionization of N_2 at $E_{SR} = 18$ eV.[2]

In the near future, we will study the decay dynamics of vibronically excited ions by means of single vibronic level dispersed fluorescence spectroscopy of an excited state produced by laser excitation of ground-state ions prepared by VUV photoionization.

References

1) M. Mizutani, M. Tokeshi, A. Hiraya and K. Mitsuke, J. Synchrotron Radiation **4**, 6 (1997).
2) M. Mizutani, H. Niikura, A. Hiraya and K. Mitsuke, J. Synchrotron Radiation **5**, (1998) *in press.*

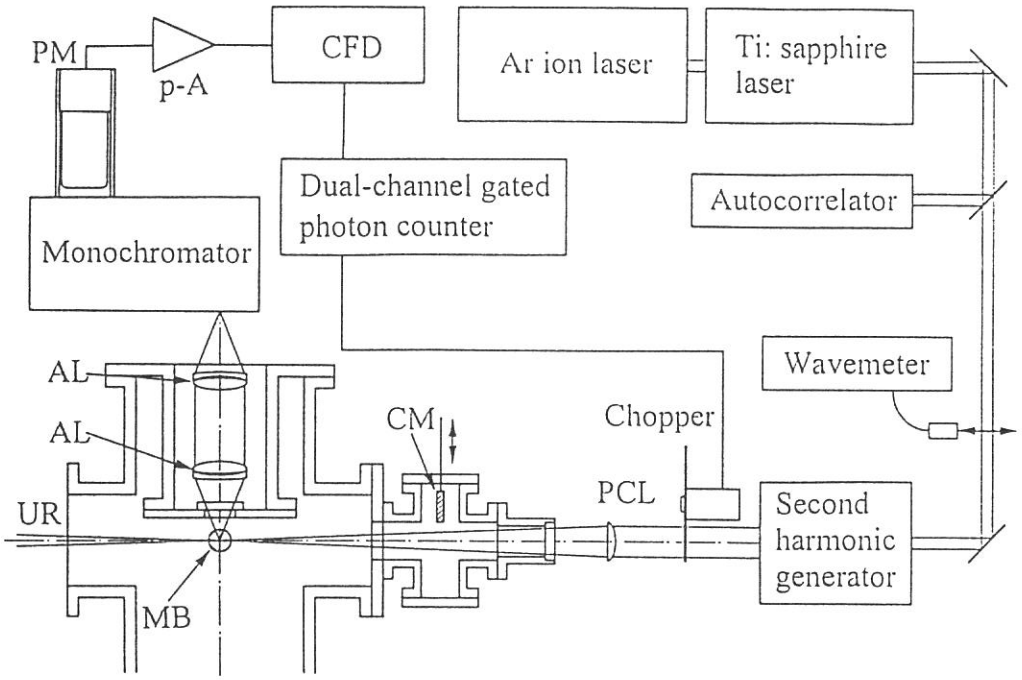

Figure 1. Schematic arrangement of the apparatus for synchrotron radiation-laser combination experiments. PM, photomultiplier; p-A, pre-amplifier; CFD, constant fraction discriminator; AL, spherical achromatic lenses; UR, monochromatized undulator radiation; MB, cross section of a molecular beam expanded from a nozzle; CM, gold-mesh current monitor; PCL, spherical plano-convex lens.

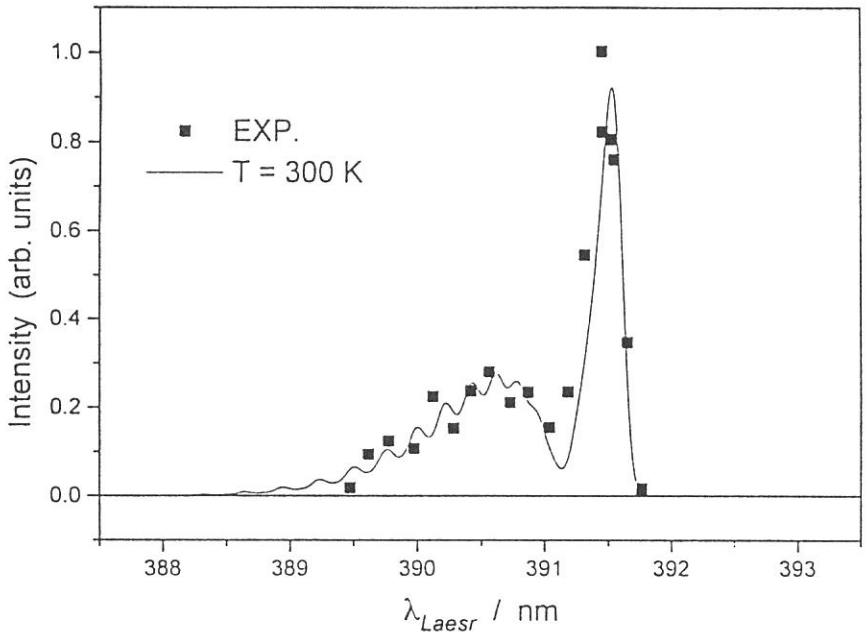

Figure 2. Laser induced fluorescence excitation spectrum of the $(B\,^2\Sigma_u^+,\ v' = 0) \leftarrow (X\,^2\Sigma_g^+,\ v_i'' = 0)$ transition of N_2^+ which is prepared by photoionization of N_2 at E_{SR} = 15.98 eV. The monitored fluorescence at 427 ± 4 nm is ascribed to the $(B\,^2\Sigma_u^+,\ v' = 0) \rightarrow (X\,^2\Sigma_g^+,\ v_f'' = 1)$ transition. The solid line represents a spectrum at T = 300 K calculated by using the theoretical intensity distribution of rotation bands convoluted with the laser spectral width of 9.2 cm^{-1}.

(BL3B)

Two-Photon Ionization Photoelectron Spectroscopy of Ar Using Visible laser and Synchrotron Radiation

Yasumasa HIKOSAKA and Koichiro MITSUKE

Department of Vacuum UV Photoscience, Institute for Molecular Science, Okazaki 444-8585 Japan

There has been a growing interest in deactivation mechanism of molecular excited states lying in the vacuum ultraviolet region. Neutral dissociation is one of major decay processes from these states. The neutral dissociation frequently yields a pair of fragments which are free from both autoionization and radiative decay and therefore difficult to detect. In order to obtain an understanding of the dissociation dynamics, we have developed a laser-synchrotron radiation (SR) combination system to conduct two-photon ionization photoelectron spectroscopy, where fragments produced by neutral dissociation are probed by laser ionization.

The geometry of the experimental setup is schematically depicted in Fig. 1. Sample gas is admitted into an ionization cell through a 1-mm diameter pipe at room temperature. The SR is dispersed using a 3 m normal incidence monochrometor and is introduced into the cell. The light beam of a frequency-doubled Nd:YAG laser (532 nm) with the repetition of 8 KHz intersects perpendicularly with the SR beam in the ionization chamber. The electric vector of the laser beam is perpendicular to that of the SR beam. A 160 ° spherical electrostatic electron energy analyzer with the mean radius of the electron orbit of 54.7 mm is placed in the parallel direction to the electronic vector of the SR beam. Energy-analyzed electrons are detected by a position sensitive detector composed of dual microchannel plate multipliers and a two-dimensional resistive anode encoder. In order to improve the signal to background ratio, the detection of electrons is inhibited when the laser is off.

Laser photoelectron spectroscopy of Ar Rydberg states has been carried out to check the performance of the present system. The Rydberg states are prepared by irradiation of the SR beam. Photoelectron spectra are measured consecutively at SR wavelength intervals of 0.3 Å in a region where the Ar*($3p^5$3d) and Ar*($3p^5$5s) states lie, and the electron yield is plotted as a function of both photon energy of SR and kinetic energy of the electron. This method is what is called two-dimensional photoelectron spectroscopy (2D-PES), and very useful for elucidating the dynamics of superexcited states.[1] Figure 2 shows the measured 2D-PES. When the photon energy of SR is tuned at the Ar*($3p^5$3d) states, increase in electron counts due to laser ionization into $Ar^+(^2P_{1/2})$ or $Ar^+(^2P_{3/2})$ are observed at specific kinetic energies. The Ar*(3d[1/2]$_1$) state, which is a Rydberg state converging to $Ar^+(^2P_{3/2})$, obviously results in not only $Ar^+(^2P_{3/2})$ but $Ar^+(^2P_{1/2})$. This fact indicates that the Rydberg electron does not preserve the spin momentum and/or that the Rydberg electron does not alter the angular momentum by ±1 on photoionization. No photoelectron signals from Ar*($3p^5$5s) states are detected on the 2D-PES, since angular distribution of the 5s electron is isotopic and hence the electrons through laser ionization is emitted in the parallel direction to the electronic vector of the laser.

[1] for example, Y. Hikosaka, H. Hattori, T. Hikida, and K. Mitsuke, J. Chem. Phys. **107**, 2950 (1997).

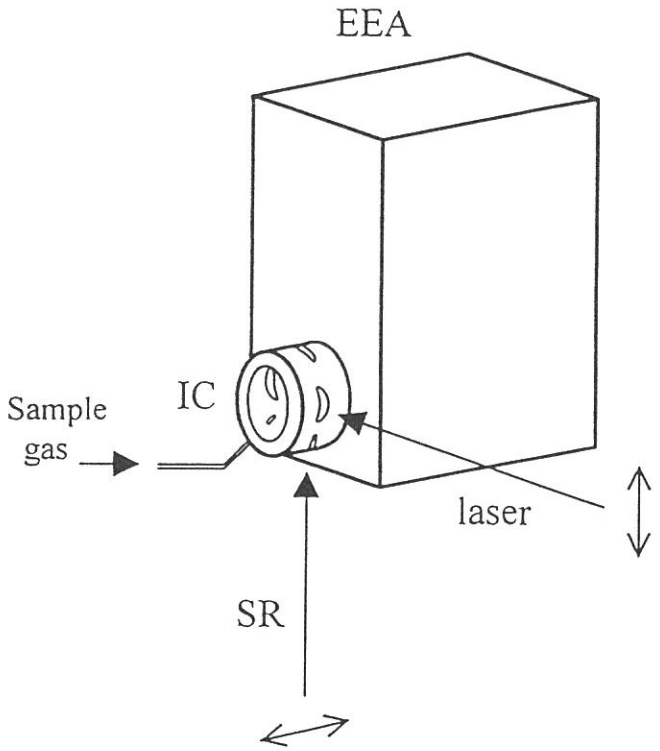

Figure 1 Geometry of the experimental setup. The synchrotron radiation (SR) beam is introduced into the ionization cell (IC) in the perpendicular direction to the laser beam. The electron energy analyzer (EEA) is placed in the parallel direction to the electronic vector of the SR beam.

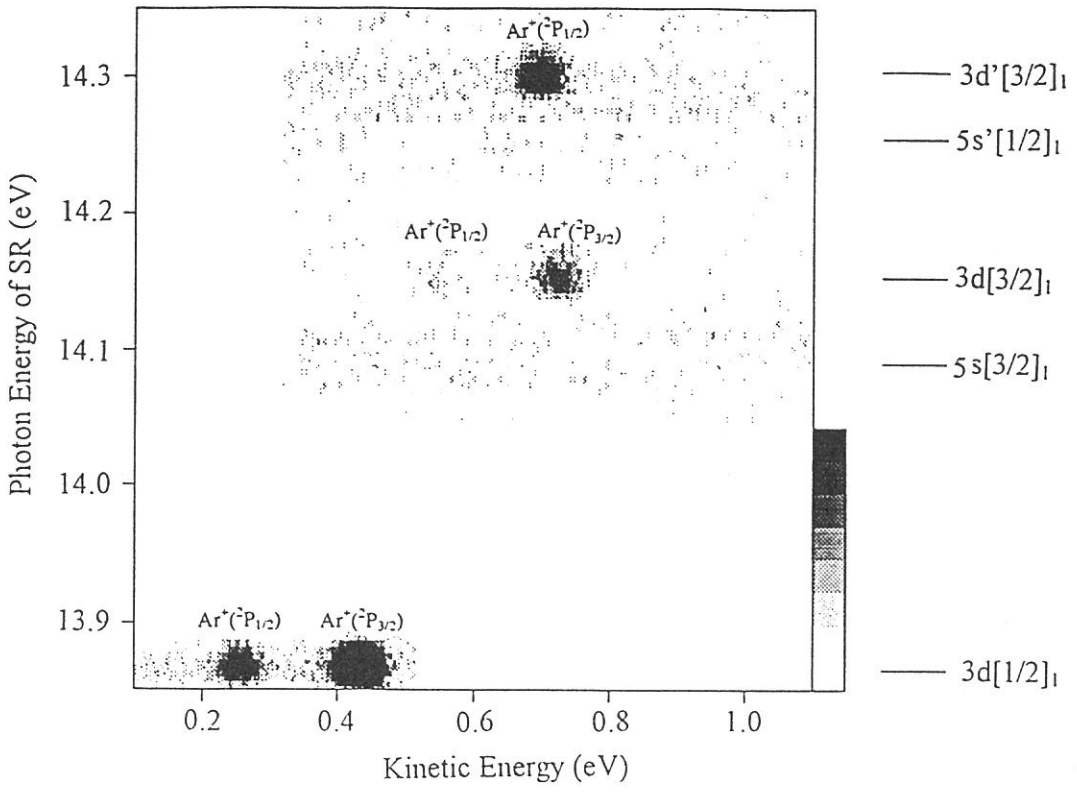

Figure 2 Two-dimensional photoelectron spectrum of Ar Rydberg states prepared by SR irradiation. The electron yield is presented by the plots with eight tones from light to dark on a liner scale.

(BL3B)

Autoionization of Superexcited Sulfur Atoms Produced from Doubly Excited Rydberg States of SO_2

Hideo HATTORI, Yasumasa HIKOSAKA, and Koichiro MITSUKE

Institute for Molecular Science, Myodaiji, Okazaki 444-8585, Japan

It is well known that superexcited states play important roles in molecular photoexcitation processes in the extreme ultraviolet (EUV) region. In particular, excitation of an inner valence electron or double-electron excitation are possible in the photon energy above 20 eV, and information on such processes is essential for a complete understanding of the molecular processes in the EUV region. However, our knowledge to date on superexcited states above 20 eV has been quite limited owing to their rapid decay and interference of a large cross section for direct photoionization. In this work, we have measured photoelectron spectra using synchrotron radiation in order to investigate doubly excited states and their decay of SO_2.

The experiment was carried out at the beamline BL3B in the UVSOR facility. Synchrotron radiation was dispersed by a 3-m normal incidence monochromator, and was focused onto a photoionization region. Photoelectron spectra of SO_2 were measured using a 160° concentric energy analyzer.

Figure 1 shows a photoelectron spectrum of SO_2 taken at the photon energy of 26.3 eV. Several sharp peaks are observed at the electron energy below 1.8 eV. These peaks have not been observed in He(II) photoelectron spectra previously reported, and cannot be assigned to any electronically excited states of SO_2^+.

Photoelectron spectra of SO_2 are measured at several photon energies between 22 and 32 eV. Three typical spectra are shown in Figure 2. It is found that some peaks appear at constant electron kinetic energies, which are independent of the photon energy. We have recently reported similar peaks in the photoelectron spectra of OCS, and attributed them to autoionization of superexcited sulfur atoms produced by neutral dissociation of superexcited states of OCS.[1] From comparison with the results of OCS, the peaks in Figure 2 are assigned to Rydberg states converging to $S^+(^2D^o)$, the first excited ionic state. Thus, the superexcited sulfur atoms are considered to be produced from SO_2 via the following processes:

1) $SO_2 + h\nu \rightarrow SO_2^{**}$ (Formation of a superexcited state)
2) $SO_2^{**} \rightarrow S^{**} + 2O$ (Neutral dissociation into three bodies)
   $\rightarrow S^{**} + O_2$ (Neutral dissociation into two bodies)
3) $S^{**} \rightarrow S^+ (^4S^o) + e^-$. (Autoionization of a superexcited sulfur atom)

Figure 3 shows a constant kinetic energy spectrum obtained by fixing the electron energy at 0.99 eV, corresponding to the formation of $S^{**}(4d\ ^1D^o)$. The spectrum indicates an onset at around 22.4 eV, where the lowest three-body dissociation limit $S^{**}(4d\ ^1D^o) + O(^3P^e) + O(^3P^e)$ lies. This suggests that S** atoms are mainly produced by the three-body dissociation, rather than by the two-body dissociation.

Furthermore, Figure 3 demonstrates a broad enhancement at 23 - 31 eV. Since previous photoelectron spectra have revealed the existence of satellite states of SO_2^+ in the ionization energy of 23 - 38 eV,[2] it is most likely that a number of doubly excited Rydberg states converging to the satellite states of SO_2^+ are responsible for the production of S**.

Reference

1) Y.Hikosaka, H.Hattori, T.Hikida, and K.Mitsuke, *J. Chem. Phys.* **107**, 2950 (1997).
2) D.M.P.Holland, M.A.MacDonald, M.A.Hayes, P.Baltzer, L.Karlsson, M.Lundqvist, B.Wannberg, and W.von Niessen, *Chem. Phys.* **188**, 317 (1994).

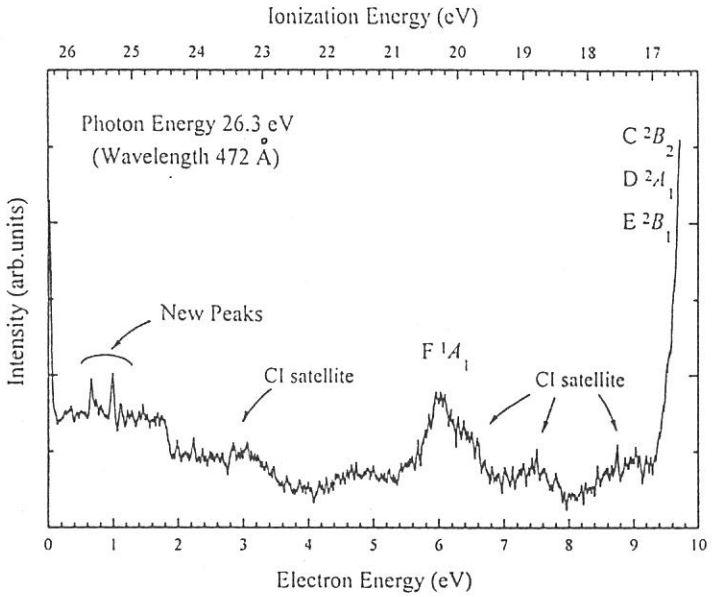

Figure 1. Photoelectron spectrum of SO_2 taken at the photon energy of 26.3 eV.

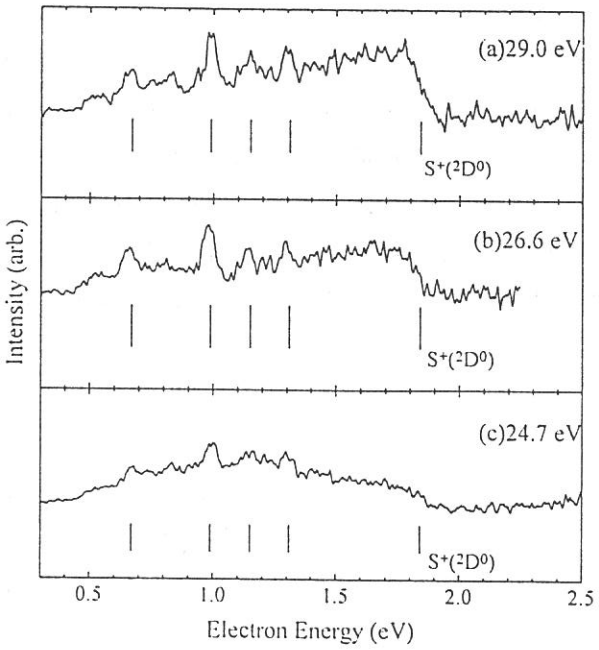

Figure 2. Photoelectron spectra of SO_2 at the photon energy of (a) 29.0, (b) 26.6, and (c) 24.7 eV. The vertical lines at 0.67, 0.99, 1.15, and 1.31 eV indicate the peaks appearing at constant electron energies, and are assigned to $5p^1F^e$, $4d^1D^o$, $6p^1F^o$, and $5d^1D^o$ states converging to $S^+(^2D^o)$, respectively. The vertical lines at 1.84 eV indicate the convergence limit of $S^+(^2D^o)$.

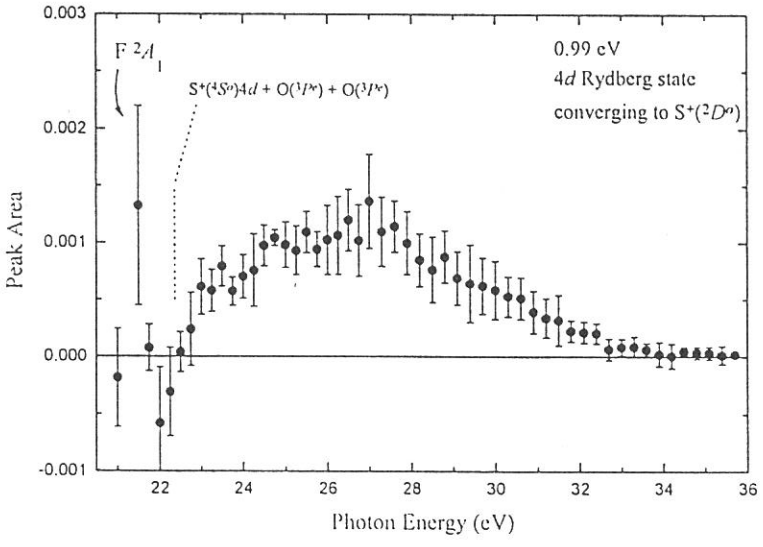

Figure 3. Constant kinetic energy spectrum for the peak at 0.99 eV in Figure 2 corresponding to the formation of the $4d\ ^1D^o$ state. The error bars represent standard deviations. The lowest limit for the three-body dissociation is indicated by the dotted line.

(BL8B1) **N AND C *K* SHELL EXCITATION OF CYANO BENZENES**

Toshio Ibuki, Kazumasa Okada[a], and Tatsuo Gejo[b]

Kyoto University of Education, Fukakusa, Fushimi-ku, Kyoto 612-0863
[a] Department of Chemistry, Hiroshima University, Higashi-Hiroshima 739-8526
[b] Institute for Molecular Science Myodaiji, Okazaki 444-8585

C_6H_5CN, C_6F_5CN, and *p*-$CF_3C_6H_4CN$ cyano benzenes have been excited at the N and C *K* shells on the soft X-ray beamline BL8B1. 3-Trifluoreomethylphenyl isocyanate, 3-$CF_3C_6H_4NCO$, was selectively exited at the N and O *K* shells. Reflectron type time-of-flight (R-TOF) mass spectrometer was installed to the main chamber to get a high resolution in mass separation. The main chamber is rotatable from –20 to 110° with respect to the electronic vector of the linearly polarized synchrotron radiation. The R-TOF mass spectra were measured at the magic angle in the present work.

The total photoabsorption (and also photoion yield) spectra of the cyano benzenes showed the distinct two or three peaks in the C and N *K* shell regions. The main band of C_6F_5CN in fig. 1, for example, would be assigned as the π*(C≡N)←N(1s) excitation. At the C *K* shell excitation the main band may be assigned as the transition to the vacant π* molecular orbital of the carbon atoms forming the phenyl group in molecule. The fragment patterns were compared between the π*←N(1s) around 400 eV and the π*←C(1s) at ≈285 eV excitations. Figure 2 shows the mass spectra measured at the π*←N(1s) resonance excitations. The difference between the two excitation modes, i.e., the π*←N(1s) and π*←C(1s), was quite small in the cyano benzenes. In the N *K* shell excitation of 3-$CF_3C_6H_4N$=C=O the small fragment ions such as H^+, N^+, O^+, N^+, and CF^+ were more produced than the terminal π*←O(1s) excitation at 530 eV, in which the relatively large fragment ions, CF_3^+, CF_2^+, and $C_6H_i^+$, survive.

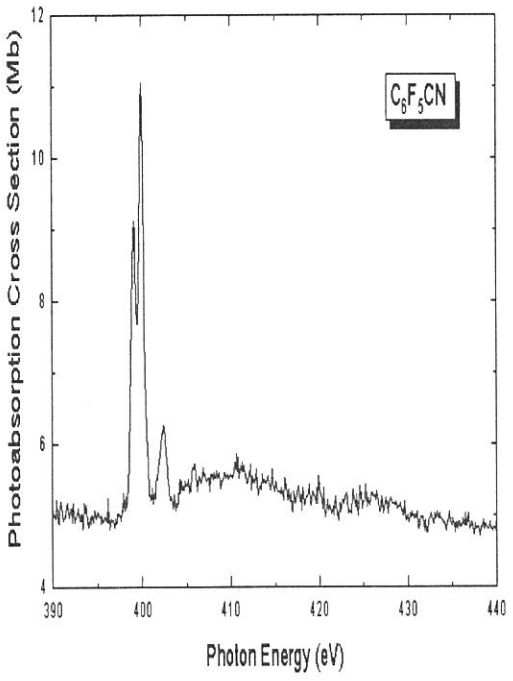

Fig. 1. Photoabsorption cross section of C_6F_5CN at the N *K* shell region.

The present observations suggest that the intramolecular energy redistribution in the *K* shell excited cyano benzene is extremely fast. In order to study the site-dependent photofragmentation it may be better to employ an aliphatic compound with functional group(s) since the selective excitation of –N=C=O group in 3-$CF_3C_6H_4NCO$ showed non-statistical

character, though it was weak.

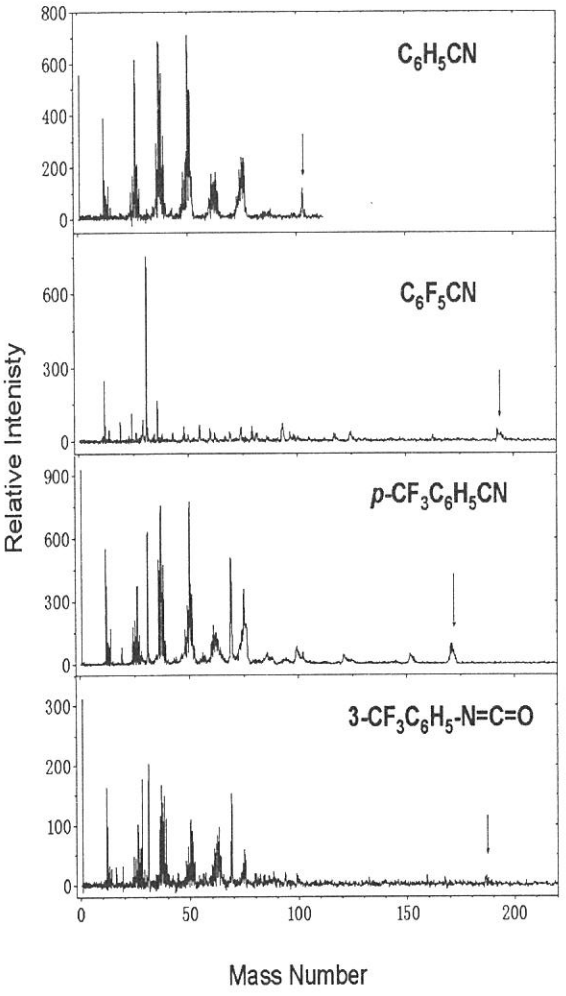

Fig. 2. R-TOF mass spectra excited at the π*← N(1s) transitions. Arrows indicate the parent ions.

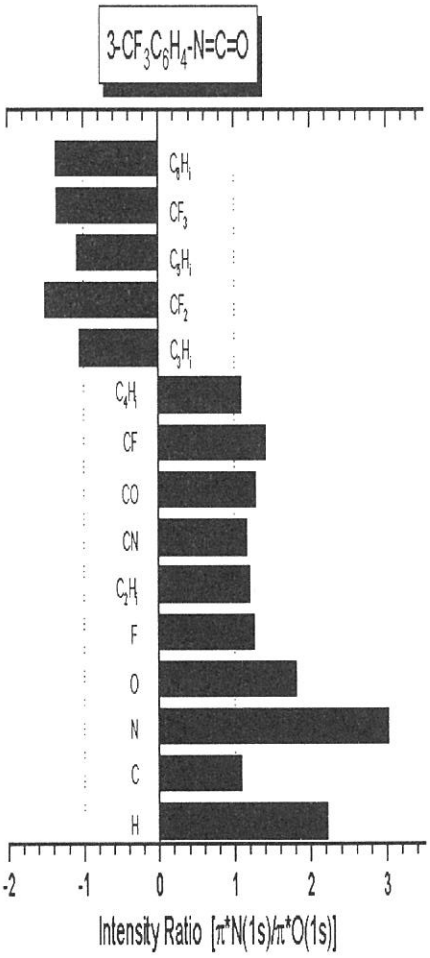

Fig. 3. Intensity ratios of the fragment ions formed at the N(1s) excitation to those at the O *K* shell excitation of 3-$CF_3C_6H_4NCO$. The fragment ions on the positive side indicate they are more produced at the central N(1s) excitation.

(BL8B1)

Photoabsorption Spectrum of Ozone in the K-edge Region

Tatsuo GEJO, Kazumasa OKADA[A] and Toshio IBUKI[B]

Institute for Molecular Science, Myodaiji, Okazaki 444-8585, Japan

[A]Department of Chemistry, Hiroshima Univ., Higashi-Hirosima 739, Japan

[B]Kyoto Univ. of Education, Fukakusa, Fushimi-ku, Kyoto 612, Japan

Ozone is one of the most important molecules in chemistry since ozone in the stratosphere absorbs UV light emitted from the sun and prohibits humanity from the exposure by the UV light. In view of this ozone effect, many experimental and theoretical exertions have been devoted to the spectroscopic studies of ozone. However, highly electronically excited states of ozone have not been fully understood yet nor have the spectroscopic data exceeding 20 eV been reported so far as we know. In order to explore the electronic states of ozone by the O(1*s*) core excitation, we have constructed an ozone supply apparatus on the beam line BL8B1. As a result, the photoabsorption and total electron yield spectra of ozone have been successfully measured for the first time in the soft-X-ray region 520-555 eV.

The photoabsorption spectrum have been measured at BL8B1. A photoabsorption cell was 25.0 cm long, which was attached to the main chamber. The typical sample pressure in the cell was 25 Pa measured by a Baratron manometer. An aluminum thin filter with a thickness of 100 nm was installed in front of the cell in order to keep the monochromator in high vacuum. The intensity of photon beam transmitted through the cell was monitored by using a silicon photodiode (IRD AXUV-100). The photoabsorption cross sections were calculated by using the Beer-Lambert expression. The data were checked to ensure that there is no line saturation effect.

The total photoabsorption cross sections of O_3 is shown in fig. 1. The corrected cross section was obtained after removal of the contribution from the coexisting O_2 component, assuming that the peak at 530.9 eV was a pure $\pi^*\leftarrow$O(1*s*) transition of O_2. The reported ionization potentials (IPs) of the O(1*s*) electrons in ozone are indicated by arrows. Fig. 1 is the first report for the absolute total photoabsorption cross section of O_3 in the soft X-ray region.

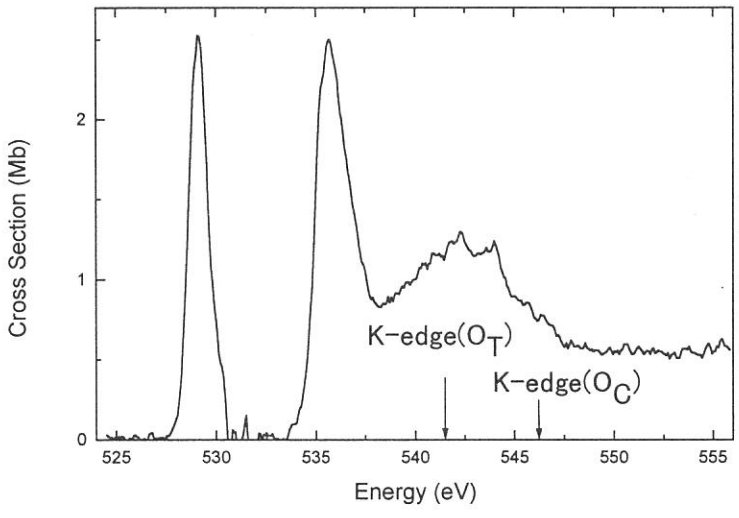

Fig. 1. Total photoabsorption cross section of ozone in the 525-555 eV energy region. Arrows show the ionization potentials of the 1s electrons at 541.5 and 546.2 eV obtained by XPS[1] of O_3.

The configuration of a molecular orbital (MO) representation in the ground state O_3 is:

Core: $1a_1^2 2a_1^2 1b_2^2$

Valence: $3a_1^2 2b_2^2 4a_1^2 5a_1^2 3b_2^2 1b_1^2 1a_2^2 4b_2^2 6a_1^2$

Vacant: $2b_1^0 7a_1^0 5b_2^0$

where the innermost $1a_1$ MO corresponds to the 1s orbital of the central oxygen atom, and the degenerate $2a_1$ and $1b_2$ MO's are almost even and odd combinations of the terminal O(1*s*) orbitals, respectively. Although the $2b_1(\pi^*)$ MO is vacant in the closed shell description, it has to be treated on an equal footing with the $1a_2$ MO because of the π biradical nature. The $7a_1$ MO is the lowest vacant σ^* level.

Two peaks definitely appear at 529 and 536 eV in fig. 1. Strong $\pi^* \leftarrow$O(1*s*) transition probability has been commonly observed at $\approx$ 530 eV in the O(1*s*) core-excitation of the compound containing O-atom. We assign the first distinct peak at 529.1 eV to be the $\pi^*(2b_1) \leftarrow 1s(2a_1)$ resonance excitation of the terminal oxygen atom of O_3 since the IP of the terminal O(1*s*) atom lies 4.7 eV lower than that of the central one, i.e., the $1a_1$ MO. Accordingly, the second peak at 536 eV may arise from the central O atom. However, the 536 eV band is convoluted at least by two Gaussian functions peaked at 535.4 and 536.3 eV.

Thus, electronic structure of the core-ionized and the core-excited states of O_3 were obtained by *ab initio* SCF calculations by using the code named GSCF3 [2, 3]. The calculations predict there exist six excited states below the K edge: two π^* and four σ^* states. Taking account of the IP difference between the central and the terminal O atoms, we assign the 535.4 eV band as the excitation to the π^* level from the center O(1*s*) MO. By comparing the term values obtained experimentally and theoretically in table 1, the proposed assignments are given in the last column.

Support of this work by New Energy and Industrial Technology Development Organization (NEDO) is gratefully acknowledged. We thank Prof. Kosugi, Dr. Adachi and Mr. Hatsui at IMS for technical assistance and for helpful discussions.

Reference

[1] M. S. Banna, D. C. Frost, C. A. McDowell, L. Noodleman and B. Wallbank, *Chem. Phys. Letters* 49 (1977) 213

[2] N. Kosugi and H. Kuroda, *Chem. Phys. Letters* 74 (1080) 490

[3] N. Kosugi, *Theor. Chim. Acta* 72 (1987) 149

Table 1. Peak positions, term values, effective principal quantum number n*, term values in the SCF calculation, and the proposed assignments.

Experiment			*ab initio* SCF calc.	Proposed assignments
Peak position (eV)	Term value (eV)	n*	Term value (eV)	
529.1	12.4(O_T)		12.0(O_T)	$\pi^*(2b_1) \leftarrow 2a_1$
535.4	10.8(O_C)		13.4(O_C)	$\pi^*(2b_1) \leftarrow 1a_1$
536.3	5.2(O_T)	1.6	3.9(O_T)	$\sigma^*(7a_1) \leftarrow (2a_1/1b_2)$
-	-	-	0.7(O_T)	$\sigma^*(5b_2) \leftarrow 2a_1$
541.5[a](O_T)				$(2a_1)^{-1}$ or $(1b_2)^{-1}$
542.31.9	3.9(O_C)	1.9	3.4(O_C)	$\sigma^*(7a_1) \leftarrow 1a_1$
544.02.5	2.2(O_C)	2.5	1.6(O_C)	$\sigma^*(5b_2) \leftarrow 1a_1$
546.2[a](O_C)				$(1a_1)^{-1}$

[a] Taken from ref. 1

(BL8B1) Vibration-resolved yield spectra of fragment ions from N_2 around the N1s to π^* resonance

Norio Saito[A] and Tatsuo Gejo

Institute for Molecular Science, Myodaiji, Okazaki 444-8585
[A] *Electrotechnical Laboratory, Umezono, Tsukuba-shi, 305-0045*

Resolution power of a soft X-ray monochromator has been developed and vibration-resolved spectra of several molecules have been obtained in these years. The fragment ion yield spectra from CO around the C-K edge shows dependence on vibration levels of excited states.[1] In this report, we have measured vibration-resolved fragment and parent ion yield spectra of N_2 around the N1s to π^* resonance.

The experiment has been performed at the beam line BL8B1 of UVSOR. A time-of-flight (TOF) mass spectrometer was used to obtain fragment ion yield spectra. An effusive flow of N_2 was introduced into the spectrometer at the presser of 2×10^{-5} Torr. A high field was applied in the collision region of the spectrometer so as to collect all kinetic ions. TOF of ions was measured with a TAC. The output pulse height from the TAC was analyzed with a MCA and SCA's. The windows of the SCA's were tuned so as to receive a pulse corresponding to N^{2+}, N^+, and N_2^+. The signals of the SCA's were counted and transferred to a computer.

Figure 1 shows an example of a TOF mass spectrum of N_2 measured at the excitation from 1s to $2p\pi_g(v=0)$. The dominantly produced ion is N^+. Yields of N^{2+} and N_2^+ are about 10% of that of N^+.

Figure 2 shows vibration-resolved ion yield spectra of N^{2+}, N^+, and N_2^+. The dots shows the experimental data and the solid curves are fitted with the Voigt function. The profiles of the N_2^+ spectrum are slightly different from those of the other spectra. These profiles agree with unpublished data measured by Saito *et al.*[2]

Reference

1) N.Saito, F.Heiser, O.Hemmers, A.Hempelmann, K.Wieliczek, J.Viefhaus, and U.Becker., Phys. Rev. A, **51**, R4313 (1995).
2) N.Saito, F.Heiser, and U.Becker, to be published.

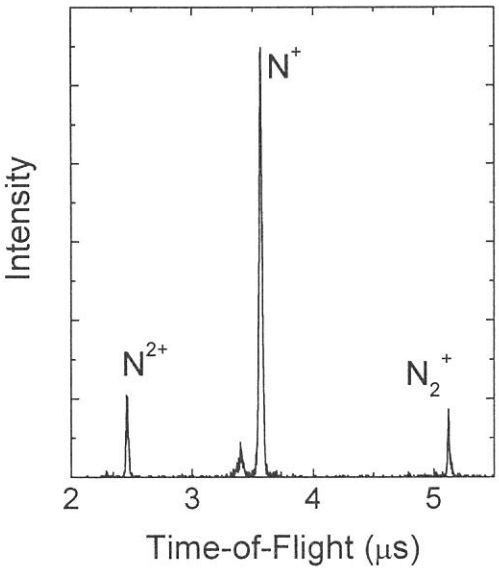

Fig.1 a TOF mass spectrum of N_2 measured at the excitation from 1s to $2p\pi_g(v=0)$.

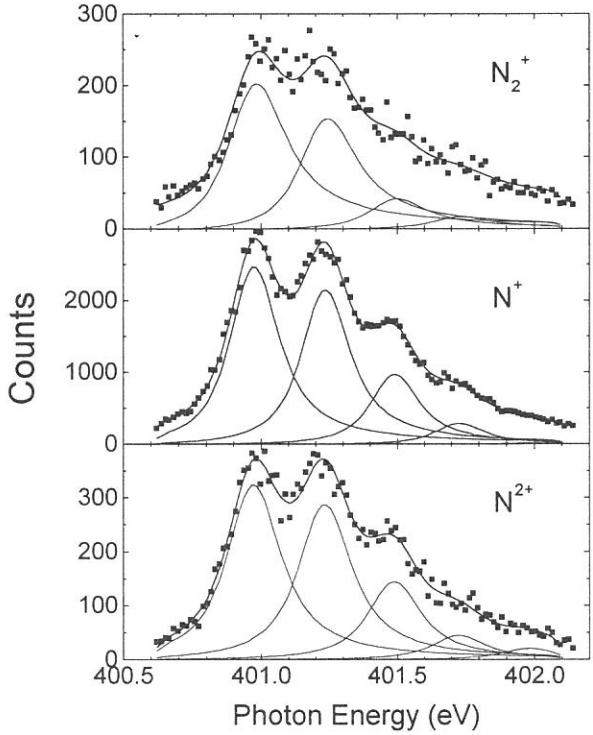

Fig.2 Vibration-resolved ion yield spectra of N^{2+}, N^+, and N_2^+ at the π^* resonance.

(BL8A)

Fourier-Transform Spectroscopy and Photon Echo in Vacuum Ultraviolet Region

S. Asaka[A] and H. Nakatsuka[B]

[A]*Equipment Development Center, Institute for Molecular Science, Okazaki 444-8585*
[B]*Institute of Applied Physics, University of Tsukuba, Tsukuba 305-0004*

We have performed accumulated photon echo experiments by using synchrotron radiation (SR) in near vacuum ultraviolet region.

Photon echo experiments generally give us information of optical T_2, or the phase relaxation time of the sample resonance lines. Among many types of photon echoes, the accumulated photon echo has excellent features in that it gives a signal magnitude and a signal-to-noise ratio much larger than other types of photon echoes by using repetitively pulsed or quasi continuous excitation source. Furthermore, the time resolution in measuring T_2 is simply determined by the correlation time (i.e. the inverse of spectral width) of the source so that a femtosecond resolution can be easily achieved by using a wide-spectral-band source.

A periodic but static change of light intensity is formed over spectral axis if time-delayed two light beams are present. This structure is copied into the inhomogeneously broadened resonance line of the sample, thus forming a "population grating". The accumulated photon echo is based on the diffraction of the excitation light by this population grating. If the electrons of the sample stay a long time at some bottleneck state other than the ground state after resonant transition, the population grating in the ground state accumulates over the bottleneck lifetime, resulting in a large echo signal.

The SR is useful as an excitation source for accumulated photon echo experiments because it is quasi continuous and it has a wide spectral band especially in short wavelength region, where other light sources cannot give sufficient light intensity for echo measurements. The echo time resolution is, for example, 40 fs if we cut out a spectral portion of SR by a width of 0.1 eV.

Before the present study, accumulated photon echo experiments by using SR have been done at UVSOR for several organic molecules embedded in polymers as sample materials[1]. Excitation wavelengths were around 300 nm in these measurements. In the present study we extended excitation wavelength to about 200 nm and applied to inorganic crystals.

The experiment was done at BL8A of UVSOR. The experimental set-up was almost the same as in reference 1, except that the beam splitter was modified and the dispersion compensator was removed. The beam splitter used here consisted of two identical half mirrors. They were made by dividing equally a single half mirror and then mounted back-to-back so that their active surfaces are in one plane. The center of the excitation wavelength was selected by selecting appropriate combination of coatings of the beam steering mirrors and the beam splitter.

We tried echo measurement for two kinds of alkali-halide crystals as sample materials: RbI, KBr. The sample temperature was about 5 K. We tuned the excitation wavelength at the foot of the exciton absorption, which is 220 nm for RbI and 230 nm for KBr, and about half of the excitation energy was absorbed. The correlation time of the excitation was about 30 fs. We also tried a mixed crystal of RbI and KI at wavelength of 230 nm expecting a broad inhomogeneous distribution.

For the samples we tried we have not obtained any detectable echo signal. We do not know about he existence of bottleneck states in the present samples, and even less about their life times. Since fluorescence quantum yields are not so small in these samples, we can conclude at least that the bottleneck states do not effectively work in the present samples if any.

Reference

[1] H. Itoh *et al.*, UVSOR Activity Report 1996, 228(1997).

[BL-8A]

Temperature-dependent dephasing characteristics of Phenol doped in hosts and long-term phase stability of interferometer

H. Itoh[1], S. Nakanishi[1], T.Fuji[2], T.Kashiwagi[2], M.Furuichi[2], N. Tsurumachi[2], H. Nakatsuka[2], S. Asaka[3] and M. Kamada[4]

[1]*Department of Advanced Materials Science, Kagawa University, Takamatsu 760-8526*
[2]*Institute of Applied Physics, University of Tsukuba, Tsukuba 305-8573*
[3]*Equipment Development Center, Institute for Molecular Science, Okazaki 444-8585*
[4]*UVSOR, Institute for Molecular Science, Okazaki 444-8585*

We have applied synchrotron radiation (SR) to investigate FM-modulated incoherent accumulated photon echo signals of simple aromatic molecules doped in Polyvinyl Alcohol(PVA) and Polymethel Methacryrate in ultraviolet wavelength region. In this paper, we show two experimental results. One is precise temperature dependent phase relaxation of Phenol doped in PVA, relating to the relaxation way of Aniline doped in same host. On the other hand, signal intensities have extremely reduced since the latter half of last year. Then we check the reliability of our experimental apparatus to make its reason clear. The experiment was performed at BL-8A. The output beam from the quartz window of the BL-8A was filtered by the bandpass filter with the center wavelength of 289 nm, the bandwidth of about 12 nm and the maximum transmission rate of about 18%.

The temporal width of field autocorrelation was measured as 25 fs, corresponding to the bandpass filter used. In that time, to compensate the dispersion of the system, we inserted a quartz plate with 3 mm thick tilting by 34 degree of angle to the SR beam path between the PBS and one of the corner cube prisms. Figure 1 shows temperature dependent dephasing characteristics of Phenol doped in PVA as a function of inverse of temperature. The dephasing time of Phenol is longer as orders than that of the Aniline at the temperature around 4 K[1]. This dephasing characteristics would be originated from the interaction between the host and the guest molecules, such as TLS transition of host molecules, i.e. non-photochemical hole burning. Because this dephasing characteristic is inferred from the results, which have been investigated in many molecules doped in hosts in visible wavelength region. It is thought from this result that the dephasing mechanism for the Aniline/PVA would be slightly different from that of the Phenol/PVA system. The short dephasing time would reflect that the potential minimum of each ground and first excited state are shifted each other in normal coordinate, so that 0-0 transition of electro-vibronic states could not satisfy the Frank-Condon principle. Resulting from fast energy relaxation in excited state(internal conversion), phase coherence between ground and excited state is not maintained so long period.

Next we check long-term phase stability of the Michelson interferometer we used. Output SR beam from the interferometer was continuously detected by p-i-n photodiode when the interferometer's arm length was fixed at a position. At the same time, interference signal of a He-Ne laser was also detected by another p-i-n photodiode using same interferometer in the same geometry as the SR beam for investigating the stability of the Michelson interferometer alone. we show both intensities of interference lights as a function of time in Fig.2, solid and dotted line correspond to the signals by the SR light and He-Ne laser, respectively. The interference intensity of the SR drastically changed at random in short period according to the phase hopping from 0 to 180 degree. On the other hand, the intensity by the He-Ne laser did not change so drastically that the main instability factor is originated from spatial hopping of SR beam. This hopping of the SR beam erases holes burned in the sample. Since echo intensities are proportional to the depth of burned phase grating, we can not get fully accumulated signals. It is needed to keep, at least, this phase variation small in one round of the detecting period. It is thought that this hopping is caused from bad vacuum condition in beam line.

Reference

[1] H.Itoh et al. UVSOR Activity Report 1996.

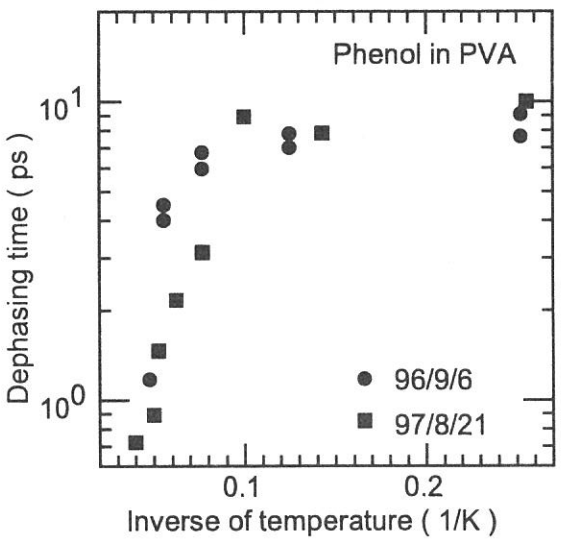

Fig. 1: Accumulated photon echo decay of Phenol doped in PVA as a function of inverse of temperature from 4.3 to 20K. The excitation wavelength is 289 nm with the bandwidth of about 12 nm. We show two results, circle denotes result of Sept.'96 and square corresponds to that of Aug.'97.

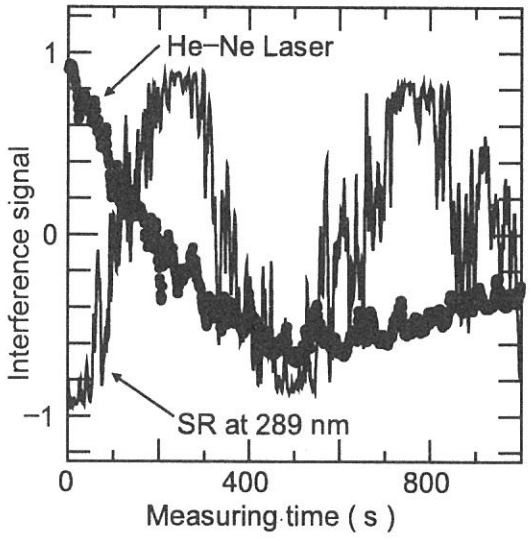

Fig. 2: Stability of interference signal with the path length in the Michelson interferometer fixed. Circle denotes the case of He-Ne laser and solid line corresponds to that of SR beam at 289 nm.

(BL1B & BL6A1)

Anisotropic reflectivity spectra of *R*PtAs (*R* = Ce, La)

S. Kimura, K.G. Nath[1], Y. Haruyama, T. Kinoshita, S. Yoshii[2] and M. Kasaya[2]

UVSOR Facility, Institute for Molecular Science, Okazaki 444-8585
[1]Department of Structural Molecular Science, The Graduate University for Advanced Studies, Okazaki 444-8585
[2]Department of Physics, Tohoku University, Aoba-ku, Sendai 980-8578

The crystal structure of CePtAs is hexagonal YPtAs-type ($P6_3/mmc$). The transport property along *c*-axis ($I \parallel c$) is semiconducting and that perpendicular to *c*-axis ($I \perp c$) is metallic. The Hall coefficient of $I \parallel c$ and $H \perp c$ is negative and small and that of $I \perp c$ and $H \parallel c$ is positive and large [1]. Here, *I* indicates current direction and *H* applied magnetic field. Therefore not only the shape of the Fermi surface and also the electronic structure attracts attention. In this study, we measured reflectivity spectra of CePtAs and of the reference material LaPtAs for the investigation of the electronic structure that makes the anisotropy of the transport and the mobility. The x-ray photoemission spectra (XPS) of valence band have also measured for the investigation of the occupied state.

The reflectivity spectra was measured at two beam lines of 1B and 6A1 for the measurements of visible - VUV (2 - 30 eV) and infrared (0.01 - 2 eV) regions, respectively. Obtained spectra of *R*PtAs are shown in Fig. 1. Anisotropy of reflectivity spectra is observed. XPS was measured by using a commercial system (FISONS Instruments, ESCALAB 220i-XL) and Mg-Kα line.

In figure 2, optical conductivity (OC) spectra of CePtAs with $E \perp c$ and $E \parallel c$ are shown. The OC spectra were determined from a Kramers-Kronig analysis of the reflectivity spectra. Optical anisotropy can be clearly observed in the whole photon energy region. Particularly, in the low energy part, the spectrum with $E \perp c$ shows metallic one because Drude type OC appears. On the other hand, the spectrum with $E \parallel c$ seems to be of a semiconductor. The result is consistent with the anisotropy of the electric resistivity.

Since the DC conductivity with $I \perp c$ at 300 K is $3.6\times10^3\ \Omega^{-1}\mathrm{cm}^{-1}$, the Drude curve of the OC with $E \perp c$ is considered to connect to DC smoothly.

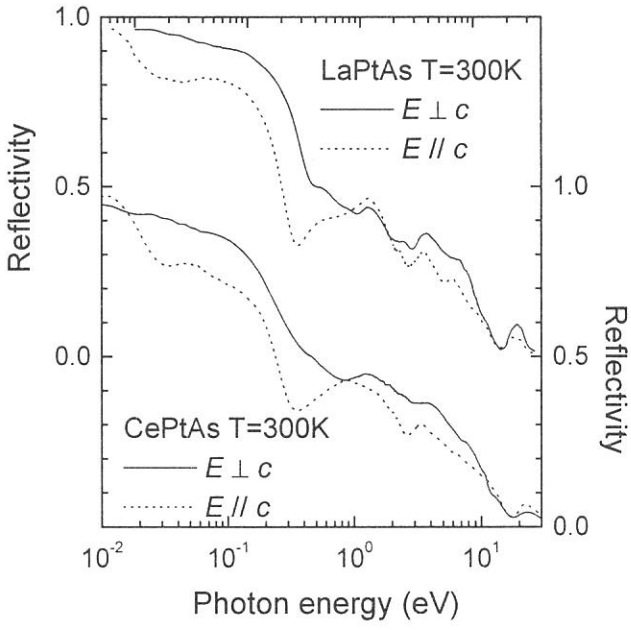

Fig. 1. Anisotropic reflectivity spectra of *R*PtAs (*R* = La, Ce) in the energy range of 0.01 - 30 eV.

And also, the OC with E // c smoothly connected to the DC conductivity with I // c because the DC conductivity is about 0.37×10^3 $\Omega^{-1}cm^{-1}$. The energies of the plasma edges with $E \perp c$ and with E // c are about 0.3 eV and about 0.03eV, respectively. Generally square of energy of plasma edge is proportional to the effective carrier density ($N\times m_0/m^*$, where N is the carrier density, m_0 the static mass of an electron and m^* the effective mass). Therefore the effective carrier density with $E \perp c$ is hundred times higher than that with E // c. Therefore the mobility (effective mass) with $E \perp c$ is hundred times larger than that with E // c. This is an origin of the anisotropy of physical properties of CePtAs.

Higher energy part of OC spectra and XPS of CePtAs are shown in Fig. 3. The binding energy of XPS is shifted by 0.5 eV from the photon energy of OC spectra. Double peak structure at 4 and 5 eV of XPS mainly originates from Pt 5*d* state. Therefore the shape of OC around 4 eV is due to the charge transfer excitation of Pt $5d \rightarrow$ Ce $4f$. The shape of the reflectivity spectra of LaPtAs around 4 eV is sharper than that of CePtAs in Fig. 1. Since the multiplet structure of $4f^2$ final state of Ce^{3+} after photo absorption is wider than that of $4f^1$ final state of La^{3+}, the difference appears in the reflectivity spectra.

---

[1] S. Yoshii et al., Proc. Int. Conf. Magn. 97. (to appear in J. Magn. Magn. Mater.)

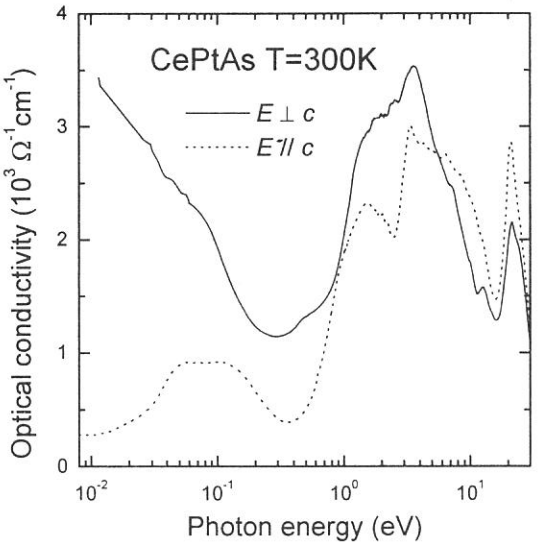

Fig. 2. Anisotropic optical conductivity of CePtAs. The spectrum with $E \perp c$ shows metallic one but that with E // c looks like an insulator.

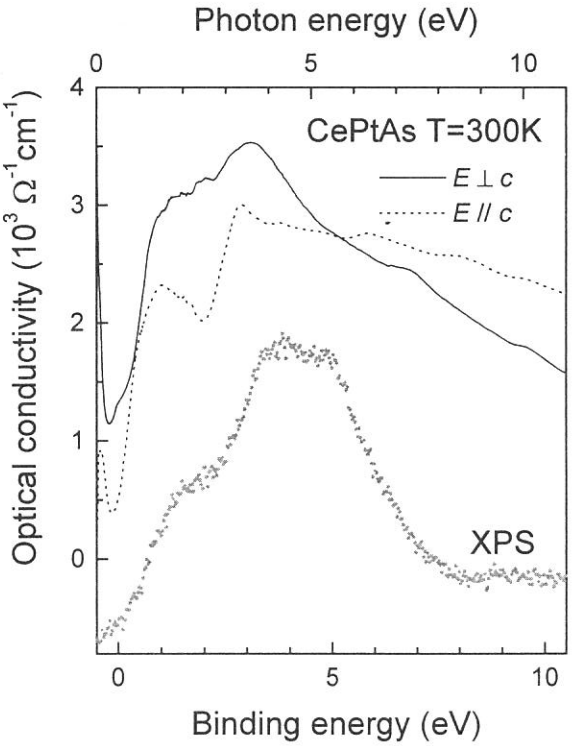

Fig. 3. Comparison of optical conductivity spectra of CePtAs with the valence band photoemission spectrum. The binding energy of photoemission spectrum shifted by 0.5 eV from the photon energy of optical conductivity spectra.

(BL-1B)

Determination of Threshold Energy of Color Center Formation in Anthracene Single Crystal

Iwao Shimoyama and [1] Kazumichi Nakagawa

Graduate School of Sci. and Tech., Kobe University, Rokkohdai, Nada-Ku, Kobe 657, Japan
[1]Faculty of Human Development, Kobe University, Tsurukabuto, Nada-Ku, Kobe657, Japan

Anthracene single crystal is a standard for radiation scintillator. Scintillation efficiency is known to be degraded by radiation induced color centers. However the detail of radiation damage of anthracene has not known yet. To clarify the lowest excitation state form which color centers are produced, we measured quenching of fluorescence of S_1 exciton as a function of irradiation time and determine the threshold energy of color center formation.

Experiments were performed at BL-1B. Anthracene crystals were grown by sublimation method from scintillation grade anthracene powder of Kantou Kagaku Company after purification by zone melting method. Samples were placed in vacuum chamber (10^{-8}Torr) and cooled at 200K. We used fluorescence quenching technique (FQT). In FQT, at first, fluorescence intensity $I_F(0)$ induced by 365nm light and intensity M of 365nm light is measured before VUV irradiation. The 365nm light is known to produce S_1 exciton and not to produce color centers. Fluctuation in the value of $I_F(0)/M$ was confirmed to be less than 1% during 110 minutes (see figure 1). Next, the sample were irradiated by VUV with various energies ($h\nu$ = 9.0, 9.5, 10, 10.8, 13.7 and 17.7 eV) during T seconds. After stopping VUV irradiation, we measured $I_F(T)/M$ as a function of T. We estimated irradiation photon numbers N_λ ($= I_\lambda T$) by measuring incident photon numbers I_λ per second. And we obtained S_1 quenching rate $I_F(N_\lambda)/I_F(0)$ as a function of N_λ. Figure 2 shows $I_F(N_\lambda)/I_F(0)$ plots for irradiation of VUV with the energies 9.0(●), 9.5(△) and 10eV(■). In the case of 9.0, $I_F(N_\lambda)/I_F(0)$ shows no quenching. Therefore we concluded that color center isn't formed at this photon energy. In the case of 9.5 eV, $I_F(N_\lambda)/I_F(0)$ shows just small values near $N_\lambda = 4\sim5\times10^{14}$ [photons]. However the data doesn't show systematically decrease, therefore we couldn't conclude whether color center is formed or not at this photon energy. While, in the case of 10eV, $I_F(N_\lambda)/I_F(0)$ decrease apparently. In other cases that photon energy are larger than 10eV, we also obtained apparent decrease of $I_F(N_\lambda)/I_F(0)$. Therefore we concluded that the threshold energy of color center formation is about 9.5eV.

It is considered that C-H bond dissociation is important reaction to form color center. For anthracene vapor, C-H bond assignment has reported only in the energy region 5～8.5 eV. In an

assignment of benzene vapor reported by Koch *et al.* [1], the highest C-H bond is assigned to 11eV, we couldn't also find C-H bond near 9.5eV. From our result, the transition energy which concern C-H bond should be near 9.5 eV. This result seems to indicate the possibility of new theory for molecular orbital calculation.

[1] E. E. Koch and A. Otto, Chem. Phys. Lett., 21,501(1973)

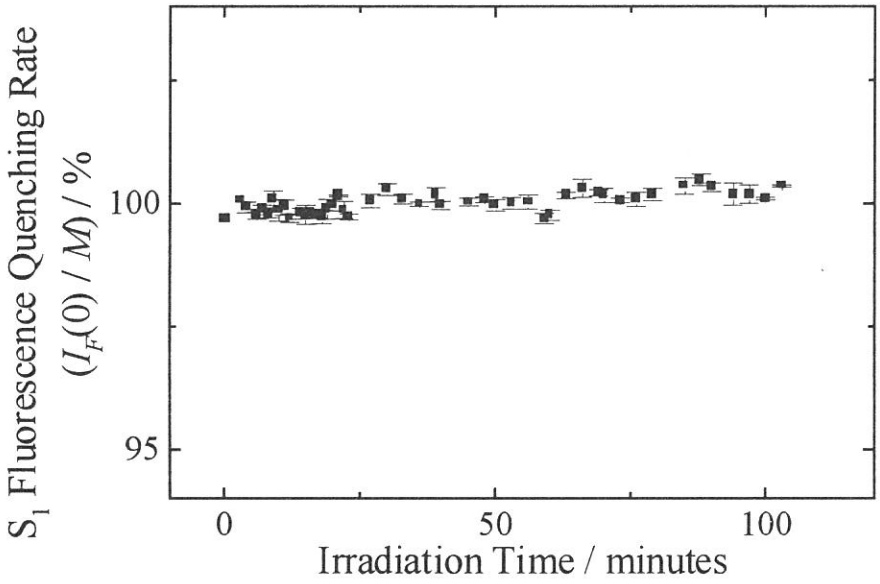

Figure 1. Stability of $I_F(0) / M$

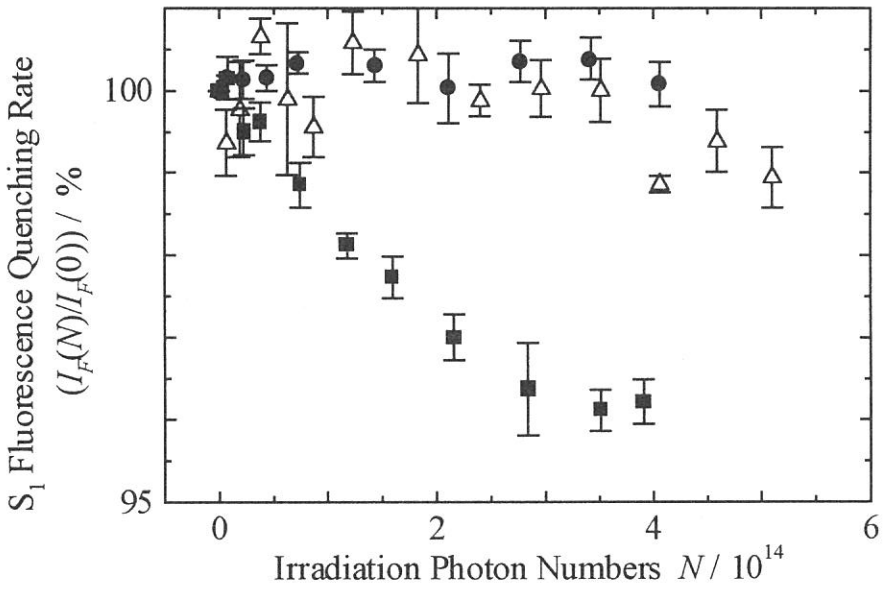

Figure 2. S1 quenching rate $I_F(T) / I_F(0)$

$h\nu$ = ● : 9.0, △ : 9.5, ■ : 10eV

(BL1B)

VUV~UV absorption spectra of thermally poled synthetic silica glass

Akihiro Kameyama, Atsushi Yokotani and Kou Kurosawa

Department of E&E Engineering, Miyazaki University, Miyazaki 889-2155

Silica glass has become much more important and also attractive for photonics engineering, because a new function of a permanent strong second-order optical nonlinearity has been observed in poled silica glass in addition to high transparency and high band-gap energy. Although the optical nonlinearity is as high as 1 pm/V in thermally poled fused silica glass by Myers et al.[1], the optical nonlinearity in thermally poled synthetic silica was about one order of magnitude smaller than in the fused silica one. We have reported[2] that the large second order nonlinearity of 0.2pm/V in high-purity synthetic silica glass exposed to X-ray before the poling procedures. Furthermore we have observed that the large second order nonlinearity in high-purity synthetic silica glass with KrF excimer laser exposure before the poling procedures. The radiation-induced defects seem to be important for the generation of second order nonlinearity.

In order to identify the defects relevant to the generation, we observed VUV absorption spectra for the poled synthetic silica glass with KrF excimer laser exposure before the poling procedures.

We used samples of synthetic silica glass supplied from Nippon Silica Glass. The samples have a plate-like shape with 20 mm in diameter and 1.5 mm in thickness and the surface were finished to optical quality. The samples were exposed to 248-nm pulses of 10000 shots of 50 mJ/cm^2 from a KrF excimer laser. The poling procedures were as follows: A sample plate was sandwiched with two electrodes maintained at a high voltage of 4.5 kV, heated up to 260°C at the rate of 10°C/min, held for 20 min, and then cooled down to room temperature at the rate of 10°C/min before removing the voltage.

In Fig. 1 are plotted SHG intensities as function of incident angle of Nd:YAG laser beam observed in the poled synthetic silica with and without the laser irradiation. The SHG intensity was observed only in the exposed sample, but not in the non-exposed sample.

We observed absorption spectra with the use of BL1B beam line at UVSOR. In Fig. 2 are shown transmittance spectra taken from samples with and without the KrF excimer laser exposure. The laser radiation apparently decreases a 6.3-eV absorption peak which is assigned to E'center, and further increases significantly a 4.7-eV absorption peak which is probably to be NBOHC (≡Si-O*) or ≡Si-O$^-$.The photon energy of 5.0 eV is very close to the center energy of absorption bands. Such speculation agrees with the result the X-ray irradiation experiments[2], namely ≡Si-O* or ≡Si-O$^-$ induced in high purity silica glass and to be close-related with the nonlinearity creation.

In summary, we investigated a VUV absorption spectra of the poled synthetic silica glass with KrF excimer laser exposure before the poling procedures. We conclude that the optical nonlinearity include defects related with Si-O at least in pure silica glasses.

Reference
1) R.A.Myers, N.Mukherjee, and S.R.J. Brueck, Opt. Lett. 16, 1732 (1991).
2) A.Kameyama, E.Muroi, A.Yokotani, K.Kurosawa and P.Herman,
J.Opt.Soc.Am. B, 14, 1088 (1997).

Fig. 1 The SHG intensities as function of incident angle of YAG laser beam in the thermally poled silica glass with (●) and without (■) KrF excimer laser exposure.

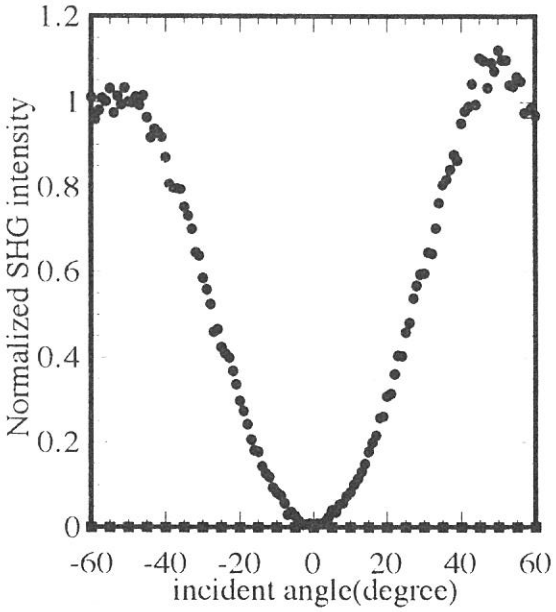

Fig. 2 Transmittance spectra taken from silica glass with (●) and without (■) KrF excimer laser exposure.

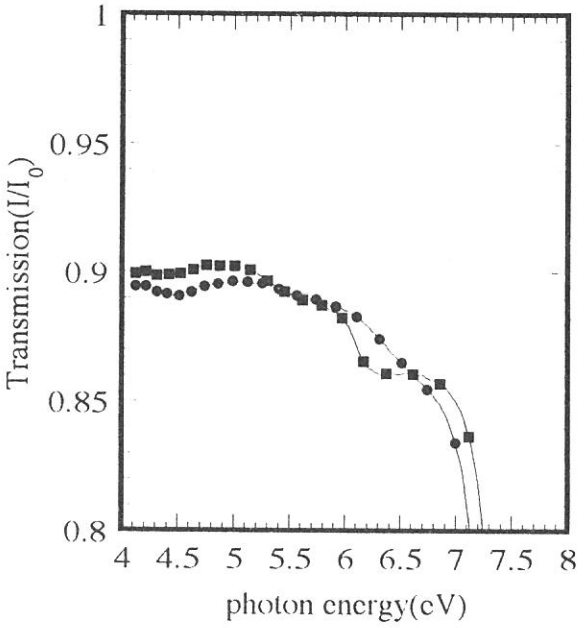

(BL1B)

Concentration of neutral oxygen vacancies in buried oxide formed by implantation of oxygen

K. S. Seol, T. Futami, and Y. Ohki

Department of Electrical, Electronics, and Computer engineering, Waseda University, 3-4-1 Ohkubo, Shinjuku-ku, Tokyo 169

Buried oxide layers in the silicon-on-insulator structure separated by implanted oxygens (SIMOX) have become widely used for a high speed metal oxide semiconductor (MOS), a radiation-hardened complementary MOS (CMOS), and other smart devices.[1,2] Many researches have been done recently on the nature of the buried oxide[3], since it plays an important role in determining the device properties. It has been considered that the buried oxide is far more oxygen-deficient than the conventional thermal oxide,[3] and that this deficiency is believed as one reason of unusual behavior of buried oxide such as enhanced electrical conductivity, charge buildup, and sensitivity to defect generation.[3]

It has been known that buried oxide contains neutral oxygen vacancies ($O_3{\equiv}Si\text{-}Si{\equiv}O_3$) which are typical in oxygen-deficient amorphous SiO_2.[4] In this study, the vacancy concentration in buried oxide is estimated by measuring the PL intensity.

In any material, the concentration (N) of photo-absorbing defects can be easily estimated from the following equation by measuring the optical absorbance (A) if their absorption cross section (σ) and the sample thickness (L) are known:

$$A = L\alpha = L\sigma N , \qquad (1)$$

where α is the optical absorption coefficient. However, in the case of the present buried oxide sample, it is impossible to measure A because of the opaqueness of the Si substrate. One possible method to estimate the concentration of oxygen vacancies is to measure the PL emitted from the vacancies. It is known that the 4.3-4.4 eV PL is the luminescence from the vacancies[5] and that its two excitation bands at 5.0 and 7.6 eV are due to absorptions by '*unrelaxed*' and '*relaxed*' oxygen vacancies, respectively.[6] Here, the unrelaxed vacancy has a larger bond length between the two silicons and the relaxed vacancy has a shorter one.[6] The PL intensity (I_{PL}) normalized by the excitation photon intensity (I_{EXC}) is given by,[5]

$$I_{PL} / I_{EXC} = \eta \cdot (1 - \exp(-\alpha L)) . \qquad (2)$$

Here, η is the quantum efficiency of the PL. It is reasonable to assume that the true quantum efficiency for a specific PL by a specific PL excitation band, namely the PL photon number induced by a certain number of incident photons, is independent of the sample whether it is a thick silica glass or a thin buried oxide layer. Of course, such a true efficiency cannot be measured in actual experiments. First, since I_{EXC} was measured with a photomultiplier coated with sodium salicylate whose fluorescent quantum yield is constant between 4 and 20 eV,[7] I_{EXC} in the present research represents only a relative number of the incident photons. Secondly, although all the experimental conditions such as the configuration of photo-detecting systems were exactly the same for the two samples, the two samples differ in the point that the buried oxide layer has a Si substrate at its back. Some of the incident photons, which should pass through the silica glass, could be reflected by the Si substrate. Reflectance at the interface between crystalline Si and vacuum is reported to be 60-70 % at 4.3, 5.0, and 7.6 eV.[8] The reflectance at the present SiO_2/Si interface should be somewhat smaller, while the reflectance at SiO_2/vacuum interface could be assumed zero. The reflectance at SiO_2/Si increases not only the effective incident photons but also the effective PL intensity. Therefore, if the reflectance at the SiO_2/Si interface is assumed to be 60 %, the effective value of η for the buried oxide sample becomes $(1.6)^2$ times as high as that for the silica glass.

PL intensities was first measured for an oxygen-deficient silica glass, the α value of which had been calculated by measuring the absorbance. Then, under the same condition, PL intensities were measured on the buried oxide layer. The PL measurement was carried out at 13 K using synchrotron radiation at the Institute for Molecular Science, Okazaki, Japan. The investigated silica glass was manufactured by the soot remelting method and its thickness is 0.7 mm. The SIMOX sample was fabricated by implanting O^+ ions up to a dose of $3.7{\times}10^{17}$ cm^{-2} with an energy of 180 keV into a Si substrate, and subsequent annealing in an Ar atmosphere followed by oxidation at 1350 °C for several hours. The thickness of the buried oxide layer is about 130 nm. For the PL measurement, the thermal oxide and the Si layer over the buried oxide were respectively removed by soaking the sample in a HF solution and subsequently in a KOH solution.

Figure 1 shows the PL spectra from the buried oxide layer excited by 5.0 and 7.6 eV photons. The PL band with a peak at 4.3-4.4 eV appears regardless of the excitation photon energy. The PL intensity shown in Fig. 1 was calibrated by taking the intensity variation of the excitation photons into consideration. Quite similar PL spectra were obtained for the glass sample. The measured apparent values of I_{PL}/I_{EXC} excited at the 5.0 eV excitation band and at the 7.6 eV band are respectively 2.0×10^{-4} and 1.1×10^{-4} for the glass sample, while they are respectively 2.6×10^{-5} and 4.8×10^{-5} for the buried oxide layer. The values of the absorption coefficient α of the glass sample are calculated to be 7.0×10^{-3} cm^{-1} and 24 cm^{-1} at 5.0 eV and 7.6 eV, respectively, by measuring the absorbance A at each photon energy. Then, by substituting the values of I_{PL}/I_{EXC}, α, and L into Eq. (2), the value of η for the silica glass measured with the present system is calculated to be 4.0×10^{-1} and 1.4×10^{-4} for the 5.0 eV photons and the 7.6 eV photons, respectively. As mentioned above, the effective values of η for the buried oxide layer are considered to be $(1.6)^2$ times as high as these values. If so, using the values of I_{PL}/I_{EXC} and L for the buried oxide layer, α can be obtained as 2.0 for the 5.0 eV absorption band and 1.1×10^{4} for the 7.6 eV band. Since σ is known to be 2×10^{-17} cm^2 and 8×10^{-17} cm^2 for the 5.0 eV and the 7.6 eV bands, respectively,[6] the concentration N of the photo-absorbing defects in the present buried oxide layer is calculated to be 1.0×10^{17} cm^{-3} for the unrelaxed neutral oxygen vacancies and 1.4×10^{20} cm^{-3} for the relaxed ones. The concentrations in the glass sample are similarly calculated to be 3.5×10^{14} cm^{-3} and 3.0×10^{17} cm^{-3} for the unrelaxed and the relaxed vacancies, respectively. It can be concluded that the vacancy concentrations in the buried oxide layer are about 300 - 400 times as high as those in the glass sample.

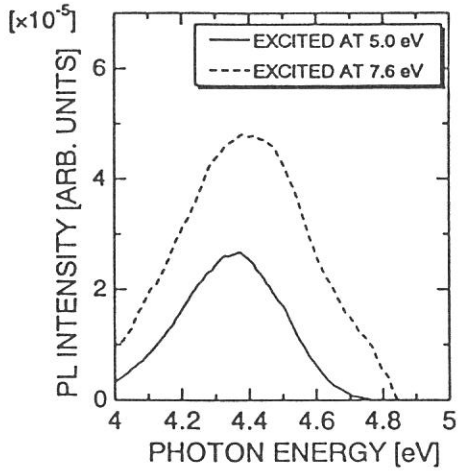

FIG. 1. PL spectra excited by 5.0 and 7.6 eV photons measured for the buried oxide layer at 13K. The PL intensity is calibrated by the intensity of excitation photons.

References

1. Y. Omura and K. Izumi, in *Proceedings of the 4th International Symposium on Silicon-on-Insulator Technology and Devices*, edited by D.N. Schmidt, PV 90-6 (The Electrochemical Society Proceedings Series, Pennington, NJ, 1990), p. 509.
2. T. Ohno, M. Shimaya, K. Izumi, and N. Shiono, IEEE Trans. Circuits Devices, CD-3, 21 (1986).
3. For example, A.G. Revesz and H.L. Hughes, Microelec. Eng. 36, 343 (1997), K. Vanheusden and A. Stesmans, Appl. Phys. Lett. 62, 2405 (1993).
4. K.S. Seol, A. Ieki, and Y. Ohki, J. Appl. Phys. 79, 412 (1996).
5. H. Nishikawa, E. Watanabe, D. Ito, and Y. Ohki, Phys. Rev. Lett. 72, 2101 (1994).
6. H. Imai, K. Arai, H. Imagawa, H. Hosono, and Y. Abe, Phys. Rev. B 38, 12772 (1988).
7. R. Allison, J. Burns, and A.J. Tuzzolino, J. Opt. Soc. Am. 54, 747 (1964).
8. H.R. Philipp, J. Phys. Chem. Solids 32, 1935 (1971).

(BL1B)

Reflection Spectra of $(CH_3NH_3)_3M_2Br_9$ (M:Sb,Bi) Single Crystals

Taketoshi Kawai[A], Akira Miyashita[B] and Makoto Iwata[B]

[A]*Department of Natural Science, Osaka Women's University, Daisen−cho, Sakai 590-0035, Japan*

[B]*Department of Applied Physics, Nagoya University, Nagoya 464-8603, Japan*

Novel crystals of alkylammonium halogenometallates $(CH_3NH_3)_3M_2X_9$ (M=Sb,Bi: X=Cl,Br,I) which contain the trivalent ion as the constituent metal exhibit several interesting structure phase transitions mainly due to the ordering of orientational motion of alkylammonium cations with the permanent dipole moment. Therefore, a number of studies on these materials have been extensively made on phase transitions and dielectric properties[1-5]. On the other hand, there are only few studies on optical properties of these novel crystals[6]. We have investigated the optical properties of the bromo derivatives $(CH_3NH_3)_3Sb_2Br_9$ (MABA) and $(CH_3NH_3)_3Bi_2Br_9$ (MABB) in the photon energy of 2.0～24eV. The compounds have a corrugated layer of the inorganic $[(M_2Br_9)^{3-}]_n$ polyanions and the $(CH_3NH_3)^+$ cations occupying the vacancies.

Single crystals of MABB and MABA were grown by slow evaporation of the HBr solution containing the stoichiometric molar ratio of Bi_2O_3 or Sb_2O_3 and CH_3NH_3Br. The obtained crystals have the form of hexagonal plates of transparent yellow color. They were cleaved along the crystallographic *ab*-plane in order to use as a reflection plane. The reflection spectra at near-normal incidence were measured at the beam line BL1B of UVSOR by using a monochromator of 1m Seya-Namioka type. The measurements were performed in the temperature range from 300K to 8K, because both crystals exhibit several structure phase transitions in this temperature range.

Figures 1(a) and 1(b) show the reflection spectra of the MABB and MABA single crystals at several temperature in the energy region of 2.0～6.0eV, respectively. As seen in these figures, several remarkable structures were observed in this energy region. The rapid drop structure at 2.73eV for MABB and 2.85eV for MABA is correspond to the energy position which each absorption spectrum exhibits a steep rise. Thus, the rapid drop structures are probably due to the reflection from the back surface of the crystals. At low temperature, the sharp reflection structure at 2.90eV for MABB and 2.95eV for MABA is attributed to the band-edge exciton state. Since the CH_3NH_3Br solution does not exhibit any absorption band in the energy region below 6.0eV, the origin of the electronic states may be interpreted on the basis of electronic states in the metal cation. Preliminary analysis of the reflection structure by the simple oscillator model provide the following values for the band-edge exciton. The transverse exciton energy and the longitudinal- transverse splitting energy are 2.90eV and 80meV for MABB, and 2.95eV and 60meV for MABA, respectively.

As the temperature increases, the reflection structures red-shift and become broader gradually. The MABB and MABA crystals have the phase transition temperatures of about 101.5, 140 and 188 K, and about 130 and 168 K, respectively. The drastic change of the reflection spectra is not observed at any phase transition temperature. This result supports that the band-edge exciton states have it's origin in electronic states in the metal ion, because the orientational motion of the $(CH_3NH_3)^+$ cations

(BL1B)

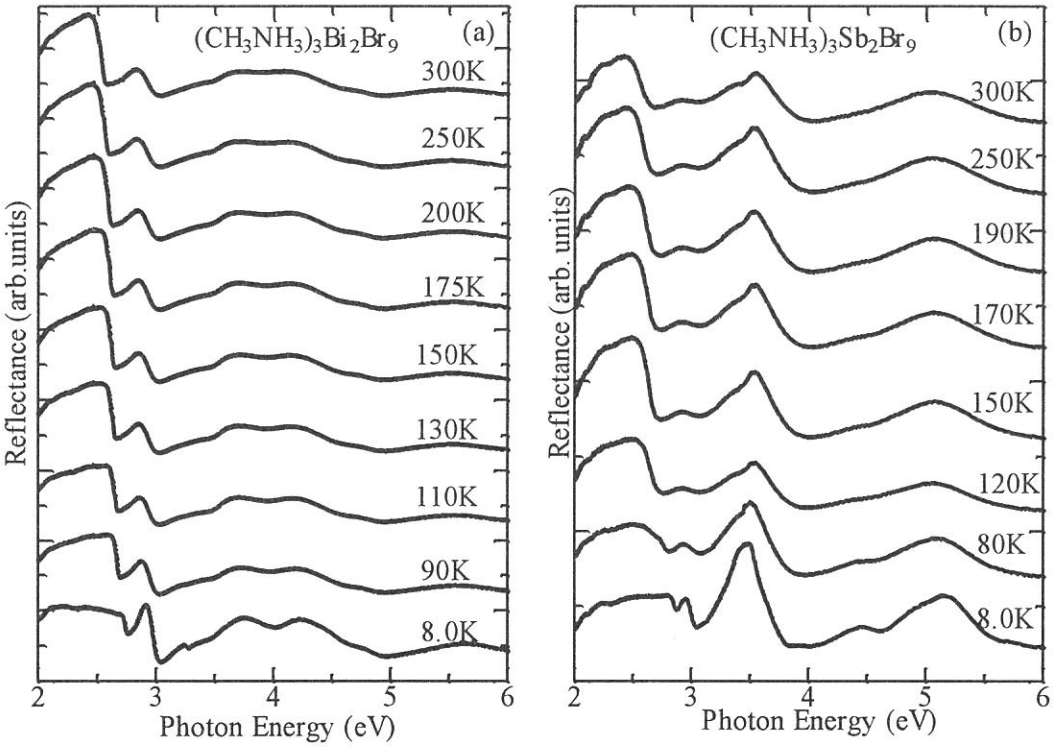

Figure 1 Reflection spectra of MABB (a) and MABA (b) at various temperature.

is not considered to distort the framework of the inorganic $[(M_2Br_9)^{3-}]_n$ polyanions. It should be noticed that the reflection peak in MABB is clearly observed even at 300K. On the other hand, the structure in MABA is hardly observed at 300K. This fact means that the band-edge exciton in MABB has a large binding energy in comparison with that in MABA. The quantitative analysis including the temperature dependence of the reflection structure in the higher energy is now in progress.

References

[1] R.Jakubas and L.Sobczyk: Phase Transitions **20** (1990) 163.

[2] R.Jakubas, Z.Galewski, L.Sobczyk and J.Matuszewski: J.Phys.C **18** (1985) L857.

[3] R.Jakubas, U.Krzewska, G.Bator and L.Sobczyk: Ferroelectrics **77** (1988) 129.

[4] P.Koziol, Y.Furukawa and D.Nakamura: J.Phys.Soc.Jpn **60** (1991) 3850.

[5] M.Iwata, M.Eguchi, Y.Ishibashi, S.Sasaki, H.Shimizu, T.Kawai and S.Shimanuki: J.Phys.Soc.Jpn **62** (1993) 3315.

[6] T.Kawai, A.Ishii, T.Kitamura, S.Shimanuki, M.Iwata and Y.Ishibashi: J.Phys.Soc.Jpn **65** (1996) 1464.

(BL1B)

Optical Properties of Cerium-doped Oxide and Fluoride Crystals for Laser Media I

Yoshiro SUZUKI, Hisashi UMEDA, Tooru HIRAYAMA and Kiyoshi INOUE
Faculty of Engineering, Tohoku University, Aoba, Sendai, 980-77

Introduction

Optical properties of cerium-doped materials have received considerable interests in recent years in connection with the application to tunable solid state laser media. [1] Several reports were made on the laser activity of cerium-doped fluoride crystals in UV region, while none of oxide crystals in visible region. This is believed to be due to optical losses by what is called the excited state absorption.[2] The excited state absorption is attributed to the transition from the lowest 5d excited state of the trivalent cerium ions (Ce^{3+}) to the conduction band of the host materials. Therefore, it is important to determine the location of the energy levels of the Ce^{3+} in the band gap for prediction of the laser activity. However, quantitative nor systematic evaluation has hardly been made because of lacking of the fundamental data.

As the first step, the measurements of the reflection spectra and the excitation spectra of the Ce^{3+} emission in several laser crystals have been carried out in the photon energy range of 4 to 17eV in order to obtain the information on the band gap energies.

Experimental

Crystals of $Y_3Al_5O_{12}$ (YAG) containing cerium were grown by Czochralski method in Tokin Inc., while those of $Gd_3Sc_2Ga_3O_{12}$ (GSGG), $YAlO_3$ (YAP), $YLiF_4$ (YLF) were furnished by the courtesy of Dr.Y.Segawa of Photodynamics Research Center, the Institute of Physical and Chemical Research. The crystals of YAP and YLF are anisotropic , then their orientations were determined through a comparison of the polarized absorption spectra with those from the literature.[3,4] The orientation of the crystals and the nominal concentrations of the Ce^{3+} are presented in each frame of Fig. 1.

The measurements were carried out at room temperature. The spectra of the reflection and the excitation of Ce^{3+} emission were measured by means of a Seya-Namioka-type VUV monochromator at the beam line BL1B. The band width for the reflection and the excitation spectra was 0.1 and 0.3nm,respectively. The reflected and emitted light were detected both at angle of 45° with the incident direction.

Experimental Results and Discussion

Solid curves in Fig.1 show the reflection spectra of the respective crystals. The measured reflectivity are normalized to the reflectance calculated using the refractive indices in the transparent region.[5] The reflection spectra were analyzed using Kramers-Kronig relationship by Roessler method.[6] Chain curves in Fig.1 present the imaginary part of the dielectric function, ε_2 thus obtained. The ε_2 spectra of YAG and YAP are essentially similar to those previously reported.[7,8] The main peaks at 9.0eV in YAG and 8.7eV in YAP were assigned to the transitions from the $O^{2-}2p^6$ to $Y^{2+}4p^6(4d+5s)$ level.[8] The structures due to exciton peaks are obscure at the leading edges of 6 to 8eV. This is characteristic manifestation in complex oxide crystals and attributed to the broadening and overlapping of multiple exciton absorption due to large atomic numbers in the unit cell.[9] The same feature is the case in GSGG and YLF. Therefore, it is difficult to determine the band gap energies only from the ε_2 spectra.

Dashed curves in Fig.1 show the excitation spectra of Ce^{3+} emission, which is caused by the transition from the lowest 5d excited state to the 4f ground state of the Ce^{3+}. The emission was detected at around the peak energy of the emission band in the respective crystals; 2.1eV in YAG and GSGG, 3.3eV in YAP and 3.8eV in YLF. The several bands due to the intraionic excitation to the higher lying 5d states are observed below 6.0eV in YAG and GSGG, while 7.0eV in YAP and YLF. Notable are the bands located around the leading edge of the fundamental absorption of the respective crystals; 6.8 to 8.0eV in YAG, 6.0 to 7.0eV in GSGG, 7.9eV in YAP and 10.3eV in YLF. These are denoted by the edge bands hereafter. Tomiki et al. reported the excitation spectra of Ce^{3+} emission from YAG:Ce and YAP:Ce powder phosphors and suggested the exciton formation by the intrinsic tail excitation.[8] Murk et al. detected the emission due to self trapped excitons (STE) in undoped YAG and YAP.[10] The excitation spectra of STE emission are very similar to the edge bands of YAG and YAP. This suggests the energy transfer from STE to Ce^{3+} and supports the exciton as the origin of the edge bands. It follows that the fallings at the high energy side of the edge bands are interpreted from the decrease of the transfer efficiency due to photoionization. The increase of the reflection loss contributes insignificantly to the falling. Figure 1 shows 40 to 90 % decreases in excitation intensity at the high energy side of the edge bands, whereas only 11 to 18% increases in reflectance is observed in the identical energy regions. Then, we may obtain indication of the electron-hole

continuum excitation from the falling edge energies of the edge bands in the respective crystals ; 8.0eV in YAG, 6.8eV in GSGG, 7.8eV in YAP and 10.5eV in YLF. It is consistent that these energies correspond to the singular points of the ε_2 spectra where steeper rises are observed. The band gap energy of YAG was determined to be 8.0eV from a photocurrent measurement.[11] The agreement with the falling edge energy of the edge band in YAG supports the validity of the falling edge as an indicator of the continuum excitation.

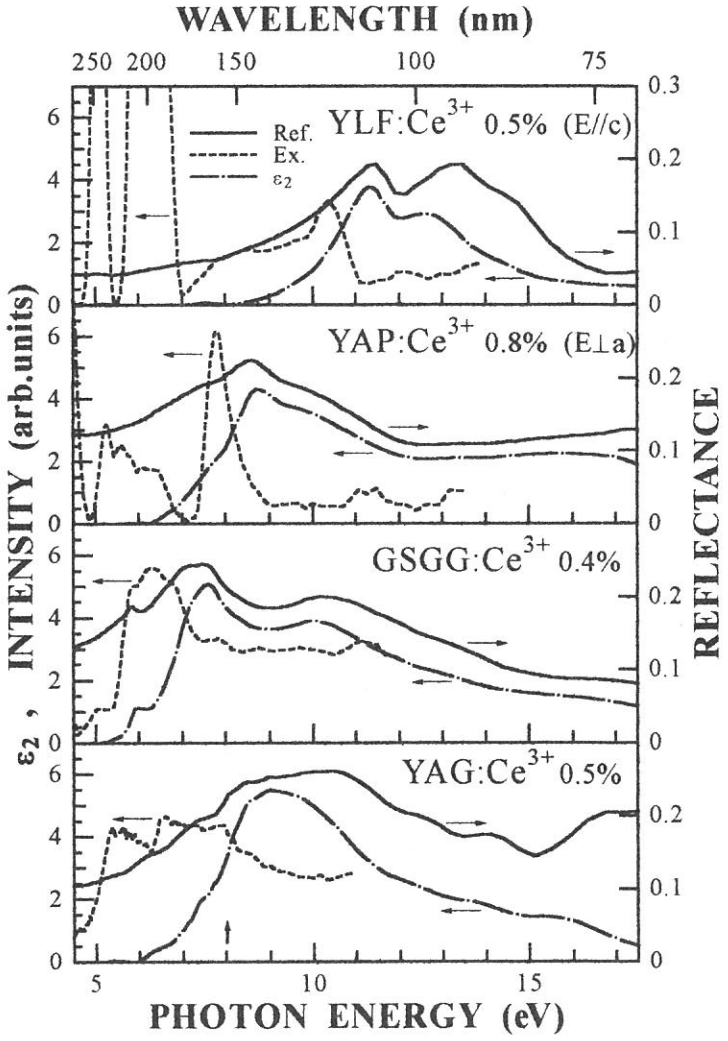

Fig.1 Spectra of Ce doped YAG, GSGG, YAP and YLF at room temperature : reflection (solid), ε_2 (chain) and excitation spectra of the Ce^{3+} emission (dashed curves) .

References

[1] See, for example, N.Sarukura : Kogaku, **25** (1996) 518 [in Japanese] .

[2] D. S. Hamilton et al. : Phys. Rev. **B 39** (1989) 8807.

[3] S. Yan, G. Yuan and Y. Zhong : Materials Lett. **16** (1993) 222.

[4] N. Sarukura et al. : IEEE J. Selected Topics in Quantum Electronics, **1** (1995) 792.

[5] L. G. DeShazer et al. : CRC Handbook of Laser Science and Technology, ed. M. J. Weber (CRC Press, Boca Raton Fla.1987) Vol. 5, p. 281.

[6] D. M. Roessler : Br. J. Appl. Phys. **16** (1965) 1119.

[7] V. N. Abramov and A. I. Kuznetsov : Sov. Phys. Solid State **20** (1978) 399.

[8] T. Tomiki et al. : J. Lumin. **40 & 41** (1988) 379.

[9] A. I. Kuznetsov et al. : Trudy Inst. Fiz. Akad. Nauk. Est. SSR. **63** (1989) 19.

[10] V. Mürk et al. : Nucl. Instrum & Methods Phys. Research **B 91** (1994) 327.

[11] N. S. Rooze and N. A. Anisimov : Trudy Inst. Fiz. Akad. Nauk. Est. SSR. **44** (1975) 163.

(BL1B)

Optical Properties of Cerium-doped Oxide and Fluoride Crystals for Laser Media II

Yoshiro SUZUKI, Hisashi UMEDA, Tooru HIRAYAMA and Kiyoshi INOUE
Faculty of Engineering, Tohoku University, Aoba, Sendai, 980-77

Introduction

Cerium-doped materials have received much attention as tunable solid state laser media. [1] The emission due to the transition from the lowest 5d excited state ($5d^1$) to the 4f ground state of the trivalent cerium ions (Ce^{3+}) is used for the laser action. The peak energy of Ce^{3+} emission varies from UV to visible region depending on the host materials. Up to date, however, the tunable energies of Ce^{3+} laser are restricted to UV region using fluoride crystals. The visible laser action using oxide crystals is believed to be hampered by so-called excited state absorption. [2] Since the excited state absorption is attributed to the transition from the $5d_1$ state to the conduction band of the host materials, the location of the energy levels of the Ce^{3+} in the band gap is crucial for the laser activity.

In the preceding report,[3] we showed that the excitation spectra of Ce^{3+} emission in VUV region give information of the band gap energies of the host crystals. In the present study, the measurements have been extended to UV and visible regions where intraionic transitions of the Ce^{3+} are observable. The quantum efficiencies of Ce^{3+} emission are known to be almost unity under the $5d_1$ excitations,[4] while those under the higher 5d excitations are unknown. Since the latter excitations may cause electron-release to the conduction band and reduce the quantum efficiency, the excitation spectra of Ce^{3+} emission have been expected to give information of the energy separation between the 4f ground state of the Ce^{3+} and the bottom of the conduction band.

Experimental

Cerium-doped crystals of $Y_3Al_5O_{12}$ (YAG), $Gd_3Sc_2Ga_3O_{12}$ (GSGG), $YAlO_3$ (YAP), $YLiF_4$ (YLF) were identical with those in the preceding report.[3] Presented in each frame of Fig.1 are the thickness and the nominal concentrations of the Ce^{3+} of the respective crystals, as well as the crystal orientation if anisotropic.

The measurements were carried out at room temperature. The excitation spectra of Ce^{3+} emission above 3.5eVwere measured at the beam line BL1B in the identical optical configuration with those in the preceding report.[3] The sufficient beam intensities facilitated the measurements and their corrections. The excitation spectra below 3.5eV were measured with a conventional optical system using a Xe lamp, since the sodium salicylate scintillater was unavailable at these energies. The absorptivity spectra of the respective crystals were also measured in order to evaluate the quantum efficiencies through comparisons with the excitation spectra. The band widths for the excitation and the absorption spectra above 3.5 eV were both 0.3nm, while those below 3.5 eV were 1.5nm.

Experimental Results and Discussion

Solid curves in Fig.1 show the absorptivity spectra of the respective crystals. The reflection losses were not corrected, while the absorbance at the transparent region were subtracted as the background. Several absorption bands observed are due to the transition from the 4f ground state to the crystal-field levels of the 5d excited states of the Ce^{3+}. The increased covalency and crystal field in oxide crystals gives the red shifts of the absorption peaks compared with those in YLF. Absorption tails due to the anisovalent cerium ions or the other impurities are obvious at the high energy region in GSGG and YAP.

Dotted curves in Fig.1 show the emission spectra under the $5d_1$ excitation. The doublet structure prominent in YLF is due to the spin-orbit splitting of the 4f ground state. The broadening of the emission bands in oxide crystals makes the structure obscure.

Dashed curves in Fig.1 show the excitation spectra of Ce^{3+} emission detected at around the peak energy of the emission band in the respective crystals. The heights were normalized to the peak heights of the $5d_1$ absorption bands. It is evident that the excitation spectra almost follow the absorptivity spectra in the whole energy region in YAG and YLF. Although the excitation spectra in GSGG and YAP apparently slip down from the absorptivity spectra at the higher energy region, the absorption tails due to the anisovalent cerium ions or the other impurities seem to be responsible for the disagreements. These behaviors of the excitation spectra of Ce^{3+} emission are unexpected. The photoionization threshold energy of the Ce^{3+} in YAG was determined to be 3.8eV from a photocurrent measurement.[5] However, no manifestation of the photoionization is observable in the present excitation spectra around 3.8 eV in YAG. The present result of YAG is not consistent with the previous one by Tomiki et al. either.[6] They reported that the relative intensity of the excitation band of Ce^{3+} emission to that of the absorption band decreased drastically at higher energy region. The reason of this discrepancy is not clear. The emission quenching may depend on the concentration of the electron-trap competitive with the photoionized Ce^{3+}.

Codoping of the electron-trap ions might be necessary for the observation of the photoionization threshold.

On the other hand, the spectral dependence of the excitation spectra is desirable for the laser performance. The Ce^{3+} is usually excited to higher lying 5d states in the laser performance because of less variety of pumping sources. The present result suggests that the Ce^{3+} emission efficiency does not decrease under such excitation as far as multiphoton processes are not induced.

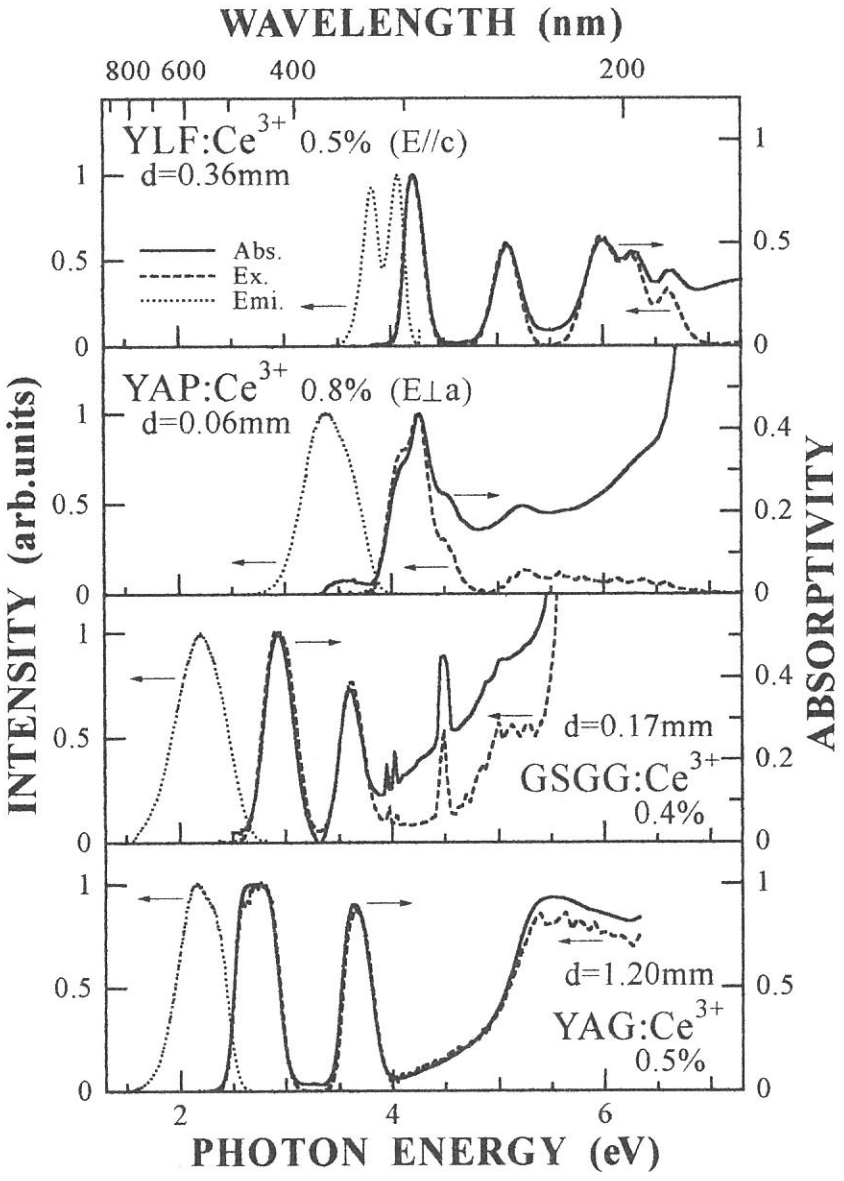

Fig.1 Spectra of Ce doped YAG, GSGG, YAP and YLF at room temperature : absorptivity (solid), emission (dotted) and their excitation spectra (dashed curves) .

References

[1] See, for example, N. Sarukura : Kogaku, **25** (1996) 518 〔in Japanese〕 .

[2] D. S. Hamilton, S. K. Gayen, G. J. Pogatshink, R. D. Ghen, and W. J. Miniscalco : Phys. Rev. **B 39** (1989) 8807.

[3] Y. Suzuki, T. Hirayama, H. Umeta and K. Inoue : this issue.

[4] Li-Ji Lyu and D. S. Hamilton : J.Lumin. **48 & 49** (1991) 251.

[5] C. Pedrini, F. Rogemond and D. S. McClure : J. Appl. Phys. **59** (1986) 1196.

[6] T. Tomiki, F. Fukutome, M. Kaminao, M. Fujisawa, Y. Tanahara and T. Futemma : J. Phys. Soc. Jpn. **58** (1989) 1801.

(BL1B) VUV Excited Luminescence in CsI (pure, Tl-doped and Na-doped) and in multilayer structures of LiF- CaF_2 and LiF- BaF_2.

A. Ejiri, E. Chin, A. Urasaki, T, Yonamine and T. Yokozawa [A]

Dept. of Science Education, College of Education, University of the Ryukyus, Nishihara, Okinawa 903-01.

[A] *Dept. of Physics, Faculty of Science, Rikkyo University, Nishi-Ikebukuro, Tokyo 171.*

CsI is an interesting material of scintillator to be revealed its luminescence mechanism. Alkali earth fluoride crystals (CaF_2 and BaF_2) are well known that they show a strong STE luminescence even at room temperature. [1] It is interesting to investigate quantum confinement effect of the luminescence in the quantum well structures of these fluorides. Samples of scintillators are pure CsI single crystal, Tl- 0. 1mol%- doped CsI and Na- 0. 1mol%- doped CsI crystals.

Present paper will report results of the luminescence measurements in those CsI crystals, and in the quantum well structures respectively consisted of 5- periods of LiF (200Å)- CaF_2 (100Å), LiF (100Å)- CaF_2 (50Å), LiF (200Å)- BaF_2 (100Å), and LiF (100Å)- BaF_2 (50Å). The specimen of 5-periods multilayer structures are fabricated with vacuum evaporation technique and annealing at 200℃ for an hour in every layer after deposition. All measurement were performed at BL-1B by the use of a Spex monochrometer for the luminescence. Excitation spectra for each luminescence band were also measured in the photon energy range up to 40eV. The luminescence spectra were not corrected for the spectral efficiency of the monochrometer and the excitation spectra were normalized by the spectral output of the Seya- Namioka monochromator.

In Fig. 1, observed luminescence spectra in pure CsI and the Tl- doped CsI excited with 12eV radiation at 7K are shown. It is characteristic to be appeared a new band at 2. 5eV in Tl- doped CsI. In Fig. 2, observed luminescence of CaF_2 (exc 1033Å) and BaF_2 (exc 1240Å) single crystals at 7K (a), those of a LiF (200Å)- CaF_2 (100Å) and a LiF (100Å)- CaF_2 (50Å) multilayers at 7K (b), and of a LiF (200Å)- BaF_2 (100Å) and a LiF (100Å)- BaF_2 (50Å) multilayers at 7K (c) are shown.

On the luminescence spectra in the multilayers, several resonance type structures are observed especially on CaF_2 (50Å) spectrum in Fig. 2(b) and BaF_2 (100Å) spectrum in Fig. 2(c). Furthermore, it was found that a line series of luminescence in LiF (200Å)- CaF_2 (100Å) multilayer excited 1050Å at room temperature as shown in Fig. 3(a).

An excitation spectra of the luminescence in the mutilayer structure of LiF(200)-CaF_2 (100) is shown in Fig 3(b). This appears a very narrow band which indicates an onset of STE and a penetration limit of radiation in the multilayer.

The resonance structures and line spectra in the luminescence can be explained in terms of interference of luminescence in the well layers (CaF_2, BaF_2) and of resonant emission in

a cavity of the multilayer.

References

1) A. Ejiri, A. Hatano, and K. Arakaki; UVSOR Act. Rep. (IMS)1995, (1996) 68.

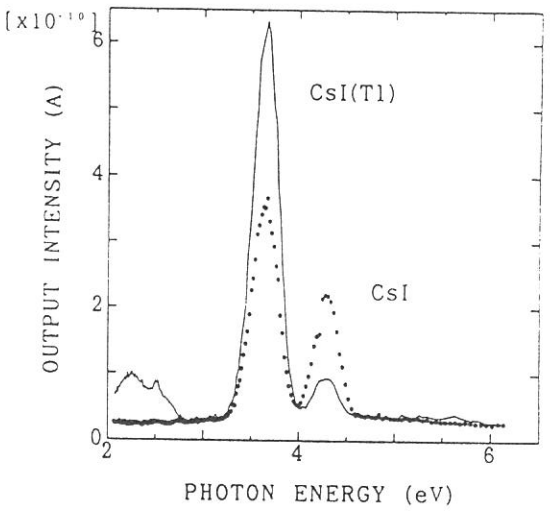

Fig. 1 Luminescence spectra of pure CsI and Tl 0. 1mol%- doped CsI excited with 12eV radiation at 7K.

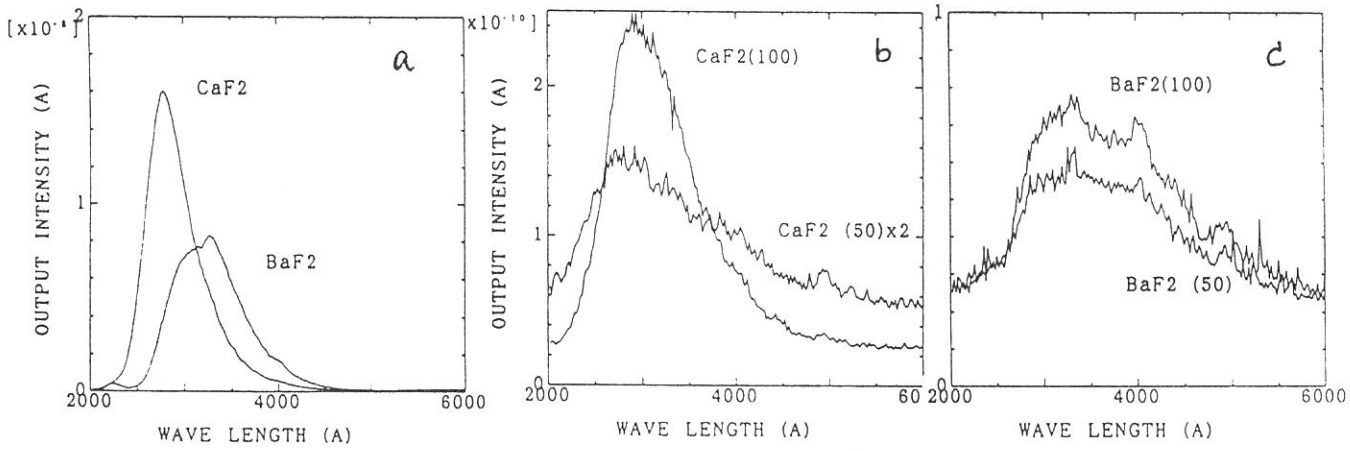

Fig. 2 Luminescence spectra of CaF_2 (excited with 1033 Å) and BaF_2 (excited with 1240Å) crystals at 7K (a), of LiF (200Å)- CaF_2 (100Å) and LiF (100Å)- CaF_2 (50Å) multilayers excited with 1033Å radiation at 7K (b) and of the LiF (200Å)- BaF_2 (100Å) and LiF (100Å)- BaF_2 (50Å) multilayers excited with 1240Å radiation at 7K (c).

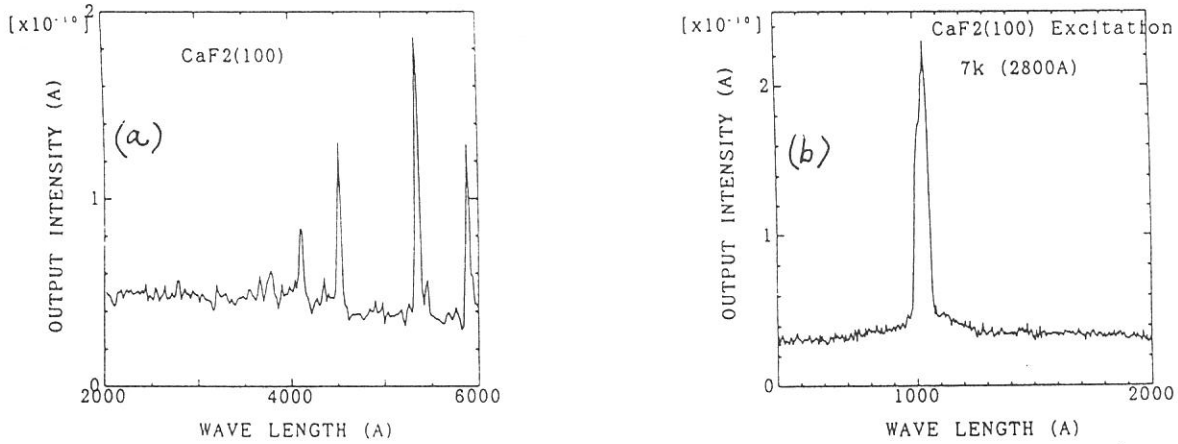

Fig. 3 Luminescence spectra of a LiF (200Å)- CaF_2 (100Å) multilayer excited 1050Å at room temperature(a) and an excitation spectrum of the multilayer luminescence of 2800Å at 7K(b).

(BL1B)

Luminescence from Self-Trapped Excitons in BaFI and $BaFBr_{1-x}I_x$ crystals

Akimasa OHNISHI[A], Ken-ichi KAN'NO[B] and Nobufumi MORI[C]

[A]*Department of Physics, Yamagata University, Yamagata 990-0021*
[B]*Department of Physics, Kyoto University, Kyoto 606-8224*
[C] *Fuji Photo Film Co., Ltd., Miyanodai, Kaisei-machi, Kanagawa 258-0023*

Balium-fluoro-halides (BaFX, X=Cl, Br, I) are important host materials of photo-stimulated luminescence phosphors activated with Eu^{2+} ions.[1] We have investigated luminescence properties from self-trapped excitons (STEs) in BaFCl, BaFBr and $BaFCl_{1-x}Br_x$, and have discussed on the STE configurations by the analogy with on- and off-center STEs in alkali halides.[2,3] In the present study, luminescence measurements have been extended to BaFI and $BaFBr_{1-x}I_x$ crystals.

BaFI and $BaFBr_{1-x}I_x$ were grown by a horizontal Bridgmann method. Experiments were made using synchrotron radiation pulses from the beam line BL1B of UVSOR. Luminescence was detected with a photomultiplier (Hamamatsu R955) through a grating monochromator (Spex 270M).

Figure 1(a) shows the emission spectrum in BaFI at 15 K. When the crystal is excited at 8.86 eV in the range of band-to-band transition, a characteristic luminescence band is observed at 4.54 eV. In Fig.1(b), is shown the excitation spectrum for the 4.54 eV band, along with positions of the halogen doublet due to I^- spin-orbit splitting reported by Nicklaus [4] (arrows at 6.5 and 7.6 eV). The spectrum indicates high emission yields above the threshold at 6.5 eV. This suggests that the 4.54 eV band is due to recombination luminescence from STE with I_2^--core in BaFI. Efficient excitation bands are observed also in the region (5.6 ~ 6.5 eV) of low energy tail of the n=1 exciton absorption band. The reason is now under consideration.

To see the effect of changing in the crystal environment on the manner of exciton self-trapping, luminescence from $BaFBr_{1-x}I_x$ has been investigated under excitation at 10.3 eV at 10 K. Their emission spectra are shown in Fig.2. As seen in Fig.2(a), an emission band is observed at 5.06 eV in the x=0.001 crystal, as far as the excitation is made at the energies of band-to-band transition of BaFBr. The peak energy and band width are in good agreement with the intrinsic luminescence band of BaFBr. This means that the STE composed of an electron and a Br_2^- core is created under excitation at 10.3 eV. However when excited at the lower energy around 6.53 eV, another emission band which can be attributed to the localized excitons with $(BrI)^-$-cores appears at 5.18 eV (dotted spectrum of Fig.2(a)). In the case of x=0.1, a new emission band is observed at 4.95 eV together with the 5.18 eV band. In this case, major part of free holes must be self-trapped on I^- sites because of the smaller electron affinity of I^- compared with Br^-. Thus the 4.95 eV band supposedly originates from the localized excitons with I_2^--cores. In fact, the 5.18 eV band disappears in the x>0.3 crystals, and the 4.95 eV band gradually

shifts to the low energy side with the increase in x and finally connects to the 4.54 eV band from the STE with I_2^--core in BaFI. It should be noted that these spectral changes in $BaFBr_{1-x}I_x$ are essentially the same as those of on-center type STE luminescence in $BaFCl_{1-x}Br_x$.[3] We suppose that the STE configurations responsible for the emission bands are also of on-center type, and the off-center instability does not take place in BaFI and $BaFBr_{1-x}I_x$.

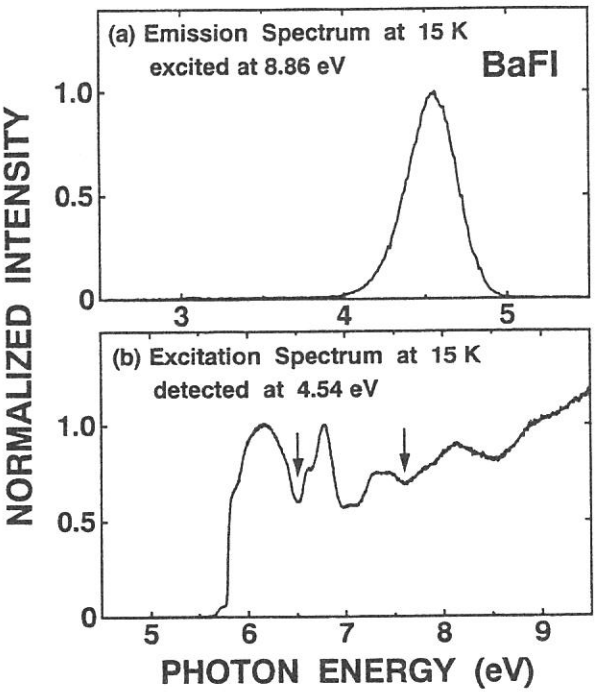

Fig.1

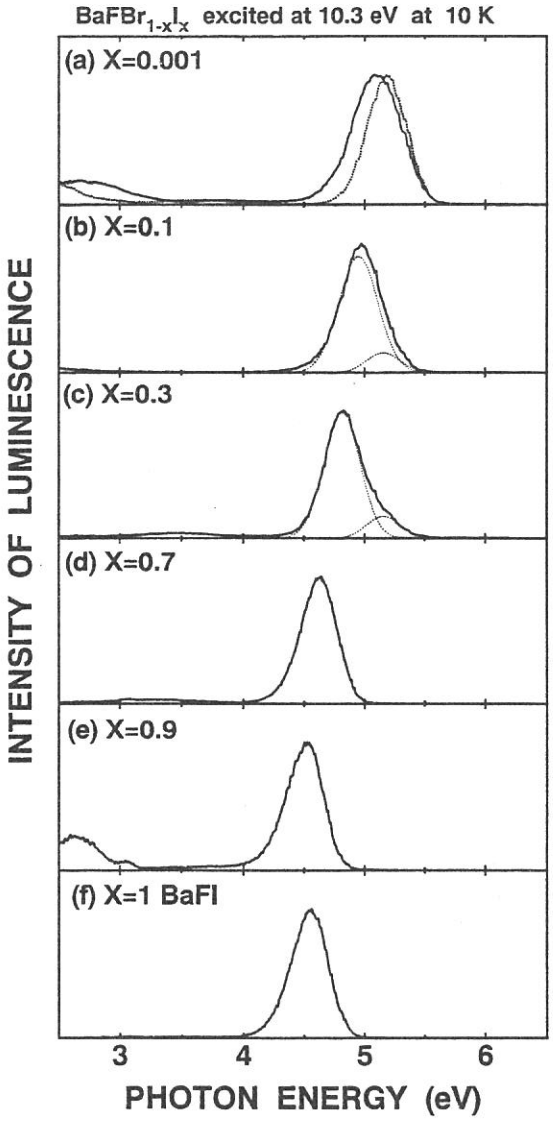

Fig.2

References

1. M. Sonoda, M. Takano, J. Miyahara and H. Kato ; Radiology, 148 (1983) 833.
2. A. Ohnishi, K. Kan'no, Y. Iwabuchi and N. Mori ; Nucl. Instr. and Meth. in Phys. Res. B91 (1994), 210.
3. A. Ohnishi, K. Kan'no, Y. Iwabuchi and N. Mori ; J. Electron Spectrosc. Relat. Phenom., 79 (1996) 163.
4. Nicklaus ; Phys. Status. Solidi (a) 53 (1979) 217

(BL1B)

Optical Spectra in Solid Superoxide KO_2

M. ASHIDA, O. MORIKAWA, S. HASHIMOTO[A], S. HIROSE[B], M. KAMADA[B] and K. KAN'NO

Department of Physics, Kyoto University, Kyoto 606

[A]Kyoto University of Education, Kyoto 612

[B]UVSOR, Institute for Molecular Science, Okazaki 444

Alkali superoxides consist of alkali metal ions and paramagnetic anion O_2^- molecules. This material shows a number of structural phase transitions due to the reorientation of O_2^- [1] and antiferromagnetic order of the spin 1/2 of O_2^-. [2] The O_2^- molecule in alkali halides is a well-known efficient luminescent center.[3] Thus characteristic optical properties reflecting the phase transition are expected in the alkali superoxides. However, there have been only a few optical studies on solid alkali superoxides, since they are highly reactive and it is difficult to obtain single crystals of appropriate size. Bösch *et al.* succeeded in growing single crystals of NaO_2 in liquid ammonia and measured reflection spectra.[4] For the other alkali superoxides, optical spectra in visible and VUV region have not been reported yet. As a first step for the study of optical properties of this system, solid KO_2 was investigated in the present experiment. Samples were prepared by cooling molten KO_2 on Al substrates in a vacuum.

Reflection spectra in KO_2 at 40K and 310K are shown in Fig. 1. The overall structure and peak positions of the spectra were reproducible, though the absolute value of the reflectivity changed within ±10% from sample to sample. It is regrettable that the spectra in the low energy region below ~4eV, where anomalous temperature change was observed in NaO_2 crystal,[4] were affected by the back reflection due to the Al substrate. Although the spectrum changed gradually with increasing temperature, characteristic changes at the phase-transition temperatures were not observed. The structures below ~7eV (e.g. the remarkable peak at 6eV) correspond to those in NaO_2 crystal.[4] Hence, the spectral features in the lower energy region (4-7eV) can be assigned to the intramolecular transition in the O_2^- molecule and those in the higher energy region are possibly caused by the charge transfer transition. The structures due to the intramolecular transition, however, cannot be explained by using the adiabatic potential diagram of a single molecule.[5] The transition $^2\Pi_g \rightarrow {}^2\Pi_u$ of an O_2^- molecule, which gives rise to a main absorption band centered at ~5eV of O_2^- centers in alkali halides,[6] does not manifest itself in Fig. 1. The effect of the interaction among the O_2^- molecules, that is, Frenkel exciton, and/or the electron-phonon interaction must be taken into account.

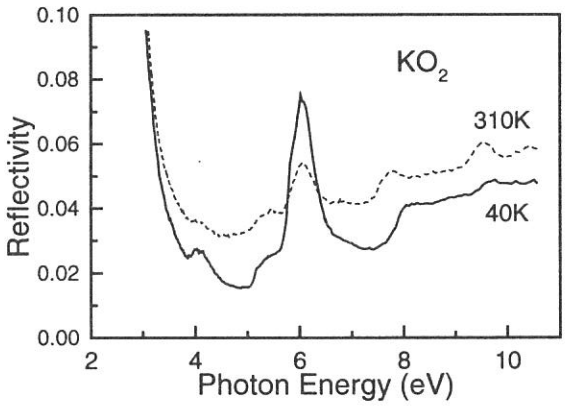

Fig. 1. Reflection spectra in solid KO_2. (Solid line: 40K, broken line: 310K.)

Photo-luminescence was observed even at room temperature. Figure 2 shows its spectrum at 310K under the excitation at ~6eV. The broad shape almost unchanged down to ~10K. The excitation spectrum of this luminescence is shown in Fig. 3. The remarkable peaks and a shoulder are in good agreement between excitation and reflection spectra. Therefore, it is confirmed that the luminescence arises from the intrinsic excited state of KO_2. The luminescence spectrum is drastically different from the spectra of O_2^- centers in alkali halides, which show sharp vibronic lines.[3] This fact indicates strong intermolecular interaction among O_2^- molecules and/or electron-phonon interaction in alkali superoxides again. For further investigation, growth of single crystals of alkali superoxides is desirable.

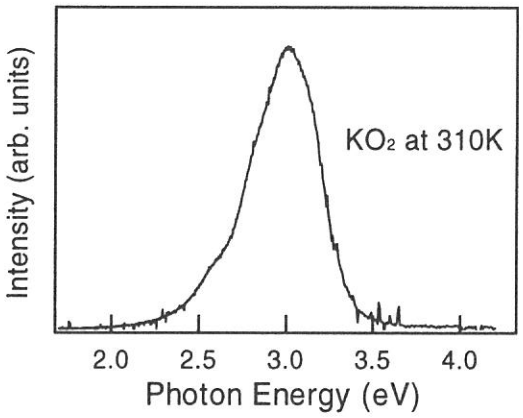

Fig. 2. Emission spectrum in KO_2 at 310K under excitation at 205nm.

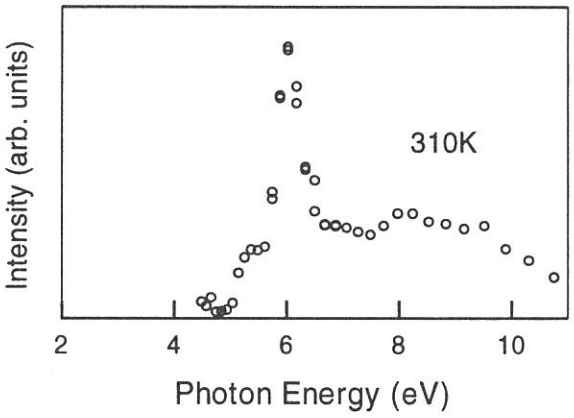

Fig. 3. Excitation spectrum of 3.0eV emission in KO_2 at 310K.

References

1) M. Ziegler *et al.*: Helv. Phys. Acta **49** (1976) 57.
2) H. G. Smith *et al.*: J. Appl. Phys. **37** (1966) 1047.
3) S. Hongo *et al.*: Memoirs of the Faculty of Science, Kyoto University, A **38** (1992)187.
4) von M. Bösch and W. Känzig: Helv. Phys. Acta **48** (1975) 743.
5) M. Krauss *et al.*: Phys. Rev. **A7** (1973) 69.
6) F. Fischer *et al.*: Z. Phys. **189** (1966)79.

(BL1B)

Reflection Spectra of Orthorhombic and Cubic PbF_2 Crystals

Masami FUJITA, Dmitri L. ALOV,[A] Minoru ITOH,[B] Jun-ichi MURAKAMI,[B]
Tetsuo SAIDA,[C] Hideyuki NAKAGAWA[C] and Mamoru KITAURA[D]

Maritime Safety Academy, Wakaba, Kure, Hiroshima 737-8512
[A]*Institute of Solid State Physics, Chernogolovka, Moscow, 142432, Russia*
[B]*Department of Electrical and Electronic Engineering, Faculty of Engineering, Shinshu University, Wakasato, Nagano 380-0922*
[C]*Department of Electrical and Electronics Engineering, Faculty of Engineering, Fukui University, Bunkyo, Fukui, 910-0017*
[D]*Fukui National College of Technology, Sabae, Fukui, 916-0064*

Lead fluoride crystallizes into two phases, one of which has an orthorhombic lattice of $PbCl_2$ type (α-PbF_2: D_{2h}^{16}, Pmnb) and the other has a cubic fluorite structure (β- PbF_2: O_h^5, Fm3m). The former is more stable phase below 320 °C, but the latter is also metastable at low temperature. Optical spectrum of β- PbF_2 reported so far[1] shows different features from the orthorhombic $PbCl_2$ and $PbBr_2$[2]. It is an interesting problem whether the difference in optical spectra comes from the difference in the crystal structure or in the halogen species. However, optical study of PbF_2 has been limited so far to the cubic phase because of the difficulty in preparing the orthorhombic crystals with enough size. Recently, orthorhombic crystals have been grown from aqueous solution and the photoluminescence experiment has been performed[3,4]. In the present study, reflection spectra of α-PbF_2 have been measured up to VUV region in order to investigate the electronic structure in lead halides.

Single crystals of α-PbF_2 were grown from the aqueous solution as thin flakes with the size of 2 x 2 mm^2. The surface of the sample was perpendicular to the c-axis. Reflection spectra were measured for the polarization parallel to the a-axis (E//a) or b-axis (E//b). Reflection spectra of cleaved surfaces of β-PbF_2 crystal and PbClBr crystal were also measured. Experiments have been performed at BL1B in UVSOR.

In the upper part of Fig. 1 are shown reflection spectra of α- and β-PbF_2 crystals at 7K. In the spectra of α-PbF_2, the first exciton band 1 appears at 5.7eV. As mentioned later, the band shows dichroism. Two prominent peaks 2 and 3 are found at 6.3 eV and 8.5 eV. These structures above 6 eV depend slightly on the polarization. The spectrum of β-PbF_2 agrees with that measured at 77K[1]. The first exciton band of β-PbF_2 appears nearly the same position of the exciton band of α-PbF_2. In the 6-7 eV region is observed a broad band 2 which seems to consist of two or three components. A large peak 3 is observed at 8.6 eV. Gross features in the spectra of α-PbF_2 resemble those of β-PbF_2, which suggests that the electronic structures in both modifications are similar to each other.

Reflection spectra in the first exciton band region of α-PbF_2 are shown in Fig. 2. The second-energy-derivative reflectance d^2R/dE^2 (2EDR) spectra were calculated numerically from the reflection spectra and are also shown in Fig. 2. The 2EDR spectra clearly indicate that the exciton band has a single peak for E//a, while it consists of two components for E//b. The peak positions determined from the 2EDR spectra are, 5.678eV (1a) for E//a, and 5.701eV (1b) and 5.829eV (1b') for E//b. The first exciton band of $PbCl_2$ and $PbBr_2$ shows similar dichroism, that is, the band has one peak for E//a and two peaks with separation of 60meV for E//b[2]. The dichroism is explained in terms of the cationic $6s^2 \rightarrow 6s6p$ ($^1S_0 \rightarrow {}^3P_1$) transition in the crystal field of Cs symmetry around the lead ion. According to the theoretical

calculation based on the point charge model, the crystal field splitting of the $6p$ levels in α-PbF_2 is about two times larger than that in $PbCl_2$ and $PbBr_2$[5]. This is in agreement with the present experimental result.

In the lower part of Fig. 1 are shown reflection spectra of $PbCl_2$, PbClBr and $PbBr_2$ at low temperature. The sharp peaks 1 and 3 in these crystals shift continuously with the change of halogen component. This indicates that the excitation associated with the peak 3 occurs also mainly at the cation site. The energy position of the peak 3 of $PbCl_2$ and $PbBr_2$ almost coincides with the C-absorption band of Pb^{2+} impurity in alkali chloride and bromide, respectively. Therefore the peak 3 of these crystals is considered to be due to the excitonic transition corresponding to the $^1S_0 \rightarrow {}^1P_1$ excitation in lead ions[2]. In PbF_2, the transition is expected to occur in the 7.5-8.0 eV region from the extrapolation of $PbBr_2$ and $PbCl_2$ indicated by the broken line in Fig. 1. However, no sharp structure is discernible at the position in the spectra of PbF_2. The peak 3 at 8.5 eV is too broad to be assigned to such transition. Present result indicates that the transition intensity corresponding to the $^1P_1$ excitation is strongly affected by the halogen species, in spite of the localized nature of the cationic excitation. The question why the transition does not appear in PbF_2 would be an important problem to understand the electronic structure in lead halides.

References

[1] J. H. Beaumont, A. J. Bourdillon and J. Bordas: J. Phys. C Solid State Phys. **10**(1977)761.

[2]M. Fujita, H. Nakagawa, K. Fukui, H. Matsumoto, T. Miyanaga and M. Watanabe: J. Phys. Soc. Jpn. **60**(1991)4393.

[3]A. B. Kulakov, A. A. Zhokhov, G. A. Emel'chenko and N. V. Klassen: J. Cryst. Growth **151**(1995)107.

[4]D. L. Alov and S. I. Rybchenko: J. Phys. Condens. Matter 7(1995)1475.

[5]K. Wada: Sci. Light **26**(1977)77.

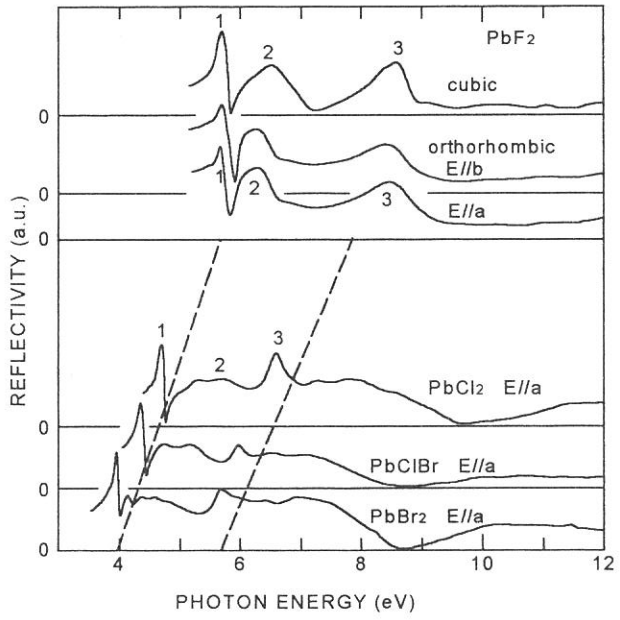

Fig. 1. Reflection spectra of lead halides at low temperature.

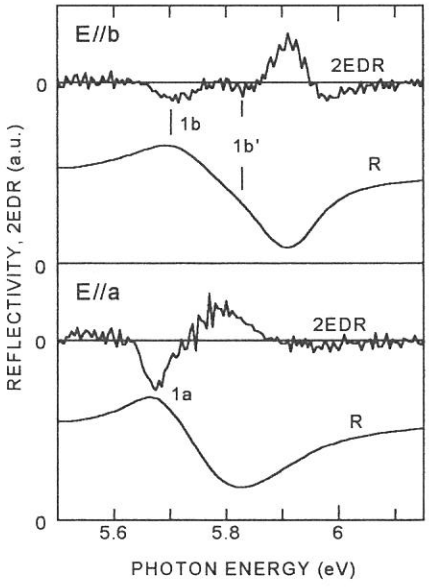

Fig. 2. Reflection and 2EDR spectra of α-PbF_2 in the first exciton band region.

(BL1B)

Time-Resolved Luminescence from Excitons Localized at Br^- Impurities in CsCl Crystals

Y. Bokumoto, M. Itoh and H. Yoshida*

Faculty of Engineering, Shinshu University, Nagano 380-8553
**NEC Kansai, Ltd., Shiga 520-8555*

In CsCl crystals containing a small amount of Br^- impurities, three luminescence bands can be seen at 3.84, 4.35 and 5.27 eV under the excitation with UV light in the low-energy region of the fundamental absorption of host CsCl [1]. It has been suggested that the 3.84-eV band is due to radiative decay of off-centered excitons localized at Br^- impurity monomer. The 4.35- and 5.27-eV bands are likely due to off- and on-centered excitons localized at Br^- impurity dimer, respectively. In the present work, we have carried out time-resolved luminescence studies on localized excitons in CsCl:Br, in order to investigate relaxation processes of the excitons in CsCl crystals with simple cubic structure.

Figure 1 shows time-resolved luminescence spectrum of $CsCl_{1-x}Br_x$ (x = 0.005) excited with 7.56-eV light under the single-bunch operation of synchrotron radiation (SR) at 10 K. Broken curve (fast component) and solid curve (slow component) represent the counts of photons measured through the time window of 0 − 2.4 ns and 37 − 60 ns after the excitation pulse, respectively. The 3.84-eV band does not change its peak position in both spectra. On the other hand, the peak position of the 4.35-eV band shifts from 4.60 eV in the fast-component spectrum to 4.35 eV in the slow-component spectrum. From Fig. 1, it is clear that the 5.27-eV band has only fast decay component (decay time = 0.55 ns).

Decay profile of the luminescence detected at 4.35 eV, i.e., the peak position of the slow-component spectrum in Fig. 1, is shown by dotted curve in Fig. 2, where the slow decay component has been subtracted. Open circles represent the pulse shape of SR. As clearly seen, this decay profile has a rise component around 1 ns.

Luminescence spectra have also been examined in the temperature ranges from 8.3 K to 200 K under stationary UV-light excitation. It is found that the 4.35-eV band exhibits remarkable blue-shift toward 4.6 eV with increasing temperature from 8.3 K up to 40 K.

All the above results suggest that there are two excited states on the pathway of the off-center relaxation of excitons localized at Br^- dimer in CsCl system; one is a stable state responsible for the 4.35-eV luminescence, and the other is a metastable state for the 4.60-eV luminescence. At low temperatures, the localized excitons first relax to the metastable state, from which the 4.60-eV photons are emitted. A part of them are then converted to the stable state over a potential barrier, resulting in the 4.35-eV luminescence. If the temperature is increased above 40 K, the relaxed excitons are repopulated at the 4.60-eV state. According to this model, decay profile of the

luminescence detected at 4.35 eV can be expressed by the formula;

$$I(t)=\int_0^{\infty} G(\xi)\cdot\left\{W_{f1}\,e^{-(W_{f1}+W_T)(t-\xi)}+C\cdot W_{f2}\left(\frac{W_T}{W_{f1}+W_T-W_{f2}}e^{-W_{f2}(t-\xi)}-\frac{W_T}{W_{f1}+W_T-W_{f2}}e^{-(W_{f1}+W_T)(t-\xi)}\right)\right\}d\xi, \quad (1)$$

where W_{f1} and W_{f2} are the radiative transition probabilities of the 4.60- and the 4.35-eV states, respectively, and W_T is the transition rate from the 4.60-eV state to the 4.35-eV state. $G(\xi)$ is the pulse shape of SR and C is a constant which includes the ratio of the luminescence yields of the 4.60- and 4.35-eV bands. The slow decay process of the 4.35-eV state is neglected in Eq. (1). From this fit we get $1/W_{f1}$ = 1.3 ns, $1/W_{f2}$ = 3.0 ns, $1/W_T$ = 1.3 ns and C = 5. Agreement between the calculated and experimental curves seems fairly good.

The present experiment reveals that the off-centered excitons localized at Br^- dimer have two different relaxed-configurations; stable and metastable ones. This situation is somewhat different from that in alkali-halide crystals with NaCl-type structure [2].

The authors are grateful to Professor K. Sawada for useful discussion.

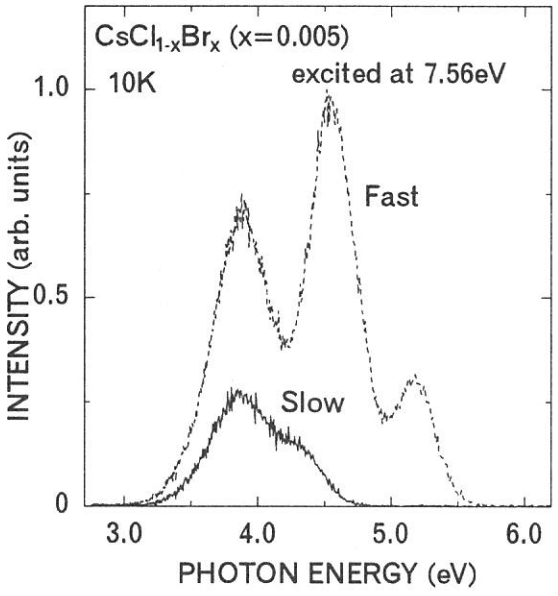

Fig.1. Time-resolved luminescence spectrum excited with 7.56-eV photons at 10K.

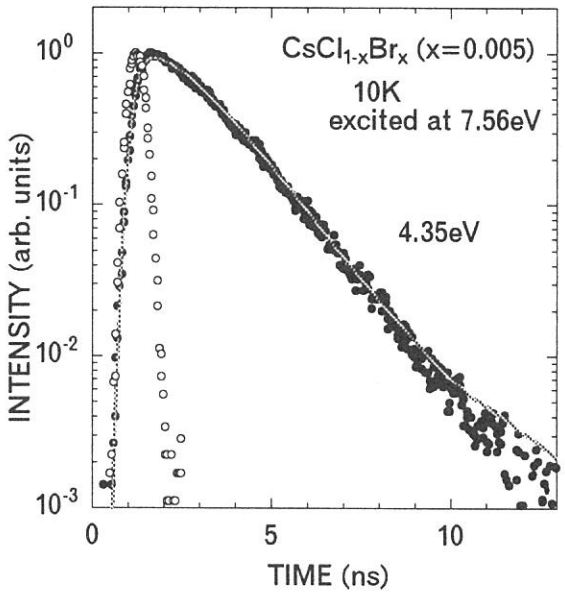

Fig.2. Decay curve (closed circles) of the luminescence detected at 4.35 eV under the excitation with 7.56-eV photon pulses at 10 K. Open circles represent the pulse shape of SR. Solid curve is the best fit of Eq. (1).

[1] H. Yoshida, N. Ohno and M. Itoh; *Proc. 2nd Int. Conf. on Excitonic Processes in Condensed Matter*, Kurort Gohrisch, edited by M. Schreiber (August, 1996) p.231.

[2] K. Kan'no, K. Tanaka and T. Hayashi; Rev. Solid State Sci. 4 (1990) 383.

(BL1B)

Two-Photon Spectroscopy of Excitons in BaF_2 by Combinational Use of Synchrotron Radiation and Laser

O. Arimoto[a], T. Tsujibayashi[b], M. Watanabe[c], S. Fujiwara[a], M. Itoh[d], S. Nakanishi[e], H. Itoh[e], S. Asaka[f], and M. Kamada[g]

[a]*Department of Physics, Okayama University, Okayama 700-8530*
[b]*Department of Physics, Osaka Dental University, Hirakata 573-1121*
[c]*Department of Fundamental Sciences, Kyoto University, Kyoto 606-8501*
[d]*Department of Electrical & Electronic Engineering, Shinshu University, Nagano 380-8553*
[e]*Department of Advanced Materials Science, Kagawa University, Takamatsu 760-8526*
[f]*Equipment Development Center, Institute for Molecular Science, Okazaki 444-8585*
[g]*UVSOR Facility, Institute for Molecular Science, Okazaki 444-8585*

One-photon spectroscopy with synchrotron radiation (SR) is a powerful and useful tool for the studies of electronic structures of various materials over a wide spectral range. On the other hand, laser has been utilized for not only one-photon spectroscopy but also multi-photon spectroscopy because of its high power and narrow spectral width. Combinational use of these two light sources is interesting and promising for the spectroscopy of solids in the VUV region. In the present study we have carried out a two-photon spectroscopy of the excitons in BaF_2 by making use of SR and laser. The valence band of BaF_2 consists of $2p$ orbital of F^-, and the conduction band $6s$ and $5d$ orbitals of Ba^{2+}. Therefore the excitons with an envelope function of S-type are one-photon allowed while the P excitons are two-photon allowed. A preliminary result at room temperature has been already reported [1, 2]. In this work, the experimental system has been improved to obtain definite results at low temperatures.

The experiments were done at BL1B of UVSOR. In Fig. 1 is shown a schematic diagram of the apparatus used for the present work. Single crystals of BaF_2 were cleaved from the ingot and mounted on a cold finger of a conduction-type cryostat. The monochromatized SR light (pulse width ~ 400 ps) was introduced into a sample chamber along the opposite direction of the second harmonic light of a Nd:YAG laser (2.33 eV, pulse width ~ 70 ns, average power ~ 12 W). The RF signal of 90 MHz from the master oscillator of the electron storage ring was divided down to 5 kHz, which triggers the YAG laser. The time interval between successive SR pulses was about 11 ns, while the time width of the laser pulse was 70 ns. Therefore, the time coincidence between the SR and laser pulses was automatically achieved, because about six pulses of the SR were involved within the time duration of a single pulse of the laser. This is an advantageous point compared to the preliminary experimental system with a short-pulse laser [1, 2], in which the temporal coincidence between the SR and laser pulses had to be carefully adjusted. Furthermore, the use of the high-repetition laser with the wide pulse-duration and low peak-power enabled us to detect weak two-photon signals more efficiently without any damage of the sample. The luminescence at about 4.1 eV, which is due to self-trapped excitons (STE's) produced by two-photon excitation, was observed by a micro-channel plate photomultiplier tube (MCP-PMT), with a combination of filters and a conventional monochromator for eliminating the scattered light from the laser. The signals from the MCP-PMT were fed to a three-channel time-gated photon counter. The photon signals just before and after the incidence of the laser pulses were counted at the channels 1 and 2, respectively: The channel 1 (CH 1) counts the background signal induced only by the SR light, while the CH 2 counts the signal due to the STE luminescence induced by the simultaneous irradiation with the SR and laser lights in addition to the background signal. The gate widths for both counters were equally set to be 4 μs by referring to the lifetime of the STE luminescence. The total signal was also counted at the CH 3 with the time-gate in full

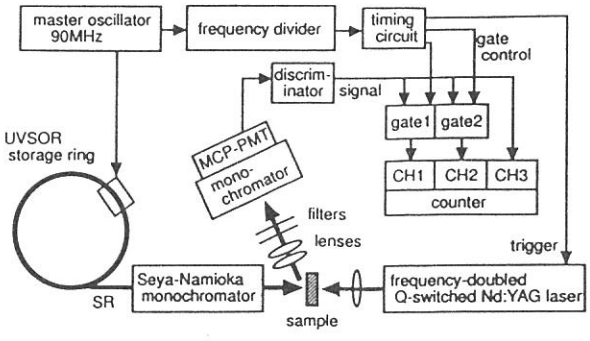

Fig. 1 Schematic diagram of the experimental system for two-photon spectroscopy with SR and laser.

open. The net luminescence signal induced by two-photon excitation was obtained by subtracting the count at CH 1 from that at CH 2. The above detection system has been specially developed for the present experiments, the details of which will be reported elsewhere [3].

Open circles in Fig. 2 show two-photon excitation spectrum of BaF_2 measured by monitoring the STE luminescence at 15 K. Its intensity corresponds to the net luminescence count obtained by subtraction of the count at CH 1 from that at CH 2. The solid curve is the total count at CH 3, which is properly normalized around 10 eV to the two-photon spectrum shown by the open circles. The closed circles are obtained by subtracting the data shown by the solid curve from those by the open circles. The count due to the net two-photon process, which is the difference between the count at CH 1 and that at CH 2, was at most 1% of that at CH 3. Accordingly the solid curve, intensity of which is proportional to the total count at CH 3, can be regarded as the one-photon spectrum induced by the SR light alone. As is easily recognized in the figure, the two-photon spectrum shown by open circles resemble the one-photon spectrum shown by solid curve. Such a similarity invokes the existence of cascade processes: Real states (or their relaxed states) excited by one photon from the SR are subsequently re-excited to the higher states by the laser, which in turn contributes to the enhancement of the STE luminescence. This is in contrast to the usual two-photon absorption process, in which virtual intermediate states are involved. In the one-photon excitation spectrum of the STE luminescence we observed weak peaks at 8.3 eV and 8.8 eV probably due to excitons bound to some unknown lattice imperfection. The energy positions of the two peaks at 10.6 eV and 11.2 eV in Fig. 2 are in good correspondence to those of the weak peaks at 8.3 eV and 8.8 eV. Therefore it is likely that the real excited states are unknown bound exciton states. Here it is noted that we made careful checks about not only the reproducibility of data but also the instruments used, especially the time-gated counter, to make sure that the obtained experimental data are reliable enough.

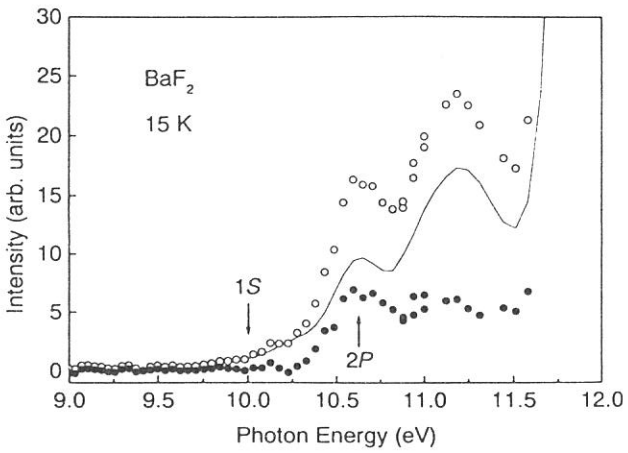

Fig. 2 The two-photon excitation spectrum of the STE luminescence in BaF_2 at 15 K (open circles). The spectrum includes two contributions: the two-photon absorption process (closed circles) and the cascade excitation process (solid curve).

As mentioned above, closed circles in Fig. 2 are the result of subtraction of the spectrum shown by the solid curve from that by the open circles. Since the former refers to the count due to the cascade process and the latter the net count due to the two-photon processes, the resultant spectrum depicted by closed circles can be regarded as the spectrum due to the usual two-photon absorption process under the assumption that the efficiency of the cascade excitation is constant. The spectrum has a broad band peaking at 10.6 eV. This is 0.6 eV higher than the $1S$ exciton whose energy position is indicated by a downward arrow. We assign this peak to the $2P$ exciton. Assuming a simple hydrogen model, the binding energy of the $1S$ exciton is estimated to be 0.8 eV, which gives the band gap energy as 10.8 eV. From measurements of reflection spectra, Rubloff has deduced the band gap energy of 11.0 eV [4], whereas Tomiki and Miyata have obtained the value of 10.6 eV [5]. It seems that the present value of 10.8 eV is more accurate because we observed the definite peak of the $2P$ exciton. Finally it is to be stressed that cascade excitation processes like the present case are not yet easy to investigate by the use of usual lasers, since their one-photon energies fall into the transparent region of the materials with wide band gap so that the real excited states can not be excited.

References

[1] T. Tsujibayashi *et al.*: UVSOR Activity Report **24** (1997) 52.
[2] M. Kamada *et al.*: *Proc. 6th Int. Conf. Synchrotron Radiation Instrum.*, Himeji, Aug. 1997 (in press).
[3] S. Asaka *et al.*: submitted to Rev. Sci. Instrum.
[4] G. W. Rubloff: Phys. Rev. **B5** (1972) 662.
[5] T. Tomiki and T. Miyata: J. Phys. Soc. Jpn. **27** (1969) 658.

(BL3A1)

Total Photoyield in Amorphous Chalcogenide Films by Undulator Radiation

Koji HAYASHI

Center for Cooperative Research, Gifu University, Gifu 501-1193

It is well-known that amorphous materials show a variety of photoinduced phenomena. The prominent photoinduced phenomenon in these materials is a time-dependent decrease in photocurrent during and after bandgap illumination.[1,2] This phenomenon is usually called photodegradation and is explained in terms of light-induced metastable defects (LIMD). In the device application of these materials, LIMD creation is a serious problem. Although a number of models have been proposed for LIMD creation[3], details of the mechanism underlying LIMD creation in these materials are still not clear. Understanding the physical mechanism underlying metastability is one of the important fundamental problems related to these materials. These phenomena were studied by exciting outer core electrons with the irradiation of the bandgap illumination. Little attention has been given to the photoinduced phenomena by exciting inner core electrons with the irradiation of higher energy photon. To obtain a wide knowledge of the photoinduced effects, it is necessary to investigate photoinduced effects on wide energy range. In the previous reports[4], we have reported the photodarkening in amorphous arsenic trisulfide (a-As_2S_3) by the vacuum ultra-violet (VUV) light. In the present study, we performed an in-situ study of the photoinduced effects by exciting inner core electrons and observed photoinduced change in total photoyield during illumination of the VUV light.

Thin films of a-As_2S_3 used for the measurements of photoyield were prepared onto quartz substrates by conventional evaporation technique. The thickness of the films was around 6000Å. An electrode using Al contact was fabricated first on the substrate for the measurements of the photoyield, before depositing the amorphous films. The experiments were performed at a BL3A1 beam line of the UVSOR facility of the Institute for Molecular Science in Okazaki. VUV light that is filtered through an Al film from undulator radiation was used to measure the photoyield. Before illumination, the samples were annealed at 443K (near the glass transition temperature) for two hours in a vacuum. To eliminate visible lights of synchrotron radiation and higher harmonics of undulator radiation, Al film was inserted between undulator and samples. The samples were fixed in sample chamber which were evacuated below 10^{-8} Torr. The photon flux of undulator radiation through Al film was estimated from the total photoelectric yield of gold mesh.

Figure 1 shows the change in the total photoyield as a function of number of photons for a-As_2S_3 at room temperature. This figure is obtained by normalizing the photoyield to the incident photon flux. As shown in the figure, the photoyield is decreased at the first stage. At the second stage, the photoyield is gradually increased and the photoyield seems to be finally saturated. This change also depends on the illumination energy of the photon. This change is similar effects with the previous report[5] in the photocurrent by VUV light. That is, the decrease and the increase in the photoyield are related with the LIMD creation (or initial defects) and photodarkening , respectively.

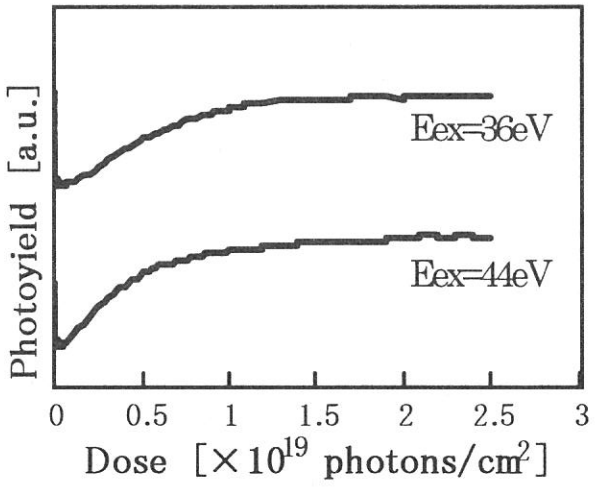

Fig.1 Change in the total photoyield for a-As_2S_3 measured at room temperature.

REFFERENCES

[1] K. Shimakawa, S. Inami, and S. R. Elliott, Phys. Rev. B, 42(1990)11857.
[2] D. L. Staebler and C. R. Wronski, Appl. Phys. Lett., 31(1977)292.
[3] K. Shimakawa, A. Kolobov, and S.R. Elliott, Adv. Phys., 44(1995)475.
[4] K. Hayashi, D. Kato, and K. Shimakawa, J. Non-Cryst. Solids., 198-200(1996)696.
[5] K. Hayashi, A. Hirai and K. Shimakawa, UVSOR Activity Report 1996, p116.

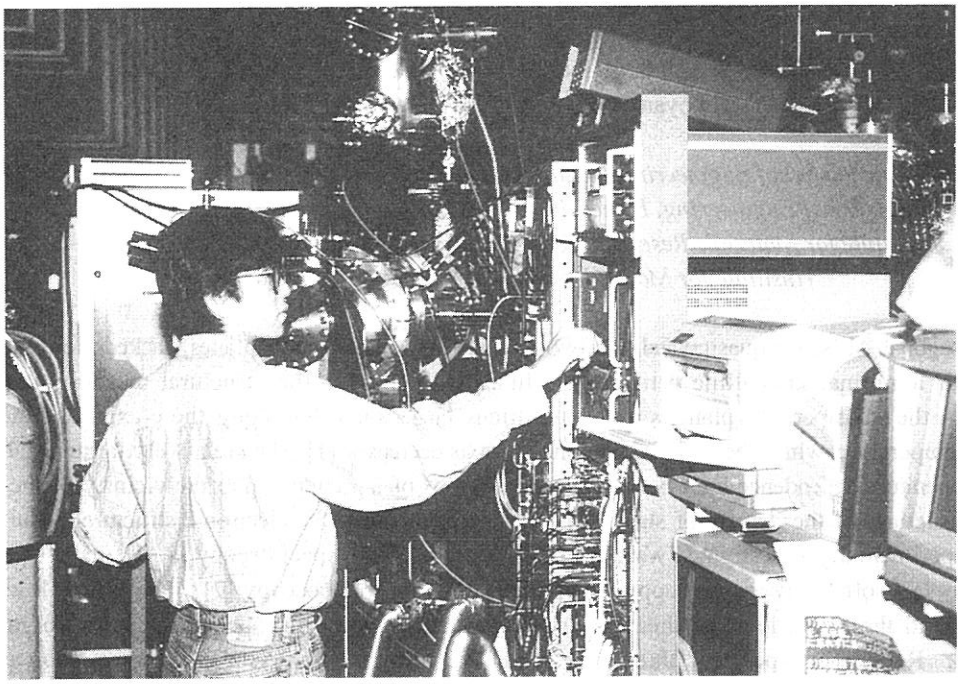

BL8B1

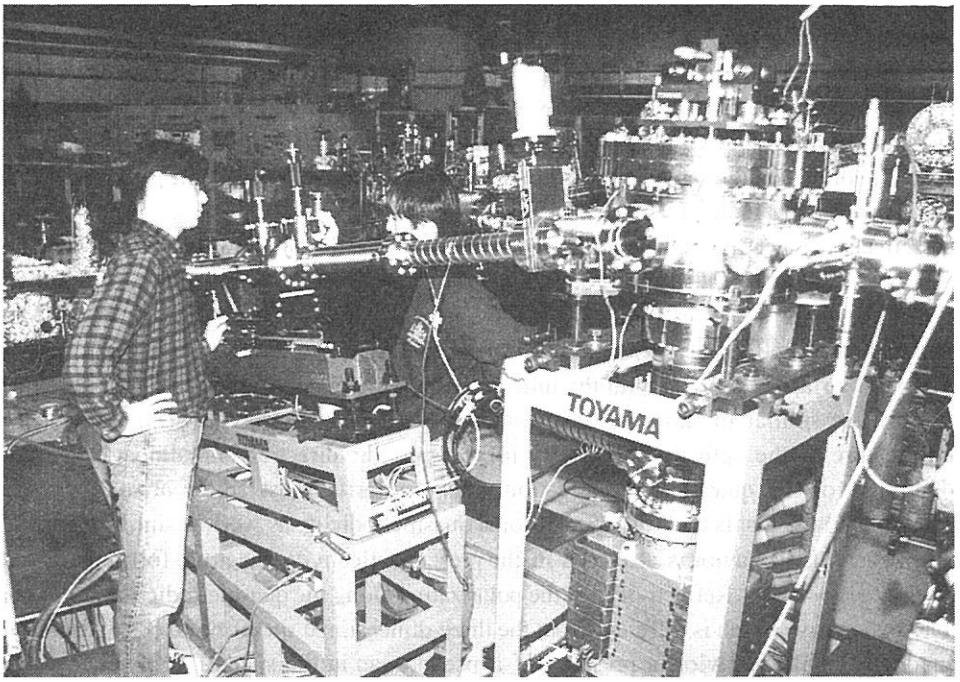

BL2B2

(BL6A1)

Infrared Reflectivity Spectra of Decagonal Al-Ni-Co Single Crystal

K. Soda, Y. Yanagida, K. Nozawa, T. Takeuchi, K. Morita, U. Mizutani,
Y. Yokoyama*, R. Note#, A. Inoue#, and S. Kimura†

Graduate School of Engineering, Nagoya University, Furo-cho, Chikusa, Nagoya 464-8603
**Faculty of Engineering, Himeji Institute of Technology, Shosha, Himeji 671-2201*
#Institute for Materials Research, Tohoku University, Katahira, Aoba, Sendai 980-8577
†Institute for Molecular Science, Myoudaiji, Okazaki 444-8585

A decagonal Al-Ni-Co quasicrystal has two-dimensional quasiperiodic planes stacked along a 10-fold axis (*c*-axis) with a normal crystalline periodicity. In accordance with the structural anisotropy, its electrical resistivity in the quasiperiodic plane is about ten times larger than that along the c-axis, and increases with decreasing temperature, while the resistivity along the axis decreases [1]. The relatively large resistivity and its negative temperature-dependence have been discussed in terms of a pseudo-gap in the vicinity of the Fermi level and spiky structures of the density of states [2]. On the other hand, the electronic structure of the quasicrystal has been experimentally investigated with use of the photoelectron spectroscopy [3, 4], inverse photoelectron spectroscopy [5], soft X-ray spectroscopy [4, 6], and tunneling spectroscopy [7]. They show lowering of the intensity around the Fermi level in their spectra, which may suggest the opening of a pseudo-gap across the Fermi level. Reflectivity spectra of three-dimensional icosahedral quasicrystals have been also studied, which shows neither Drude- nor semiconductor-type frequency dependence of their optical conductivity [8]. Here, we report a preliminary result on infrared reflectivity measurements of a decagonal single quasicrystal $Al_{72}Ni_{12}Co_{16}$ in order to obtain its optical conductivity and clarify its electronic structure.

Infrared reflectivity spectra for the incident photons polarized linearly in perpendicular and parallel with the *c*-axis, *i.e.* in the quasiperiodic and periodic directions, respectively, were measured with a standard setup of a Fourier interferometer at the beamline 6A1 of UVSOR at the temperatures of 300, 80 and 10 K. Specimens of single quasicrystals grown by a Czochralski method [9] were cut into a size of 5 mm in diameter and 1 mm in thickness, and mechanically polished along or perpendicular to the *c*-axis. Measured area was restricted to 2 mm in diameter by a conical aperture in front of the specimen. In order to correct contributions of such as surface roughness and small scratches and to obtain an absolute value of the reflectivity, we measured infrared reflectivity spectra of gold, evaporated on the same surfaces that were used for the reflectivity measurement of the specimen, and compared them with data in the reference [10].

Infrared reflectivity spectra obtained at the temperature of 300 K are shown in Fig. 1 together with those measured at BL-1 of SOR-RING, the Synchrotron Radiation Laboratory of the Institute for Solid State Physics, the University of Tokyo, in a photon energy range between 2 and 30 eV. Since we measured the photon-energy dependence of the relative reflectivity in the visible-vacuum ultraviolet (VUV) region, the visible-VUV data in the figure is plotted so as to coincide with the infrared data extrapolated to the visible region. These infrared reflectivity spectra are similar to those reported for other decagonal Al-Co-Cu-(Si) quasicrystals [11], which reveal a Drude feature in the optical conductivity for the periodic direction and almost frequency-independent optical conductivity for the quasiperiodic direction. This similarity most likely arises from the long-range ordering of these materials, that is their two-dimensional quasiperiodicity, as well as similarity in the constituent elements. The Drude-like behavior is also seen in the present reflectivity spectrum for the polarization parallel to the *c*-axis below $h\nu = 1$ eV. Reflectivity for the polarization along the quasiperiodic direction is almost unity for the low photon energy, which is different from the three-dimensional quasicrystal [8]. At present, we do not find the semiconductor-like behavior or presence of a pseudo-gap in the spectra. However, we recognize the anisotropy in the reflectivity below the photon energy $h\nu$ of 1 eV, which is apparently consistent with that in the electrical resistivity. By assuming the Drude-type frequency dependence in the low photon energy region for both directions, we can estimate the concentration of free carriers in the periodic direction to be larger than that in the quasiperiodic plane by a factor of about ten. The reflectivity spectra in the visible-VUV region do not show much difference in shape; they start to decrease at around $h\nu = 4$ eV, and show humps at $h\nu = 12$ and 18 eV. This suggests that the electronic structure relevant at least to this photon energy region is similar for both directions parallel and perpendicular to the *c*-axis. The 18-eV structure may be related to the plasmon loss peak

observed in the electron energy loss spectra of quasicrystals [11], and the 12-eV feature might be attributed to an interband transition relevant to the constituent transition metal. For further detailed discussion, we have to obtain optical conductivity or dielectric function by a Kramers-Kronig analysis, which is now in progress and will be reported elsewhere.

References

[1] T. Shibuya *et al.*, *J. Phys. Soc. Jpn.* **59** (1990) 1917.
[2] G. Trambly de Laissardiére and T. Fujiwara, *Phys. Rev.* **B50** (1994) 9843.
[3] Z. M. Stadnik *et al.*, *Phys. Rev.* **B51** (1995) 11358.
[4] K. Soda *et al.*, *Proc. of the 7th Int. Conf. on Quasicrystals, to be published.*
[5] K. Soda *et al.*, *J. Electron Spectrosc. Relat. Phenom., to be published.*
[6] E. Belin-Ferré *et al.*, *J. Phys.: Condens. Matter* **8** (1996) 9213.
[7] D. N. Davydov *et al.*, *Phys. Rev. Lett.* **77** (1996) 3173.
[8] C. C. Homes *et al.*, *Phys. Rev. Lett.* **67** (1991) 2694.
[9] Y. Yokoyama *et al.*, *Sci. Rep. RITU* **A42** (1996) 185.
[10] E. D. Palik (ed.), *Handbook of Optical Constants of Solids*, (Academic Inc., Orlando, 1985).
[11] D. N. Basov *et al.*, *Phys. Rev. Lett.* **72** (1994) 1937.
[12] M. Terauchi *et al.*, *Phil. Mag. Lett.* **74** (1996) 107.

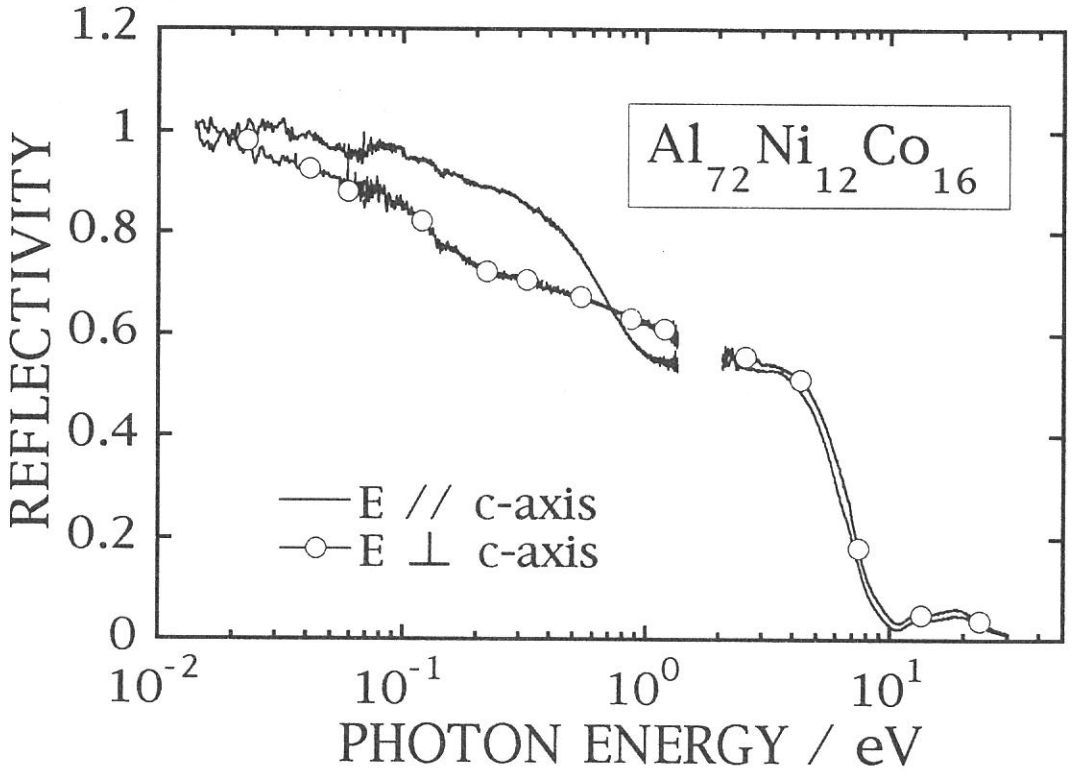

Figure 1. Reflectivity spectra of $Al_{72}Ni_{12}Co_{16}$ for the incident photons polarized in parallel with (solid curve with open circles) and in perpendicular to (solid curve) the c-axis.

(BL6A1)

Infrared magnetic circular dichroism of magnetic exciton of GdAs

Shin-ichi KIMURA, Dexin LI[1], Yoshinori HAGA[2] and Takashi SUZUKI[3]

UVSOR Facility, Institute for Molecular Science, Okazaki 444-8585
[1]Oarai Branch, Institute for Material Research, Tohoku University, Oarai 311-13
[2]Advanced Science Research Center, Japan Atomic Energy Research Institute, Tokai 319-11
[3]Department of Physics, Tohoku University, Sendai 980-77

In the last fiscal year, an infrared magneto-optical apparatus has been constructed at BL6A1 [1]. The main purpose is to measure infrared magnetic circular dichroism (IRMCD) of magnetic materials using circularly polarized infrared synchrotron radiation [2]. The experiment is expected to obtain informations of electronic structures with magnetic moments near the Fermi level. In the case of strongly correlated electron systems, the electronic structure that is made by coupling between carriers and magnetic moments appears near the Fermi level. Then the IRMCD is one of powerful tools for the investigation of such electronic structure.

GdAs is one of strongly correlated electron systems with low-carrier concentration. The physical properties are simple because it is a Heisenberg-type antiferromagnetic material with the Néel temperature of 18.7 K [3]. However, an absorption structure with strong temperature and magnetic field dependences has been found around 0.4 eV [4]. According to the temperature dependence, the absorption is considered to be due to an exciton. However, its magnetic field dependence is anomalous. To investigate the origin of the magnetic field dependence, IRMCD was performed.

Reflectivity spectra with circularly polarized infrared light in the energy range of 10 meV - 2 eV were measured under magnetic field up to 6 T and at the temperature of 6 - 60 K. The measurement was done by using fixed circular polarization direction (left circular polarization) and by using changed magnetic field direction. The reflectivity spectra in the energy range of 2 - 30 eV were measured at BL1B. After the connection of these spectra, optical conductivity spectra were derived from the Kramers-Kronig transformation of the reflectivity spectra. From here and in figures, the spectrum in the case of the magnetic field direction parallel to the polar direction of light is denoted by Δl = +1 and antiparallel is denoted by Δl = -1.

The magnetic field dependences of circularly polarized optical conductivity spectra at 6 K were shown in Fig. 1 (a). Peak energies around 0.4 eV of Δl = ±1 spectra are different from each other, i. e.,

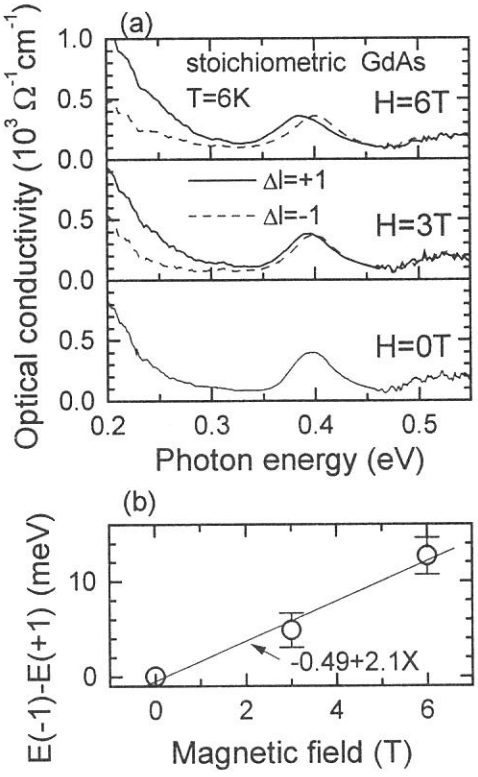

Fig. 1. (a) Magnetic field dependence of circularly polarized optical conductivity spectra at 6 K. Magnetic circular dichroism of absorption at 0.4 eV of GdAs appears. (b) The different energy (E(-1)-E(+1)) between the two peaks of Δl = ±1 as the function of applied magnetic field. The energy difference linearly changes as the magnetic field increases.

magnetic circular dichroism appears in the 0.4 eV absorption of GdAs. The difference between the two peaks ($E(-1)$-$E(+1)$) linearly increases with increasing magnetic field as shown in Fig. 1 (b). This just indicates Zeeman splitting of an exciton. The slope is determined to be 2.1 meV/T by a least square method. The value is about ten times larger than normal electron response. However, since the magnetic field applied to the exciton is induced by Gd^{3+} ions, the induced field should be considered. According to the magnetization data [3], the magnetization has linear response to applied magnetic field up to 13 T. The relation is $M = 0.4\ H$ per Gd^{3+} ion, where M means magnetization and H applied field. From the relation of $E(-1) - E(+1) = 2g\mu_B\ (H + nM)$, where g is g-factor ≈ 2, μ_B Bohr magneton and n the number of Gd^{3+} ion which makes the induced magnetic field to an exciton, the area of one exciton can be determined. The n becomes 20, i. e., one exciton expands in the volume of twenty Gd^{3+} ions.

On the other hand, the temperature dependences of circularly polarized optical conductivity spectra at ±6 T are shown in Fig. 2 (a). In comparison with the spectra at 60 K, the peak energy difference at 6 K is larger. The energy difference is plotted in Fig. 2 (b). The splitting energy increases as the temperature decreases above 20 K. However, the energy difference becomes almost constant below 20 K. Since the Néel temperature of GdAs is 18.7 K, the change of the slope comes from the magnetic transition. Therefore, the Zeeman splitting of the exciton is a signal of the magnetic transition.

---

[1] S. Kimura, UVSOR Activity Report 1996 (1997) p. 170.

[2] S. Kimura, in this issue.

[3] D. X. Li, Y. Haga, H. Shida, T. Suzuki, T. Koide and G. Kido, Phys. Rev. B **53** (1996) 8453.

[4] S. Kimura, D. X. Li, Y. Haga and T. Suzuki, UVSOR Activity Report 1996 (1997) p. 172; J. Magn. Magn. Mater. **177-181** (1998) in press.

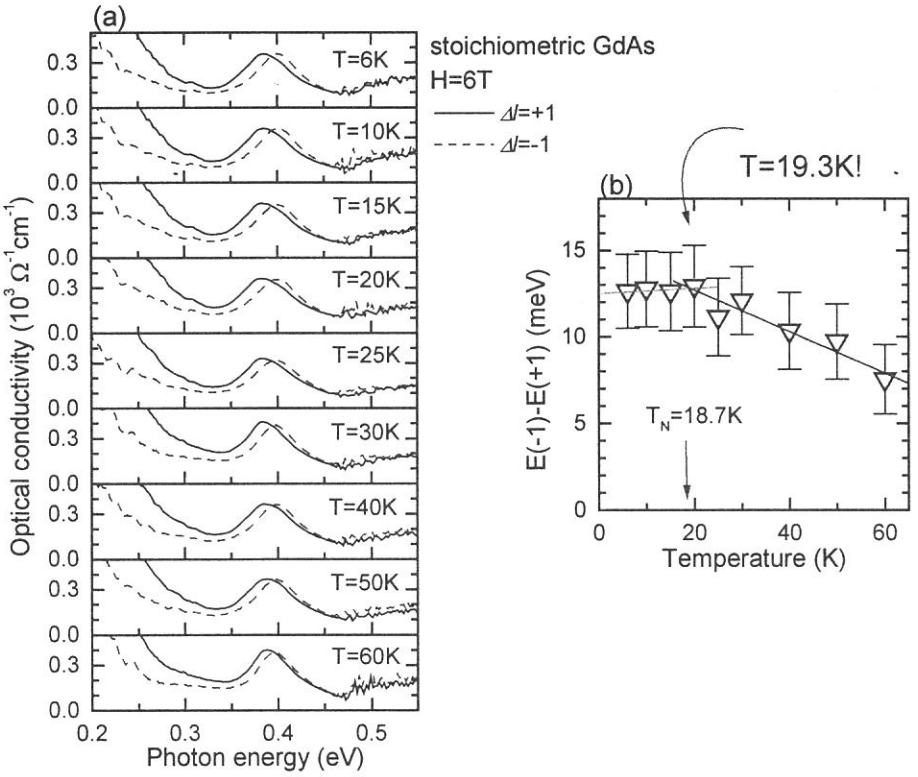

Fig. 2. (a) Temperature dependence of circularly polarized optical conductivity at ±6 T. (b) The energy difference of two peaks of $\Delta l = \pm 1$ as the function of temperature.

(BL6A1)

Heavy-Fermion-Like Optical Conductivity of Yb_4As_3

Shin-ichi KIMURA, Akira OCHIAI[1], and Takashi SUZUKI[2]

UVSOR Facility, Institute for Molecular Science, Okazaki 444-8585
[1]Department of Material Science and Technology, Niigata University, Niigata 950-21
[2]Department of Physics, Tohoku University, Sendai 980-77

Yb_4As_3 is a typical strongly correlated 4*f*-electron system with low carrier concentration. The temperature dependence of optical conductivity (OC) spectrum has been measured in the photon energy of 2 meV – 50 eV at several temperature of 39 – 320 K in the last fiscal year [1]. The result indicates that there is an absorption with strong temperature dependence around 0.4 eV. The electronic structure from which the absorption originates crosses the Fermi level and changes to conduction band with short relaxation time. Physical properties at higher temperature come from the electronic structure. After that, we measured reflectivity spectra at several temperatures down to 6 K form the investigation of the electronic structure at lower temperature and reported here.

Reflectivity spectra were measured at an infrared beam line 6A1. The magneto-optical system which was constructed in the last fiscal year [2] was used in spite of no magnetic field because measuring of temperature dependence below 100 K is easier than normal optical system of BL6A1. We discuss using OC spectra that were determined from a Kramers-Kronig analysis of the reflectivity spectra.

The OC spectra at several temperatures are shown in Fig. 1. The spectra are plotted with the DC conductivity and the carrier number derived from the Hall coefficient. Above 700 meV, the OC spectra originates from interband transitions. Therefore the temperature dependence is small. On the other hand, below 700meV, the spectrum strongly changes with temperature. The origin of a peak at 0.4 eV has already discussed [1] and mentioned before. Here, we discuss the origin of structures below 8 meV and around 30 meV. Note that some sharp peaks around 15 meV come from TO phonons. We do not discuss them in this

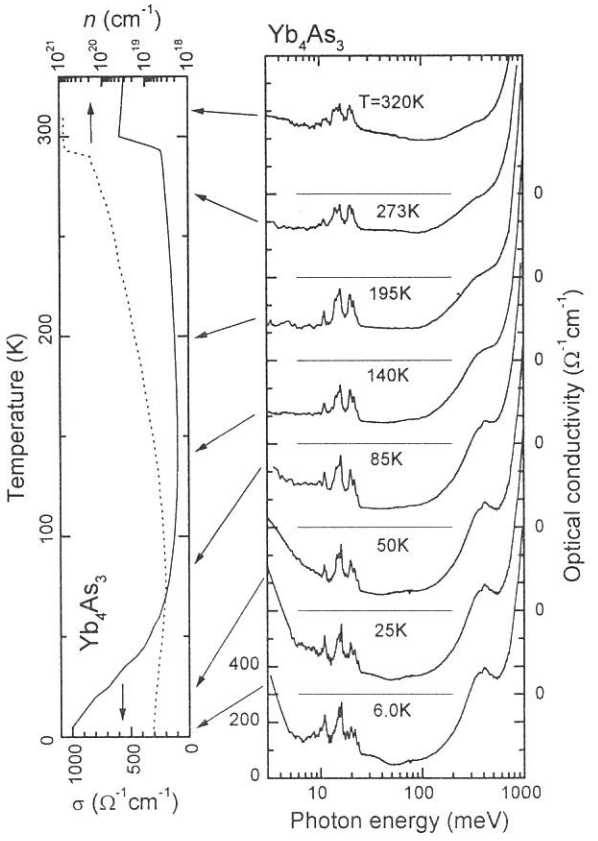

Fig. 1. Temperature dependence of optical conductivity spectrum of Yb_4As_3 with the DC conductivity and the carrier number derived from the Hall coefficient.

report.

Drude-type optical conductivity appears below 8 meV. From the carrier number and the DC conductivity, we can get a Drude function,

$$\sigma(\omega) = \left(\frac{Nm_0}{m^*}\right)\frac{e^2\tau}{m_0(\omega^2\tau^2+1)}$$

with a parameter of the effective mass, m^*. After the fitting, the effective mass is determined to be $0.7m_0$, which is equal to that of cyclotron mass derived from microwave resonance [3]. The relaxation time is 3.1×10^{-12} sec, which value is hundred times larger than that of normal metals.

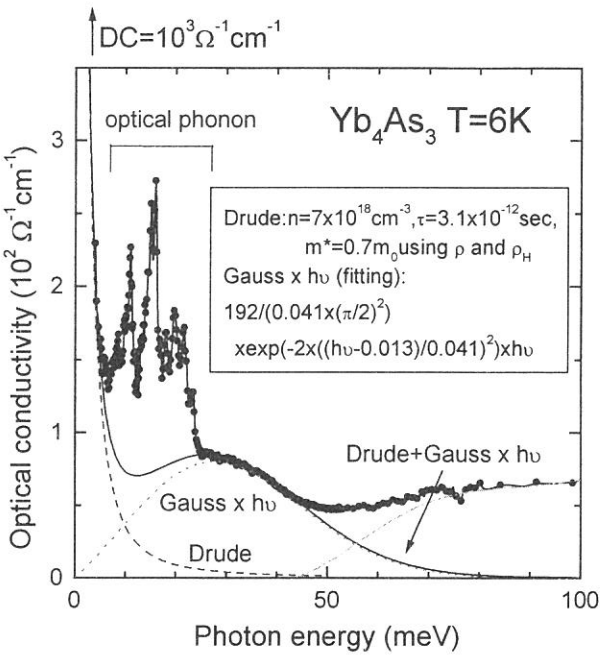

Fig. 2. Optical conductivity spectrum of Yb_4As_3 at 6 K and the fitting curves.

Around 30 meV, a shoulder develops as temperature decreases. Then we fitted the spectrum of 25 - 45 meV at 6 K. We can get a good fitting by a function of Gaussian×$h\nu$. The fitting function shows there is a peak around 30 meV, i. e., a small gap opens on the Fermi level.

According to a theory of Coleman [4], the spectrum can be explained by a Kondo lattice model. The Kondo temperature (T_K) of Yb_4As_3 is estimated to be about 100 K (8.6 meV) by the DC conductivity. Therefore the width of Drude part becomes 1 T_K and the energy of the gap becomes 3 T_K. The results are equal to the theory of Coleman. However, it is thought that the charge of Yb_4As_3 does not couple with the magnetism [5]. And also similar spectrum shape appears in organic materials, which originates from the CDW nature. Therefore the origin of the spectrum shape should be considered.

[1] S. Kimura, M. Ikezawa, A. Ochiai and T. Suzuki, J. Phys. Soc. Jpn. **65** (1996) 3591; S. Kimura, A. Ochiai and T. Suzuki, UVSOR Activity Report 1996 (1997), p. 174.
[2] S. Kimura, UVSOR Activity Report 1996 (1997), p. 170.
[3] H. Matsui *et al.*, private communication.
[4] P. Coleman, Phys. Rev. Lett. **59** (1987) 1026.
[5] A. Ochiai, private communication.

(BL6A1)

Optical reflectivity study of the Kondo insulator YbB_{12}

H. Okamura, H. Sinozaki, T. Nanba, S. Kimura[A],
F. Iga[B], N. Simizu[B] and T. Takabatake[B]

Department of Physics, Kobe University, Kobe 657-8501.
[A]UVSOR, Institute for Molecular Science, Okazaki 444
[B]Department of Materials Science, Hiroshima University, Higashi-Hiroshima 739

YbB_{12} is one of the strongly correlated electron systems known as "Kondo insulators".[1] It is paramagnetic at high temperatures, but with lowering the temperature below 75 K, χ decreases and the electrical resistivity (ρ) increases. The temperature dependences of both χ and ρ show thermally activated behaviors, and indicate the presence of an energy gap of about 10 meV. These unique behaviors are believed to arise from strong interactions between the localized f-electrons and free carriers, but the mechanism responsible for them is not exactly known yet. In particular, it is important to obtain more information about the behaviors of energy gap at low temperatures. Although infrared reflectivity measurements are very useful for this purpose, earlier optical measurements on YbB_{12} suffered from a lack of high-quality single crystal.[2,3] Recently, however, Iga, Shimizu and Takabatake have successfully grown single crystals of YbB_{12} [4]. Using BL6A1 we have measured the optical reflectivity of single crystals of YbB_{12} at various temperatures between 20 K and 300 K. Figure 1(a) shows the reflectivity spectrum of YbB_{12} at 290 K, 160 K, 78 K, and 20 K, and Fig. 1(b) shows the corresponding optical conductivity $\sigma(\omega)$ obtained from the reflectivity spectra via Kramers-Kronig analyses. At 290 K, there is a strong absorption peaked around 0.2 eV, superimposed on a broad, Drude-like free carrier contribution. This absorption peak at 0.2 eV is not seen for LuB_{12}, which has a filled f-shell and non-magnetic, and is likely to arise from f-levels located near the Fermi level. Upon cooling, the free carrier contribution is rapidly suppressed, and below 80 K the spectral weight below 20 meV in $\sigma(\omega)$ is completely depleted. Figure 2 shows the detailed temperature dependence of the gap structure seen in $\sigma(\omega)$ below 80 K. From this we can see that the gap structure in $\sigma(\omega)$ appears just below 78 K. This temperature nearly coincides with the temperature below which χ decreases rapidly, hence the gap appearance seen in $\sigma(\omega)$ is correlated with the magnetic properties. To clarify further the characteristics of the energy gap, we plan to study the reflectivity of $Yb_{1-x}Lu_xB_{12}$ with several values of x, including their response to magnetic field.

References

[1] G. Aeppli and Z. Fisk, Comments Cond. Mat. Phys. **16**, 155 (1992).

[2] P. Wachter and G. Travaglini, J. Magn. Magn. Mater. **47&48**, 423 (1985).

[3] H. Okamura et al, UVSOR Annual Report 1997, p162.

[4] F. Iga, N. Shimizu, and T. Takabatake, J. Magn. Magn. Mater. to be published.

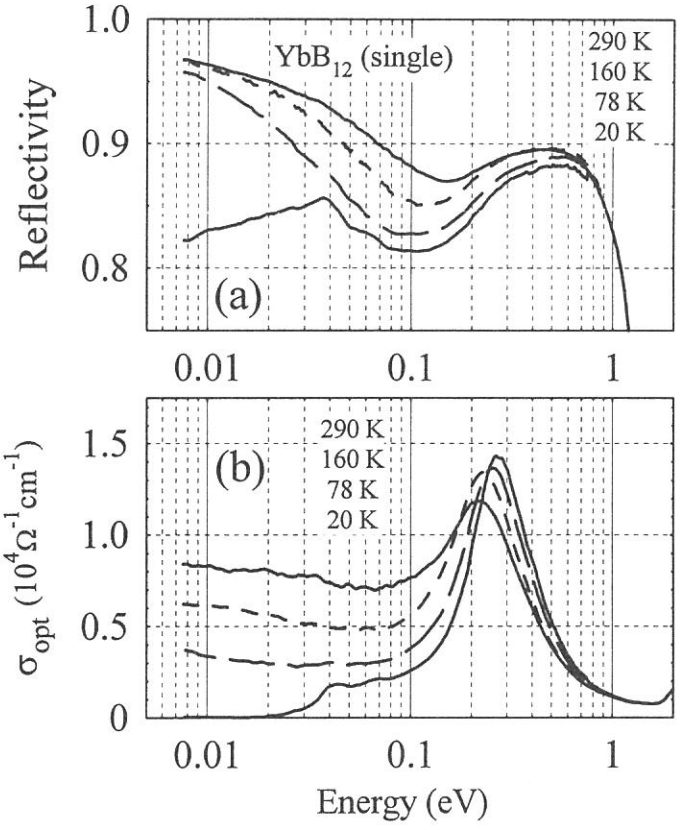

Fig.1: Reflectivity (a) and optical conductivity (b) of YbB_{12} single crystal at several temperatures.

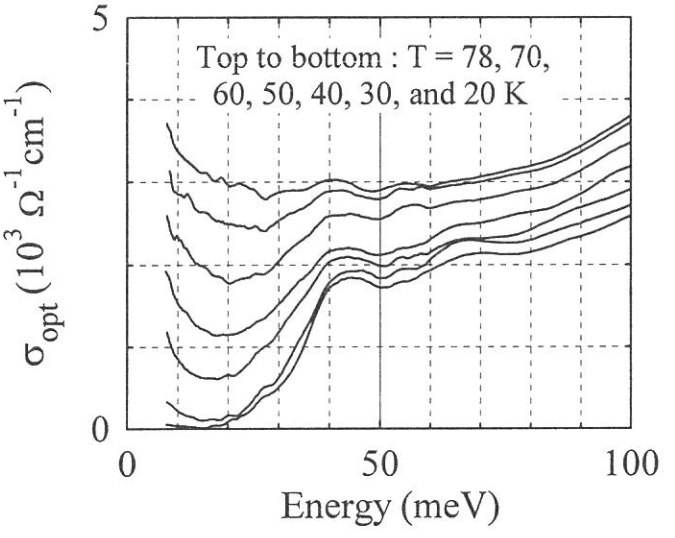

Fig. 2: Optical conductivity of YbB_{12} below 78 K.

(BL6A1)

Millimeter Wave Reflection Measurement of Secondary Battery Substance $LiNiO_2$

Hitoshi OHTA, Yoji IKEUCHI, Shunsuke ONO, Takao NANBA, Atushi HIRANO* and Ryoji KANNO*

Department of Physics, Faculty of Science, Kobe University,1-1 Rokkodai, Nada, Kobe 657

**Department of Chemistry, Faculty of Science, Kobe University,1-1 Rokkodai, Nada, Kobe 657*

Nowadays Li ion secondary battery has attracted much attention because it is a promising secondary battery due to its high energy density and light weight.[1] Although $LiCoO_2$ is already in commercial use as an electrode material in secondary Li batteries, $LiNiO_2$ is a promising candidate to replace $LiCoO_2$ from the economical point of view. This is due to the fact that Ni atoms is cheaper and easy to obtain than Co atoms. However, the composition of $LiNiO_2$ is very sensitive to the synthesis condition, especially the sintered temperature, and it can be easily lead to a decomposition to $Li_{1-x}Ni_{1+x}O_2$. The non-stoichiometry degrades the charge and discharge characteristics significantly. However, Kanno *et al.* succeeded in synthesizing nearly stoichiometric $LiNiO_2$ and they opened the way to use $LiNiO_2$ as an electrode material in secondary Li batteries.[2] The aim of our study is to obtain the information about the diffusive motion of Li^+ ions by observing "ionic plasmon" whose existence can be proved as a definite increase in a reflectivity towards a low energy side in the millimeter wave region because the mass of Li^+ ion is larger than that of electron. The first observation of ionic plasmon has been performed previously for alkali silver iodide super-ionic conductors MAg_4I_5 (M=Rb, K and NH_4) by Awano *et al.*[3]

The reflection measurements of the nearly stoichiometric $LiNiO_2$ sintered at 650°C has been performed in the spectral region from 6 to 50 cm^{-1} using the beam line BL6A1 of UVSOR. Low pass filter below 22 cm^{-1} was used for the low energy region. The temperature was varied from 79 K to 380 K and the liquid He cooled InSb detector was used. Figure 1 shows the results of our measurements. The reflection is almost flat for the observed region below 197 K. The previous measurements also showed similar behavior for 11 K.[4] However, the reflection in the low energy region increases monotonically as the temperature is increased above 300 K. This result is consistent with the fact that diffusive motion of Li^+ ions is low at low temperature but starts to increase above 300 K. Therefore the temperature dependence strongly suggests that the increase of the reflection in the low energy side is due to the ionic plasmon of Li^+ ion. The detailed analysis of the data is underway.

Acknowledgments: One of the authors (HO) is grateful to Murata Science Foundation for the financial support.

References

[1] S. Megahed and B. Scrosati: The Electrochemical Society Interface, Winter (1995) 34.

[2] R. Kanno *et al.*: J. Solid State Chem. **110** (1994) 216.

[3] T. Awano *et al.*: Solid State Ionics **53-56** (1992) 1269.

[4] H. Ohta et al.: UVSOR Activity Report (1996) 182.

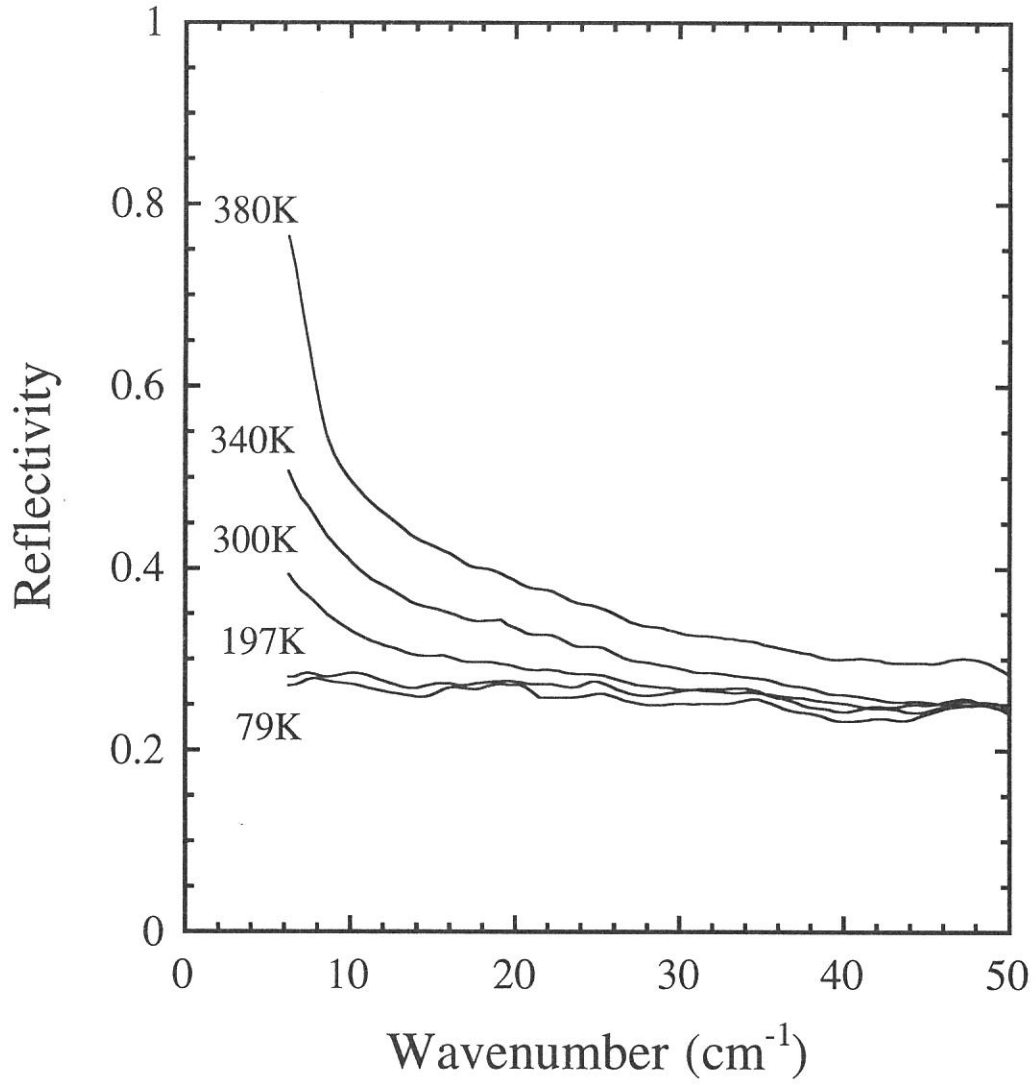

Fig. 1 The reflection spectra of the nearly stoichiometric $LiNiO_2$ sintered at 650°C.

(BL6A1)

Far-infrared Reflection Spectrum of Ice Ⅷ

Masato Hayashi and Takao Nanba[A]

Faculty of Natural Science , Kobe University, Nada-ku, Kobe 657-8501
[F]*aculty of Science, Kobe University, Nada-ku, Kobe 657-8501*

Ice has more than ten stable phase according to the environment of pressure and temperature. At Ⅶ, the oxygen atom of the hydrogen molecule forms two net works with a diamond structure (Fig.1). Two net works intersect each other and the position of the proton atoms is in disorder. At Ⅷ, on the other hand, the oxygen atoms form the same two net works with a diamond structure, but the position of proton forming the hydrogen bonding with oxygen atom is in order. Consequently, Th. orientation of the dipole moment of the water molecule in the one net work has the same direction and the one in the other net work has the opposite direction. That is, the only difference between two phases in structure is the order-disorder on the proton configuration.

Hitherto, various types of spectroscopic studies have been done on ice. However, the far infrared spectroscopy on ice under pressure has not been done except only one [1] because of the difficulty in doing the experiment using a diamond anvil cell (DAC). The transmission light intensity through DAC is too weak to detect. Kobayashi *et al* made the transmission measurement on very thin ice at low temperature and observed the anomalous pressure dependence of the phonon frequencies of ice at the phase Ⅷ[1]. Unfortunately, the signal showed a saturation around the region of the absorption peak due to the infrared active phonon mode because of the strong absorption. We made a far-infrared reflection measurement on ice under pressure using a DAC and synchrotron radiation (UVSOR) , and succeeded ,for the first time, to measure the change in the far-infrared reflection spectra on ice due to the phase transition between Ⅶ and Ⅷ phases.

Fig.2 shows the developments of the power spectra on ice under pressure in the far-infrared region. The sample was compressed up to 2.6 GPa at room temperature (Ⅶ) and then cooled down to Ⅷ phase. A new peak was resolved around 220 cm^{-1} at Ⅷ phase which corresponds to the TO phonon mode at Ⅷ phase. The ratios of spectra at Ⅷ phase to that at Ⅶ phase was shown in Fig.3. The peak at Ⅷ phase showed a blue shift of about 17 cm^{-1}/GPa to pressure .

[1] M.Kobayashi; Solid State Physiscs (Japan) 31,(1996)127.

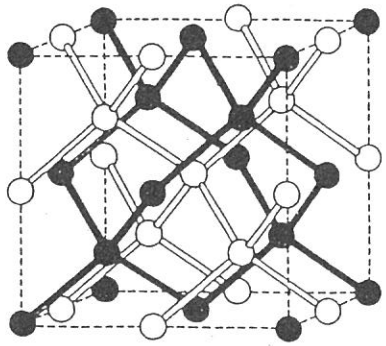

Fig.1 Crystal structure of ice at Ⅶ and Ⅷ phases. The open and closed circles corespond to oxgen atoms and show two net works with a diamond structure.

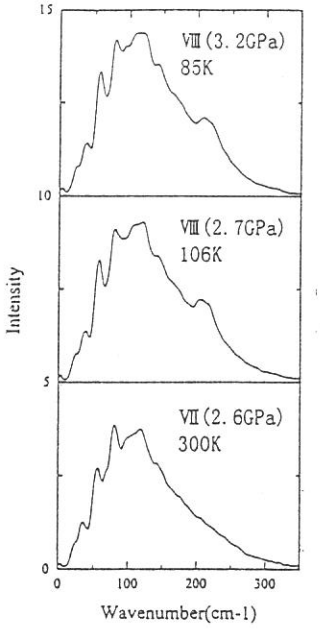

Fig.2 shows the development of the spectra of ice under pressure.

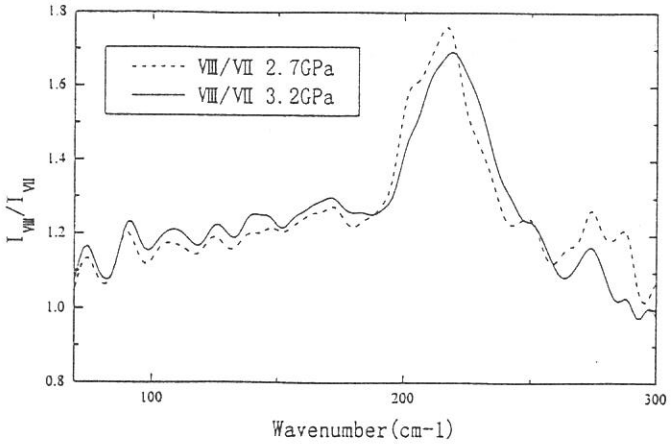

Fig.3 shows the ratios of spectra at Ⅷ phase at 2.7(dot) and 3.2 GPa(solid curve) to that at Ⅶ phase.

(BL6A1)

IR reflection and magneto-reflection of the $Yb_4(As_{1-x}Sb_x)_3$ system

Raniero Pittini [a], Mikihiko Ikezawa [a], Akira Ochiai [b], Hidekazu Aoki [c] and Takashi Suzuki [c]

[a] *Research Institute for Scientific Measurements, Tohoku University, Sendai 980-77, Japan*
[b] *Department of Material Science and Technology, Niigata University, Niigata950-21, Japan*
[c] *Department of Physics, Faculty of Science, Tohoku University, Sendai 980-77, Japan*

After the study of the optical response of $Yb_4(As_{0.88}Sb_{0.12})_3$ and $Yb_4(As_{0.71}Sb_{0.29})_3$ performed extensively last year over a wide energy range from 1 meV to 5.5 eV, this year we focused on two points, i.e. *a)* the temperature dependence of the IR optical signal (in the photon energy region of the free carrier absorptions and phonon absorptions) and *b)* the field dependence of the optical absorption of the $4f \rightarrow 5d$ transitions.

a) Temperature dependence of the IR optical signal

The free carrier contributions to the optical signal can be fitted with a Drude model, yielding the plasma frequency ω_p and the scattering rate γ as parameters. Repeating this fit for all the measured temperatures, one can determine the effective mass of the charge carriers from the plasma frequency, taking the carrier density from the Hall data. The result is shown in Fig. 1.

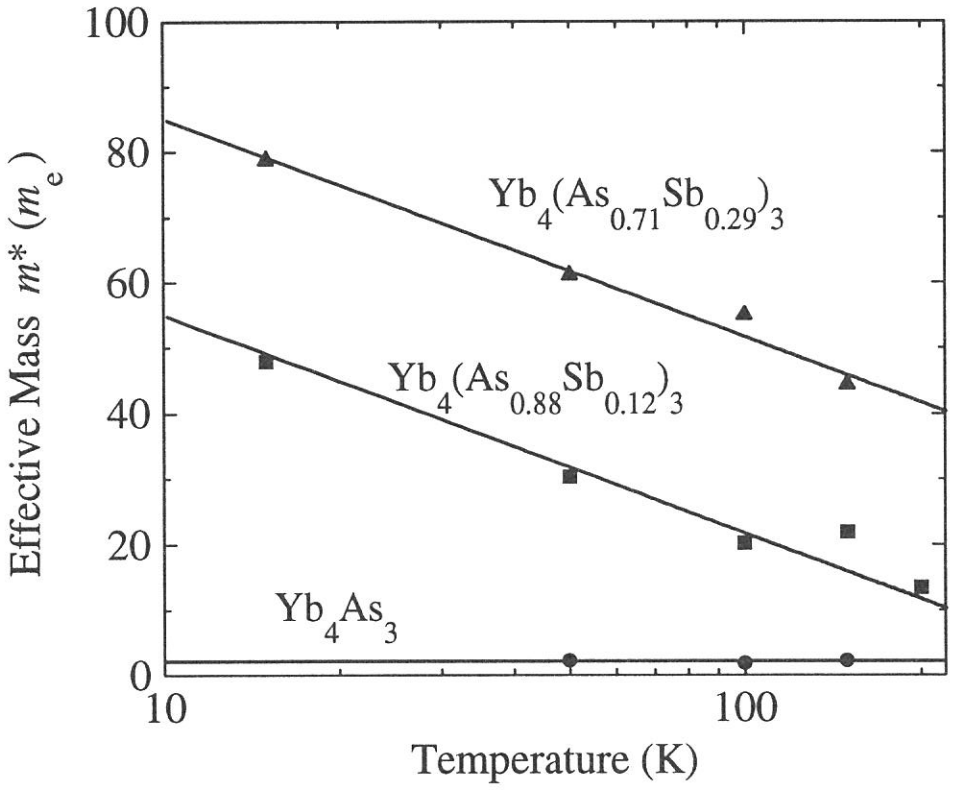

Fig. 1: Temperature dependence of the effective mass in the Yb_4X_3 system, obtained from the optical data (R. Pittini et al., ICM'97, scheduled for J. Magn. Magn. Mat. **177-181** (1998)).

The effective mass of the carriers in Yb_4As_3 is not particularly enhanced and temperature independent, while the effective masses in $Yb_4(As_{0.88}Sb_{0.12})_3$ and $Yb_4(As_{0.71}Sb_{0.29})_3$ have a logarithmic temperature dependence, and reach the values of 55 m_e and 85 m_e at 10 K, respectively. Therefore, the Sb-substituted samples are nearer to a heavy fermion than 'pure' Yb_4As_3.

b) Field dependence of the optical absorption of the $4f \rightarrow 5d$ transitions

The magneto-reflection of the $4f \rightarrow 5d$ transitions in $Yb_4(As_{0.88}Sb_{0.12})_3$ and $Yb_4(As_{0.71}Sb_{0.29})_3$ is very strong (Fig. 2), in particular the sharp peak at 0.4 eV. This indicates that the magnetic dichroism is strong in the Sb-substituted samples, while it appears to be weak in 'pure' Yb_4As_3. For the peaks between 0.1 and 0.3 eV and at 0.5 eV, the origin is still unclear. But similar effects have been reported recently at very high fields in low dimensional systems (J.S. Brooks, RHMF'97). The Yb_4X_3 materials are indeed low dimensional systems, as the $4f$ bands are one-dimensional. But the $Yb_4(As_{1-x}Sb_x)_3$ system is particular because the anomalies appear already at moderately low fields.

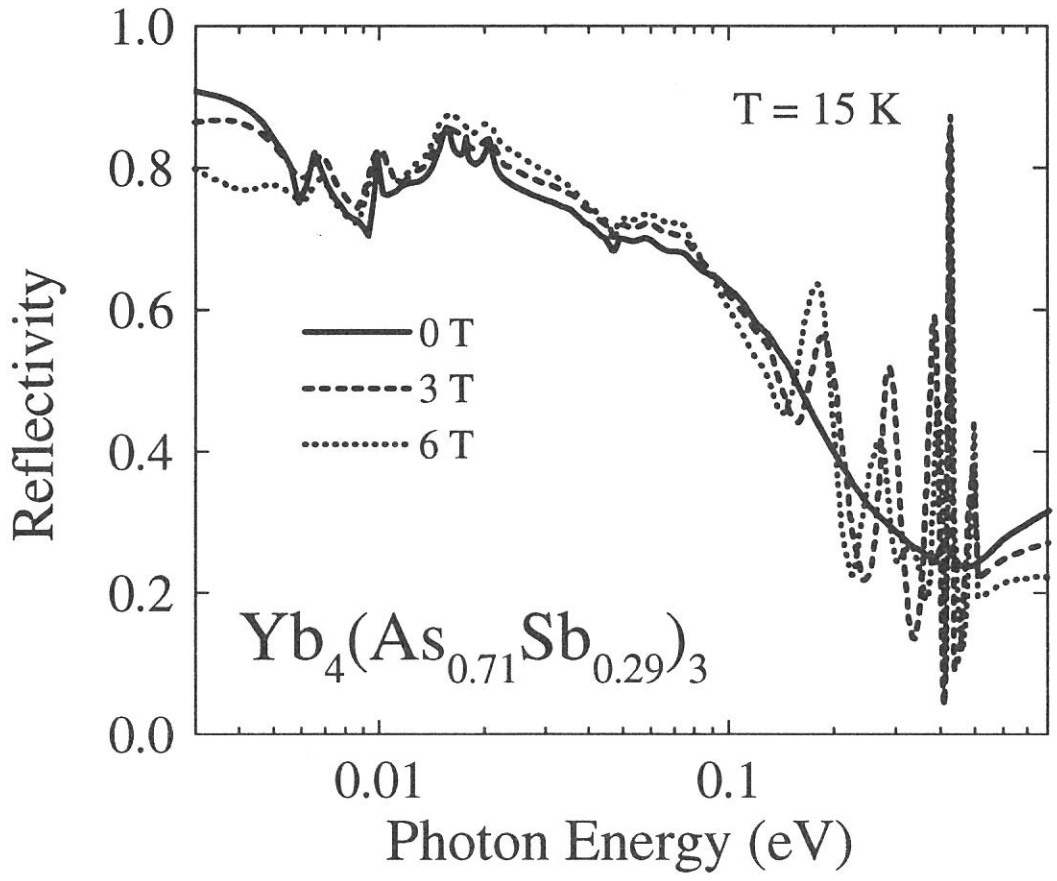

Fig. 2: Field dependence of the optical reflection in $Yb_4(As_{0.71}Sb_{0.29})_3$ at 15 K. (R. Pittini et al., RHMF'97, to be published in Phys. B).

(BL6A1)

Millimeter Wave Spectroscopy of Superionic Conducting Glasses

Naotake Sasaki, Katsuyoshi Handa and Teruyoshi Awano

Department of Applied Physics, Tohoku Gakuin University, Tagajo 985-0873

There are few precise optical measurements of superionic conducting glasses in the spectral region between millimeter wave and far-infrared. An optical absorption band by a collective motion of mobile ions may appear in this spectral region, in which motion of mobile ions switches from translation to vibration. Such collective motion may be one reason of the high ionic conductivity of these glasses even at low temperature.

We had investigated far-infrared and millimeter wave spectra of some silver or copper ion conductors to study the dynamics of mobile ions. In AM_4X_5 (A=alkali metal; M=Ag or Cu; X=halogen) crystal, a structure by "ionic plasmon" was observed in the spectral region below 10 cm^{-1} in silver ion conductors or 30 cm^{-1} in copper ion conductors in energy loss function spectra at temperatures of superionic conducting phase[1].

In this study, we report results on $(AgI)_x(AgPO_3)_{1-x}$, $(TMAI)_{0.1}(TEAI)_{0.1}(AgI)_{0.8}$, (TMAI=$(CH_3)_4NI$, TEAI=$(C_2H_5)_4NI$) superionic conducting glasses comparing the results of copper ion conducting glasses in the millimeter wave region. Large alkylammonium ions disperse randomly into AgI in organic-inorganic glasses in contrast to oxide tetrahedrons in inorganic glasses.

Optical constants were obtained from reflectivity spectra by K-K analysis. In the millimeter wave region, the transmittance spectra of samples with different thickness were measured directly. Absorption coefficient spectra of this spectral region were calculated from them.

Fig. 1 shows AgI composition dependence of intensity of absorption bands in millimeter wave region. As the AgI composition decreased, the absorption intensity around 7 cm^{-1} decreased. Fig. 2 shows temperature dependence of this absorption band. The 7 cm^{-1} band decreased as temperature decreased. This suggest that the absorption around 7 cm^{-1} is due to a sort of diffusive motion of conduction ions. The 7 cm^{-1} band in AgI-$AgPO_3$ shifted to 9 cm^{-1} in CuI-$CuPO_3$. The square root of mass ratio of silver and copper ion is 1.3. Therefore the wave number shift of these absorption bands means that these bands are due to movements of conduction ions.

Fig. 3 shows the spectral change of the absorption spectra in millimeter wave region of $(TMAI)_{0.1}(TEAI)_{0.1}(AgI)_{0.8}$ glass as temperature decreased. The same spectral change as AgI-$AgPO_3$ was observed. Fig. 4 shows spectral change of the absorption band in millimeter wave region between $(TMAI)_{0.1}(TEAI)_{0.1}(AgI)_{0.8}$ and $(TMAI)_{0.15}(TEAI)_{0.1}(CuI)_{0.75}$. The 8 cm^{-1} peak in $(TMAI)_{0.1}(TEAI)_{0.1}(AgI)_{0.8}$ shifted to 11 cm^{-1} in $(TMAI)_{0.15}(TEAI)_{0.1}(CuI)_{0.75}$. This shift coincides with the inverse square root of mass ratio of sliver and copper. This suggest that this band is due to a motion of conduction ions.

The absorption band in millimeter wave region is due to a sort of diffusive motion of conduction ions. Detail of this motion of conduction ions is under investigation.

References

1) T. Awano, T. Nanba and M. Ikezawa, Solid State Ionics, **53-56**, 1269 (1992).

2) J. Kawamura et al., Solid State Ionics, **86-88**, 517 (1996).

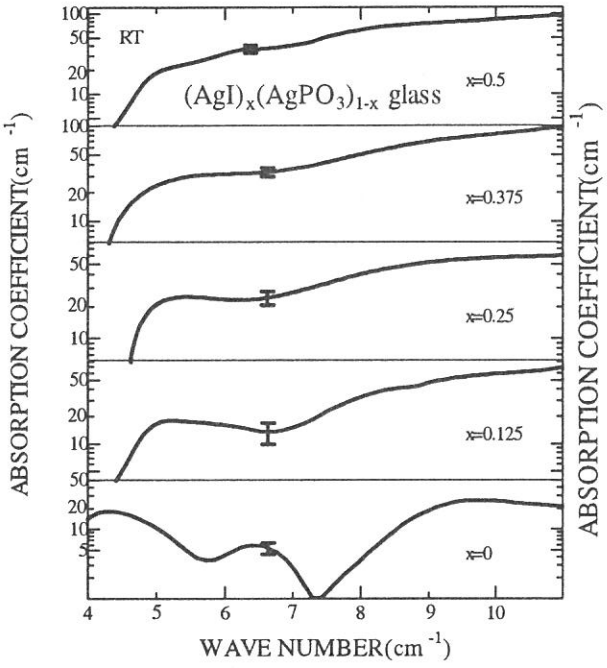

Fig. 1. Spectral change in millimeter wave region of $(AgI)_x(AgPO_3)_{1-x}$ to AgI composition.

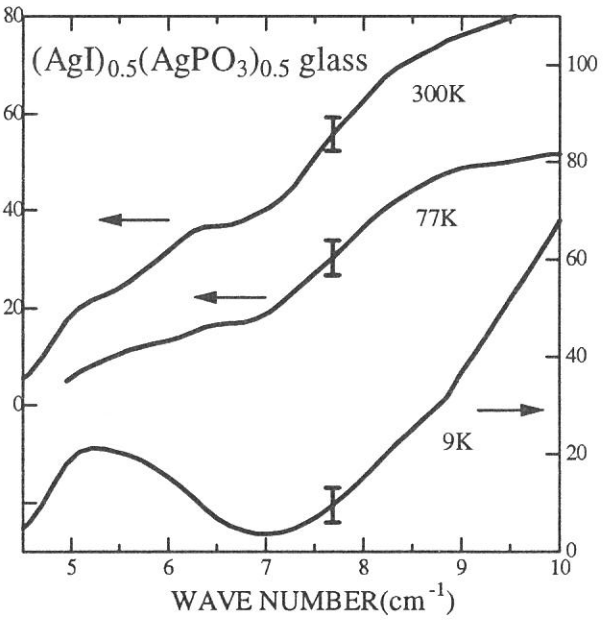

Fig. 2. Spectral change in millimeter wave region of $(AgI)_x(AgPO_3)_{1-x}$ to temperature.

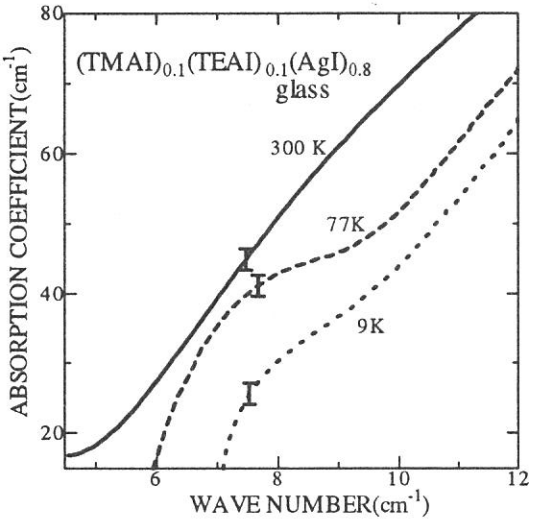

Fig. 3. Spectral change in millimeter wave region of $(TMAI)_{0.1}(TEAI)_{0.1}(AgI)_{0.8}$ to temperature.

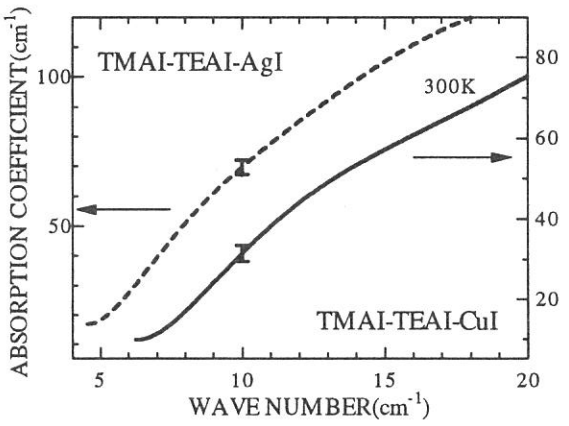

Fig. 4. Spectral change between $(TMAI)_{0.1}(TEAI)_{0.1}(AgI)_{0.8}$ and $(TMAI)_{0.15}(TEAI)_{0.1}(CuI)_{0.75}$ in millimeter wave region.

(BL6A1)

Effect of Photo-excited Carriers on Infrared Reflectivity in InGaN Single Quantum Well Structures

Takahiro DEGUCHI, Takayuki SOTA, Shigefusa CHICHIBU[A],
Takashi AZUHATA[B], Shingo ONO[B], Shinji IZUMIDA[B], Hideyuki OHTAKE[B],
Nobuhiko SARUKURA[B], and Shuji NAKAMURA[C]

Department of Electrical, Electronics, and Computer Engineering, Waseda University, 3-4-1 Ohkubo, Shinjuku, Tokyo 169-8555, Japan
[A]Faculty of Science and Technology, Science University of Tokyo, 2641 Yamazaki, Noda, Chiba 278-8510, Japan
[B]Laser Research Center, Institute for Molecular Science, 38 Nishigonaka, Myodaiji, Okazaki, Aichi 444-8585, Japan
[C]Department of Research and Development, Nichia Chemical Industries Ltd., 491 Oka, Kaminaka, Anan, Tokushima 774-8601, Japan

Recent development of growth techniques for GaN and related nitrides has realized the commercial production of superbright blue and green light emitting diodes based on InGaN single quantum wells, [1] and the room temperature cw operation of InGaN multi-quantum-well laser diodes in the purplish-blue energy region. [2] The life time of laser diodes is more than 10,000 hours. [3] Although it has been reported the excitons localized into certain potential minima caused by the fluctuation of In mole fraction in InGaN contribute to the spontaneous emission in the purplish-blue, blue, and green light emitting diodes, [4,5] the lasing mechanism in the purplish-blue laser diodes is not clear at present. It is important to study the effect of carriers created in InGaN quantum wells.

We investigated the reflectivity change of InGaN single quantum well structures in the infrared region, which would be caused by photo-excited carriers. The samples used here were prepared by the two-flow metalorganic chemical vapor deposition method [6] on the c-plane of sapphire substrates with low-temperature-grown GaN buffer layers. The exact sample structure was p-GaN(0.5 μm)/p-AlGaN(100 nm)/$In_xGa_{1-x}N$(3 nm)/n-GaN(4 μm)/GaN buffer(30 nm)/sapphire substrate. The values of x were 0.3 and 0.45, which correspond to blue and green light emitting diodes, respectively. Infrared reflectivity spectra were measured using BL6A1 at room temperature and 80 K. As light sources to create carriers, 325.0 nm line of a He-Cd laser and 476.5, 488.0, and 514.5 nm lines of an Ar^+ laser were used. Maximum powers for respective lines were 0.02, 1.2, 3.1, and 1.2 W.

The infrared reflectivity spectra measured without laser irradiation show intrinsic phonon structures from GaN layers. The signal from InGaN layer was too thin to be observed. When the laser was irradiated, unfortunately, no change were observed. Some of possible reasons are that the laser powers were too low to cause observable reflectivity changes and that the absorption coefficient of the samples in the visible wavelength region was too small to excite carriers effectively.

The authors are grateful to Dr. S. Kimura for his experimental support, and also to Profs. H. Nakanishi and K. Suzuki and Monsieur T. Gejo for their continuous encouragement.

[1] S. Nakamura, M. Senoh, N. Iwasa, S. Nagahama, T. Yamada, and T. Mukai, Jpn. J. Appl. Phys. 2 **34**, L1332(1995).
[2] S. Nakamura, M. Senoh, S. Nagahama, N. Iwasa, T. Yamada, T. Matsushita, Y. Sugimoto, and H. Kiyoku, Appl. Phys. Lett. **69**, 4056(1996); S. Nakamura, M. Senoh, S. Nagahama, N. Iwasa, T. Yamada, T. Matsushita, Y. Sugimoto, and H. Kiyoku, Jpn. J. Appl. Phys. 2 **36**, L1059(1997).
[3] S. Nakamura, M. Senoh, S. Nagahama, N. Iwasa, T. Yamada, T. Matsushita, H. Kiyoku, Y. Sugimoto, T. Kozaki, H. Umemoto, M. Sano, and K. Chocho, the 2nd International Conference on Nitride Semiconductors, Tokushima, Japan, 1997.
[4] S. Chichibu, T. Azuhata, T. Sota, and S. Nakamura, Appl. Phys. Lett. **69**, 4188(1996).
[5] Y. Narukawa, Y. Kawakami, Sz. Fujita, Sg. Fujita, and S. Nakamura, Phys. Rev. B **55**, R1938(1997).
[6] S. Nakamura, Y. Harada, and M. Senoh, Appl. Phys. Lett. **58**, 2021(1991).

(BL6A1)

Complex refractive index measurement of various semiconductors in the far-infrared region

Hideyuki OHTAKE, Takashi AZUHATA, Shingo ONO[A], Takeyo TSUKAMOTO[A],
Zhenlin LIU, Shinji IZUMIDA, Takahiro DEGUCHI[B], Takayuki SOTA[B],
and Nobuhiko SARUKURA

Laser Research Center for Molecular Science,
Institute for Molecular Science (IMS), Myodaiji, Okazaki 444-8585,
[A]Faculity of Science, Department of Applied Physics, Science University of Tokyo,
1-3, Kagurazaka, Shinjuku, Tokyo 162-0825
[B]Department of Electrical, Electronics and Computer Engineering, Waseda University,
3-4-1, Ohkubo, Shinjuku, Tokyo 169-8555

The devices and applications to ultrafast opt-electronics of THz radiation or far infrared light from various devices have been intensively studied. [1,2] For the design of various devices in the THz-radiation region, precise information of material properties is strongly required. In particular, precise index refractive and optically and electrically induced index change of typical semiconductors are matter of interest. However, there were few reliable reports of such complex index measurement in the THz-radiation region. Development of complex index measurement system in the far infrared region will open up possibilities for the material research of new high-speed opt-electric devices utilizing THz radiation. There are a few reports[4] that describe how photoexcited carriers in semiconductors change complex-index in the far-infrared region. These works [4,5] have led to not only picosecond time resolved index change measurement [6] but also THz-tomography [7] and THz-ranging[8].

We measured reflectivity change of GaAs and InAs in the THz-region at room and liquid nitrogen temperature by irradiating an Ar ion laser (e.g. 488 nm to 514.5 nm) and HeCd laser light. Infrared reflectivity spectra were obtained by using BL6A1. We investigated exciting wavelength dependence of infrared reflectivity. At room temperature, we did not observe any changes among them. It means that the number of photoexcited carriers in GaAs and InAs do not have any excitation wavelength dependence, because their carrier densities are almost the same due to penetration depths. At liquid nitrogen temperature, unfortunately, we can not obtain reasonable data. Some possible reasons are that the laser power was so high that local heating effect took place and that As component vaporized by heat. To overcome these problems, we should make thin semiconductor films or well defined clear semiconductor surfaces preparing in ultra high vacuum.

The authors are grateful to Dr. S. Kimura for his helpful experimental support, and also to Dr. T. Gejo for his strong encouragement.

References

[1] D. H. Auston, Appl. Phys. Lett. 43, 713 (1983).
[2] P. C. M. Planken, M. C. Nuss, W. H. Knox, D. A. B. Miller, and K. W. Goossen, Appl. Phys. Lett. 61, 2009 (1992).
[3] P. B. Corkum and D. Keith, J. Opt. Soc. Am. B2, 1873 (1985).
[4] H. Ohtake, Z. Liu, S. Izumida, T. Yamanaka, N. Sarukura, K. Koyama, and T. Suemoto, CLEO Pacific Rim '97, paper P50.
[5] S. L. Chuang, S. Schmitt-Rink, B. I. Greene, P. N. Saeta, and A. F. J. Levi, Phys. Rev. Lett. 68, 102 (1992).
[6] B. I. Greene, J. F. Federici, D. R. Dykaar, A. F. J. Levi, and L. Pfeiffer,Opt. Lett. 16, 48 (1991).
[7] D. M. Mittelman, S. Hunsche, L. Boivin, and M. C. Nuss, Opt. Lett. 22, 904 (1997).
[8] R. A. Cheville, R. W. McGowan, and D. Grischkowsky, OSA TOPS Vol. 13 Ultrafast Electronics and Optoelectronics, 222-227 (1997).

(BL8A)

Fourier-Transform Spectroscopy and Photon Echo in Vacuum Ultraviolet Region

S. Asaka[A] and H. Nakatsuka[B]

[A]*Equipment Development Center, Institute for Molecular Science, Okazaki 444-8585*
[B]*Institute of Applied Physics, University of Tsukuba, Tsukuba 305-0004*

We have performed accumulated photon echo experiments by using synchrotron radiation (SR) in near vacuum ultraviolet region.

Photon echo experiments generally give us information of optical T_2, or the phase relaxation time of the sample resonance lines. Among many types of photon echoes, the accumulated photon echo has excellent features in that it gives a signal magnitude and a signal-to-noise ratio much larger than other types of photon echoes by using repetitively pulsed or quasi continuous excitation source. Furthermore, the time resolution in measuring T_2 is simply determined by the correlation time (i.e. the inverse of spectral width) of the source so that a femtosecond resolution can be easily achieved by using a wide-spectral-band source.

A periodic but static change of light intensity is formed over spectral axis if time-delayed two light beams are present. This structure is copied into the inhomogeneously broadened resonance line of the sample, thus forming a "population grating". The accumulated photon echo is based on the diffraction of the excitation light by this population grating. If the electrons of the sample stay a long time at some bottleneck state other than the ground state after resonant transition, the population grating in the ground state accumulates over the bottleneck lifetime, resulting in a large echo signal.

The SR is useful as an excitation source for accumulated photon echo experiments because it is quasi continuous and it has a wide spectral band especially in short wavelength region, where other light sources cannot give sufficient light intensity for echo measurements. The echo time resolution is, for example, 40 fs if we cut out a spectral portion of SR by a width of 0.1 eV.

Before the present study, accumulated photon echo experiments by using SR have been done at UVSOR for several organic molecules embedded in polymers as sample materials[1]. Excitation wavelengths were around 300 nm in these measurements. In the present study we extended excitation wavelength to about 200 nm and applied to inorganic crystals.

The experiment was done at BL8A of UVSOR. The experimental set-up was almost the same as in reference 1, except that the beam splitter was modified and the dispersion compensator was removed. The beam splitter used here consisted of two identical half mirrors. They were made by dividing equally a single half mirror and then mounted back-to-back so that their active surfaces are in one plane. The center of the excitation wavelength was selected by selecting appropriate combination of coatings of the beam steering mirrors and the beam splitter.

We tried echo measurement for two kinds of alkali-halide crystals as sample materials: RbI, KBr. The sample temperature was about 5 K. We tuned the excitation wavelength at the foot of the exciton absorption, which is 220 nm for RbI and 230 nm for KBr, and about half of the excitation energy was absorbed. The correlation time of the excitation was about 30 fs. We also tried a mixed crystal of RbI and KI at wavelength of 230 nm expecting a broad inhomogeneous distribution.

For the samples we tried we have not obtained any detectable echo signal. We do not know about he existence of bottleneck states in the present samples, and even less about their life times. Since fluorescence quantum yields are not so small in these samples, we can conclude at least that the bottleneck states do not effectively work in the present samples if any.

Reference

[1] H. Itoh *et al.*, UVSOR Activity Report 1996, 228(1997).

[BL-8A]

Temperature-dependent dephasing characteristics of Phenol doped in hosts and long-term phase stability of interferometer

H. Itoh[1], S. Nakanishi[1], T.Fuji[2], T.Kashiwagi[2], M.Furuichi[2], N. Tsurumachi[2], H. Nakatsuka[2], S. Asaka[3] and M. Kamada[4]

[1]*Department of Advanced Materials Science, Kagawa University, Takamatsu 760-8526*
[2]*Institute of Applied Physics, University of Tsukuba, Tsukuba 305-8573*
[3]*Equipment Development Center, Institute for Molecular Science, Okazaki 444-8585*
[4]*UVSOR, Institute for Molecular Science, Okazaki 444-8585*

We have applied synchrotron radiation (SR) to investigate FM-modulated incoherent accumulated photon echo signals of simple aromatic molecules doped in Polyvinyl Alcohol(PVA) and Polymethel Methacryrate in ultraviolet wavelength region. In this paper, we show two experimental results. One is precise temperature dependent phase relaxation of Phenol doped in PVA, relating to the relaxation way of Aniline doped in same host. On the other hand, signal intensities have extremely reduced since the latter half of last year. Then we check the reliability of our experimental apparatus to make its reason clear. The experiment was performed at BL-8A. The output beam from the quartz window of the BL-8A was filtered by the bandpass filter with the center wavelength of 289 nm, the bandwidth of about 12 nm and the maximum transmission rate of about 18%.

The temporal width of field autocorrelation was measured as 25 fs, corresponding to the bandpass filter used. In that time, to compensate the dispersion of the system, we inserted a quartz plate with 3 mm thick tilting by 34 degree of angle to the SR beam path between the PBS and one of the corner cube prisms. Figure 1 shows temperature dependent dephasing characteristics of Phenol doped in PVA as a function of inverse of temperature. The dephasing time of Phenol is longer as orders than that of the Aniline at the temperature around 4 K[1]. This dephasing characteristics would be originated from the interaction between the host and the guest molecules, such as TLS transition of host molecules, i.e. non-photochemical hole burning. Because this dephasing characteristic is inferred from the results, which have been investigated in many molecules doped in hosts in visible wavelength region. It is thought from this result that the dephasing mechanism for the Aniline/PVA would be slightly different from that of the Phenol/PVA system. The short dephasing time would reflect that the potential minimum of each ground and first excited state are shifted each other in normal coordinate, so that 0-0 transition of electro-vibronic states could not satisfy the Frank-Condon principle. Resulting from fast energy relaxation in excited state(internal conversion), phase coherence between ground and excited state is not maintained so long period.

Next we check long-term phase stability of the Michelson interferometer we used. Output SR beam from the interferometer was continuously detected by p-i-n photodiode when the interferometer's arm length was fixed at a position. At the same time, interference signal of a He-Ne laser was also detected by another p-i-n photodiode using same interferometer in the same geometry as the SR beam for investigating the stability of the Michelson interferometer alone. we show both intensities of interference lights as a function of time in Fig.2, solid and dotted line correspond to the signals by the SR light and He-Ne laser, respectively. The interference intensity of the SR drastically changed at random in short period according to the phase hopping from 0 to 180 degree. On the other hand, the intensity by the He-Ne laser did not change so drastically that the main instability factor is originated from spatial hopping of SR beam. This hopping of the SR beam erases holes burned in the sample. Since echo intensities are proportional to the depth of burned phase grating, we can not get fully accumulated signals. It is needed to keep, at least, this phase variation small in one round of the detecting period. It is thought that this hopping is caused from bad vacuum condition in beam line.

Reference

[1] H.Itoh et al. UVSOR Activity Report 1996.

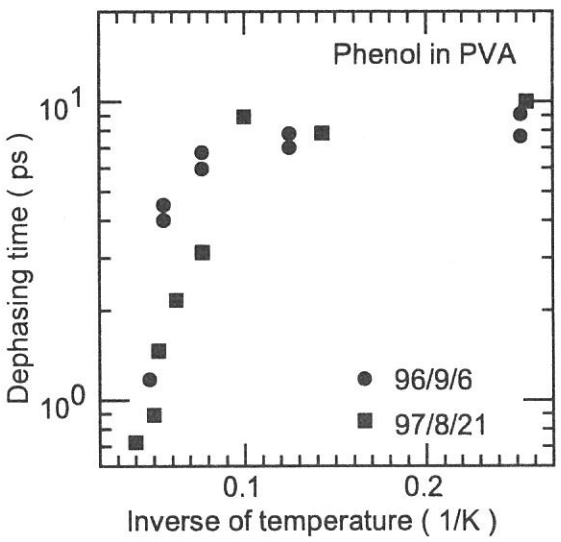

Fig. 1: Accumulated photon echo decay of Phenol doped in PVA as a function of inverse of temperature from 4.3 to 20K. The excitation wavelength is 289 nm with the bandwidth of about 12 nm. We show two results, circle denotes result of Sept.'96 and square corresponds to that of Aug.'97.

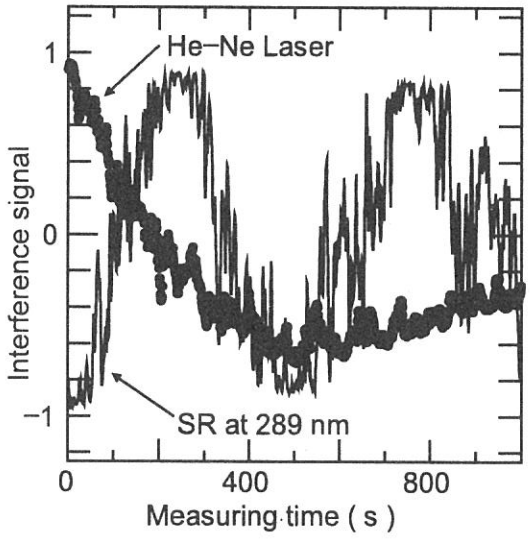

Fig. 2: Stability of interference signal with the path length in the Michelson interferometer fixed. Circle denotes the case of He-Ne laser and solid line corresponds to that of SR beam at 289 nm.

(BL1B & BL6A1)

Anisotropic reflectivity spectra of *R*PtAs (*R* = Ce, La)

S. Kimura, K.G. Nath[1], Y. Haruyama, T. Kinoshita, S. Yoshii[2] and M. Kasaya[2]

UVSOR Facility, Institute for Molecular Science, Okazaki 444-8585
[1]Department of Structural Molecular Science, The Graduate University for Advanced Studies, Okazaki 444-8585
[2]Department of Physics, Tohoku University, Aoba-ku, Sendai 980-8578

The crystal structure of CePtAs is hexagonal YPtAs-type ($P6_3/mmc$). The transport property along *c*-axis ($I \parallel c$) is semiconducting and that perpendicular to *c*-axis ($I \perp c$) is metallic. The Hall coefficient of $I \parallel c$ and $H \perp c$ is negative and small and that of $I \perp c$ and $H \parallel c$ is positive and large [1]. Here, *I* indicates current direction and *H* applied magnetic field. Therefore not only the shape of the Fermi surface and also the electronic structure attracts attention. In this study, we measured reflectivity spectra of CePtAs and of the reference material LaPtAs for the investigation of the electronic structure that makes the anisotropy of the transport and the mobility. The x-ray photoemission spectra (XPS) of valence band have also measured for the investigation of the occupied state.

The reflectivity spectra was measured at two beam lines of 1B and 6A1 for the measurements of visible - VUV (2 - 30 eV) and infrared (0.01 - 2 eV) regions, respectively. Obtained spectra of *R*PtAs are shown in Fig. 1. Anisotropy of reflectivity spectra is observed. XPS was measured by using a commercial system (FISONS Instruments, ESCALAB 220i-XL) and Mg-Kα line.

In figure 2, optical conductivity (OC) spectra of CePtAs with $E \perp c$ and $E \parallel c$ are shown. The OC spectra were determined from a Kramers-Kronig analysis of the reflectivity spectra. Optical anisotropy can be clearly observed in the whole photon energy region. Particularly, in the low energy part, the spectrum with $E \perp c$ shows metallic one because Drude type OC appears. On the other hand, the spectrum with $E \parallel c$ seems to be of a semiconductor. The result is consistent with the anisotropy of the electric resistivity.

Since the DC conductivity with $I \perp c$ at 300 K is $3.6\times10^3\ \Omega^{-1}\mathrm{cm}^{-1}$, the Drude curve of the OC with $E \perp c$ is considered to connect to DC smoothly.

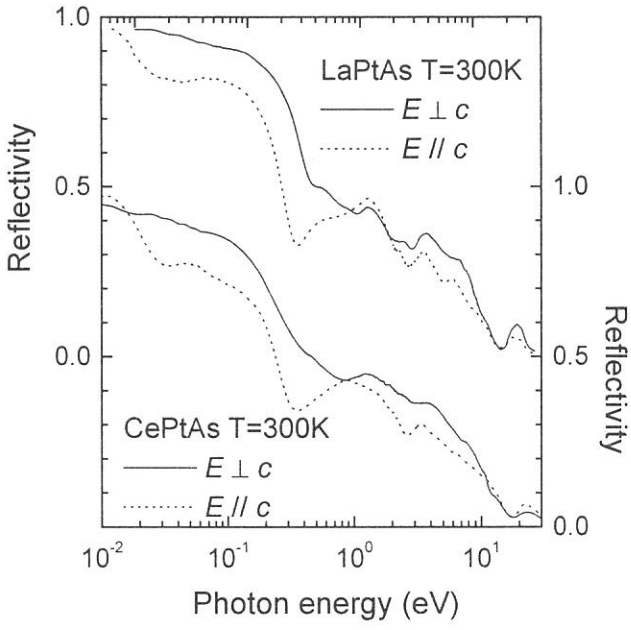

Fig. 1. Anisotropic reflectivity spectra of *R*PtAs (*R* = La, Ce) in the energy range of 0.01 - 30 eV.

And also, the OC with E // c smoothly connected to the DC conductivity with I // c because the DC conductivity is about 0.37×10^3 $\Omega^{-1}cm^{-1}$. The energies of the plasma edges with $E \perp c$ and with E // c are about 0.3 eV and about 0.03eV, respectively. Generally square of energy of plasma edge is proportional to the effective carrier density ($N\times m_0/m^*$, where N is the carrier density, m_0 the static mass of an electron and m^* the effective mass). Therefore the effective carrier density with $E \perp c$ is hundred times higher than that with E // c. Therefore the mobility (effective mass) with $E \perp c$ is hundred times larger than that with E // c. This is an origin of the anisotropy of physical properties of CePtAs.

Higher energy part of OC spectra and XPS of CePtAs are shown in Fig. 3. The binding energy of XPS is shifted by 0.5 eV from the photon energy of OC spectra. Double peak structure at 4 and 5 eV of XPS mainly originates from Pt 5*d* state. Therefore the shape of OC around 4 eV is due to the charge transfer excitation of Pt $5d \rightarrow$ Ce $4f$. The shape of the reflectivity spectra of LaPtAs around 4 eV is sharper than that of CePtAs in Fig. 1. Since the multiplet structure of $4f^2$ final state of Ce^{3+} after photo absorption is wider than that of $4f^1$ final state of La^{3+}, the difference appears in the reflectivity spectra.

---

[1] S. Yoshii et al., Proc. Int. Conf. Magn. 97. (to appear in J. Magn. Magn. Mater.)

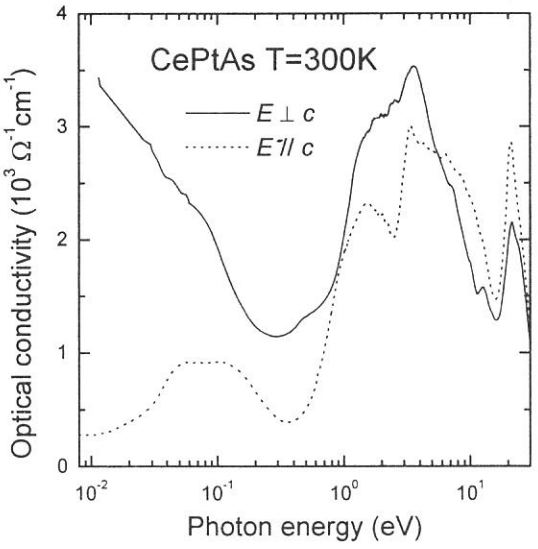

Fig. 2. Anisotropic optical conductivity of CePtAs. The spectrum with $E \perp c$ shows metallic one but that with E // c looks like an insulator.

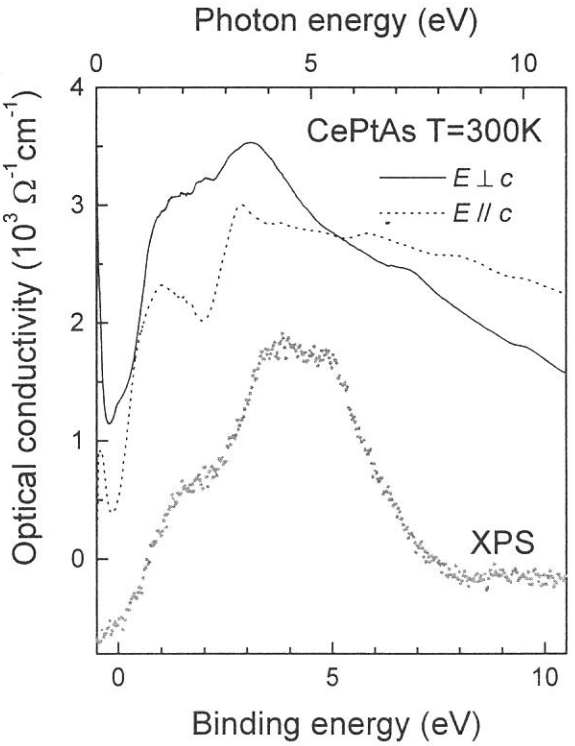

Fig. 3. Comparison of optical conductivity spectra of CePtAs with the valence band photoemission spectrum. The binding energy of photoemission spectrum shifted by 0.5 eV from the photon energy of optical conductivity spectra.

(BL-1B)

Determination of Threshold Energy of Color Center Formation in Anthracene Single Crystal

Iwao Shimoyama and [1] Kazumichi Nakagawa

Graduate School of Sci. and Tech., Kobe University, Rokkohdai, Nada-Ku, Kobe 657, Japan
[1]Faculty of Human Development, Kobe University, Tsurukabuto, Nada-Ku, Kobe657, Japan

Anthracene single crystal is a standard for radiation scintillator. Scintillation efficiency is known to be degraded by radiation induced color centers. However the detail of radiation damage of anthracene has not known yet. To clarify the lowest excitation state form which color centers are produced, we measured quenching of fluorescence of S_1 exciton as a function of irradiation time and determine the threshold energy of color center formation.

Experiments were performed at BL-1B. Anthracene crystals were grown by sublimation method from scintillation grade anthracene powder of Kantou Kagaku Company after purification by zone melting method. Samples were placed in vacuum chamber (10^{-8}Torr) and cooled at 200K. We used fluorescence quenching technique (FQT). In FQT, at first, fluorescence intensity $I_F(0)$ induced by 365nm light and intensity M of 365nm light is measured before VUV irradiation. The 365nm light is known to produce S_1 exciton and not to produce color centers. Fluctuation in the value of $I_F(0)/M$ was confirmed to be less than 1% during 110 minutes (see figure 1). Next, the sample were irradiated by VUV with various energies ($h\nu$ = 9.0, 9.5, 10, 10.8, 13.7 and 17.7 eV) during T seconds. After stopping VUV irradiation, we measured $I_F(T)/M$ as a function of T. We estimated irradiation photon numbers N_λ ($= I_\lambda T$) by measuring incident photon numbers I_λ per second. And we obtained S_1 quenching rate $I_F(N_\lambda)/I_F(0)$ as a function of N_λ. Figure 2 shows $I_F(N_\lambda)/I_F(0)$ plots for irradiation of VUV with the energies 9.0(●), 9.5(△) and 10eV(■). In the case of 9.0, $I_F(N_\lambda)/I_F(0)$ shows no quenching. Therefore we concluded that color center isn't formed at this photon energy. In the case of 9.5 eV, $I_F(N_\lambda)/I_F(0)$ shows just small values near $N_\lambda = 4\sim5\times10^{14}$ [photons]. However the data doesn't show systematically decrease, therefore we couldn't conclude whether color center is formed or not at this photon energy. While, in the case of 10eV, $I_F(N_\lambda)/I_F(0)$ decrease apparently. In other cases that photon energy are larger than 10eV, we also obtained apparent decrease of $I_F(N_\lambda)/I_F(0)$. Therefore we concluded that the threshold energy of color center formation is about 9.5eV.

It is considered that C-H bond dissociation is important reaction to form color center. For anthracene vapor, C-H bond assignment has reported only in the energy region 5～8.5 eV. In an

assignment of benzene vapor reported by Koch *et al.* [1], the highest C-H bond is assigned to 11eV, we couldn't also find C-H bond near 9.5eV. From our result, the transition energy which concern C-H bond should be near 9.5 eV. This result seems to indicate the possibility of new theory for molecular orbital calculation.

[1] E. E. Koch and A. Otto, Chem. Phys. Lett., 21,501(1973)

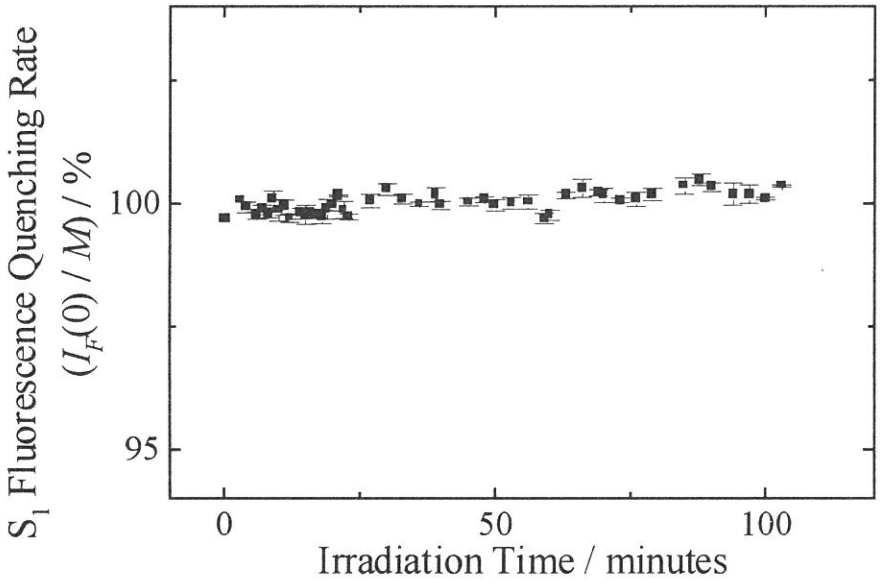

Figure 1. Stability of $I_F(0) / M$

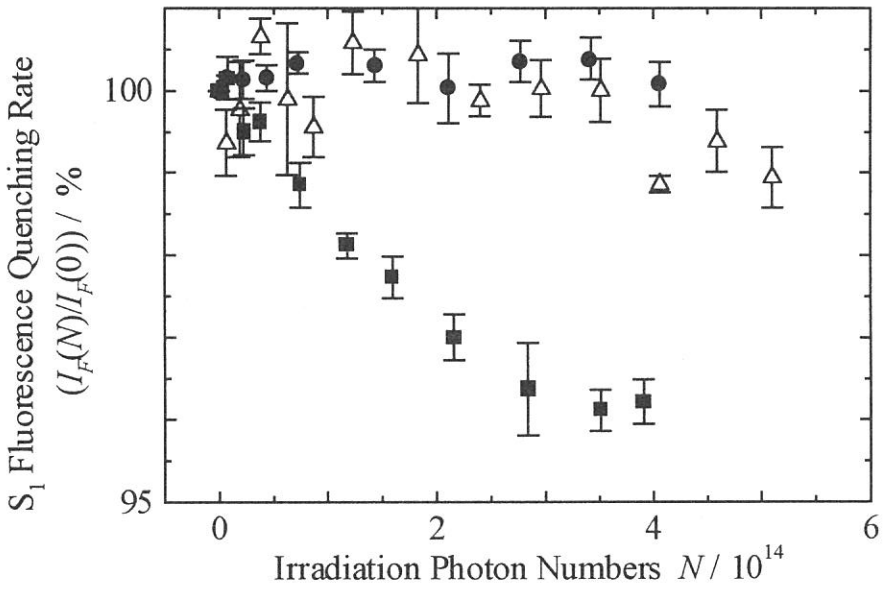

Figure 2. S1 quenching rate $I_F(T) / I_F(0)$

$h\nu$ = ● : 9.0, △ : 9.5, ■ : 10eV

(BL1B)

VUV~UV absorption spectra of thermally poled synthetic silica glass

Akihiro Kameyama, Atsushi Yokotani and Kou Kurosawa

Department of E&E Engineering, Miyazaki University, Miyazaki 889-2155

Silica glass has become much more important and also attractive for photonics engineering, because a new function of a permanent strong second-order optical nonlinearity has been observed in poled silica glass in addition to high transparency and high band-gap energy. Although the optical nonlinearity is as high as 1 pm/V in thermally poled fused silica glass by Myers et al.[1], the optical nonlinearity in thermally poled synthetic silica was about one order of magnitude smaller than in the fused silica one. We have reported[2] that the large second order nonlinearity of 0.2pm/V in high-purity synthetic silica glass exposed to X-ray before the poling procedures. Furthermore we have observed that the large second order nonlinearity in high-purity synthetic silica glass with KrF excimer laser exposure before the poling procedures. The radiation-induced defects seem to be important for the generation of second order nonlinearity.

In order to identify the defects relevant to the generation, we observed VUV absorption spectra for the poled synthetic silica glass with KrF excimer laser exposure before the poling procedures.

We used samples of synthetic silica glass supplied from Nippon Silica Glass. The samples have a plate-like shape with 20 mm in diameter and 1.5 mm in thickness and the surface were finished to optical quality. The samples were exposed to 248-nm pulses of 10000 shots of 50 mJ/cm^2 from a KrF excimer laser. The poling procedures were as follows: A sample plate was sandwiched with two electrodes maintained at a high voltage of 4.5 kV, heated up to 260°C at the rate of 10°C/min, held for 20 min, and then cooled down to room temperature at the rate of 10°C/min before removing the voltage.

In Fig. 1 are plotted SHG intensities as function of incident angle of Nd:YAG laser beam observed in the poled synthetic silica with and without the laser irradiation. The SHG intensity was observed only in the exposed sample, but not in the non-exposed sample.

We observed absorption spectra with the use of BL1B beam line at UVSOR. In Fig. 2 are shown transmittance spectra taken from samples with and without the KrF excimer laser exposure. The laser radiation apparently decreases a 6.3-eV absorption peak which is assigned to E'center, and further increases significantly a 4.7-eV absorption peak which is probably to be NBOHC (≡Si-O*) or ≡Si-O$^-$.The photon energy of 5.0 eV is very close to the center energy of absorption bands. Such speculation agrees with the result the X-ray irradiation experiments[2], namely ≡Si-O* or ≡Si-O$^-$ induced in high purity silica glass and to be close-related with the nonlinearity creation.

In summary, we investigated a VUV absorption spectra of the poled synthetic silica glass with KrF excimer laser exposure before the poling procedures. We conclude that the optical nonlinearity include defects related with Si-O at least in pure silica glasses.

Reference
1) R.A.Myers, N.Mukherjee, and S.R.J. Brueck, Opt. Lett. 16, 1732 (1991).
2) A.Kameyama, E.Muroi, A.Yokotani, K.Kurosawa and P.Herman,
J.Opt.Soc.Am. B, 14, 1088 (1997).

Fig. 1 The SHG intensities as function of incident angle of YAG laser beam in the thermally poled silica glass with (●) and without (■) KrF excimer laser exposure.

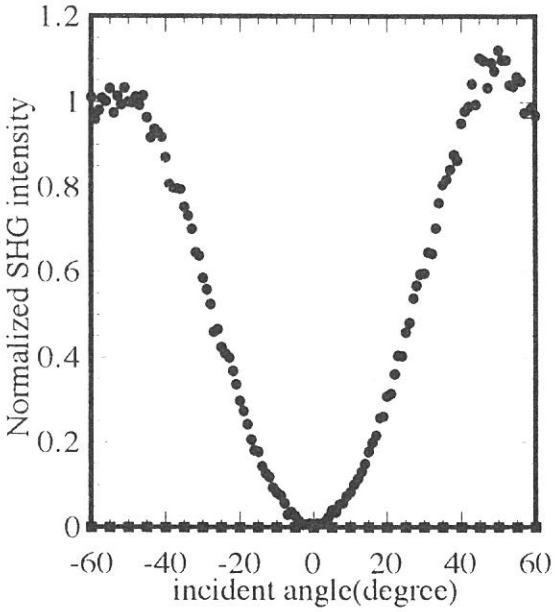

Fig. 2 Transmittance spectra taken from silica glass with (●) and without (■) KrF excimer laser exposure.

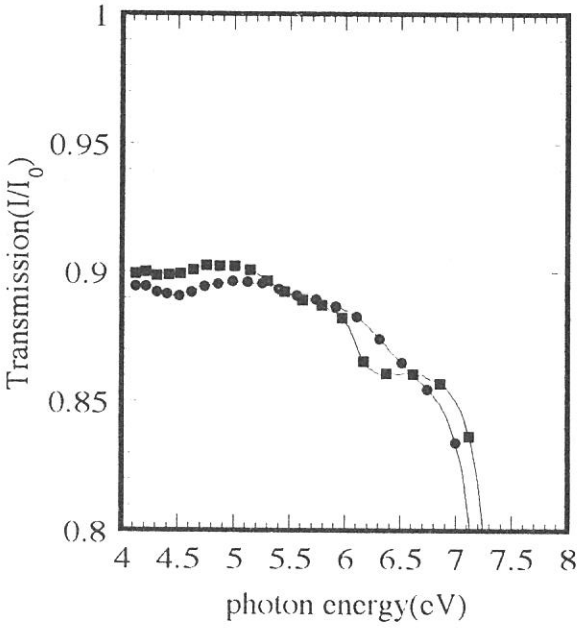

(BL1B)

Concentration of neutral oxygen vacancies in buried oxide formed by implantation of oxygen

K. S. Seol, T. Futami, and Y. Ohki

Department of Electrical, Electronics, and Computer engineering, Waseda University, 3-4-1 Ohkubo, Shinjuku-ku, Tokyo 169

Buried oxide layers in the silicon-on-insulator structure separated by implanted oxygens (SIMOX) have become widely used for a high speed metal oxide semiconductor (MOS), a radiation-hardened complementary MOS (CMOS), and other smart devices.[1,2] Many researches have been done recently on the nature of the buried oxide[3], since it plays an important role in determining the device properties. It has been considered that the buried oxide is far more oxygen-deficient than the conventional thermal oxide,[3] and that this deficiency is believed as one reason of unusual behavior of buried oxide such as enhanced electrical conductivity, charge buildup, and sensitivity to defect generation.[3]

It has been known that buried oxide contains neutral oxygen vacancies ($O_3{\equiv}Si\text{-}Si{\equiv}O_3$) which are typical in oxygen-deficient amorphous SiO_2.[4] In this study, the vacancy concentration in buried oxide is estimated by measuring the PL intensity.

In any material, the concentration (N) of photo-absorbing defects can be easily estimated from the following equation by measuring the optical absorbance (A) if their absorption cross section (σ) and the sample thickness (L) are known:

$$A = L\alpha = L\sigma N , \qquad (1)$$

where α is the optical absorption coefficient. However, in the case of the present buried oxide sample, it is impossible to measure A because of the opaqueness of the Si substrate. One possible method to estimate the concentration of oxygen vacancies is to measure the PL emitted from the vacancies. It is known that the 4.3-4.4 eV PL is the luminescence from the vacancies[5] and that its two excitation bands at 5.0 and 7.6 eV are due to absorptions by '*unrelaxed*' and '*relaxed*' oxygen vacancies, respectively.[6] Here, the unrelaxed vacancy has a larger bond length between the two silicons and the relaxed vacancy has a shorter one.[6] The PL intensity (I_{PL}) normalized by the excitation photon intensity (I_{EXC}) is given by,[5]

$$I_{PL} / I_{EXC} = \eta \cdot (1 - \exp(-\alpha L)) . \qquad (2)$$

Here, η is the quantum efficiency of the PL. It is reasonable to assume that the true quantum efficiency for a specific PL by a specific PL excitation band, namely the PL photon number induced by a certain number of incident photons, is independent of the sample whether it is a thick silica glass or a thin buried oxide layer. Of course, such a true efficiency cannot be measured in actual experiments. First, since I_{EXC} was measured with a photomultiplier coated with sodium salicylate whose fluorescent quantum yield is constant between 4 and 20 eV,[7] I_{EXC} in the present research represents only a relative number of the incident photons. Secondly, although all the experimental conditions such as the configuration of photo-detecting systems were exactly the same for the two samples, the two samples differ in the point that the buried oxide layer has a Si substrate at its back. Some of the incident photons, which should pass through the silica glass, could be reflected by the Si substrate. Reflectance at the interface between crystalline Si and vacuum is reported to be 60-70 % at 4.3, 5.0, and 7.6 eV.[8] The reflectance at the present SiO_2/Si interface should be somewhat smaller, while the reflectance at SiO_2/vacuum interface could be assumed zero. The reflectance at SiO_2/Si increases not only the effective incident photons but also the effective PL intensity. Therefore, if the reflectance at the SiO_2/Si interface is assumed to be 60 %, the effective value of η for the buried oxide sample becomes $(1.6)^2$ times as high as that for the silica glass.

PL intensities was first measured for an oxygen-deficient silica glass, the α value of which had been calculated by measuring the absorbance. Then, under the same condition, PL intensities were measured on the buried oxide layer. The PL measurement was carried out at 13 K using synchrotron radiation at the Institute for Molecular Science, Okazaki, Japan. The investigated silica glass was manufactured by the soot remelting method and its thickness is 0.7 mm. The SIMOX sample was fabricated by implanting O^+ ions up to a dose of $3.7{\times}10^{17}$ cm^{-2} with an energy of 180 keV into a Si substrate, and subsequent annealing in an Ar atmosphere followed by oxidation at 1350 °C for several hours. The thickness of the buried oxide layer is about 130 nm. For the PL measurement, the thermal oxide and the Si layer over the buried oxide were respectively removed by soaking the sample in a HF solution and subsequently in a KOH solution.

Figure 1 shows the PL spectra from the buried oxide layer excited by 5.0 and 7.6 eV photons. The PL band with a peak at 4.3-4.4 eV appears regardless of the excitation photon energy. The PL intensity shown in Fig. 1 was calibrated by taking the intensity variation of the excitation photons into consideration. Quite similar PL spectra were obtained for the glass sample. The measured apparent values of I_{PL}/I_{EXC} excited at the 5.0 eV excitation band and at the 7.6 eV band are respectively 2.0×10^{-4} and 1.1×10^{-4} for the glass sample, while they are respectively 2.6×10^{-5} and 4.8×10^{-5} for the buried oxide layer. The values of the absorption coefficient α of the glass sample are calculated to be 7.0×10^{-3} cm^{-1} and 24 cm^{-1} at 5.0 eV and 7.6 eV, respectively, by measuring the absorbance A at each photon energy. Then, by substituting the values of I_{PL}/I_{EXC}, α, and L into Eq. (2), the value of η for the silica glass measured with the present system is calculated to be 4.0×10^{-1} and 1.4×10^{-4} for the 5.0 eV photons and the 7.6 eV photons, respectively. As mentioned above, the effective values of η for the buried oxide layer are considered to be $(1.6)^2$ times as high as these values. If so, using the values of I_{PL}/I_{EXC} and L for the buried oxide layer, α can be obtained as 2.0 for the 5.0 eV absorption band and 1.1×10^{4} for the 7.6 eV band. Since σ is known to be 2×10^{-17} cm^2 and 8×10^{-17} cm^2 for the 5.0 eV and the 7.6 eV bands, respectively,[6] the concentration N of the photo-absorbing defects in the present buried oxide layer is calculated to be 1.0×10^{17} cm^{-3} for the unrelaxed neutral oxygen vacancies and 1.4×10^{20} cm^{-3} for the relaxed ones. The concentrations in the glass sample are similarly calculated to be 3.5×10^{14} cm^{-3} and 3.0×10^{17} cm^{-3} for the unrelaxed and the relaxed vacancies, respectively. It can be concluded that the vacancy concentrations in the buried oxide layer are about 300 - 400 times as high as those in the glass sample.

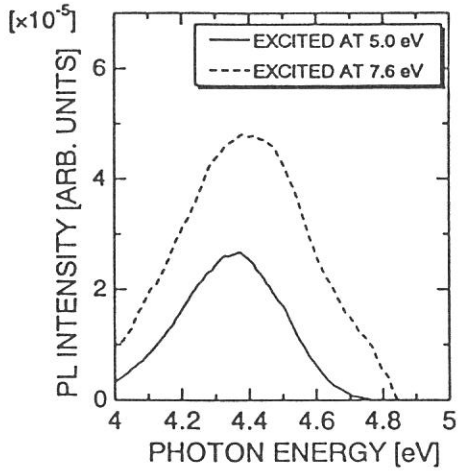

FIG. 1. PL spectra excited by 5.0 and 7.6 eV photons measured for the buried oxide layer at 13K. The PL intensity is calibrated by the intensity of excitation photons.

References

1. Y. Omura and K. Izumi, in *Proceedings of the 4th International Symposium on Silicon-on-Insulator Technology and Devices*, edited by D.N. Schmidt, PV 90-6 (The Electrochemical Society Proceedings Series, Pennington, NJ, 1990), p. 509.
2. T. Ohno, M. Shimaya, K. Izumi, and N. Shiono, IEEE Trans. Circuits Devices, CD-3, 21 (1986).
3. For example, A.G. Revesz and H.L. Hughes, Microelec. Eng. 36, 343 (1997), K. Vanheusden and A. Stesmans, Appl. Phys. Lett. 62, 2405 (1993).
4. K.S. Seol, A. Ieki, and Y. Ohki, J. Appl. Phys. 79, 412 (1996).
5. H. Nishikawa, E. Watanabe, D. Ito, and Y. Ohki, Phys. Rev. Lett. 72, 2101 (1994).
6. H. Imai, K. Arai, H. Imagawa, H. Hosono, and Y. Abe, Phys. Rev. B 38, 12772 (1988).
7. R. Allison, J. Burns, and A.J. Tuzzolino, J. Opt. Soc. Am. 54, 747 (1964).
8. H.R. Philipp, J. Phys. Chem. Solids 32, 1935 (1971).

(BL1B)

Reflection Spectra of $(CH_3NH_3)_3M_2Br_9$ (M:Sb,Bi) Single Crystals

Taketoshi Kawai[A], Akira Miyashita[B] and Makoto Iwata[B]

[A]*Department of Natural Science, Osaka Women's University, Daisen−cho, Sakai 590-0035, Japan*

[B]*Department of Applied Physics, Nagoya University, Nagoya 464-8603, Japan*

Novel crystals of alkylammonium halogenometallates $(CH_3NH_3)_3M_2X_9$ (M=Sb,Bi: X=Cl,Br,I) which contain the trivalent ion as the constituent metal exhibit several interesting structure phase transitions mainly due to the ordering of orientational motion of alkylammonium cations with the permanent dipole moment. Therefore, a number of studies on these materials have been extensively made on phase transitions and dielectric properties[1-5]. On the other hand, there are only few studies on optical properties of these novel crystals[6]. We have investigated the optical properties of the bromo derivatives $(CH_3NH_3)_3Sb_2Br_9$ (MABA) and $(CH_3NH_3)_3Bi_2Br_9$ (MABB) in the photon energy of 2.0～24eV. The compounds have a corrugated layer of the inorganic $[(M_2Br_9)^{3-}]_n$ polyanions and the $(CH_3NH_3)^+$ cations occupying the vacancies.

Single crystals of MABB and MABA were grown by slow evaporation of the HBr solution containing the stoichiometric molar ratio of Bi_2O_3 or Sb_2O_3 and CH_3NH_3Br. The obtained crystals have the form of hexagonal plates of transparent yellow color. They were cleaved along the crystallographic *ab*-plane in order to use as a reflection plane. The reflection spectra at near-normal incidence were measured at the beam line BL1B of UVSOR by using a monochromator of 1m Seya-Namioka type. The measurements were performed in the temperature range from 300K to 8K, because both crystals exhibit several structure phase transitions in this temperature range.

Figures 1(a) and 1(b) show the reflection spectra of the MABB and MABA single crystals at several temperature in the energy region of 2.0～6.0eV, respectively. As seen in these figures, several remarkable structures were observed in this energy region. The rapid drop structure at 2.73eV for MABB and 2.85eV for MABA is correspond to the energy position which each absorption spectrum exhibits a steep rise. Thus, the rapid drop structures are probably due to the reflection from the back surface of the crystals. At low temperature, the sharp reflection structure at 2.90eV for MABB and 2.95eV for MABA is attributed to the band-edge exciton state. Since the CH_3NH_3Br solution does not exhibit any absorption band in the energy region below 6.0eV, the origin of the electronic states may be interpreted on the basis of electronic states in the metal cation. Preliminary analysis of the reflection structure by the simple oscillator model provide the following values for the band-edge exciton. The transverse exciton energy and the longitudinal- transverse splitting energy are 2.90eV and 80meV for MABB, and 2.95eV and 60meV for MABA, respectively.

As the temperature increases, the reflection structures red-shift and become broader gradually. The MABB and MABA crystals have the phase transition temperatures of about 101.5, 140 and 188 K, and about 130 and 168 K, respectively. The drastic change of the reflection spectra is not observed at any phase transition temperature. This result supports that the band-edge exciton states have it's origin in electronic states in the metal ion, because the orientational motion of the $(CH_3NH_3)^+$ cations

(BL1B)

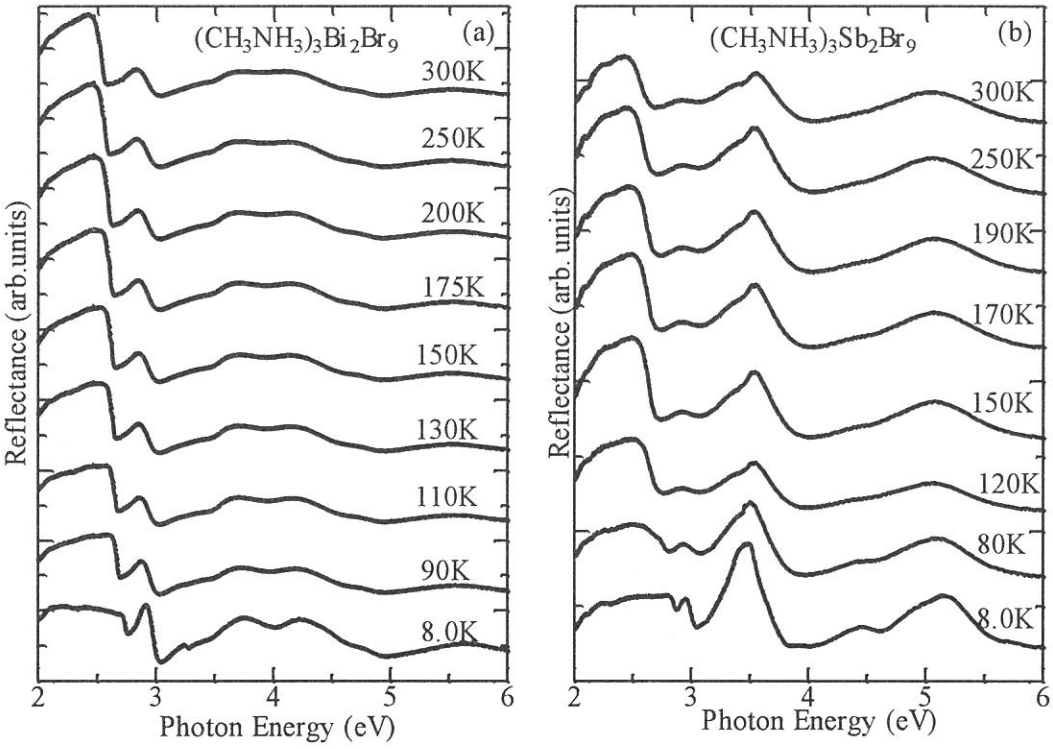

Figure 1 Reflection spectra of MABB (a) and MABA (b) at various temperature.

is not considered to distort the framework of the inorganic $[(M_2Br_9)^{3-}]_n$ polyanions. It should be noticed that the reflection peak in MABB is clearly observed even at 300K. On the other hand, the structure in MABA is hardly observed at 300K. This fact means that the band-edge exciton in MABB has a large binding energy in comparison with that in MABA. The quantitative analysis including the temperature dependence of the reflection structure in the higher energy is now in progress.

References

[1] R.Jakubas and L.Sobczyk: Phase Transitions **20** (1990) 163.

[2] R.Jakubas, Z.Galewski, L.Sobczyk and J.Matuszewski: J.Phys.C **18** (1985) L857.

[3] R.Jakubas, U.Krzewska, G.Bator and L.Sobczyk: Ferroelectrics **77** (1988) 129.

[4] P.Koziol, Y.Furukawa and D.Nakamura: J.Phys.Soc.Jpn **60** (1991) 3850.

[5] M.Iwata, M.Eguchi, Y.Ishibashi, S.Sasaki, H.Shimizu, T.Kawai and S.Shimanuki: J.Phys.Soc.Jpn **62** (1993) 3315.

[6] T.Kawai, A.Ishii, T.Kitamura, S.Shimanuki, M.Iwata and Y.Ishibashi: J.Phys.Soc.Jpn **65** (1996) 1464.

(BL1B)

Optical Properties of Cerium-doped Oxide and Fluoride Crystals for Laser Media I

Yoshiro SUZUKI, Hisashi UMEDA, Tooru HIRAYAMA and Kiyoshi INOUE
Faculty of Engineering, Tohoku University, Aoba, Sendai, 980-77

Introduction

Optical properties of cerium-doped materials have received considerable interests in recent years in connection with the application to tunable solid state laser media. [1] Several reports were made on the laser activity of cerium-doped fluoride crystals in UV region, while none of oxide crystals in visible region. This is believed to be due to optical losses by what is called the excited state absorption.[2] The excited state absorption is attributed to the transition from the lowest 5d excited state of the trivalent cerium ions (Ce^{3+}) to the conduction band of the host materials. Therefore, it is important to determine the location of the energy levels of the Ce^{3+} in the band gap for prediction of the laser activity. However, quantitative nor systematic evaluation has hardly been made because of lacking of the fundamental data.

As the first step, the measurements of the reflection spectra and the excitation spectra of the Ce^{3+} emission in several laser crystals have been carried out in the photon energy range of 4 to 17eV in order to obtain the information on the band gap energies.

Experimental

Crystals of $Y_3Al_5O_{12}$ (YAG) containing cerium were grown by Czochralski method in Tokin Inc., while those of $Gd_3Sc_2Ga_3O_{12}$ (GSGG), $YAlO_3$ (YAP), $YLiF_4$ (YLF) were furnished by the courtesy of Dr.Y.Segawa of Photodynamics Research Center, the Institute of Physical and Chemical Research. The crystals of YAP and YLF are anisotropic , then their orientations were determined through a comparison of the polarized absorption spectra with those from the literature.[3,4] The orientation of the crystals and the nominal concentrations of the Ce^{3+} are presented in each frame of Fig. 1.

The measurements were carried out at room temperature. The spectra of the reflection and the excitation of Ce^{3+} emission were measured by means of a Seya-Namioka-type VUV monochromator at the beam line BL1B. The band width for the reflection and the excitation spectra was 0.1 and 0.3nm,respectively. The reflected and emitted light were detected both at angle of 45° with the incident direction.

Experimental Results and Discussion

Solid curves in Fig.1 show the reflection spectra of the respective crystals. The measured reflectivity are normalized to the reflectance calculated using the refractive indices in the transparent region.[5] The reflection spectra were analyzed using Kramers-Kronig relationship by Roessler method.[6] Chain curves in Fig.1 present the imaginary part of the dielectric function, ε_2 thus obtained. The ε_2 spectra of YAG and YAP are essentially similar to those previously reported.[7,8] The main peaks at 9.0eV in YAG and 8.7eV in YAP were assigned to the transitions from the $O^{2-}2p^6$ to $Y^{2+}4p^6(4d+5s)$ level.[8] The structures due to exciton peaks are obscure at the leading edges of 6 to 8eV. This is characteristic manifestation in complex oxide crystals and attributed to the broadening and overlapping of multiple exciton absorption due to large atomic numbers in the unit cell.[9] The same feature is the case in GSGG and YLF. Therefore, it is difficult to determine the band gap energies only from the ε_2 spectra.

Dashed curves in Fig.1 show the excitation spectra of Ce^{3+} emission, which is caused by the transition from the lowest 5d excited state to the 4f ground state of the Ce^{3+}. The emission was detected at around the peak energy of the emission band in the respective crystals; 2.1eV in YAG and GSGG, 3.3eV in YAP and 3.8eV in YLF. The several bands due to the intraionic excitation to the higher lying 5d states are observed below 6.0eV in YAG and GSGG, while 7.0eV in YAP and YLF. Notable are the bands located around the leading edge of the fundamental absorption of the respective crystals; 6.8 to 8.0eV in YAG, 6.0 to 7.0eV in GSGG, 7.9eV in YAP and 10.3eV in YLF. These are denoted by the edge bands hereafter. Tomiki et al. reported the excitation spectra of Ce^{3+} emission from YAG:Ce and YAP:Ce powder phosphors and suggested the exciton formation by the intrinsic tail excitation.[8] Murk et al. detected the emission due to self trapped excitons (STE) in undoped YAG and YAP.[10] The excitation spectra of STE emission are very similar to the edge bands of YAG and YAP. This suggests the energy transfer from STE to Ce^{3+} and supports the exciton as the origin of the edge bands. It follows that the fallings at the high energy side of the edge bands are interpreted from the decrease of the transfer efficiency due to photoionization. The increase of the reflection loss contributes insignificantly to the falling. Figure 1 shows 40 to 90 % decreases in excitation intensity at the high energy side of the edge bands, whereas only 11 to 18% increases in reflectance is observed in the identical energy regions. Then, we may obtain indication of the electron-hole

continuum excitation from the falling edge energies of the edge bands in the respective crystals ; 8.0eV in YAG, 6.8eV in GSGG, 7.8eV in YAP and 10.5eV in YLF. It is consistent that these energies correspond to the singular points of the ε_2 spectra where steeper rises are observed. The band gap energy of YAG was determined to be 8.0eV from a photocurrent measurement.[11] The agreement with the falling edge energy of the edge band in YAG supports the validity of the falling edge as an indicator of the continuum excitation.

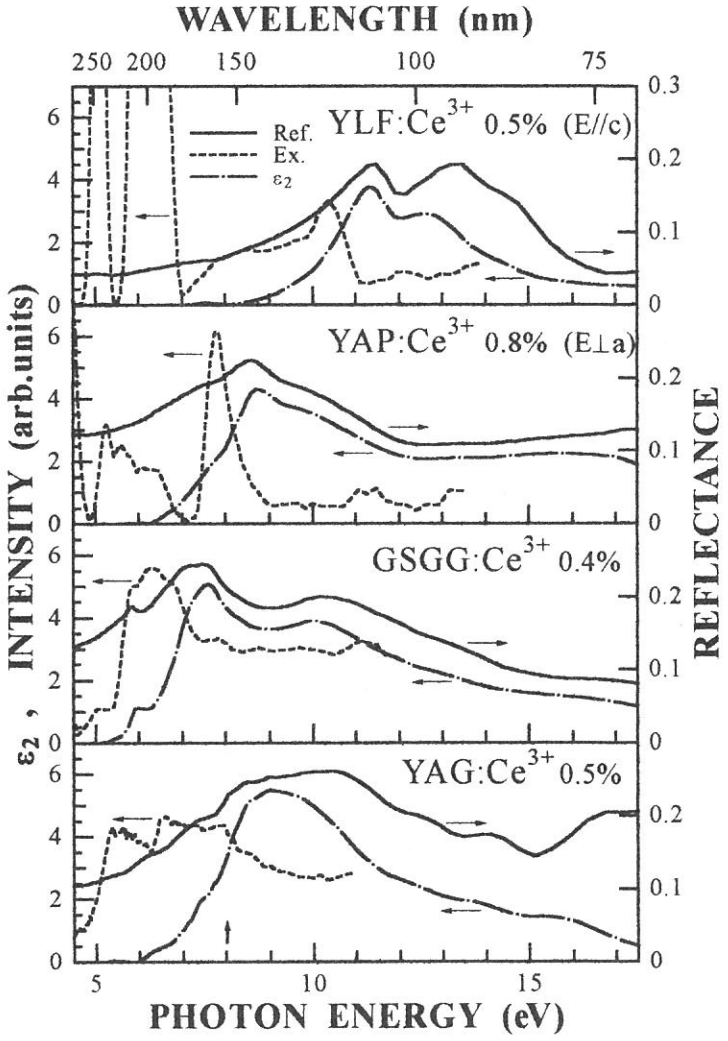

Fig.1 Spectra of Ce doped YAG, GSGG, YAP and YLF at room temperature : reflection (solid), ε_2 (chain) and excitation spectra of the Ce^{3+} emission (dashed curves) .

References

[1] See, for example, N.Sarukura : Kogaku, **25** (1996) 518 [in Japanese] .

[2] D. S. Hamilton et al. : Phys. Rev. **B 39** (1989) 8807.

[3] S. Yan, G. Yuan and Y. Zhong : Materials Lett. **16** (1993) 222.

[4] N. Sarukura et al. : IEEE J. Selected Topics in Quantum Electronics, **1** (1995) 792.

[5] L. G. DeShazer et al. : CRC Handbook of Laser Science and Technology, ed. M. J. Weber (CRC Press, Boca Raton Fla.1987) Vol. 5, p. 281.

[6] D. M. Roessler : Br. J. Appl. Phys. **16** (1965) 1119.

[7] V. N. Abramov and A. I. Kuznetsov : Sov. Phys. Solid State **20** (1978) 399.

[8] T. Tomiki et al. : J. Lumin. **40 & 41** (1988) 379.

[9] A. I. Kuznetsov et al. : Trudy Inst. Fiz. Akad. Nauk. Est. SSR. **63** (1989) 19.

[10] V. Mürk et al. : Nucl. Instrum & Methods Phys. Research **B 91** (1994) 327.

[11] N. S. Rooze and N. A. Anisimov : Trudy Inst. Fiz. Akad. Nauk. Est. SSR. **44** (1975) 163.

(BL1B)

Optical Properties of Cerium-doped Oxide and Fluoride Crystals for Laser Media II

Yoshiro SUZUKI, Hisashi UMEDA, Tooru HIRAYAMA and Kiyoshi INOUE
Faculty of Engineering, Tohoku University, Aoba, Sendai, 980-77

Introduction

Cerium-doped materials have received much attention as tunable solid state laser media. [1] The emission due to the transition from the lowest 5d excited state ($5d^1$) to the 4f ground state of the trivalent cerium ions (Ce^{3+}) is used for the laser action. The peak energy of Ce^{3+} emission varies from UV to visible region depending on the host materials. Up to date, however, the tunable energies of Ce^{3+} laser are restricted to UV region using fluoride crystals. The visible laser action using oxide crystals is believed to be hampered by so-called excited state absorption. [2] Since the excited state absorption is attributed to the transition from the $5d_1$ state to the conduction band of the host materials, the location of the energy levels of the Ce^{3+} in the band gap is crucial for the laser activity.

In the preceding report,[3] we showed that the excitation spectra of Ce^{3+} emission in VUV region give information of the band gap energies of the host crystals. In the present study, the measurements have been extended to UV and visible regions where intraionic transitions of the Ce^{3+} are observable. The quantum efficiencies of Ce^{3+} emission are known to be almost unity under the $5d_1$ excitations,[4] while those under the higher 5d excitations are unknown. Since the latter excitations may cause electron-release to the conduction band and reduce the quantum efficiency, the excitation spectra of Ce^{3+} emission have been expected to give information of the energy separation between the 4f ground state of the Ce^{3+} and the bottom of the conduction band.

Experimental

Cerium-doped crystals of $Y_3Al_5O_{12}$ (YAG), $Gd_3Sc_2Ga_3O_{12}$ (GSGG), $YAlO_3$ (YAP), $YLiF_4$ (YLF) were identical with those in the preceding report.[3] Presented in each frame of Fig.1 are the thickness and the nominal concentrations of the Ce^{3+} of the respective crystals, as well as the crystal orientation if anisotropic.

The measurements were carried out at room temperature. The excitation spectra of Ce^{3+} emission above 3.5eVwere measured at the beam line BL1B in the identical optical configuration with those in the preceding report.[3] The sufficient beam intensities facilitated the measurements and their corrections. The excitation spectra below 3.5eV were measured with a conventional optical system using a Xe lamp, since the sodium salicylate scintillater was unavailable at these energies. The absorptivity spectra of the respective crystals were also measured in order to evaluate the quantum efficiencies through comparisons with the excitation spectra. The band widths for the excitation and the absorption spectra above 3.5 eV were both 0.3nm, while those below 3.5 eV were 1.5nm.

Experimental Results and Discussion

Solid curves in Fig.1 show the absorptivity spectra of the respective crystals. The reflection losses were not corrected, while the absorbance at the transparent region were subtracted as the background. Several absorption bands observed are due to the transition from the 4f ground state to the crystal-field levels of the 5d excited states of the Ce^{3+}. The increased covalency and crystal field in oxide crystals gives the red shifts of the absorption peaks compared with those in YLF. Absorption tails due to the anisovalent cerium ions or the other impurities are obvious at the high energy region in GSGG and YAP.

Dotted curves in Fig.1 show the emission spectra under the $5d_1$ excitation. The doublet structure prominent in YLF is due to the spin-orbit splitting of the 4f ground state. The broadening of the emission bands in oxide crystals makes the structure obscure.

Dashed curves in Fig.1 show the excitation spectra of Ce^{3+} emission detected at around the peak energy of the emission band in the respective crystals. The heights were normalized to the peak heights of the $5d_1$ absorption bands. It is evident that the excitation spectra almost follow the absorptivity spectra in the whole energy region in YAG and YLF. Although the excitation spectra in GSGG and YAP apparently slip down from the absorptivity spectra at the higher energy region, the absorption tails due to the anisovalent cerium ions or the other impurities seem to be responsible for the disagreements. These behaviors of the excitation spectra of Ce^{3+} emission are unexpected. The photoionization threshold energy of the Ce^{3+} in YAG was determined to be 3.8eV from a photocurrent measurement.[5] However, no manifestation of the photoionization is observable in the present excitation spectra around 3.8 eV in YAG. The present result of YAG is not consistent with the previous one by Tomiki et al. either.[6] They reported that the relative intensity of the excitation band of Ce^{3+} emission to that of the absorption band decreased drastically at higher energy region. The reason of this discrepancy is not clear. The emission quenching may depend on the concentration of the electron-trap competitive with the photoionized Ce^{3+}.

Codoping of the electron-trap ions might be necessary for the observation of the photoionization threshold.

On the other hand, the spectral dependence of the excitation spectra is desirable for the laser performance. The Ce^{3+} is usually excited to higher lying 5d states in the laser performance because of less variety of pumping sources. The present result suggests that the Ce^{3+} emission efficiency does not decrease under such excitation as far as multiphoton processes are not induced.

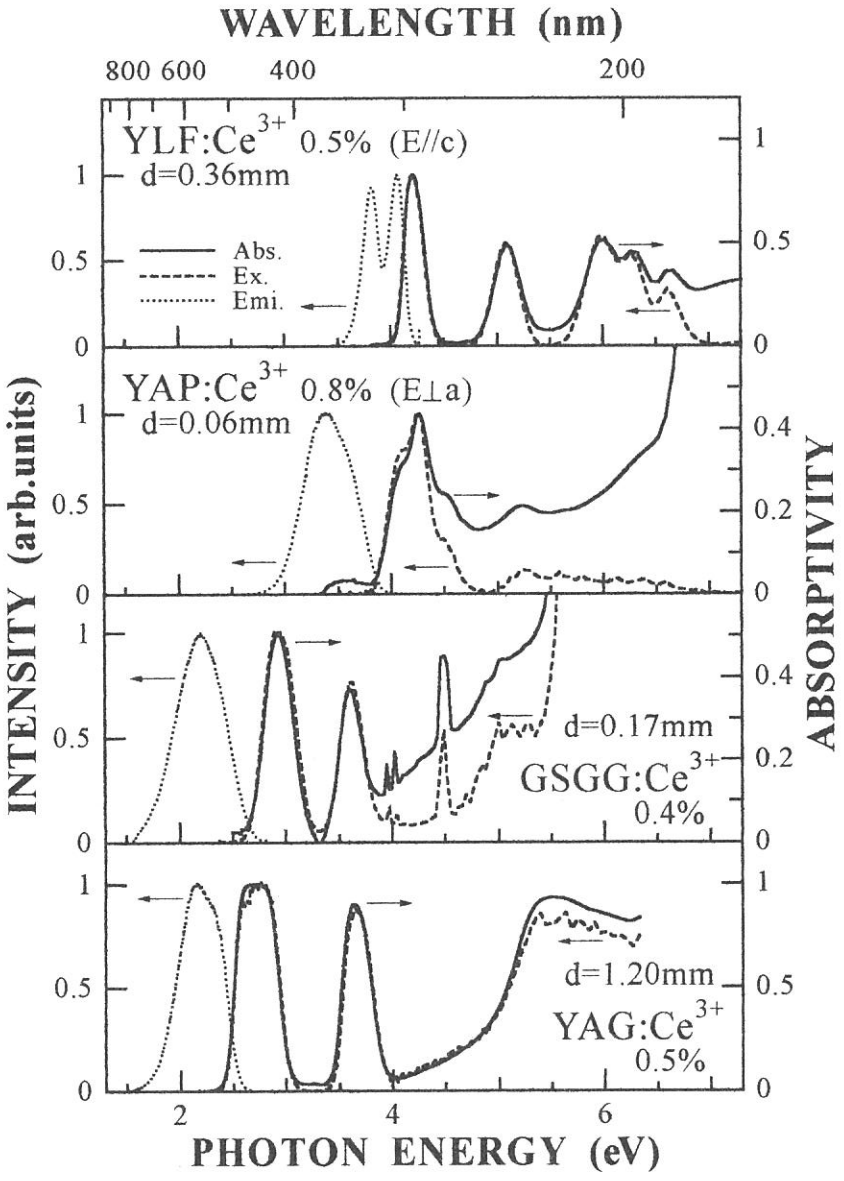

Fig.1 Spectra of Ce doped YAG, GSGG, YAP and YLF at room temperature : absorptivity (solid), emission (dotted) and their excitation spectra (dashed curves) .

References

[1] See, for example, N. Sarukura : Kogaku, **25** (1996) 518 〔in Japanese〕 .

[2] D. S. Hamilton, S. K. Gayen, G. J. Pogatshink, R. D. Ghen, and W. J. Miniscalco : Phys. Rev. **B 39** (1989) 8807.

[3] Y. Suzuki, T. Hirayama, H. Umeta and K. Inoue : this issue.

[4] Li-Ji Lyu and D. S. Hamilton : J.Lumin. **48 & 49** (1991) 251.

[5] C. Pedrini, F. Rogemond and D. S. McClure : J. Appl. Phys. **59** (1986) 1196.

[6] T. Tomiki, F. Fukutome, M. Kaminao, M. Fujisawa, Y. Tanahara and T. Futemma : J. Phys. Soc. Jpn. **58** (1989) 1801.

(BL1B) VUV Excited Luminescence in CsI (pure, Tl-doped and Na-doped) and in multilayer structures of LiF- CaF_2 and LiF- BaF_2.

A. Ejiri, E. Chin, A. Urasaki, T, Yonamine and T. Yokozawa [A]

Dept. of Science Education, College of Education, University of the Ryukyus, Nishihara, Okinawa 903-01.

[A] *Dept. of Physics, Faculty of Science, Rikkyo University, Nishi-Ikebukuro, Tokyo 171.*

CsI is an interesting material of scintillator to be revealed its luminescence mechanism. Alkali earth fluoride crystals (CaF_2 and BaF_2) are well known that they show a strong STE luminescence even at room temperature. [1] It is interesting to investigate quantum confinement effect of the luminescence in the quantum well structures of these fluorides. Samples of scintillators are pure CsI single crystal, Tl- 0. 1mol%- doped CsI and Na- 0. 1mol%- doped CsI crystals.

Present paper will report results of the luminescence measurements in those CsI crystals, and in the quantum well structures respectively consisted of 5- periods of LiF (200Å)- CaF_2 (100Å), LiF (100Å)- CaF_2 (50Å), LiF (200Å)- BaF_2 (100Å), and LiF (100Å)- BaF_2 (50Å). The specimen of 5-periods multilayer structures are fabricated with vacuum evaporation technique and annealing at 200℃ for an hour in every layer after deposition. All measurement were performed at BL-1B by the use of a Spex monochrometer for the luminescence. Excitation spectra for each luminescence band were also measured in the photon energy range up to 40eV. The luminescence spectra were not corrected for the spectral efficiency of the monochrometer and the excitation spectra were normalized by the spectral output of the Seya- Namioka monochromator.

In Fig. 1, observed luminescence spectra in pure CsI and the Tl- doped CsI excited with 12eV radiation at 7K are shown. It is characteristic to be appeared a new band at 2. 5eV in Tl- doped CsI. In Fig. 2, observed luminescence of CaF_2 (exc 1033Å) and BaF_2 (exc 1240Å) single crystals at 7K (a), those of a LiF (200Å)- CaF_2 (100Å) and a LiF (100Å)- CaF_2 (50Å) multilayers at 7K (b), and of a LiF (200Å)- BaF_2 (100Å) and a LiF (100Å)- BaF_2 (50Å) multilayers at 7K (c) are shown.

On the luminescence spectra in the multilayers, several resonance type structures are observed especially on CaF_2 (50Å) spectrum in Fig. 2(b) and BaF_2 (100Å) spectrum in Fig. 2(c). Furthermore, it was found that a line series of luminescence in LiF (200Å)- CaF_2 (100Å) multilayer excited 1050Å at room temperature as shown in Fig. 3(a).

An excitation spectra of the luminescence in the mutilayer structure of LiF(200)-CaF_2 (100) is shown in Fig 3(b). This appears a very narrow band which indicates an onset of STE and a penetration limit of radiation in the multilayer.

The resonance structures and line spectra in the luminescence can be explained in terms of interference of luminescence in the well layers (CaF_2, BaF_2) and of resonant emission in

a cavity of the multilayer.

References

1) A. Ejiri, A. Hatano, and K. Arakaki; UVSOR Act. Rep. (IMS)1995, (1996) 68.

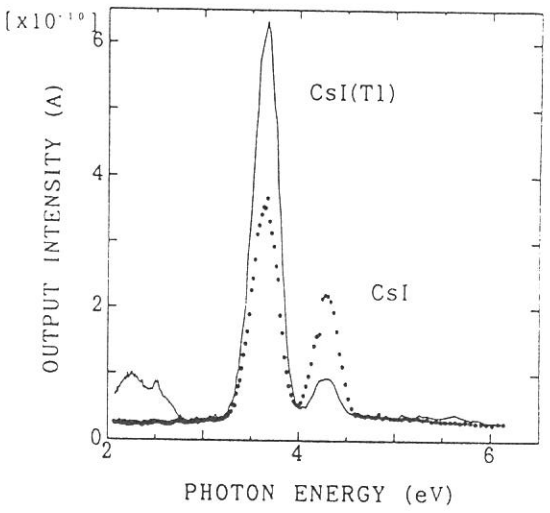

Fig. 1 Luminescence spectra of pure CsI and Tl 0. 1mol%- doped CsI excited with 12eV radiation at 7K.

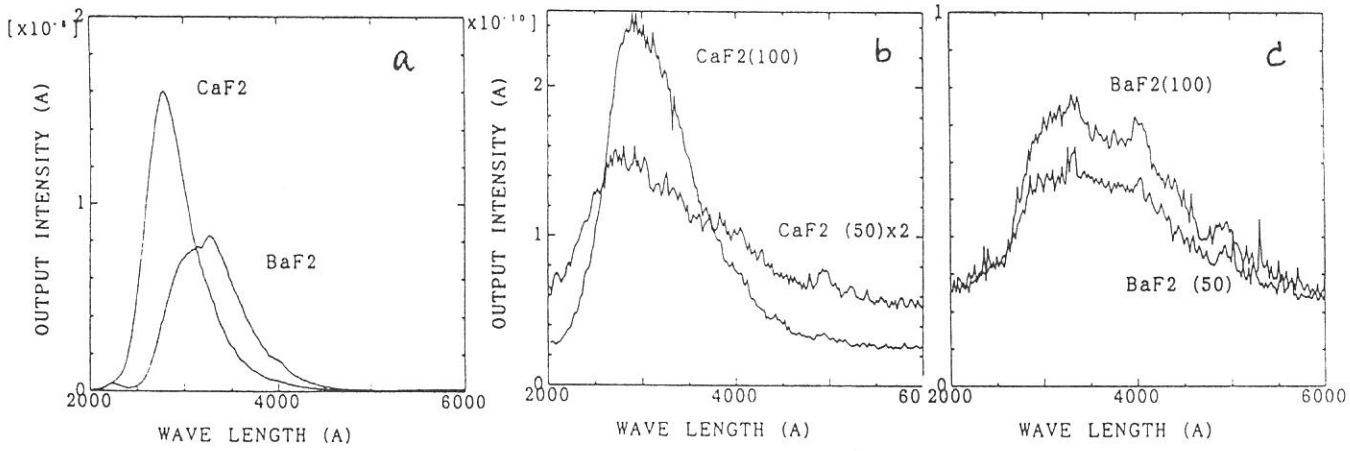

Fig. 2 Luminescence spectra of CaF_2 (excited with 1033 Å) and BaF_2 (excited with 1240Å) crystals at 7K (a), of LiF (200Å)- CaF_2 (100Å) and LiF (100Å)- CaF_2 (50Å) multilayers excited with 1033Å radiation at 7K (b) and of the LiF (200Å)- BaF_2 (100Å) and LiF (100Å)- BaF_2 (50Å) multilayers excited with 1240Å radiation at 7K (c).

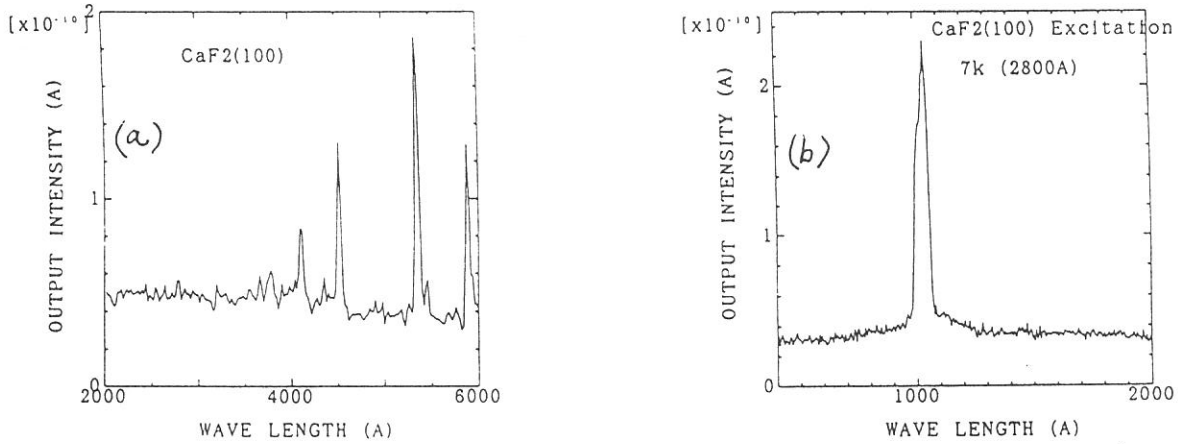

Fig. 3 Luminescence spectra of a LiF (200Å)- CaF_2 (100Å) multilayer excited 1050Å at room temperature(a) and an excitation spectrum of the multilayer luminescence of 2800Å at 7K(b).

(BL1B)

Luminescence from Self-Trapped Excitons in BaFI and $BaFBr_{1-x}I_x$ crystals

Akimasa OHNISHI[A], Ken-ichi KAN'NO[B] and Nobufumi MORI[C]

[A]*Department of Physics, Yamagata University, Yamagata 990-0021*
[B]*Department of Physics, Kyoto University, Kyoto 606-8224*
[C] *Fuji Photo Film Co., Ltd., Miyanodai, Kaisei-machi, Kanagawa 258-0023*

Balium-fluoro-halides (BaFX, X=Cl, Br, I) are important host materials of photo-stimulated luminescence phosphors activated with Eu^{2+} ions.[1] We have investigated luminescence properties from self-trapped excitons (STEs) in BaFCl, BaFBr and $BaFCl_{1-x}Br_x$, and have discussed on the STE configurations by the analogy with on- and off-center STEs in alkali halides.[2,3] In the present study, luminescence measurements have been extended to BaFI and $BaFBr_{1-x}I_x$ crystals.

BaFI and $BaFBr_{1-x}I_x$ were grown by a horizontal Bridgmann method. Experiments were made using synchrotron radiation pulses from the beam line BL1B of UVSOR. Luminescence was detected with a photomultiplier (Hamamatsu R955) through a grating monochromator (Spex 270M).

Figure 1(a) shows the emission spectrum in BaFI at 15 K. When the crystal is excited at 8.86 eV in the range of band-to-band transition, a characteristic luminescence band is observed at 4.54 eV. In Fig.1(b), is shown the excitation spectrum for the 4.54 eV band, along with positions of the halogen doublet due to I^- spin-orbit splitting reported by Nicklaus [4] (arrows at 6.5 and 7.6 eV). The spectrum indicates high emission yields above the threshold at 6.5 eV. This suggests that the 4.54 eV band is due to recombination luminescence from STE with I_2^--core in BaFI. Efficient excitation bands are observed also in the region (5.6 ~ 6.5 eV) of low energy tail of the n=1 exciton absorption band. The reason is now under consideration.

To see the effect of changing in the crystal environment on the manner of exciton self-trapping, luminescence from $BaFBr_{1-x}I_x$ has been investigated under excitation at 10.3 eV at 10 K. Their emission spectra are shown in Fig.2. As seen in Fig.2(a), an emission band is observed at 5.06 eV in the x=0.001 crystal, as far as the excitation is made at the energies of band-to-band transition of BaFBr. The peak energy and band width are in good agreement with the intrinsic luminescence band of BaFBr. This means that the STE composed of an electron and a Br_2^- core is created under excitation at 10.3 eV. However when excited at the lower energy around 6.53 eV, another emission band which can be attributed to the localized excitons with $(BrI)^-$-cores appears at 5.18 eV (dotted spectrum of Fig.2(a)). In the case of x=0.1, a new emission band is observed at 4.95 eV together with the 5.18 eV band. In this case, major part of free holes must be self-trapped on I^- sites because of the smaller electron affinity of I^- compared with Br^-. Thus the 4.95 eV band supposedly originates from the localized excitons with I_2^--cores. In fact, the 5.18 eV band disappears in the x>0.3 crystals, and the 4.95 eV band gradually

shifts to the low energy side with the increase in x and finally connects to the 4.54 eV band from the STE with I_2^--core in BaFI. It should be noted that these spectral changes in $BaFBr_{1-x}I_x$ are essentially the same as those of on-center type STE luminescence in $BaFCl_{1-x}Br_x$.[3] We suppose that the STE configurations responsible for the emission bands are also of on-center type, and the off-center instability does not take place in BaFI and $BaFBr_{1-x}I_x$.

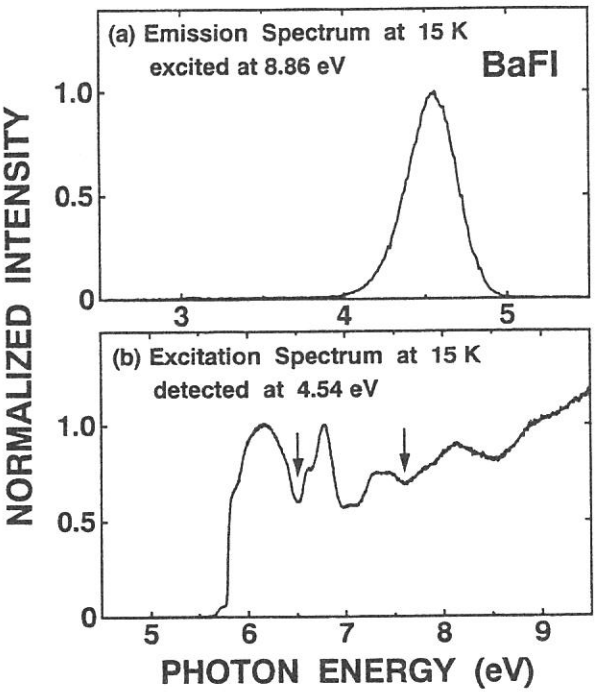

Fig.1

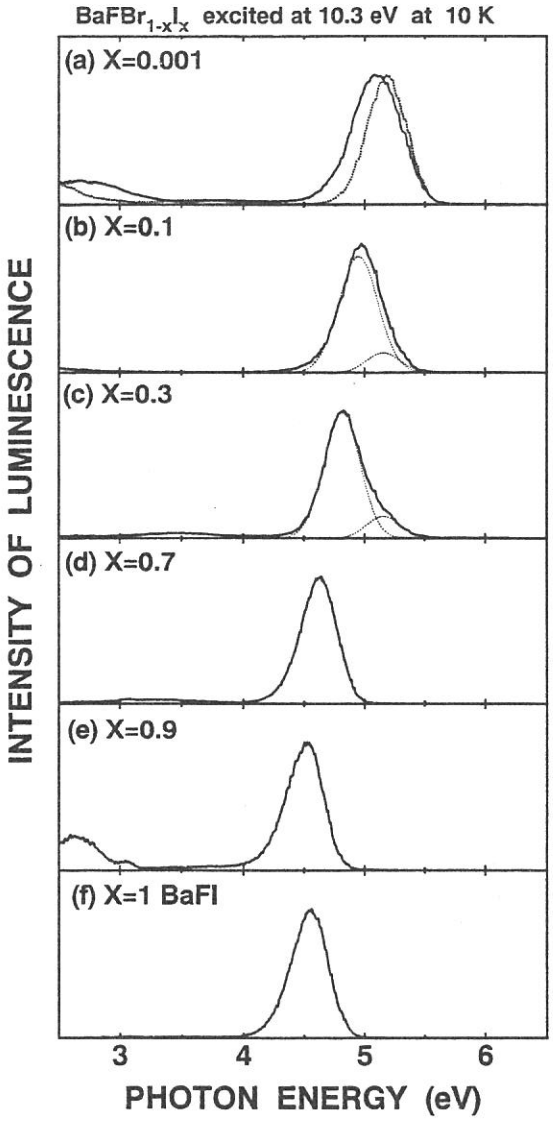

Fig.2

References

1. M. Sonoda, M. Takano, J. Miyahara and H. Kato ; Radiology, 148 (1983) 833.
2. A. Ohnishi, K. Kan'no, Y. Iwabuchi and N. Mori ; Nucl. Instr. and Meth. in Phys. Res. B91 (1994), 210.
3. A. Ohnishi, K. Kan'no, Y. Iwabuchi and N. Mori ; J. Electron Spectrosc. Relat. Phenom., 79 (1996) 163.
4. Nicklaus ; Phys. Status. Solidi (a) 53 (1979) 217

(BL1B)

Optical Spectra in Solid Superoxide KO_2

M. ASHIDA, O. MORIKAWA, S. HASHIMOTO[A], S. HIROSE[B], M. KAMADA[B] and K. KAN'NO

Department of Physics, Kyoto University, Kyoto 606

[A]Kyoto University of Education, Kyoto 612

[B]UVSOR, Institute for Molecular Science, Okazaki 444

Alkali superoxides consist of alkali metal ions and paramagnetic anion O_2^- molecules. This material shows a number of structural phase transitions due to the reorientation of O_2^- [1] and antiferromagnetic order of the spin 1/2 of O_2^-. [2] The O_2^- molecule in alkali halides is a well-known efficient luminescent center.[3] Thus characteristic optical properties reflecting the phase transition are expected in the alkali superoxides. However, there have been only a few optical studies on solid alkali superoxides, since they are highly reactive and it is difficult to obtain single crystals of appropriate size. Bösch *et al.* succeeded in growing single crystals of NaO_2 in liquid ammonia and measured reflection spectra.[4] For the other alkali superoxides, optical spectra in visible and VUV region have not been reported yet. As a first step for the study of optical properties of this system, solid KO_2 was investigated in the present experiment. Samples were prepared by cooling molten KO_2 on Al substrates in a vacuum.

Reflection spectra in KO_2 at 40K and 310K are shown in Fig. 1. The overall structure and peak positions of the spectra were reproducible, though the absolute value of the reflectivity changed within ±10% from sample to sample. It is regrettable that the spectra in the low energy region below ~4eV, where anomalous temperature change was observed in NaO_2 crystal,[4] were affected by the back reflection due to the Al substrate. Although the spectrum changed gradually with increasing temperature, characteristic changes at the phase-transition temperatures were not observed. The structures below ~7eV (e.g. the remarkable peak at 6eV) correspond to those in NaO_2 crystal.[4] Hence, the spectral features in the lower energy region (4-7eV) can be assigned to the intramolecular transition in the O_2^- molecule and those in the higher energy region are possibly caused by the charge transfer transition. The structures due to the intramolecular transition, however, cannot be explained by using the adiabatic potential diagram of a single molecule.[5] The transition $^2\Pi_g \rightarrow {}^2\Pi_u$ of an O_2^- molecule, which gives rise to a main absorption band centered at ~5eV of O_2^- centers in alkali halides,[6] does not manifest itself in Fig. 1. The effect of the interaction among the O_2^- molecules, that is, Frenkel exciton, and/or the electron-phonon interaction must be taken into account.

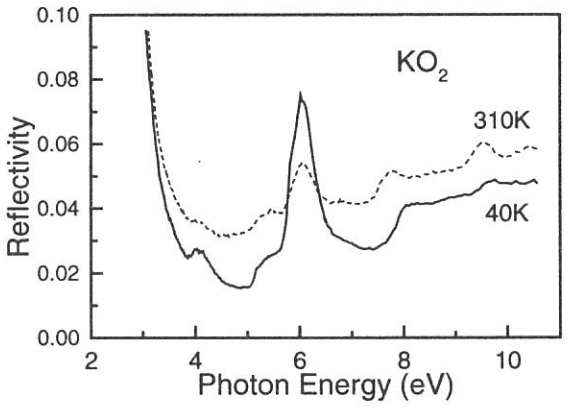

Fig. 1. Reflection spectra in solid KO_2. (Solid line: 40K, broken line: 310K.)

Photo-luminescence was observed even at room temperature. Figure 2 shows its spectrum at 310K under the excitation at ~6eV. The broad shape almost unchanged down to ~10K. The excitation spectrum of this luminescence is shown in Fig. 3. The remarkable peaks and a shoulder are in good agreement between excitation and reflection spectra. Therefore, it is confirmed that the luminescence arises from the intrinsic excited state of KO_2. The luminescence spectrum is drastically different from the spectra of O_2^- centers in alkali halides, which show sharp vibronic lines.[3] This fact indicates strong intermolecular interaction among O_2^- molecules and/or electron-phonon interaction in alkali superoxides again. For further investigation, growth of single crystals of alkali superoxides is desirable.

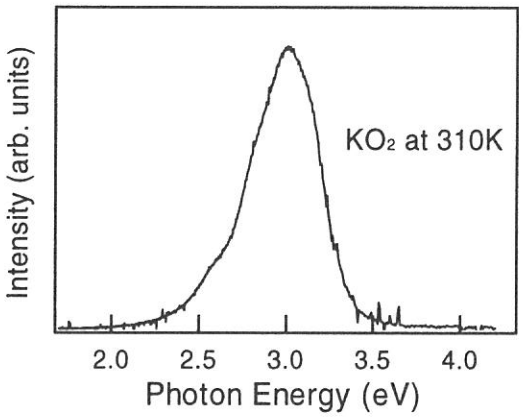

Fig. 2. Emission spectrum in KO_2 at 310K under excitation at 205nm.

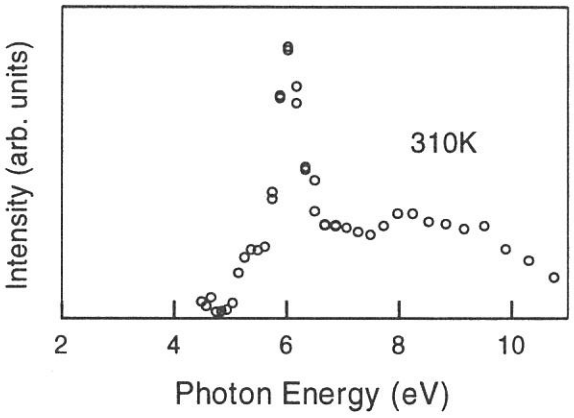

Fig. 3. Excitation spectrum of 3.0eV emission in KO_2 at 310K.

References

1) M. Ziegler *et al.*: Helv. Phys. Acta **49** (1976) 57.
2) H. G. Smith *et al.*: J. Appl. Phys. **37** (1966) 1047.
3) S. Hongo *et al.*: Memoirs of the Faculty of Science, Kyoto University, A **38** (1992)187.
4) von M. Bösch and W. Känzig: Helv. Phys. Acta **48** (1975) 743.
5) M. Krauss *et al.*: Phys. Rev. **A7** (1973) 69.
6) F. Fischer *et al.*: Z. Phys. **189** (1966)79.

(BL1B)

Reflection Spectra of Orthorhombic and Cubic PbF_2 Crystals

Masami FUJITA, Dmitri L. ALOV,[A] Minoru ITOH,[B] Jun-ichi MURAKAMI,[B]
Tetsuo SAIDA,[C] Hideyuki NAKAGAWA[C] and Mamoru KITAURA[D]

Maritime Safety Academy, Wakaba, Kure, Hiroshima 737-8512
[A]*Institute of Solid State Physics, Chernogolovka, Moscow, 142432, Russia*
[B]*Department of Electrical and Electronic Engineering, Faculty of Engineering, Shinshu University, Wakasato, Nagano 380-0922*
[C]*Department of Electrical and Electronics Engineering, Faculty of Engineering, Fukui University, Bunkyo, Fukui, 910-0017*
[D]*Fukui National College of Technology, Sabae, Fukui, 916-0064*

Lead fluoride crystallizes into two phases, one of which has an orthorhombic lattice of $PbCl_2$ type (α-PbF_2: D_{2h}^{16}, Pmnb) and the other has a cubic fluorite structure (β- PbF_2: O_h^5, Fm3m). The former is more stable phase below 320 °C, but the latter is also metastable at low temperature. Optical spectrum of β- PbF_2 reported so far[1] shows different features from the orthorhombic $PbCl_2$ and $PbBr_2$[2]. It is an interesting problem whether the difference in optical spectra comes from the difference in the crystal structure or in the halogen species. However, optical study of PbF_2 has been limited so far to the cubic phase because of the difficulty in preparing the orthorhombic crystals with enough size. Recently, orthorhombic crystals have been grown from aqueous solution and the photoluminescence experiment has been performed[3,4]. In the present study, reflection spectra of α-PbF_2 have been measured up to VUV region in order to investigate the electronic structure in lead halides.

Single crystals of α-PbF_2 were grown from the aqueous solution as thin flakes with the size of 2 x 2 mm^2. The surface of the sample was perpendicular to the c-axis. Reflection spectra were measured for the polarization parallel to the a-axis (E//a) or b-axis (E//b). Reflection spectra of cleaved surfaces of β-PbF_2 crystal and PbClBr crystal were also measured. Experiments have been performed at BL1B in UVSOR.

In the upper part of Fig. 1 are shown reflection spectra of α- and β-PbF_2 crystals at 7K. In the spectra of α-PbF_2, the first exciton band 1 appears at 5.7eV. As mentioned later, the band shows dichroism. Two prominent peaks 2 and 3 are found at 6.3 eV and 8.5 eV. These structures above 6 eV depend slightly on the polarization. The spectrum of β-PbF_2 agrees with that measured at 77K[1]. The first exciton band of β-PbF_2 appears nearly the same position of the exciton band of α-PbF_2. In the 6-7 eV region is observed a broad band 2 which seems to consist of two or three components. A large peak 3 is observed at 8.6 eV. Gross features in the spectra of α-PbF_2 resemble those of β-PbF_2, which suggests that the electronic structures in both modifications are similar to each other.

Reflection spectra in the first exciton band region of α-PbF_2 are shown in Fig. 2. The second-energy-derivative reflectance d^2R/dE^2 (2EDR) spectra were calculated numerically from the reflection spectra and are also shown in Fig. 2. The 2EDR spectra clearly indicate that the exciton band has a single peak for E//a, while it consists of two components for E//b. The peak positions determined from the 2EDR spectra are, 5.678eV (1a) for E//a, and 5.701eV (1b) and 5.829eV (1b') for E//b. The first exciton band of $PbCl_2$ and $PbBr_2$ shows similar dichroism, that is, the band has one peak for E//a and two peaks with separation of 60meV for E//b[2]. The dichroism is explained in terms of the cationic $6s^2 \rightarrow 6s6p$ ($^1S_0 \rightarrow {}^3P_1$) transition in the crystal field of Cs symmetry around the lead ion. According to the theoretical

calculation based on the point charge model, the crystal field splitting of the $6p$ levels in α-PbF_2 is about two times larger than that in $PbCl_2$ and $PbBr_2$[5]. This is in agreement with the present experimental result.

In the lower part of Fig. 1 are shown reflection spectra of $PbCl_2$, PbClBr and $PbBr_2$ at low temperature. The sharp peaks 1 and 3 in these crystals shift continuously with the change of halogen component. This indicates that the excitation associated with the peak 3 occurs also mainly at the cation site. The energy position of the peak 3 of $PbCl_2$ and $PbBr_2$ almost coincides with the C-absorption band of Pb^{2+} impurity in alkali chloride and bromide, respectively. Therefore the peak 3 of these crystals is considered to be due to the excitonic transition corresponding to the $^1S_0 \rightarrow {}^1P_1$ excitation in lead ions[2]. In PbF_2, the transition is expected to occur in the 7.5-8.0 eV region from the extrapolation of $PbBr_2$ and $PbCl_2$ indicated by the broken line in Fig. 1. However, no sharp structure is discernible at the position in the spectra of PbF_2. The peak 3 at 8.5 eV is too broad to be assigned to such transition. Present result indicates that the transition intensity corresponding to the $^1P_1$ excitation is strongly affected by the halogen species, in spite of the localized nature of the cationic excitation. The question why the transition does not appear in PbF_2 would be an important problem to understand the electronic structure in lead halides.

References

[1] J. H. Beaumont, A. J. Bourdillon and J. Bordas: J. Phys. C Solid State Phys. **10**(1977)761.

[2]M. Fujita, H. Nakagawa, K. Fukui, H. Matsumoto, T. Miyanaga and M. Watanabe: J. Phys. Soc. Jpn. **60**(1991)4393.

[3]A. B. Kulakov, A. A. Zhokhov, G. A. Emel'chenko and N. V. Klassen: J. Cryst. Growth **151**(1995)107.

[4]D. L. Alov and S. I. Rybchenko: J. Phys. Condens. Matter 7(1995)1475.

[5]K. Wada: Sci. Light **26**(1977)77.

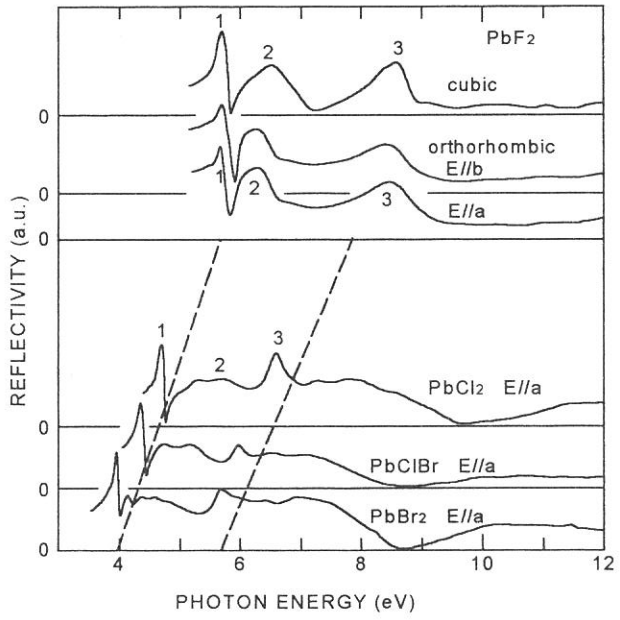

Fig. 1. Reflection spectra of lead halides at low temperature.

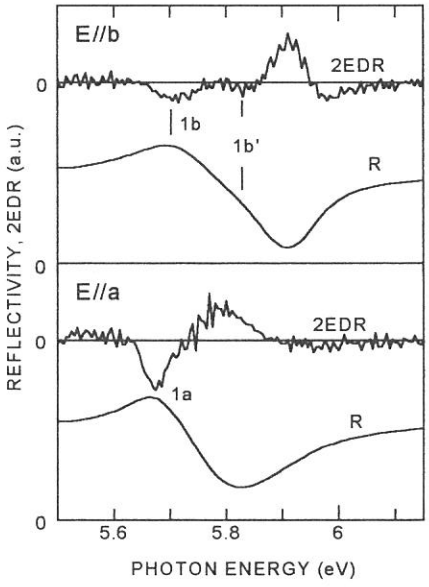

Fig. 2. Reflection and 2EDR spectra of α-PbF_2 in the first exciton band region.

(BL1B)

Time-Resolved Luminescence from Excitons Localized at Br^- Impurities in CsCl Crystals

Y. Bokumoto, M. Itoh and H. Yoshida*

Faculty of Engineering, Shinshu University, Nagano 380-8553
**NEC Kansai, Ltd., Shiga 520-8555*

In CsCl crystals containing a small amount of Br^- impurities, three luminescence bands can be seen at 3.84, 4.35 and 5.27 eV under the excitation with UV light in the low-energy region of the fundamental absorption of host CsCl [1]. It has been suggested that the 3.84-eV band is due to radiative decay of off-centered excitons localized at Br^- impurity monomer. The 4.35- and 5.27-eV bands are likely due to off- and on-centered excitons localized at Br^- impurity dimer, respectively. In the present work, we have carried out time-resolved luminescence studies on localized excitons in CsCl:Br, in order to investigate relaxation processes of the excitons in CsCl crystals with simple cubic structure.

Figure 1 shows time-resolved luminescence spectrum of $CsCl_{1-x}Br_x$ (x = 0.005) excited with 7.56-eV light under the single-bunch operation of synchrotron radiation (SR) at 10 K. Broken curve (fast component) and solid curve (slow component) represent the counts of photons measured through the time window of 0 − 2.4 ns and 37 − 60 ns after the excitation pulse, respectively. The 3.84-eV band does not change its peak position in both spectra. On the other hand, the peak position of the 4.35-eV band shifts from 4.60 eV in the fast-component spectrum to 4.35 eV in the slow-component spectrum. From Fig. 1, it is clear that the 5.27-eV band has only fast decay component (decay time = 0.55 ns).

Decay profile of the luminescence detected at 4.35 eV, i.e., the peak position of the slow-component spectrum in Fig. 1, is shown by dotted curve in Fig. 2, where the slow decay component has been subtracted. Open circles represent the pulse shape of SR. As clearly seen, this decay profile has a rise component around 1 ns.

Luminescence spectra have also been examined in the temperature ranges from 8.3 K to 200 K under stationary UV-light excitation. It is found that the 4.35-eV band exhibits remarkable blue-shift toward 4.6 eV with increasing temperature from 8.3 K up to 40 K.

All the above results suggest that there are two excited states on the pathway of the off-center relaxation of excitons localized at Br^- dimer in CsCl system; one is a stable state responsible for the 4.35-eV luminescence, and the other is a metastable state for the 4.60-eV luminescence. At low temperatures, the localized excitons first relax to the metastable state, from which the 4.60-eV photons are emitted. A part of them are then converted to the stable state over a potential barrier, resulting in the 4.35-eV luminescence. If the temperature is increased above 40 K, the relaxed excitons are repopulated at the 4.60-eV state. According to this model, decay profile of the

luminescence detected at 4.35 eV can be expressed by the formula;

$$I(t)=\int_0^{\infty} G(\xi)\cdot\left\{W_{f1}\,e^{-(W_{f1}+W_T)(t-\xi)}+C\cdot W_{f2}\left(\frac{W_T}{W_{f1}+W_T-W_{f2}}e^{-W_{f2}(t-\xi)}-\frac{W_T}{W_{f1}+W_T-W_{f2}}e^{-(W_{f1}+W_T)(t-\xi)}\right)\right\}d\xi, \quad (1)$$

where W_{f1} and W_{f2} are the radiative transition probabilities of the 4.60- and the 4.35-eV states, respectively, and W_T is the transition rate from the 4.60-eV state to the 4.35-eV state. $G(\xi)$ is the pulse shape of SR and C is a constant which includes the ratio of the luminescence yields of the 4.60- and 4.35-eV bands. The slow decay process of the 4.35-eV state is neglected in Eq. (1). From this fit we get $1/W_{f1}$ = 1.3 ns, $1/W_{f2}$ = 3.0 ns, $1/W_T$ = 1.3 ns and C = 5. Agreement between the calculated and experimental curves seems fairly good.

The present experiment reveals that the off-centered excitons localized at Br^- dimer have two different relaxed-configurations; stable and metastable ones. This situation is somewhat different from that in alkali-halide crystals with NaCl-type structure [2].

The authors are grateful to Professor K. Sawada for useful discussion.

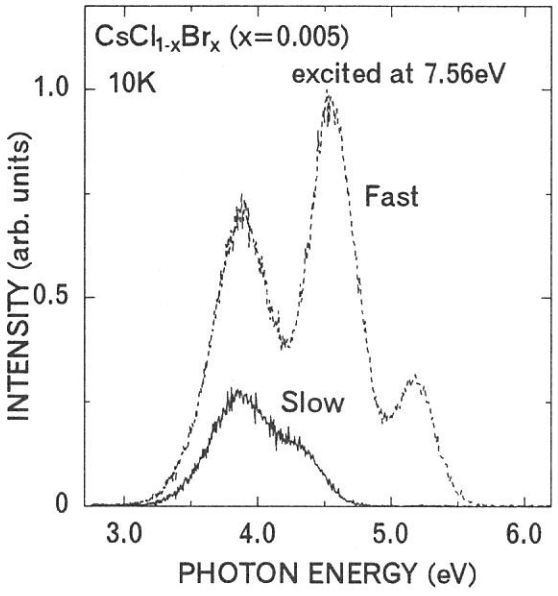

Fig.1. Time-resolved luminescence spectrum excited with 7.56-eV photons at 10K.

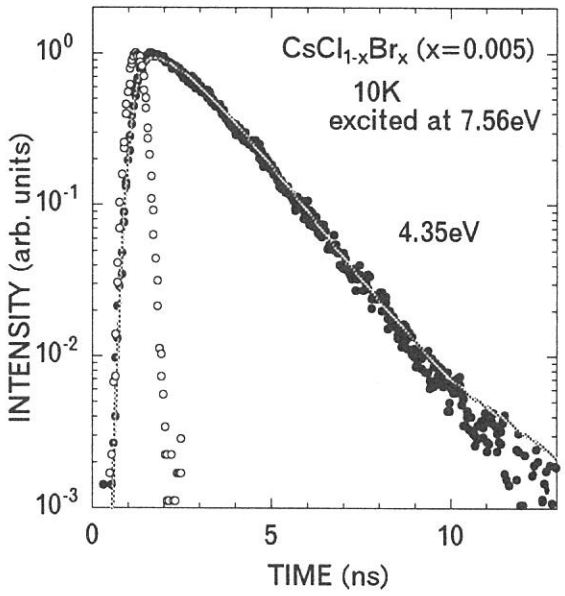

Fig.2. Decay curve (closed circles) of the luminescence detected at 4.35 eV under the excitation with 7.56-eV photon pulses at 10 K. Open circles represent the pulse shape of SR. Solid curve is the best fit of Eq. (1).

[1] H. Yoshida, N. Ohno and M. Itoh; *Proc. 2nd Int. Conf. on Excitonic Processes in Condensed Matter*, Kurort Gohrisch, edited by M. Schreiber (August, 1996) p.231.

[2] K. Kan'no, K. Tanaka and T. Hayashi; Rev. Solid State Sci. 4 (1990) 383.

(BL1B)

Two-Photon Spectroscopy of Excitons in BaF_2 by Combinational Use of Synchrotron Radiation and Laser

O. Arimoto[a], T. Tsujibayashi[b], M. Watanabe[c], S. Fujiwara[a], M. Itoh[d], S. Nakanishi[e], H. Itoh[e], S. Asaka[f], and M. Kamada[g]

[a]*Department of Physics, Okayama University, Okayama 700-8530*
[b]*Department of Physics, Osaka Dental University, Hirakata 573-1121*
[c]*Department of Fundamental Sciences, Kyoto University, Kyoto 606-8501*
[d]*Department of Electrical & Electronic Engineering, Shinshu University, Nagano 380-8553*
[e]*Department of Advanced Materials Science, Kagawa University, Takamatsu 760-8526*
[f]*Equipment Development Center, Institute for Molecular Science, Okazaki 444-8585*
[g]*UVSOR Facility, Institute for Molecular Science, Okazaki 444-8585*

One-photon spectroscopy with synchrotron radiation (SR) is a powerful and useful tool for the studies of electronic structures of various materials over a wide spectral range. On the other hand, laser has been utilized for not only one-photon spectroscopy but also multi-photon spectroscopy because of its high power and narrow spectral width. Combinational use of these two light sources is interesting and promising for the spectroscopy of solids in the VUV region. In the present study we have carried out a two-photon spectroscopy of the excitons in BaF_2 by making use of SR and laser. The valence band of BaF_2 consists of $2p$ orbital of F^-, and the conduction band $6s$ and $5d$ orbitals of Ba^{2+}. Therefore the excitons with an envelope function of S-type are one-photon allowed while the P excitons are two-photon allowed. A preliminary result at room temperature has been already reported [1, 2]. In this work, the experimental system has been improved to obtain definite results at low temperatures.

The experiments were done at BL1B of UVSOR. In Fig. 1 is shown a schematic diagram of the apparatus used for the present work. Single crystals of BaF_2 were cleaved from the ingot and mounted on a cold finger of a conduction-type cryostat. The monochromatized SR light (pulse width ~ 400 ps) was introduced into a sample chamber along the opposite direction of the second harmonic light of a Nd:YAG laser (2.33 eV, pulse width ~ 70 ns, average power ~ 12 W). The RF signal of 90 MHz from the master oscillator of the electron storage ring was divided down to 5 kHz, which triggers the YAG laser. The time interval between successive SR pulses was about 11 ns, while the time width of the laser pulse was 70 ns. Therefore, the time coincidence between the SR and laser pulses was automatically achieved, because about six pulses of the SR were involved within the time duration of a single pulse of the laser. This is an advantageous point compared to the preliminary experimental system with a short-pulse laser [1, 2], in which the temporal coincidence between the SR and laser pulses had to be carefully adjusted. Furthermore, the use of the high-repetition laser with the wide pulse-duration and low peak-power enabled us to detect weak two-photon signals more efficiently without any damage of the sample. The luminescence at about 4.1 eV, which is due to self-trapped excitons (STE's) produced by two-photon excitation, was observed by a micro-channel plate photomultiplier tube (MCP-PMT), with a combination of filters and a conventional monochromator for eliminating the scattered light from the laser. The signals from the MCP-PMT were fed to a three-channel time-gated photon counter. The photon signals just before and after the incidence of the laser pulses were counted at the channels 1 and 2, respectively: The channel 1 (CH 1) counts the background signal induced only by the SR light, while the CH 2 counts the signal due to the STE luminescence induced by the simultaneous irradiation with the SR and laser lights in addition to the background signal. The gate widths for both counters were equally set to be 4 μs by referring to the lifetime of the STE luminescence. The total signal was also counted at the CH 3 with the time-gate in full

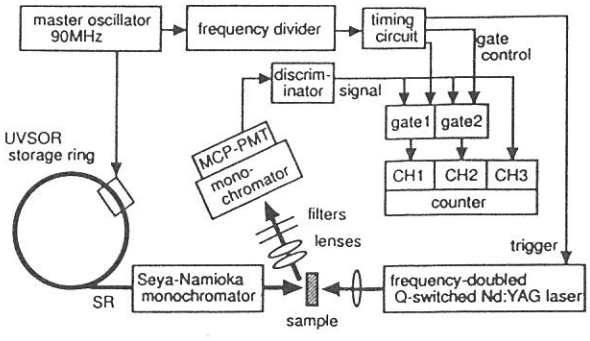

Fig. 1 Schematic diagram of the experimental system for two-photon spectroscopy with SR and laser.

open. The net luminescence signal induced by two-photon excitation was obtained by subtracting the count at CH 1 from that at CH 2. The above detection system has been specially developed for the present experiments, the details of which will be reported elsewhere [3].

Open circles in Fig. 2 show two-photon excitation spectrum of BaF_2 measured by monitoring the STE luminescence at 15 K. Its intensity corresponds to the net luminescence count obtained by subtraction of the count at CH 1 from that at CH 2. The solid curve is the total count at CH 3, which is properly normalized around 10 eV to the two-photon spectrum shown by the open circles. The closed circles are obtained by subtracting the data shown by the solid curve from those by the open circles. The count due to the net two-photon process, which is the difference between the count at CH 1 and that at CH 2, was at most 1% of that at CH 3. Accordingly the solid curve, intensity of which is proportional to the total count at CH 3, can be regarded as the one-photon spectrum induced by the SR light alone. As is easily recognized in the figure, the two-photon spectrum shown by open circles resemble the one-photon spectrum shown by solid curve. Such a similarity invokes the existence of cascade processes: Real states (or their relaxed states) excited by one photon from the SR are subsequently re-excited to the higher states by the laser, which in turn contributes to the enhancement of the STE luminescence. This is in contrast to the usual two-photon absorption process, in which virtual intermediate states are involved. In the one-photon excitation spectrum of the STE luminescence we observed weak peaks at 8.3 eV and 8.8 eV probably due to excitons bound to some unknown lattice imperfection. The energy positions of the two peaks at 10.6 eV and 11.2 eV in Fig. 2 are in good correspondence to those of the weak peaks at 8.3 eV and 8.8 eV. Therefore it is likely that the real excited states are unknown bound exciton states. Here it is noted that we made careful checks about not only the reproducibility of data but also the instruments used, especially the time-gated counter, to make sure that the obtained experimental data are reliable enough.

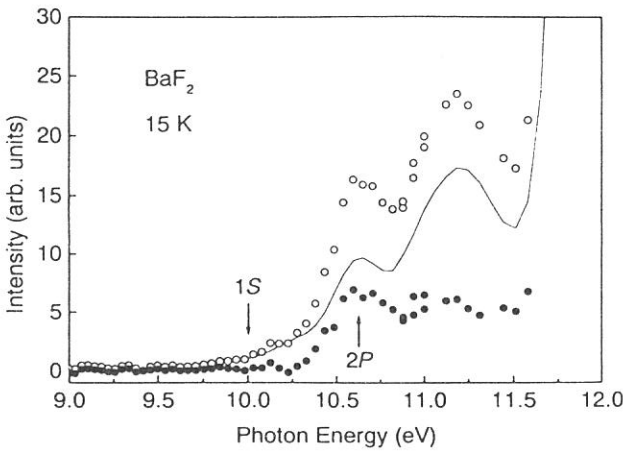

Fig. 2 The two-photon excitation spectrum of the STE luminescence in BaF_2 at 15 K (open circles). The spectrum includes two contributions: the two-photon absorption process (closed circles) and the cascade excitation process (solid curve).

As mentioned above, closed circles in Fig. 2 are the result of subtraction of the spectrum shown by the solid curve from that by the open circles. Since the former refers to the count due to the cascade process and the latter the net count due to the two-photon processes, the resultant spectrum depicted by closed circles can be regarded as the spectrum due to the usual two-photon absorption process under the assumption that the efficiency of the cascade excitation is constant. The spectrum has a broad band peaking at 10.6 eV. This is 0.6 eV higher than the $1S$ exciton whose energy position is indicated by a downward arrow. We assign this peak to the $2P$ exciton. Assuming a simple hydrogen model, the binding energy of the $1S$ exciton is estimated to be 0.8 eV, which gives the band gap energy as 10.8 eV. From measurements of reflection spectra, Rubloff has deduced the band gap energy of 11.0 eV [4], whereas Tomiki and Miyata have obtained the value of 10.6 eV [5]. It seems that the present value of 10.8 eV is more accurate because we observed the definite peak of the $2P$ exciton. Finally it is to be stressed that cascade excitation processes like the present case are not yet easy to investigate by the use of usual lasers, since their one-photon energies fall into the transparent region of the materials with wide band gap so that the real excited states can not be excited.

References

[1] T. Tsujibayashi *et al.*: UVSOR Activity Report **24** (1997) 52.
[2] M. Kamada *et al.*: *Proc. 6th Int. Conf. Synchrotron Radiation Instrum.*, Himeji, Aug. 1997 (in press).
[3] S. Asaka *et al.*: submitted to Rev. Sci. Instrum.
[4] G. W. Rubloff: Phys. Rev. **B5** (1972) 662.
[5] T. Tomiki and T. Miyata: J. Phys. Soc. Jpn. **27** (1969) 658.

(BL3A1)

Total Photoyield in Amorphous Chalcogenide Films by Undulator Radiation

Koji HAYASHI

Center for Cooperative Research, Gifu University, Gifu 501-1193

It is well-known that amorphous materials show a variety of photoinduced phenomena. The prominent photoinduced phenomenon in these materials is a time-dependent decrease in photocurrent during and after bandgap illumination.[1,2] This phenomenon is usually called photodegradation and is explained in terms of light-induced metastable defects (LIMD). In the device application of these materials, LIMD creation is a serious problem. Although a number of models have been proposed for LIMD creation[3], details of the mechanism underlying LIMD creation in these materials are still not clear. Understanding the physical mechanism underlying metastability is one of the important fundamental problems related to these materials. These phenomena were studied by exciting outer core electrons with the irradiation of the bandgap illumination. Little attention has been given to the photoinduced phenomena by exciting inner core electrons with the irradiation of higher energy photon. To obtain a wide knowledge of the photoinduced effects, it is necessary to investigate photoinduced effects on wide energy range. In the previous reports[4], we have reported the photodarkening in amorphous arsenic trisulfide (a-As_2S_3) by the vacuum ultra-violet (VUV) light. In the present study, we performed an in-situ study of the photoinduced effects by exciting inner core electrons and observed photoinduced change in total photoyield during illumination of the VUV light.

Thin films of a-As_2S_3 used for the measurements of photoyield were prepared onto quartz substrates by conventional evaporation technique. The thickness of the films was around 6000Å. An electrode using Al contact was fabricated first on the substrate for the measurements of the photoyield, before depositing the amorphous films. The experiments were performed at a BL3A1 beam line of the UVSOR facility of the Institute for Molecular Science in Okazaki. VUV light that is filtered through an Al film from undulator radiation was used to measure the photoyield. Before illumination, the samples were annealed at 443K (near the glass transition temperature) for two hours in a vacuum. To eliminate visible lights of synchrotron radiation and higher harmonics of undulator radiation, Al film was inserted between undulator and samples. The samples were fixed in sample chamber which were evacuated below 10^{-8} Torr. The photon flux of undulator radiation through Al film was estimated from the total photoelectric yield of gold mesh.

Figure 1 shows the change in the total photoyield as a function of number of photons for a-As_2S_3 at room temperature. This figure is obtained by normalizing the photoyield to the incident photon flux. As shown in the figure, the photoyield is decreased at the first stage. At the second stage, the photoyield is gradually increased and the photoyield seems to be finally saturated. This change also depends on the illumination energy of the photon. This change is similar effects with the previous report[5] in the photocurrent by VUV light. That is, the decrease and the increase in the photoyield are related with the LIMD creation (or initial defects) and photodarkening , respectively.

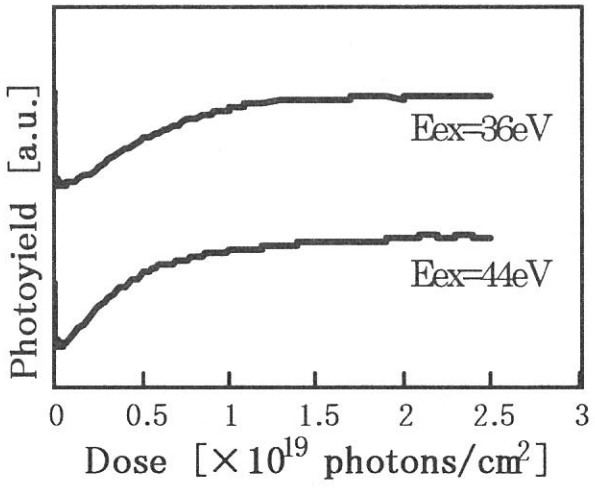

Fig.1 Change in the total photoyield for a-As_2S_3 measured at room temperature.

REFFERENCES

[1] K. Shimakawa, S. Inami, and S. R. Elliott, Phys. Rev. B, 42(1990)11857.
[2] D. L. Staebler and C. R. Wronski, Appl. Phys. Lett., 31(1977)292.
[3] K. Shimakawa, A. Kolobov, and S.R. Elliott, Adv. Phys., 44(1995)475.
[4] K. Hayashi, D. Kato, and K. Shimakawa, J. Non-Cryst. Solids., 198-200(1996)696.
[5] K. Hayashi, A. Hirai and K. Shimakawa, UVSOR Activity Report 1996, p116.

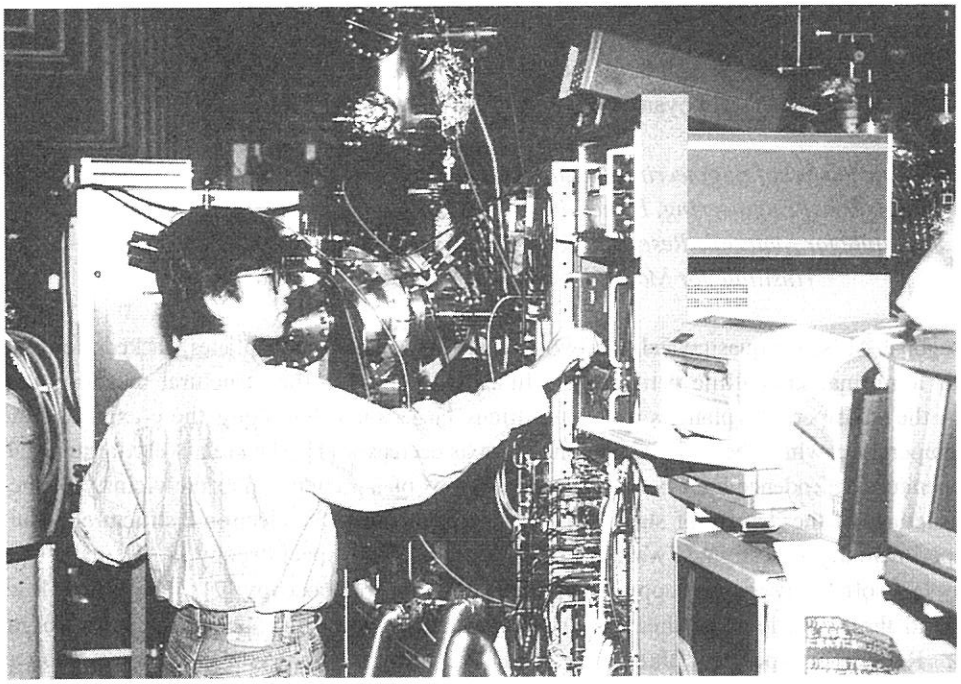

BL8B1

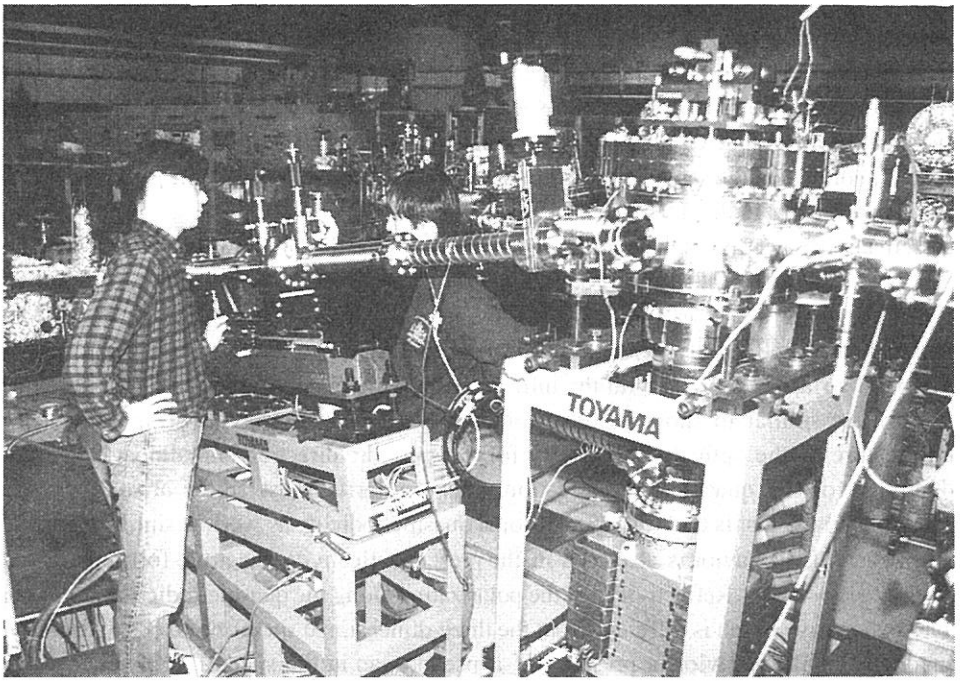

BL2B2

(BL6A1)

Infrared Reflectivity Spectra of Decagonal Al-Ni-Co Single Crystal

K. Soda, Y. Yanagida, K. Nozawa, T. Takeuchi, K. Morita, U. Mizutani,
Y. Yokoyama*, R. Note#, A. Inoue#, and S. Kimura†

Graduate School of Engineering, Nagoya University, Furo-cho, Chikusa, Nagoya 464-8603
**Faculty of Engineering, Himeji Institute of Technology, Shosha, Himeji 671-2201*
#Institute for Materials Research, Tohoku University, Katahira, Aoba, Sendai 980-8577
†Institute for Molecular Science, Myoudaiji, Okazaki 444-8585

A decagonal Al-Ni-Co quasicrystal has two-dimensional quasiperiodic planes stacked along a 10-fold axis (*c*-axis) with a normal crystalline periodicity. In accordance with the structural anisotropy, its electrical resistivity in the quasiperiodic plane is about ten times larger than that along the c-axis, and increases with decreasing temperature, while the resistivity along the axis decreases [1]. The relatively large resistivity and its negative temperature-dependence have been discussed in terms of a pseudo-gap in the vicinity of the Fermi level and spiky structures of the density of states [2]. On the other hand, the electronic structure of the quasicrystal has been experimentally investigated with use of the photoelectron spectroscopy [3, 4], inverse photoelectron spectroscopy [5], soft X-ray spectroscopy [4, 6], and tunneling spectroscopy [7]. They show lowering of the intensity around the Fermi level in their spectra, which may suggest the opening of a pseudo-gap across the Fermi level. Reflectivity spectra of three-dimensional icosahedral quasicrystals have been also studied, which shows neither Drude- nor semiconductor-type frequency dependence of their optical conductivity [8]. Here, we report a preliminary result on infrared reflectivity measurements of a decagonal single quasicrystal $Al_{72}Ni_{12}Co_{16}$ in order to obtain its optical conductivity and clarify its electronic structure.

Infrared reflectivity spectra for the incident photons polarized linearly in perpendicular and parallel with the *c*-axis, *i.e.* in the quasiperiodic and periodic directions, respectively, were measured with a standard setup of a Fourier interferometer at the beamline 6A1 of UVSOR at the temperatures of 300, 80 and 10 K. Specimens of single quasicrystals grown by a Czochralski method [9] were cut into a size of 5 mm in diameter and 1 mm in thickness, and mechanically polished along or perpendicular to the *c*-axis. Measured area was restricted to 2 mm in diameter by a conical aperture in front of the specimen. In order to correct contributions of such as surface roughness and small scratches and to obtain an absolute value of the reflectivity, we measured infrared reflectivity spectra of gold, evaporated on the same surfaces that were used for the reflectivity measurement of the specimen, and compared them with data in the reference [10].

Infrared reflectivity spectra obtained at the temperature of 300 K are shown in Fig. 1 together with those measured at BL-1 of SOR-RING, the Synchrotron Radiation Laboratory of the Institute for Solid State Physics, the University of Tokyo, in a photon energy range between 2 and 30 eV. Since we measured the photon-energy dependence of the relative reflectivity in the visible-vacuum ultraviolet (VUV) region, the visible-VUV data in the figure is plotted so as to coincide with the infrared data extrapolated to the visible region. These infrared reflectivity spectra are similar to those reported for other decagonal Al-Co-Cu-(Si) quasicrystals [11], which reveal a Drude feature in the optical conductivity for the periodic direction and almost frequency-independent optical conductivity for the quasiperiodic direction. This similarity most likely arises from the long-range ordering of these materials, that is their two-dimensional quasiperiodicity, as well as similarity in the constituent elements. The Drude-like behavior is also seen in the present reflectivity spectrum for the polarization parallel to the *c*-axis below $h\nu = 1$ eV. Reflectivity for the polarization along the quasiperiodic direction is almost unity for the low photon energy, which is different from the three-dimensional quasicrystal [8]. At present, we do not find the semiconductor-like behavior or presence of a pseudo-gap in the spectra. However, we recognize the anisotropy in the reflectivity below the photon energy $h\nu$ of 1 eV, which is apparently consistent with that in the electrical resistivity. By assuming the Drude-type frequency dependence in the low photon energy region for both directions, we can estimate the concentration of free carriers in the periodic direction to be larger than that in the quasiperiodic plane by a factor of about ten. The reflectivity spectra in the visible-VUV region do not show much difference in shape; they start to decrease at around $h\nu = 4$ eV, and show humps at $h\nu = 12$ and 18 eV. This suggests that the electronic structure relevant at least to this photon energy region is similar for both directions parallel and perpendicular to the *c*-axis. The 18-eV structure may be related to the plasmon loss peak

observed in the electron energy loss spectra of quasicrystals [11], and the 12-eV feature might be attributed to an interband transition relevant to the constituent transition metal. For further detailed discussion, we have to obtain optical conductivity or dielectric function by a Kramers-Kronig analysis, which is now in progress and will be reported elsewhere.

References

[1] T. Shibuya *et al.*, *J. Phys. Soc. Jpn.* **59** (1990) 1917.
[2] G. Trambly de Laissardiére and T. Fujiwara, *Phys. Rev.* **B50** (1994) 9843.
[3] Z. M. Stadnik *et al.*, *Phys. Rev.* **B51** (1995) 11358.
[4] K. Soda *et al.*, *Proc. of the 7th Int. Conf. on Quasicrystals, to be published.*
[5] K. Soda *et al.*, *J. Electron Spectrosc. Relat. Phenom., to be published.*
[6] E. Belin-Ferré *et al.*, *J. Phys.: Condens. Matter* **8** (1996) 9213.
[7] D. N. Davydov *et al.*, *Phys. Rev. Lett.* **77** (1996) 3173.
[8] C. C. Homes *et al.*, *Phys. Rev. Lett.* **67** (1991) 2694.
[9] Y. Yokoyama *et al.*, *Sci. Rep. RITU* **A42** (1996) 185.
[10] E. D. Palik (ed.), *Handbook of Optical Constants of Solids*, (Academic Inc., Orlando, 1985).
[11] D. N. Basov *et al.*, *Phys. Rev. Lett.* **72** (1994) 1937.
[12] M. Terauchi *et al.*, *Phil. Mag. Lett.* **74** (1996) 107.

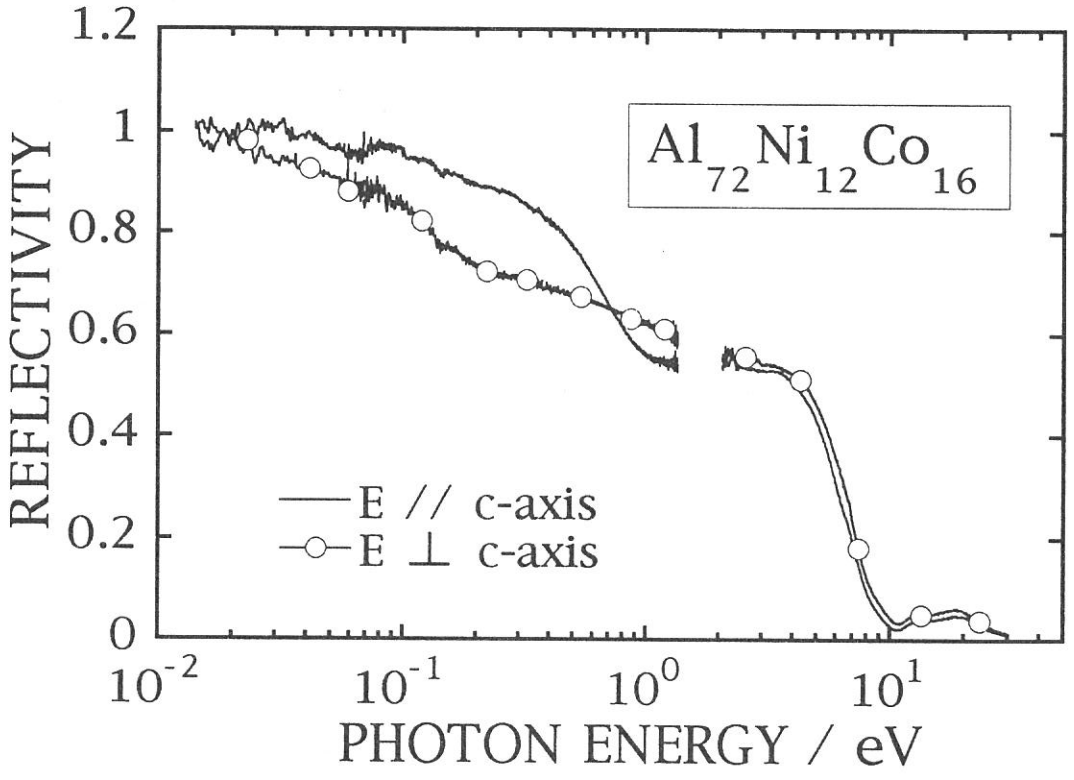

Figure 1. Reflectivity spectra of $Al_{72}Ni_{12}Co_{16}$ for the incident photons polarized in parallel with (solid curve with open circles) and in perpendicular to (solid curve) the c-axis.

(BL6A1)

Infrared magnetic circular dichroism of magnetic exciton of GdAs

Shin-ichi KIMURA, Dexin LI[1], Yoshinori HAGA[2] and Takashi SUZUKI[3]

UVSOR Facility, Institute for Molecular Science, Okazaki 444-8585
[1]Oarai Branch, Institute for Material Research, Tohoku University, Oarai 311-13
[2]Advanced Science Research Center, Japan Atomic Energy Research Institute, Tokai 319-11
[3]Department of Physics, Tohoku University, Sendai 980-77

In the last fiscal year, an infrared magneto-optical apparatus has been constructed at BL6A1 [1]. The main purpose is to measure infrared magnetic circular dichroism (IRMCD) of magnetic materials using circularly polarized infrared synchrotron radiation [2]. The experiment is expected to obtain informations of electronic structures with magnetic moments near the Fermi level. In the case of strongly correlated electron systems, the electronic structure that is made by coupling between carriers and magnetic moments appears near the Fermi level. Then the IRMCD is one of powerful tools for the investigation of such electronic structure.

GdAs is one of strongly correlated electron systems with low-carrier concentration. The physical properties are simple because it is a Heisenberg-type antiferromagnetic material with the Néel temperature of 18.7 K [3]. However, an absorption structure with strong temperature and magnetic field dependences has been found around 0.4 eV [4]. According to the temperature dependence, the absorption is considered to be due to an exciton. However, its magnetic field dependence is anomalous. To investigate the origin of the magnetic field dependence, IRMCD was performed.

Reflectivity spectra with circularly polarized infrared light in the energy range of 10 meV - 2 eV were measured under magnetic field up to 6 T and at the temperature of 6 - 60 K. The measurement was done by using fixed circular polarization direction (left circular polarization) and by using changed magnetic field direction. The reflectivity spectra in the energy range of 2 - 30 eV were measured at BL1B. After the connection of these spectra, optical conductivity spectra were derived from the Kramers-Kronig transformation of the reflectivity spectra. From here and in figures, the spectrum in the case of the magnetic field direction parallel to the polar direction of light is denoted by Δl = +1 and antiparallel is denoted by Δl = -1.

The magnetic field dependences of circularly polarized optical conductivity spectra at 6 K were shown in Fig. 1 (a). Peak energies around 0.4 eV of Δl = ±1 spectra are different from each other, i. e.,

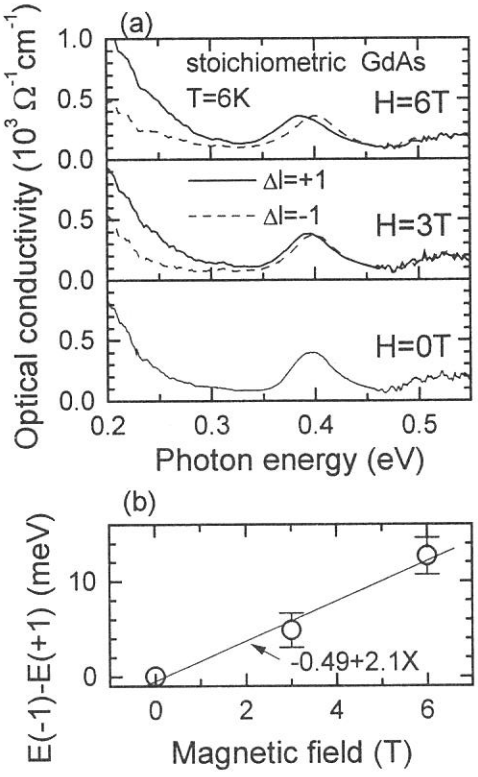

Fig. 1. (a) Magnetic field dependence of circularly polarized optical conductivity spectra at 6 K. Magnetic circular dichroism of absorption at 0.4 eV of GdAs appears. (b) The different energy (E(-1)-E(+1)) between the two peaks of Δl = ±1 as the function of applied magnetic field. The energy difference linearly changes as the magnetic field increases.

magnetic circular dichroism appears in the 0.4 eV absorption of GdAs. The difference between the two peaks ($E(-1)$-$E(+1)$) linearly increases with increasing magnetic field as shown in Fig. 1 (b). This just indicates Zeeman splitting of an exciton. The slope is determined to be 2.1 meV/T by a least square method. The value is about ten times larger than normal electron response. However, since the magnetic field applied to the exciton is induced by Gd^{3+} ions, the induced field should be considered. According to the magnetization data [3], the magnetization has linear response to applied magnetic field up to 13 T. The relation is $M = 0.4\ H$ per Gd^{3+} ion, where M means magnetization and H applied field. From the relation of $E(-1) - E(+1) = 2g\mu_B\ (H + nM)$, where g is g-factor ≈ 2, μ_B Bohr magneton and n the number of Gd^{3+} ion which makes the induced magnetic field to an exciton, the area of one exciton can be determined. The n becomes 20, i. e., one exciton expands in the volume of twenty Gd^{3+} ions.

On the other hand, the temperature dependences of circularly polarized optical conductivity spectra at ±6 T are shown in Fig. 2 (a). In comparison with the spectra at 60 K, the peak energy difference at 6 K is larger. The energy difference is plotted in Fig. 2 (b). The splitting energy increases as the temperature decreases above 20 K. However, the energy difference becomes almost constant below 20 K. Since the Néel temperature of GdAs is 18.7 K, the change of the slope comes from the magnetic transition. Therefore, the Zeeman splitting of the exciton is a signal of the magnetic transition.

---

[1] S. Kimura, UVSOR Activity Report 1996 (1997) p. 170.

[2] S. Kimura, in this issue.

[3] D. X. Li, Y. Haga, H. Shida, T. Suzuki, T. Koide and G. Kido, Phys. Rev. B **53** (1996) 8453.

[4] S. Kimura, D. X. Li, Y. Haga and T. Suzuki, UVSOR Activity Report 1996 (1997) p. 172; J. Magn. Magn. Mater. **177-181** (1998) in press.

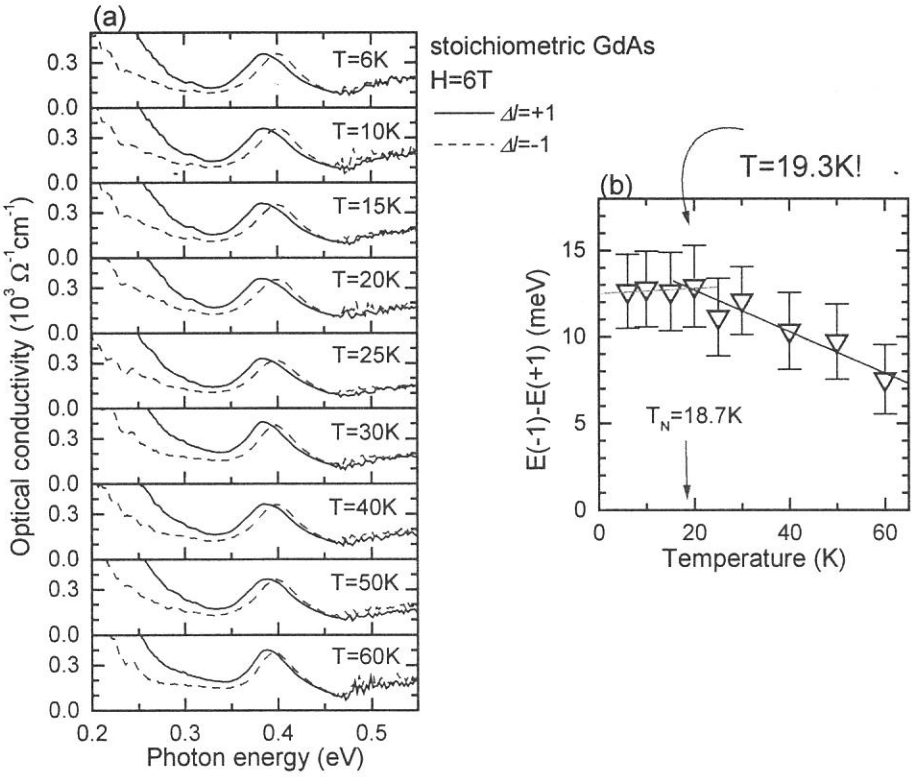

Fig. 2. (a) Temperature dependence of circularly polarized optical conductivity at ±6 T. (b) The energy difference of two peaks of $\Delta l = \pm 1$ as the function of temperature.

(BL6A1)

Heavy-Fermion-Like Optical Conductivity of Yb_4As_3

Shin-ichi KIMURA, Akira OCHIAI[1], and Takashi SUZUKI[2]

UVSOR Facility, Institute for Molecular Science, Okazaki 444-8585
[1]Department of Material Science and Technology, Niigata University, Niigata 950-21
[2]Department of Physics, Tohoku University, Sendai 980-77

Yb_4As_3 is a typical strongly correlated 4*f*-electron system with low carrier concentration. The temperature dependence of optical conductivity (OC) spectrum has been measured in the photon energy of 2 meV – 50 eV at several temperature of 39 – 320 K in the last fiscal year [1]. The result indicates that there is an absorption with strong temperature dependence around 0.4 eV. The electronic structure from which the absorption originates crosses the Fermi level and changes to conduction band with short relaxation time. Physical properties at higher temperature come from the electronic structure. After that, we measured reflectivity spectra at several temperatures down to 6 K form the investigation of the electronic structure at lower temperature and reported here.

Reflectivity spectra were measured at an infrared beam line 6A1. The magneto-optical system which was constructed in the last fiscal year [2] was used in spite of no magnetic field because measuring of temperature dependence below 100 K is easier than normal optical system of BL6A1. We discuss using OC spectra that were determined from a Kramers-Kronig analysis of the reflectivity spectra.

The OC spectra at several temperatures are shown in Fig. 1. The spectra are plotted with the DC conductivity and the carrier number derived from the Hall coefficient. Above 700 meV, the OC spectra originates from interband transitions. Therefore the temperature dependence is small. On the other hand, below 700meV, the spectrum strongly changes with temperature. The origin of a peak at 0.4 eV has already discussed [1] and mentioned before. Here, we discuss the origin of structures below 8 meV and around 30 meV. Note that some sharp peaks around 15 meV come from TO phonons. We do not discuss them in this

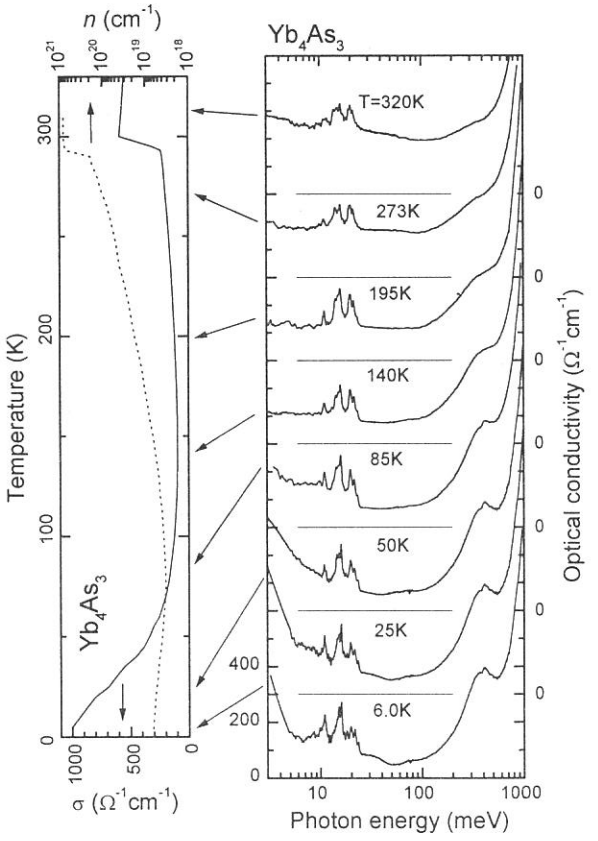

Fig. 1. Temperature dependence of optical conductivity spectrum of Yb_4As_3 with the DC conductivity and the carrier number derived from the Hall coefficient.

report.

Drude-type optical conductivity appears below 8 meV. From the carrier number and the DC conductivity, we can get a Drude function,

$$\sigma(\omega) = \left(\frac{Nm_0}{m^*}\right)\frac{e^2\tau}{m_0(\omega^2\tau^2+1)}$$

with a parameter of the effective mass, m^*. After the fitting, the effective mass is determined to be $0.7m_0$, which is equal to that of cyclotron mass derived from microwave resonance [3]. The relaxation time is 3.1×10^{-12} sec, which value is hundred times larger than that of normal metals.

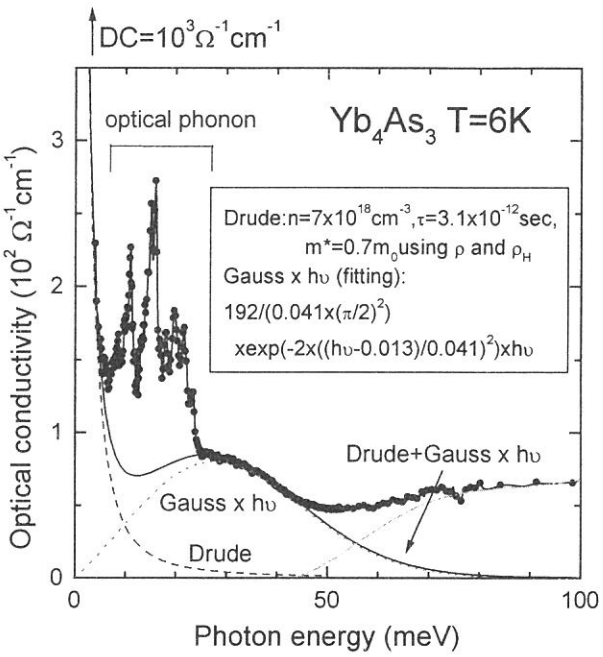

Fig. 2. Optical conductivity spectrum of Yb_4As_3 at 6 K and the fitting curves.

Around 30 meV, a shoulder develops as temperature decreases. Then we fitted the spectrum of 25 - 45 meV at 6 K. We can get a good fitting by a function of Gaussian×$h\nu$. The fitting function shows there is a peak around 30 meV, i. e., a small gap opens on the Fermi level.

According to a theory of Coleman [4], the spectrum can be explained by a Kondo lattice model. The Kondo temperature (T_K) of Yb_4As_3 is estimated to be about 100 K (8.6 meV) by the DC conductivity. Therefore the width of Drude part becomes 1 T_K and the energy of the gap becomes 3 T_K. The results are equal to the theory of Coleman. However, it is thought that the charge of Yb_4As_3 does not couple with the magnetism [5]. And also similar spectrum shape appears in organic materials, which originates from the CDW nature. Therefore the origin of the spectrum shape should be considered.

[1] S. Kimura, M. Ikezawa, A. Ochiai and T. Suzuki, J. Phys. Soc. Jpn. **65** (1996) 3591; S. Kimura, A. Ochiai and T. Suzuki, UVSOR Activity Report 1996 (1997), p. 174.
[2] S. Kimura, UVSOR Activity Report 1996 (1997), p. 170.
[3] H. Matsui *et al.*, private communication.
[4] P. Coleman, Phys. Rev. Lett. **59** (1987) 1026.
[5] A. Ochiai, private communication.

(BL6A1)

Optical reflectivity study of the Kondo insulator YbB_{12}

H. Okamura, H. Sinozaki, T. Nanba, S. Kimura[A],
F. Iga[B], N. Simizu[B] and T. Takabatake[B]

Department of Physics, Kobe University, Kobe 657-8501.
[A]UVSOR, Institute for Molecular Science, Okazaki 444
[B]Department of Materials Science, Hiroshima University, Higashi-Hiroshima 739

YbB_{12} is one of the strongly correlated electron systems known as "Kondo insulators".[1] It is paramagnetic at high temperatures, but with lowering the temperature below 75 K, χ decreases and the electrical resistivity (ρ) increases. The temperature dependences of both χ and ρ show thermally activated behaviors, and indicate the presence of an energy gap of about 10 meV. These unique behaviors are believed to arise from strong interactions between the localized f-electrons and free carriers, but the mechanism responsible for them is not exactly known yet. In particular, it is important to obtain more information about the behaviors of energy gap at low temperatures. Although infrared reflectivity measurements are very useful for this purpose, earlier optical measurements on YbB_{12} suffered from a lack of high-quality single crystal.[2,3] Recently, however, Iga, Shimizu and Takabatake have successfully grown single crystals of YbB_{12} [4]. Using BL6A1 we have measured the optical reflectivity of single crystals of YbB_{12} at various temperatures between 20 K and 300 K. Figure 1(a) shows the reflectivity spectrum of YbB_{12} at 290 K, 160 K, 78 K, and 20 K, and Fig. 1(b) shows the corresponding optical conductivity $\sigma(\omega)$ obtained from the reflectivity spectra via Kramers-Kronig analyses. At 290 K, there is a strong absorption peaked around 0.2 eV, superimposed on a broad, Drude-like free carrier contribution. This absorption peak at 0.2 eV is not seen for LuB_{12}, which has a filled f-shell and non-magnetic, and is likely to arise from f-levels located near the Fermi level. Upon cooling, the free carrier contribution is rapidly suppressed, and below 80 K the spectral weight below 20 meV in $\sigma(\omega)$ is completely depleted. Figure 2 shows the detailed temperature dependence of the gap structure seen in $\sigma(\omega)$ below 80 K. From this we can see that the gap structure in $\sigma(\omega)$ appears just below 78 K. This temperature nearly coincides with the temperature below which χ decreases rapidly, hence the gap appearance seen in $\sigma(\omega)$ is correlated with the magnetic properties. To clarify further the characteristics of the energy gap, we plan to study the reflectivity of $Yb_{1-x}Lu_xB_{12}$ with several values of x, including their response to magnetic field.

References

[1] G. Aeppli and Z. Fisk, Comments Cond. Mat. Phys. **16**, 155 (1992).

[2] P. Wachter and G. Travaglini, J. Magn. Magn. Mater. **47&48**, 423 (1985).

[3] H. Okamura et al, UVSOR Annual Report 1997, p162.

[4] F. Iga, N. Shimizu, and T. Takabatake, J. Magn. Magn. Mater. to be published.

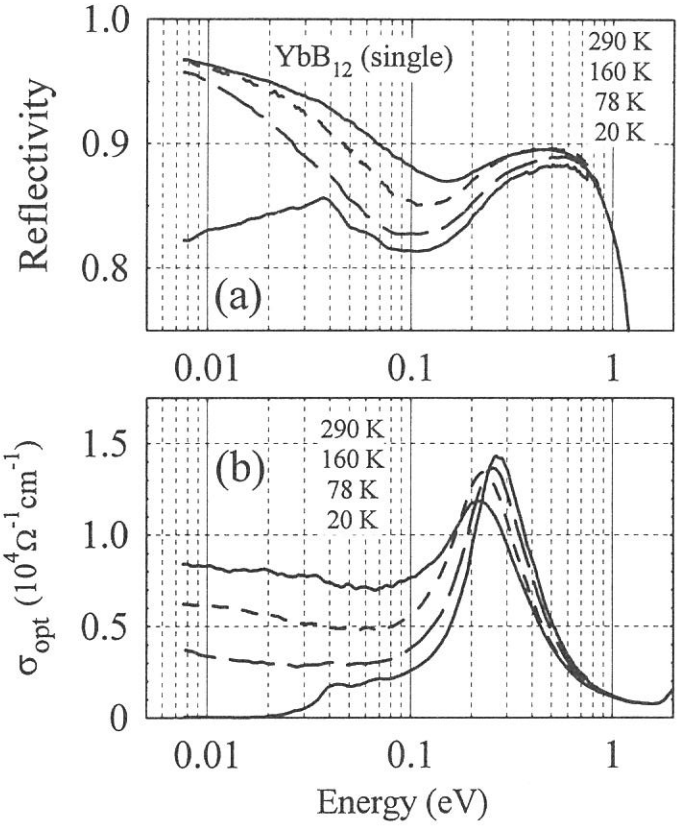

Fig.1: Reflectivity (a) and optical conductivity (b) of YbB_{12} single crystal at several temperatures.

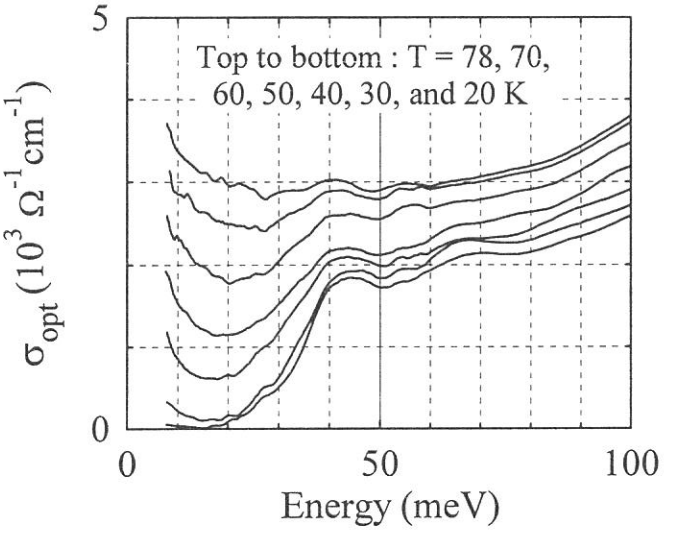

Fig. 2: Optical conductivity of YbB_{12} below 78 K.

(BL6A1)

Millimeter Wave Reflection Measurement of Secondary Battery Substance $LiNiO_2$

Hitoshi OHTA, Yoji IKEUCHI, Shunsuke ONO, Takao NANBA, Atushi HIRANO* and Ryoji KANNO*

Department of Physics, Faculty of Science, Kobe University,1-1 Rokkodai, Nada, Kobe 657

**Department of Chemistry, Faculty of Science, Kobe University,1-1 Rokkodai, Nada, Kobe 657*

Nowadays Li ion secondary battery has attracted much attention because it is a promising secondary battery due to its high energy density and light weight.[1] Although $LiCoO_2$ is already in commercial use as an electrode material in secondary Li batteries, $LiNiO_2$ is a promising candidate to replace $LiCoO_2$ from the economical point of view. This is due to the fact that Ni atoms is cheaper and easy to obtain than Co atoms. However, the composition of $LiNiO_2$ is very sensitive to the synthesis condition, especially the sintered temperature, and it can be easily lead to a decomposition to $Li_{1-x}Ni_{1+x}O_2$. The non-stoichiometry degrades the charge and discharge characteristics significantly. However, Kanno *et al.* succeeded in synthesizing nearly stoichiometric $LiNiO_2$ and they opened the way to use $LiNiO_2$ as an electrode material in secondary Li batteries.[2] The aim of our study is to obtain the information about the diffusive motion of Li^+ ions by observing "ionic plasmon" whose existence can be proved as a definite increase in a reflectivity towards a low energy side in the millimeter wave region because the mass of Li^+ ion is larger than that of electron. The first observation of ionic plasmon has been performed previously for alkali silver iodide super-ionic conductors MAg_4I_5 (M=Rb, K and NH_4) by Awano *et al.*[3]

The reflection measurements of the nearly stoichiometric $LiNiO_2$ sintered at 650°C has been performed in the spectral region from 6 to 50 cm^{-1} using the beam line BL6A1 of UVSOR. Low pass filter below 22 cm^{-1} was used for the low energy region. The temperature was varied from 79 K to 380 K and the liquid He cooled InSb detector was used. Figure 1 shows the results of our measurements. The reflection is almost flat for the observed region below 197 K. The previous measurements also showed similar behavior for 11 K.[4] However, the reflection in the low energy region increases monotonically as the temperature is increased above 300 K. This result is consistent with the fact that diffusive motion of Li^+ ions is low at low temperature but starts to increase above 300 K. Therefore the temperature dependence strongly suggests that the increase of the reflection in the low energy side is due to the ionic plasmon of Li^+ ion. The detailed analysis of the data is underway.

Acknowledgments: One of the authors (HO) is grateful to Murata Science Foundation for the financial support.

References

[1] S. Megahed and B. Scrosati: The Electrochemical Society Interface, Winter (1995) 34.

[2] R. Kanno *et al.*: J. Solid State Chem. **110** (1994) 216.

[3] T. Awano *et al.*: Solid State Ionics **53-56** (1992) 1269.

[4] H. Ohta et al.: UVSOR Activity Report (1996) 182.

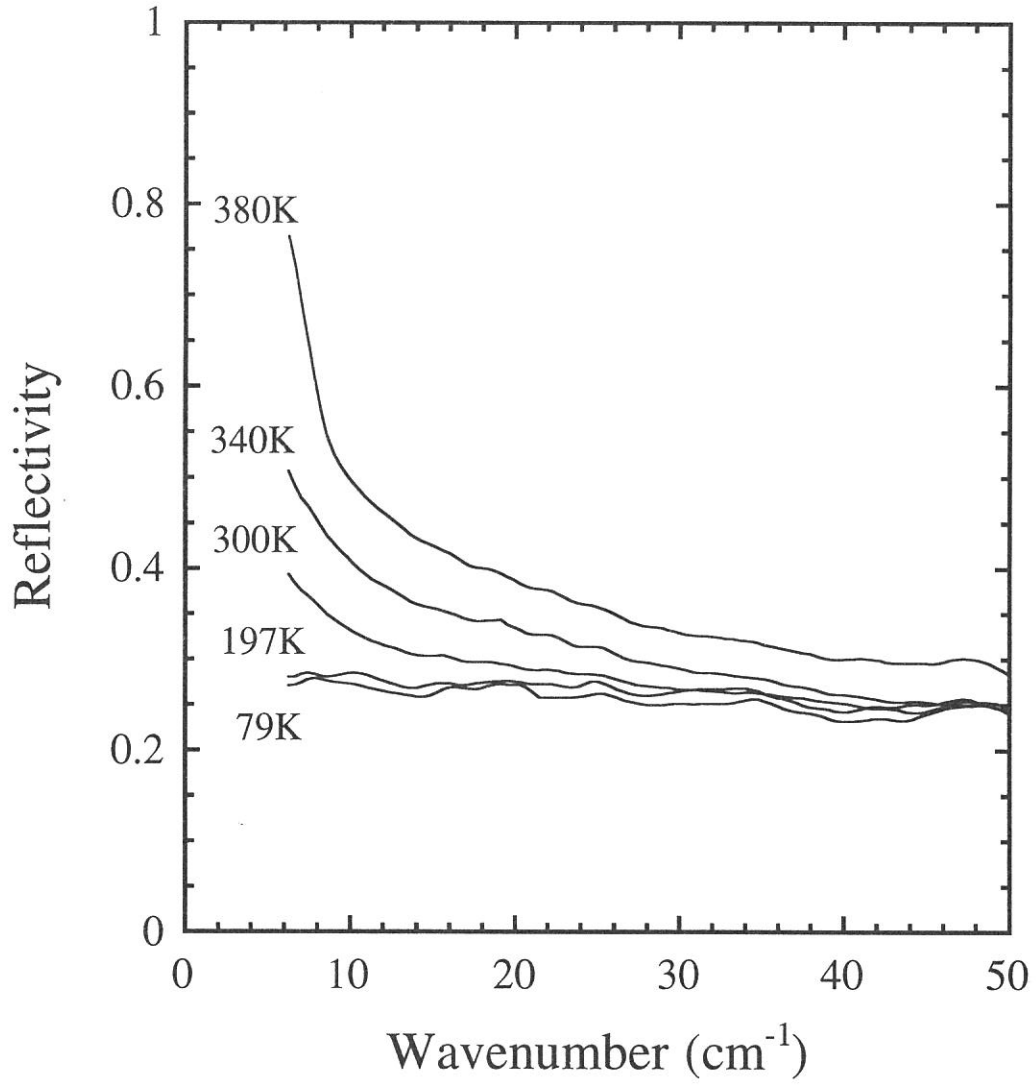

Fig. 1 The reflection spectra of the nearly stoichiometric $LiNiO_2$ sintered at 650°C.

(BL6A1)

Far-infrared Reflection Spectrum of Ice Ⅷ

Masato Hayashi and Takao Nanba[A]

Faculty of Natural Science , Kobe University, Nada-ku, Kobe 657-8501
[F]*aculty of Science, Kobe University, Nada-ku, Kobe 657-8501*

Ice has more than ten stable phase according to the environment of pressure and temperature. At Ⅶ, the oxygen atom of the hydrogen molecule forms two net works with a diamond structure (Fig.1). Two net works intersect each other and the position of the proton atoms is in disorder. At Ⅷ, on the other hand, the oxygen atoms form the same two net works with a diamond structure, but the position of proton forming the hydrogen bonding with oxygen atom is in order. Consequently, Th. orientation of the dipole moment of the water molecule in the one net work has the same direction and the one in the other net work has the opposite direction. That is, the only difference between two phases in structure is the order-disorder on the proton configuration.

Hitherto, various types of spectroscopic studies have been done on ice. However, the far infrared spectroscopy on ice under pressure has not been done except only one [1] because of the difficulty in doing the experiment using a diamond anvil cell (DAC). The transmission light intensity through DAC is too weak to detect. Kobayashi *et al* made the transmission measurement on very thin ice at low temperature and observed the anomalous pressure dependence of the phonon frequencies of ice at the phase Ⅷ[1]. Unfortunately, the signal showed a saturation around the region of the absorption peak due to the infrared active phonon mode because of the strong absorption. We made a far-infrared reflection measurement on ice under pressure using a DAC and synchrotron radiation (UVSOR) , and succeeded ,for the first time, to measure the change in the far-infrared reflection spectra on ice due to the phase transition between Ⅶ and Ⅷ phases.

Fig.2 shows the developments of the power spectra on ice under pressure in the far-infrared region. The sample was compressed up to 2.6 GPa at room temperature (Ⅶ) and then cooled down to Ⅷ phase. A new peak was resolved around 220 cm^{-1} at Ⅷ phase which corresponds to the TO phonon mode at Ⅷ phase. The ratios of spectra at Ⅷ phase to that at Ⅶ phase was shown in Fig.3. The peak at Ⅷ phase showed a blue shift of about 17 cm^{-1}/GPa to pressure .

[1] M.Kobayashi; Solid State Physiscs (Japan) 31,(1996)127.

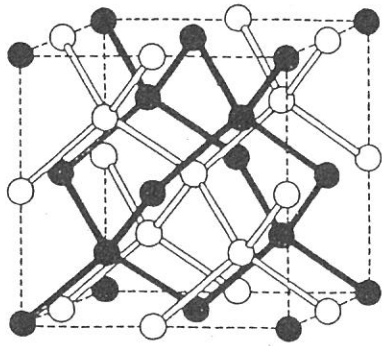

Fig.1 Crystal structure of ice at Ⅶ and Ⅷ phases. The open and closed circles corespond to oxgen atoms and show two net works with a diamond structure.

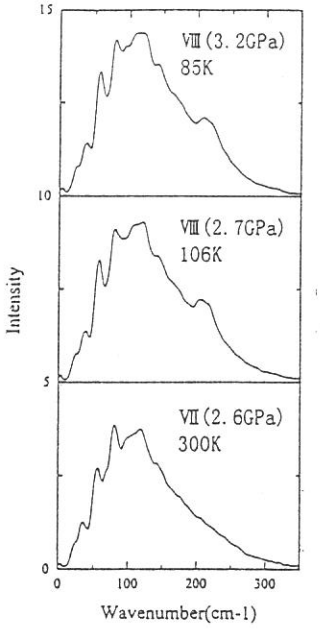

Fig.2 shows the development of the spectra of ice under pressure.

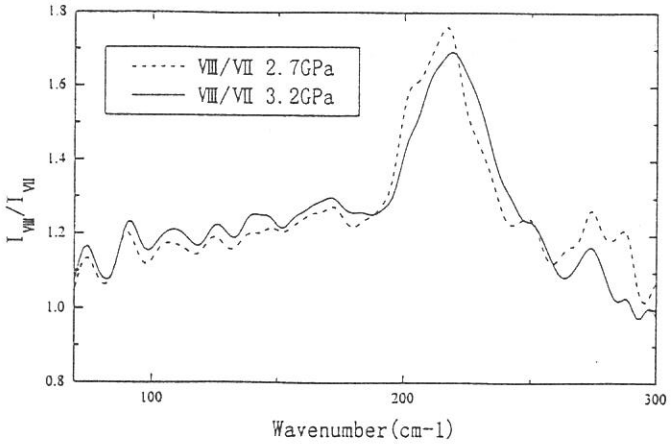

Fig.3 shows the ratios of spectra at Ⅷ phase at 2.7(dot) and 3.2 GPa(solid curve) to that at Ⅶ phase.

(BL6A1)

IR reflection and magneto-reflection of the $Yb_4(As_{1-x}Sb_x)_3$ system

Raniero Pittini [a], Mikihiko Ikezawa [a], Akira Ochiai [b], Hidekazu Aoki [c] and Takashi Suzuki [c]

[a] *Research Institute for Scientific Measurements, Tohoku University, Sendai 980-77, Japan*
[b] *Department of Material Science and Technology, Niigata University, Niigata950-21, Japan*
[c] *Department of Physics, Faculty of Science, Tohoku University, Sendai 980-77, Japan*

After the study of the optical response of $Yb_4(As_{0.88}Sb_{0.12})_3$ and $Yb_4(As_{0.71}Sb_{0.29})_3$ performed extensively last year over a wide energy range from 1 meV to 5.5 eV, this year we focused on two points, i.e. *a)* the temperature dependence of the IR optical signal (in the photon energy region of the free carrier absorptions and phonon absorptions) and *b)* the field dependence of the optical absorption of the $4f \rightarrow 5d$ transitions.

a) Temperature dependence of the IR optical signal

The free carrier contributions to the optical signal can be fitted with a Drude model, yielding the plasma frequency ω_p and the scattering rate γ as parameters. Repeating this fit for all the measured temperatures, one can determine the effective mass of the charge carriers from the plasma frequency, taking the carrier density from the Hall data. The result is shown in Fig. 1.

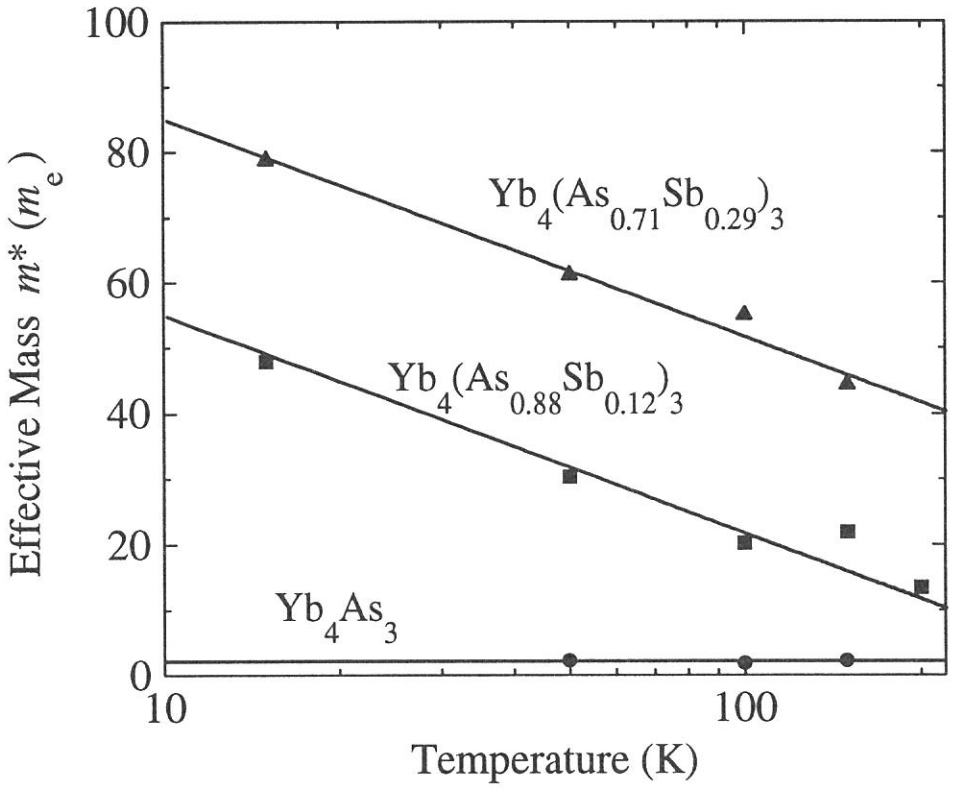

Fig. 1: Temperature dependence of the effective mass in the Yb_4X_3 system, obtained from the optical data (R. Pittini et al., ICM'97, scheduled for J. Magn. Magn. Mat. **177-181** (1998)).

The effective mass of the carriers in Yb_4As_3 is not particularly enhanced and temperature independent, while the effective masses in $Yb_4(As_{0.88}Sb_{0.12})_3$ and $Yb_4(As_{0.71}Sb_{0.29})_3$ have a logarithmic temperature dependence, and reach the values of 55 m_e and 85 m_e at 10 K, respectively. Therefore, the Sb-substituted samples are nearer to a heavy fermion than 'pure' Yb_4As_3.

b) Field dependence of the optical absorption of the $4f \rightarrow 5d$ transitions

The magneto-reflection of the $4f \rightarrow 5d$ transitions in $Yb_4(As_{0.88}Sb_{0.12})_3$ and $Yb_4(As_{0.71}Sb_{0.29})_3$ is very strong (Fig. 2), in particular the sharp peak at 0.4 eV. This indicates that the magnetic dichroism is strong in the Sb-substituted samples, while it appears to be weak in 'pure' Yb_4As_3. For the peaks between 0.1 and 0.3 eV and at 0.5 eV, the origin is still unclear. But similar effects have been reported recently at very high fields in low dimensional systems (J.S. Brooks, RHMF'97). The Yb_4X_3 materials are indeed low dimensional systems, as the $4f$ bands are one-dimensional. But the $Yb_4(As_{1-x}Sb_x)_3$ system is particular because the anomalies appear already at moderately low fields.

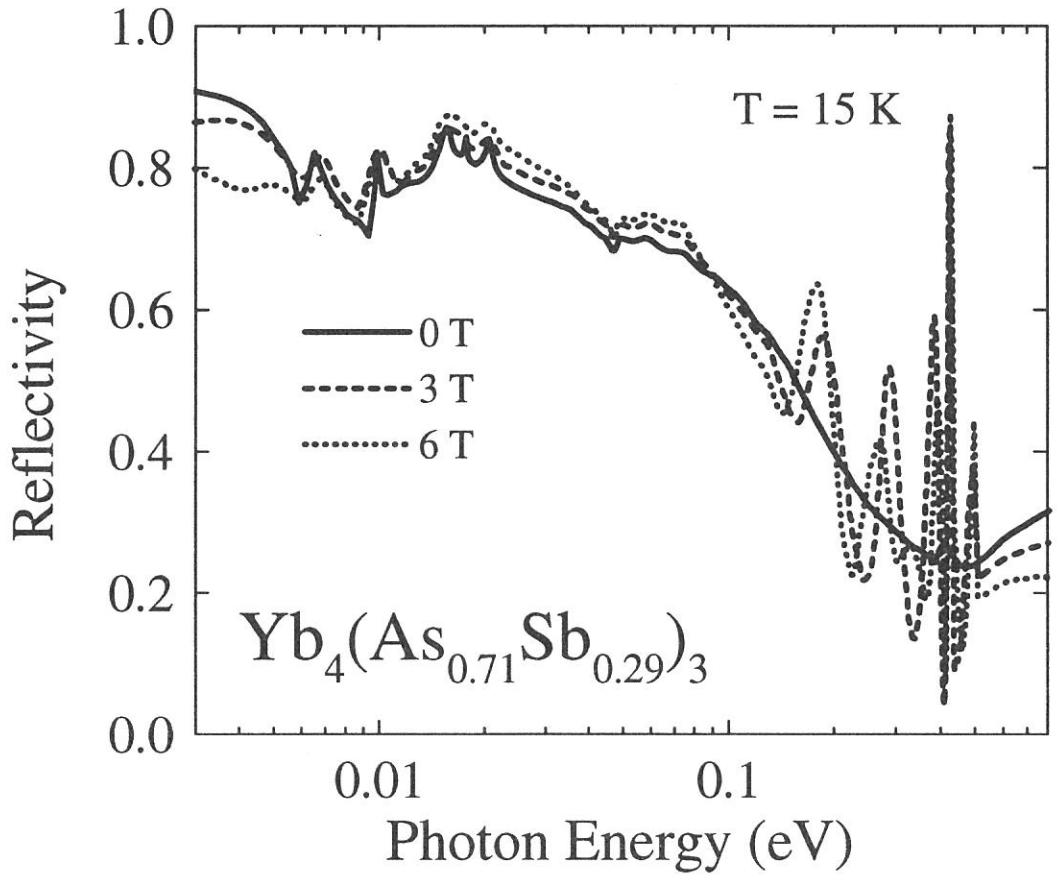

Fig. 2: Field dependence of the optical reflection in $Yb_4(As_{0.71}Sb_{0.29})_3$ at 15 K. (R. Pittini et al., RHMF'97, to be published in Phys. B).

(BL6A1)

Millimeter Wave Spectroscopy of Superionic Conducting Glasses

Naotake Sasaki, Katsuyoshi Handa and Teruyoshi Awano

Department of Applied Physics, Tohoku Gakuin University, Tagajo 985-0873

There are few precise optical measurements of superionic conducting glasses in the spectral region between millimeter wave and far-infrared. An optical absorption band by a collective motion of mobile ions may appear in this spectral region, in which motion of mobile ions switches from translation to vibration. Such collective motion may be one reason of the high ionic conductivity of these glasses even at low temperature.

We had investigated far-infrared and millimeter wave spectra of some silver or copper ion conductors to study the dynamics of mobile ions. In AM_4X_5 (A=alkali metal; M=Ag or Cu; X=halogen) crystal, a structure by "ionic plasmon" was observed in the spectral region below 10 cm^{-1} in silver ion conductors or 30 cm^{-1} in copper ion conductors in energy loss function spectra at temperatures of superionic conducting phase[1].

In this study, we report results on $(AgI)_x(AgPO_3)_{1-x}$, $(TMAI)_{0.1}(TEAI)_{0.1}(AgI)_{0.8}$, (TMAI=$(CH_3)_4NI$, TEAI=$(C_2H_5)_4NI$) superionic conducting glasses comparing the results of copper ion conducting glasses in the millimeter wave region. Large alkylammonium ions disperse randomly into AgI in organic-inorganic glasses in contrast to oxide tetrahedrons in inorganic glasses.

Optical constants were obtained from reflectivity spectra by K-K analysis. In the millimeter wave region, the transmittance spectra of samples with different thickness were measured directly. Absorption coefficient spectra of this spectral region were calculated from them.

Fig. 1 shows AgI composition dependence of intensity of absorption bands in millimeter wave region. As the AgI composition decreased, the absorption intensity around 7 cm^{-1} decreased. Fig. 2 shows temperature dependence of this absorption band. The 7 cm^{-1} band decreased as temperature decreased. This suggest that the absorption around 7 cm^{-1} is due to a sort of diffusive motion of conduction ions. The 7 cm^{-1} band in AgI-$AgPO_3$ shifted to 9 cm^{-1} in CuI-$CuPO_3$. The square root of mass ratio of silver and copper ion is 1.3. Therefore the wave number shift of these absorption bands means that these bands are due to movements of conduction ions.

Fig. 3 shows the spectral change of the absorption spectra in millimeter wave region of $(TMAI)_{0.1}(TEAI)_{0.1}(AgI)_{0.8}$ glass as temperature decreased. The same spectral change as AgI-$AgPO_3$ was observed. Fig. 4 shows spectral change of the absorption band in millimeter wave region between $(TMAI)_{0.1}(TEAI)_{0.1}(AgI)_{0.8}$ and $(TMAI)_{0.15}(TEAI)_{0.1}(CuI)_{0.75}$. The 8 cm^{-1} peak in $(TMAI)_{0.1}(TEAI)_{0.1}(AgI)_{0.8}$ shifted to 11 cm^{-1} in $(TMAI)_{0.15}(TEAI)_{0.1}(CuI)_{0.75}$. This shift coincides with the inverse square root of mass ratio of sliver and copper. This suggest that this band is due to a motion of conduction ions.

The absorption band in millimeter wave region is due to a sort of diffusive motion of conduction ions. Detail of this motion of conduction ions is under investigation.

References

1) T. Awano, T. Nanba and M. Ikezawa, Solid State Ionics, **53-56**, 1269 (1992).

2) J. Kawamura et al., Solid State Ionics, **86-88**, 517 (1996).

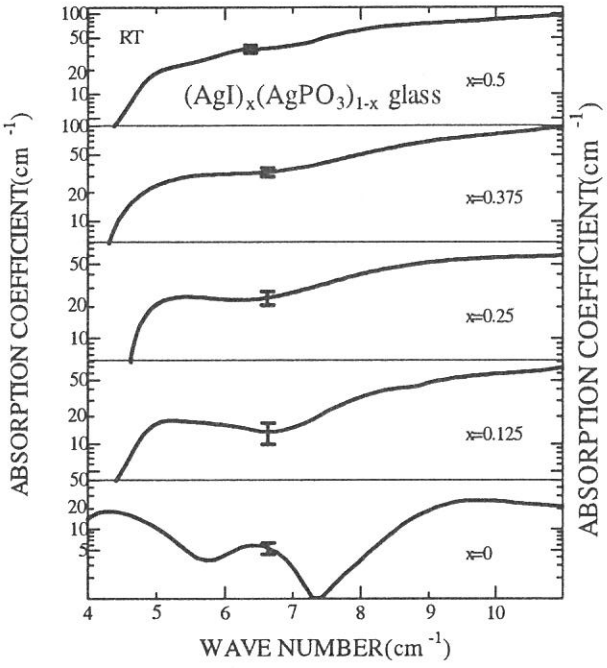

Fig. 1. Spectral change in millimeter wave region of $(AgI)_x(AgPO_3)_{1-x}$ to AgI composition.

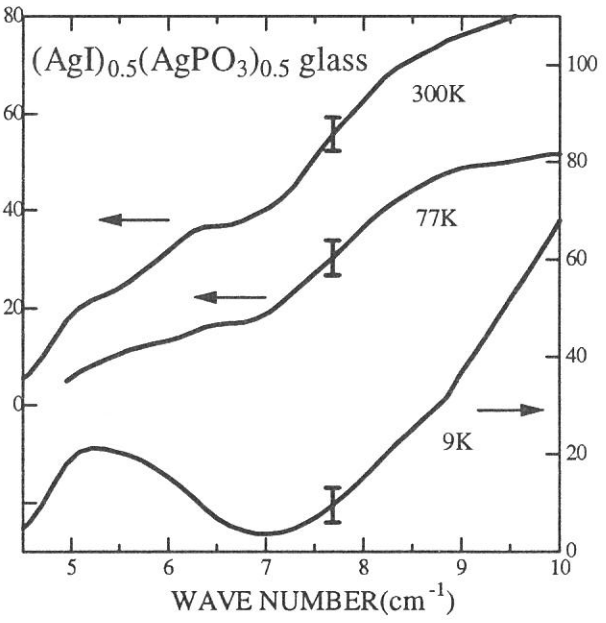

Fig. 2. Spectral change in millimeter wave region of $(AgI)_x(AgPO_3)_{1-x}$ to temperature.

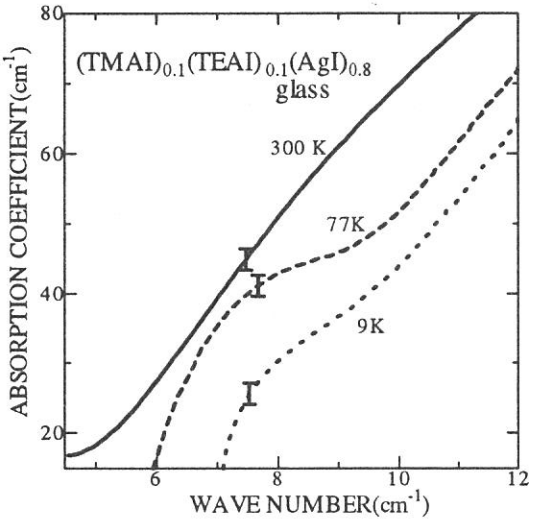

Fig. 3. Spectral change in millimeter wave region of $(TMAI)_{0.1}(TEAI)_{0.1}(AgI)_{0.8}$ to temperature.

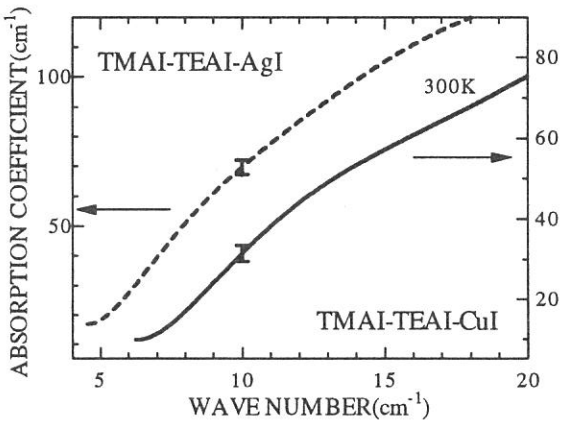

Fig. 4. Spectral change between $(TMAI)_{0.1}(TEAI)_{0.1}(AgI)_{0.8}$ and $(TMAI)_{0.15}(TEAI)_{0.1}(CuI)_{0.75}$ in millimeter wave region.

(BL6A1)

Effect of Photo-excited Carriers on Infrared Reflectivity in InGaN Single Quantum Well Structures

Takahiro DEGUCHI, Takayuki SOTA, Shigefusa CHICHIBU[A],
Takashi AZUHATA[B], Shingo ONO[B], Shinji IZUMIDA[B], Hideyuki OHTAKE[B],
Nobuhiko SARUKURA[B], and Shuji NAKAMURA[C]

Department of Electrical, Electronics, and Computer Engineering, Waseda University, 3-4-1 Ohkubo, Shinjuku, Tokyo 169-8555, Japan
[A]Faculty of Science and Technology, Science University of Tokyo, 2641 Yamazaki, Noda, Chiba 278-8510, Japan
[B]Laser Research Center, Institute for Molecular Science, 38 Nishigonaka, Myodaiji, Okazaki, Aichi 444-8585, Japan
[C]Department of Research and Development, Nichia Chemical Industries Ltd., 491 Oka, Kaminaka, Anan, Tokushima 774-8601, Japan

Recent development of growth techniques for GaN and related nitrides has realized the commercial production of superbright blue and green light emitting diodes based on InGaN single quantum wells, [1] and the room temperature cw operation of InGaN multi-quantum-well laser diodes in the purplish-blue energy region. [2] The life time of laser diodes is more than 10,000 hours. [3] Although it has been reported the excitons localized into certain potential minima caused by the fluctuation of In mole fraction in InGaN contribute to the spontaneous emission in the purplish-blue, blue, and green light emitting diodes, [4,5] the lasing mechanism in the purplish-blue laser diodes is not clear at present. It is important to study the effect of carriers created in InGaN quantum wells.

We investigated the reflectivity change of InGaN single quantum well structures in the infrared region, which would be caused by photo-excited carriers. The samples used here were prepared by the two-flow metalorganic chemical vapor deposition method [6] on the c-plane of sapphire substrates with low-temperature-grown GaN buffer layers. The exact sample structure was p-GaN(0.5 μm)/p-AlGaN(100 nm)/$In_xGa_{1-x}N$(3 nm)/n-GaN(4 μm)/GaN buffer(30 nm)/sapphire substrate. The values of x were 0.3 and 0.45, which correspond to blue and green light emitting diodes, respectively. Infrared reflectivity spectra were measured using BL6A1 at room temperature and 80 K. As light sources to create carriers, 325.0 nm line of a He-Cd laser and 476.5, 488.0, and 514.5 nm lines of an Ar^+ laser were used. Maximum powers for respective lines were 0.02, 1.2, 3.1, and 1.2 W.

The infrared reflectivity spectra measured without laser irradiation show intrinsic phonon structures from GaN layers. The signal from InGaN layer was too thin to be observed. When the laser was irradiated, unfortunately, no change were observed. Some of possible reasons are that the laser powers were too low to cause observable reflectivity changes and that the absorption coefficient of the samples in the visible wavelength region was too small to excite carriers effectively.

The authors are grateful to Dr. S. Kimura for his experimental support, and also to Profs. H. Nakanishi and K. Suzuki and Monsieur T. Gejo for their continuous encouragement.

[1] S. Nakamura, M. Senoh, N. Iwasa, S. Nagahama, T. Yamada, and T. Mukai, Jpn. J. Appl. Phys. 2 **34**, L1332(1995).
[2] S. Nakamura, M. Senoh, S. Nagahama, N. Iwasa, T. Yamada, T. Matsushita, Y. Sugimoto, and H. Kiyoku, Appl. Phys. Lett. **69**, 4056(1996); S. Nakamura, M. Senoh, S. Nagahama, N. Iwasa, T. Yamada, T. Matsushita, Y. Sugimoto, and H. Kiyoku, Jpn. J. Appl. Phys. 2 **36**, L1059(1997).
[3] S. Nakamura, M. Senoh, S. Nagahama, N. Iwasa, T. Yamada, T. Matsushita, H. Kiyoku, Y. Sugimoto, T. Kozaki, H. Umemoto, M. Sano, and K. Chocho, the 2nd International Conference on Nitride Semiconductors, Tokushima, Japan, 1997.
[4] S. Chichibu, T. Azuhata, T. Sota, and S. Nakamura, Appl. Phys. Lett. **69**, 4188(1996).
[5] Y. Narukawa, Y. Kawakami, Sz. Fujita, Sg. Fujita, and S. Nakamura, Phys. Rev. B **55**, R1938(1997).
[6] S. Nakamura, Y. Harada, and M. Senoh, Appl. Phys. Lett. **58**, 2021(1991).

(BL6A1)

Complex refractive index measurement of various semiconductors in the far-infrared region

Hideyuki OHTAKE, Takashi AZUHATA, Shingo ONO[A], Takeyo TSUKAMOTO[A],
Zhenlin LIU, Shinji IZUMIDA, Takahiro DEGUCHI[B], Takayuki SOTA[B],
and Nobuhiko SARUKURA

Laser Research Center for Molecular Science,
Institute for Molecular Science (IMS), Myodaiji, Okazaki 444-8585,
[A]Faculity of Science, Department of Applied Physics, Science University of Tokyo,
1-3, Kagurazaka, Shinjuku, Tokyo 162-0825
[B]Department of Electrical, Electronics and Computer Engineering, Waseda University,
3-4-1, Ohkubo, Shinjuku, Tokyo 169-8555

The devices and applications to ultrafast opt-electronics of THz radiation or far infrared light from various devices have been intensively studied. [1,2] For the design of various devices in the THz-radiation region, precise information of material properties is strongly required. In particular, precise index refractive and optically and electrically induced index change of typical semiconductors are matter of interest. However, there were few reliable reports of such complex index measurement in the THz-radiation region. Development of complex index measurement system in the far infrared region will open up possibilities for the material research of new high-speed opt-electric devices utilizing THz radiation. There are a few reports[4] that describe how photoexcited carriers in semiconductors change complex-index in the far-infrared region. These works [4,5] have led to not only picosecond time resolved index change measurement [6] but also THz-tomography [7] and THz-ranging[8].

We measured reflectivity change of GaAs and InAs in the THz-region at room and liquid nitrogen temperature by irradiating an Ar ion laser (e.g. 488 nm to 514.5 nm) and HeCd laser light. Infrared reflectivity spectra were obtained by using BL6A1. We investigated exciting wavelength dependence of infrared reflectivity. At room temperature, we did not observe any changes among them. It means that the number of photoexcited carriers in GaAs and InAs do not have any excitation wavelength dependence, because their carrier densities are almost the same due to penetration depths. At liquid nitrogen temperature, unfortunately, we can not obtain reasonable data. Some possible reasons are that the laser power was so high that local heating effect took place and that As component vaporized by heat. To overcome these problems, we should make thin semiconductor films or well defined clear semiconductor surfaces preparing in ultra high vacuum.

The authors are grateful to Dr. S. Kimura for his helpful experimental support, and also to Dr. T. Gejo for his strong encouragement.

References

[1] D. H. Auston, Appl. Phys. Lett. 43, 713 (1983).
[2] P. C. M. Planken, M. C. Nuss, W. H. Knox, D. A. B. Miller, and K. W. Goossen, Appl. Phys. Lett. 61, 2009 (1992).
[3] P. B. Corkum and D. Keith, J. Opt. Soc. Am. B2, 1873 (1985).
[4] H. Ohtake, Z. Liu, S. Izumida, T. Yamanaka, N. Sarukura, K. Koyama, and T. Suemoto, CLEO Pacific Rim '97, paper P50.
[5] S. L. Chuang, S. Schmitt-Rink, B. I. Greene, P. N. Saeta, and A. F. J. Levi, Phys. Rev. Lett. 68, 102 (1992).
[6] B. I. Greene, J. F. Federici, D. R. Dykaar, A. F. J. Levi, and L. Pfeiffer,Opt. Lett. 16, 48 (1991).
[7] D. M. Mittelman, S. Hunsche, L. Boivin, and M. C. Nuss, Opt. Lett. 22, 904 (1997).
[8] R. A. Cheville, R. W. McGowan, and D. Grischkowsky, OSA TOPS Vol. 13 Ultrafast Electronics and Optoelectronics, 222-227 (1997).

(BL1A)

Ni 3p and 3s resonant photoionization at the Ni 2p excitation of Ni

Yasutaka Takata, Takaki Hatsui and Nobuhiro Kosugi

The Graduate University for Advanced Studies, Institute for Molecular Science, Myodaiji, Okazaki 444-8585

Recently core excitation and deexcitation processes have been investigated in detail for various systems. For the planar nickel complexes, a number of satellite series in the Ni 3p and 3s regions are strongly enhanced by the Ni 2p resonant excitations and lowers its kinetic energy for the higher resonance energy, showing one-to-one correspondence with the excited state [1–3]. Furthermore, it was revealed that the kinetic energy shift relative to the photon energy is strongly influenced by the intermolecular interaction [3].

In the present study, we have measured resonant photoelectron spectra in the Ni 3p and 3s ionization regions at the Ni 2p edge of Ni. It is interesting to know the resonant behaviors in Ni which has metallic bond with a much shorter Ni–Ni distance than those of the molecular solids.

Experiments were performed at BL1A soft x-ray beamline. A sample of Ni was evaporated on Ni plate in a vacuum of 2×10^{-10} Torr. A pair of beryl ($10\bar{1}0$) crystal was used as a monochromator. The Ni 2p photoabsorption spectra were measured by monitoring the total electron yield. A SCIENTA SES200 electron energy analyzer was used to measure the photoelectron spectra. The total energy resolution in the photoelectron spectra was about 0.7 eV.

Figure 1 shows the Ni 2p photoabsorption spectrum of Ni. Figure 2 shows the resonant photoelectron spectra in the Ni 3p and 3s ionization regions measured at the excitation energies (0–6) marked in Fig. 1. The normal Auger spectrum (N) measured at the photon energy of 900 eV is also shown. Similarly to the case of Ni planar complexes, Ni 3p and 3s primary ionization peaks labeled with an asterisk (*) are not enhanced by the resonant excitation. On the other hand, the weak satellite bands (a–e) in the non-resonant spectrum (0) are strongly enhanced at the lowest Ni $2p_{3/2}$ resonance (1). The kinetic energies of these bands are linearly dispersive as a function of the photon energy below the resonance maximum (1). Above the maximum, photon energy dependence changes drastically; i.e., the kinetic energies are independent of the photon energy and are the same as those in the normal Auger spectrum (N). These photon energy dependences of the kinetic energy shift have been reported by Weinelt at al. for the 6 eV satellite in the valence band of Ni [4]. However, the observed photon energy dependence in Ni is different from that in the planar nickel complexes and indicates that the photoexcited electron in the intermediate and/or the Auger final states does not strongly localized. In the Ni $2p_{1/2}$ excitation region, the new satellite bands (a'–e') are enhanced and show similar photon energy dependence as in the Ni $2p_{1/2}$ excitation region.

References

[1] Y. Takata, M. Nakamura and N. Kosugi, UVSOR Active. Rep. (1995) 50.

Y. Takata, M. Nakamura and N. Kosugi, Chem. Phys. Lett., in press.

[2] Y. Takata, M. Nakamura, Y. Yamamoto, T. Yokoyama, T. Ohta and N. Kosugi, UVSOR Active. Rep. (1996) 48.

Y. Takata, M. Nakamura and N. Kosugi, J. Electron Spectrosc. in press.

[3] Y. Takata, T. Hatsui and N. Kosugi, ibid.

[4] M. Weinelt, A. Nilsson, M. Magunson, T. Wiell, N. Wassdahl, O. Karis, A. Föhlisch, N. Mårtensson, J. Stöhl and M. Samant, Phys, Rev. Lett., 78 (1997) 967.

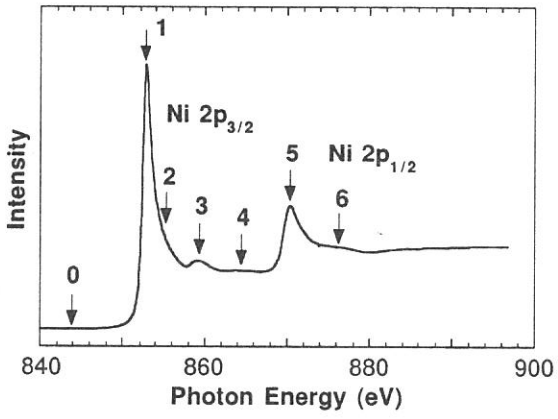

Fig. 1. Ni 2p photoabsorption spectrum of Ni.

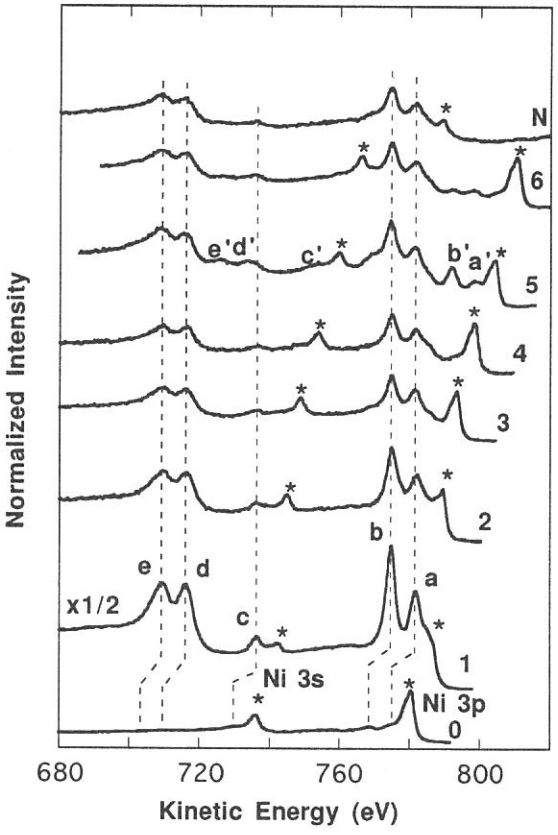

Fig. 3. Resonant photoelectron spectra in the Ni 3p and 3s regions of Ni at the photon energies marked in Fig. 2.

(BL1A)

Polarized Ni 2p photoabsorption spectra of $Ni^{II}(mnt)_2^{2-}$ and $Ni^{III}(mnt)_2^{1-}$.

Takaki HATSUI, Yasutaka TAKATA, Nobuhiro KOSUGI

The Graduate University for Advanced Studies, Myodaiji, Okazaki 444-0864
Institute for Molecular Science, Myodaiji, Okazaki 444-0864

The metal *2p* photoabsorption spectra of *3d* transition metal compounds have been extensively studied. For ionic compounds such as oxides and halides, the spectra are successfully explained by model hamiltonians taking into account the crystal field, intra-atomic multiplet coupling and, if necessary, ligand-to-metal charge transfer (LMCT) effect, or covalency hybridization between ligand and unoccupied metal *3d** orbitals. On the other hand, for compounds with π-backbonding such as organometallic compounds, the metal *2p* excitation is not well understood. One of the reasons is the insufficient knowledge of the metal-to-ligand charge transfer (MLCT) transitions, namely transitions to unoccupied low-lying ligand π* orbitals hybridized with occupied metal *3d* orbitals. In the previous studies, we measured linearly polarized Ni *2p* photoabsorption spectra of $K_2Ni(CN)_4 \cdot H_2O$ and nickel dimethylglyoxime, and revealed that strong bands above the most intense *2p-3d** atomic lines are associated with MLCT transitions [1]. In this study, we measured linearly polarized Ni *2p* photoabsorption spectra of two nickel complexes $[(C_4H_9)_4N]_2[Ni^{II}(mnt)_2]$ and $[(C_2H_5)_4N][Ni^{III}(mnt)_2$ (mnt = 1,2-dicyano-ethylene-1,2-dithiolato (maleonitrile-dithiolate)). The observed polarization dependence was interpreted in terms of the symmetry and the character of unoccupied molecular orbitals (MO).

Single crystal samples were prepared as described in ref. [2]. The molecular axes *x*, *y* and *z* are determined by X-ray diffraction analyses (the axes are chosen as shown in Fig. 1). Both the $Ni^{II}(mnt)_2^{2-}$ and $Ni^{III}(mnt)_2^{1-}$ anions have D_{2h} symmetry in a good approximation [2]. The Ni *2p* photoabsorption spectra were measured at the BL1A soft X-ray beamline with a pair of beryl (1010) crystals by monitoring total electron yields.

Fig. 2 shows the polarized Ni *2p* photoabsorption spectra of single crystalline $[(C_4H_9)_4N]_2[Ni^{III}(mnt)_2]$. Distinct anisotropy is observed for three isolated peaks B, C, D and E. Because $Ni^{II}(mnt)_2^{2-}$ in the ground state has low-spin Ni $3d^8$ configuration, the only unoccupied metal *3d* orbital is $3d_{xy}\sigma^*$ with b_{1g} symmetry. Thus, it is reasonable to assign peak B to the intra-atomic transition to b_{1g}^* ($3d_{xy}\sigma^*$) orbital. Employing the dipole selection rule, the transition to $3d_{xy}\sigma^*$ is allowed in E//*x* and E//*y* directions and forbidden in E//*z*, which is consistent with the observed polarization dependence of peak B. Peaks C and D are plausibly described in terms of intra-atomic multiplet, LMCT, or MLCT effects. The intra-atomic multiplet effect, however, cannot explain the polarization dependence of peak C because it is expected to cause the second lowest peak stronger in E//*z* than the other directions [3]. Peaks C and D cannot be interpreted as LMCT satellites, or transitions to $\underline{2p}3d^0\underline{L}$ ($\underline{2p}$ and $\underline{L}$ denotes 2p and ligand hole, respectively) which should show the same polarization dependence as peak B. On the other hand, the mnt^{2-} ligand has unoccupied ligand π* orbitals. Two mnt ligands produce two low-lying unoccupied b_{3g}^* (d_{yz} in central symmetry) and a_g^* (d_{x2-y2}, d_{z2}, *s*) orbitals, which may cause MLCT transitions. Based on the observed polarization dependencies, the peaks C and D can be assigned to the MLCT transitions to the b_{3g}^* and a_g^* orbitals, respectively.

Fig. 3 shows the polarized Ni *2p* photoabsorption spectra of $[(C_2H_5)_4N][Ni(^{III}mnt)_2]$. A strong peak A is observed on the lower energy side of the peak B. Peak A is strong in E//*z*, weak in E//*x*, and very weak in E//*y*. Because $Ni(mnt)_2^{1-}$ anions are not completely parallel to one another [2], peak A should be forbidden in E//*y*. Thus, peak A can be assigned to the transition to an orbital with b_{2g} (d_{xz}) symmetry. This is consistent with the electronic structure of $Ni(mnt)_2^{1-}$ with an singly occupied $3b_{2g}$ orbital. Peaks C and D can be assigned to the transition to b_{3g}^* and a_g^* orbitals, respectively on the basis of the polarization dependence,

In conclusion, the peak C and D (Fig. 2 and Fig. 3) are undoubtedly assigned to the transitions

to MLCT transitions. These results indicate that the MLCT effect is indispensable in interpreting the metal *2p* photoabsorption spectra of compounds with π-backbonding. Furthermore, the symmetry of the singly occupied $3b_{2g}$ orbital in $Ni(mnt)_2^{1-}$ is successfully determined by polarized Ni *2p* photoabsorption.

References

[1] T. Hatsui, et al., J. Electron Spectrosc. Relat. Phenom., in press.

[2] A. Kobayashi and Y. Sasaki, Bull. Chem. Soc. Jpn., 50, 2650 (1977)

[3] G. van der Laan, et al., Phys. Rev. B37, 6587 (1988)

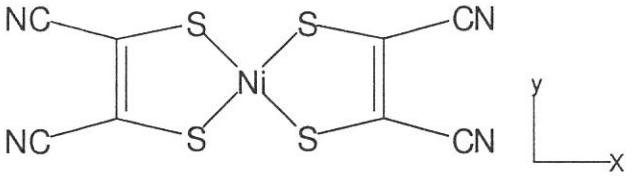

Fig. 1 The structural formula of $Ni(mnt)_2^{n-}$ (n=1,2) with D_{2h} symmetry.

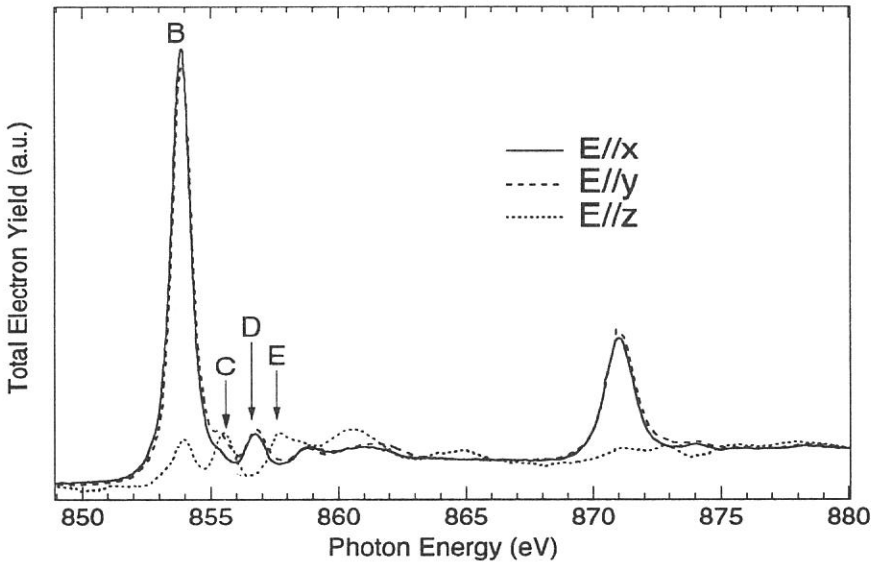

Fig. 2 Polarized Ni *2p* photoabsorption spectra of $[(C_4H_9)_4N]_2[Ni^{II}(mnt)_2]$.

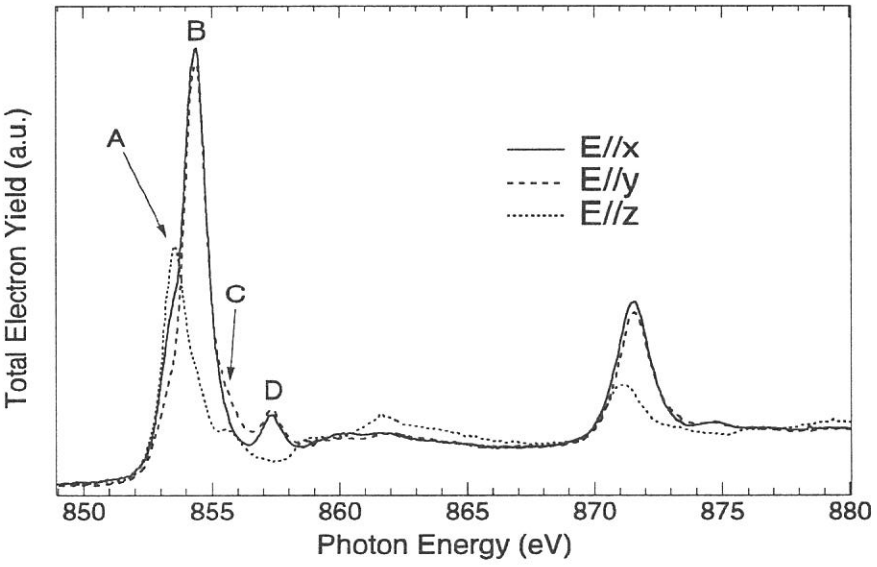

Fig. 3 Polarized Ni *2p* photoabsorption spectra of $[(C_2H_5)_4N][Ni^{III}(mnt)_2]$.

(BL1A)

Resonant behavior of satellite photoelectrons in the Ni 3p and 3s regions at the Ni 2p excitation of $Ni(Hgly)_2$

Yasutaka Takata, Takaki Hatsui and Nobuhiro Kosugi

The Graduate University for Advanced Studies, Institute for Molecular Science, Myodaiji, Okazaki 444-8585

We have investigated resonant behavior of photoelectrons at the Ni 2p excitation for nickel compounds. For the planar nickel complexes, $K_2Ni(CN)_4$[1] and Ni(Hdmg)2 [bis-(2,3butanedione dioximato)nickel(II)] [2], a number of satellite series in the Ni 3p and 3s regions, which are mostly forbidden in the non-resonant spectrum, become strongly observable via the resonant excitations. For both samples, each satellite lowers its kinetic energy for the higher resonance energy, showing one-to-one correspondence with the excited state. This behavior is characteristic of molecular system in solid. It was also revealed that kinetic energy shift relative to the increment of the excitation energy differs considerably between these samples. One possible reason for the difference supposed to be the different degree of the intermolecular interaction.

In the present study, the resonant behavior of satellite electrons in the Ni 3p and 3s regions at the Ni 2p excitation of $Ni(Hgly)_2$ [bis-(dioximato)nickel(II)] was investigated to clarify the effect of intermolecular interaction upon the kinetic energy shift. $Ni(Hgly)_2$ is a good sample for this purpose because the local bonding character around the Ni atom is nearly the same as in $Ni(Hdmg)_2$ as shown in Fig.1 but the intermolecular (Ni-Ni) distance (4.20Å) is much longer than $Ni(Hdmg)_2$ (3.25Å).

Experiments were performed at BL1A soft x-ray beamline. A sample of $Ni(Hgly)_2$ was evaporated on a gold plate in a vacuum of $1x10^{-9}$ Torr. A pair of beryl $(10\bar{1}0)$ crystal was used as a monochromator. The Ni 2p photoabsorption spectra were measured by monitoring the total electron yield. A SCIENTA SES200 electron energy analyzer was used to measure the photoelectron spectra. The total energy resolution in the photoelectron spectra was about 0.7 eV.

Figure 2 shows the Ni 2p photoabsorption spectrum of $Ni(Hgly)_2$. The shape is nearly the same as that of the $Ni(Hdmg)_2$[3]. This is reasonable because both the complexes have almost the same local bonding character around the Ni atom. Figure 3 shows the resonant photoelectron spectra in the Ni 3p and 3s ionization regions measured for three resonant excitations (1-3) in Fig. 2, together with an non-resonant photoelectron spectrum (0). Two weak peaks labeled as sharp (#) are the Au $4f_{5/2}$ and $4f_{7/2}$ photoelectron lines originating from the substrate. Similarly to the case of Ni(Hdmg)2, Ni 3p and 3s primary ionization peaks labeled with an asterisk (*) are not enhanced by the resonant excitation but satellite bands (a–e) weakly observed or absent in the non-resonant spectrum (0) are enhanced. Peaks (a, b), (c) and (d, e) are attributable to the resonant photoionization $\underline{2p_{3/2}}\varphi i - \underline{3p3d}\psi i$, $\underline{2p_{3/2}}\varphi i - \underline{3s3d}\psi i$ and $\underline{2p_{3/2}}\varphi i - \underline{3p3p}\psi i$, respectively. Here, each under bar denotes a single hole. φi is an excitonic electron bound by the $\underline{2p_{3/2}}$ singly charged state, and ψi is an excitonic electron bound by the doubly charged state such as $\underline{3p3d}$.

The kinetic energies of the distinct peak (a) were measured then the slopes ($\Delta K.E./\Delta h\nu$) were obtained, where $\Delta K.E.$ and $\Delta h\nu$ denote the increments of the kinetic energy and the photon energy, respectively. The slopes have a nearly constant value of -0.42 ± 0.05 between the resonance (1) and (3), and are considerably different from the results in $Ni(Hdmg)_2$ [2]. In $Ni(Hdmg)_2$, the slope between the resonance (1) and (2) is about -0.7 but is only about -0.1 between the resonance (2) and

(3) [2]. The molecular orbitals to which the Ni 2p electron is excited are the in-plane Ni 3d* and the out-of-plane ligand orbitals for the resonance (1) and the resonances (2, 3), respectively[3]. Therefore, the effect of the intermolecular interaction upon the kinetic energy shift is stronger in the case that the molecules are more closely stacked with one another. The intermolecular (Ni-Ni) distance is much longer in $Ni(Hgly)_2$ so that the effect is much weaker than those in $Ni(Hdmg)_2$. As a result the kinetic energy shift is not so influenced by the intermolecular interaction in $Ni(Hgly)_2$ and shows strong photon energy dependence as in the ionic complex $K_2Ni(CN)_4$[1].

References

[1] Y. Takata, M. Nakamura and N. Kosugi, UVSOR Active. Rep. (1995) 50.
Y. Takata, M. Nakamura and N. Kosugi, Chem. Phys. Lett., in press.

[2] Y. Takata, M. Nakamura, Y. Yamamoto, T. Yokoyama, T. Ohta and N. Kosugi, UVSOR Active. Rep. (1996) 48.
Y. Takata, M. Nakamura and N. Kosugi, J. Electron Spectrosc. in press.

[3] T. Hatsui, Y. Takata, N. Kosugi, K. Yamamoto, T. Yokoyama and T. Ohta, UVSOR Active. Rep., (1996) 46.
T. Hatsui, Y. Takata, N. Kosugi, K. Yamamoto, T. Yokoyama and T. Ohta, J. Electron Spectrosc., in press.

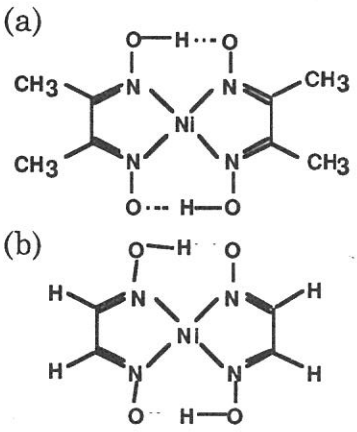

Fig. 1. Molecular structure of (a) $Ni(Hdmg)_2$ and (b) $Ni(Hgly)_2$.

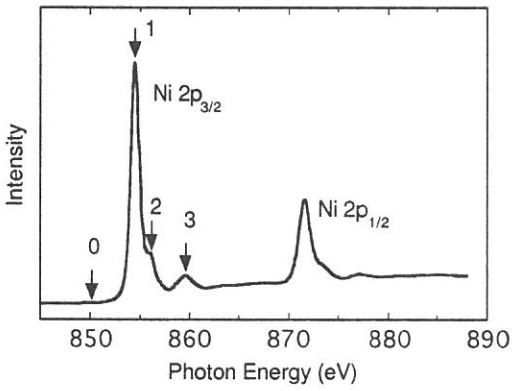

Fig. 2. Ni 2p photoabsorption spectrum of $Ni(Hgly)_2$.

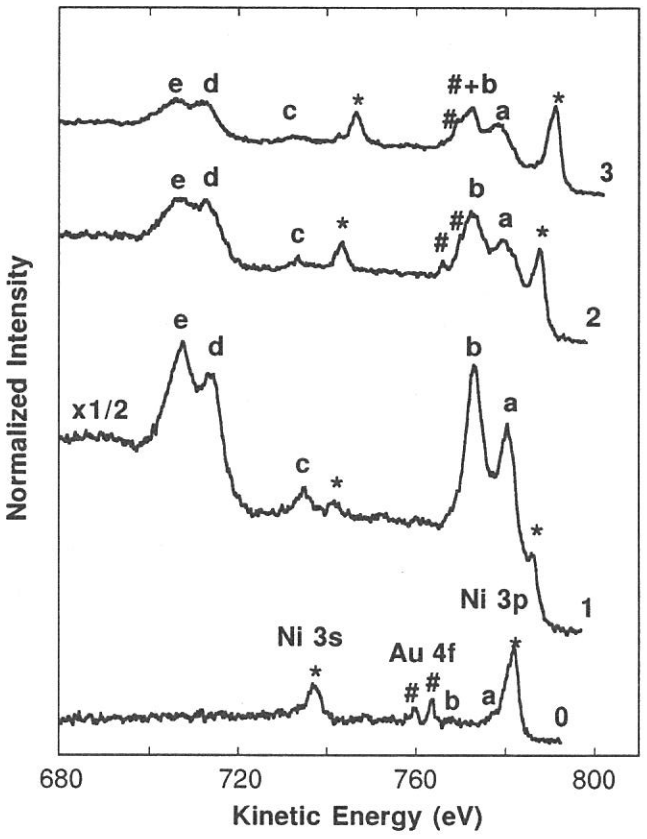

Fig. 3. Resonant photoelectron spectra in the Ni 3p and 3s regions of Ni $(Hgly)_2$ at the photon energies marked in Fig. 2.

(BL1A)

Resonant Photoemission Study of Temperature-Induced Valence Transition Material $EuNi_2(Si_{1-x}Ge_x)_2$

Heralu Pathirannehelage Nihal Jayalath GUNASEKARA*, Yasutaka TAKATA, Shin-ichi KIMURA, Toyohiko KINOSHITA, Nobuhiro KOSUGI, Krishna Gopal NATH[1], Hirofumi WADA[2], Akihiro MITSUDA[2] and Masayuki SHIGA[2]

Institute for Molecular Science, Myodaiji, Okazaki 444-8585, Japan

[1]Department of Structural Molecular Science, Graduate University for Advanced Studies, Okazaki 444-8585, Japan

[2]Department of Materials Science and Engineering, Kyoto University, Kyoto 606-01, Japan

Study of the electronic structures of rare earth compounds has been attracted much attention because of their interesting physical properties which are derived from the localized nature of $4f$ electrons. Among the intermediate valent systems, Eu compounds are known to exhibit strong temperature dependence of the mean valence. Very recently, it was found that the $EuNi_2(Si_{1-x}Ge_x)_2$ compounds with $0.70 \leq x \leq 0.82$ show a temperature induced valence transition below room temperature[1)] and magnetic field induced transition. In the previous report[2)], it has been concluded that the $3d$-$4f$ resonant photoemission of such kind of mixed valent $4f$ compounds is a useful technique to clarify the different $4f$ electronic states owing to different valence. In this study, we have applied the $3d$-$4f$ resonant photoemission method to investigate the valence transition of the $EuNi_2(Si_{1-x}Ge_x)_2$ compound. We have also measured the photoemission spectra around the Ni $2p$-$3d$ resonant excitation region in order to investigate the Ni $3d$ states of the same sample. The sample of x=0.75 which shows the mean valence transition from ~2.3 (high temperature) to ~2.8 (low temperature) at T=110K was used.

The samples were prepared by melting stoichiometric amount of constituent elements in argon furnace. The ingots were annealed in an evacuated quartz tube at 800°C for one week. The resonant photoemission experiments were performed at the double crystal monochromator beamline BL1A, where the high performance photoemission spectroscopy system SCIENTA SES-200 is equipped. A pair of beryl $(10\bar{1}0)$ crystals was used to obtain the monochromatized light around both the Eu $3d$-$4f$ and Ni $2p$-$3d$ excitation regions. The total energy resolution of the photoelectron spectra was estimated to be about 0.7 eV. Photoelectron total yield (TY) spectra around these excitation condition were also measured by recording sample drain current as a function of photon energy. The clean surface of the sample was obtained by filing in ultra high vacuum condition.

Figure 1 shows the TY spectra around the Eu $3d$-$4f$ excitation region ($M_{IV, V}$ edge) at about 300K and 80K. Several peaks are appeared due to the final state multiplet and mixed valent nature of the sample. It is noticed from Fig. 1 that the peaks 2, and 3 are enhanced at the low temperature phase. From the comparison with the previous report of L_{III} edge spectra[1)], it is concluded that these peaks are enhanced due to increasing the trivalent Eu ion component at low temperature. The resonant photoemission spectra around these excitation conditions are shown in Fig. 2. It is found that the trivalent components of Eu $4f$ states are enhanced at the excitation conditions of 2 and 3. On the other hand, the divalent 4f states are dominant at 1, 4 and 5. From these results, the features around 0-4eV binding energy are estimated to be mostly divalent $4f$ states and those around 6-12eV are trivalent ones in these on-resonant spectra. The features of the off-resonant spectrum at "0" might be mainly hybridized states of divalent Eu $4f$ and Ni $3d$.

The Ni $2p$-$3d$ resonant photoemission spectra have also been measured (not shown here). It was considered that the spectra reflect the contribution of the Ni $3d$ bands. The resonant behavior of the Ni $3d$ band is almost same as that reported for the Ni metal[3)]. It is noted that the $3d$ bands seem to be situated higher binding energy (about 0.8-0.9eV) than those of Ni metal.

It is concluded that the $3d$-$4f$ resonant photoemission spectra and the Eu $M_{IV, V}$ edges absorption spectra behave as similar manner as the Eu L_{III} edge spectra[1)] in their temperature dependence, which reflects

valence transition from Eu^{2+} at room temperature to Eu^{3+} at low temperature. To clarify each valence state, the 3*d*-4*f* resonant photoemission is very useful as reported for Tm compounds[2]. The estimation procedure of the mean valence for each temperature is now in progress as will be described elsewhere[4].

Acknowledgements

Authors would like to thank to the staff members of the UVSOR facility for the support.

References

* Permanent Address; Ceylon Institute for Scientific and Industrial Research, P.O.Box 787, 363, Bauddhaloka Mawatha, Colombo 7, Sri Lanka.

1) H. Wada, A. Nakamura, A. Mitsuda, M. Shiga, T. Tanaka, H. Mitamura and T. Goto, *J. Phys., Condens. Matter.* 9 (1997) 7913.

2) T. Kinoshita, Y. Ufkutepe, K. G. Nath, S. Kimura, H. Kumigashira, T. Takahashi, T. Matsumura, T. Suzuki, H. Ogasawara and A. Kotani, *J. Electron Spectrosc. Relat. Phenomn.* (1998), in press: Y. Ufkutepe, S. Kimura, K. G. Nath, T. Kinoshita, H. Kumigashira, T. Takahashi, T. Matsumura, T. Suzuki and H. Ogasawara, *UVSOR Activity Report* (1996) p.200.

3) For example, M. Weinelt, A. Nilsson, M. Magnuson, T. Wiel, N. Wassdahl, O. Karis, A. Föhlisch and N. Mårtennsson, *Phys. Rev. Lett.* 78 (1997) 967.

4) H. P. N. J. Gunasekara, Y. Takata, S. Kimura, T. Kinoshita, N. Kosugi, K. G. Nath, H. Wada, A. Mitsuda and M. Shiga, in preparation.

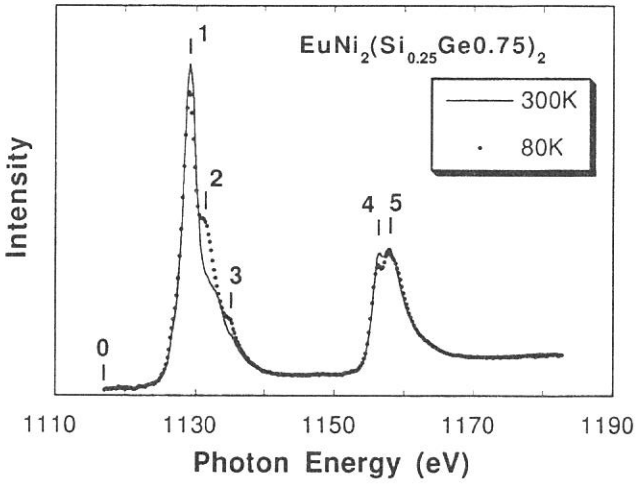

↑

Figure 1. TY spectra for $EuNi_2(Si_{1-x}Ge_x)_2$ (x=0.75) around Eu $M_{IV, V}$ edges at 300K and 80K.

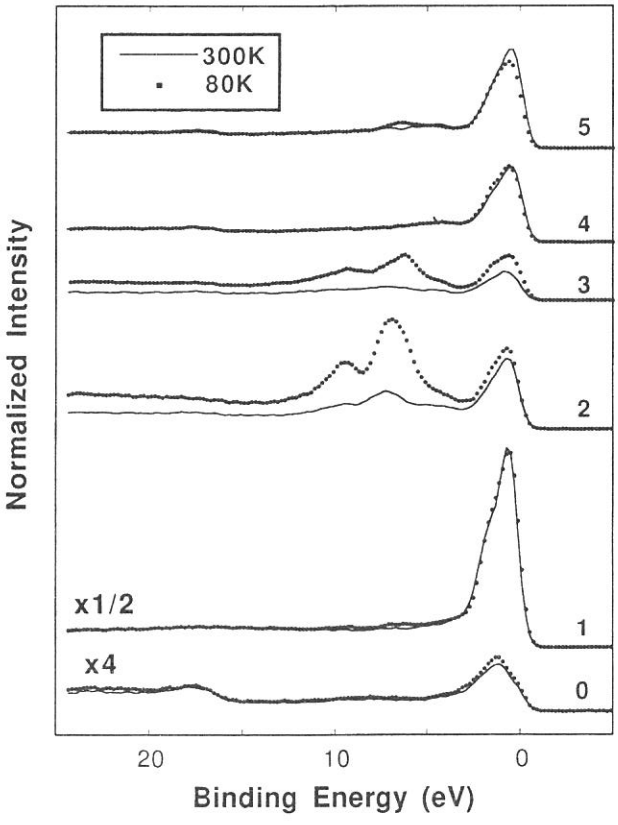

→

Figure 2. Resonant photoemission spectra of $EuNi_2(Si_{1-x}Ge_x)_2$ (x=0.75) around Eu $M_{IV, V}$ edges at 300K and 80K. The photon energy position of each spectrum corresponds to the peak position of the TY spectrum in Fig. 1.

(BL2B1) X-ray absorption study of $Ce_{1-x}Sr_xTiO_3$

T. Yokoya, T. Sato, A. Chainani[A], and T. Takahashi

Department of Physics, Tohoku University, Sendai 980-8578, Japan
[A] *Institute for Plasma Research, Gandhinagar 382428, India*

Titanium oxide with a perovskite structure is classified as a Mott-Hubbard (M-H) type by the phase diagram based on the work of Zaanen, Allen, and Sawatzky, where early transition metal compounds (TMC's) are a M-H type and late TMC's are a charge transfer type [1]. However, in our previous study on $CeTiO_{3+\delta}$, we have observed spectral changes across the δ-controlled metal-insulator (M-I) transition due to doped hole states in the O 1s x-ray absorption spectra and showed that M-H system can have a charge-transfer (C-T) character due to a strong hybridization [2]. In this study, to further investigate the electronic structure of Titanium oxide, we have performed x-ray absorption spectroscopy (XAS) on $Ce_{1-x}Sr_xTiO_3$, which exhibits M-I transition by a substitution of trivalent Ce with divalent Sr.

XAS was carried out at BL2B1 in the total electron yield mode at a resolution of 1 eV. Samples were scraped *in-situ* with a diamond file to obtain clean surfaces. Fig. 1 shows O 1s XAS of $Ce_{1-x}Sr_xTiO_3$ [x=0 (semiconducting), 0.05 and 0.2(metallic)]. We find two structures in the spectrum of $CeTiO_3$. One is a prominent peak centered at 535 eV and the other is a weak shoulder around 532eV. The overall spectral shape is similar to that of $LaTiO_3$ [3], where a feature at 532 eV is ascribed to O 2p states hybridized with the upper Hubbard band and a feature at 535 eV corresponds to Ce 5d states with O 2p admixture. In the spectrum of x=0.05 compound, we can clearly see that the weak feature at 532 eV observed in x=0.0 compound is strongly enhanced, forming a peak structure. The intensity of the peak structure is stronger in x=0.2 compound than in x=0.05 compound. This indicates that the new hole-doped state evolves as a function of x, and may cause the M-I transition. The spectral changes across the x-controlled M-I transition are similar to that across the δ-controlled one [2]. These results provide a direct confirmation of the C-T nature of early TMC's due to a strong hybridization.

We thank Prof. M. Onoda for providing us $Ce_{1-x}Sr_xTiO_3$ samples.

[1] J. Zaanen, G.A. Sawatzky, and J.W. Allen, Phys. Rev. Lett. 55, 418 (1985).
[2] O. Akaki et al., Phys. Rev. B 56, 12050 (1997).
[3] A. Fujumori et al, Phys. Rev. B 46, 9841 (1996).

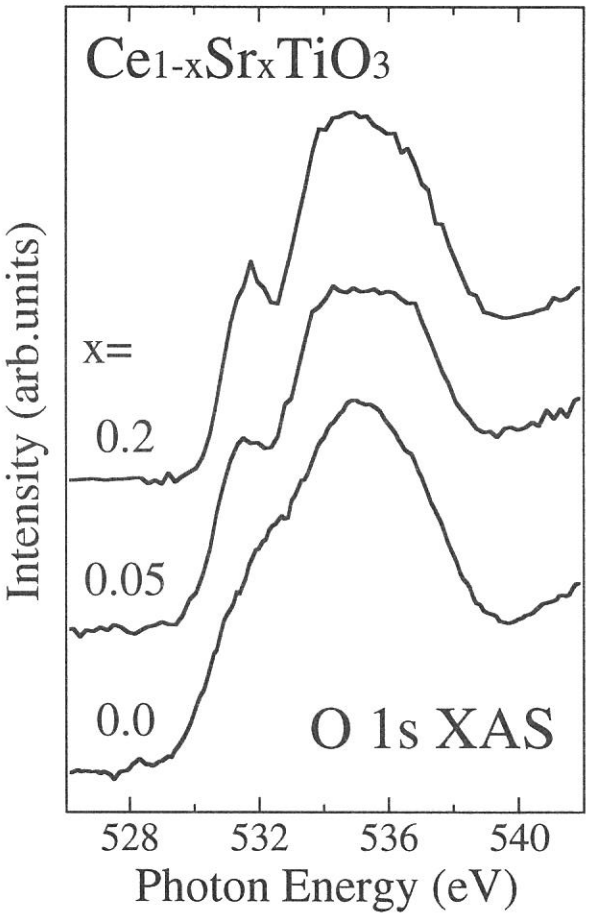

Fig. 1. O 1s-p XAS of $Ce_{1-x}Sr_xTiO_3$ (x=0.0, 0.05 and 0.2).

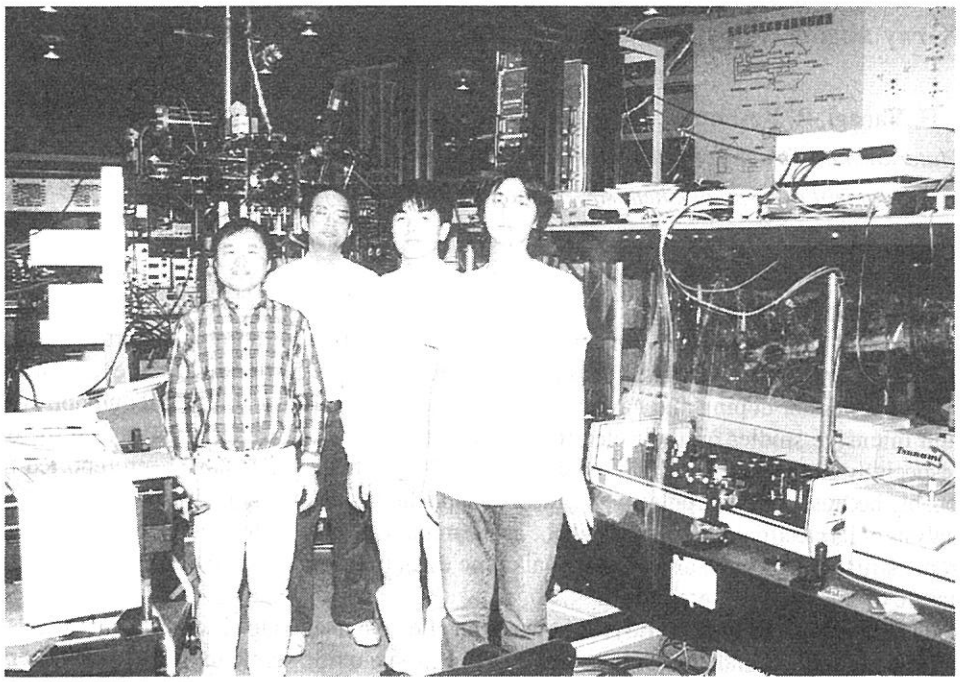

Mitsuke Group at BL3A2

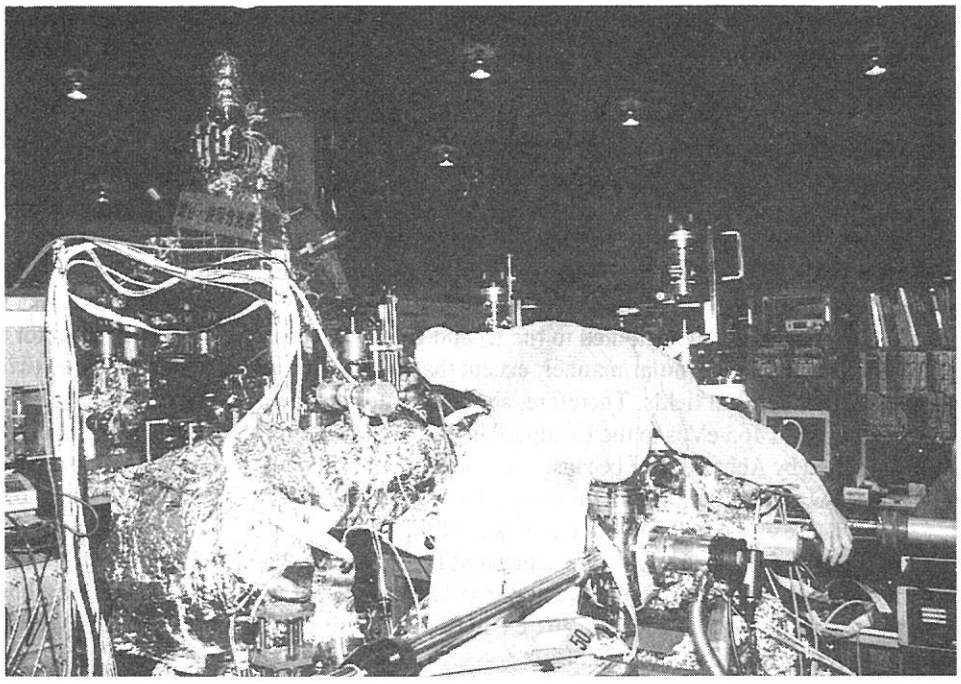

Investigation at BL1A

(BL2B1)

X-ray absorption spectra for Ca $L_{2,3}$, Ti $L_{2,3}$, and O K edges in $CaTiO_3$

K. Ueda, H. Yanagi, R. Noshiro, H. Hosono, H. Kawazoe, M. Takemoto[A], N. Miyagawa[A], and H. Ikawa[A]

Materials and Structures Laboratory, Tokyo Institute of Technology, Yokohama 226-8503

[A] Department of Applied Chemistry, Kanagawa Institute of Technology, Atsugi 243-0292

$CaTiO_3$ is one of alkaline earth titanates with perovskite structure. However, the crystal structure of $CaTiO_3$ is not an ideal cubic perovskite type but a $GdFeO_3$ type with orthorhombic distortion, because the ionic radius of Ca ions is smaller than that of Sr or Ba ions.[1] These alkaline earth titanates are known to show n-type conduction by proper donor doping and have several fascinating properties in electrical and optical applications. Extensive and intensive studies on their electronic structures have been undertaken to find the origins of the properties, especially in the cases of $SrTiO_3$ and $BaTiO_3$. Only a few studies have been reported in the case of $CaTiO_3$, probably because of less popularity in practical applications and the complication in the crystal structure. However, analysis of its electronic structure would be as meaningful as that of other titanates', because understanding of the electronic structures through a series of the alkaline earth titanates may provide us with an essential clue to reveal the nature of the attractive properties.

Photoemission spectroscopy (PES) is known as an effective method to observe valence bands of materials. However, since conduction bands play important roles in n-type oxide semiconductors, the observation of the conduction bands is significant to understand the electroconductive properties of the n-type oxide semiconductors. Therefore, inverse photoemission spectroscopy (IPES), X-ray absorption spectroscopy (XAS), and electron energy loss spectroscopy (EELS) are more useful for the n-type oxide semiconductors than PES. In the present report, the XAS spectra of $CaTiO_3$ were measured and compared with the EELS spectra obtained on a transmission electron microscope and the results of an energy band calculation, mainly the partial density of states (PDOS).

Single crystals of $CaTiO_3$ were prepared by the floating zone method using an infrared furnace. H_2-reduced crystals doped with Y 0.01at% were used in the XAS measurements to avoid charging effects. On the other hand, nominally non-doped crystals were used in the EELS measurements. XAS measurements for Ca $L_{2,3}$ edges, Ti $L_{2,3}$ edges and O K edge were carried out on BL2B1 of UVSOR in Institute for Molecular Science. The surface of a sample was scraped by a diamond file at a pressure of $\sim 10^{-9}$ Torr before the measurements and the spectra were obtained under a vacuum of $\sim 10^{-10}$ Torr. EELS spectra for Ca $L_{2,3}$ edges, Ti $L_{2,3}$ edges and O K edge were measured on the transmission electron microscope (Hitachi : H9000NAR) equipped with a LaB_6 electron source and an electron energy loss spectrometer (Gatan : 676). An empirical energy band calculation by the tight-binding method was carried out to interpret the spectra.

Figure 1 shows the XAS and EELS spectra for (a) Ca $L_{2,3}$, (b) Ti $L_{2,3}$, and (c) O K edges in $CaTiO_3$. The XAS spectra are adjusted to the EELS spectra in energy scale so that the energy of peak tops will meet each other between these spectra. Intensities of these spectra are arbitrarily arranged to enable a comparison of the spectra. The XAS spectra and EELS spectra provide analogous structure in the three absorption edges although the former gives sharper bands because of the higher energy resolution. Two bands were observed at 348 and 351 eV in the Ca $L_{2,3}$ edges (fig.1a), and they are attributed to the L_2 and L_3 edges, respectively. The spectra for Ti $L_{2,3}$ edges (fig.1b) are also interpreted in the similar manner, except that each unoccupied band is split into two bands under the influence of octahedral crystal fields. Therefore, a pair of bands at 458 and 460 eV is ascribed to the L_2 edge, and the other one at 463 and 465 eV is to the L_3 edge. The XAS spectrum for the Ti $L_{2,3}$ edges in $CaTiO_3$ is similar to that in $SrTiO_3$ reported by Abbate et.al.[2] because of analogous environments for Ti ions. Although the observation of Ca and Ti L_1 edges was tried, no prominent absorption was detected. The O K edge (fig.1c) shows four bands at 531, 534, 536 and 544 eV. Since the relative intensity of the O K edge was lower than those of the Ca $L_{2,3}$ and Ti $L_{2,3}$ edges, the spectra of the O K edge were somewhat noisy, especially for the EELS spectrum. The energies of the absorption edges are approximately estimated from the lower-energy edge of the observed bands to be 346 and 349 eV for the Ca L_2, L_3 edges, 456 and 461 eV for the Ti L_2, L_3 edges, 530 eV for the O K edge, which are close to the energies reported by Bearden and Burr.[3]

XAS and EELS spectra generally provide PDOSs of conduction bands. Therefore, the spectra correspond mainly to intra-atomic excitations and they are unique to each element in materials. Recalling the selection rule for the electric dipole transition, transitions to s or d orbitals are allowed for $L_{2,3}$ edges and transitions to p orbitals are permitted for a K edge. Therefore, it is expected that the Ca $L_{2,3}$ edges show the transition to a Ca 4s band, the Ti $L_{2,3}$ edges do the transition to Ti 3d and 4s bands, and the O K edge does the transition to an O 2p band in the anti-bonding states. If we assume that the band width of the initial states, that is the core levels, in each transition is negligibly small, the structure of the spectra is substantially derived from the structure of the final states, that is, the PDOSs of the conduction bands for each element. Therefore, the XAS spectra were

compared with the results of an energy band calculation. In the cases of the Ca and Ti spectra, the L_3 edges were eliminated in the way that the high energy sides of the L_2 edges were smoothly extrapolated to zero. Although this operation erases the information about PDOSs at higher energy such as the PDOS of a Ti 4s band, the processing of the spectra is clear and reproducible because of its simplicity.

Figure 2 shows the comparison of the XAS spectra with the PDOSs obtained by the tight-binding energy band calculation. Although there is no relation in intensity between the XAS spectra and PDOSs, the XAS spectra of Ca, Ti, and O edges or the PDOSs of these elements are relatively arranged in intensity among themselves. The bottom of the conduction band is set to zero in energy scale for the PDOSs. The energy scale for the XAS spectra was taken so that they will fit to the respective PDOSs. Although the comparison may be somewhat artificial, it is based on the selection rule and provides reasonable results; The degree of the energy splitting by crystal fields for Ti ions is almost the same between its XAS spectrum and PDOS, and the energies of three bands in the O K edge agree well with the energies of the cations' bands in the XAS spectra indicating the anti-bonding states of O 2p bands. Although some deviation can be seen between the XAS spectra and PDOSs in intensity because of the neglect of the transition probability, they agree with each other qualitatively.

In conclusion, the XAS and EELS spectra of $CaTiO_3$ were measured to understand the electronic structure of the conduction band. The XAS and EELS spectra gave almost the same features between them, and the energy resolution of the XAS spectra was higher than that of the EELS spectra in the present experiments. It was understood from the comparison of the XAS spectra with the calculated PDOSs that the conduction band mainly consists of Ca 4s and Ti 3d bands with a small contribution of the O 2p anti-bonding bands.

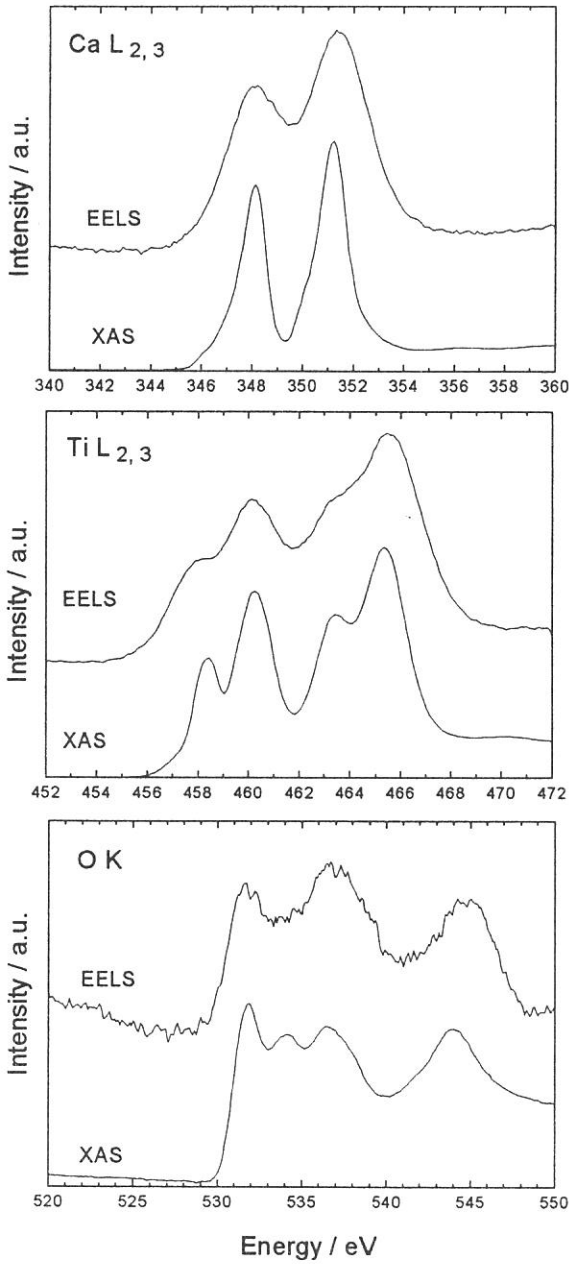

Figure 1 The XAS and EELS spectra for Ca $L_{2,3}$ (a), Ti $L_{2,3}$ (b), O K (c) edges in $CaTiO_3$.

References

[1] S. Sasaki, C.T. Prewitt, J.D. Bass, and W.A. Schulze, Acta Cryst. C43, 1668 (1987)

[2] M. Abbate, F.M.F. de Groot, J.C. Fuggle, A. Fujimori, Y. Tokura, Y. Fujishima, O. Strebel, M. Domke, G. Kaindl, M. Sacchi and N. Tsuda, Phys. Rev. B 44, 5419 (1991)

[3] J.A. Bearden, and A.F. Burr, Rev. Mod. Phys. 39, 125 (1967)

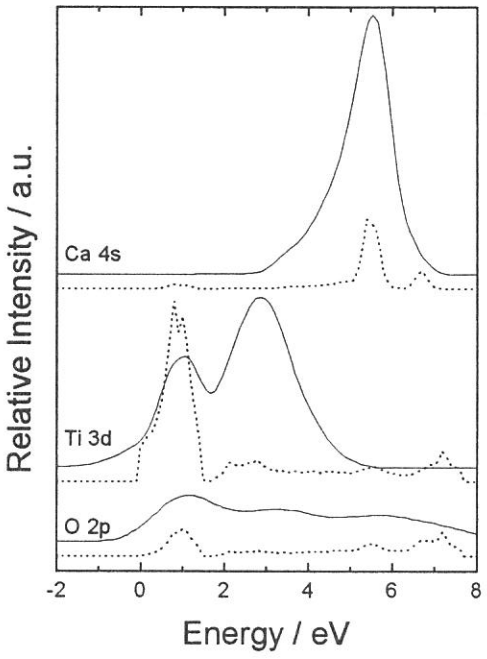

Figure 2 The comparison of the XAS spectra (solid lines) for Ca L_2 (top), Ti L_2 (middle), and O K (bottom) edges with the PDOSs (dotted lines) of Ca 4s, Ti 3d, and O 2p orbitals.

(BL2B1)

Tm5*p* resonant photoemission study of TmX (X=S, Se and Te) around 4*d*-excitation region

Krishna G. NATH, Yüksel UFUKTEPE[A*], Shin-ichi KIMURA[A], Toyohiko KINOSHITA[A], Takeshi MATSUMURA[B], Takashi SUZUKI[B], Haruhiko OGASAWARA[C] and Akio KOTANI[C]

Department of Structural Molecular Science, Graduate University for Advanced Studies, Okazaki 444 -8585
A) UVSOR facility, Institute for Molecular Science, Okazaki 444-8585
B) Department of Physics, Tohoku University, Sendai 980-77
C) Institute for Solid State Physics, University of Tokyo, Tokyo 106

In the 4*d*-4*f* resonant process of rare earth compounds, study of resonance behavior of core levels (5*p* or 5*s*) is important to understand overall decay processes related to different electronic states. In fact, the core level photoemission spectra in rare earth systems show complex multiplet structures due to existence of unfilled and localized 4*f*-shell[1]. Sometimes it is rather difficult to separate the spin-orbit peaks and the valence components if the system is mixed-valence. In this point of view, the resonance study of core levels is also significant to get clear picture of complex muliplet structures. Recently we have measured the resonant photoemission of 4*f*-states at the 4*d*-4*f* excitation condition of thulium compounds (TmS, TmSe, and TmTe) for divalent and trivalent Tm-ions[2]. It was found in that experiment that a large resonant enhancement occurs in Tm 4*f* emission around Tm4*d* absorption edges. As a consequence of that experiment, we measured the resonant photoemission of 5*p* levels around 4*d* threshold. In this report, we present the Tm-5*p* photoemission results at the 4*d*-4*f* absorption edges (hν = 150-200eV) of Tm-compounds.

The experiments were performed at the beam line, BL2B1, with Grasshopper monochromator. Photoelectrons from the sample were collected and analyzed by a double-pass cylindrical mirror analyzer. The base pressure of the chamber was 2×10^{-10} torr. The overall energy resolution was less than 0.5eV. The clean surfaces of the single crystal were obtained by scraping with diamond filler.

Figure 1(a) shows the on- and off- resonant 5*p* resonant photoemission results of mostly divalent compounds TmTe. The excitation energies are selected from the total yield (TY) spectra in Fig.1 (b). The peak position (~173eV) in Fig. 1(b) corresponds to 4*d*-4*f* resonance of Tm^{2+}. The shoulder at photon energy of ~178eV indicates the presence of small amount of Tm^{3+} in this mostly divalent compound. All dotted curves represent the calculation. The on-resonance spectra for 5*p* (Tm^{2+}) are shown in the upper panel in Fig.1 (a). The off-resonance spectra taken at hν=169eV are in the lower panel. It can be easily seen that Tm5*p* states show resonance enhancement at on-resonance condition. It is noticed that the resonance effect is larger for higher binding energy states, i.e. around 30eV than lower ones around 24eV.

In Figure 2(a), it is shown the resonance behavior of trivalent Tm5*p* of TmSe, a typical mixed-valent compound. Though the mostly trivalent TmS is the best to show the trivalent characteristics, the 5*p*-photoemission peaks taken at several on-resonance conditions are overlapped by LMM Auger transition from sulfur (S). So the true resonance effect can not be separated easily for TmS. Figure 2(b) represents the 4*d*-4*f* absorption spectrum for the both Tm^{3+} and Tm^{2+} components. This absorption spectrum is considered as a superposition of two spectra for two Tm-valences as shown by the calculated curves. The off –resonance photoemission spectrum taken at hν=169eV is shown in the lower panel of Fig. 2(a). At this photon energy position in the TY spectra, the both valence components are present with different ratio. As a result, the photoemission also shows the both Tm^{3+} and Tm^{2+} components as seen by comparing the calculated curves for two valences. In the upper panel, the on-resonance spectrum taken at the photon energy of ~178eV reflects the trivalent characteristics. It is found that the spectrum shows the enhancement in trivalent parts due to the resonant effect.

The decay channel 4*d*5*p*4*f* explains the resonance behavior of Tm5p at 4*d*-4*f* resonance. Though the intrinsic photoionization cross-section of 5*p* level is not so strong as compared with the 4*f* level at the 4*d*-4*f* absorption ranges, the 5*p*-photoemission still shows resonance at this 4*d*5*p*4*f*-decay channel. 5*p*-photoemission cross section (total) for photon energy $h\nu_{4d}$ near 4*d* edge can be written as:

$$\sigma(h\nu_{4d}) = \sigma^{0}(h\nu_{4d}), \text{ normal part } + \sigma^{res}(h\nu_{4d}), \text{ resonance part.}$$

The resonance contrast can be written as:

$$\xi_{nl}(h\nu_{4d}) = \sigma(h\nu_{4d})/\sigma^{0}(h\nu_{4d}).$$

For 5*p*(Tm^{3+} in TmSe), the value of resonance contrast is about 3. On the other hand this value is 4.25 for 4*f*(Tm^{3+} in TmSe). So at 4*d*-4*f* resonance,

$$[\xi_{5p}/\xi_{4f}] \times 100\% = 70\%$$

This indicates that 4*d*5*p*4*f*-decay channel is also active but not so strong as 4*d*4*f*4*f* decay channel.

Another interesting observation of this 5*p* resonant photoemission is that the apparent values of spin-orbit splitting between $5p_{3/2}$ and $5p_{1/2}$ states are not easily defined because of multiplet structure. Oh and co-workers[3] have reported the values of 5*p* spin-orbit splitting of Tm^{3+} and Tm^{2+} for TmSe. They did not mention the multiplet structure in 5*p* photoemission. Recently, resonant effect of 5*p* for Tm-metal has been studied by Nicklin *et al*[4]. Though they mentioned multiplet peaks by the help of calculation, they also defined $5p_{3/2}$ and $5p_{1/2}$ states for several peaks. In fact, there is no meaning to estimate the values 5*p* spin-orbit-splitting peaks or to define directly the $5p_{3/2}$ and $5p_{1/2}$ peaks in the presence

of multiplet structures. Our experiments show broadened feature of $5p$ photoemission peaks due to complex structure in both figures, 1(a) and 2(a). At the same time the calculated line and convoluted spectra indicate the same feature like experiment.

In conclusion, the $5p$ photoemission shows resonance behavior at $4d$-$4f$ excitation range for Tm-compounds. The strength of $5p$-decay channel is comparable with $4f$-decay channel in 4d-$4f$ excitation process. The photoemission spectra for two Tm-valences are defined by complex multiplet structures, not by single $5p_{3/2}$ or $5p_{1/2}$ peak.

We would like to thank the staff members of UVSOR facility staff for their technical support.

*Visiting Scientist on leave from Physics Department, University of Cukurova, 01330 Adana, Turkey

1. A.Kotani, Inner shell photoelectron process in solids, (Hand book on synchrotron Radiation, vol.2, edited by G.V.Marr (North-Holland Physics publishing, Amsterdam, 1987).
2. Y.Ufuktepe et al. submitted to J. Phys. Soc. Jpn.: UVSOR activity report (1996), p102.
3. S. -J. Oh *et al.*, Phys. Rev. B **30,** 1937 (1984).
4. C. L. Nicklin *et al.*, Phys. Rev. B **52,** 4815 (1995).

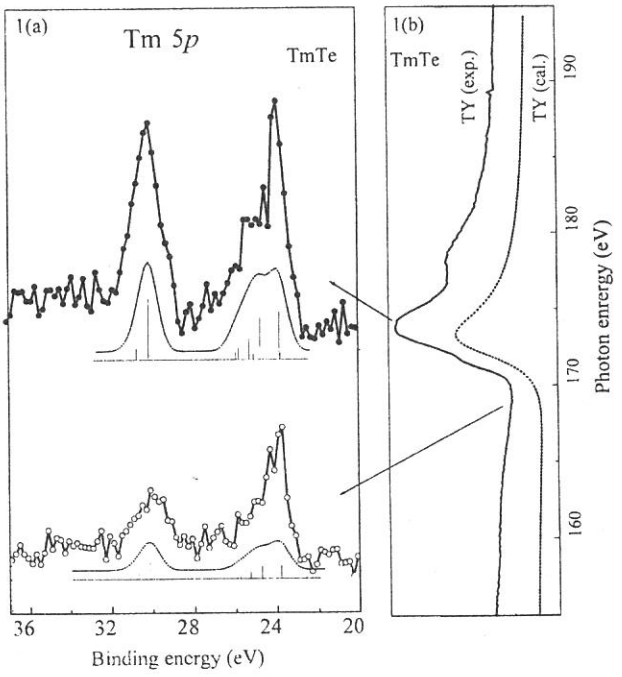

Figure 1. (a):Tm $5p$ resonant photoemission spectra for TmTe. (Upper): the on resonant. (Lower): the off resonant. The dotted curves represent the calculation. The excitation energies are taken from the total yield (TY) spectrum given in Fig. 1(b). In this absorption spectrum, the peak at ~173eV is the on-resonance condition of divalent Tm-ion.

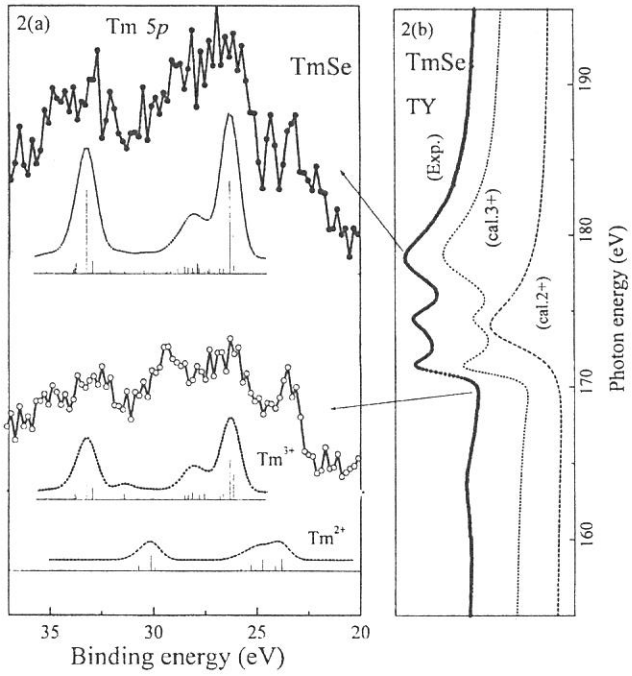

Figure 2. (a):Tm $5p$ resonant photoemission spectra for TmSe. (Upper): the on-resonance spectrum to show the trivalent characteristics. (Lower): the off resonant one. The dotted curves represent the calculation. The excitation energies are taken from the total yield (TY) spectrum given in Fig. 2(b). The TY shows the mixed valent characteristics as shown by calculation. Because of long tail of the divalent part, the off-resonance $5p$-photoemission show mixed behavior. This is also shown by calculation.

(BL5B)

Photoelectron Spectromicroscopy Study of $(DI\text{-}DCNQI)_2M$ (M=Ag, Cu)

Yuichi Haruyama[A], Krishna G. Nath[B], Yüksel Ufuktepe[C], Ko-ichi Hiraki[D,A], Kazushi Kanoda[D,A], Shin-ichi Kimura[A], and Toyohiko Kinoshita[A]

[A] *Institute for Molecular Science, Myodaiji, Okazaki 444-8585, Japan*

[B] *Department of Structural Molecular Science, Graduate University for Advanced Studies, Okazaki 444-8585, Japan*

[C] *Physics Department, University of Cukurova, 01330 Adana, Turkey*

[D] *Department of Applied Physics, University of Tokyo, Bunkyo-ku, Tokyo 113-0033, Japan*

The crystal structures of $(DI\text{-}DCNQI)_2M$ (M=Ag, Cu), where DI-DCNQI is 2,5-diiodo-*N*,*N'*-dicyanoquinonediimine, are isostructural with a space group $I4_1/a$, whereas the physical properties are quite different from each other. In the electrical resistance [1], $(DI\text{-}DCNQI)_2Cu$ (abbreviated DI-Cu) shows metallic conductivity down to low temperature, on the other hand, $(DI\text{-}DCNQI)_2Ag$ (DI-Ag) shows semiconducting nature with a gap of 490K. The difference in the physical properties is considered to arise from the *d* band position of M ion. Although the photoemission is a direct method to investigate these electronic structures, the photoemission study for the single crystals DI-Ag and DI-Cu has not been performed so far. The reason is that the size of these single crystals is not large enough to carry out the photoemission experiments. However, photoelectron spectromicroscopy apparatus can do the experiment. Therefore, we have measured the photoemission spectra for DI-Ag and DI-Cu using the photoelectron spectromicroscopy [2].

Needlelike shaped single crystals of DI-Ag and DI-Cu were synthesized by electrochemical reduction as reported elsewhere [1]. The typical sample size used here was smaller than $\phi 100\times1000\mu m^2$. These samples were characterized by x-ray diffraction, electrical resistance, magnetic susceptibility and NMR measurements [1]. The clean sample surfaces were obtained by 0.5 keV Ar ion sputtering for 10 min. The cleanliness was confirmed by x-ray photoemission spectroscopy for the absence of extra features arising from the contaminations. Photoemission experiments were carried out by using a conventional UHV system (FISONS, ESCALAB-220i-XL) at a base pressure of 2×10^{-8} Pa [2]. Total instrumental energy resolution was 0.3 ~ 0.6 eV full width at half maximum (FWHM), depending on the photon energy ($h\nu$) in the energy range of 30 ~ 200 eV. All experiments were performed at room temperature.

Figures 1(a) and 1(b) show the photoemission spectra of DI-Ag and DI-Cu, respectively. The detection area of the photoemission spectra was 50μm, which is smaller than the sample size. The light polarization (**E**) was parallel to the c-axis of DI-Ag and DI-Cu. The photoemission spectra were normalized to the maximum intensity of the valence band. For DI-Ag, four features in this valence band are observed at ~1.0, 3.5, 5.0 and 8.0 eV labeled A, B, C and D, respectively. Although the prominent feature C has the maximum intensity for every photon energy, the relative intensity of these features is varied as the photon energy changes. From the photon energy dependence of the photoionization cross section [3], the features A, B and D are predominantly derived from N and C 2*p*, and the feature C is from Ag 4*d* bands. Another feature is observed at ~10 eV with $h\nu$ = 40 eV. This feature is assigned to the Auger signal. For DI-Cu, three features are observed at ~3.5, 6.5 and 10.0 eV labeled E, F and G, respectively. The relative intensity of the features F and G to the feature E is gradually decreased with increasing $h\nu$. This photon energy dependence shows that the features F and G are predominantly derived from N and C 2*p*, and the feature E is from Cu 3*d* bands. Here, we compare the *d* bands of the M ion in both DI-Ag and DI-Cu. As assigned above, the Ag 4*d* bands for DI-Ag are located around 5 eV and localized within 2.5 eV width. For DI-Cu, the Cu 3*d* bands are situated around 3.5 eV and show broader

band width. This is a direct evidence of the localized nature of Ag 4*d* electrons and the itinerant nature of Cu 3*d* electrons. As Ag has much deeper *d* levels than Cu, DI-Ag has smaller $p\pi$-*d* hybridization with the DCNQI molecule than DI-Cu. These results are consistent with the band calculation [4].

In figures 2(a) and 2(b), the polarization dependence of the photoemission spectra is shown for DI-Ag and DI-Cu, respectively. The photoemission spectra were normalized to the background intensity at ~12 eV. Although the polarization dependence of both DI-Ag and DI-Cu is observed reflecting the anisotropy of the crystal structure, the stronger dependence is seen for DI-Ag as compared with that for DI-Cu. This results indicate that the anisotropy of the electronic states is stronger for DI-Ag than DI-Cu.

References

[1] K. Hiraki and K. Kanoda, Phys. Rev. **B 54**(1996)17276.

[2] T. Kinoshita, K. G. Nath, Y. Haruyama, M. Watanabe, S. Yagi, S. Kimura, and A. Fanelsa, submitted to J. Electron Spectrosc. Relat. Phenom.; T. Kinoshita, K. G. Nath, M. Watanabe, S. Yagi, S. Kimura, and A. Fanelsa, UVSOR Activity Report 1996, p.154.

[3] J. J. Yeh and I. Lindau, Atomic Data and Nuclear Data Tables **32**(1985)1.

[4] T. Miyazaki and K. Terakura, Phys. Rev. **B 54**(1996)10452.

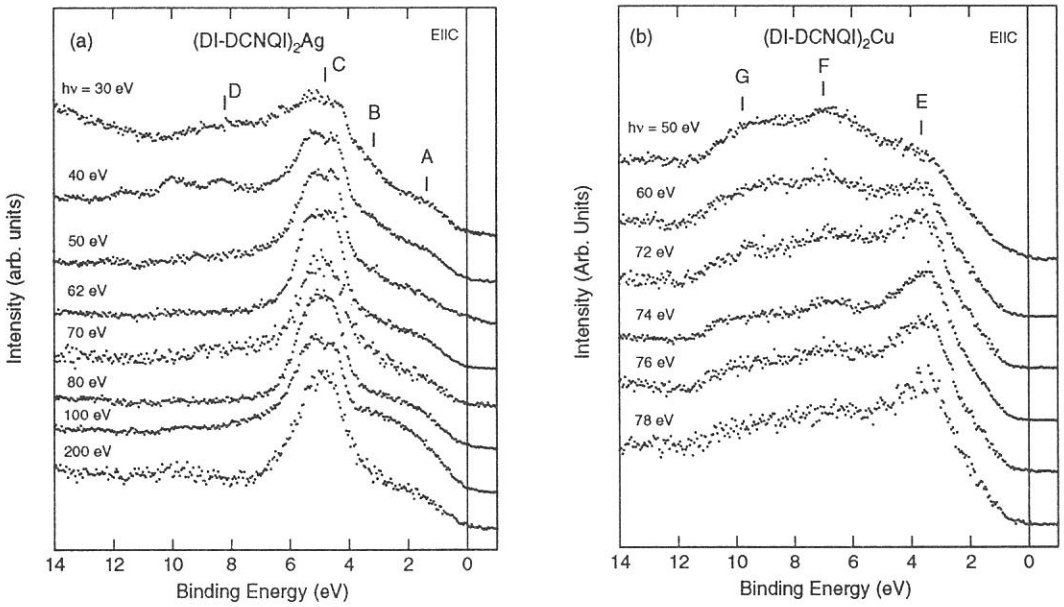

Figure 1. The photon energy dependence of the photoemission spectra (a) of $(DI\text{-}DCNQI)_2Ag$, (b) of $(DI\text{-}DCNQI)_2Cu$. The detection area was 50μm.

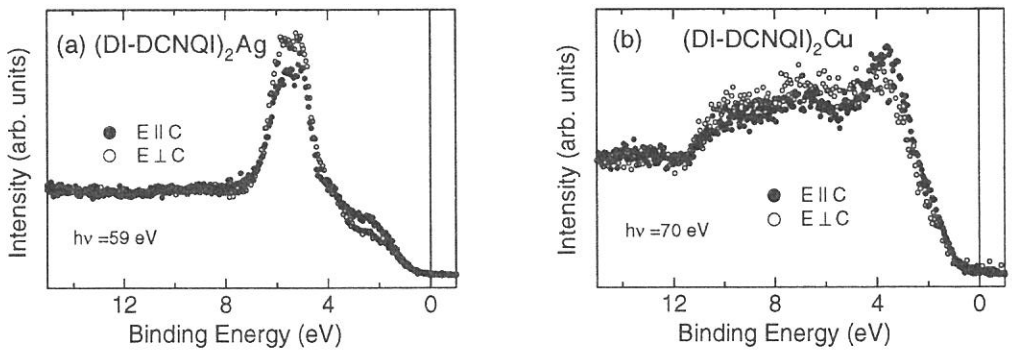

Figure 2. The polarization dependence of the photoemission spectra (a) of $(DI\text{-}DCNQI)_2Ag$, (b) of $(DI\text{-}DCNQI)_2Cu$. The detection area was 50μm.

(BL5B)

Study of magnetism in Ni-thin film by magnetic linear dichroism (MLD) of Ni-3*d* states around the Ni-3*p* threshold

Krishna G. NATH, Yuichi HARUYAMA[A], Shin-ichi KIMURA[A]

Yüksel UFUKTEPE[A*] and Toyohiko KINOSHITA[A]

Department of Structural Molecular Science, Graduate University for Advanced Studies, Okazaki 444-8585
A) UVSOR facility, Institute for Molecular Science, Okazaki 444-8585

It is now well known and firm established that the ultrathin film in nanometer range of 3*d*-materials often shows very interesting and striking magnetic properties different from its bulk. Because of rich variety of unusual magnetic properties in these nearly two-dimensional systems, the thin film magnetism is getting much more interest from both experimentalists and theoreticians[1]. By varying the preparation conditions, i.e., different substrates (non-magnetic, magnetic or semiconductor), substrate temperatures or deposition rate, film thickness, one can modify the structural properties as well as the magnetic properties of the film.

Magnetic Dichroism (MD) effect in both the photoemission and photoabsorption is considered to be one of the most powerful methods to study the magnetism. It provides information of both the surface and interface magnetism. The absolute value of MD intensity can be used to identify the degree of magnetic ordering, since it is proportional to the net system magnetization[2]. The study of element specific magnetism can be done easily by the MD effect selecting different electronic levels of multilayer component. MD experiment in the photoelectron spectroscopy can be performed by using circularly, linearly, or unpolarized light. By using linearly polarized light in the UVSOR facility, it is possible to perform successfully the dichroism experiment for studying the magnetism in thin film system. Here we report the results of magnetic linear dichroism (MLD) of Ni-3*d* states around the Ni-3*p* threshold of ultrathin Ni film grown on fct Co (100).

In order to perform these experiments, the VG ESCALAB 220i-XL[4] system with base pressure of 2×10^{-10} mbar was connected to the beam line. The total energy resolution of the photoelectron spectra at photon energy of 67.2eV was 300meV, which is estimated from the width of the Fermi edge in the spectra of Ni. The photoemission experiments and film evaporation were carried out in room temperature. The Cu (100) substrate was prepared by several cycles of Ar ion sputtering and subsequent careful annealing until sharp LEED pattern was seen. The magnetic substrate Co (100) was grown on Cu (100) to thickness of approximately 10 ML (~18Å). The Co film in this range of thickness exhibits a tetragonally distorted fcc structure having layer spacing of ~1.73Å along Cu [001] direction[3]. The Ni film evaporated on the fct Co (100) also shows same growth structure like Co on Cu (100) that was confirmed by LEED. All films were evaporated from a water-cooled evaporator. High purity (4N) Ni and Co rods were used for the evaporation. The deposition rate, ~0.8ML/min, was calibrated by a quartz thickness monitor placing the same position of sample before and after the deposition.

The geometry of the MLD experiment is described in Figure 1. The sample surface is parallel to the XY plane. Cu [100] direction is along Y-axis. The electric vector (E) of s-polarized light impinges on the sample surface at an angle $\alpha=15°$ out of XY-plane. Electrons are collected at an angle $\theta=8°$ out of the sample Z-axis (see inset). Thin film is magnetized along the both X and Y-directions in the XY-plane (in-plane magnetization). The dichroism signal is obtained by calculating the asymmetry; i.e. the difference between those two spectra divided by sum of them. In the linear dichroism measurements, the asymmetry between two spectra depends on the experimental geometry of light electric vector, electron emission and magnetization direction in the presence of spin-orbit (SO) splitting and exchange interaction[5].

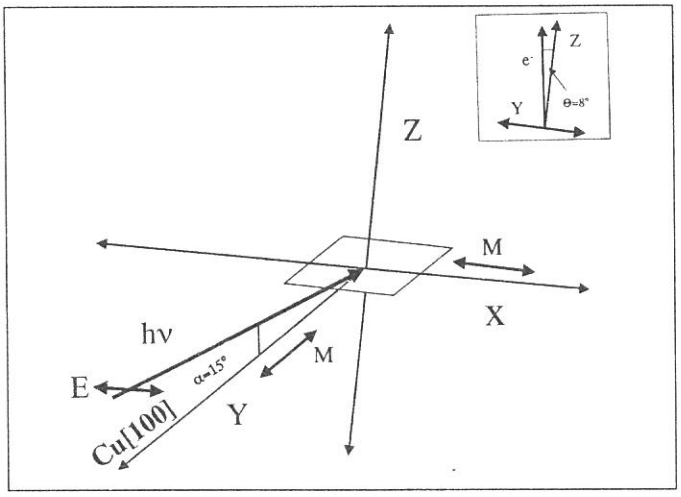

Figure 1. Schematic geometry of MLD experiment (see text).

In Figure 2, we show the Ni-3*d* MLD result for Ni(8ML)/Co(10ML)/Cu(100) taken at the photon energy of 67.2eV, i.e. the Ni-3*p* excitation energy.

The photoemission spectra (upper panel) show the two dominant peaks. One is near the Fermi level stated as main peak with $3d^9$ configuration. Other peak stays at 6eV below of the main peak. This is the so-called 6eV satellite peak assigning as $3d^8$ final state configuration. This satellite peak shows a strong resonant enhancement at the $3p$-excitation energy that was explained via super-Coster-Kronig (sCK) process[6]. The lower panel in Fig. 2 shows the intensity asymmetry between the two spectra taken for two magnetization directions parallel to X and Y-axes as in Fig. 1. This MLD signal is the direct evidence of the long-range ferromagnetic orderings on the Ni-film.

In the lower panel in Fig.2, both the main peak ($3d^9$) and the satellite peak ($3d^8$) show asymmetry but in opposite direction from each other. The $3p$-resonance effect on dichroism of different $3d$ states has been reported by S. Ueda *et al.* for Ni(110) sample[7]. In this previous result, the MLDAD (magnetic linear dichroism in angular distribution) does not show any asymmetry for 6eV-satellite region. But the MCDAD (magnetic circular dichroism in angular distribution) in their results shows asymmetry for 6eV-satellite region with an opposite direction of main peak. Our results are similar to this MCDAD result. Moreover we did not find any asymmetry for satellite peak at other off-resonance conditions. It can be interpreted that the resonance effect on MLD for satellite region is mainly guided by sCK process. A detailed theoretical interpretation is needed for clear understanding of dichroism behavior in this satellite region.

We can use these dichroism results to explorer the magnetic property in Ni-thin film. It has been reported that Ni-film on Cu (100) shows a transition from in-plane magnetization to perpendicular magnetization in the average region of ~7ML up to ~12 ML[8-9]. It was also reported by XMCD measurement[9] that Ni-film of above 9 ML on Cu (100) does not show any in-plane magnetization. But the situation is different for Ni/Co/Cu (100) system. In our MLD experiment, we found the in-plane magnetization for 11 ML Ni-film growth on magnetic Co substrate. But Ni of 12 ML on Cu (100) does not show any in-plane magnetization in our measurement, which is consistent with previous results.

Our dichroism measurement concludes that the resonance effect is present on MLD of 6eV satellite in the valence band photoemission whereas the main valence band peak shows same MLD signal for the both on and off resonance conditions. Magnetic orderings on different Ni-films are also verified by this experiment. The calculation of Ni-MLD is in progress.

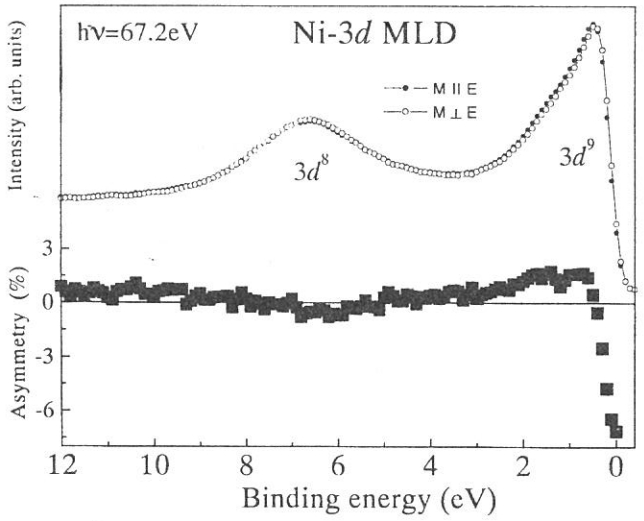

Figure 2. (Upper): Ni-3*d* photoemission spectra taken at 67.2eV- photon energy with s-polarized light (E||X). Dark circles: M ||E and open circles: M ⊥ E. Lower: Asymmetry of those two EDC's showing MLD in photoemission.

We would like to thank the staff members of UVSOR facility for their technical support.

* Visiting Scientist on leave from Physics Department, University of Cukurova, 01330 Adana, Turkey

1. M. T. Johnson *et al.,* Magnetic anisotropy in metallic multilayers: Rep. Prog. Phys. **59** (1996) 1409.
2. W. L. O'Brien *et al.*, Surf. Sci. **334** (1995) 10.
3. J. R. Cerdá *et al.*, J. Phys. Cond. Matt. **5** (1993) 2055.
4. T.Kinoshita *et al.*,UVSOR Activity Report, 96 (1997) 154: J. Electron Spectrosc. Relat. Phenom., in press.
5. R. Feder *et al.*, Magnetic Dichroism and Spin Polarization in Valence Band Photoemission, in Spin-Orbit-Influenced Spectroscopies of Magnetic Solids, edited by H. Ebert and G. Schütz, Springer (Berlin, 1995), p.85.
6. C. Guillot et *al.*, Phys. Rev. Lett. **39** (1977) 1632.
7. S. Ueda *et al.* J. Electron Spectrosc. Relat. Phenom., in print (private communication).
8. B. Schulz *et al.*, Vacuum **46** (1995) 1189.
9. W. L. O'Brien *et al.*, Phys. Rev. B **49** (1994) 15370.

(BL6A2)

SIMULTANEOUS MEASUREMENTS OF PHOTOELECTRON AND LUMINESCENCE OF BARIUM HALIDES

Masao Kamada, Shigeki Fujiwara,[a] Osamu Arimoto,[a] Yasuo Fujii,[b] and Shin-ichiro Tanaka

UVSOR Facility, Institute for Molecular Science, Myodaiji, Okazaki 444-8585, JAPAN
[a]Dept. of Physics, Okayama University, Okayama 700-8530, JAPAN
[b]Dept. of Appl. Physics, Osaka City University, Osaka 558, JAPAN

Barium halides have attracted much interest in recent years, because they show a variety of luminescence and resonant photoemission processes. The so-called Auger-free luminescence (AFL) due to a radiative transition between the valence band and a core level is observed in BaF_2 (1,2). A strong recombination luminescence is observed in BaFCl and BaFBr, which include impurities of rare-earth elements (3). Photoelectron spectra of barium halides show clear solid-state effects on the resonant photoelectron spectra (4). The luminescence has been applied to fast scintillation or registration of x-rays, but the detailed mechanism of the luminescence is sill not clear. Detailed comparison of the photoelectron and luminescence spectra is strongly desired. However, photoelectron and luminescence of barium halides have been measured independently so far. In this work, the irradiation effect on BaF_2 films is investigated using both photoelectron and luminescence spectroscopies. Time-correlation between photoelectrons and AFL photons is also studied for the first time, bringing additional information on the relaxation process of the core-level excited states.

Experiments were carried out at plane-grating monochromator beam line BL6A2. Photoelectron spectra were observed by using a hemispherical energy analyzer installed on a two-axes goniometer in an analyzer chamber, the base pressure of which was about 2×10^{-8} Pa. The angle of incidence of the exciting photon was 60°. The emission angle of the photoelectrons and the angular resolution were about 15° and 1.1°, respectively. Luminescence was collected with a quartz lens mounted in the analyzer chamber, and was focused in a conventional monochromator (Jobin-Yvon HR-320). The luminescence was observed by a photomultiplier (HAMAMATSU R943-02) or a CCD system (Princeton Inc.). The present spectra were not corrected for the spectral sensitivity of the detection system. To avoid charging up effects, BaF_2 thin films of 10-20 nm in thickness were prepared on the gold substrate by in-situ evaporation in a preparation chamber, the base pressure of which was 5×10^{-8} Pa, and then transferred to the analyzer chamber. The Baf_2 films were irradiated with zero-th order light from the plane-grating monochromator through an aluminum filter in order to investigate the irradiation effects. The energy range and flux of the incident photons were 17-150 eV and about 10^{14} phs/s/mm^2, respectively. The time-correlation between the photoelectrons and the AFL photons was observed by using a time-to-amplitude converter (TAC) system with a micro-channel plate photomultiplier (MCP-PM).

Figure 1 shows the luminescence spectra observed at every five-minute's irradiation intervals. The spectra consist of two luminescence bands at about 4.1 and 5.5 eV. The 4.1-eV band may be attributed to the self-trapped exciton (STE), although the energy position of the STE luminescence in BaF_2 films is slightly different from that in single crystals. The 5.5-eV band is AFL, which is due to an electron transition from a valence band to a Ba 5p core-level. Obviously, intensities of the STE luminescence and AFL decrease as the irradiation dose is increased. This figure shows that the decrease in AFL is larger than that in STE luminescence. It should be noted that the spectral shapes of the STE luminescence and AFL changed with irradiation. Especially, a shoulder becomes clear at 5.2 eV as the irradiation dose is increased. This result cannot be interpreted with the simple idea based on the density of states in the valence band. The present result indicates that AFL may be strongly affected by the crystal field around a core hole. This is consistent with the lattice-relaxation model proposed by Kayamuma et al (5).

Figure 2 shows the photoelectron spectra observed at every-five minute's irradiation intervals. The excitation photon energy is 90 eV, and the binding energy is presented relative to the maximum of the valence band. The valence band, Ba 5p3/2, and Ba 5p1/2 photoelectrons are observed at 2.5, 8.5, and 10.5 eV binding energy, respectively. The intensity of these photoelectrons decreases as the irradiation dose is increased, while new bands acquire appreciable intensity at +1.8 and +3.7 eV. According to Karlsson et al. (6), the F 2p states of CaF_2 on Si(111) are redistributed in energy by irradiation, and a new state with an initial-state energy of +5.5 eV is created. A half-filled band due to metallic surface and the suface Ca in a 1+ oxidation state are also observed near fermi level in their spectra. The present photoelectron spectra of BaF_2 show no clear structures due to Ba+1 states and metallic states near fermi level, but new structures are observed around +1.8 and +3.7 eV.

These irradiation-induced structures may be due to the F 2p states, which is different from unirradiated BaF_2. The decrease in intensity of the valence band and Ba-5p photoelectrons may also be attributed to irradiation effects of BaF_2 thin films.

Before irradiation, the condition Evc<Eg is satisfied, resulting in AFL, where Evc and Eg are the energy difference between a valence band and a Ba-5p core level and the band gap energy between a maximum of the valence band and a minimum of the conduction band, respectively. The irradiation-induced structures are produced at Ex (Ex=1.8-3.7 eV) above valence band, and then the condition changes to Evc>Eg-Ex. This causes the decrease in intensity of AFL as the irradiation dose is increased. The decrease in the intensity of the STE luminescence may be due to the defect-induced nonradiative decay process.

The time-correlation between Ba-4d photoelectrons and AFL photons was also observed. The result indicates that photoemission and luminescence processes correlate with each other.

REFERENCES

1) S. Kubota, M. Itoh, J. Ruan(Gen), S. Sakuragi, and S. Hashimoto, Phys. Rev. Lett. 60 (1988) 2319.
2) M. Itoh, S. Kubota, J. Ruan(Gen) and S. Hashimoto, Solid State Sci. 4(1990) 467.
3) A. Onishi, K. Kan'no, Y. Iwabuchi, and N. Mori, Nucl. Instrum. Methods B91 (1994) 210.
4) M. Kamada, K. Ichikawa, and O. Aita, Phys. Rev. B47 (1993) 3511.
5) Y. Kayanuma and A. Kotani, J. Electron Spectrosc. Relat. Phenom. 79 (1996) 219.
6)U. O. Karlsson, F. J. Himpsel, J. F. Morar, F. R. McFeely, D. Rieger, and J. A. Yarmoff, Phys. Rev. Lett. 57 (1986) 1247.

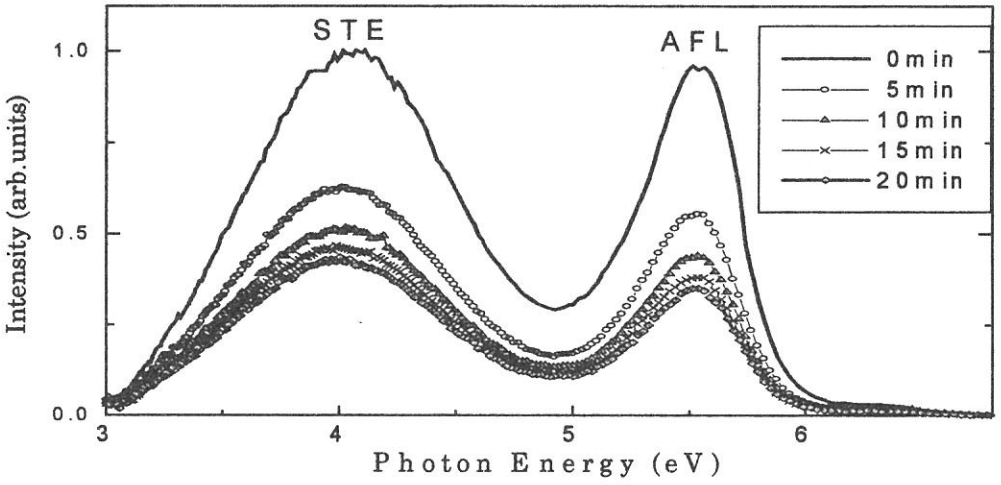

Fig. 1. Luminescence spectra of BaF2.

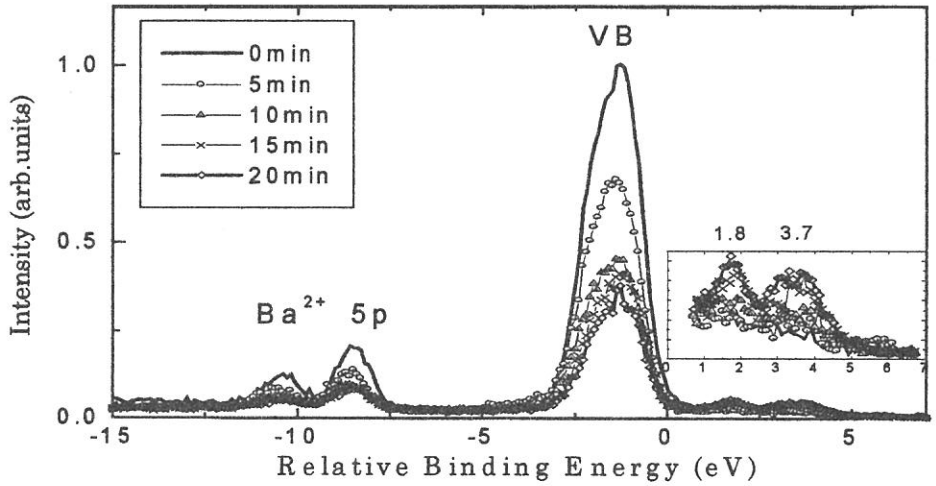

Fig. 2. Photoelectron spectra of BaF2.

(BL6A2)

Valence-Band Photoemission from PbF_2 and $PbCl_2$

M. Itoh, T. Shiokawa, K. Sawada and M. Kamada*

Faculty of Engineering, Shinshu University, Nagano 380-8553
**UVSOR Facility, Institute for Molecular Science, Okazaki 444-8585*

Lead-halide crystals exhibit a variety of interesting physical properties, with possible applications to high-energy particle detectors. Although there have been some earlier photoemission studies of Pb-halides, the nature of their valence bands (VB's) has not yet been understood satisfactorily. In the present experiment, we have performed ultraviolet photoemission spectroscopy (UPS) of PbF_2 and $PbCl_2$ with use of synchrotron radiation as a light source.

Photoelectron spectra were measured with an angle-resolved hemi-spherical analyzer, its resolution being kept at 0.2 eV. Thin film samples were fabricated *in-situ* by evaporation on gold substrates in a preparation chamber, and were then transferred into an analyzing chamber. Reagent-grade powders of PbF_2 and $PbCl_2$ from Merck were used as the starting materials. Thickness of the specimens was maintained at about 100 Å to avoid any charging effect.

For PbF_2, it was found that the spectral shape in the valence region changes seriously with irradiation time. A typical example observed under the excitation with 100-eV photons is shown in Fig. 1. Here, the measurements progressed repeatedly from (a) to (e), with a scanning time of 8 min for each spectrum. The curve (a) is the spectrum taken for a previously unexposed sample. The sample was exposed to 100-eV photons for 25 min before the next measurement. The binding energy is given relative to the top of the VB. Judging from the spectrum (a), the VB in PbF_2 is composed of, at least, three unresolved bands. As obviously seen, the central part of the VB spectra is reduced remarkably with irradiation time. On the other hand, the intensity of the Pb^{2+} 5*d* doublet around 20 eV increases slightly during the measurements, and its peaks shift toward the lower binding-energy side.

In contrast to PbF_2, the VB spectra of $PbCl_2$ did not change seriously even when a sample was exposed to photons for more than 1 hr. Figure 2 shows UPS spectra of $PbCl_2$ excited at different photon energies. It is clear that spectral shape of the VB in $PbCl_2$ is not sensitive to the change in excitation energies in the range 60 to 120 eV.

It seems very likely that the VB spectra of PbF_2 are deformed as a result of photon-stimulated desorption of fluorine atoms from the sample surface. In alkali and alkaline-earth halides, it has been believed that the decay of excited electronic states results in the formation of F-H defect pairs, which leads to ejection of the halogen atom from the sample surface [1]. We suppose that the similar dynamical process of defect formation, occurring within a few atomic layers of the surface, is also responsible for the fluorine desorption in PbF_2 which has fluorite

structure. On the other hand, $PbCl_2$ crystallizes in orthorhombic structure, where the interstitial space is not so open as PbF_2. Accordingly, the defect formation process leading to the chlorine desorption may not be easy to occur in $PbCl_2$.

Based on the present results, we suggest strongly that the central part of the VB in PbF_2 is dominated by fluorine $2p$ state, and the remaining upper and lower parts have lead $6s$ character with small contribution of fluorine $2p$ state. This is consistent with the theoretical calculation of the electronic structures of the VB in PbF_2 [2,3]. Furthermore, because of the similarity in the VB shape between PbF_2 and $PbCl_2$, it is also supposed that the electronic structure of the VB in PbC_2 is essentially the same as that in PbF_2.

Finally, it is noted in Fig. 1 that, when a PbF_2 sample is continuously exposed to photons, the Pb^{2+} $5d$ doublet shifts toward the low-binding-energy side, accompanied by a slight increase in intensity. This is likely due to environmental changes around Pb^{2+} ions induced by the fluorine desorption, with the result that the upper surface layer becomes increasingly lead enriched.

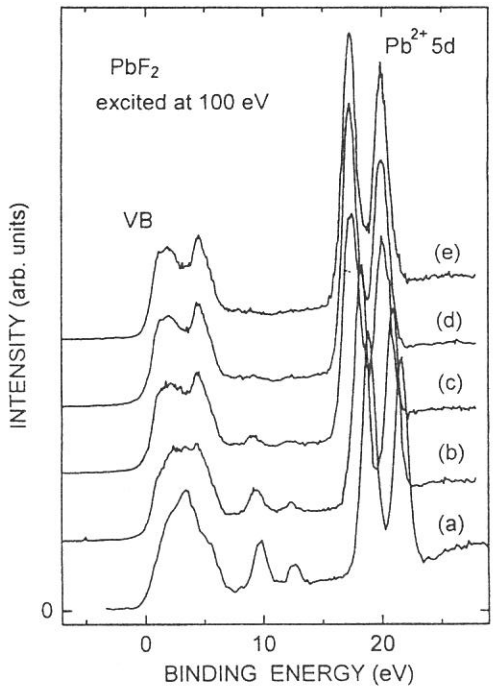

Fig. 1. UPS spectra of PbF_2 excited at 100 eV.

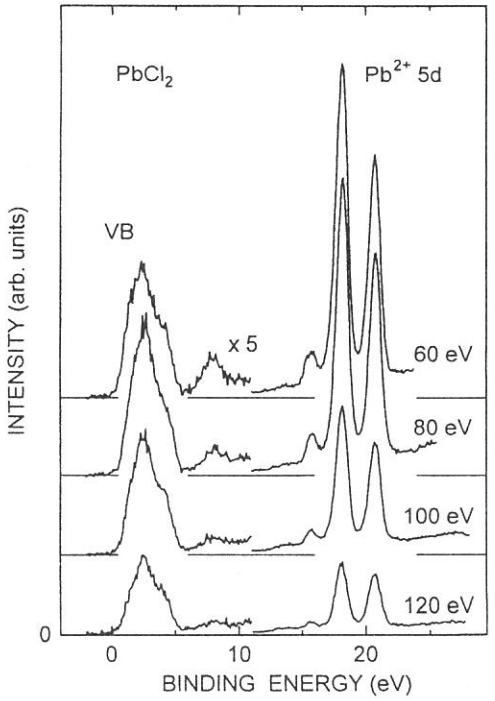

Fig. 2. UPS spectra of $PbCl_2$ excited at 60, 80, 100 and 120 eV.

[1] R.T. Williams: Rad. Effects and Defects in Solids 109 (1989) 175.

[2] M. Nizam, Y. Bouteiller, B. Silvi, C. Pisani, M. Causa and R. Dovesi: J. Phys. C: Solid State Phys. 21 (1988) 5351.

[3] R.A. Evarestov, I.V. Murin and A. V. Petrov: Sov. Phys. Solid State 26 (1984) 1563.

(6A2) **Photoemission studying of Ca-Mg-Ga amorphous alloys**

Nobuhiko Takeichi, Kazuo Soda and Uichiro Mizutani

Department of Crystalline Material Science, Nagoya University, Chikusa-Ku, Nagoya, 464-8603

Introduction

The electron transport properties of many nonmagnetic amorphous alloys have been reported. Especially a number of Ca-based amorphous alloys have been studied because of the fascinating electron transport properties. The resistivity is only 40μΩcm for Ca-Mg binary amorphous alloys, whereas more than 400μΩcm for Ca-Al and Ca-Ga binary ones. Mizutani et al.[1][2] revealed that the replacement of Al and Mg by Ga further increases the resistivity in the Ca-Al-Ga and Ca-Mg-Ga ternary amorphous alloys.

In the present work, We have measured UPS spectra for a series of $Ca_{10}Mg_{90-x}Ga_x$ amorphous alloys (x=0, 10, 20, 30, and 40) and the valence band structure has been discussed in comparison with the XPS spectra measured with the use of the laboratory XPS spectrometers. We show that the narrow Mg-Ga bonding states are formed immediately below the Fermi level as a result of the hybridization of Mg-3p and Ga-4p states and that the formation of this narrow p-states are responsible for the rapid increase in resistivity upon addition of Ga.

Experimental technique

UPS spectra were measured at the BL 6A2 in UVSOR of Institute for Molecular Science, Okazaki, Japan. The excitation energies in the range 12-20 eV was used to study the fine structure of the valence band structure near the Fermi level. Here the Fermi level was determined with reference to that of pure Au. The working pressure of the main chamber during measurement was kept less than 3.0×10^{-10} torr. A clean surface was achieved by using Argon sputtering technique.

Result and Discussion

We have measured the XPS valence band spectra for a series of the amorphous alloys in our laboratory (Surface Science). As is clearly seen in Fig 1, the XPS spectrum for the amorphous $Ca_{10}Mg_{90}$ alloy is well extended only with a shallow depression at the binding energy of 4 eV. However, we can see a substantial growth in the density of states immediately below the Fermi level when Ga is added to the amorphous $Ca_{10}Mg_{90}$ binary alloy. From the XPS valence band profile of the Mg_2Ga compound we conclude that the peak at 1.5 eV can be attributed to the formation of the bonding states between the Ma and Ga atom.

Further detailed information about valence band structure near the Fermi level can be extracted by studying the excitation energy dependence of the photoemission valence band spectra.This is accomplished by using the synchrotron radiation in the energy range 10-20eV. Fig 2 shows the photoemission spectra with different excitation energies for the two amorphous alloys with x=0and 30.

As is clearly from observed spectra, the intensities just below the Fermi level are high when the excitation energy is below 14 eV and are much stronger in the x=30 than in the x=0 amorphous alloy. Intensities just below the Fermi level gradually

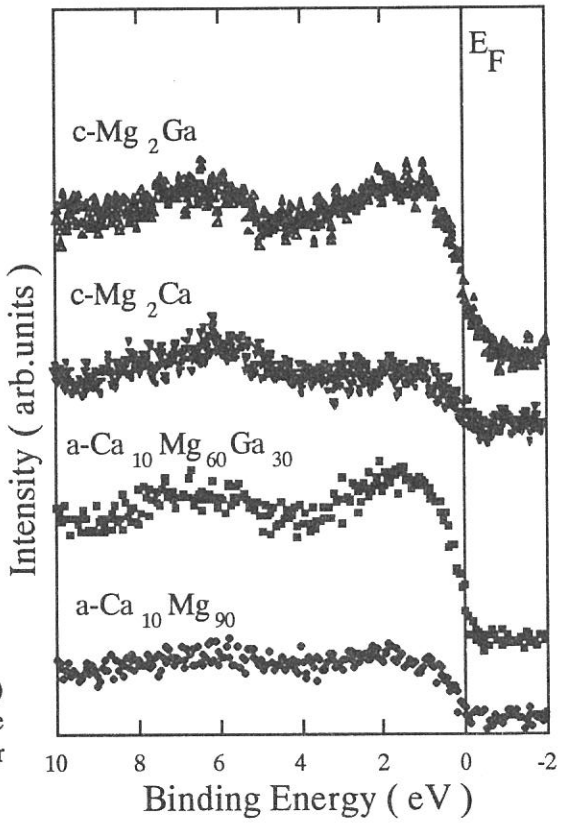

Figure 1.
XPS spectra for two amorphous $Ca_{10}Mg_{90-x}Ga_x$ (x=0,30) alloys. The data for $MgZn_2$-type Mg_2Ca and $LiSb_2$-type Mg_2Ga intermetallic compounds are also shown for comparison.

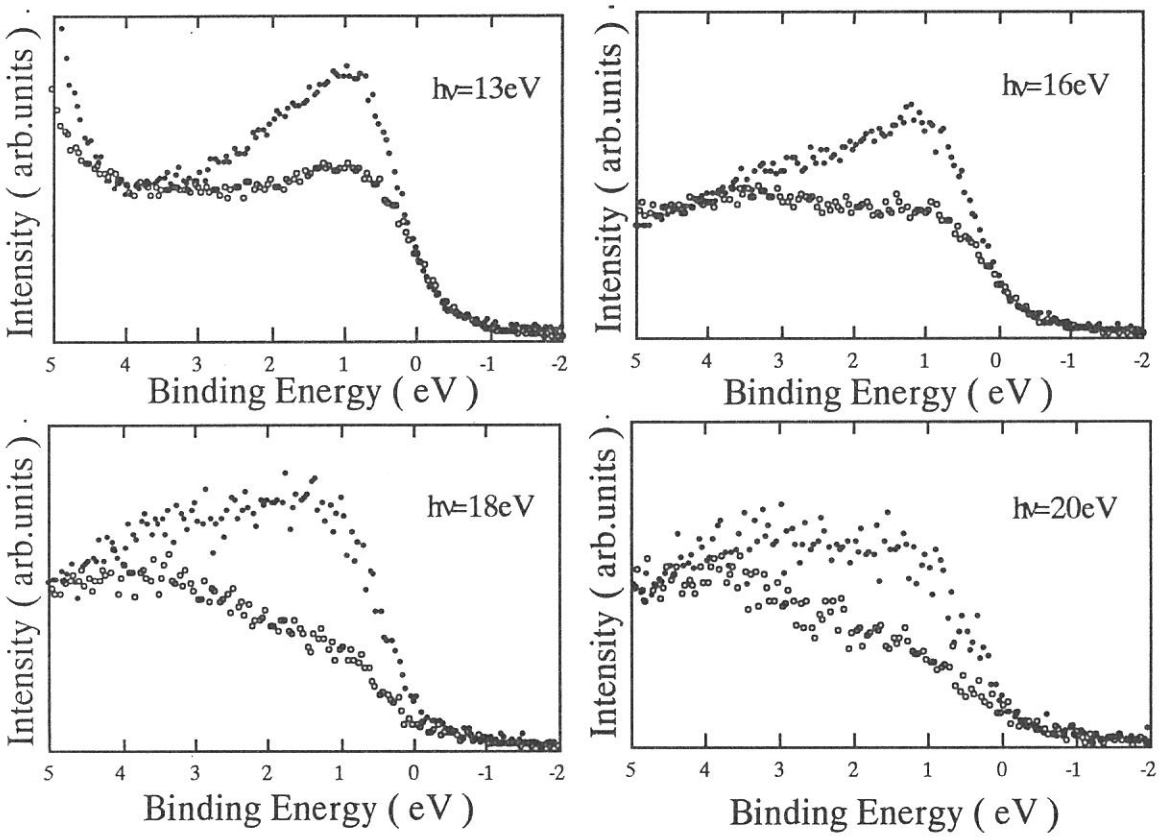

Figure. 2.
UPS spectra for two amorphous $Ca_{10}Mg_{90}$ (○) and $Ca_{10}Mg_{60}Ga_{30}$ (●) alloys.The spectra were taken with the excitation energies of hn = 13, 16, 18 and 20 eV.

decrease with increasing excitation energies in both amorphous alloys. In contrast, the intensities at the binding energy around 4eV increase with increasing excitation energy in both amorphous alloys. According to the calculations of the atomic subshell photoionization cross section[3], the cross section due to p electrons is larger than that of the s electrons in the excitation energy range below 14 eV. But this situation reverses when the excitation energy is increased above 14 eV. The valence band in the $Ca_{10}Mg_{90}$ amorphous alloy is dominated by the Mg-3p,3s states. From the excitation energy dependence of the cross section, We conclude that the Mg-3p states dominate near the Fermi level and the Mg-3s states at binding energy around 4eV.

In contrast to the x=0 amorphous alloy, the intensities immediately below the Fermi level are greatly increased in the x=30 amorphous alloy. This enhancement can be now attributed to the growth of the Ga-4p states hybridized with the Mg-3p states. This hybridization produces the narrow density of states immediately below the Fermi level for the x=30 amorphous alloys and leads to a substantial increase in resistivity in this system.

[1]U. Mizutani, M. Sasaura, Y. Yamada and T. Matsuda; J. Phys. F: Metal Phys. **17** (1987) 667
[2]Z. Diao, Y. Yamada, T. Fukunaga, T. Matsuda and U. Mizutani; Mat. Sci. Eng. **A181/A182** (1994) 1047
[3]J. J. Yeh and I. Lindau; At. Data Nucl. Data Tables **32** (1985) 1

(BL7A)

Mo L_3-edge XANES Study of Hydrogen Molybdenum Bronze

Kentaro NAKAMURA, Kazuo EDA, Noriyuki SOTANI

Department of Chemistry, Faculty of Science,
Kobe University, Nada, Kobe, 657, Japan

Introduction

Hydrogen molybdenum bronze, H_xMoO_3 ($0<x\leqq 2$), is obtained from MoO_3 by reduction of hydrogen in an acidic media or by hydrogen spillover. Four distinct phases have been confirmed in the region $0<x\leqq 2$ by Birtill and Dickens.[1] Eda[2] has studied the thermal decomposition of Type-I ($0.21\leqq x\leqq 0.4$) in a nitrogen atmosphere and discussed the decomposition mechanism. He suggested that the decomposition process took two ways depending on the density of defect in the sample. One is the way to MoO_2 through high defect density and the other, to MoO_3 through the MoO_3 like structure. In both cases, the removal of lattice oxygen in nitrogen or *in vacuo* produces a defect structure. The defect structure can be expected to be effective for catalytic reaction, so that it is interesting to know the detailed structure. We investigated Type-I by heat treatment *in vacuo* by XANES.

Experimental

Hydrogen molybdenum bronze, H_xMoO_3, (x=0.25:Type-I) was obtained by the method described previously.[3]

XANES (X-ray Absorption Near Edge Structure) spectrum was measured at BL-7A of UVSOR at Institute of National Laboratory for Molecular Science, Okazaki, Japan, using a Ge (111) two-crystal monochrometer. After the sample was evacuated to $< 1.0\times10^{-7}$ torr in the sample chamber, the spectrum was measured in total electron yield mode at room temperature.

Result and Discussion

We measured the XANES spectra by the total electron yield mode method and the penetration range of the spectra was possibly several tens angstroms into the bulk. The observed XANES spectra can reflect the surface and/or near the surface structure of the sample. Figure 1 shows the Mo L_3-edge XANES spectra of standard materials of Type-I, MoO_3, and MoO_2. Type-I and MoO_3 has a octahedral symmetry and the spectra show two distinct peaks. The peak at a lower energy side is higher than that at a higher one. The peaks are attributed to the electron transition from $2p_{3/2}$ to a vacant 4d state, t_{2g} (d_{xy}, d_{xz} and d_{yz}) and e_g ($d_{x^2-y^2}$ and d_{z^2}). The peak height at the low energy side differs from that at the high energy side. This difference is due to the difference in the transition cross section of the molecular orbital of Mo(4d)-O(2p); theoretically, the intensity is $t_{2g} : e_g = 3 : 2$ for octahedron. The spectrum of Type-I appeared at little lower energy side than that of MoO_3. Type-I make a minor rearrangement in the Mo-O framework of MoO_6 octahedron which is caused by insertion of hydrogen into MoO_3 intra-layer.[4] The hydrogen atoms are stabilized by bonding to the lattice oxygens in the intra-layer.[4] The energy gap between the peak to peak width, Δ, is used as a parameter of the ligand field splitting of the final state 4d orbital because of reflecting the coordinated environment around Mo atom.[5-7] The second derivatives as shown in Fig.1(II) are used to determine the energy gap. Δ of Type-I and MoO_3 was determined to be 3.2 and 3.4eV, respectively. This result is very reasonable because Δ takes 3.1~4.5eV for the octahedral compounds as shown in Table 1. We obtained Δ=2.5eV for MoO_2. This value was good agreement with that of the reported value of 2.4eV.[7] Δ of MoO_2 having Mo^{4+} ions should be smaller than that of the material having Mo^{6+} ions, because of the less effect of perturbation by the ligand field of six O ions. This result indicates clearly that the reduction of Mo ions leads to the condensation of a total 4d state, and makes the energy gap much smaller.

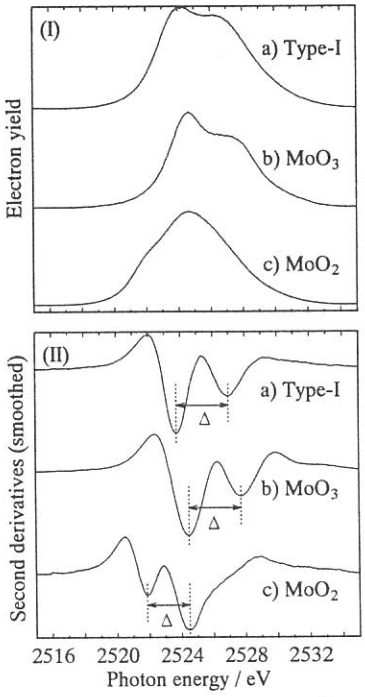

Fig.1 Mo L_3-edge XANES spectra (I) and the second derivatives (II) of reference compounds; a) Type-I, b) MoO_3 and c) MoO_2.

Figure 2 shows the Mo L_3-edge XANES patterns (I) and their second derivatives (II) of Type-I treated at various temperatures *in vacuo*. Δ is summarized in Table 1. The XANES spectra looked like no change at all treated temperature. The second derivative above 723K showed the interesting peak at around 2522eV. Below 673K Δ took 3.1~3.2eV, and above 673K, that gave two value, 3.1~3.2eV and 2.2eV. The former Δ is due to Type-I and/or MoO_3 which have octahedral symmetry, and the later, to MoO_2. We observed MoO_2 by XRD when Type-I was treated at 573K *in vacuo*. It suggests the formation of MoO_2 is easier by about 150K in the bulk than that on the surface. Moreover, we have reported that the formation of MoO_2 is accompanied by the formation of the defect structure. This result strongly suggests the formation of the defect structure in the bulk of Type-I and its diffuse to the surface. We are now studying to reveal the surface composition and their proportion.

Table 1 d-orbital splitting, Δ, of molybdenum compounds.

Sample	Local Structure	Δ / eV
$CoMoO_4$	octahedral	3.3[6]
MoO_3	octahedral	3.4*, 4.0[6], 3.4[7]
Type-I **	octahedral	3.2*, 3.1[7]
Type-II **	octahedral	3.1[7]
$(NH_4)_6Mo_7O_{24}$	octahedral	3.6[6], 2.9[7],
Ba_2CaMoO_6	octahedral	4.5[6]
MoO_2	octahedral	2.5*, 2.4[7]
	treated temperature	
Type-I $H_{0.25}MoO_3$	R.T	3.2
	373K	3.2
	473K	3.1
	523K	3.2
	573K	3.2
	623K	3.2
	673K	3.1
	723K	2.2 3.2
	773K	2.2 3.1
	873K	2.2 3.1

*: present work, **: hydrogen molybdenum bronze

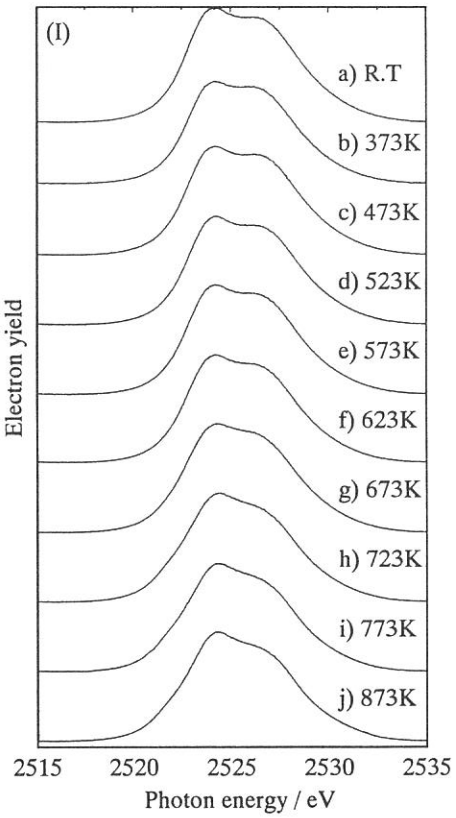

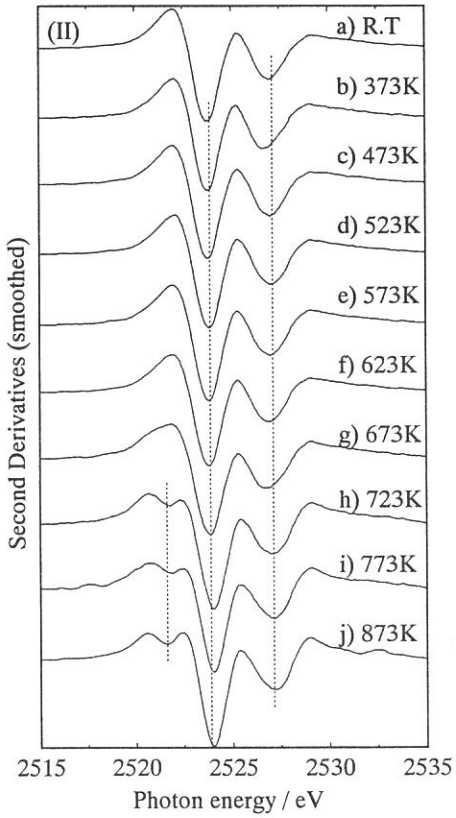

Fig.2 Mo L_3-edge XANES spectra (I) and their second derivatives (II) of Type-I treated at a)room temperature, b)373K, c)473K, d) 523K, e)573K, f)623K, g)673K, h)723K, i)773K, and j)873K in vacuo.

References

1. J. J. Birtill and P. G. Dickens, *Mater Res. Bull.*, **13**, 311 (1978).
2. K. Eda, *J. Mater. Chem.*, **2**, 533 (1992).
3. O. Glemser and G. Lutz, *Z. Anorg. Allg. Chem.*, **264**, 17 (1951); **269**, 93 (1952); **285**, 173 (1956).
4. N. Sotani, K. Eda, and M. Kunitomo, *Trends in Inorganic. Chemistry.*, **1**, 23 (1991).
5. K. Nakamura, K. Eda, N. Sotani, and S. Hasegawa, submitted *J. Chem. Soc. Trans Faraday*.
6. S. R. Bare, G. E. Mitchell, J. J. Maj, G. E. Vrieland and J. L. Gland, *J. Phys. Chem.*, **97**, 6048 (1993).
7. H. Aritani, T. Tanaka, T. Funabiki, S. Yoshida, N. Sotani, K. Eda, and S. Hasegawa, *J. Phys. Chem.*, **100**, 19495 (1996).

(BL7A)

Zr L_3-edge XANES Study of Some ZrO_2 catalysts

Tomomi KOSAKA, Tsutomu OHNARI, Yoshiaki TAKAHASHI and Sadao HASEGAWA

Department of Chemistry, Tokyo Gakugei University, Koganei, Tokyo 184-8501

1 Introduction

Zirconium oxide is a very interesting material because of its thermal stability, its mechanical properties and its acidic, basic surface properties[1]. Sulfated ZrO_2 was known as superacid, for example, which has catalytic function of skeletal isomerization for alkane. Comelli et. al. reported the catalytic activity of sulfated ZrO_2 is not dependent of the precursor salts and of the $Zr(OH)_4$ preparation method[2]. These prompt us to carry out systematic studies on the electron states and catalytic activity of sulfated ZrO_2 catalysts.

In the present study, we described the change of localized electron states and its effect to catalytic activity of sulfated and non-sulfated ZrO_2 catalysts against calcination temperature by Zr L_3-edge XANES analysis.

2 Experiment

Zirconium oxychloride was dissolved in water at R. T., then stirring and slowly added aqueous ammonia (25% NH_3) to obtain $Zr(OH)_4$ until the solution change into pH8. After $Zr(OH)_4$ was washed by a large quantity water, dried at 383K for 24h. Sulfated ZrO_2 was prepared in a solution of 1N H_2SO_4 for 6h with stirring after the mixture were filtered, dried at 383K for 24h. Each $Zr(OH)_4$ calcined at 873K for 3h in air, then non-sulfated ZrO_2 (hereafter it is referred to as ZrO_2) and sulfated one were obtained.

The measurements of Zr L_3-edge XANES spectra were carried out on a facility of BL-7A station of soft X-ray beamline. Each sample was prepared for measurement by grinding with hexane, and mixed with active carbon then spread on a Cu-Be dinode which was attached to a first position of electron multiplier into the beamline chamber. After the chamber had been evacuated, the spectrum was recorded in a total electron yield mode at R. T., using a Ge(111) double crystal monochromator.

3 Results and Discussion

In Fig.1 (A) and (B) shows Zr L_3-edge XANES spectra of ZrO_2 and sulfated ZrO_2 calcined at different temperature. The two peaks (2334 eV (first) and 2336 eV (second)) observed in these spectra that were corresponding to transfer from $2s_{3/2}$ to t_{2g} and e_g of 4d orbital, respectively.

While XRD results of ZrO_2 and sulfated ZrO_2 are exhibited in Fig.2 (A) and (B). The both of catalysts calcined at 473K have amorphous phase. Calcined at 873K, the main structure is metastable tetragonal phase, however a mixture of the tetragonal and monoclinic phase of ZrO_2 was also observed. And calcined at 1073K, practically the monoclinic phase is detected. Zirconium oxide generally changes its crystalline from amorphous to metastable tetragonal, and then monoclinic with increasing calcination temperature[2]. It is explained that SO_4 ion existed in sulfated ZrO_2 was lead to prevent crystal growth. When sulfated ZrO_2 maintained metastble tetragonal phase, activity of skeletal isomerization for n-butane (See as Fig.3) was recognized. In case of monoclinic phase (calcined above 1073K), SO_4 ion was separated from catalyst and sulfated ZrO_2 have no activity of skeletal isomerization.

Thus, these catalysts calcined at 473K has amorphous phase, two peaks was broad and indistinct (in Fig.1). This is supposed that hydroxyl group was obtained in the catalyst cause action, as function of electron donor. When sulfated ZrO_2 catalyst calcined at 873K, the remarkable change of XANES spectra was observed, that is, the intensity of second peak was increased more than that of first peak. It is expected that the electron density between zirconium and oxygen atoms were drawn toward oxygen atom side because SO_4 ion of sulfated ZrO_2 has been electron-accepting. So Zr 4d e_g is nearly empty orbital, electron transfer the higher energy states easily. Calcined above 873K, each spectra are similar shape which intensity of the first peak is higher than that of second peak. It is explained that localization of electron density has became weak due to SO_4 ion desorption

from catalyst, and then reactivity also decreased.

Accordingly, the effect of SO_4 ion addition to electron density of ZrO_2 was depend on the calcined temperature. Sulfated ZrO_2 has a unique electron structure when it was most active for skeletal isomerization. However, further theoretical effort so as to include the electron interaction between catalysts and n-butane is need for understanding of this catalysts activity in detail.

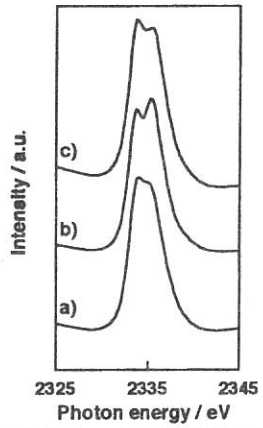

Fig.1 (A) Zr L_3-edge XANES spectra on sulfated ZrO_2 calcined at a) 473K, b) 873K and c) 1073K.

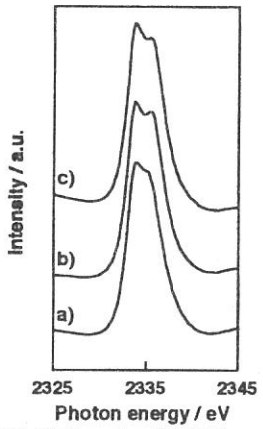

Fig.1 (B) Zr L_3-edge XANES spectra on ZrO_2 calcined at a) 473K, b) 873K and c) 1073K.

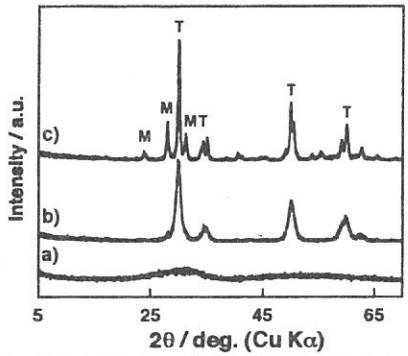

Fig.2 (A) XRD patterns of sulfated ZrO_2 calcined at a) 473K, b) 873K and c)1073K.
T: Tetragonal
M: Monoclinic

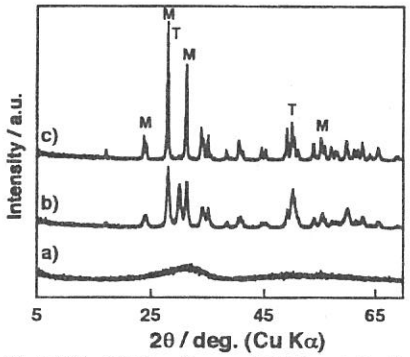

Fig.2 (B) XRD patterns of ZrO_2 calcined at a) 473K, b) 873K and c)1073K.
T: Tetragonal
M: Monoclinic

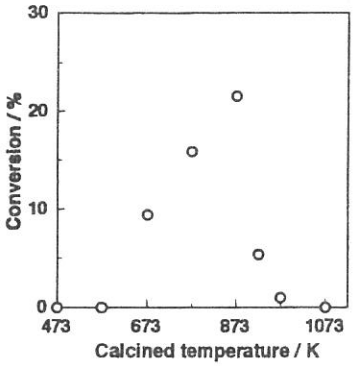

Fig.3 Skeletal isomerization for n-butane on sulfated ZrO_2 against calcined temperature.

1) Y. Nakano, T. Iizuka, H. Hattori, and K. Tanabe., *J. Catal.* **57**, 1 (1979)
2) Raul A. Comelli, Carlos R. Vera, and Jose M. Parera., *J. Catal.* **151** 96 (1995)

(BL7A)

Si K-edge XAFS study of dense vitreous silica

N. Kitamura, H. Mizoguchi, K. Fukumi, H. Kageyama, K. Kadono and M. Makihara

Osaka National Research Institute, AIST, Midorigaoka, Ikeda, Osaka 563-8577

Introduction

Permanent densification of glassy materials is of interest to understand the glass structure and mechanism of the compaction. The structure of densified silica glass has been investigated using infrared absorption, Raman[1] and neutron[2] scattering. However, detail of change in local structure is not clear yet. In this work, we have observed Si K-edge x-ray near-edge structure for pure synthetic and permanently densified silica glasses.

Experimental procedure and results

Synthetic silica glass (Nihon Silica Glass Yamaguchi Co. Ltd.) was used for starting material. Silica glass (3mm in diameter) was densified by heating at 400°C for 2min under 6 GPa with a 6-8 multi-anvil type high pressure apparatus (UHP-2000, Sumitomo Heavy Industry Co. Ltd.). Density of undensified and densified glasses are 2.20 and 2.44 g/cm^3, respectively. X-ray absorption experiments were performed at the double crystal monochromator beam line BL7A. InSb was used as the monochromator crystal. At first, spectra of undensified silica glass were recorded at room temperature by using Total Electron Yield (TEY), Transmission (TR), Drain Current (DC) and Electron Yield (EY) methods. The electron yield spectrum was obtained by an electron multiplier (EM) and an x-ray photo diode (PD) equipped with sample chamber at position of about 45° against beam direction. Non-bias photocurrent is recorded on the PD measurement. Bulk sample put on a manipulator using carbon tape was used on the DC and EY measurements. Powder sample was put on the first photocathode made of Cu-Be of the electron multiplier on the TEY measurement. Powder dispersed film and pure film were used on the TR measurement in the chamber of about 10^{-8} torr. Figure 1 shows the results of the Si K-edge absorption spectra obtained by five methods (EM, PD, TR, DC and EY). The DC curve shows abrupt down in intensity at higher energy side of sharp peak. Since the drop down is suppressed with the increase of scan speed. It will be due to charge up of the sample. The other curves did not depend on scan speed. In the TEY and DC curves, the sharp peak is smaller in intensity than that in the EM or PD curves, although the reason is not clear yet. The EM and PD curves are quite similar with each other. The S/N ratio on the PD measurement is slightly better than in the EM measurement. Since the size of densified glass is small, comparison of absorption spectra for undensified and 11% densified silica glasses was performed by using the TEY measurement. Figure 2 shows the TEY curves for two glasses. They are almost same, but slight difference (small peak) is found near the sharp peak in the XANES spectra. Dominant change in glass structure under densification is decrease of Si-O-Si bond angle[1,2]. An elongation of Si-O bond length is expected from low energy shift of band gap energy which was observed in the vacuum uv reflection spectra at the BL7B[3]. Speculation of the difference in the XANES spectra remains unclear, but the similar behavior is found for some lithium silicate glasses.

References

[1] G. E. Walrafen and M. S. Hokmabadi, Structure and Bonding in Non-Crystalline Solids, ed. By G. E. Walrafen and A. G. Revesz(Plenum, New York, 1986), p.185.

[2] A. Hiramatsu, M. Arai, H. Shibazaki, M. Tsunekawa, T. Otomo, A. C. Hannon, S. M. Bennington, N. Kitamura and A. Ondera, Physica **B219&220**(1996)287.

[3] N. Kitamura, K. Fukumi, K. Kadono, H. Yamashita and K. Suito, Phys. Rev. **B50**(1994)132.

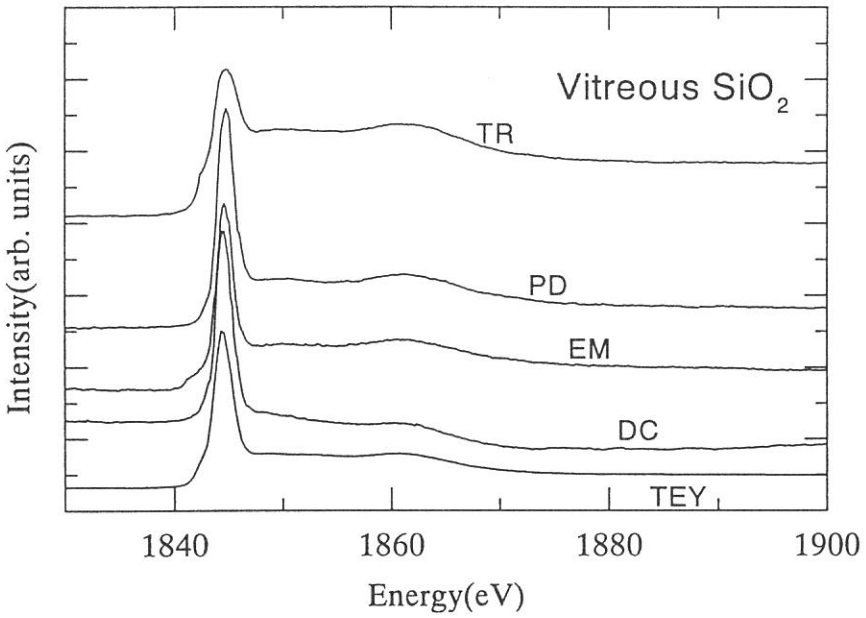

Figure 1 Si K-edge x-ray absorption spectra obtained by total electron yield (TEY), transmission (TR), drain current (DC), electron yield (EM) and x-ray photodiode (PD).

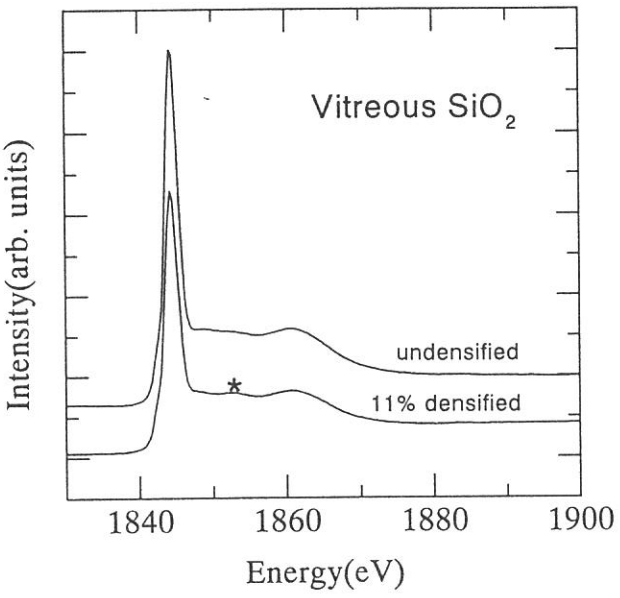

Figure 2 Si K-edge x-ray absorption spectra for undensified and 11% densified silica glasses obtained by total electron yield.

(BL7A)

Si K-edge XANES Study of High Energy Particle Irradiated Silica Glasses

Tomoko Yoshida, Hisao Yoshida[A] and Tetsuo Tanabe

Center for Integrated Research in Science and Engineering, Nagoya University, Furo-cho, Chikusa-ku, Nagoya 464-8603
[A]Department of Applied Chemistry, Graduate School of Engineering, Nagoya University, Furo-cho, Chikusa-ku, Nagoya 464-8603

Introduction

Neutron or high energy ion irradiation effects on silica glass are one of the main concerns for its application for optical windows, insulators and optical fibers in fusion reactors as well as fission reactors. We have studied on the dynamic effects of the irradiation mainly by neutron or ion induced luminescence of silica and revealed that both the electron excitation and the lattice displacement are caused under the irradiation [1,2]. These processes are closely related to the defect formation in silica. However, the structure and the electronic state of the irradiated silica glass are still unclear. In the present study, we investigated the change of local structure and the electronic state of silica glass before and after neutron or He^+ ion irradiation.

Experimental

Synthesized silica glass plates (T-4040) of 15 mm diameter and 2 mm thickness were obtained from Toshiba Ceramics, Japan.

Neutron irradiation experiments were carried out at the nuclear reactor YAYOI. During the experiments YAYOI was operated with a power of 2 kW with an average neutron energy of 1.3 MeV. The fluence of neutron was 6×10^{15} n/cm^2. He^+ ions accelerated up to 20 KeV and mass-analyzed were injected to a silica sample at room temperature through an aperture of 5 mm in diameter. The vacuum of the chamber during the irradiation was maintained below 1×10^{-6} Pa. The fluence of He^+ ions was 2×10^{17} ions/cm^2.

X-ray absorption experiments were carried out on the beam line 7A at UVSOR, Institute for Molecular Science, Okazaki, Japan with a ring energy 750 MeV and stored current 80-200 mA. Spectra were recorded at room temperature in a total electron yield mode, using a two-crystal InSb monochromator. To avoid the charge up by X-ray and to measure a spectrum of only the irradiated part of a sample, unirradiated part of a sample was covered with carbon sheet and Cu sheet having adequate thickness. The sample was put on the first photocathode made of Cu-Be of the electron multiplier.

Results and Discussion

Fig.1 shows Si K-edge XANES spectra of a virgin silica sample (a), its neutron or He^+-irradiated samples (b,c), and a silicon crystal (d). XANES spectrum of a virgin silica glass plate (a) was identical to those of its ground sample and a powder amorphous silica [3]. Therefore, we regarded the charge up effect on the spectrum of a virgin silica sample (plate sample) as negligible. XANES spectrum of a virgin silica sample shows a sharp and prominent peak at around 8 eV (relative energy to Si K-edge). This absorption is possibly due to atomic-like Si 1s to 3p transition. In case of silica, a silicon atom is located at a center of the regular tetrahedron of oxygen atoms. Therefore, Si 3p orbitals should be degenerated resulting in such a sharp absorption.

XANES spectrum of the neutron irradiated silica sample (b) is similar to that of a virgin silica sample (a) , indicating that the local structure around Si atom in silica sample does not change by the neutron irradiation. The neutron fluence, 6×10^{15} n/cm^2 would be too small to bring about a considerable structural change.

On the other hand, XANES spectrum of He^+-irradiated silica sample (c) is different from that of a virgin silica sample (a). The prominent peak at around 8 eV shown in Fig.1 (a) disappears in Fig.1 (c) while a new sharp peak appears at lower energy position. This result may indicate that the reduced Si ion species are formed by He^+ irradiation. According to the TRIM92 calculation, the atomic (oxygen) displacement takes place in the depth region from surface to ca. 300 nm in the present He^+ irradiation experiment. Taking into account this, the presence of the reduced Si ions may be correlated with the formation of Si precipitate due to atomic displacement. Only the irradiated part on surface of silica glass plate was gray and the transmittance of visible light in wavelength region from 300 to 700 nm reduced by He^+ irradiation, supporting the formation of Si precipitate in the vicinity of the surface of a silica glass plate. Since Si K-edge XANES spectra were measured in a total electron yield mode, which mainly monitors X-ray energy dependence of Si KLL Auger electrons yield, the spectrum would reflect such a structural change in the vicinity of the surface. It is clear that the Si precipitate in this He^+-irradiated sample (Fig. 1 c) is not like a Si metal crystalline (Fig. 1 d) . Further approach by EXAFS analysis should be carried out to clarify the local structure of the Si precipitate.

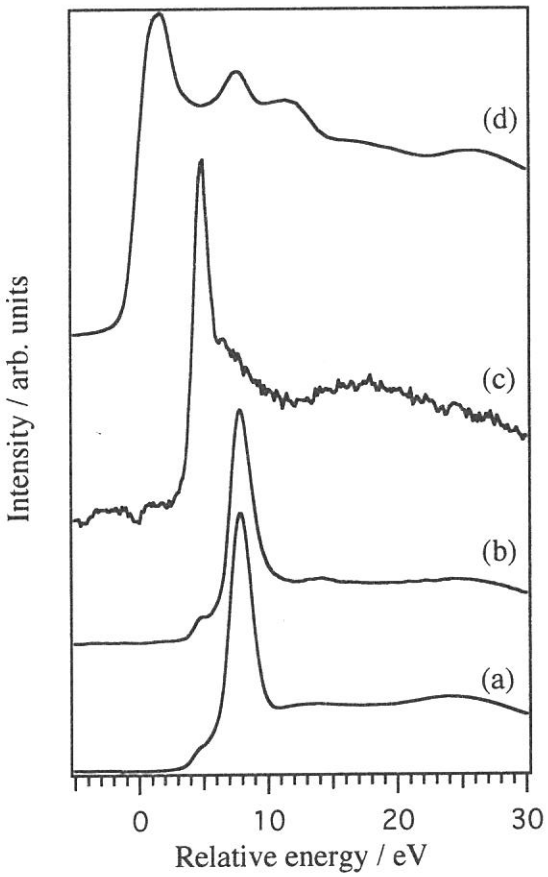

Fig. 1 Si K-edge XANES spectra of a virgin silica sample (a),
its neutron or He^+ -irradiated samples (b,c), and a silicon crystal (d).

References

[1] M. Fujiwara, T. Tanabe, H. Miyamaru and K. Miyazaki, *Nucl. Instr. and Meth. B*, 116 (1996) 536-541.

[2] T. Tanabe, S. Tanaka, K. Yamaguchi. N. Otsuki, T. Iida and M. Yamawaki, *J. Nucl. Mater.*, 212-215 (1994) 1050-1055.

[3] T. Tanaka, S. Yoshida, R. Kanai, T. Shishido, H. Hattori, Y. Takata and K. Kosugi, *J. Phys. IV France*, 7 (1997) 913-914.

(BL7A)

Al K XANES Spectra of Synthetic and Natural Alumina

Takatoshi Murata[A], Giancarlo Della Ventura[B.C], Giannantonio Cibin[C], Augusto Marcelli[C] and Annibale Mottana[B.C]

[A]*Department of Physics, Kyoto University of Education, Kyoto 612-0863, Japan*

[B]*Università di Roma Tre, Dipartimento di Scienze Geologiche, Roma, Italy*

[C]*I.N.F.N.-Laboratori Nazionali di Frascati, Frascati, Italy*

X-ray absorption fine spectra at the Al K-edge were measured experimentally on a chemically pure and physically perfect synthetic α-Al_2O_3 (α-alumina) powder, a natural "ruby/sapphire" (corundum) crystal and a series of artificial "corundums" produced for technical purposes, some of which are physically homogeneous although chemically impure (max. 30,000 atoms per formula unit), and others are impure inhomogeneous phases containing up to 10 vol.% admixed β-alumina. Measurements were done at the soft X-ray beamline BL7A using total yield of the photoelectron. Samples were ground homogeneously to a 3-5 micron size and spread as a fine film on a piece of adhesive tape, which is sticked onto the first photocatode of the Hamamatsu R595 photomultiplier. All measurements were constantly carried out using 0.1 eV steps, so as to assure maximum reproducibility, and warrant meaningful comparison among spectra.

Figure 1 show the XANES spectra fitted to account for the baseline. The Al K edge XANES spectra of α-alumina, "ruby/sapphire" and homogeneous "corundums" differ despite of the identical six-fold co-ordination (short-range arrangement) assumed by O around Al, and vary slightly in relation to the slightly different chemistries of the materials (substitutional defects) as well as on account of the location taken by foreign atoms in the structural lattices (positional defects). The Al K edge XANES spectra of inhomogeneous "corundums" containing the admixed β-alumina phase show additional XANES features reflecting the presence of Al in four-fold co-ordination besides the prevailing six-fold co-ordinated one.

Figure 2 shows the quantitative treatment of the observed changes, which is interpreted in terms of short-range modification of the co-ordination polyhedron and of medium- to long-range modifications in the overall structure; both of them induced by substitutions.

These experiments clearly shows that XAFS spectroscopy it is a reliable technique for both investigate a light element such as Al, and detecting minor co-ordination changes and substitutions (ca. 1~3 wt.% as oxide) of the absorber by dilute other atoms, at least under favourable conditions as those occurring in this system are.

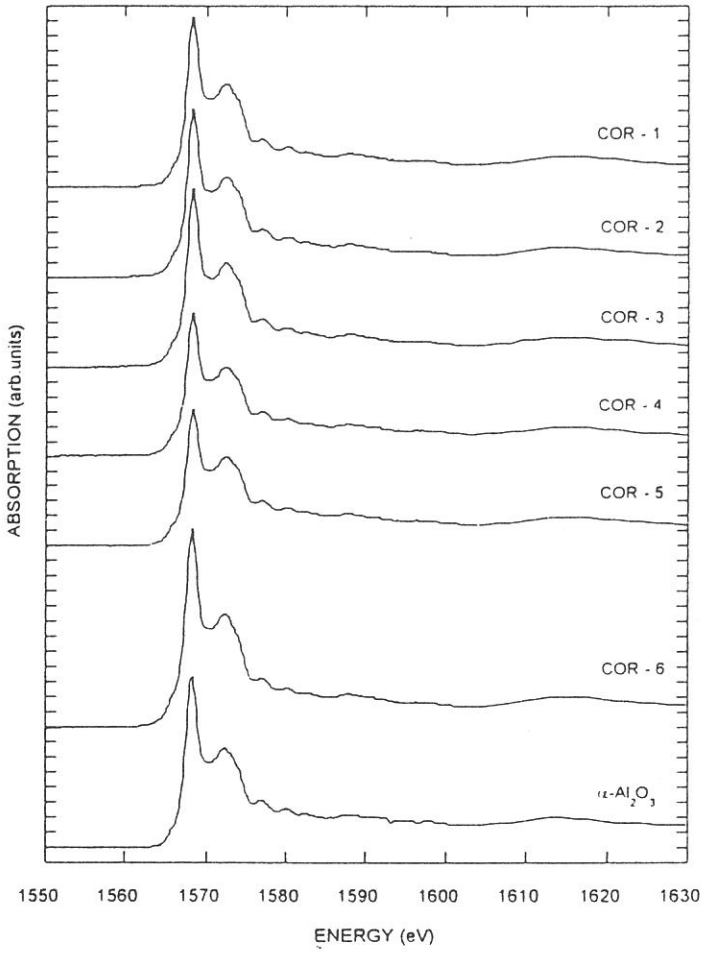

Figure 1

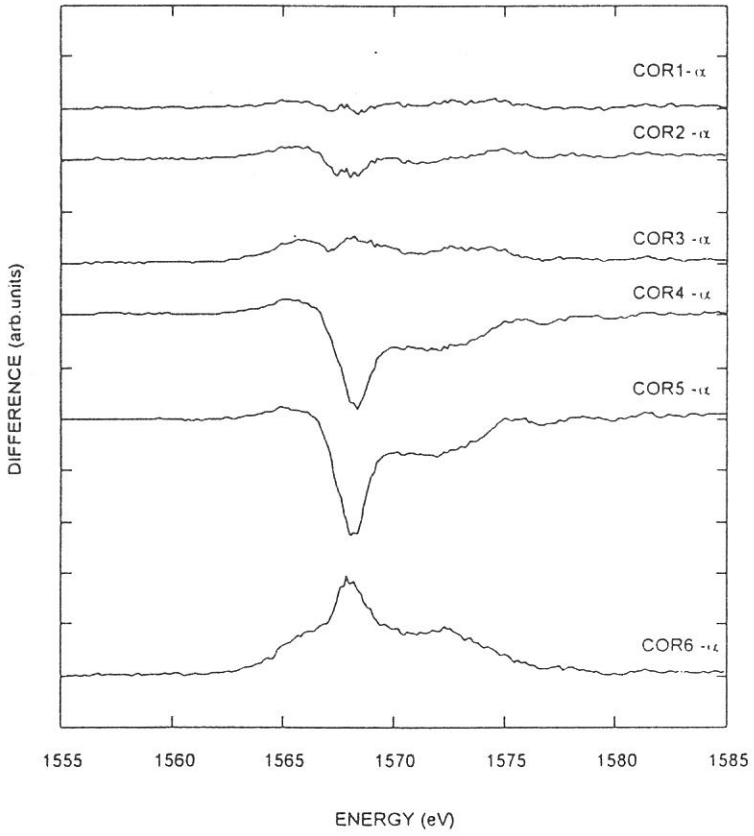

Figure 2

(BL7A)

Polarization-Dependent Alminum K-edge Absorption of AlN and AlGaN

Kazutoshi FUKUI, Ryousuke HIRAI
Faculty of Engineering, Fukui University, Fukui 910-0017, Japan
Fax +81-776-27-8749 fukui@wbase.fuee.fukui-u.ac.jp
Syun-ichi NAOE
Faculty of Engineering, Kanazawa University, Kanazawa 920-11, Japan

The soft X-ray absorption (SXA) around aluminum K-edge have been measured to investigate the electronic structure of the wurzite III-V nitrides (AlN and AlGaN), especially the structure of the unoccupied states. The Al K absorption spectra of III-V nitrides near the Al K-edge in principle represent the partial density of the final states with p symmetry (p-like p-DOS) according to the selection rule. Furthermore, the Al K absorption spectrum gives us the site-specific (aluminum ion site) information, since the core levels are very localized in space. The Al K absorption spectrum also gives us the information about the final states symmetry p_{xy} and p_z, because the incidence soft X-ray light is linearly polarized.

The experiments were carried out at BL7A. Resolutions under the experimental conditions were about 0.8 eV at about 1500 eV. The soft X-ray absorption measurement was performed by using the total photoelectron yield (TY) method. The both AlN and AlGaN thin films which have about 1 μm thickness on SiC were made by the MOCVD method at Riken. All films were cleaned with organic solvents just before the installation into the vacuum chamber, and the measurements were performed at room temperature in the range of 10^{-9} Torr. The sample holder was able to rotate in the vacuum chamber for the angle dependence measurement. The polarization angle α is defined as the angle between the incident light and the normal to the sample surface, i.e., c axis. The α dependence measurements were performed under the p-polarization configuration which means $E \parallel c$ at $\alpha \sim 90$ degree.

Figure 1 shows the Al K absorption spectra of AlN and AlGaN mixed crystals. The energy scale is relative to the threshold energy which correspond to the conduction-band minimum. The threshold energies of AlN, $Al_{0.7}Ga_{0.3}N$, $Al_{0.5}Ga_{0.5}N$ and $Al_{0.3}Ga_{0.7}N$ are 1557.1, 1556.7, 1556.6 and 1555.6 eV respectively. The intensity of each spectrum is normalized at the maximum peak for convenience. They show the similar spectrum shape, but some differences can be seen between AlN and the other AlGaN. This similarity represents that the structure of the p-like p-DOS around the Al ion site almost independent on Ga content, and the differences between AlN and AlGaN show that there are some sensitive Al native electric structures. The energy separation between the lowest energy peak and the main one is gradually decreasing with increasing Ga concentration.

The α dependece absorption measurement was performed each sample which was shown in Fig. 1. Figure 2, for example, shows the Al K absorption of AlN as function of angle α. All spectra are normalized. AlN result in Fig.2 also shows a clear α dependence as well as the other samples. To investigate the symmetry of the unoccupied states, the component analysis of the partial density of the final states with p symmetry (K absorption spectra) have been performed under the assumption as follows; (i) the partial density of the final states with p symmetry consists of p_{xy}, p_z and the α independent components, (ii) the absorption coefficients for $1s \rightarrow p_{xy}$ and $1s \rightarrow p_z$ are proportional to $\cos^2\alpha$ and $\sin^2\alpha$, respectively, where z axis is taken to be parallel to the c axis of the sample. Figure 3 shows the results of the component analysis of the Al K absorption for AlN. The spectrum labeled a represents the α independent component, b the p_z component and c the p_{xy} component, respectively. The component analyses of the Al K absorption for AlGaN were also performed as the same manner. From these results each peak of the p_{xy} and the p_z components is found around the same energy. It suggests that the unoccupied states with p symmetry of III-V nitrides have the similar structure near aluminum site.

The authors would like to thank Dr.S.Tanaka, Dr.Y.Aoyagi (RIKEN) for supply of AlN and AlGaN samples.

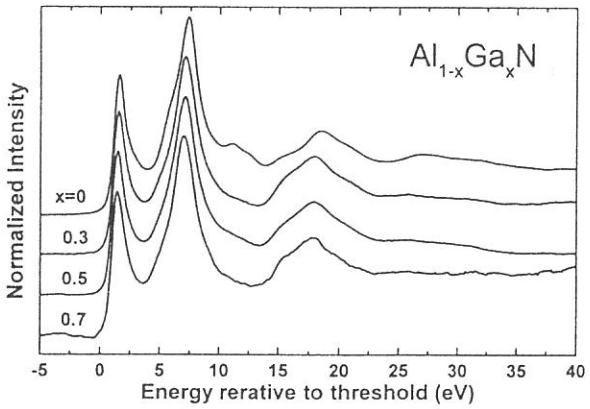

Fig.1 N K absorption spectra of AlN, $Al_{0.7}Ga_{0.3}N$, $Al_{0.5}Ga_{0.5}N$ and $Al_{0.3}Ga_{0.7}N$. The energy scale is relative to the threshold energy.

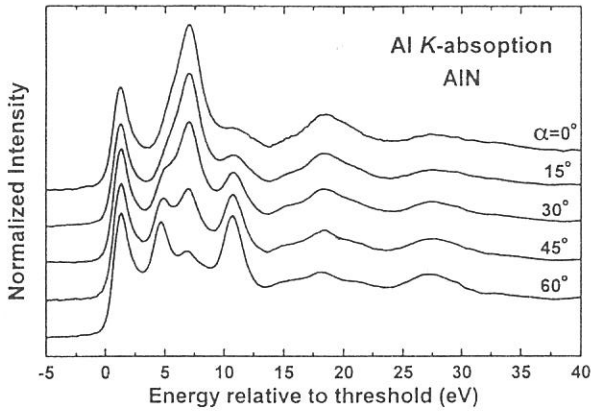

Fig.2 N K absorption spectra of AlN as function of angle which is defined as the angle between the incident light and the normal to the sample surface (c-axis).

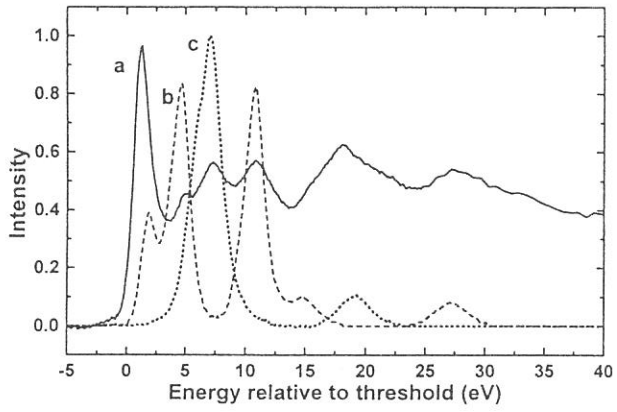

Fig.3 The component analysis results of Fig.2. The spectra labeled a, b and c show the α independent component, p_z and p_{xy} component, respectively.

(BL-7A)

Br L Spectra Measured with YB66 crystal

Tokuo MATSUKAWA, Hiroaki OKUTANI, Kazunori MATSUDA
and Toyohiko KINOSHITA*

Dep. of science, Naruto University of Eduction, Naruto 772-8502, Japan
**UVSOR, Institute for Molecular Science, Okazaki 444-8585, Japan*

1. Introduction

YB_{66} is a new synthesized crystal which has a proper nature to monochromatize soft x-rays from synchrotron radiation.[1] The 2d value of x-ray reflecting (400) plane is 10.76 A , which covers the energy region of 1.2 to 2keV and is suitable for Mg K, Al K and Si K EXAFS experiments.

In this report, we present the recent results of the experiments by using the YB_{66} crystal at the soft x-ray beam line of the UVSOR facility in the Institute for Molecular Science, OKAZAKI. The measurements were carried out on the absorption fine structures at the Br L edges of alkali bromides. As far as we know, there has been no report on the *2p* absorption spectra of bromine ion, whereas a lot of *2p* absorption spectra of chlorine ion had been studied from the very early stages in the history of the synchrotron radiation science. The one of the reasons may be that spectroscopic studies were due to photographic recording in those days and absorption by Br ion in AgBr grains in photographic plates interfere with the spectral features. The other reason is that there has been only few proper crystal with a large 2d value of around 10A for SR studies.

2. Results and discussions

At first, we have tried to use beryl crystal to measure Br L spectra. Figure 1 shows a result on RbBr. The dotted curve I shows a reference signal spectrum and the solid curve I/I0 shows a corrected absorption spectrum with a reference spectrum. At the Br L edge, the both spectra show fluctuating structures which reflect the sharp absorption structures due to the constituent Al atom in beryl crystal. The Al K absorption edge lies accidentally at the Br L_3 edge. The effects of the anomalous dispersion could hardly remove even with a proper correction method. Thus the beryl crystal could not be applied to the spectroscopic studies at Br L edge..

We have measured the Br L_3 absorption spectra of the alkali-bromides by use of YB_{66} crystal. Figure 2 shows the Br L spectra obtained with total photoelectron yield method. No obstructing structure is observed. The L_2 edge is separated well above the L_3 edge The photon energy was referred to the metallic Al K absorption edge. The resolution was also estimated to be 0.8 eV with a width of a derivative curve of the Al K edge. The spectrum shows characteristic structures which are common among the samples. They are designated A through D. In order to fix the bottom of the conduction band, we evaluated the binding energy of the Br *2p* level and the top of the valence band. The high resolution XPS spectra had been measured by monochromatized Al K x-ray source, and the binding energies were measured carefully referred to Au *4f* line. The binding energy of Br *2p* level was determined by adding the photon energy of the Br $L_{\alpha 1}$ (*3d* to *2p* transition) characteristic x-ray to the binding energy of Br *3d* line. The band gap of the bromides was determined from the binding energy of the top of the valence band. In Fig.2 , the energy of the bottom of the conduction band is shown by an arrow.

The fine structures designated A is bellow the conduction band threshold, and may be due to the x-ray exiton absorption. It is interesting that the spectral features are like those of chlorine L_3 spectra[2], considering a difference in a life time broadening between the case of the chlorine and the bromine ions. It has been well known that chlorine L spectra show several

sharp peaks at the chlorine absorption edges. The separations of the peaks correspond well to those of the characteristic structures of the bromides. Table 1 exhibits the relative energies of the characteristic structures to the bottom of the conduction band. Thus the fine structures at Br-L_3 edge may be interpreted on a same way as in the case of chlorides.

References

1) J.Wong *et al., Nucl. Insr. and Meth.,* A195, 243 (1990)
2) O.Aita *et al., J. Phys. Soc. Japan,* 30, 1414 (1971)

Table 1. Energy positions of characteristic structures measured relative to the bottom of the conduction band .

Energy relative to the bottom of the conduction band (eV)					
	A	B	C	D	E
NaBr	-0.6	1.4	3.8	10.3	12.1
KBr	-1.5	0.0	2.0	8.4	6
RbBr	-0.6	0.6	3.2	8.9	

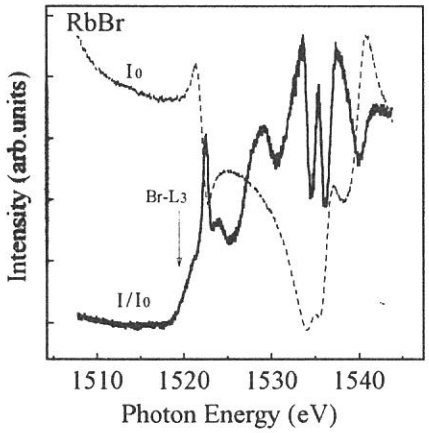

Fig.1. The throughput spectrum with beryl monochromator (I_0) and absorption curve (I/I_0) of RbBr at the Br L_3 edge.

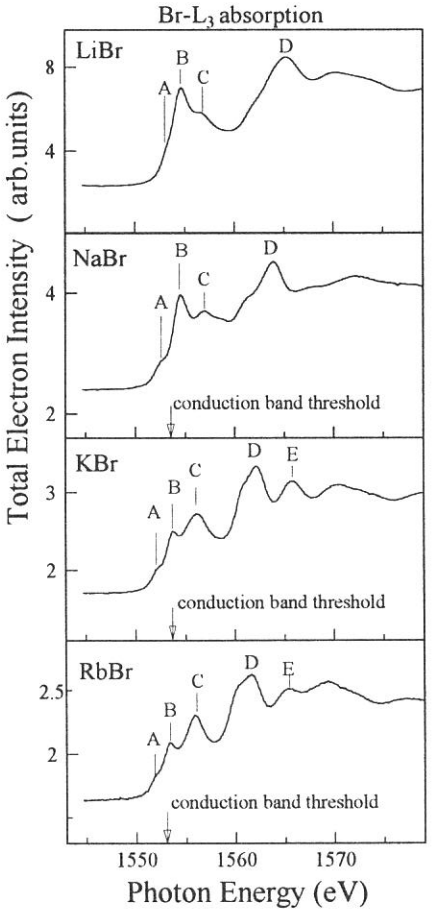

Fig.2. Br L_3 absorption spectra of alkali-bromides. The arrow shows the bottom of the conduction band obtained by XPS .

(BL-7A)

Cu L-edge Absorption Spectra of Copper-aluminate Catalysts

Ken-ichi Shimizu, Hajime Maeshima, Hisao Yoshida and Tadashi Hattori[A]

Department of Applied Chemistry, Graduate School of Engineering, Nagoya University, Chikusa-ku, Nagoya 464-8603

[A]Research Center for Advanced Waste and Emission Management, Nagoya University, Chikusa-ku, Nagoya 464-8603

It is widely accepted that the selective catalytic reduction of NO by hydrocarbons is a potential method to remove NOx practically in excess O_2 [1]. Recently, we have reported that copper-aluminate catalysts having the spinel-type structure show high de-NOx performance, and Cu^{2+} cation interacted with γ-Al_2O_3 matrix is considered to be related to the active species. In this study, we have measured Cu L_3-edge absorption spectra to clarify the local structure of Cu^{2+} cation in Al_2O_3 matrix.

Copper-aluminate samples (Cu-Al_2O_3) with Cu content of 1-30 wt% were prepared by a coprecipitation method. Solutions of copper acetate and aluminum nitrate at the required concentration were coprecipitated using aqueous ammonia. The precipitates were washed, filtered and dried at 395K then calcined in air for 12h at 1073K. Cu-Al_2O_3 with 30 wt% Cu content almost corresponds to $CuAl_2O_4$ (stoichiometric spinel), whose crystal phase was confirmed by XRD.

Cu L-edge X-ray absorption spectra were measured on BL-7A at UVSOR with a ring energy of 750 MeV and a stored current of 70-220 mA in a mode of total electron yields. A double crystal beryl monochromator was used, and the absolute energy scale was calibrated to the Cu2$p_{3/2}$ peak in CuO at 931.3 eV [4]. From each absorption spectrum, subtraction of a sloping background was performed by extrapolating it from the linear region below the threshold. The intensity of the spectra have not been normalized because of missing of an adequate normalizing procedure.

Fig. 1 illustrates Cu L_3-edge absorption spectra of Cu-Al_2O_3 catalysts and $CuAl_2O_4$ (Cu=30 wt%). For 1wt% Cu-Al_2O_3, a peak are seen at 930.8 eV, while for 16wt% Cu-Al_2O_3 and $CuAl_2O_4$, two peaks are seen at 930.1 eV and at 930.8 eV. These peaks exhibited the positions similar to that observed for copper (II) compounds [3,4], and has been considered to be mainly due to $2p \rightarrow 3d$ transitions [4]. By assuming that a single absorption peak results from a single unoccupied d state of Cu^{2+} with an atomic configuration of d^9, the result suggests that the samples contain at least two kinds of Cu^{2+} species with different chemical states and the fraction of such species varies with Cu content.

For a qualitative estimation of the local environment of Cu^{2+} in Cu-Al_2O_3, diffuse reflectance UV-vis spectra were measured. The results showed that Cu^{2+} cations in 16wt% Cu-Al_2O_3 and $CuAl_2O_4$ were both in tetrahedral (λ =7000 cm^{-1}) and octahedral (λ =13000 cm^{-1}) sites, while those in 1wt% Cu-Al_2O_3 were predominantly in octahedral site. Therefore, it is considered that the

absorption peaks at 930.1 eV and at 930.8 eV in Cu L_3-edge spectra should correspond to Cu^{2+} cations in tetrahedral and octahedral sites, respectively.

To estimate the fraction of Cu^{2+} cations in tetrahedral and octahedral sites, we carried out deconvolution of the Cu L_3-edge spectra with two set of curves of a Lorenzians. From the deconvoluted spectrum of $CuAl_2O_4$ (Cu=30 wt%) shown in Fig. 1c, the ratio of the areas of 930.1 eV peak and 930.8 eV peak were determined to be 60/40, which is in good agreement with the ratio of tetrahedral/octahedral obtained by diffraction analysis [5]. Therefore, it is concluded that the ratio of tetrahedral/octahedral can be estimated quantitatively from Cu L_3-edge absorption spectra. By using this method, the ratio of Cu^{2+} cations in tetrahedral and octahedral sites was estimated for a series of Cu-Al_2O_3 and plotted as a function of Cu content (Fig. 2). The result shows that the ratio of tetrahedral/octahedral is a function of composition; it increases as Cu content increases.

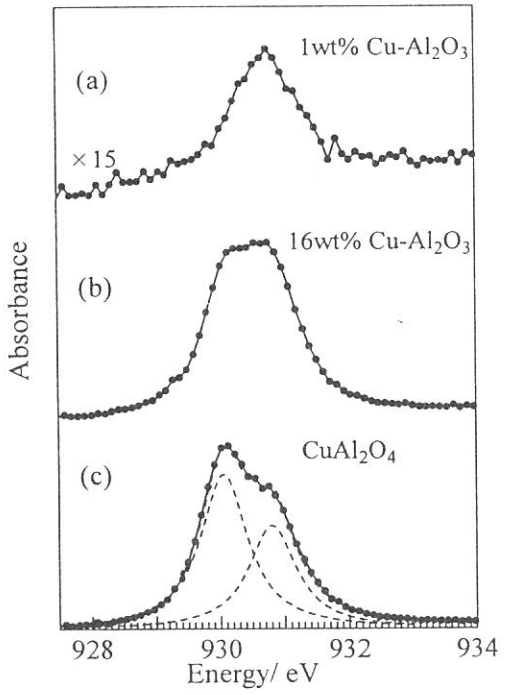

Fig. 1 Cu L_3-edge absorption spectra of (a) 1wt% Cu-Al_2O_3, (b) 16wt% Cu-Al_2O_3 and (c) $CuAl_2O_4$ (Cu=30 wt%) and its deconvoluted spectrum (dotted lines).

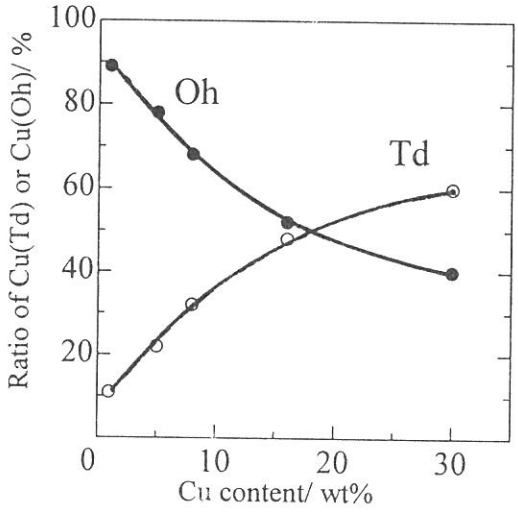

Fig. 2 Ratio of Cu(Td) or Cu(Oh) as a function of Cu content.

[1] M. Iwamoto and H. Yahiro, Catal. Today, 22 (1994) 5.

[2] K. Shimizu, A. Satsuma and T. Hattori, Appl. Catal. B, accepted.

[3] A. S. Koster, Molec. Phys., 26 (1973) 625.

[4] M. Grioni *et al.*, Phys. Rev. B, 39 (1989) 1541.

[5] R. Mark, M. Friedman, J. J. Freeman and F. W. Lytle, J. Catal., 55 (1978) 10.

(BL7A)

Tm4*d* core level resonant photoemission study of TmX (X=S, Se &Te) around Tm3*d* threshold

Krishna G. NATH, Yüksel UFUKTEPE[A*], Shin-ichi KIMURA[A], Toyohiko KINOSHITA[A], Takeshi MATSUMURA[B], Takashi SUZUKI[B], Haruhiko OGASAWARA[C] and Akio KOTANI[C]

Department of Structural Molecular Science, Graduate University for Advanced Studies, Okazaki 444-8585
A) UVSOR facility, Institute for Molecular Science, Okazaki 444-8585
B) Department of Physics, Tohoku University, Sendai 980-77
C) Institute for Solid State Physics, University of Tokyo, Tokyo 106

The applications of resonant photoemssion (RESPES) are important especially for studies of rare earth systems where the multiplet structures are complex due to existence of unfilled and localized 4*f*-shell[1]. In the previous reports[2,3], thulium compounds have been studied by RESPES to know the 4*f* electronic structures for two kinds of ions, Tm^{2+} and Tm^{3+}. It was found in these experiments that a large resonant enhancement occurs in Tm 4*f* emission around Tm4*d* absorption edges[2] and also around Tm3*d* absorption edges[3]. On the other hand, the resonance behavior of deeper core levels such as 4*d* has not been studied extensively so far. The efficiency of other decay channels of core-4*f* resonant transition can be derived using core level RESPES. In addition, the dynamics of collapsing core hole to its ground state can be directly observed through the lifetime-broadened features in the core level photoemission spectra.

In this report, we present the Tm-4*d* RESPES results at the 3*d*-4*f* resonance absorption edges (hν= 1450-1520eV) for mixed-valence Tm-compounds TmS, TmSe and TmTe. Because of different Tm ionic states, these compounds show different physical and electrical properties. The results of this study give us the resonant behaviors of the peaks of 4*d* multiplet and two Tm-valences. The lifetime broadening effect in the 4*d* emission depending on the multiplet structure is discussed herewith. The results of the theoretical calculation are compared with the experimental ones.

The experiments were performed at the beam line, BL7A, with an YB_{66} double crystal monochromator. The VG ESCALAB 220i-XL photoelectron analyzer system with a base pressure of less than $2x10^{-10}$ mbar was connected to the beam line for these experiments. The overall energy resolution of the core level photoemission spectra was less than 1eV both for on- and off-resonant condition. The surfaces of the single crystal samples were cleaned by Ar ion bombardment or by scraping. Oxygen contamination was checked by monitoring the O (1*s*) XPS peak and found to be negligible.

Figures 1(a-d) show the on- and off- resonant 4*d* core level photoemission results for TmS at various photon energies

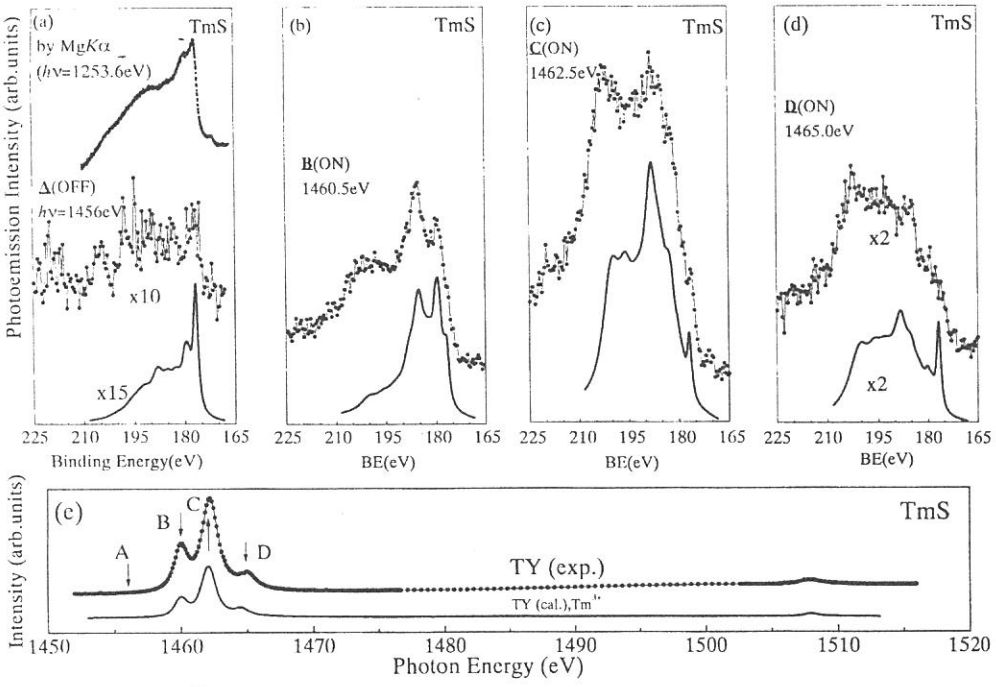

Figure 1. (a-d):Tm 4*d* photoemission spectra of TmS. All solid curves represent the calculated for each resonance condition of the trivalent Tm ion. (a):Off-resonant spectrum along with the XPS spectrum excited by MgKα radiation. (b-d): On-resonant spectra. (e): 3*d*-4*f* total photoelectron yield spectrum of TmS. The marks B, C and D indicate the resonance peak maxima of trivalent features.

along with the XPS spectrum excited by Mg$K\alpha$ radiation. The observed spectra show mostly trivalent nature, but there is small amount of the divalent component. The excitation energies indicated by alphabet (A-D) are selected from the total yield (TY) spectrum shown in Fig.1 (e). Three of these excitation energies (B-D) represent the resonant conditions of trivalent Tm ion, namely correspond to $^3H_6$, $^3G_5$, and $^1H_5$ intermediate states. It is noticed that the 4*d* spectra are strongly enhanced (about 10 times of off-resonant one) under the 3*d*-4*f* resonant condition. The resonance effect of spectra in Figs.1 (b-d) is explained by considering the interference between the direct 4*d* photoemission and the 4*d* excitation to continuum state due to the decay channel, $3d^{10}4d^{10}4f^{12} + h\nu \rightarrow 3d^{9}4d^{10}4f^{13} \rightarrow 3d^{10}4d^{9}4f^{12} + \varepsilon l$. We observed several multiplet peaks in both off- and on-resonant spectra in Figs. 1(b-d). Each 4*d*-multiplet spectrum is extended over the binding energy width of 40eV. The off-resonant spectrum excited by Mg$K\alpha$ radiation in Fig.1 (a) also has the complex multiplet structures.

In Figure 2, we show the resonance effect of the 4*d* spectrum corresponding to Tm^{2+} ion for TmSe, which is considered as a typical mixed valent compound. Figures 2 (b-c) correspond to on- and off- resonant 4*d*-XPS results for TmSe around the 3*d*-excitation region. In order to clarify the divalent component of 4*d* core level, the off-resonant XPS spectra for TmSe, TmS and TmTe, are shown together in Fig.2 (a). The TY spectrum for TmSe in Fig.2 (d) has to be considered as a superposition of Tm^{3+} and Tm^{2+} peaks. The dominant features of the TY spectra are similar to that of TmS in Fig. 1(e), i.e., trivalent peaks at the photon energy of 1460.5, 1462.5, 1465 and 1508eV. In addition, there exits obviously a shoulder at the photon energy of 1459.6eV that belongs to the divalent component as shown in the calculated curve. This is the condition for on-resonant photoemission spectrum of divalent 4*d*-level in Fig.2 (c) that shows also large resonance enhancement comparing with off-resonant one.

The lifetime broadening of the several core-states in the multiplet structure strongly varies with their binding energy that was explained in details by Ogasawara and co-workers[4]. The lifetime of core hole depends on the super-Coster-Kronig transition rate involving 4*f* electrons. The broadening effect according to the selective Auger transition can be easily understood by spin-selection rule and electron correlation effect[5]. The general tendency of 4*d* spectrum is to be more broadened at higher binding energy than the lower one, so that the lower binding energy peaks are sharp with long lifetime as seen for different on- and off-resonant spectra in the Fig.1 and 2. In the lower binding energy sides in the 4d-spectra for TmS and TmSe, the experiments show good agreement with calculation. But there are some disagreements in the higher binding energy sides as seen it the both figures. The origin of this disagreement is not still known.

The core level RESPES study gives us the different spectral features of 4*d* multiplet in the final state vary according to the excitation conditions and different Tm-valences. At the same time, the lifetime broadening phenomenon is also introduced to describe the variation of spectral shape.

We would like to thank the staff members of UVSOR facility staff for their technical support.

*Visiting Scientist on leave from Physics Department, University of Cukurova, 01330 Adana, Turkey

1. A. Kotani, Inner shell photoelectron process in solids, (Handbook on synchrotron Radiation, vol.2, edited by G.V.Marr (North-Holland Physics publishing, Amsterdam, 1987): A.Kotani et al. J. Electron Spectrosc. Relat. Phenom. **60**, 257 (1992).
2. S.-J. Oh *et al.*, Phys. Rev. B **30,** 1937 (1984), Y. Ufuktepe *et al.*, submitted to J. Phys. Soc. Jpn. ;UVSOR Act.Rept. (1996) P.102.
3 T. Kinoshita *et al.*, J. Electron Spectrosc. Relat. Phenom., in print :C.Laubschat *et al.*, Physica. Scripta. **41**, 124 (1990).
4 H. Ogasawara *et al.*, Phys. Rev. B **50,** 12332 (1994).
5. M. Ohno *et al.*, Phys. Rev. A **31**, 2318 (1985): E. G. McGuire, Phys. Rev. A **9**,1840 (1974).

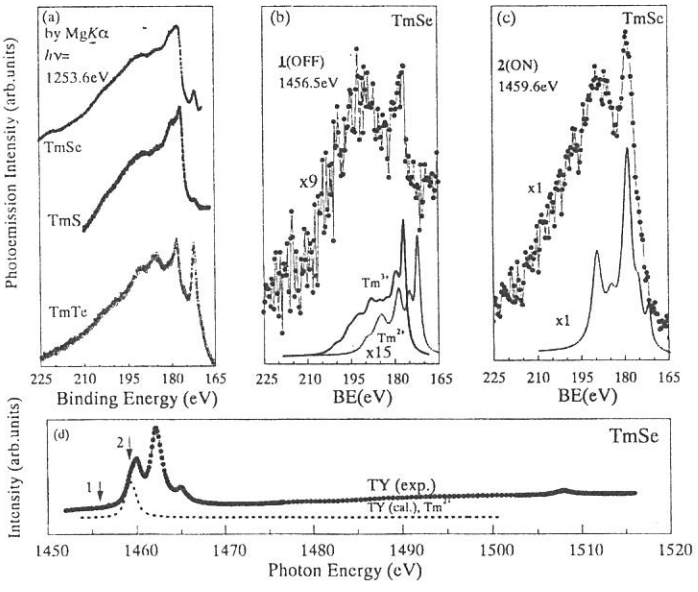

Figure 2. (a): The XPS spectra of TmX (X=S, Se & Te) excited by Mg$K\alpha$ line are used to clarify the divalent and trivalent nature of the 4*d* core level spectra. (b,c): Tm-4*d* core level photoemission spectra near the 3*d*-4*f* excitation conditions for TmSe. (d): 3*d*-4*f* TY spectra of TmSe where the positions 1 and 2 for ON and OFF resonance conditions of divalent component respectively.

(BL7A)

EXAFS Studies in Defective Perovskite Type Oxides Such as $Ba_2In_2O_5$ and $La_{1-x/2}Y_xSc_{1-x/2}O_3$

Yoshiharu UCHIMOTO, Takeshi YAO, Yoshiyuki ITO, and Koichi KAJIHARA

Department of Fundamental Energy Science,
Graduate School of Energy Science, Kyoto University,
Yoshida, Sakyo-ku, Kyoto 606-8317, JAPAN

Recently, a significant amount of work has been devoted to solid oxide fuel cells (SOFCs) utilizing oxide ion conductors as electrolyte. When the operating temperature is reduced to intermediate temperature range (700-800°C), SOFCs could be constructed by less costly materials for interconectors, for example alloys, and technical advantages such as increase reliability and life time will be attained. Since oxide ion conductivity of stabilized zirconia decreases at such temperatures, the development of electrolyte materials having high oxide ion conductivity at the intermediate temperatures is of considerable interest.

Defective perovskite type oxides are excellent candidates for electrolytes of SOFCs operating at intermediate temperature. The perovskite type of oxides such as $Ba_2In_2O_5$ doped with Ca and/or $La_{1-x/2}Y_xSc_{1-x/2}O_3$ are the most promising candidate for electrolytes of intermediate SOFCs. In the perovskite oxides, there are two kinds of cation sites, that is A-site:12 coordination with larger space and B-site:6 coordination with smaller space. Crystal structure, especially local structure of cations must influence the oxide ionic conductivity. In this work, the crystal structure were analyzed by powder X-ray Rietveld method and EXAFS analysis.

Pure and Ca doped $Ba_2In_2O_5$ powder was prepared by usual solid state reaction starting with $BaCO_3$, In_2O_3 and CaO. For the Preparation of $La_{1-x/2}Y_xSc_{1-x/2}O_3$, lanthanum oxide, scandium oxide and yttrium oxide were weighed with molar ratio as La:Y:Sc=1-x/2:x:1-x/2(x=0.00, 0.10, 0.20, 0.30, 0.40) and mixed for 5 h by electric mortar. The mixtures were pressed into disk, heat-treated at 1600℃ for 5 h in air, then left cool in the furnace.

Figure 1 shows fourier transform of Sc K-edge EXAFS function for $La_{0.90}Y_{0.20}Sc_{0.90}O_3$. A peak between 1.0 and 2.5 Å was observed for each sample. This peak was attributed to oxide ions neighboring the absorbing Sc^{3+} ion. Figure 2 shows the inverse Fourier transform of the peak and the result of the parameter fit for each sample. Table 1 shows obtained parameters by the parameter fit. The local interatomic distances of Sc-O which are obtained by the EXAFS analysis are increase with increase of Y dopant content.

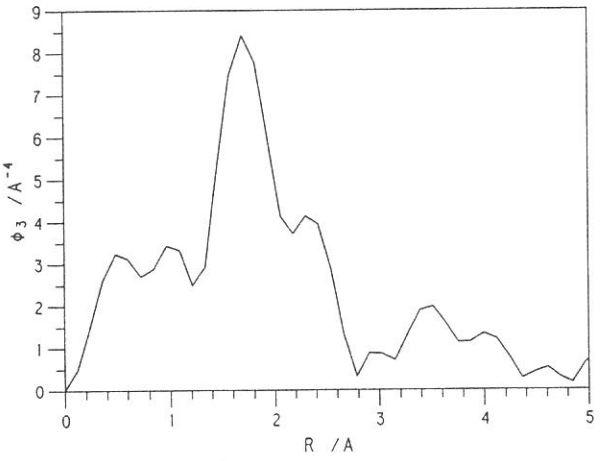

Figure 1 Fourier transform of Sc K-edge EXAFS function for $La_{0.90}Y_{0.20}Sc_{0.90}O_3$

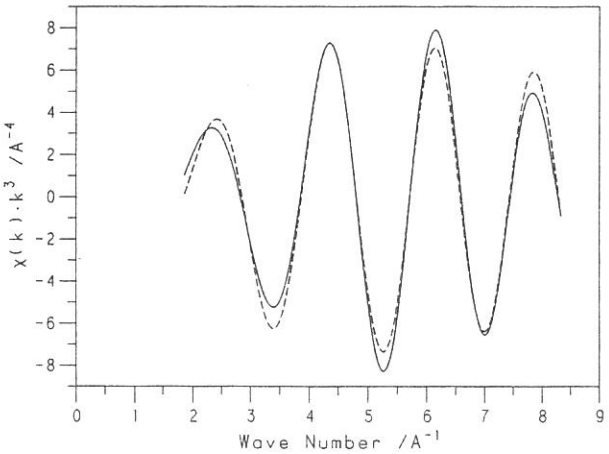

Figure 2 Results of the parameter fitting of the EXAFS function for $La_{0.90}Y_{0.20}Sc_{0.90}O_3$. The solid and broken lines present the experiment and calculation, respectively.

Table 1 Refined parameters of $La_{1-x/2}Y_xSc_{1-x/2}O_3$(x= 0.10, 0.20, 0.30) and reliability factors obtained by the Rietveld analysis.

x	Sc-O / Å	a / Å	b / Å	c / Å
0.0	2.09	5.7973	8.1014	5.6833
0.2	2.10	5.8327	8.1326	5.6867
0.3	2.12	5.8513	8.1545	5.6948

(BL8B1)

Oxidation States in $LiMn_2O_4$ Spinel Oxides from Manganese L-edge Spectroscopy

Yoshiharu UCHIMOTO, Takeshi YAO, Dan ISHIZAKI, and Koichi KAJIHARA

Department of Fundamental Energy Science,
Graduate School of Energy Science, Kyoto University,
Yoshida, Sakyo-ku, Kyoto 606-8317, JAPAN

$LiMn_2O_4$ based spinel type oxides are one of the most promising cathode materials used in lithium ion batteries because their low cost, high theoretical energy density. It is important to clarify valency change and structural change during charge and discharge process in order to understand their electrochemical properties. In the present study, oxidation state of manganese ion in the $LiMn_2O_4$ spinels were determined by using a measurement of Mn L_{23}-edge X-ray absorption near edge structure.

A mixture of Li_2CO_3 and $MnCO_3$ in a mole ratio of 1:4 was heated at 850 ℃ for 48 h in air. The crystal structure of the product was determined by XRD using CuKα radiation to confirm the formation of a well characterized $LiMn_2O_4$. Figure 1 shows a low rate discharge curve of $LiMn_2O_4$. The $LiMn_2O_4$ shows mainly 2 different regions. Between x = 0.2 to 0.5 ($Li_xMn_2O_4$), the discharge voltage was of 4.10 to 4.0 V and then the voltage fell rapidly down to 2.9 V at x = 0.5. XANES analysis were performed to clarify the oxidation state of manganese for various x values in $Li_xMn_2O_4$.

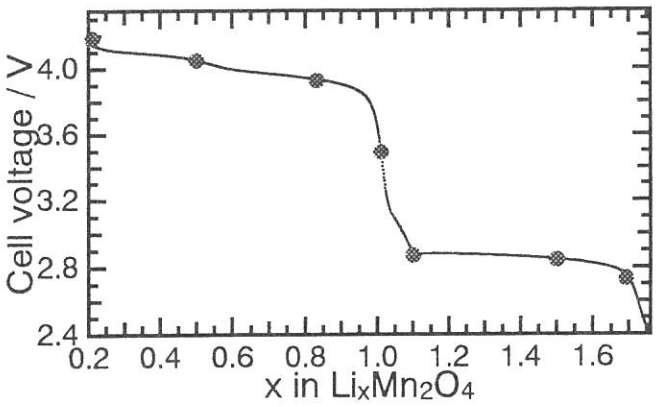

Fig. 1 Variations of electrode potential with capacity upon first discharging of $LiMn_2O_4$.

Fig. 2 shows the Mn L-edge X-ray absorption spectrum of $Li_xMn_2O_4$ (x=0.22, 0.50, 0.87, 0.98, 1.10, 1.50, and 1.70) together with MnO_2 (Mn^{4+}) and Mn_2O_3 (Mn^{3+}). The spectra correspond to $Mn2p^63d^n$ to $Mn2p^53d^{n+1}$ transitions. Figure 2 shows that the Mn L_3 absorption edge of Mn_2O_3 is about 642.0 eV and that of MnO_2 is 643.4 eV. These results indicated that increasing the oxidation state of manganese, the Mn L_3 absorption edge shift to higher energy.

As shown in Fig. 2, the peak of $Li_{0.98}Mn_2O_4$ is a combination of peak of Mn_2O_3 and MnO_2. At high x value such as x = 1.70, contribution of Mn^{3+} increase. On the other hand, at low x values of 0.22, contribution of Mn^{4+} increase. In conclusion, the average manganese valence in $LiMn_2O_4$ is between 3 and 4 and the valence is increase during the electrochemical extraction of lithium.

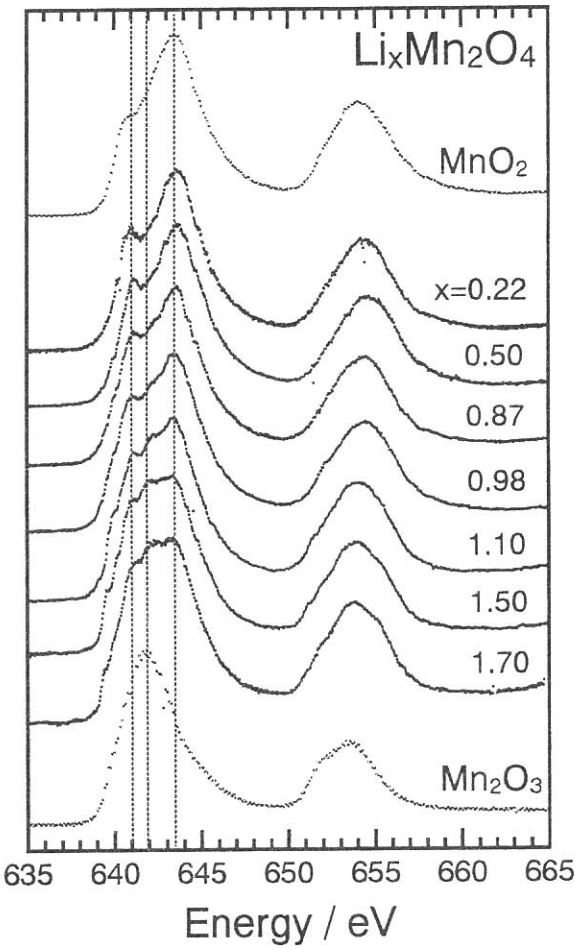

Fig. 2. Mn L-edge XANES of $LiMn_2O_4$ at various x values ($Li_xMn_2O_4$) potentials. x = x=0.22, 0.50, 0.87, 0.98, 1.10, 1.50, and 1.70

(BL8B1)

Mn-*L* absorption spectra in the paramagnetic and antiferromagnetic state in the intermetallic compounds YMn_2 and YMn_{12}

I.S. Dubenko[1], T. Gejo[2], E. Gratz[3], Y. Hosokoshi[2], K. Inoue[2],

S. Kimura[2], T. Kinoshita[2], A.S. Markosyan[2,1],

[1]*Faculy of Physics, Moscow State University, 119899 Moscow, Russia.*

[2]*Institute for Molecular Science, Myodaiji, Okazaki 444-8585, Japan,*

[3]*Institute for Experimental Physics, Technical University Vienna, A-1040 Wien Austria*

The nature of magnetism of the intermetallic compound YMn_2 is a subject of a long term discussion. It orders antiferromagnetically by a first order type phase transition with a wide hysteresis over a range 80 - 105 K. This transition is accompanied by a large volume expansion of ≈6 % and a tetragonal distortion. In the paramagnetic state, the thermal expansion of YMn_2 is essentially enhanced and $\alpha = d(\ln L)/dT$ attains 55×10^{-6} K^{-1}. Different models, geometrical frustration, metamagnetism, critical Mn-Mn distance [1-3], proposed to account for the anomalous properties of YMn_2 have a descriptive character and do not analyse the mechansims of magnetic instability. Recently was found that the paramagnetic thermal expansion coefficient is strongly enhanced in other binary Y-Mn compounds, too [4]. It was suggested that the anomalous properties of the binary Y-Mn compounds are related to the Mn electronic structure instability; one of the possible explanations could be a continuous temperature induced change in the Mn electronic structure (an itinerant analog of the intermadiate valence state), which can provide a strong temperature dependence of the local spin density on Mn sites and, hence, give rise to an enhancement of the thermal expansion. A change in the Mn electronic structure was recently observed by XAS investigation performed at the Mn *K*-edge in the $Y(Mn_{1-x}Ni_x)_2$ system [5].

In this work an attempt is made to observe directly the possible co-existence of different Mn-states in YMn_2 and YMn_{12} by recording the soft X-ray absorption spectra of the $2p$ (Mn) and $4d$ (Y) core levels at different temperatures above and below the Neel temperature (52, 85, 125 and 300 K) by using the BL8B1 beam line.

Table. Basic characteristics of YMn_2 and YMn_{12}.

Compound	YMn_2	YMn_{12}
Crystal structure and paramaters (Å)	Cubic, *Fd3m*, a = 7.675	Tetragonal, *I4/mm*, a = 8.579, c = 4.760
T_N (K)	80 - 105	110
μ_{Mn} at 4 K (μ_B)	2.7	0.66 (Mn(8i)) 0.66 (Mn(8j)) 0.22 (Mn(8f))

In Fig. 1 the Mn *L*-egde absorption spectra of YMn_2 and YMn_{12} are shown at different temperatures. The spectra correspond to Mn $2p^63d^n \rightarrow 2p^53d^{n+1}$ transitions and present two well resolved peaks separated by the spin-orbital interaction of the Mn $2p$ core hole.

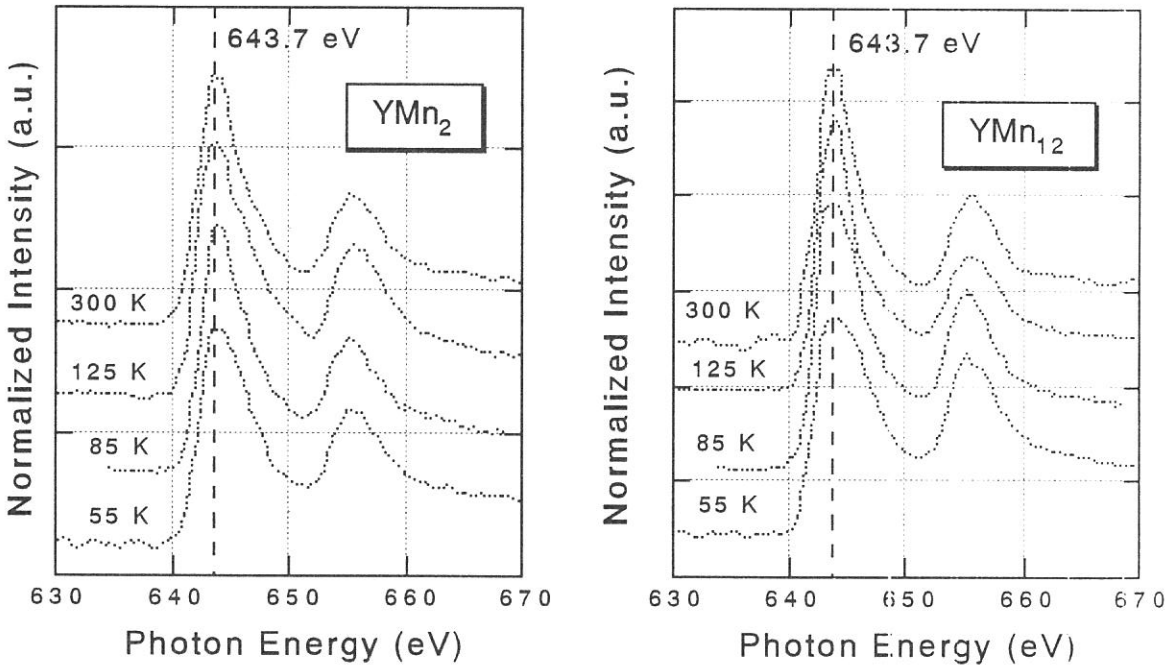

Fig. 1 Mn L-edge absorption spectra of YMn_2 and YMn_{12} at differen temperatures.

The position of the L_3 absorption edge, 643.7 eV, is very near to that observed in MnO_2 (Mn^{4+}) by XANES measurements [6]. From the magnetic data, the Mn state in YMn_2 is rather close to Mn^{3+}, while in YMn_{12} it is close to Mn^{6+}. A close inspection of the linewidth shows a weak temperature variation with a broadening below T_N (Fig. 2). This can be ascribed to a change in the Mn-electronic structure induced by a magnetic order. However, in order to investigate the influence of the 3*d*-electron shell on the Mn core levels, higher resolution is required. Similar behavior was observed when collecting Y K-egde absorption spectra of these intermetallics.

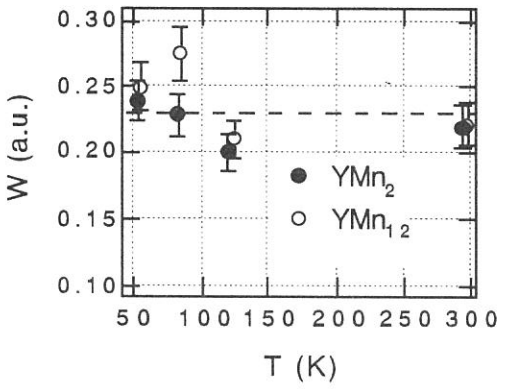

Fig. 2. Linewidth vs. T for YMn_2 and YMn_{12}

References

1. R. Ballou, J. Deportes, R. Lemaire and B. Ouladdiaf, J. Appl. Phys. **63**, 3487 (1988).
2. I.Yu. Gaidukova, I.S. Dubenko, R.Z. Levitin, A.S. Markosyan and A.N. Pirogov, Zh. Eksp. Teor. Fiz. **94**, 234 (1988) [Sov. Phys. JETP **67**, 2522 (1988)].
3. M. Shiga, Physica **B 149**, 249 (1988).
4. I.S. Dubenko, I.Yu. Gaidukova, S.A. Granovsky, E. Gratz, D. Gurjazkas, A.S. Markosyan and H. Mueller, Sol. State Commun. **103**, 495 (1997).
5. J. Chaboy, A. Marcelli, M.R. Ibarra and A. del Moral, Sol. State Commun. **91**, 859 (1994).
6. R.S. Liu, L.Y. Jang, J.M. Chen, Y.C. Tsai, Y.D. Hwang and R.G. Liu, J. Sol. State Chem. **128**, 326 (1997).

(BL8B1)

Polarization-Dependent Nitrogen K-edge Absorption of AlN, GaN, InN and AlGaN

Kazutoshi FUKUI, Ryousuke HIRAI, Akio YAMAMOTO
Faculty of Engineering, Fukui University, Fukui 910-0017, Japan
Fax +81-776-27-8749 fukui@wbase.fuee.fukui-u.ac.jp

The soft X-ray absorption (SXA) around nitrogen K-edge have been measured to investigate the electronic structure of the wurzite III-V nitrides, especially the structure of the unoccupied states. The N K absorption spectra of III-V nitrides near the N K-edge in principle represent the partial density of the final states with p symmetry according to the selection rule. Furthermore, the N K absorption spectrum gives us the site-specific (nitrogen ion site) information, since the core levels are very localized in space. The N K absorption spectrum also gives us the information about the final states symmetry p_{xy} and p_z, because the incidence soft X-ray light is linearly polarized.

The experiments were carried out at BL8B1. Resolutions under the experimental conditions were about 0.5 eV at 400 eV. The soft X-ray absorption measurement was performed by using the total photoelectron yield (TY) method. Thin films were made by the MOCVD method at Nichia Chemical (GaN), Riken (AlN and AlGaN) and Fukui University (InN). GaN thin film is 2.8 μm thickness on α-Al_2O_3 substrate. Both AlN and AlGaN thin films are 1 μm on SiC, and InN thin film is 0.1 μm on GaAs(111). All films were cleaned with organic solvents just before the installation into the vacuum chamber, and the measurements were performed at room temperature in the range of 10^{-8} Torr. The sample holder was able to rotate in the vacuum chamber for the angle dependence measurement. The polarization angle α is defined as the angle between the incident light and the normal to the sample surface, i.e., c axis. The α dependence measurements were performed under the p-polarization configuration which means $E \parallel c$ at $\alpha \sim 90$ degree. We were also performed the α dependence measurements at the N K absorption under the s-polarization configuration ($E \perp c$ at any α), and found that there was no angle dependence.

Figure 1(a) shows the N K absorption spectra of AlN, GaN and InN, and Fig.1(b) shows those of AlGaN mixed crystal. The energy scale is relative to the threshold energy which correspond to the conduction-band minimum. The threshold energies of AlN, GaN and InN are 395.0, 395.0 and 392.2 eV respectively. The labels A to G are corresponding to those for GaN in Ref. 1. The intensity of each spectrum is normalized at the peak B for convenience. The spectra feature of GaN and InN are good agreement with the previous works [1-3]. All spectra seem to be explained by the same labelling. It may be suggested that the electric structures of the unoccupied states around nitrogen ion for III-V nitrides basically consist of the similar components.

The α dependence absorption measurement was performed each sample which was shown in Fig. 1(a) and (b). Figure 2, for example, shows the N K absorption of AlN as function of angle α. All spectra are normalized. AlN result in Fig.2 also shows a clear α dependence as well as the other samples. Both the angle independence under the s polarization configuration and the clear angle dependence under the p polarization configuration are good agreement with the fact that the III-V nitrides are hexagonal and their c axes are perpendicular to the surface. To investigate the symmetry of the unoccupied states, the component analysis of the partial density of the final states with p symmetry (K absorption spectra) have been performed under the assumption as follows; (i) the partial density of the final states with p symmetry consists of p_{xy}, p_z and the α independent components, (ii) the absorption coefficients for $1s \rightarrow p_{xy}$ and $1s \rightarrow p_z$ are proportional to $\cos^2 \alpha$ and $\sin^2 \alpha$, respectively, where z axis is taken to be parallel to the c axis of the sample. Figure 3 shows the results of the component analysis of the N K absorption for AlN. The spectrum labeled a represents the α independent component, b the p_z component and c the p_{xy} component, respectively. The component analyses of the N K absorption for GaN, InN and AlGaN were also performed as the same manner. From these results each peak of the p_{xy} and the p_z components is found around the same energy. It suggests that

the unoccupied states with p symmetry of III-V nitrides have the similar structure near nitrogen site. Our results also show that the intensity ratio of the α independent component to the α dependent components is increasing with decreasing the cation mass. They will give us the information about the ionisity and the covalency of III-V nitrides.

The authors would like to thank Dr.S.Tanaka, Dr.Y.Aoyagi (RIKEN) for supply of AlN and AlGaN samples and Dr.S.Nakamura (Nichia Chemical) for supply of GaN samples.

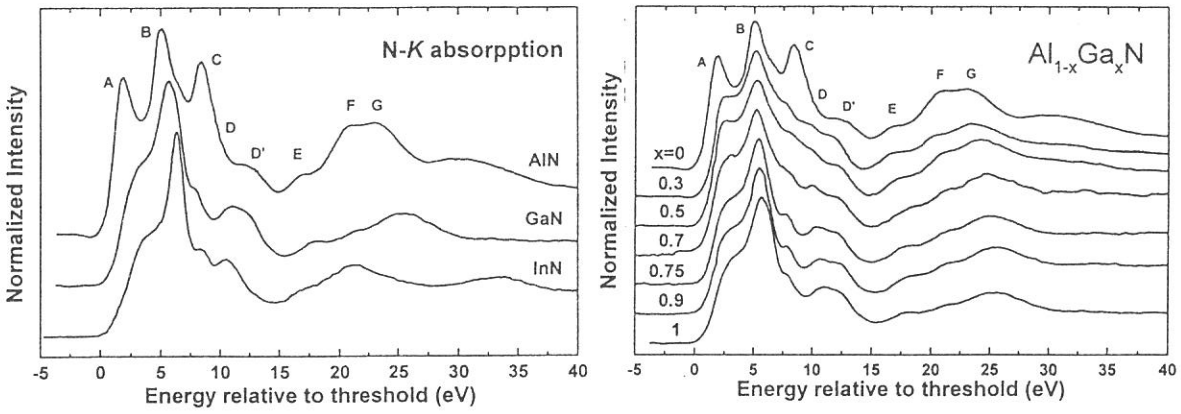

Fig.1 N K absorption spectra of AlN, GaN and InN(a), and those of AlGaN(b). The energy scale is relative to the threshold energy.

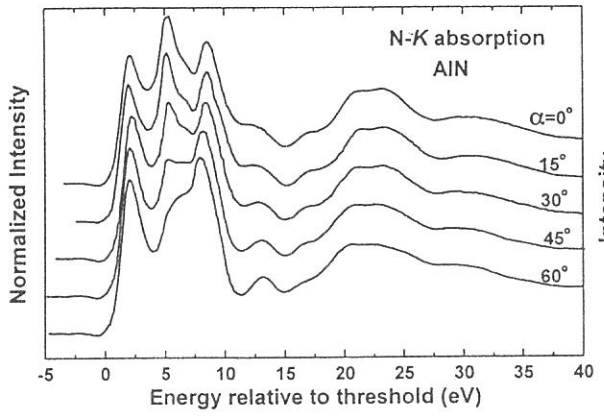

Fig.2 N K absorption spectra of AlN as function of angle which is defined as the angle between the incident light and the normal to the sample surface (c-axis).

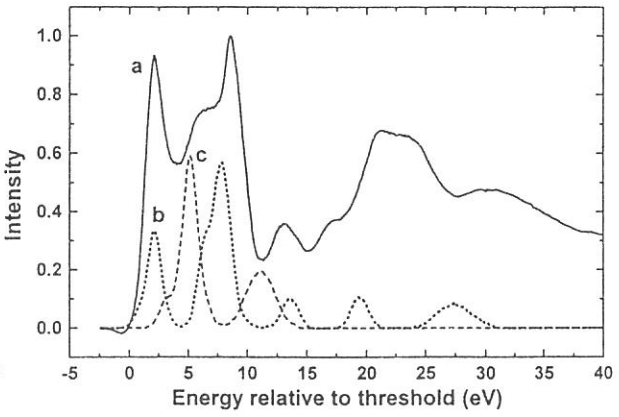

Fig.3 The coponent analysis results of Fig.2. The spectra labeled a, b and c show the α independent component, p_z and p_{xy} component, respectively.

References

[1] W.R.L.Lambrecht et al., Phys. Rev. B **55** (1997) 2612.

[2] C.B.Stagarescu et al., Phys. Rev. B **54** (1996) R17335.

[3] K.Fukui, M.Ichikawa, A.Yamamoto and M.Kamada, Solid State Electronics **41** (1997) 299.

(BL8B2)

Angle-resolved UPS of thin films of chloroalminium phthalocyanine (ClAlPc) on MoS_2 Surfaces

K.K.Okudaira[a], M.Tutui[b], T.Hasebe[b], Y.Azuma[a], A.Aoki[c], Y.Harada[a], and N.Ueno[d]

aDepartment of Material Science, Faculty of Engineering, Chiba University, Chiba 263
bGraduate School of Science and Technology, Chiba University, Chiba 263
cCollege of Arts and Sciences, The University of Tokyo, Tokyo 153
dInstitute for Molecular Science. Okazaki, 444

The angle-resolved ultraviolet photoelectron spectroscopy (ARUPS) using synchrotron radiation is a powerful method to investigate the geometrical structure of the ultrathin films of functional organic molecules as well as the electronic structure.

In the previous work we analyzed the take-off angle (θ) and azimuthal angle (ϕ) dependences of ARUPS of thin films of large organic molecules using the independent-atomic-center and single-scattering approximations combined with molecular orbital calculation (IAC/MO and SS/MO) and succeeded to determine the molecular orientation of copper phthalocyanine[1] and bis(1,2,5-thiadiazolo)-*p*-quinobis(1,3-dithiole) on MoS_2 surfaces.[2]

In the present work we found that the θ dependences of the photoelectron intensities from the HOMO band of thin films of chloroalminium phthalocyanine (ClAlPc) on MoS_2 surfaces depend on the temperature. The purpose of this report is to investigate the temperature dependences of molecular orientation by the analysis of the photoelectron angular distribution. The molecular structure of ClAlPc is shown in Fig.1.

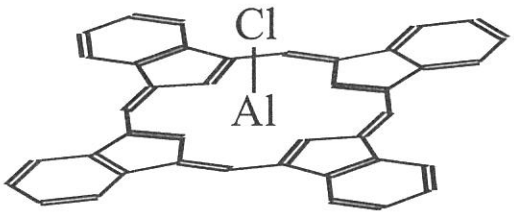

Figure 1 Structure of ClAlPc molecule.

ARUPS measurements were carried out at the beam line BL8B2 at Institute for Molecular Science. The θ dependences of photoelectron spectra were measured at normal incidence [incidence angle of photon (α)=0°] and at hν=40eV. ClAlPc molecules were deposited on the MoS_2 substrate cooled at about -100℃. The film thickness was 8 Å.

Figure 2 shows the ARUPS (i) observed at -150℃ for as-deposited film, (ii) observed at room temperature (RT) for the film annealed at RT for 12 h, and (iii) observed at -150℃ for the film annealed at 110℃ for 8 h after 12-h annealing at RT. It is noted that the feature B, which originates from MoS_2, appearing in the ARUPS spectra of the as-deposited film disappears by the annealing at RT. Furthermore, while the energy position of HOMO band A which originates from the single π band shifts to the higher binding energy by about 0.2eV with the annealing at RT, it does not change after the additional annealing at 110℃. These results indicate that the as-deposited film consists of islands, and by annealing at RT the molecules spread over the substrate surface.

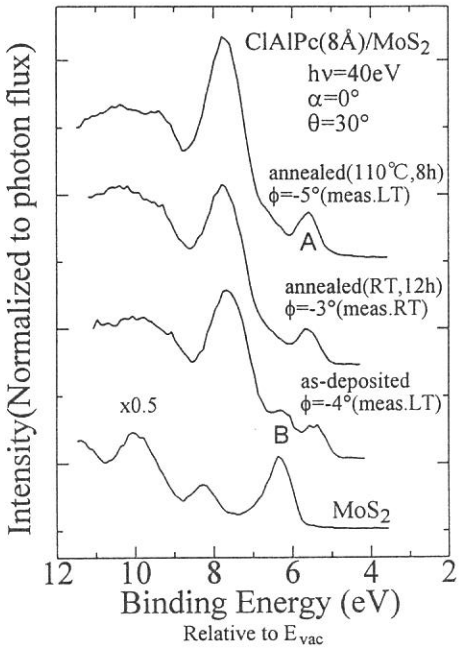

Figure 2 ARUPS spectra of ClAlPc films (8 Å) on the cooled MoS_2 (-100℃) at hν=40eV, α=0° and θ=30°. The ARUPS of as-deposited film, the film annealed at RT for 12 h, and the film annealed at 110℃ for 8 h after 12-h annealing at RT are measured at -150℃, RT, and -150℃, respectively. The substrate spectrum observed at RT is shown for comparison.

Figure 3 shows the θ dependences of photoelectron intensity from the HOMO band for the as-deposited film and for the film annealed at 110℃. For the annealed film, the θ dependence at RT is slightly broader than that at -150℃. It is

considered that the origin of the broadening is due to the vibrational excitations of ClAlPc molecules at RT. On the other hand, the θ dependence observed at -150℃ for the annealed film is sharper than that for the as-deposited film. It means that the molecular orientation changes by the annealing.

To estimate the change of the molecular orientation quantitatively, we calculate the θ dependences of photoelectron intensity from the HOMO band. We used SS/MO method to calculate the photoelectron intensity. The phase shifts and radial matrix elements were calculated using Muffin-tin potential.[3] The theoretical formula of SS/MO approximation were described in Ref.4. In this calculation we averaged the six azimuthal molecular orientations which are expected from analyses of LEED and ϕ dependences of photoelectron intensity.

The calculated and observed θ dependences are compared in Figs.4 (a) and (b). In Fig.4(a), the observed θ dependence for the as-deposited film agrees with calculated one for β=5°, where β is the molecular inclination angle. For the film annealed at 110℃, the observed θ dependence is in good agreement with calculated one for β=0° as shown in Fig.4 (b). These results indicate that on the cooled MoS_2, the molecules incline at about 5° with respect to the substrate surface, and after annealing at 110℃ they lie flat.

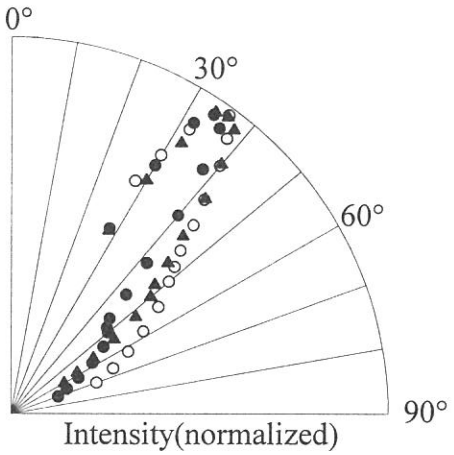

Figure 3 The take-off angle (θ) dependences of the photoelectron intensity of the HOMO band of ClAlPc films (8Å) on the cooled MoS_2 (-100℃) at hν=40eV and α=0°. The result of as-deposited film is shown by ○ (measured at -150℃). The results for the film annealed at 110℃ for 8 h after 12-h annealing at RT are shown by ▲ (measured at RT) and ● (measured at -150℃).

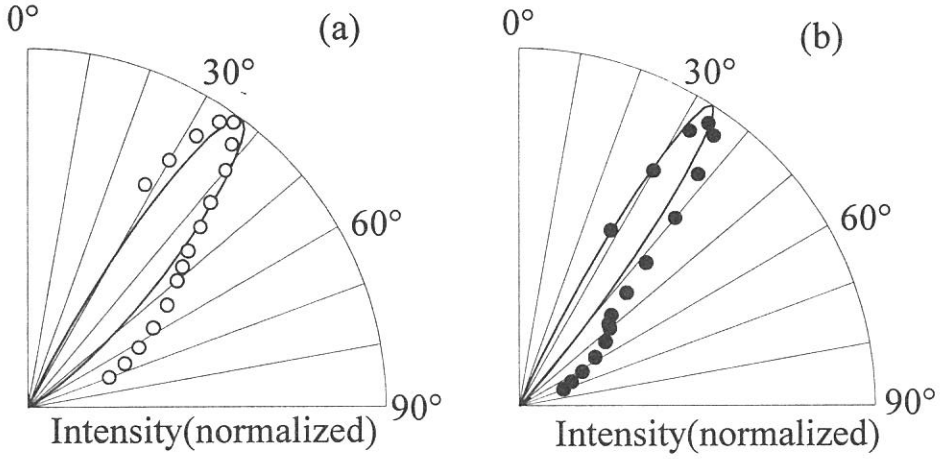

Figure 4 The comparison between calculated (——) and observed take-off angle (θ) dependences. The experimental results at -150℃ are shown by ○ (as-deposited film) and ● (the film annealed at 110℃ for 8 h after 12-h annealing at RT). The calculations were performed with SS/MO approximation at hν=40eV and α=0° for β=5° (panel(a)) and for β=0° (panel (b)).

REFERENCES

[1]K.Kamiya, M.Momose, A.Kitamura, Y.Harada, N.Ueno, S.Hasegawa, T.Miyazaki, H.Inokuchi, S.Narioka, H.Ishii, and K.Seki, J.Electron Spectrosc.Relat.Phenom., **76** 213 (1995).

[2]N.Ueno, A.Kitamura, K.K.Okudaira, T.Miyamae, S.Hasegawa, H.Ishii, H.Inokuchi, T.Fujikawa, T.Miyazaki, and K.Seki, J.Chem.Phys., **107** 2079(1997).

[3]D.Dill and J.L.Dehmer, J.Chem.Phys., **61** 692 (1974).

[4]N.Ueno, J.Electron Spectrosc.Relat.Phenom., **78** 345 (1996).

(BL8B2) Photoelectron spectra of metallofullerenes, GdC_{82} and La_2C_{80}

Shojun Hino[a,b], Kazunori Umishita [a,b] Kentaro Iwasaki [a], Takafumi Miyazaki[c]*, Takayuki Miyamae [b,c], Koichi Kikuchi [d] and Yohji Achiba [c]

[a] *Faculty of Engineering, Chiba University, Inage-ku, Chiba 263-8522 Japan*
[b] *Graduate School of Science and Technology, Chiba University, Inage-ku, Chiba 263-8522 Japan*
[c] *Institute for Molecular Science, Myoudaiji, Okazaki, Japan 444-8585*
[d] *Faculty of Science, Tokyo Metropolitan University, Hachioji, Tokyo 192-0397 Japan*

Metallofullerenes have attracted a lot of attentions such as their structures including the position of the metal atom(s), their electronic structures as well as the amounts of transferred electrons from the metal atom(s) to the cage, their reactivity and so on. Photoelectron spectroscopy is a powerful tool to clarify their electronic structures. In this article, our recent results of the photoelectron spectroscopy on metallofullerenes, GdC_{82} and La_2C_{80} are presented and their electronic structures are discussed.

Figure 1 shows the incident photon energy dependence of the UPS of the solution dried-up GdC_{82} film heated up to 300 °C in ultrahigh vacuum. Note that the specimen is not vacuum deposited film. The spectral onset is 0.3 eV below the Fermi level and six distinct structures labeled A – E and N are observed in this energy region. In the spectra obtained with lower excitation energy, superposition of secondary electrons is heavy in the higher binding energy region; structure C can be vaguely discerned in the $h\nu$ = 15 – 25 eV spectra and a dip between structures C and D is discerned only in the $h\nu$ = 30 eV spectra. A clear intensity oscillation is observed in structures A and B, as in other fullerenes. Their intensity in the $h\nu$ = 20 and 40 eV spectra is nearly equal, but structure B in other spectra is about one and half times more intense than structure A. This intensity dependence of structures A and B on the incident photon energy is essentially the same as those of C_{82} [1] and LaC_{82} [2].

Figure 2 shows the photoelectron spectra of GdC_{82}, C_{82} and LaC_{82} (excited by $h\nu$ = 20 eV photon). The intensity of the high binding energy region of the spectrum of GdC_{82} is stronger than those of the other two spectra, which is due to the overlap of secondary electrons. Structures A – E have one to one correspondence with those of C_{82} and LaC_{82}. Note the presence of structure N that is also observed in LaC_{82} but absent in C_{82}. The appearance of structure N is the result of electron transfer from the metal atom to the fullerene cage. In order to estimate the amount of transferred electrons, a difference spectrum is obtained by subtracting the spectrum of C_{82} from that of GdC_{82}: both spectra are normalized at the peak position of structure B (3.3 eV). The difference spectrum is shown in the inset of Fig. 2. It can be deconvoluted into two parts, α and β; their peak positions are 0.85 and 1.45 eV, respectively. Their intensity ratio is roughly 1 : 2. This finding and the electron configuration of the Gd atom, $(6s)^2(4f)^7(5d)^1$, support that three electrons are transferred from the metal atom to the C_{82} cage. The difference spectrum between LaC_{82} and C_{82} is very close to the present result [2]. This fact and the resemblance of their absorption spectra [3,4] indicate that the electronic structures of LaC_{82} and GdC_{82} are analogous and that three electrons of the metal are transferred to the cage in both metallofullerenes.

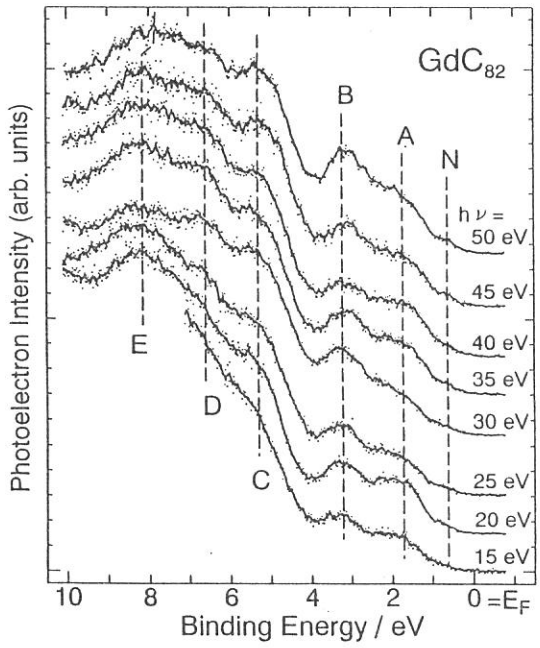

Fig.1 Incident photon energy dependence of the photoelectron spectra of GdC_{82}. Approximate peak positions are indicated by broken lines.

When three electrons are transferred from the Gd metal, the C_{82} cage has odd number electrons to form an open shell molecule. A solid composed of open shell molecules is considered to be metallic, but GdC_{82} is not metallic since the spectral onset does not cross the E_F but is 0.3 eV below the E_F. Both X-ray diffraction study of YC_{82} [5] and a theoretical consideration of metallofullerenes containing one metal atom [6] indicate that the metal atom is located at the off-centered position in the cage. This also seems to hold in GdC_{82}, so that the molecule might have a large dipole moment. In GdC_{82} solid, the molecules might be arranged to cancel its dipole moment to lower the total energy of the solid, and probably pairing of the molecules takes place so that molecular aggregates tend to behave like closed shell molecules. This could be the reason for its semi-conductive nature.

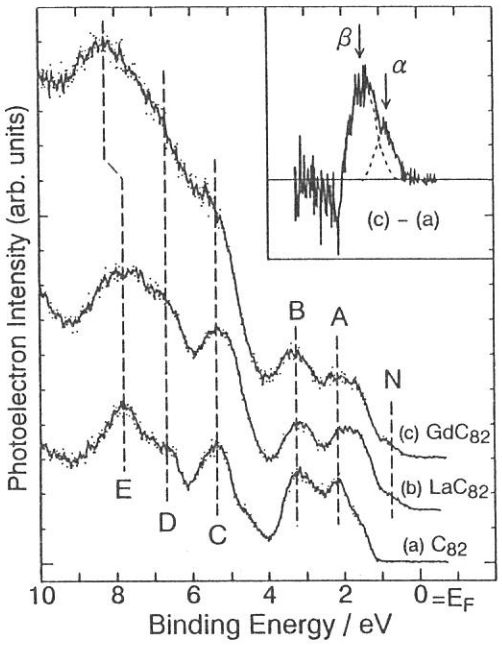

Fig.2 Photoelectron spectra of empty C_{82}, LaC_{82} and GdC_{82} obtained with hν = 20 eV excitation energy. Inset is the difference spectrum obtained by subtracting the C_{82} spectrum from the GdC_{82} spectrum. The intensity of both spectra is normalized at the 3.3 eV peak that seems to be least affected by superposition of secondary electron. The difference spectrum can be deconvoluted into two peak components α and β with an intensity ratio of 1 : 2.

A photoelectron spectrum of the solvent dried-up La_2C_{80} film heated up to 400 °C begins at the Fermi level and show poor structures. The spectrum resembles that of vitreous carbon. A straightforward interpretation of this analogousity brings a conclusion that the electronic structure of La_2C_{80} is somewhat like that of amorphous carbon or La carbide. That is, the metal atoms could be at any place; outside or inside the carbon cage or just in the carbon plane. This is inconsistent with the conclusion obtained from the reactivity of 1,1,2,2,-tetramesityl-1,2-disilirane to La_2C_{80} and the analysis of its nuclear magnetic resonance spectrum [7]; they strongly support its endohedral form. A further investigation is required to settle the conflicting results on La_2C_{80}.

References

[1] S. Hino *et al.*, Phys. Rev. B 48, 8418 (1993).

[2] S. Hino *et al.*, Phys. Rev. Letters 71, 4261 (1993).

[3] K. Kikuchi *et al.*, Chem. Phys. Letters 216, 67 (1993).

[4] T. Suzuki et al., Tetrahedron 52, 4973 (1996).

[5] M. Takada *et al.*, Nature 377, 46 (1995).

[6] S. Nagase *et al.*, Bull. Chem. Soc. Jpn. 69, 2131 (1996), and references there in.

[7] T. Akasaka *et al.*, Angew. Chem. 109, 1716 (1997).

(BL8B2)

UV PHOTOEMISSION OF n-$C_{44}H_{90}$ / Cu(100) : MOLECULAR ORIENTATION OF A LONG-CHAIN OLIGOMER / METAL INTERFACE

H. Ishii[a], D. Yoshimura[a], E. Ito[a], K. Okudaira[b], T. Miyamae[c], S. Hasegawa[c], N. Ueno[b, c], and K. Seki[a]

[a)] *Faculty of Science, Nagoya University, Furo-cho, Chikusa-ku, Nagoya 464-8602, Japan*
[b)] *Faculty of Engineering, Chiba University, 1-33 Yayoi-cho, Inage-ku, Chiba 263-8522, Japan*
[c)] *Institute for Molecular Science, Myodaiji, Okazaki 444-8585, Japan.*

INTRODUCTION

Recently various polymers have attracted wide attention in close relation to electronic devices. The elucidation of geometrical and electronic structure of polymer / metal interfaces is crucial for understanding and improving the performance of such devices. Especially, the study for a simple system with a well-ordered structure is highly desired. However, it is not easy for polymers. The use of the shorter oligomers instead of polymers is one of the solutions because of their definite molecular weight, better crystallinity, and possibility of preparing well ordered thin films by vacuum deposition. In fact, oligomers such as *p*-sexiphenyl (6P) and a-sexithiophene (α-6T) have been applied to devices, and their oriented films have been prepared by vacuum deposition. Very recently, we have found that even for 6P with small number N of repeating units (6), the wavenumber (k) of the valence electron is still a good quantum number but much blurred because of small N [1], indicating that translational nature is still far from that of a polymer with full translational symmetry. Thus the study for a longer oligomer is desired for investigating polymer.

In this study, we investigated the molecular orientation of a long-chain alkane, tetratetracontane (n-$C_{44}H_{90}$, TTC) in thin films on Cu(100) single crystal surface, using low energy electron diffraction (LEED) and angle-resolved UV photoemission (ARUPS). TTC is a model compound of poly(ethylene) which is one of the fundamental polymers. In the case of TTC, the blurring of k is much smaller than that of shorter oligomer such as 6P [2] because of its large number of repeating units of 22. Thus this TTC / Metal system can be regarded as a prototype of polymer/metal interface.

EXPERIMENTAL

The sample of TTC was purchased from Tokyo Chemical Industries Co.Ltd., and purified by recrystallization from the benzene solution. Cu(100) surface was cleaned by several cycles of annealing and Ar^+ ion sputtering. TTC film was prepared by vacuum vapor deposition. The thickness was about 0.4nm in average that corresponds to monolayer thickness in flat-lying orientation. UPS measurement was performed at the beamline 8B2 of the UVSOR synchrotron radiation facility at IMS. Photon energy for UPS was 40 eV. The incidence angle of photon was 70° relative to surface normal.

RESULTS AND DISCUSSION

TTC/Cu(100) surface exhibited LEED pattern as shown in Fig.1, indicating two-dimensional order of the surface. The analysis of this pattern suggested that there are two domains where TTC chain aligns to [110] ([1 $\bar{1}$ 0] in the other domain) direction of the Cu(100) surface. This was confirmed by UPS measurement.

Fig.2 shows UPS spectra of TTC/Cu(100). The abscissa is binding energy relative to the Fermi level of Cu. The polarization vector of photons and the wave vector of emitted electrons were located in the mirror plane which includes surface normal and [110] direction of Cu(100) surface. The spectral features are ascribed as follows: structure A is due to Cu 3d orbital and upper edge of C2p-derivd orbital of TTC. Structures B and C

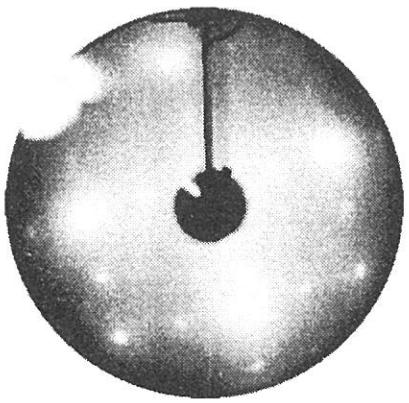

Fig.1 LEED pattern of TTC on Cu(100). Four large spots are [1,0] spots from the Cu substrate.

are due to C2p and C2s-derived orbitals, respectively. Their lineshape exhibited drastic variation by changing the take-off angle θ due to intramolecular band dispersion of TTC. The band structure derived from the spectra observed for a wide range of θ well corresponded to that reported for thick TTC film [2], suggesting that the formation of the interface does not change the translational nature of TTC. This can be explained by weak chemical interaction between TTC and Cu surface.

The simulated spectra for the C2p bands are also shown in Fig.2 as solid lines. They were calculated with independent-atomic-center (IAC) approximation combined with *ab-initio* molecular orbital calculation [3]. The photoemission intensity was calculated for two domains in which TTC axis is parallel to [110] direction with the molecular plane parallel to the surface. As seen in Fig.2, each simulated spectrum is well consistent with the observed one, clearly indicating the flat-on orientation of TTC on Cu(100).

In conclusion, two-dimensionally well-ordered TTC ultrathin film was successfully prepared on Cu(100) as a prototype of polymer / metal interface. The molecular orientation was determined by LEED and ARUPS combined with the theoretical analysis by IAC approximation. This type of experiment for well-defined interface will be useful for obtaining deeper insight for polymer/metal interfaces.

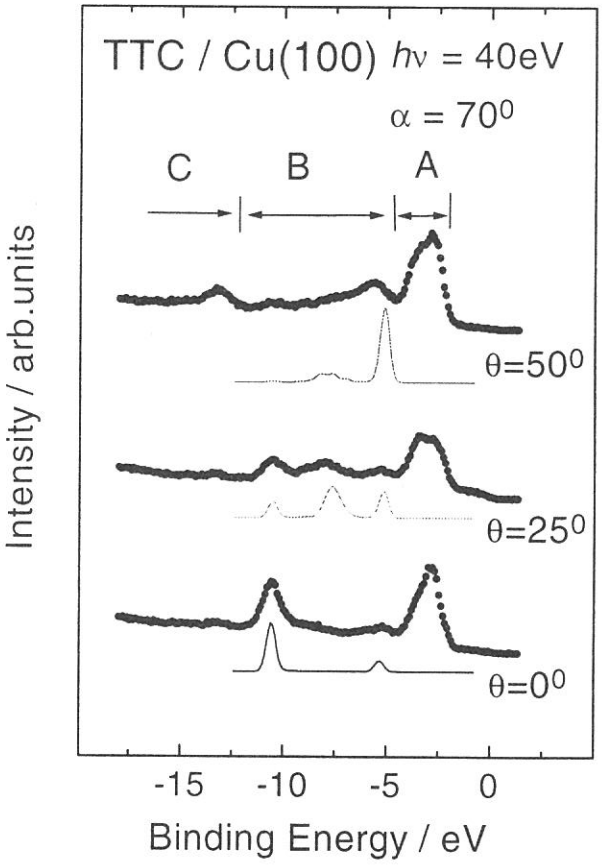

Fig2. Observed ARUPS spectra (dot) and the simulated spectra (solid line) of TTC on Cu(100).

REFERENCES

[1] S. Narioka, H. Ishii, K. Edamatsu, K. Kamiya, S. Hasegawa, T. Ohta, N. Ueno, and K. Seki, *Phys. Rev.*, **B52**, p2362 (1995).
[2] K. Seki, N. Ueno, U.O. Karlsson, R. Engelhardt, and E. Koch, Chem. Phys., **105**, p247 (1986).
[3] S. Hasegawa, S. Tanaka, Y. Yamashita, H. Inokuchi, H. Fujimoto, K. Kamiya, K. Seki and N. Ueno, *Phys. Rev.*, **B48**, p2596 (1993).

(BL1B)

One-Photon Photoionization Thresholds of Aromatic Molecules on Water Surface in Ambient Condition

Teiichiro Ogawa[A], Shin-ya Sasaki[A], Manabu Tokeshi[B], and Takanori Inoue[A]

[A]*Department of Molecular Science and Technology, Kyushu University*
Kasuga-shi, Fukuoka, 816-8580
[B]*Falculty of Engneering, The University of Tokyo,*
Hongo, Tokyo, 113-1111

Photoionization behavior at the solution surface is different from that in the bulk solution. Photoionization threshold in solution has been determined in a single-photon process using synchrotron radiation or hydrogen discharge lamp, and in a two-photon process using laser radiation. Although there are a few measurements on photoionization threshold of aromatic molecules on solution surface using laser two-photon excitation, no measurements have been carried out using one-photon excitation on solution surface. We have tried to measure one-photon ionization spectra (wavelength dependence of photoionization efficiency) and photoionization thresholds of aromatic molecules on water surface using synchrotron radiation.

The experimental apparatus is shown in Fig.1. Synchrotron radiation of wavelength from 160 to 240 nm was used as an excitation source. The beam power was 10^{10} photons/sec as monitored using a photomultiplier to calibrate its wavelength dependence. The beam was not focused and irradiated the solution surface horizontally. The solution was kept in a stainless-steel vessel (0.5mL) of 1.5 cm in diameter, and the vessel was served as the current collecting electrode. A disk electrode was located 5 mm above the solution surface and was connected to a high-voltage power supply unit. The photoionization current was measured using a current amplifier(Keithley, 617). The perylene, pyrene and methylanthracene (guaranted grade, Nacalai Tesque) were used without further purification. The water was distilled, deionized, filtered and distill again in a quartz vessel.

The one-photon ionization spectra have been measured for the three molecules on the water surface. The blank signal (signal of pure water) was relatively small and negligible. The photoionization of perylene on water surface in the concentration range between 10^{-6}M – 10^{-8}M has showed linear dependence on concentration. The photoionization spectrum was normalized by beam power and solution concentration.

The photoionization current near threshold can be represent by a power law,

$$I = c\,(E_{excess})^{5/2} = c(h\nu - I_{th})^{5/2}$$

where E_{excess} is the excess energy of the ionized pair, $h\nu$ is the photon energy and I_{th} is the ionization threshold. A plot of the (2/5)th power of the normalized photoionization current versus the photon energy should give a straight line, and its onset on the abscissa should give I_{th}, because there would be no photoionization current below I_{th}. Figure 2 shows the photoionization spectrum for the three aromatic molecules on water surface, and I_{th} of perylene, pyrene, and methylanthracene have been determined to be 6.0, 6.3 and 5.9 eV, respectively. I_{th} of perylene was determined to be 5.95 eV by a two-photon process using a Ti-sapphire laser and agree with the present value within experimental errors.

The photoionization threshold on the surface has been related with the ionization potential in gas phase, I_p, as:

$$I_{th} = I_p + P^+,$$

where P^+ is the polarization energy of the positive ion. This equation should be applicable to these molecules in this study, because the electron escapes directly from the surface and so the electron affinity of the solvent is able to be negligible. P^+ of perylene on water can be determined as –0.9eV. The value of P^+ can be obtained from Born equation using the dielectric constant and the radius of the molecule. The observed value of P^+ was about half as much as the calculated value, this indicates that the effective dielectric constant of water surface should be much smaller than that of bulk water, 80.4 at 20°C.

Reference

1. Inoue, T.: Masuda, K.: Nakashima, K.: Ogawa, T., *Anal.Chem.*, 66(1994)1012.
2. Watanabe, I.: Ono, K.: Ikeda, S., *Bull.Chem.Soc.Jpn.*, 64(1991)352.
3. Ogawa, T.: Chen, H.: Inoue, T.: Nakashima, K., *Chem.Phys.Lett.*, 229(1994)328.
4. Born, M., *Z.Physik*, 1(1920)45

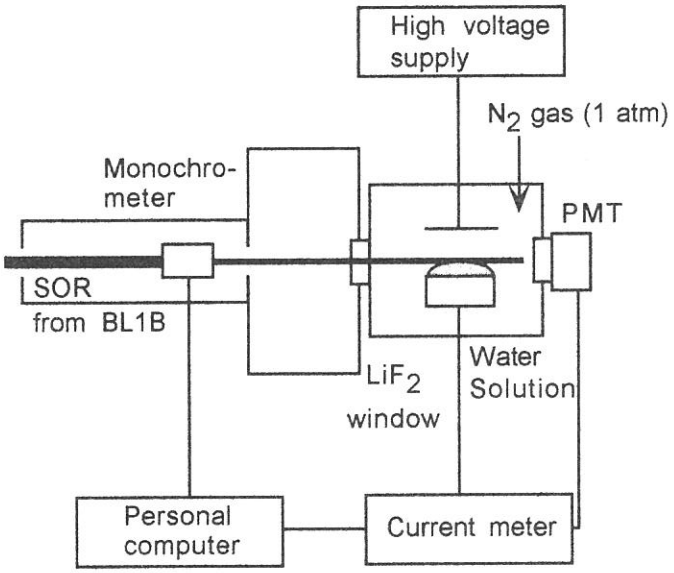

Fig.1 Schematic diagram of the experimental appatus

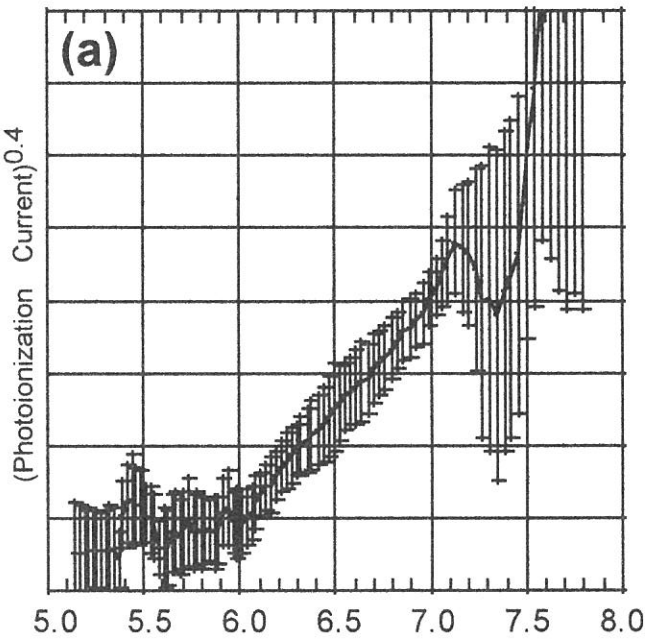

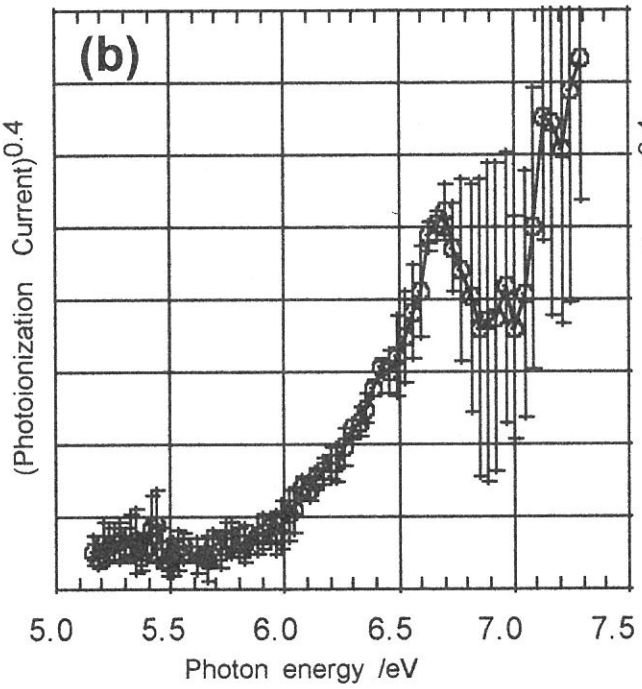

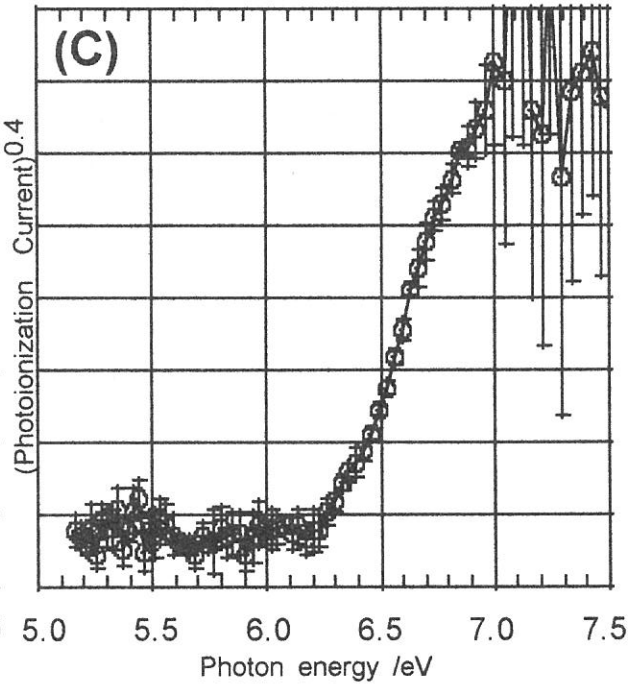

Fig.2 Photoionization current spectra of (a) perylene, (b) methylanthracene, (c) pyrene.

(2B1) SELECTION OF ORIENTED OXYGEN ADMOLECULES ON A PT(133) STEPPED SURFACE

Manami Sano, Yoshiyuki Seimiya, Yuichi Ohno, Tatsuo Matsushima, Shin-ichiro Tanaka[A] and Masao Kamada[A]

Catalysis Research Center and Graduate School of Environmental Earth Science, Hokkaido University, Sapporo 060-0811, Japan

[A] Institute for Molecular Science, Myodaiji Okazaki 444-0867, Japan.

Oxygen admolecules on Pt(133)=(s)3(111)x(111) were characterized with thermal desorption (TDS) and near edge X-ray absorption fine structure (NEXAFS). Three desorption peaks from the admolecules are found at 150 K (α_3-O_2), 170 K (α_2-O_2) and 220 K (α_1-O_2). The admolecules due to α_1-O_2 lie along the step edge. The α_2-O_2 axis is rotated significantly from the trough direction. α_3-O_2 on the terrace is more rotated. The admolecules with different orientations can be separately prepared on this surface.

A typical TDS spectrum of the oxygen desorption from the molecular adsorption states is shown in Fig. 1. α_1-O_2 was concluded to be located on or near the step, because it is suppressed completely by preadsorbed atomic oxygen. On the other hand, α_2-O_2 and α_3-O_2 are on the declining (111) terrace because their desorption is hardly affected by oxygen adatoms on the step. α_2-O_2 is suppressed by preadsorbed oxygen populated on the terrace. The α_3-O_2 desorption increases with increasing amount of oxygen atoms except for a high coverage range. α_3-O_2 is far from the step sites.

NEXAFS spectra were obtained at 110 K for modified surfaces by atomic oxygen which yielded each of the three α-O_2 species in the subsequent heating. Oxygen adatoms were present on the pre-treated surface and a remarkable electron yield was found around 530 eV, as shown in Fig. 2 (a). Therefore, the spectra were examined in the differential form between raw spectra and those of oxygen adatoms in the same amount. The orientation of the electric vector, E, of the X-ray, θ, is measured from the surface parallel in a plane parallel to the trough.

Only the σ^* resonance appears at $\theta = 0^\circ$ in the spectra of α_1-O_2. However, with increasing θ, the σ^* resonance fades and the π^* resonance grows rapidly. Moreover, the σ^* resonance disappears completely in a wide angle range, when E is perpendicular to the trough. α_1-O_2 is oriented along the trough. The two other α-O_2 species show different angle dependence. In the spectra of α_3-O_2, both π^* and σ^* states of resonance appear at $\theta = 0^\circ$ as shown in Fig. 2 (b). This molecule appears to be rotated from the trough direction.

The rotation angle was determined from a simple simulation of the angle dependence of the relative intensity of both resonance signals. Each peak area was determined by curve fitting using two Gaussian functions as indicated by the broken curve. In the simulation, the molecular axes of all the species were assumed to be parallel to the surface plane, in accord with HREELS work. As shown in Fig. 3, we concluded that the admolecule yielding α_1-O_2 lies along the step edge, whereas α_2-O_2 and α_3-O_2 lie on the declining (111) terraces and are inclined 35~45° and 50~60° from the trough direction, respectively.

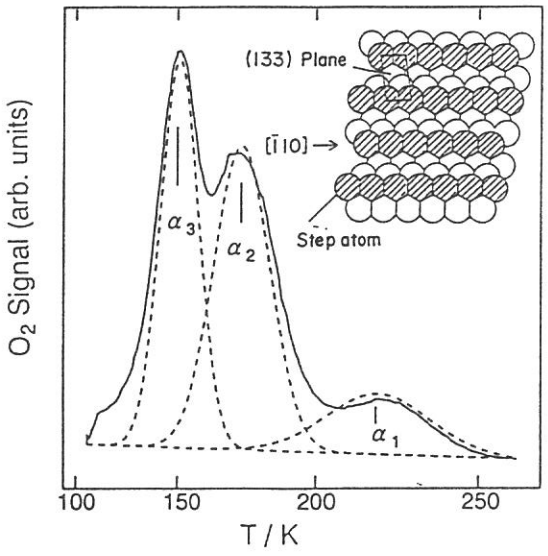

Fig. 1 A TDS spectrum of oxygen admolecules. The surface structure is inserted.

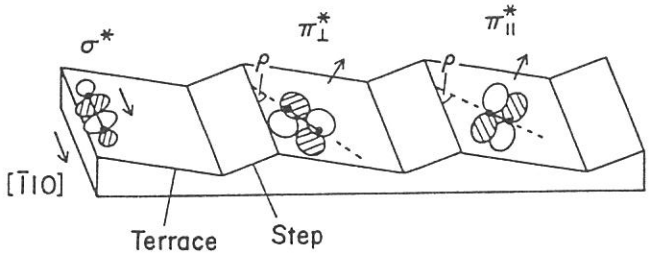

Fig. 3 Molecular and orbital orientation. ρ defines the rotation angle of the molecular axis.

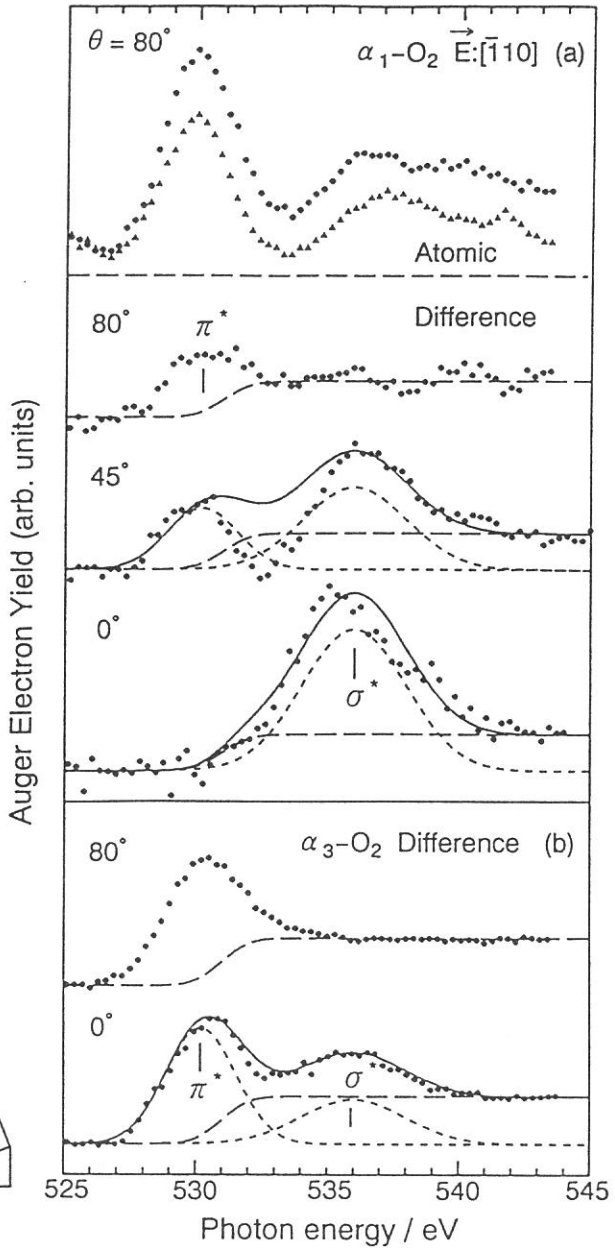

Fig. 2 NEXAFS spectra of (a) α_1-O_2 and (b) α_3-O_2. The X-ray electric vector is in a plane in the [1̄10] direction.

(BL2B1)

ELECTRONIC STRUCTURES IN THE VALENCE REGION OF CHEMISORBED AND PHYSISORBED SPECIES ON Pd(110)

Jun Yoshinobu[1,2], Maki Kawai[1], Shin-ichiro Tanaka[3], Kazuo Watanabe[3], Yoshiyasu Matsumoto[3,4] and Masao Kamada[3]

1) The Institute of Physical and Chemical Research (RIKEN), 2-1 Hirosawa, Wako 351-01. 2) The Institute for Solid State Physics, The University of Tokyo, 7-22-1 Roppongi, Minato-ku, Tokyo 106. 3) Institute for Molecular Science, Myodaiji-cho, Okazaki 444. 4) The Graduate University for Advanced Studies, Shonan village, Hayama, Kanagawa 240-01.

When an atom or a molecule is adsorbed on a metal surface, discrete electronic energy levels are chang due to the interaction with the surface. In the case of weak interaction, adsorbate-induced levels are shifted to lower energy and broadened [1]. This broadening is referred as adsorbate-induced resonance. If the interaction is very strong, the broadened band will be split into a pair of a bonding state below valence band and an antibonding state at the top of valence band. This case may be relevant for chemisorption on transition metals which are characterized by a narrow d-band in addition to a broad sp-band.

As a typical model for molecular chemisorption, the valence electronic structure (in particular, near the Fermi level) of adsorbed CO on metal surfaces is still of interest and a controversial subject. There are two models for extreme cases; (1) the surface complex model (the Blyholder model [2]), where a σ-bond is formed between the CO 5σ molecular orbital (MO) and a metal d-orbital (donation) and also a π-bond between the CO 2π MO and a metal d-orbital (back-donation). (2) the surface resonance model [3,4], where the unoccupied 2π state is shifted and broadened due to the interaction with metal bands. Since the low energy side of the resonance is located below the Fermi energy (EF), this region is bonding in character.

We have investigated the electronic structures of CO, CH_4 and Xe on Pd(110) by means of photoelectron spectroscopy (PES) using UVSOR BL2B1 in Institute of Molecular Science. In order to enhance the sensitivity for the adsorbate-derived states in valence PE spectra, photon energy at the Cooper minimum (hν = 120-130 eV) was utilized.[5-7] In the case of the CO saturated Pd(110) surface at 90 K, peaks are observed at ~3.4 eV, 8.0 eV (with a shoulder at ~7.2eV), 11.0 eV and 14.4 eV below the Fermi level (EF). In addition to the previously reported peaks (1π & 5σ at ~8 eV and 4σ at ~11 eV),[8] two peaks were newly observed. The 3.4 eV peak could be assigned to the bonding state hybridized between CO 2p and Pd 4d orbitals. The 14.4eV peak is tentatively assigned to the CO 4s shake-up satellite. In the "physisorption" systems, i.e., CH_4 and Xe on Pd(110), only the smooth attenuation of photoemission from the Pd 4d band was observed in the PE spectra.[9] The study is to be published.[10]

[1] B. I. Lundqvist, H. Hjelmberg and O. Gunnarsson, in: Photoemission and the electronic properties of surfaces (John Wiley & Sons, New York, 1978).
[2]G. Blyholder, J. Phys. Chem., 68 (1964) 2772.
[3]B. Gumhalter, K. Wandelt, and Ph. Avouris, Phys. Rev. B 37 (1988) 8048.
[4]Ph. Avouris, Physica Scripta., 35 (1987) 47.
[5]J.W. Cooper, Phys. Rev., 128 (1962) 681.
[6]P.S. Wehner, S.D. Kevan, R.S. Williams, R.F. Davis and D.A. Shirley, Chem. Phys. Lett., 57 (1978) 334.
[7]E. Miyazaki, I. Kojima, M. Orita, K. Sawa, N. Sanada, T. Miyahara and H. Kato, Surf. Sci. 176(1986) L841.
[8]H. Conrad, G. Ertl, J. Küppers and E.E.Latta, Disc. Farad. Soc. 58 (1974) 116.
[9]K. Jacobi and and H.H. Rotermund, Surf. Sci., 133 (1983) 401.
[10]J. Yoshinobu, M. Kawai, S. Tanaka, K. Watanabe, Y. Matsumoto and M. Kamada, J. Electry. *in press.*

(BL2B1)

Study of Site-Specific Ion Desorption from a Si(100) Surface Saturated by Fluorine Using Photoelectron Photoion Coincidence Spectroscopy

Kazuhiko Mase, Sinya Hirano, Shin-ichiro Tanaka, and Tsuneo Urisu

Institute for Molecular Science, Okazaki 444-8585, Japan

Since a core-electron is localized at an atom, site-specific fragmentation is expected to be induced by core-electron excitations. Site-specific fragmentation is important not only as the fundamental science of molecular dynamics but also as the fundamental technology of the reaction control for the new material production. Photoelectron photoion coincidence (PEPICO) spectroscopy is an ideal tool for site-specific ion desorption study because it provides ion mass spectra of the sites related to the selected photoelectrons [1]. In the present article, we describe a study of site-specific ion desorption from a Si(100) surface saturated by Fluorine at the room temperature (Si(100)-F).

Figure 1 shows PEPICO spectra of Si(100)-F. PEPICO F^+ signal was observed for Si:2*p* photoelectron with kinetic energies of 101 eV. Figure 2 shows potoelectron spectra (PES) and potoelectron energy dependence of the PEPICO F^+ yield (PEPICO F^+ yield spectrum). The peak position and shape of the PEPICO F^+ yield spectrum was observed to be similar to those of the difference PES between Si(100)-F and a clean Si(100) surface, which corresponds to the ≡SiF, $=SiF_2$, and $-SiF_3$ species. These results directly verify that F^+ ion desorption is induced by Si:2*p* photoionizations at the ≡SiF, $=SiF_2$, and $-SiF_3$ sites on the surface.

References

[1] S. Nagaoka *et al.*, *J. Chem. Phys.*, **107**, 10751 (1997); K. Mase *et al.*, *Surf. Sci.* **377-379**, 376 (1997).

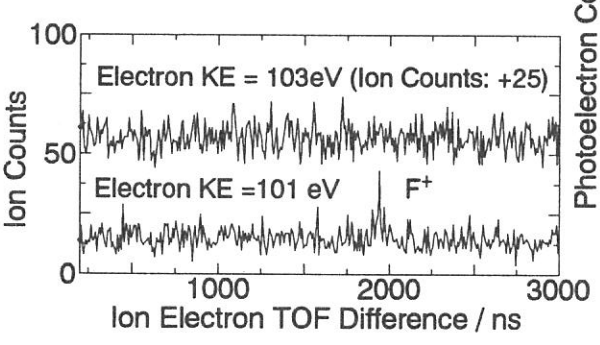

Figure 1. PEPICO spectra of Si(100)-F in coincidence with Si:2*p* photoelectron with kinetic energies of 101 eV and 103 eV.

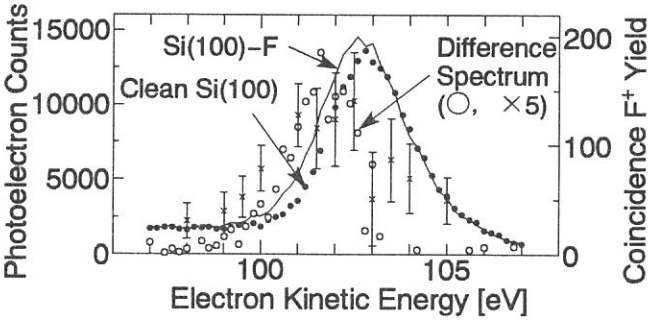

Figure 2. PES of Si(100)-F (dot line) and a clean Si(100) surface (solid line). The open circles denote the difference PES between Si(100)-F and Si(100). The crosses with an error bar denote a PEPICO F^+ yield spectrum.

(BL2B1)

Surface-NEXAFS and photo-stimulated ion desorption spectra at the C-K and O-K edges of the CO/Si(100) surface

S. Tanaka, M. Mase, M. Nagasono and M. Kamada

Institute for Molecular Science, Okazaki, 444-8585, Japan

The interaction of carbon monoxide (CO) with the solid surfaces is one of test cases for the gas-surface interaction study, and has been extensively studied on the many kinds of solid surfaces. However, only few studies have been made on the Si surface, although the surface chemistry of the Si has been attractive by the viewpoint of not only the pure science but also the technological application. In this report, we show the NEXAFS and photo-stimulated desorption spectra of CO adsorbed on the Si(100) surface at 80K, and discuss about the bonding orientation of CO on the Si(100) surface.

All the experiments were carried out at the UHV chamber at BL2B1 of UVSOR. For the measurements of the surface sensitive NEXAFS (Near-Edge X-ray Absorption Fine Structure) spectroscopy, the Auger electron yield method was used, in which the yield of the Auger electron yield of the atoms of adsorbates (C-KVV for C-K edge, and O-KVV for O-K edge) were measured as a function of the photon energy. The photo-stimulated ion desorption spectra were observed by detecting the total (positive) ion yield. The Si(100) wafer was cleaned by the resistive heating in the UHV. The sample was cooled by liquid nitrogen all through the experiments. The CO-exposure was made by the use of the dosing system of pulse valve. The pressure of the gas reservoir was about 0.8 Torr, the time of the opening was 10 msec, and the doses were made for 10 times. They were enough to make the surface saturated with CO, and all the results reported here are for the the Si(100) surface with 1 mono-layer of CO.

Figure 1 shows the NEXAFS spectra of the CO/Si(100) surface at the C-K edge as a function of the incident angle of the photons. The angle from the surface normal was 60° and 20° for the upper and lower curves, respectively. It was difficult to estimate the difference of the efficiency of the photoelectron detection two spectra, and the intensities of the spectra were normalized by the intensity of the first peak at the threshold. The photon energy is shown referred from the energy position of the first peak for convenience. The spectra observed are similar to the NEXAFS spectra of the CO-adsorbed metal surfaces, and the first peak are ascribed to the transition to the π* resonance state, and the broad peak around 20 eV for the upper curve is ascribed to the transition to the σ* shape resonance. The intensity of the σ* shape resonance was too small to be observed in the spectrum taken at 20° of the photon incidence. Considering the polarization of the incident photons and symmetry of the molecular orbital, it is interpreted as that the CO axis on the Si(100) surface is aligned near to the surface

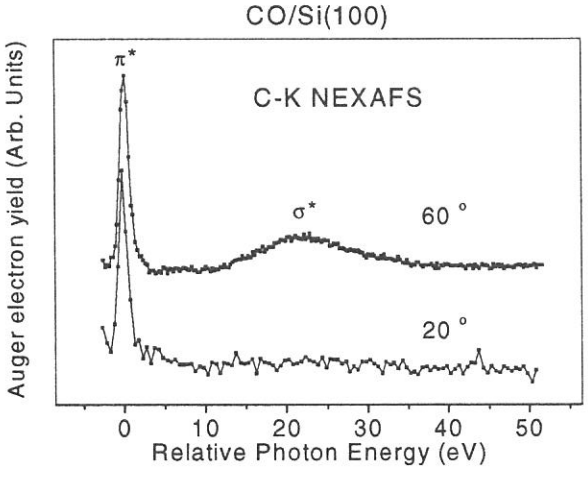

Figure 1

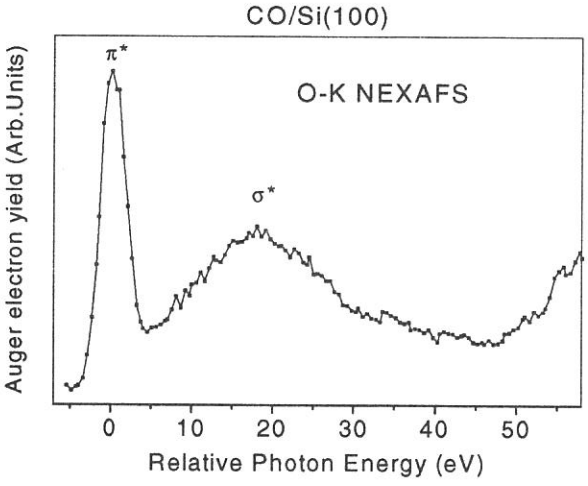

Figure 2

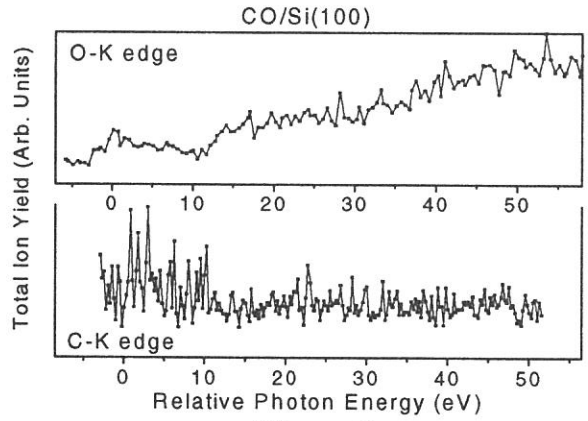

Figure 3

normal. Ho et.al. concluded that CO is bonded to the dangling bond of the Si(100) surface, and the angle of the molecular axis is about 18.6° from the surface normal, which is consistent with our observation. It is noted that it is difficult to discuss quantitatively the angle of the molecular axis, partly because the lack of the detailed data, and partly because the ambiguity of the azimuth of the Si(100)(2x1) surface.

Figure 2 shows the NEXAFS spectra at O-K edge of CO/Si(100). The incident angle of the photons was 60°. Two peaks are observed and ascribed to π^* and σ^* resonance as well as C-K edge. The peaks are broader than those in the spectrum for C-K edge because of poorer resolution of the instruments at higher energies. The enhancement at >50 eV is due to the direct excitation of photoelectrons, and not the NEXAFS signal.

Figure 3 shows the total ion yield spectra for C-K edge and O-K edge from CO/Si(100). At the O-K edge, the increase of the ion yield is observed at about 0eV, 10eV and 25 eV. The increase of the ion yield at 0eV was not reproducible, and may be due to the H^+ desorption from the ice layer adsorbed on the surface during the experiment. The increases at 10 eV and 35 eV are corresponding to the σ^* excitation and the shake-up excitation, respectively, and are similar to the case of CO adsorbed on the metal surface. The desorbing species for the CO/metal are O^+, and it is reasonable to assume a similar photon-induced dissociation takes place on the Si(100) surface. Meanwhile, no structure was observed for the ion yield at the C-K edge. It indicates that the CO molecule adsorbs on the Si(100) surface via the C atom. In this configuration, if a core hole is created at the C atom, the screening due to the electrons at the substrate will be very quick because the C atom is directly bonded to the substrate, and the relaxation without any desorption will occur. Meanwhile, a core hole at the O atom, and holes at the valence level created by the Auger transition may be possible to survive during the process of the bond breaking.

In conclusion, we have measured the NEXAFS and photo-stimulated desorption spectra of CO adsorbed on the Si(100) surface at 80K, and have shown that CO is bonded nearly perpendicular to the surface via the C atom on the Si(100) surface.

(BL2B1)

Study of ion desorption induced by the core-level excitation on the CaF_2(111) surface

S. Tanaka, M. Mase, M. Nagasono and M. Kamada

Institute for Molecular Science, Okazaki, 444-8585, Japan

Desorption of F^+ induced by core-level excitation with synchrotron radiation has been investigated on the CaF_2(111) film produced on Si(111). All the experiments were carried out at a UHV (base pressure was $1x10^{-10}$ Torr) chamber installed at BL2B1 of UVSOR at Institute for Molecular Science. CaF_2 was deposited from a boron nitride crucible onto a Si(111) surface, which has been cleaned by resistive heating in UHV.

Figure 1 shows partial electron (open circles) and total ion (lines) yields spectra of CaF_2(111) films at 80K in the region of the (a) F-1s and (b) Ca-2p edges. At the onset of the Ca-2p edge, ion yield is nearly proportional to electron yield [fig.1(b)], whereas it shows a clear enhancement at the first peak compared to electron yield in the region of the F-1s edge [fig.1(a)]. The first peak at the onset of the F-1s edge in the electron yield is ascribed to the core exciton [$(F\text{-}1s)^{-1}(Ca\text{-}4s)^1$], whereas the second peak to a transition into an unbound state in the conduction band (Ca-4s and Ca-3d). It was also observed that the peak around 688 eV for the ion yield was shifted by about -1.2 eV compared to that in the electron yield.

The left-hand panels of figure 2 show photoelectron spectra of CaF_2(111) at 300K taken at (a) hv=688eV [corresponding to the first peak observed in the ion yield spectra at the onset of the F-1s edge in fig.1(a)] and (b) at hv=349eV [corresponding to the first large peak at the onset of the Ca-2p edge in fig.1(b)]. The right-hand panels of figure 2 show coincidence signals between positive ions and electrons of kinetic energies which are indicated as A - D in their left-hand panels. All coincidence spectra have periodic backgrounds, which is considered to be related to the time structure of the electron bunchs in the storage ring of UVSOR, because the period in the backgrounds is the same as one cycle of the storage ring (178 ns). The peaks A and B in the photoelectron spectrum in fig. 2(a) are ascribed to the F-$KL_{2,3}L_{2,3}$, and F–$KL_1L_{2,3}$ Auger electron emissions, respectively, and the peaks C and D in fig.2(b) are to the Ca-$L_{2,3}M_{2,3}M_{2,3}$ Auger electron and Ca-3p photoelectron emissions, respectively.

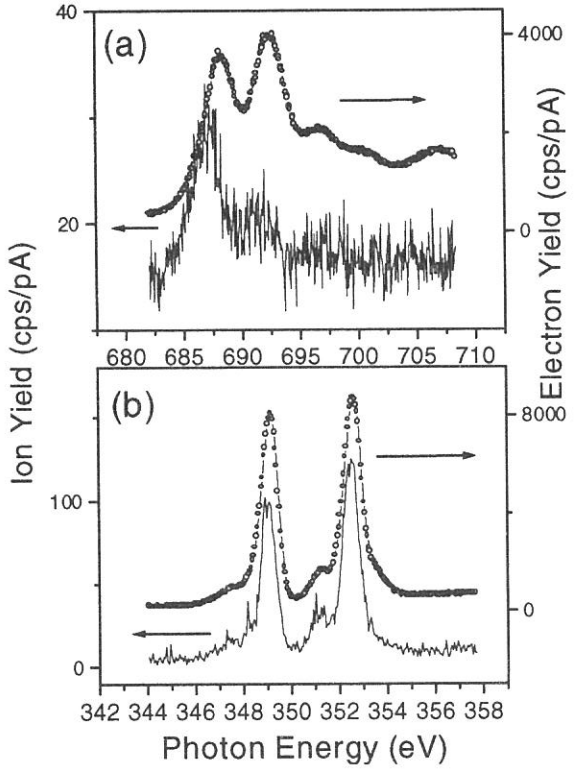

Figure 1

The electron-ion coincidence spectra [fig.2(a)] have shown clear evidence that desorption of F^+ takes place directly via a decay of the F-1s core-exciton. It is in agreement with the observation that the ion yield is enhanced compared to the electron yield at the photon energy for the F-1s core-exciton [fig.1(a)].

Meanwhile, the ion yield is nearly proportional to electron yield at the onset of the Ca-2p edge of CaF_2(111) [fig.1(b)], and no peaks were observed in the coincidence spectra corresponding to the decay of the Ca-2p hole [fig.2(b)]. It indicates that the ion desorption observed in the total ion spectrum is stimulated by the secondary electron current followed by the relaxation of the Ca-2p hole.

It should be noted that the peak observed in the ion yield spectrum is shifted by about -1.2 eV compared to that in the electron yield at the F-1s edge [fig.1(a)]. It is attributed to the "surface" shift of the excitation energy for the core-exciton, because it is reasonable to assume that ion desorbs only from the surface layer, and that the ion yield predominantly reflects the electronic property at the surface in case of desorption via the direct process. Two contributions should be considered. One is an initial state contribution due to the change of binding energies of F-1s and Ca-4s levels at the surface, and the other is a final state contribution due to the change of the core-exciton binding energy at the surface. The dominant mechanism giving rise to the change in the binding energy at the surface of the ionic material is considered to be a change in the Madelung energy. According to the calculation for the CaF_2(111) surface by Rotenberg et.al., the difference in the Madelung energy at the top layer consisting of F^+ and that at the second layer consisting of Ca^{2+} are about -1.05 eV and +0.3 eV, respectively, compared to the bulk value. Therefore, the photon energy for interatomic excitation at the surface is estimated to be shifted by about -1.35 eV compared to bulk, which shows rather good agreement with the observed value (-1.2eV). Accordingly, the origin of the energy shift is mainly attributed to the change in the Madelung energy at the surface of CaF_2(111) film. Although there may be other contributions, e.g., a change in the core-exciton binding energy at the surface, they seem to be smaller. This may be due to the high degree of localization of the F-1s core hole.

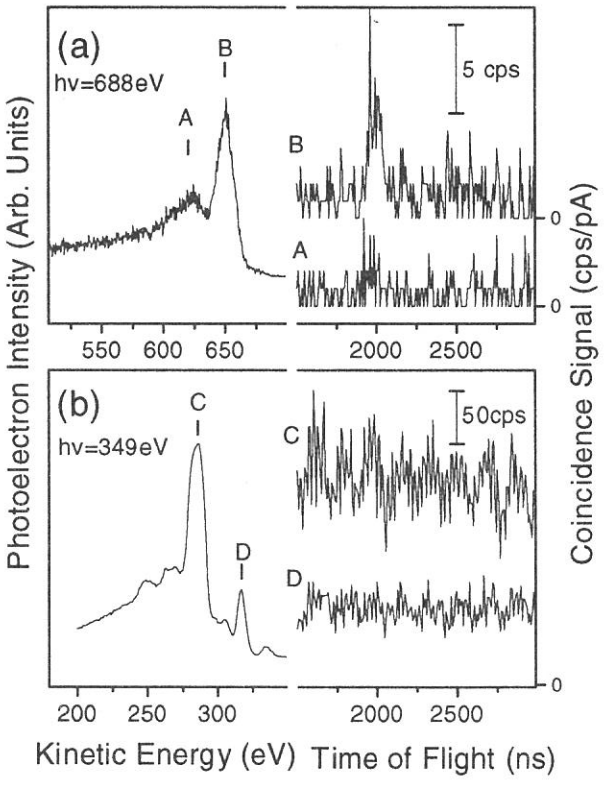

Figure 2

In summary, desorption of F^+ induced by core-level excitation with synchrotron radiation has been investigated on the CaF_2(111) surface produced on Si(111). The ion yield was proportional to electron yield in the region of Ca-2p edge, while an enhancement of the ion yield was observed at the photon energy for the F-1s core-exciton. The peak corresponding to the F-1s excitation observed in the ion yield is shifted from that in the electron yield by about -1.2eV, which is predominantly ascribed to the change in the Madelung potential at the surface. The electron-ion coincidence study showed that F^+ desorption is directly stimulated via a decay of the F-1s surface core-exciton, while secondary-electron stimulated desorption is the predominant process after the creation of Ca-2p hole.

(BL2B1)

Resonant Auger Spectra of Condensed Acetonitrile Molecules Following Carbon and Nitrogen Core Excitation

Eiji Ikenaga[a], Hideki Matsuo[a], Chiaki Kato[a], Tetsuji Sekitani[a], Mitsuru Nagasono[b], Sin-ichiro Tanaka[b], Kazuhiko Mase[b], Tsuneo Urisu[b], and Kenichiro Tanaka[a]

(a) Department of Materials Science, Hiroshima University, Higashi-Hiroshima 739-8526

(b) Institute for Molecular Science, Okazaki 444-8585

Site-specific reactions have been found in photon stimulated ion desorption (PSID) induced by core excitation. The Auger stimulated ion desorption (ASID) mechanism is now proposed as a model for explanation of PSID. Recently, Mase et al. developed an electron-ion coincidence analyzer [1], and we measured Auger electron-photoion coincidence (AEPICO) spectra for condensed acetonitrile (CH_3CN) following carbon excitation [2, 3]. In the present work, we have measured resonant Auger spectra for condensed CH_3CN following carbon and nitrogen core excitation for clarifying the resonant Auger process and the ion desorption mechanism related to the Auger process. The sample was prepared by exposing a gold foil with 100L of CH_3CN at 80K.

Figure 1 shows resonant Auger electron spectra following carbon core excitation. The major contributions of the peaks were assigned on the basis of a comparison with the Auger spectra by calculation [4] and gas phase normal Auger spectra by experiment [5]. The normal Auger transition is dominant in the σ^*_{CC} and σ^*_{CN} excitation which lie above the threshold. (Fig.1e,f,g) because the excited electron promptly goes far from the parent molecule through autoionization and/or electron transfer to neighboring molecules. Auger spectra are drastically changed at the π^*_{CN} and C-H* excitation from the normal Auger spectrum (Fig.1b,d,g). The peak X is attributed to the participant Auger transition. Other peaks are attributed to the spectator Auger transition of carbon 1s. The difference in AES between the π^*_{CN} excitation and the C-H* excitation can be explained as follows: At the π^*_{CN} excitation, the transition of a C1s(CN) electron to the π^*_{CN} orbital occurs rather than that of the C1s(CH_3) electron to π^*_{CN} because the π^*_{CN} orbital is localized on the CN group. Then the spectator Auger transition which makes holes at the orbital localized on the CN group occurs selectively. In the case of the C-H* excitation, the C1s(CH_3) electron to C-H* orbital transition mainly occurs, so that the spectator Auger transition which makes holes at the orbital localized on the CH_3 group occurs selectively.

Figure 2 shows resonant Auger spectra following the nitrogen core excitation. Auger electron spectra are different from that of the carbon core excitation. At the π^*_{CN} excitation (Fig.2b), spectral feature except for the peak X is similar to the normal Auger spectrum (Fig.2f),but the peaks are shifted to high energy. The peak X is ascribed to the participant Auger transition, and other peaks are attributed to the spectator Auger transition of the nitrogen 1s hole. The difference in spectra between Fig.1b and Fig.2b, which both correspond to resonant excitation to the π^*_{CN} orbital,

indicates that the spectator Auger transition depends on the site of core hole.

These results clearly show that primary excitation depends on the localized character of unoccupied orbital and the subsequent Auger transition depends on the site of core hole. The comparison of AEPICO measurements with the resonant Auger spectra at various resonant excitation supports the previous results, that the ion desorption depends on the bonding/anti-bonding character and the localized character of the excited state and the Auger final state [2, 3].

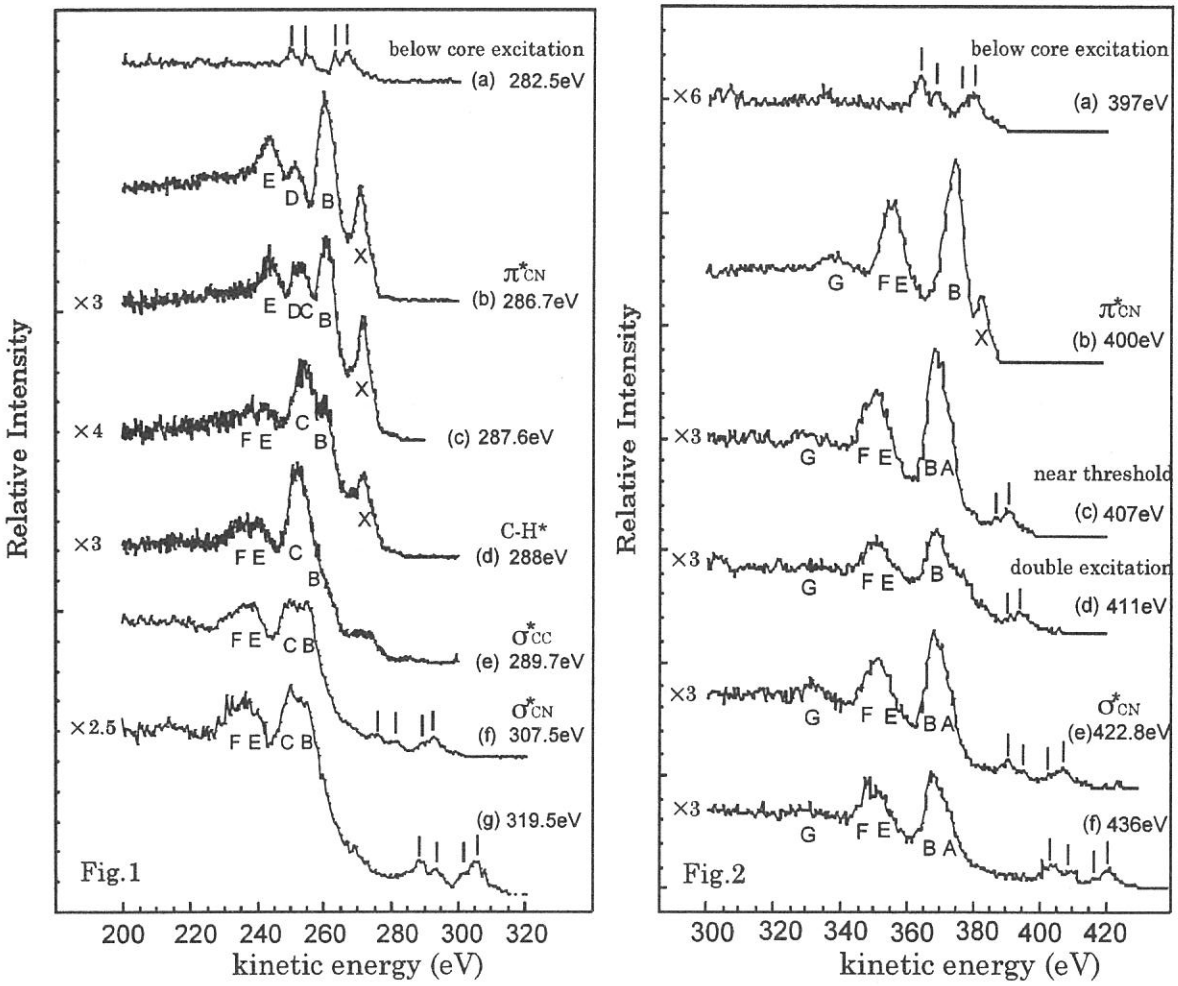

FIG.1 and FIG.2. Resonant Auger spectra for condensed CH_3CN following carbon core excitation (Fig.1), and nitrogen core excitation (Fig.2). Bars show peaks owing to emission of a valence electron. Photon energies are indicated at the right end.

Reference

[1] K. Mase et al., Rev. Sci. Instrum. 68 (1997) 1703.

[2] E. Ikenaga et al., UVSOR Activity Reports BL2B1. (1996) 108.

[3] T. Sekitani et al., Surf. Sci. 390 (1997) 107.

[4] J. V. Ortiz, J. Chem. Phys. 83 (1985) 4604.

[5] R. R. Rye and J. E. Houston, J. Chem. Phys. 75 (1981) 2085.

(BL2B1)

Site-specific fragmentation following C:1*s* core-level photoionization of CF_3CH_3 condensed on a Au surface

Shin-ichi Nagaoka, Kazuhiko Mase,[A] Mitsuru Nagasono,[A] Shin-ichiro Tanaka[A] and Tsuneo Urisu[A]

Department of Chemistry, Faculty of Science, Ehime University, Matsuyama 790-8577

[A]Institute for Molecular Science, Okazaki 444-8585

Synchrotron radiation has provided a powerful means to obtain information about core-level excitations, and the dynamic processes following the core-level excitations in molecules have long been a subject of interest. In contrast to valence electrons that are often delocalized over the entire molecule, the core electrons are localized near the atom of origin. Although core electrons do not participate in the chemical bonding, the energy of an atomic core-level in the molecule depends on the chemical environment around the atom. A shift in the energy levels of core electrons that is due to a specific chemical environment is called a chemical shift.

Monochromatized synchrotron radiation can excite core electrons of an atom in a specific chemical environment selectively, discriminating the core electrons from those of like atoms having different chemical environments. This site-specific excitation often results in site-specific fragmentation, which is of importance in understanding localization phenomena in chemical reactions and which is potentially useful for synthesizing materials through selective bond breaking.

To elucidate the site-specific fragmentation, we have studied the spectroscopy and dynamics following core-level photoionization of various molecules condensed on surfaces [1,2]. To observe the dissociation processes following core-level ionization of a site selectively, we use the energy-selected-photoelectron photoion coincidence (ESPEPICO) method and the Auger-electron photoion coincidence (AEPICO) method. The measurements of fragment ions coincidentally produced with energy-selected photoelectrons or Auger-electrons allow selective observation of the processes initiated by the electron ejection.

In the present work, we have used photoelectron spectroscopy and these coincidence methods to study the site-specific fragmentation following C:1*s* photoionization of CF_3CH_3 condensed on a Au surface. The chemical environment of a C atom bonded to three F atoms (C[F]) is very different from that of one bonded to three H atoms (C[H]), so it seems likely that CF_3CH_3 will show site-specific fragmentation. It is also interesting that the site-specific fragmentation pattern on a Au surface is compared with that in the vapor phase [3,4].

Since the accidental coincidences carried the time structure of the synchrotron source that was operated with a partial-filling mode, we had to remove the time-structure background with a period of 177 ns from the coincidence spectrum. Accordingly, we performed its fast-Fourier-transformation (FFT), subtracted the 177 ns component and then made its inverse FFT. This technique seems to work rather well such that we are able to discern even weak true coincidence

features rather well.

Figures 1(a) and 1(b) show the ESPEPICO spectra obtained with emission of the C[H]:1*s* and C[F]:1*s* electrons, respectively. $C_2H_n^+$ (n=0-3) and $CFCH_m^+$ (m=2,3) ions are predominantly desorbed coincidentally with the C[F]:1*s* electrons. The ionic fragmentation occurs selectively around the C atom where the photoionization has taken place: synchrotron radiation can indeed play the part of an optical knife for molecules. It is also interesting that the ratio of the coincidence count for CH_3^+ to that for CF_3^+ is larger in the case of C[H]:1*s* photoionization than in C[F]:1*s*. The site-specific fragmentation pattern obtained from excitation on the Au surface is very different from that obtained from excitation in the vapor phase [3,4].

Figure 2 shows the AEPICO spectrum obtained for the electron kinetic energy (E_k) corresponding to the C[H](*KVV*) normal-Auger transition. The AEPICO yield for CH_3^+ is greatly enhanced at the high-E_k edge of the C[H](*KVV*) normal-Auger peak. This result shows that the character of HOMO is C-C σ-bonding and the electronic transition from HOMO to C[H]:1*s* induces ionic fragmentation of the C-C bond.

[1] S. Nagaoka, K. Mase, M. Nagasono, S. Tanaka, T. Urisu and J. Ohshita, J. Chem. Phys., in press.

[2] S. Nagaoka, K. Mase and I. Koyano, Trends Chem. Phys., in press.

[3] K. Müller-Dethlefs, M. Sander, L. A. Chewter and E. W. Schlag, J. Phys. Chem. 88, 6098 (1984).

[4] W. Habenicht, H. Baiter, K. Müller-Dethlefs and E. W. Schlag, J. Phys. Chem. 95, 6774 (1991).

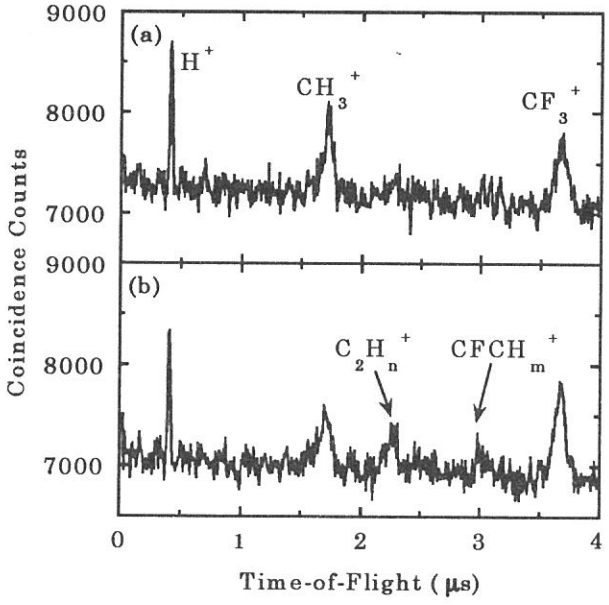

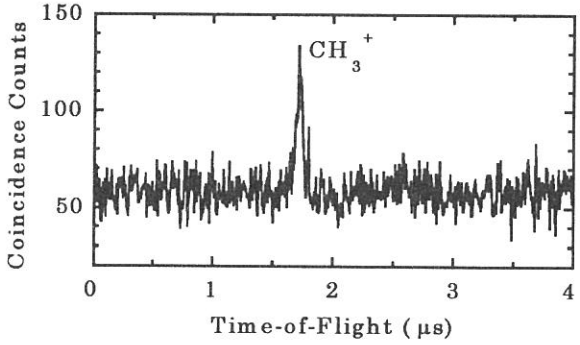

Figure 1 (left-hand side). ESPEPICO spectra of CF_3CH_3 taken at a photon energy of 393 eV. Data collection time is 5000 s. (a) C[H]:1*s* electron emission. (b) C[F]:1*s* electron emission.

Figure 2 (right-hand side). AEPICO spectrum obtained at a photon energy of 293 eV for E_k = 260 eV, which corresponds to the high E_k edge of the C[H](*KVV*) normal-Auger peak. Data collection time is 1080 s.

(BL2B1)

Site-specific fragmentation following Si:2*p* core-level photoionization of bridged trihalosilyl-trimethylsilyl system condensed on a Si(111) surface

Shin-ichi Nagaoka, Kazuhiko Mase,[A] Mitsuru Nagasono,[A] Shin-ichiro Tanaka[A] and Tsuneo Urisu[A]

Department of Chemistry, Faculty of Science, Ehime University, Matsuyama 790-8577

[A]Institute for Molecular Science, Okazaki 444-8585

In a previous paper [1], we used photoelectron spectroscopy and the energy-selected-photoelectron photoion coincidence (ESPEPICO) method to study site-specific fragmentation following Si:2*p* photoionization of 1-trifluorosilyl-2-trimethylsilylethane [$F_3SiCH_2CH_2Si(CH_3)_3$, FSMSE] condensed on a Au surface. The photoelectron spectrum of FSMSE had two peaks for 2*p*-electron emission: one for the Si atom bonded to three methyl groups (Si[Me]) and one for the Si atom bonded to three F atoms (Si[F]). H^+ and F^+ ions were predominantly desorbed coincidentally with the Si[Me]:2*p* and Si[F]:2*p* electrons.

The site-specific fragmentation is potentially useful for synthesizing materials through selective bond breaking. Synchrotron radiation can indeed play the part of an optical knife for molecules. When bond dissociation around an atomic site is required in the synthesis, one can use the optical knife that has the photon energy corresponding to the specific excitation of that site. In this context, the dependence of the site-specific fragmentation on the distance between the sites is interesting [2]. How far must the atomic site of interest be separated from any other atomic site around which bond dissociation is undesirable, in order for the site-specific process to work? This point is closely related to the application to the construction of future molecular electric devices, in which the control of very localized reactions will play a crucial role. Accordingly, in the present study, we have studied the site-specific fragmentation following Si:2*p* photoionization of 1,1,1-trimethyltrichlorodisilane [$Cl_3SiSi(CH_3)_3$, MCDS], 1-trifluorosilyl-2-trimethylsilylmethane [$F_3SiCH_2Si(CH_3)_3$, FSMSM] and FSMSE condensed on a Si(111) surface. The measurements of fragment ions coincidentally produced with energy-selected photoelectrons allow selective observation of the processes initiated by the electron ejection.

Figures 1(a), 1(b) and 1(c) show the total electron yield (TEY) spectrum of MCDS, FSMSM and FSMSE condensed on Si(111), respectively. Assignments of peaks in the spectra, inferred by comparison with the photoabsorption spectra of $SiCl_4$, SiF_4 and $Si(CH_3)_4$, are given in the figure. The TEY spectra of FSMSM and FSMSE are made up of the superposition of those of $Si(CH_3)_4$ and SiF_4, but that of MCDS seems to be close to that of $Si(CH_3)_4$. These results show that the site-specific excitation occurs in FSMSM and FSMSE but it does not in MCDS.

Figures 2(a), 2(b) and 2(c) respectively show the photoelectron spectra of MCDS, FSMSM and FSMSE in the region of Si:2*p* electron emission. The photoelectron spectra of FSMSM and FSMSE have two peaks in this region. The peaks at the lower- and higher-energy sides are respectively thought to correspond to Si[Me]:2*p* and Si[F]:2*p* electron emissions. However, under

the same experimental conditions, the photoelectron spectrum of MCDS has only one peak.

Figures 2(a), 2(b) and 2(c) also show the ESPEPICO yield spectra in MCDS, FSMSM and FSMSE respectively in the region of Si:2*p* electron emission. In FSMSM and FSMSE, the ESPEPICO yield for H^+ shows a peak around the binding energy of Si[Me]:2*p*, and the yield for F^+ shows a peak around that of Si[F]:2*p*, although the peak for F^+ is less remarkable in FSMSM than in FSMSE. However, H^+ is the only primary species desorbed coincidentally with the Si:2*p* electron in MCDS. These results show that the site-specific fragmentation takes place in FSMSM and FSMSE but it does not in MCDS.

From the above-mentioned results, it is considered that the site-specific excitation and fragmentation are observed in molecule in which the two Si sites are located far from each other. This is because the electron-migration between the two Si-containing groups located far from each other (for example, F_3Si- and -$Si(CH_3)_3$ in FSMSE) is not effective, as described previously [2].

[1] S. Nagaoka, K. Mase, M. Nagasono, S. Tanaka, T. Urisu and J. Ohshita, J. Chem. Phys., in press.

[2] S. Nagaoka, T. Fujibuchi, J. Ohshita, M. Ishikawa and I. Koyano, Int. J. Mass Spectrom. Ion Processes, in press.

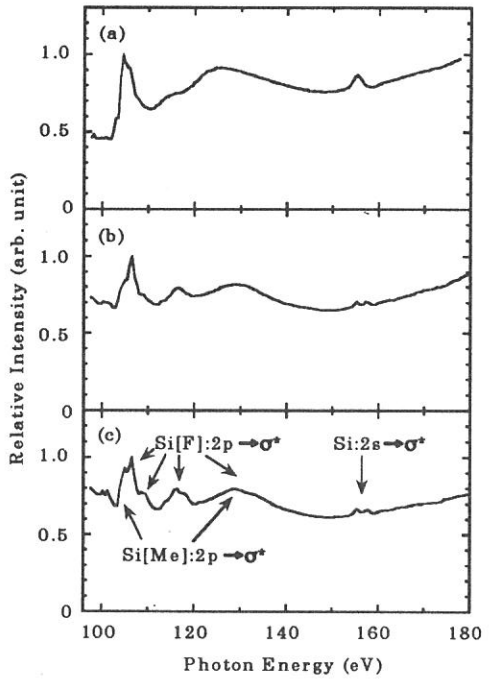

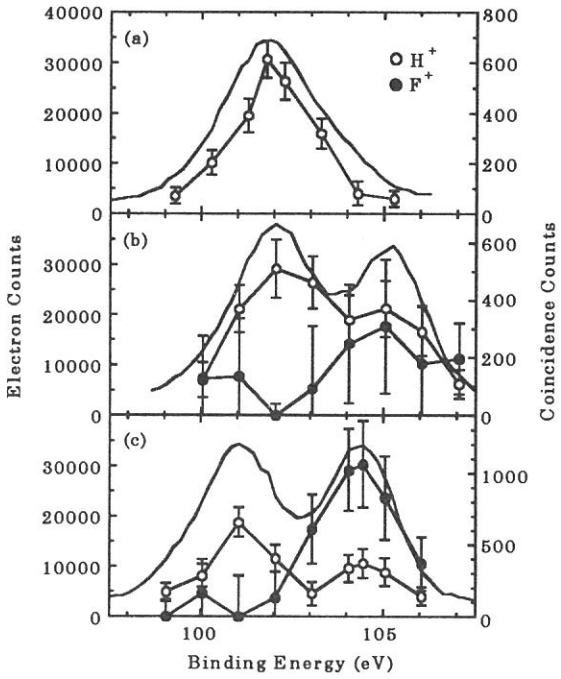

Figure 1 (left-hand side). TEY spectrum. (a) MCDS. (b) FSMSM. (c) FSMSE. Each channel was measured for 2 s at a step of 0.5 eV.

Figure 2 (right-hand side). ESPEPICO yield spectra and the photoelectron spectrum as a function of electron binding energy in the region of Si:2*p* electron emission. Each channel in the photoelectron spectrum was measured for 0.5 s at a step of 0.2 eV. (a) MCDS. Data collection time for each data point in an ESPEPICO yield spectrum is 1800 s. (b) FSMSM. Data collection time is 1200 s. (c) FSMSE. Data collection time is 1320 s.

(BL2B1)

Study of ion desorption induced by resonant core–electron excitations of condensed methanol using Auger electron photoion coincidence (AEPICO) spectroscopy combined with synchrotron radiation

Kazuhiko Mase, Mitsuru Nagasono, Shin–ichiro Tanaka, and Tsuneo Urisu

Institute for Molecular Science, Okazaki 444–8585, Japan

Ion desorption induced by resonant core–electron excitations of molecules condensed on a surface is a prospective topic in molecular dynamics, surface science, and synchrotron radiation researches [1]. Auger electron photoion coincidence (AEPICO) spectroscopy is an ideal tool in this field, because it provides ion desorption yield derived from the selected Auger transitions [2]. In the present article, we describe an ion desorption study in the region of resonant excitations of Carbon 1*s* core–electron of condensed methanol using total ion and Auger electron yield spectroscopy (TIYS and AEYS), non–derivative Auger electron spectroscopy (AES), and AEPICO spectroscopy. Figure 1(a) shows TIYS of condensed CH_3OD, CH_3OH, and CD_3OH in the Carbon K–edge region. Since the desorption probability of D^+ and polyatomic ions such as CH_3^+ is much smaller than that of H^+, the total ion yield corresponds to the H^+ yield [3]. CH_3OD and CH_3OH exhibited TIYS which resemble to each other, while ions are scarcely desorbed from CD_3OH. This result shows that H^+ desorption from the hydroxyl group is suppressed as compared with that from the methyl group, which is in consistent with the results of an electron–stimulated desorption study of condensed methanol [3]. We ascribed this phenomenon to the hydrogen bonding due to the trimer and dimer formation [4] on the surface. The AEYS exhibited a peak at $h\nu$ = 287.8 eV and a broad peak around $h\nu$ = 292.3 eV. The spectrum of TIY/AEY, on the other hand, exhibited a small peak at $h\nu$ = 287.8 eV and a slight suppression at $h\nu$ = 292.3 eV. Therefore we assigned $h\nu$ = 287.3 eV to the resonance into weakly C–H anti–bonding orbital (C–H*), $h\nu$ = 292.8 eV to the resonance into C–H non–bonding orbital, and $h\nu$ = 292.8 eV to C:1*s* ionization, respectively. Figure 2 shows series of AEPICO spectra at $h\nu$ = 287.8, 292.3, and 315.3 eV for the electron kinetic energies of 220–275 eV corresponding to the C:KVV Auger transitions. H^+ was found to be the only ion species desorbed in all the cases. Figure 3 shows the electron kinetic energy dependence of the AEPICO yield (AEPICO yield spectra) at $h\nu$ = 287.8, 292.3, and 315.3 eV. The valence electronic configuration of CH_3OH is $(3a')^2(4a')^2(5a')^2(1a'')^2(6a')^2(7a')^2(2a'')^2$ [5]. At $h\nu$ = 315.3 eV, the AEPICO yield spectrum exhibited the maximal peak at the electron kinetic energy of 255 eV, which corresponds to $(1a'')^{-2}$, $(1a'')^{-1}(6a')^{-1}$, and $(6a')^{-2}$ Auger final states [6], where 1a" and 6a' are the C–H bonding orbital [5]. This result indicates that the normal–Auger stimulated ion desorption (normal–ASID) mechanism is responsible at $h\nu$ = 315.3 eV. At $h\nu$ = 287.8 eV, the AEPICO yield spectrum exhibited a peak at the electron kinetic energy of

260 eV which was assigned to $(1a'')^{-2}(C\text{-}H^*)^1$, $(1a'')^{-1}(6a')^{-1}(C\text{-}H^*)^1$, and $(6a')^{-2}(C\text{-}H^*)^1$ spectator–Auger final states. This result suggests that spectator–ASID mechanism and/or ultrafast ion desorption mechanism is predominant at $h\nu$ = 287.8 eV. At $h\nu$ = 292.3 eV, on the other hand, the AEPICO yield spectrum displayed a remarkable suppression at the electron kinetic energy of 260 eV in contrast to the case at $h\nu$ = 287.8 eV. This suppression was ascribed to the reduction of the hole–hole Coulomb repulsion due to the shield effect of the electron in the non-bonding orbital. This result suggests that spectator–ASID mechanism is probable at $h\nu$ = 292.3 eV.

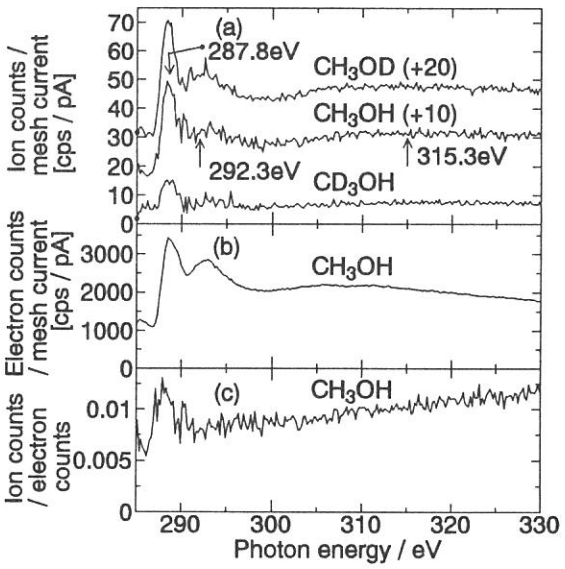

Figure 1. (a) TIYS of condensed CH_3OD, CH_3OH, and CD_3OH. (b) AEYS, and (c) spectrum of TIY/AEY of condensed CH_3OH.

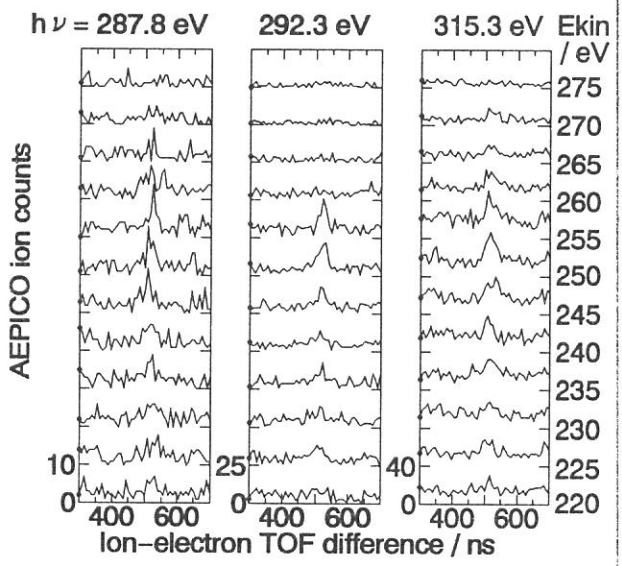

Figure 2. Series of AEPICO spectra at $h\nu$ = 287.8, 292.3, and 315.3 eV.

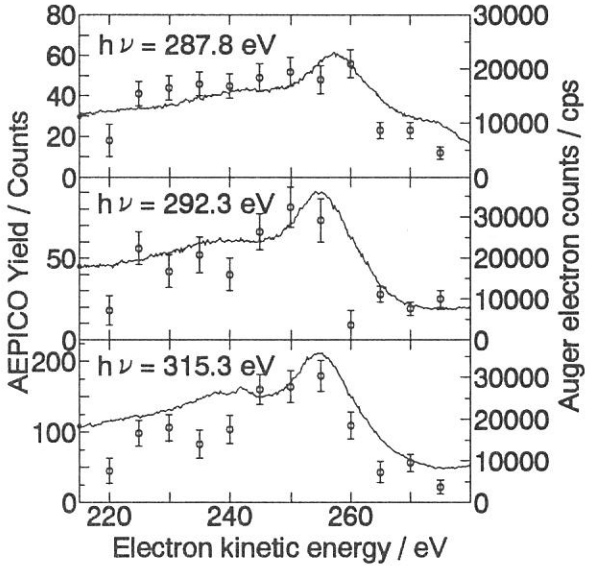

Figure 3. (a) AEPICO H^+ signal intensities as a function of the electron kinetic energy (AEPICO yield spectra) at $h\nu$ = 287.8, 292.3, and 315.3 eV. The solid lines show the AES.

References

[1] K. Mase *et al.*, *Surf. Sci.* **390**, 97 (1997); M. Nagasono *et al.*, *Surf. Sci.* **390**, 102 (1997); T. Sekitani *et al.*, *Surf. Sci.* **390**, 107 (1997).

[2] K. Mase *et al.*, *Rev. Sci. Inst.* **68**, 1703 (1997).

[3] R. Stockbauer *et al.*, *J. Chem. Phys.* **76**, 5639 (1982).

[4] O. Mó *et al.*, *J. Mol. Struct. (Theochem)* **314**, 73 (1994).

[5] M. B. Robin and N. A. Kuebler, *J. Electron Spectros. Relat. Phenom.* **1**, 13 (1972/73).

[6] N. Kosugi, Master's thesis (1978).

(BL3A1) Fine Processing of PMMA with Synchroton Radiation

Akitaka Yoshigoe, Takanori Hayakawa, Hitoshi Sato, Akihiro Wakahara and Akira Yoshida

Department of Electrical and Electronic Engineering, Toyohashi University of Technology, Tenpaku-cho, Toyohashi, 441, Japan

Recently, semiconductor devices on a small Si chip have been remarkably integrated. The lithography technology generally accepted at present can't follow this development. Therefore, the superior dry processing using vacuum-ultra-violet light is required in the future. In this study, we have demonstrated that PMMA (polymethyl-methacrylate) films, which are widely used as an electron beam and X-ray positive resist, were irradiated by SR in vacuum and oxygen gas.

The PMMA was spin coated on the Si wafer with a few micrometer thick. The sample was introduced into the high vacuum reaction chamber. The exposure to undulator light (undulator gap: 60mm) was performed directly through differential pumping systems. Figure 1 shows the reduced thickness of PMMA films which is normalized by the initial thickness as a function of SR exposure doses with and without the oxygen gas. The substrate temperature was room temperature during the SR irradiation. It was found that the reduced thickness increased with increasing the SR exposure dose at the low SR exposure and then it was saturated. On the other hand, it was found that the PMMA films were etched and removed with oxygen gas during SR irradiation.

Figure 2 shows the XPS (X-ray photoelectron spectroscopy) spectra of PMMA films and the samples after SR irradiation with and without oxygen gas. It should be pointed out that Si2p signals of the substrate were observed when the oxygen gas exists during the SR irradiation. No Si signals, however, were observed in the case of vacuum.

From the results of the XPS and the thickness measurements, it was found that the PMMA films were not etched up to the Si substrate in vacuum, however, completely removed to the substrate surface in oxygen gas.

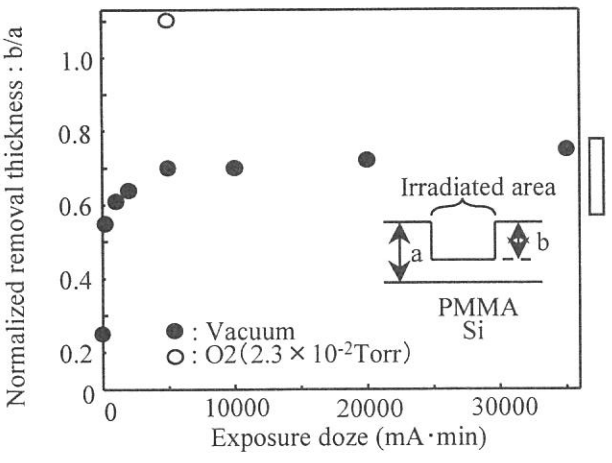

Fig. 1. The reduced thickness of PMMA after SR irradiation in vacuum and oxygen gas.

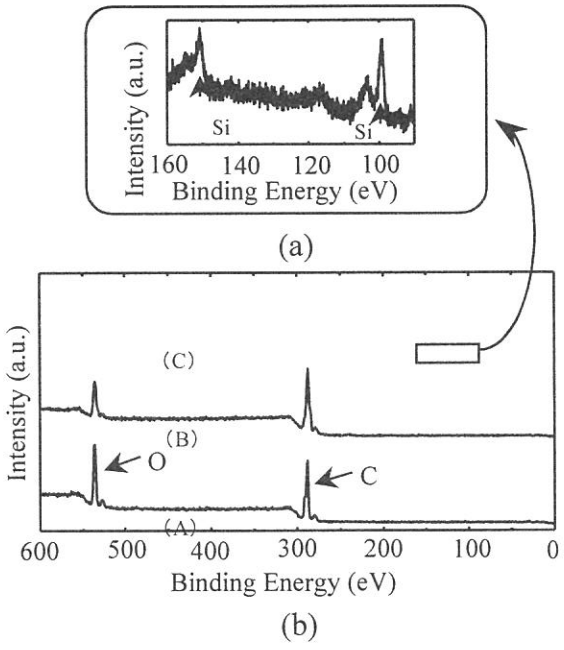

Fig. 2. XPS spectra. (A) PMMA, (B)SR irradiation in vacuum, (C) in oxgen gas.

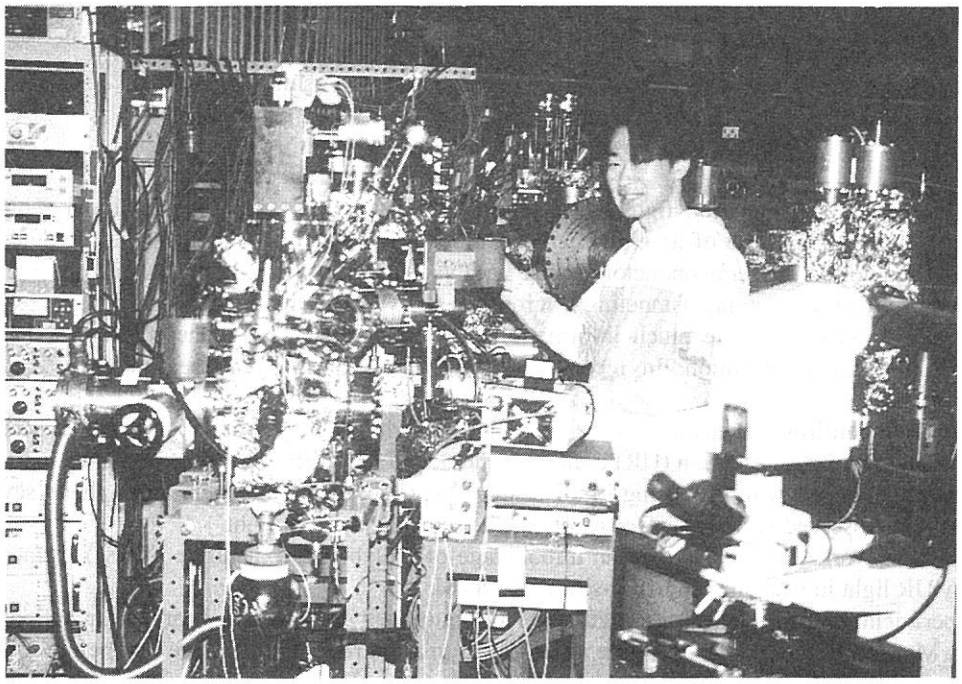

Photoreaction Chamber at BL8A

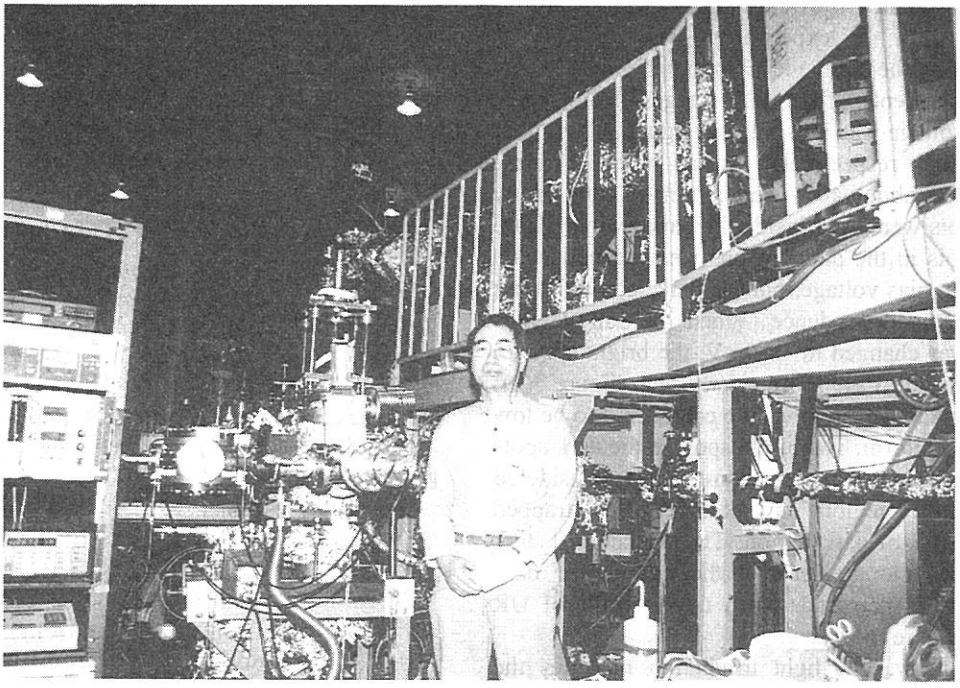

Prof. Murata (Univ. of Kyoto Edu.) at BL7A and BL7B

(BL3A-1)

Observation of MoS_2 surface reaction irradiated by Undulator Radiation Light Using Scanning Tunneling Microscope

T.Hayakawa, A.Yoshigoe and A.Yoshida

Toyohashi University of Technology, Toyohashi 441-8580

Recently, synchrotron radiation light has been exploited to give a new possibility in semiconductor processing technology because of its high energy photons. Investigations to understand the defect creation and atomic behavior on the semiconductor surface with vacuum ultra-violet-light give important clues to the semiconductor process. Scanning Tunneling Microscope (STM) is a direct method working in real space on an atomic scale. STM can give much information of electronic states and the surface topography with extremely high spatial resolution. In recent years, STM has been often used to analyze the surface characterization.

Last year, we confirmed that the depression region and ring pattern were found on the MoS_2 surface irradiated with Undulator Radiation (UR) light in vacuum, and these patterns became greater and the number of the patterns increased with increasing irradiation UR light dose. In the oxygen atmosphere, several kinds of patterns were observed in these surface reactions the same dose of UR light.

In the present work, we have studied an initial stage of molybdenum disulfide (MoS_2) surface reactions induced by UR light in vacuum with an in-situ UHV-STM.

The experimental set-up is shown in Figure 1. This equipment consists of preparation, reaction, and STM chambers. MoS_2 was used as the substrate and cleaved in air at room temperature just before it was loaded into the preparation chamber. The sample was transferred into the reaction chamber under a base pressure below 1×10^{-7} Torr and irradiated by UR light at room temperature. The amount of UR light dose was 25mA·min, 100mA·min, 200mA·min and 300mA·min. After the irradiation, the sample was transferred to the UHV-STM chamber and the surface topography was observed. STM images were obtained both in the constant-height mode and the constant-current mode at the sample bias voltage in the range of -500mV～500mV.

Figure 2(a) shows the STM image of MoS_2 clean surface on 60Å×60Å scale with the sample bias voltage of -150mV and the tunneling current of 1nA. The atomic structure in the top layer of sulfur atoms was seen clearly. Figure 2(b) shows the cross section of STM image of MoS_2 clean surface. The lattice constant estimated from this figure is consistent with that calculated from X-ray diffraction pattern of this sample within the experimental error of 2%. The images obtained with this STM are reasonable. Furthermore, the atomic level image of graphite sample was observed.

The dependence of the STM images of MoS_2 surface irradiated by UR light for 25mA·min in vacuum on the bias voltage was illustrated in figure 3. The sample bias voltages in figure 3(a) and 3(b) are both 150mV and -150mV, respectively. As can be seen from figure 3(a), the dark circular regions with an average diameter of about 40Å were observed, and many bright spots were seen inside the dark region. These bright spots in the dark regions were dependent on the sample bias voltage, but the dark region did not show such a dependence. When the sample bias voltage was changed to -150mV, the bright spots in the dark region were more clearly seen.(figure 3(b)) Therefore, the dark regions are considered to be low area at a landform. The bright spots in the dark spots are due to the electronic structure, so it is considered that some dark regions have some electrons trapped on the center of dark region. The diameter of dark regions became greater and the number of dark regions were increased, when the amounts of UR light dose were increased.

In summary, UR light irradiation modifies the MoS_2 surface, and the modified surface structure has been made clear on a atomic scale with STM.

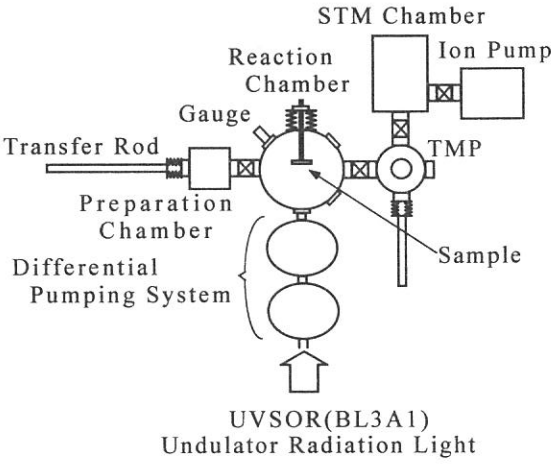

Fig.1 Experimental set-up

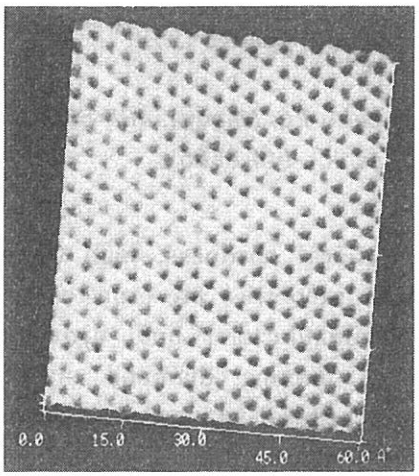

(a) STM image of the MoS_2 clean surface (60 Å × 60 Å)

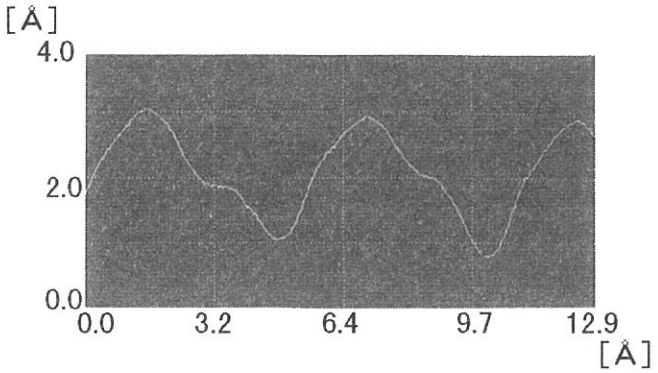

(b) Cross section of STM image of the MoS_2 clean surface

Fig.2 MoS_2 clean surface

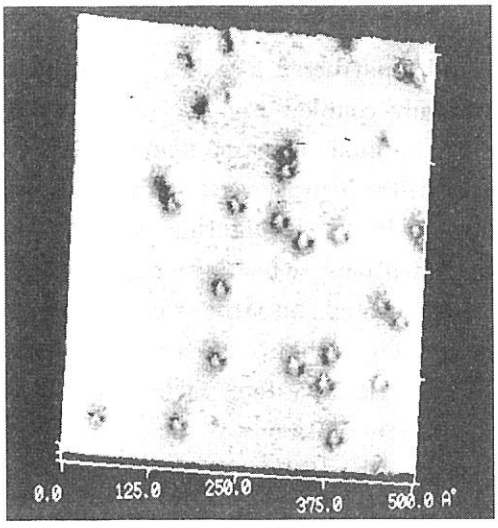

(a) Sample bias voltage 150mV (500 Å × 500 Å)

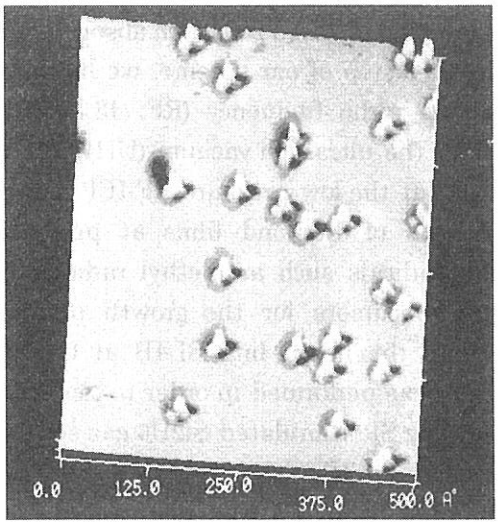

(b) Sample bias voltage -150mV (500 Å × 500 Å)

Fig.3 STM images of the MoS_2 irradiated for 25mA·min in vacuum

(BL4B)

Investigation of diamond growth mechanism using infrared reflection absorption spectroscopy

Mineo Hiramatsu, Hideyuki Noda, Masahito Nawata and Tsuneo Urisu[A]

Faculty of Science and Technology, Meijo University, Tempaku-ku, Nagoya, 468-8502
[A]Institute for Molecular Science, Myodaiji, Okazaki, 444-8585

Diamond has many excellent properties, including mechanical hardness, high thermal conductivity, chemical inertness, and a wide band gap. These properties are expected to be applied to mechanical cutting tools, heat sinks of semiconductors, and high-energy light-emitting materials. Therefore, various techniques of forming diamond such as plasma-enhanced chemical vapor deposition and hot-filament chemical vapor deposition have been developed. For the application of diamond film to the electronic devices in nanometer scale, area-selective growth of diamond must be one of key technologies for the formation of diamond films in extremely fine pattern. To accomplish this object, synchrotron radiation (SR) is expected to be useful because it provides a high spatial resolution with high photon energy.

In the present work, we are planning to deposit diamond film area-selectively using radical injection technique[1,2] with the assistance of SR-induced chemical reaction. For this purpose, first of all, it is necessary to make clear of diamond growth mechanism on the substrate. Our primary goal is to investigate the surface reaction of diamond growth in the early stage of deposition using infrared reflection absorption spectroscopy (IRAS).

As the first step of our scheme, we have designed and constructed a radical source using a low pressure radio frequency (RF; 13.56 MHz) inductively coupled plasma (ICP), which is specified for the ultrahigh vacuum (UHV) equipment. By the basic research using ICPs, it was confirmed that the low pressure RF-ICP using methanol-water-hydrogen system was useful for the formation of diamond films at pressures below 15 Pa[3]. Using this radical source, important radicals such as methyl radicals and hydrogen atoms, which are regarded as the important precursors for the growth of diamond, are injected into the reaction chamber connected to the beam line BL4B at UVSOR, Institute for Molecular Science. Preliminary experiment was performed in order to confirm the validity of IRAS system. SiHx on the Si (100) surface during SR-stimulated Si2H6 gas source molecular beam epitaxy was detected by means of IRAS using a CoSi2 buried metal layer (BML) substrate. The IRAS system installed to the UHV chamber at BL4B was re-arranged for the observation of the surface reaction on the substrate under irradiation of SR beam and injection of radicals. The detection of CHx is being carried out using BML and metal (copper and platinum) substrates.

[1] M. Hiramatsu, M. Inayoshi, K. Yamada, E. Mizuno, M. Nawata, M. Ikeda, M. Hori, and T. Goto, Rev. Sci. Instrum., 67 (1996) 2360.

[2] M. Ikeda, E. Mizuno, M. Hori, T. Goto, K. Yamada, M. Hiramatsu, and M. Nawata, Jpn. J. Appl. Phys., 35 (1996) 4826.

[3] H. Noda, M. Hiramatsu, M. Nawata, M. Hori, and T. Goto, Bulletin Am. Phys. Soc., 42 (1997) 1753.

(BL4B)

Quantum Dot Formation Using Synchrotron Radiation-excited Etching

Youichi Nonogaki[a], Tsuneo Urisu[a] and Yoshikazu Takeda[b]

[a]*Institute for Molecular Science, Myodaiji, Okazaki 444-8585, Japan*
[b]*Department of Materials Science and Engineering, Graduate School of Engineering, Nagoya University, Furo-cho, Chikusa-ku, Nagoya 464-8603, Japan*

Semiconductor structures with reduced dimensionality are subject of significant interest in modern solid state physics and device application. Recently the formation of quantum-sized InAs and InGaAs dots self-organized on GaAs surfaces using molecular beam epitaxy (MBE) was demonstrated[1]. We have been studying formation of InAs dots on InP substrate by novel droplet heteroepitaxy[2,3], because the quantum dots can emit light at technologically important wavelength of 1.5 μm. Although emission from the single dot has very sharp line, the total emission from the sample has broad peak of which full width at half maximum is about 100-150 meV, probably due to size fluctuation between each dot. Suppression of the fluctuation to sharpen the emission is necessary to fabricate the new optical devices which have higher performance than quantum laser diodes.

We suggested a new method to form ordered array of the quantum dots which includes synchrotron radiation (SR) -excited etching process. The SR-excited etching process has great potentials for fabrication of semiconductor devices. The etching reaction occurs only at SR irradiated area, then the etching progresses straight with no lateral etching. Furthermore, damage induced by SR-excited etching is much lower than commonly used reactive ion etching, because SR-excited etching involves no sputter process.

Figure 1 (a) and (b) show schematic illustrations of our proposal to form the ordered array of the quantum dots. The SR-excited etching process is performed as shown in Fig. 1 (a), where SiO_2 on InP substrate is exposed to SR in SF_6 and O_2 ambient. Therefore, SiO_2 is patterned by masking of Al_2O_3 plate with ordered holes. After preparation of patterned substrate, InAs or InGaAs quantum dots are formed by selective growth technique using organometallic vapor phase epitaxy (OMVPE), as shown in Fig. 1 (b).

We are now improving and reconstructing of etching chamber and differential pumping system to start SR-excited etching experiments.

References

[1]D. Leonard, K. Pond and P.M. Petroff, Phys. Rev. B **50**, (1994) 11687.
[2]Y. Nonogaki, Y. Fujiwara, Y. Takeda et al., Appl. Surf. Sci. **117/118**, (1997) 665.
[3]Y. Nonogaki, Y. Fujiwara, Y. Takeda et al., Mat. Sci. & Eng. B (in press).

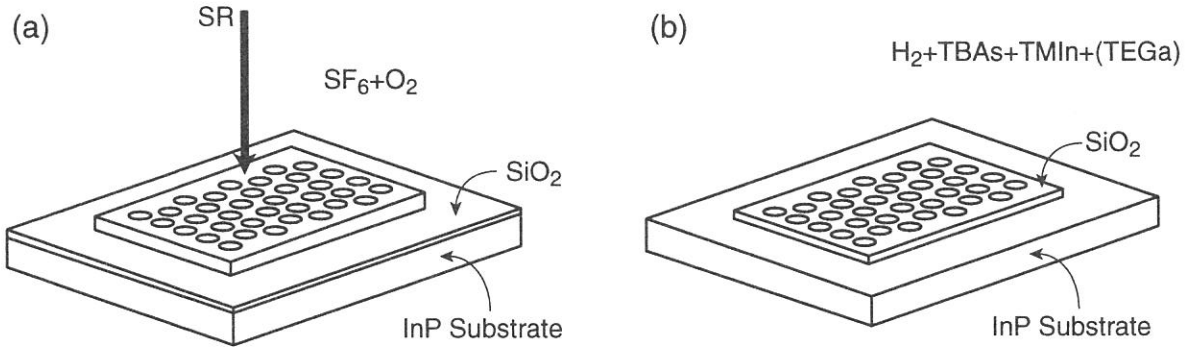

Fig. 1. Schematic illustrations of (a) the SR eching process and (b) subsequent selective growth process to form ordered array of the quantum dots.

(BL5A) **Interpretation of the photoelectron spectrum of H_2O/Si(100) surface**

Shin-ichiro Tanaka, Junichi Murakami and Masao Kamada

Institute for Molecular Science, Okazaki, 444-8585, Japan

The adsorbed states of water on the Si surface has been studied by many experimental methods, because not only it is important process of the wet oxidation of the Si, but also it is one the model case of the adsorption of the molecule on the semiconductor surface. Schmeisser et.al. [1] studied this system by the use of the photoelectron spectroscopy, and concluded the adsorption in the molecular form. Meanwhile, Ibach et.al. [2] and Nishijima et.al.[3] used HREELS (High-resolution electron energy loss spectroscopy) and concluded that water is dissociated into OH and H on the Si surfaces. Chabal et.al. [4] also stated the dissociative adsorption by the use of the infrared spectroscopy. It is considered that the vibrational spectroscopy is supreme to the photoelectron spectroscopy in order to determine the bonding configuration of the surface, and thus, the dissociative adsorption is generally accepted for this system. However, it means that the results of the photoelectron spectroscopy should be re-interpreted, but the situation is rather contradictory. Ciraci et.al. [5] made a theoretical calculations and stated that the photoelectron spectrum can be interpreted according to their model, however, their results is not agreement with the experimental results by the use of the synchrotron radiation as shown below. Schmeisser et.al. [6] made an *in-situ* experiments by using the HREELS and photoelectron spectroscopy and concluded that the water dissociation occur due to the electron beam of HREELS, however, it is not consistent with the results by Chabal et. al. [4], and can be denied.

Figure 1 shows the photoelectron spectroscopy of the Si(100) surface, which was cleaned by the resistive heating, exposed to 5L of water at the room temperature. Measurements were made by the SGM-TRAIN monochromator and Omicron EA-125HR analyzer installed at the BL5A of UVSOR. The photon energy was 52 eV, and the total resolution including photons and electrons was about 0.15eV. The angle of the incident photon and the detection of the electron was 45° and 0° from the surface normal. Energy positions (shifted by 2.2 eV to cancel the reference level difference) of peaks observed in the photoelectron spectrum of gaseous water and their assignments are also shown together with energy positions of calculated DOS (density of states) for the Si-OH and Si-H surface species. In the assignments of the calculation, "2σ" and "3σ" indicate the MOs (molecular orbital) of mainly the O-H bond, "O-σ" indicates the MO of mainly the Si-O bond, "O-π" indicates the lone pair of the O atom, and "H" indicates the MO of the Si-H bond. The calculation for upper one was made by Ciraci et.al.[5], and the lower one was made by Katircioglu [7]. Obviously, the calculations seems not to be agreement not only each other but also with the experimental results even if they are shifted by a constant energy to compensate the uncertainty of energy reference, and the interpretation can not be made by comparison to the calculation. Previously, Ciraci et. al. [5]. and Oellig et. al. [8]. made an assignments as the peak B to "H" and C

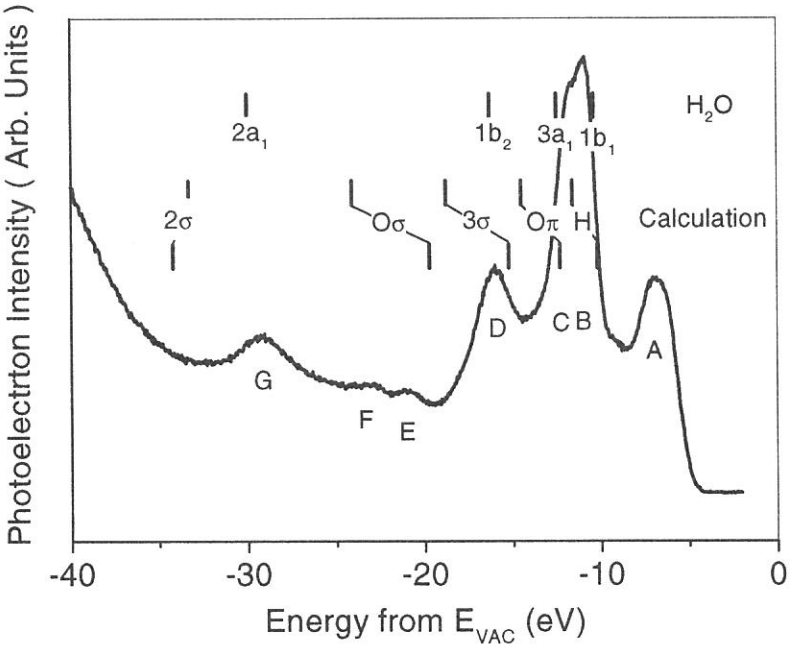

Figure 1

to "O-π". However, Schmeisser claimed that, based upon the comparison with their photoelectron spectroscopic study of the Si surface exposed to the atomic hydrogen, the peak B could not be ascribed to the Si-H species because the intensity was too high, and because the decrease taken at the higher photon energies, which was observed for the Si-H system, was not observed. It seems that the emission due to the Si-H species may be hidden in the peak A. Larsson et.al.[9] assigned both of the peaks B and C to "O-σ", which was divided to two components because the Si-O bond axis is tilted from the surface normal. However, their assignment does not agree the experimental results below, and can be denied.

We measured the photon energy dependence of the photoelectron spectra in order to get an information of the origin of the peaks in the spectrum (figure 2). The intensities of peak C (indicated in fig.1) are obviously changed depending upon photon energies. The intensity of the peak C is smaller than that of the peak B in the spectrum taken at hν=52 eV, however, it is larger taken at around 27 eV. According to the spectrum taken by the use of the He-discharge lamp, the peak C is smaller, again, taken at hν=22eV. Thus, it seems that the peak C resonantly enhances in intensity for the photon energy of around 30 eV, and that the origin of the peaks B and C are of different characters, which is inconsistent with the assignments by Larsson et.al. The resonance enhancement of the photoelectron peaks at photon energy of around 30 eV was observed for the "4σ" photoelectron peak of the carbon monoxide chemisorbed on metal surfaces [10]. It is ascribed to the "σ resonance", that is the enhancement of the photoelectron emission intensity of the molecular orbital with σ symmetry when the excitation energy corresponds to the transition to the σ* quasi-bound state. In the spectrum of the OH on the Si(100) surface, similar resonance may be expected, and the peak C may be interpreted to the molecular orbital with σ symmetry, thus, to "3σ" molecular orbital. Other peaks are assigned as follows. The peak B is assigned to "O-π". Based on the Schmeiser's discussion, the molecular orbital of Si-H bond is considered to be hidden in the peak A. The peak A also contain the contribution of the emission from the valence band of the Si substrate. The peaks D and G are assigned to "O-σ" and "2s", respectively. The peaks E and F have not reported until this report. The intensity is small, and may not be assigned to the single electron excitation from any particular molecular orbital, but satellite due to the multi-electron excitation and/or energy loss peaks of the peaks B-D due to the surface plasmon.

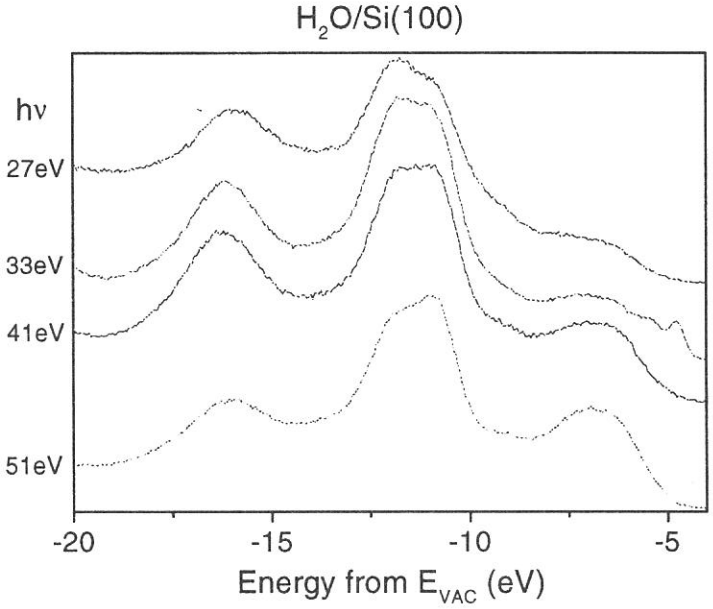

Figure 2

[1] D. Schmeisser et.al., Phys. Rev. B27, 7813(1983).
[2] H. Ibach et.al., Solid State Commun. 42, 457(1982).
[3] M. Nishijima et.al., J. Chem. Phys. 84, 6458(1986).
[4] Y. J. Chabal et.al., Phys. Rev. B29, 6974(1984).
[5] S. Ciraci et.al., Phys. Rev. B27, 5180(1983).
[6] D. Schmeisser et.al., Phys. Rev. B33, 4223 (1986).
[7] S. Katircioglu, Surf. Sci. 187, 569(1987).
[8] E. M. Oellig et.al., Solid State Commun. 51, 7(1984).
[9] C. U. S. Larsson et.al., Vacuum 42, 297(1991).
[10] F. Greuter et.al., Phys. Rev. B27, 7117(1983).

(BL5B)

Photon stimulated desorption of excited dimer from the surface of solid Ne by exciton creation

T. Hirayama*, T. Adachi, A. Hayama, I. Arakawa, K. Mitsuke[A] and M. Sakurai[A]

Department of Physics, Gakushuin University, 1-5-1 Mejiro, Toshimaku, Tokyo 171-8588
[A]*Institute for Molecular Science, Myodaiji, Okazaki 444-8585*

We have been studying the desorption of excited particles from the surface of rare gas solids (RGSs) induced by exciton creation using photon- and electron- stimulated desorption (PSD and ESD) techniques.[1-3] As to the excited atom desorption, two mechanisms, excimer dissociation (ED) and cavity ejection (CE), have been proposed[4] and confirmed experimentally. ED process is similar to the dissociation of an excited dimer (excimer) in the gas phase, i.e., the energetic fragment desorbs from the surface by the dissociation of a molecular-type exciton. Negative electron affinity of the matrix is known to be essential for the CE process to have a repulsive interaction between the excited atom and the surrounding ground state atoms, so that desorbed atoms via the CE mechanism are essentially in excited states. The desorption via CE mechanism can be observed only for solid Ne and Ar, but not for solid Kr and Xe because of their positive electron affinities in the bulk, while ED process is known to occurs for all rare gas solids.

Desorption of an excimer from the surface of RGSs has been predicted theoretically for solid Ne[5], Ar[6], and Kr[7], but the experimental evidence has been obtained only for solid Ar[8]. We have previously observed the emission from the desorbed particles with long lifetime from the surface of solid Ne, which was thought to be closely related to Ne_2^* desorption[9]. In order to confirm the desorption of Ne_2^*, we have measured the spatial distribution of the emitted VUV photons from the desorbed particles initiated by the creation of the surface and bulk excitons.

Experiments have been done at the beam line BL5B in UVSOR. The experimental setup is schematically shown in fig.1, which is similar to the one used in our previous work[3] equipped with a pin hole camera in order to observe the spatial distribution of the emitted light. Briefly, the sample substrate is a Pt(111) attached to the head of a rotatable liquid He cryostat installed in an UHV chamber (base pressure $< 10^{-8}$ Pa). The pin hole camera consists of a MCP with 75mm in diameter, two dimensional position sensitive detector, and a pin hole with 5mm in diameter. The distance between the sample and the pin hole is 90mm and the magnification is unity.

Figure 2 shows a typical image of the spatial distribution of the emitted VUV light from the desorbed excited particles measured at the excitation energy of the 1st order bulk exciton (B1, 70.7nm). Photons emitted from the sample are not detected because of a special geometry of the

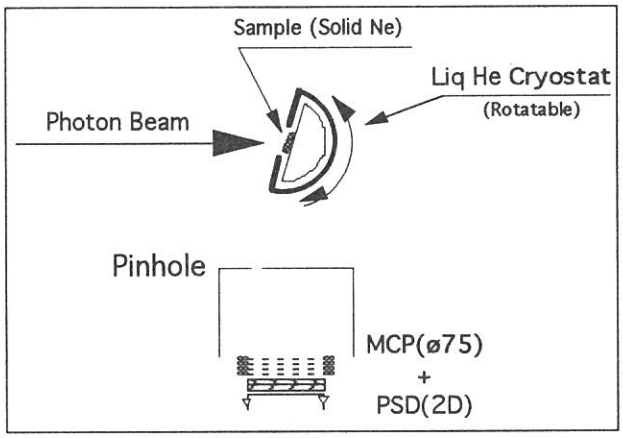

Fig.1. Schematic view of the experimental setup.

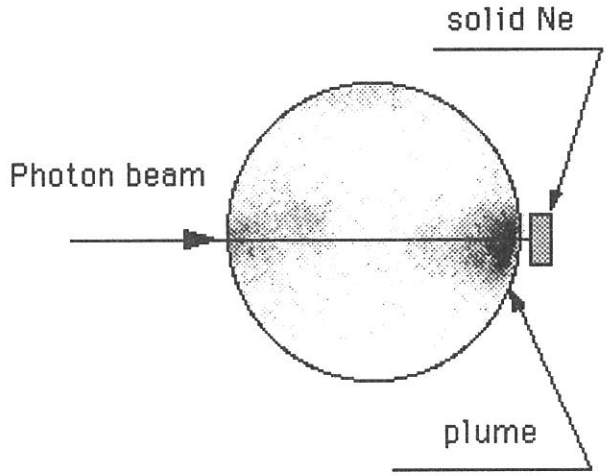

Fig.2. Typical two dimensional image of the spatial distribution of the VUV emission from the desorbed particles from the surface of solid Ne at the excitation of the 1st order bulk exciton (B1, 70.7nm).

* Fax: 03-3987-6732, e-mail: takato.hirayama@gakushuin.ac.jp

experimental setup where the pin hole camera can not directly see the sample surface. The plume, which is observed just in front of the sample surface, is due to the photons emitted from the desorbed particles, and the others are the background signals mainly due to the photons reflected by the chamber wall. From the size of the plume (~15mm) and assuming that the desorbed particle is an excimer with the kinetic energy of 0.23eV which is a calculated result by Chen et al.[5], the radiative lifetime of the desorbed particle is estimated to be about 10μsec. Considering that this value is consistent with the radiative lifetime of the excimer, $Ne_2^*(^3\Sigma_u)$, in the gas phase (11.9μsec)[10], and that the radiative lifetimes of the atomic excited states ($2p^53s$) in the gas phase are in the order of 10^{-9}sec for optically allowed states ($^3P_1$, $^1P_1$), and longer than 10sec for optically forbidden states ($^3P_{0,2}$), we conclude that the plume is due to VUV emissions from the excimer desorbed from the surface of solid Ne. We have done the ESD experiment in Gakushuin University using a similar experimental setup in order to take the decay spectra of the plume intensity, which was not possible in PSD experiment because of very low signal intensity. By using a pulsed electron beam (pulse width ~1μsec, 10kHz repetition) we have obtained time spectra of the plume intensity (not shown). The radiative lifetime measured by the ESD experiment is found to be the same as PSD experiment within an experimental uncertainty.

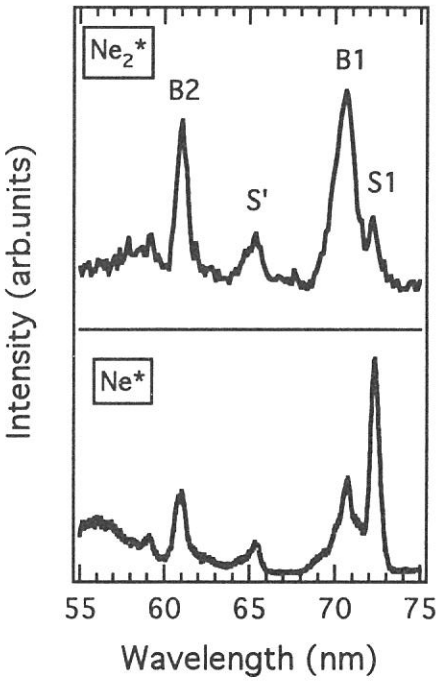

Fig.3. Desorption yield of Ne_2^* and Ne* as a function of wavelength of incident light. Assignments of the surface (S1, S') and bulk (B1, B2) excitons are shown.

Figure 3 shows the plume intensity, i.e., the desorption yield of $Ne_2^*(^3\Sigma_u)$, as a function of wavelength of the incident light together with the result for Ne* desorption[1] from the surface of solid Ne. The spectra show that the excimer desorption is also stimulated by the exciton creation on the surface and in the bulk as in the case of excited atom desorption. The main difference in the excimer desorption compared to the atomic desorption is the decrease of the relative intensity of the 1st order surface exciton (S1, 72.3nm). This can be due to the less number of the nearest neighbor atoms on the surface compared to the bulk, and the efficient desorption of excited atoms on the surface, both of which result in the decrease of the efficiency of the excimer formation on the surface. It is interesting to note that the relative intensity of $2p^53p$-type surface exciton (S', 65.4nm) remains almost constant compared to those of bulk intensities. We do not have a clear explanation for this result at present. Further PSD and ESD experiments are in progress.

References.

[1] T. Hirayama, A. Hayama, T. Koike, T. Kuninobu, I. Arakawa, K. Mitsuke, M. Sakurai and E. V. Savchenko, Surf. Sci. **390**, (1997) 266.
[2] T. Hirayama, T. Nagai, M. Abo, I. Arakawa, K. Mitsuke and M. Sakurai, J. Electr. Spectr. Rel. Phen. **80**, (1996) 101.
[3] I. Arakawa, D. E. Weibel, T. Nagai, M. Abo, T. Hirayama, M. Kanno, K. Mitsuke and M. Sakurai, Nucl. Instrum. Meth. Phys. Res. B**101**, (1995) 195.
[4] T. Kloiber and G. Zimmerer, Radiat. Eff. Def. Solids **109**, (1989) 219.
[5] L. F. Chen, G. Q. Huang and K. S. Song, Nucl. Instrum. Meth. Phys. Res. B **116**, (1996) 61.
[6] S. T. Cui, R. E. Johnson, C. T. Reimann and J. W. Boring, Phys. Rev. B **39**, (1989) 12345.
[7] W. T. Buller and R. E. Johnson, Phys. Rev. B **43** (1991) 6118.
[8] C. T. Reimann, W. L. Brown, D. E. Grosjean and M. J. Nowakowski, Phys. Rev. B **45** (1992) 43.
[9] E. V. Savchenko, T. Hirayama, A. Hayama, T. Koike, T. Kuninobu, I. Arakawa, K. Mitsuke and M. Sakurai, Surf. Sci. **390**, (1997) 261.
[10] B. Schneider and J. H. Cohen, J. Chem. Phys. **61**, (1974) 3240.

(BL6A2) The interaction of Diamond (100) surface with gas particles

N. Takagi, T. Kubo, M. Z. Hossain, S. Hasegawa, T. Aruga and M. Nishijima,

Department of Chemistry, Graduate School of Science, Kyoto University, Kyoto 606

Diamond is promising as an electronic-device material superior to Si or GaAs owing to intrinsic properties such as the large band gap, high saturation carrier velocity and high thermal conductivity. The recent development in the epitaxial growth methods of diamond promotes a number of researches from both fundamental and technological points of view. One of the most important themes is the microscopic understanding of the epitaxial growth mechanism. Although several models are proposed, as far as we know, clear solution for this problem has not been given. It is important to understand the chemical reactivity of the diamond surfaces in order to answer this. From the technological points of view, diamond is a suitable candidate for a negative electron affinity (NEA) device, since its large band gap of $\sim$ 5.5 eV makes the conduction band minimum lie close to the vacuum level. It is well known that the adsorption of alkali metal atoms on solid surfaces induce marked decrease of the work function. In that point of view, the alkali-adsorbed diamond surfaces have a potential to be used as NEA devices.

We have investigated the electronic states of C(100)(2x1)-H and C(100)(2x1), the adsorption of CO on C(100)(2x1) and the adsorption of alkali metals (K and Cs) on C(100)(1x1)+streak. In this report, we present these results.

The B-doped diamond films were grown epitaxially, by using the microwave plasma-assisted chemical vapor deposition (CVD) method, on the (100) surface of synthesized single-crystalline diamond (Ib type). The growth condition is described in ref. [1].The size of the surface was 4x4x0.3mm^3. The CVD-grown diamond surface was H-terminated, and hence the clean surface was obtained by heating the sample up to 1400 K. The clean surface shows the sharp (2x1) low energy electron diffraction (LEED) pattern. The (2x1)-H surface was prepared by exposure of the sample to H atoms produced by a hot W filament ($\sim$1800 K).

The normal emission spectra of the C(100)(2x1)-H surface were measured with the incident photon energy, hv, of 30-70 eV. Peaks at -1.2 and -4.0 eV relative to Fermi level were observed for hv = 40 eV. The peak positions depend on hv reflecting dispersion, and hence these are related to bulk states. After the sample was heated up to 1400 K and H adatoms were fully removed, normal emission spectra of the clean C(100)(2x1) surface were measured (hv = 35-50 eV). For hv = 50eV, a peak related to surface states is observed at -1.8eV. This peak is overlapped with the bulk emission and is not separately observed for hv = 35-40 eV. When the clean surface was exposed to atomic H, the intensity of the peak at -1.8 eV is gradually decreased and finally is disappeared for the (2x1)-H surface. Therefore, this peak is associated with the dangling bond π surface state. The angular resolved spectra of C(100)(2x1) were also measured with hv = 50 eV and the incidence angle of 45 degrees from the surface normal. The dangling bond π surface state shows little dispersion. These results are in good agreement with the results of Graupner et al. [2] for a natural type II-b diamond (100) surface.

When the clean surface was exposed to 1000 L (1L = 1x10^{-6} Torr s) CO at 180 K, normal emission spectra for CO-exposed surface were measured with hv = 35-50 eV. The difference spectra between those for the clean and CO-exposed surfaces were analyzed in detail, but no evidence of CO adsorption on the C(100)(2x1) surface was obtained. The interaction of the other gas molecules (O_2, C_2H_2, N_2O) with C(100)(2x1) has been studied

(experiments were carried out at Kyoto University), but the C(100)(2x1) surface is not reacted with these gas molecules. The chemical reactivity of the C(100)(2x1) surface is very low.

The adsorption of K and Cs on the C(100)(1x1)+streak surface has been studied at room temperature. The work function change ($\Delta\phi$) has been measured by the threshold of the secondary electron as a function of the coverage of alkali atom which is determined by the area intensity of the K 3p and Cs 4d emission. $\Delta\phi$ of -3.0 and -3.3eV are obtained for K and Cs, respectively. The work function change of semiconductor surfaces is generally composed of the adsorbate-induced changes in both band bending and electron affinity. The band bending was not observed for K- and Cs-covered surface and the vacuum level lies close to the conduction minimum for the C(100)(2x1) surface (The electron affinity of the C(100)(2x1) surface is estimated to be 0.8 [3]) , and hence the electron affinity of alkali-covered diamond surfaces is negative.

This work was supported in part by Grants-in-Aid from the Ministry of Education, Science, Sports and Culture, and Sumitomo Electric Industries, Ltd.

Reference

[1] T. Tsuno, T, Imai, Y. Nishibayashi, K. Hamada and N. Fujimori, Jpn. J. Appl. Phys. 30 (1991) 1063.
[2] R. Graupner, M. Hollering, A. Ziegler, J. Ristein, L. Ley and A. Stampfl, Phys. Rev. B55 (1997) 10841.
[3] Z. Chang, M. Wensell and J. Bernholc, Phys, Rev. B51 (1995) 5291.

(BL6A2,BL2B1)

SRPES study on surface core-level shift for GaP(001)-(2×4)

N. Sanada, S. Mochizuki, M. Shimomura, Y. Suzuki, G. Kaneda, T. Takeuchi, N. Utsumi, and Y. Fukuda

Res. Inst. Electronics, Shizuoka University, Hamamatsu 432-8061, Japan.

The surface structure of III-V semiconductors is of interest because it affects the electric properties of III-V semiconductor devices. It is well known that III-group metal-stabilized (001) surfaces of GaAs, InAs, and InSb show a (4×2) or c(8×2) reconstruction with 4× periodicity in the [1$\bar{1}$0] direction[1]. The surface structure has three Ga-(or In-) dimers with a missing dimer in a (4×2) unit cell, obeying electron counting model concept[2]. On the other hand, it is recently suggested by ion scattering measurements that Ar ion bombardment and annealing (IBA) treatments of a GaP (001) surface result in a Ga-stabilized (2×4) reconstruction with 4× periodicity along the [110] direction[3]. The X-ray photoelectron diffraction and STM results also support the above structure[4]. The surface structure of the Ga-stabilized GaP(001)-(2x4) surface is not understood yet in detail. In this study, we present for the first time the surface core-level shift of the Ga 3*d* line for the GaP(001) surface, and discuss the surface structure of GaP(001)-(2×4).

The clean n-GaP(001) surface was obtained by Ar ion bombardment(500V) and annealing at 450°C under 3×10^{-8} Pa. Low energy electron diffraction (LEED) shows (2×4) spots. Photoemission spectra were obtained with a hemispherical energy analyzer. A photon energy of 67 eV was used to enhance the surface sensitivity in the SRPES study.

Figure 1 shows Ga 3*d* SRPES spectra collected from the clean GaP(001)-(2×4) surface at θ=0°, 60°, and 80° along the [110] direction. The spectra can be fitted by three spin-orbit doublet components. The components having a lower binding energy by 0.5 eV and a higher binding energy by 0.4 eV than that of bulk are found. The intensity of the former increases as increases in θ and that of the latter keeps almost constant. On the basis of the energy shift and polar angle dependence of these components, the former peak would originate from topmost surface gallium atoms bonded to other gallium atom. The latter peak is suggested to be due to the gallium atoms with a dangling bond near the surface. The previous model for GaP[2] can not explain both the results of the surface core-level shift and STM observation[4,5]. The new model will be presented on the basis of the result of the surface core-level shift and STM.

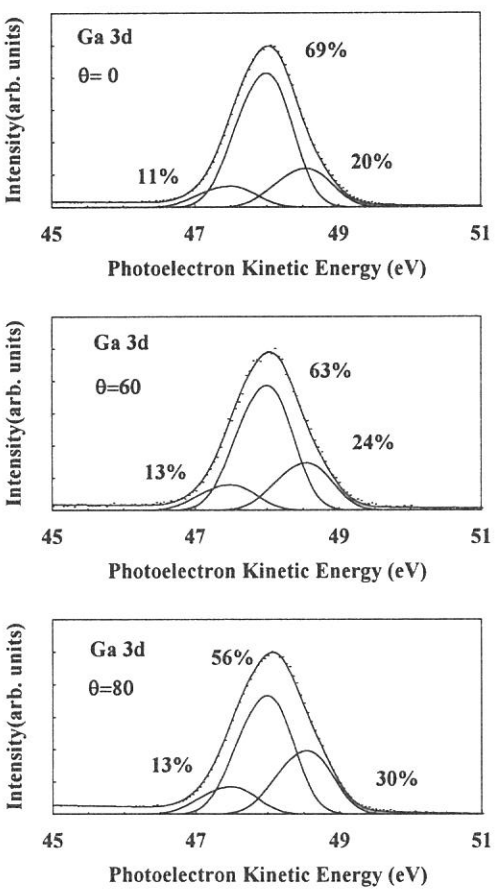

Fig. 1. Ga 3*d* photoemission data acquired at 0°, 60°, and 80°. The three best-fit spin-orbit doublets are shown with solid lines.

References

[1] P.R.Varekamp, et al., Surf. Sci., **350** L221 (1996).
[2] M.D.Pashley, Phys. Rev. B **47**, 10481 (1989).
[3] M.M.Sung and J.W.Ravalais, Surf. Sci., **365**, 136 (1996).
[4] in preparation.
[5] N. Sanada, et al., Appl. Phys. Lett., **67**, 1432 (1995).

List of Publications

LIST OF PUBLICATIONS (1997)

O. Akaki, A. Chainani, T. Yokoya, H. Fujisawa, T. Takahashi and M. Onoda
Unconventional Spectral Changes Acrocc the Metal-insulator Transition in $CeTiO_{3+\delta}$
Phys. Rev., **B56** (1997) 12050.

I. Akimoto, K. Kan'no, M. Shirai, F. Okino,H. Touhara, M. Kamada and V. G. Stankevitch
Photoluminescence from Fluorinated Fullerene $C_{60}Fx(x\leq 48)$thin Films
J. Luminescence, **72-74** (1997) 503.

M. Fujimaki, Y. Ohki and H. Nishikawa
Energy States of Ge-doped SiO_2 Glass Estimated Through Absorption and Potoluminescence
J. Appl. Phys., **81** (1997) 1042.

E. Feldbach, M. Kamada, M. Kirm, A. Lushchik, Ch. Lushchik, and I. Martinson
Direct Excitation of Tl+ impurity Ions by Hot Photoelectrons in Wide-gap Crystals
Phys. Rev., **B56** (1997) 13908.

T. Gejo, K. Okada and T. Ibuki
Photoabsorption Spectrum of Ozone in the K-edge Region
Chem. Phys. Let., **277** (1997) 497.

Q.Guo, M. Ikejira, M. Nishio and H. Ogawa
Optical Properties of Zinc Telluride in Vacuum Ultraviolet Region
Solid State Comm., **100** (1996) 813.

Q. Guo, H. Ogawa and A. Yoshida
Optical Properties of Indium Nitride in Vacuum Ultraviolet Region
J. Electron Spectrosc. Relat. Phenom., **79** (1996) 9.

Q. Guo, M. Nishio, H. Ogawa and A. Yoshida
Optical Properties of Aluminum Nitride
Phys. Rev., **B55** (1997) R15987.

H. Hama, K. Kimura, M. Hosaka J. Yamazaki and T. Kinoshita
Testing for Qualification of a Helical Optical Klystron for UV Storage-ring Free Electron Lasers
Nucl. Instr. and Meth., A **393** (1997) 23.

H. Hattori, Y. Hikosaka, T. Hikida and K. Mitsuke
Tow-dimensional Photoelectron Spectroscopy of Acetylene: Rydberg-valence Interaction between the $(3\sigma_g)^1(3p\sigma_u)^1$and $(3\sigma_g)^1(3\sigma_u)^1$ States
J. Chem. Phys., **106** (1997) 4902.

Y. Hikosaka, H. Hattori, T. Hikida and K. Mitsuke
Superexcited States of OCS Probed by Using Photoelectron Spectroscopy for Autoionizing Atomic Sulfur
J. Chem. Phya., **107** (1997) 2950.

M. Hosaka, H. Hama, K. Kimura, J. Yamazaki and T. Kinoshita
Observation of Intracavity Compton Backscattering of the UVSOR Free Electron Laser
Nucl. Instr. and Meth., A **393** (1997) 525.

T. Ibuki, M. Kono, Y. Asari, A. Hiraya and K. Shobatake
Photoabsorption and Fluorescence Cross Sections of $SiCl_4$ in the Region of 6.2-31eV
J. Chem. Phys., **106** (1997) 4853.

R. Inanami, T. Uchida and S. Morita
Si Wafer Etching with Synchroton Radiation in a CF_4 Gas Atmosphere
J. Electrochem. Soc., **143** (1996) 3754.

R. Inanami, T. Yamada, S. Ohsaki, S. Ogawa and S. Morita
50 nm Pattern Etching of Si Wafer by Synchrotron Radiation Excited CF_4 Plasma
Jpn, J. Appl. Phys. **36** (1997) 7706.

T. Ishii, R. Sekine, T. Enoki, E. Miyazaki, T. Miyamae and T. Miyazaki
DV-Xα Calculation and Ultraviolet Photoelectron Spectra of Gold Trichloride-Graphite Intercalation Compound ($AuCl_3$-GIC)
J. Phys. Soc. Jpn., **66** (1997) 3424.

K. Ishii, A. Takami and Y. Ohki
Effects of Fluorine Addition on the Structure and Optical Properties of SiO_2 Films Formed by Plasma-enhanced Chemical Vapor Deposition
J. Appl. Phys., **81** (1997) 1470.

M. Itoh, M. Kamada, and N. Ohno
Temperature Dependence of Auger-Free Luminescence in Akai and Alkaline-Earth Halides
J. Phys. Soc. Jpn., **66** (1997) 2502.

M. Itoh, K. Sawada, H. Hara, N. Ohno, and M. Kamada
Phonon Broadening of Line Widths of Auger-free Luminescence in Wide-gap Ionic Crystals
J. Luminescence, **72** (1997) 762.

M. H. Jung, Y. S. Kwon T. Kinoshita and S. Kimura
Optical Properties of $LaTe_2$ and $CeTe_2$
Physca B, **230-232** (1997) 151.

M. Kamada and S. Hirose
Laser-induced Fluorescence Study of Fast Desorption of Ground-State K Atoms from Potassium Halides Excited by Synchrotron Radiation
Surface Sci., **390** (1997) 194.

K. Kanda
Photodissociation Spectroscopy of ICN in the Vacuum Ultraviolet Region
Chem. Phys., **218** (1997) 199.

K. Kan'no
Fluorinated Fullerenes - Optical Spectra and Photo-Desorption
Materials Science Forum, **239-241** (1997) 197.

K. Kan'no, T. Matsumoto and Y. Kayanuma
Parity-broken and -unbroken Self-trapped Excitons in Alkali Halides
Pure & Appl. Chem., **69** (1997) 1227.

K. Kimura, S. Takano, J. Yamazaki, T. Kinoshita, M. Hosaka and H. Hama
Demonstration and Consideration for UV Free-electron Laser Oscillation around 270 nm
Nucl. Instr. and Meth., A **393** (1997) 28.

S. Kimura, Y. S. Kwon and T. Suzuki
Mixed Valence of Yb_3S_4
Physica, **B 230-232** (1997) 301.

S. Kimura, A. Ochiai and T. Suzuki
Low Energy Excitation of Yb_4As_3
Physica, **B 230-232** (1997) 705.

N. Kitamura, K. Fukumi, H. Mizoguchi, M. Makihara, A. Higuchi and N. Ohno
Structure of Densified Lithium Silicate Glasses
The Review of High Pressure Science and Technology, **7** (1998) in press.

H. Kumagai, K. Toyoda, K. Kabayashi, M. Obara and Y. Iimura
Titanium Oxide/aluminum Oxide Multilayer Reflectors for "water-window" Wavelengths
Appl. Phys. Lett., **70** (1997) 2338.

K. Mase, M. Nagasono, S. Tanaka, M. Kamada, T. Urisu and Y. Murata
Development of Electron-ion Coincidence Spectroscopy for the Study of Surface Dynamics Combined with Synchrotron Radiaton
Rev. Sci. Instrum., **68** (1997) 1703.

K. Mase, M. Nagasono, S. Tanaka, T. Urisu and S. Nagaoka
Study of Ion Desorption Induced by Core-level Excitations of Condensed $Si(CH_3)_4$ by Using Photoelectron-photoion Coincidence Spectroscopy (PEPICO) Combined with Synchrotron Radiation
Surface Sci., **377-379** (1997) 376.

K. Mase, M. Nagasono, S. Tanaka, T. Urisu, E. Ikenaga, T. Sekitani and K. Tanaka
Study of Ion Desorption Induced by a Resonant Core-level Excitation of Condensed H_2O Using Auger Electron Photo-ion Coincidence (AEPICO) Spectroscopy Combined with Synchrotron Radiation
Surface Sci., **390** (1997) 97.

T. Masuoka
Single, Double, and Triple Photoionization of Molecules Using Synchrotron Radiation
Can. J. Phys., **74** (1996) 850.

T. Masuoka
Single- and Double-Photoionization of Sulfur Dioxide
Mem. Fac. Eng., Osaka City Univ., **38** (1997) 147.

T. Mito, S. Fujino, H. Takebe, K. Morinaga, S. Todoroki and S. Sakaguchi
Refractive Index and Material Dispersions of Multi-component Oxide Glasses
J. Non-Crystalline Solids, **210** (1997) 155.

M. Mizutani, M. Tokeshi, A. Hiraya and K. Mitsuke
Development of a Tunable UV Laser System Synchronizing Precisely with Synchrotron Radiation Pulses from UVSOR
J. Synchrotron Rad., **4** (1997) 6.

T. Miyazaki, T. Doi, T. Miyamae and I. Matsuura
Structure and Catalysis of $Li_xNi_{2-x}O_2$ Oxide Systems for Oxidative Coupling of Methane
Proc. 3rd World Congress on Oxidation Catalysis, (San Diego, 1997) p245.

S. Nagaoka, K. Mase, M. Nagasono, S. Tanaka, T. Urisu and J. Ohshita
Site-specific Fragmentation Following Si:2p Core-level Photoionization of $F_3SiCH_2CH_2Si(CH_3)_3$ Condensed on a Au Surface
J. Chem. Phys., **107** (1997) 10751.

M. Nagasono, K. Mase, S. Tanaka and T. Urisu
Auger-final-state Selected Ion Desorption Study of Condensed NH_3 and ND_3 by Using Auger Electron-photoion Coincidence Spectroscopy
Surface Sci., **377-379** (1997) 380.

M. Nagasono, K. Mase, S. Tanaka and T. Urisu
Study of Ion Desorption Induced by a Resonant Core-level Excitation of Condensed NH3 by Using Auger-electron Photo-ion Coincidence (AEPICO) Spectroscopy Combined with Synchrotron Radiation
Surface Sci., **390** (1997) 102.

S. Nagata, H. Hara, T. Sakao, T. Shimizu, S. Tsuneta, T. Yoshida, W. Ishiyama, K. Murakami and T. Oshino
Development of the Multilayer Mirrors for XUV Doppler Telescope
Proc. SPIE, **3113**, in press

T. Nanba, Y. Nodake, M. Muneyasu, G. P. Williams and S. Hayashi
Size-Dependence of Phase Transition of CdS Microcrystals
J. Phys. Soc. Jpn., **66** (1997) 1526.

T. Nanba and M. Ikezawa
Far-Infrared Interferometry by Using Synchrotron Radiation
Chapter 3 in 「 Principles and Applications of Polarization-Division Interferometry」

K. Ozawa, T. Iwasaki, K. Edamoto, S. Tanaka and S. Otani
Na Adsorption Process on a ZrC(100) Surface
Applied Surface Science, **121/122** (1997) 142.

R. Pittini, M. Ikezawa, A. Ochiai, H. Aoki and T. Suzuki
Yb_4As_3 and $Yb_4(As_{0.71}Sb_{0.29})_3$, two ways to heavy fermion character
J. Magn. Magn. Mat. 177-181 (1998), contributed to ICM'97
(Cairns, Australia)

R. Pittini, M. Ikezawa, A. Ochiai, and T. Suzuki
Correlation effects in $Yb_4(As_{0.88}Sb_{0.12})_3$ and $Yb_4(As_{0.71}Sb_{0.29})_3$
Physica B (1998), contributed to RHMF'97 (Sydney, Australia)

T. Sekitani, E. Ikenaga, K. Tanaka, K. Mase, M. Nagasono, S. Tanaka and T. Urisu
Auger-electron-ion Coincidence Study of Photon-stimulated Ion Desorption for Condensed Acetonitrile
Surface Sci., **390** (1997) 107.

K. Shimizu, M. Takamatsu, K. Nishi, H. Yoshida, A. Satsuma and T. Hattori
Influence of Local Structure on the Catalytic Activity of Gallium Oxide for the Selective Reduction of NO by CH_4
Chem.Commun., (1996) 1827.

C. Sugiura, A. Kamata, T. Kashiwakura, H. Tezuka, K. Suzuki and S. Nakai
Phosphorus K-Edge X-Ray Absorption Spectra of $Ca_3(PO_4)_2$, $CaHPO_4 \cdot 2H_2O$, $Ca(H_2PO_4)_2 \cdot H_2O$ and $Ca(H_2PO_2)_2$
J. Phys. Soc. Jpn., **66** (1997) 274.

Y. Tamenori and I. Koyano
Dissociative Photoionization of Iron Pentacarbonyl in the Range 38-120 eV
J. Phys. Chem. A, **120** (1998) 368.

S. Tanaka, K. Mase, M. Nagasono and M. Kamada
Desorption of H Ions from Water Chemisorbed on Si(100) by O 1s Excitation - an Auger Electron-photoion Coincidence Spectroscopy Study
Surface Sci., **390** (1997) 204.

N. Takahashi, S. Tanaka, M. Ichikawa, Y. Q. Cai and M. Kamada
Photoelectron Spectroscopic Study of Coadsorbed States of Cs and O on GaAs(100)
J. Phys. Soc. Jpn., **66** (1997) 2798.

I. Tokue and T. Ibuki
Photoabsorption Cross Sections and Radiative Processes of $SnCl_4$ and $Sn(CH_3)_4$ in the 6-31 eV Region
Chem. Phys. Lett., **273** (1997) 247.

T. Urisu, T. Ibuki, Y. Imaizumi and M. Kawasaki
Potential of Site Specific Photochemical Processing Using Synchrotron Radiation
Nucl. Instr. and Meth. in Phys. Res., **B122** (1997) 364.

H. Yoshida, T. Yoshida, T. Tanaka, T. Funabiki, S. Yoshida, T. Abe, K. Kimura, T. Hattori
Mg K-Edge XAFS Study of Silica-Magnesia Systems
J. Phys. IV France, **7** (1997), C2-911.

H. Yoshida, T. Tanaka, M. Yamamoto, T. Yoshida, T. Funabiki and S. Yoshida
Epoxidation of Propene by Gaseous Oxygen over Silica and Mg-Loaded Silica under Photoirradiation
J. Catal., **171** (1997) 351.

Y. Takata, M. Nakamura and N. Kosugi
Ni L-Edge Absorption Structure of $K_2Ni(CN)_4$ Ionic Solid Investigated with Resonant Photoelectron Spectroscopy
J. Phys. IV France, C2 (1997) 489.

K.S. Seol, T. Karasawa, H. Koike, Y. Ohki and M. Tachimori
Effect of Post-Oxidation on the Oxygen Deficiency of Buried Oxides
Mat. Res. Soc. Symp. Proc. Vol.446 (1997) 219.

M. Ishii, S. Iwai, H. Kawata, T. Ueki and Y. Aoyagi
Atomic layer epitaxy of AlP and its application to X-ray multilayer mirror
J. Crystal Growth, 180 (1997) 15.

(Japanese)

H. Kumagai
Recent Progress in Soft-X-Ray Multilayer Mirrors though Atomic Layer Deposition/Epitaxy Methods
Laser Review, **25** (1997) 355

K. Mase, M.Nagasono, S.Tanaka and S. Nagaoka
Study of Ion Desorption Induced by Core-Electron Excitations of Molecules on Surface by Using Electron Ion Coincidence Spectroscopy
Journal of the Japanese Society for Synchrotron Radiation Research, **10** (1997) 375.

K. Mitsuke and M. Mizutani
Synchrotron Radiation-Laser Combination Studies of Molecular Ionization and Dissociation
Journal of the Japanese Society for Synchrotron Radiation Research, **10** (1997) 463.

Y.Ohki, K. Ishii, K.S. Seol and H. Nishikawa
A New Detection Method of Point Defects in Silicon Dioxide Thin Films
Trans. IEE of Japan, **116-A** (1996) 387.

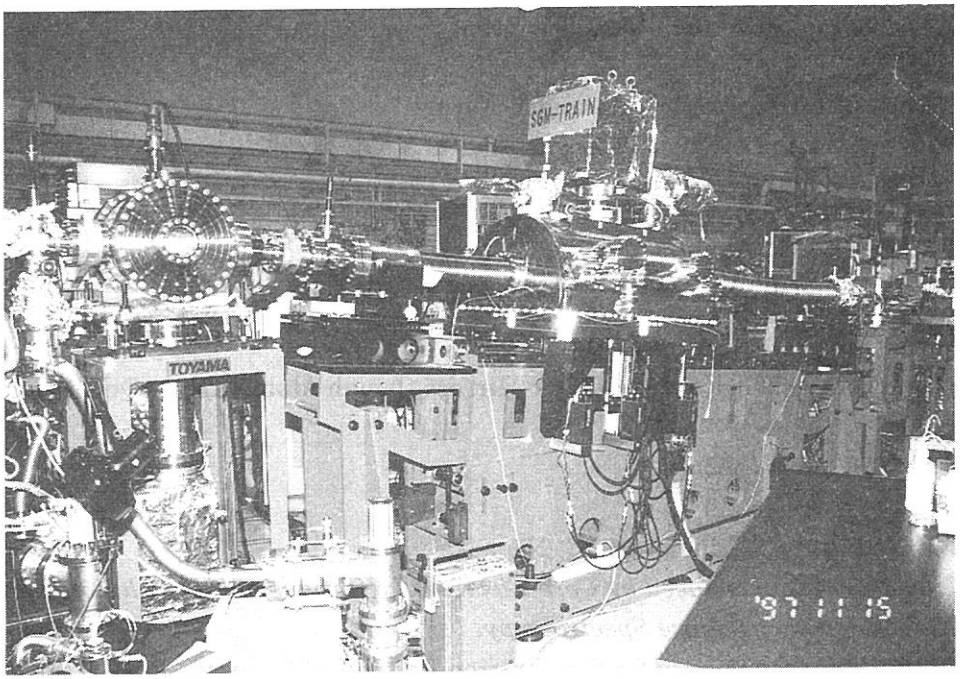

SGM-TRAIN Monochromator at BL5A

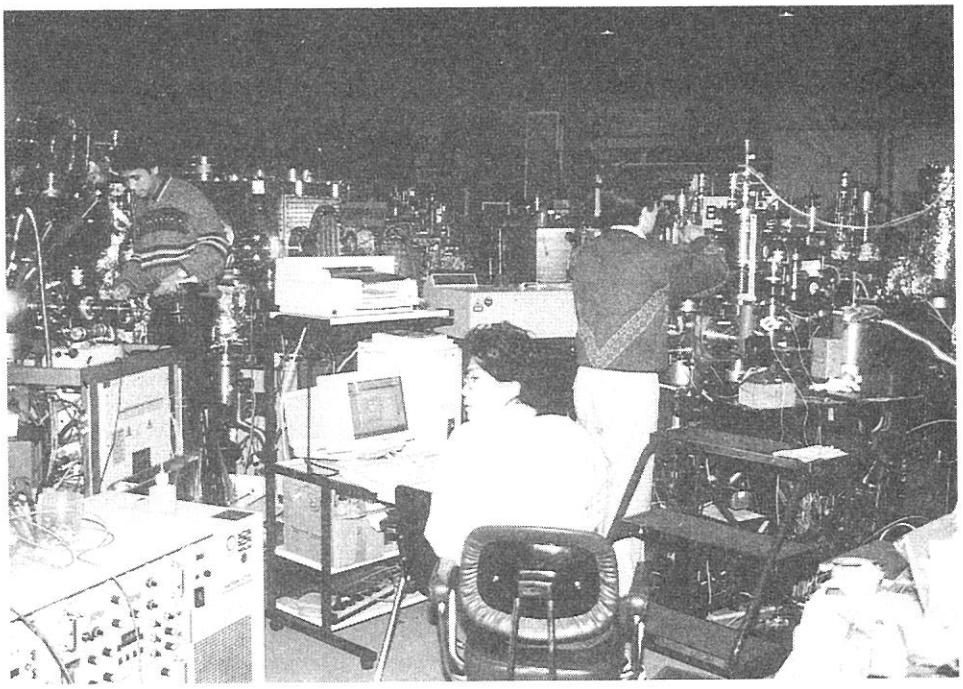

Men at work(BL5B and BL6A1)

Workshop

UVSOR Workshop IV
----Designs and applications of grazing incidence monochromators---

February 23 and 24, 1998
Okazaki Conference Center, Conference Room B
Okazaki National Research Institutes

Feb. 23 (Mon.)

Chairman: E. Ishiguro (Univ. Ryukyus)

1. 13：30-13：50
   " Opening remark---Present Status of the UVSOR" T. Kinoshita (IMS)
2. 13：50-14：25
   " Optical design of soft X-ray grazing incidence monochromator" M. Fujisawa (ISSP)
3. 14：25-15：00
   " Optical design of the valid-line-spacing plane-grating-grazing-incidence-monochromator (VLS-PGM) for third generation light source" M. Koike (JAERI)
4. 15：00-15：25
   " Present status of the VLS-PGM at the PF-BL-2C" M. Watanabe (KEK-PF)
5. 15：25-15：50
   " Experience of the construction and the commissioning of the VLS-PGM at the PF-BL-11A" Y. Kitajima (KEK-PF)

Coffee Break 15：50-16：00

Chairman: M. Kamada (IMS)

6. 16：00-16：25
   " Soft X-ray grating monochromator at the BL27-SPring8" E. Ishiguro (Univ. Ryukyus)
7. 16：25-16：50
   " Valid line spacing grating made by ruling engine" S. Tanaka (HITACHI Co.)
8. 16：50-17：15
   " Holographic grating for VUV-Soft X-ray (Including VLS)" Y. Harada (SHIMADZU Co.)
9. 17：15-17：40
   " Optical design of the VLS spherical grating grazing incidence monochromator " K. Ono (Univ. Tokyo)
10. 17：40-18：15
    " VUV-Soft X-ray beamlines at the third generation light source planned at Tohoku University" S. Suzuki (Tohoku Univ.)

18：15- Party

Feb. 24 (Tue)

Chairman: S. Kimura (IMS)

1. 9：05-9：30
   " VUV-Soft X-ray beamlines at the HiSOR" A. Hiraya (Hiroshima Univ.)
2. 9：30-9：50
   " An example of the grazing incidence monochromator with parabola mirrors at ELETRA" T. Kinoshita (IMS)
3. 9：50-10：20
   " Present status of the BL8B1 and design of BL4B at the UVSOR" T. Gejo (IMS)

Coffee Break 10：20-10：30

Chairman: T. Gejo (IMS)

4. 10：30-11：00
" Characteristics and activities of BL8B2 (Past , present and future)" K. Seki (Nagoya Univ.)
5. 11：00-11：30
" Recent activities at BL8B2: Problems: Scrap & build of BL8B2" N. Ueno (IMS)
6. 11：30-11：55
" Construction of a new grazing incidence monochromator at the UVSOR-BL2B2"
H. Yoshida (Hiroshima Univ.)

11:55-13:20 Lunch

Chairman: T. Kinoshita (IMS)

5. 13：20-13：50
" Present status of the SGM-TRAIN at BL5A and the PGM at BL6A2"
M. Kamada (IMS)
6. 13：50-14：20
" Activities at the UVSOR BL2B1：Coincidence spectroscopy, Surface chemistry"
S. Tanaka (IMS)
8. 14：20-14：50
" Future plan of the UVSOR" N. Kosugi (IMS)
9. 14：50-15：50
" Free discussion"
Remarks T. Harada (Tokyo Metropolitan Univ.)
H. Fujimoto (Kumamoto Univ.)

16：00 End

Appendix

Dear Professor Kosugi ,

It is just over ten years since I was last privileged to work at I.M.S. - and at UVSOR -for any substantial period of time . During the intervening period and particularly for the past four or five years . I have watched and appreciated a very significant growth in the scale and the quality of the science program supported by the UVSOR facility .

The Facilty : UVSOR now has 20 user stations (including 2 undulators and 1 superconducting wiggler) operating for periods of up to 3000 hours per year and a total user community of between 600 and 1000 scientists . This is , in itself , a very considerable achievement given the extremely small number , compared with staff numbers at synchrotron radiation user facilities elsewhere, of dedicated and extremely hardworking scientific and technical staff who support the UVSOR machine, beamlines and stations . In this context , the level of machine improvements including the unique short wavelength FEL and the characterization of the UVSOR operating modes during recent years are a worthy "Highlight" . *Future for the Facility* : These achievements of course maintain a challenge for the future since the primary objective of every facility must be to provide at all times , a functioning , reliable and predictable synchrotron radiation source . To be scientifically (and cost) effective it has to provide the maximum possible number of hours per year of photon beams with the optical properties matched to the needs of each different experiment . This is particularly important since many users travel significant distances to use the facility and now that the demand for beamtime exceeds the supply . One solution for the future would be to increase the supply of beamtime, although the total number of user stations at least , is probably already at or close to the maximum .

In order to maintain the current position and certainly to generate fresh scientific initiatives . resources of extra staff and money are needed by the UVSOR to continue the sound " scrap and build " policy which has already begun . That is , to replace older , less scientifically competitive stations and replace them with new and (usually !) more expensive ones.

Future growth should be achieved wherever feasible by support from sources *external* to I.M.S. For example outside Research Institutes or Universities , perhaps sometimes with support from researchers based in industry , could be encouraged to provide their own "private" beamlines or stations (a successful policy called PRT's and CRT's in USA and Europe respectively) . Beamlines or stations on UVSOR which are the property of outside Universities or Institutes would be an alternative way in which the level of exploitation and use of the UVSOR could be increased - and this mechanism also gives a very good signals about the competitiveness and merits of the UVSOR facility .

The Research Program: The overall scientific research output from UVSOR is extremely impressive. Over the past few years the number of reports has increased to more than 110 per year (in 1996) and the number of refereed publications has risen to around 80. The published science in 1996 showed that about one third of the overall programme was related to solid state research . The research on organic conductors , superconductors and ionic solids , together with a substantial number of publications on photoemission and exciton-luminescence studies and also work on glassy materials and catalysts often using XANES for low Z structural information are notable . Some of the work in this area, for example on angle resolved resonant photoemission has been very highly cited in the literature . Around one third of the research publications relate primarily to surface studies and the study of surface chemical reactions, surface structures , thin films , overlayers , interfaces and buried layers . This research incorporates infra-red and soft x-ray spectroscopies and also includes research on the physics and chemistry of surface processing and on photon assisted reactions at surfaces . Many of these activities have considerable relevance to future manufacturing and processing technologies and must be seen as important areas for future investment and growth . Approximately *one quarter of the UVSOR programme focuses on basic studies in the gas phase* - an area for which the work at I.M.S, has justly achieved world-wide recognition using both laser and synchrotron radiation photo-excitation. Much of this research exploits to the full the great advantage to IMS of " owning " a synchrotron radiation facility . It permits the inclusion of experimental stations of considerable complexity and gives an opportunity to conduct experiments where the timescales involved for data collection are very long . Notable work in this area includes molecular spectroscopy and the study of molecular dynamics , excitation , ionisation and fragmentation using a wide variety of angle and energy resolved methods and time of flight studies .

In this work , the links within I.M.S. between theoreticians and experimentalists help play a vital role in defining the good quality of the research programme . Wherever possible , this excellent combination of the oretical and experimental skills within I.M.S. should be further strengthened and increased beyond the Department of VUV Photochemistry to cover other areas such as magnetic materials , nano assemblies , molecules at surfaces etc..

The final group of research publications from the UVSOR facility include *the technicai and experimental developments* . This category includes machine instrumentation (eg., the helical undulator and UV FEL) , novel research instrumentation (eg. the potentially very important new combined synchrotron radiation /laser research activities) and "multi technique" research where synchrotron radiation is combined with a range of characterisation methods (such as STM and perhaps AFM, RAS etc.) . The vitality of the UVSOR facility will always depend

importantly upon the development of new techniques and equipment such as monochromators and detectors . Whenever possible , the instrumentation resources within other Centres and Departments in I.M.S. should be pooled to achieve some kind of a "critical mass " in this area , when required , in order to ensure the most rapid completion of new projects .

Genera Comments : UVSOR was built about 15 years ago to help create new fields in Molecular Science. It is now a reliable and productive Facility - of medium to large size - with a science programme which has derived largely from the excellent skills and interests of the staff of the VUV Photochemistry Department and the UVSOR facility within I. M. S. There is now an opportunity to capitalise further on this substantial long term investment by seeking wider usage within I.M.S. . Staff in almost all IMS Departments could and should be users and certainly must take the lead in stimulating new collaborations with (chemistry orientated) molecular science outside user groups . New broad objectives for example in the areas of new materials , combined laser with synchrotron radiation experiments , surface chemical reactions and thin film studies are well chosen and offer excellent and realistic targets for the medium term . I think that within UVSOR the level of activity in the area of molecular biological and biochemical spectroscopy and imaging is a little low . Outside Japan, bio-science represents - from 15% to 20% of all SR activity (~ 25% in the UK) and is predicted to rise to around 30% within 5 years or so across Europe and the USA. Much of this activity is linked to crystallographic structure studies and small angle diffraction and scattering mainly at around 12keV using high energy (> 2 GeV) storage rings but there is significant interest - and potentially growth - in the use of SXR and VUV radiation for biological spectroscopy and imaging .
In any case , the proximity on the same site as UVSOR of two world class bio-science Institutes (i.e. of N.I.B.B. and N.I.P.S.) - in addition to IMS itself , obviously offers a unique opportunity to create a good bio-molecular science program. There are many potential areas of research using VUV/SXR from UVSOR including, for example , low Z XAFS , VUV/SXR absorption, polarisation and fluorescence spectroscopies, laser/synchrotron radiation time resolved studies , radiation damage and VUV confocal and SXR biological imaging etc. . The study of wet samples in the VUV / SXR is feasible in principle and could give quite new information to the biologist , The use of far I.R. radiation and future exploitation of I.R. FELs Will probably also find many important applications in the study of wet biological samples .

The long term plan ------UVSOR 2 ?

In the long term , the proposal for any new Facility and, certainly the achievement of a successful outcome will require at least as much "political " as scientific insight. Any new Facility will have to come with an "operational and reliability guarantee"-like SPring 8, ESRF, APS etc.. In the USA and Europe at least , the days of hoping that new science might somehow emerge from an expensive and often not fully tested technology have essentially disappeared .

The Okazaki Institutes may be unique in world terms in their concentration of science expertise in the area of the molecular sciences . There are probably more opportunities now to carry out " ground breaking" molecular science using synchrotron radiation than ever before . For the past few years there has been an increasing convergence of attention on the behaviour of all systems at a molecular level .This has undoubtedly been stimulated by the great ease with which the atomic structures of exceedingly complex " molecules " (chemical or biological) can be measured by using SR for diffraction and scattering studies .
However it is also driven by the desire to understand and to manipulate large molecular assemblies to carry out new functions -for the greater benefit of mankind and no doubt also of industry . This emphasis on "molecular microscrence" has been further enhanced by the recent discovery of many new materials . The desire to fabricate new structures implies working at the interface between small molecule and solid state science . It will be crucial to understand at a theoretical and an experimental level all that science needed to underpin the electronic and communication devices likely to shape human activity in the next century. This will include Si ULSI mesoscopic single electron devices , nanoparticle based lasers , display materials , all types of quantum device ,thin layer research , lithography of all kinds , nanofabricated catalysts and no doubt many others .

In Europe and the USA , the current message to potential researchers is that the intellectual challenge to study "real" systems is at least as great as any other . Resources are a little more likely to be given to projects which are applied or strategic rather than basic (which is sometimes mistakenly equated with open ended and uncontrolled .) Inside Japan there are other (new) storage ring facilities which are capable of undertaking molecular studies but non of which has made it their exclusive objective .
There is a niche now - in world terms - for an insertion device storage ring with small source size , high fiux , primary photon range from - 6eV to 1 keV and with perhaps a superconducting magnet array to give some access to ~ 10 - 20 keV radiation) to be exploited

primarily for "Applied Molecular Science" , "Molecular Microscience" or "Molecular Materials Science" . The research agenda should include molecuiar science associated with industrial , environmental and biological fields . It would require the support ofresearchers in the fields of molecular and material science , coordination chemistry , biochemistry and applied and industrial molecular science (for example , in the areas of surface modification , thin film studies , photo processing , bonding in solids etc.). The reputation and experience of the Okazaki Institutes combined with their location in Chubu / Aichi would perhaps be a significant point in this debate . The ring could specialise on "two color " experiments and exploit to the full these new activities started at IMS . There could be some growth stimulated now in the area of materials science covering magnetism and magnetic structures , disordered systems buried interfaces etc , and perhaps in the use of SR for routine analysis . " UVSOR 2" should support all spectroscopies in VUV/SXR range and would be capable of low Z XAFS and some diffraction and scattering .

The strength of such a Facility would lie in its incorporation of interdisciplinary research efforts beyond the traditional boundaries of chemistry and biology and could include for example pharmaceutical science material science and medicine .

In conclusion , whatever the long term plans might be for the future of UVSOR and IMS , it is quite clear that the UVSOR facility is already a major player both in Japan and at world level as a source for synchrotron radiation science and technology and that it will continue remain so for a very considerable time to come .

Yours sincerely .

Ian H. Munro

(Professor Ian Munro)

September 28, 1997

Dear Professor Kosugi :

Thank you for your invitation to comment on my visit to IMS and UVSOR earlier this month (Sep 4,5, 1 997). First I would like to thank you and the members of your group for the outstanding hospitality during my brief stay. It was a real pleasure to share social as well as scientific activities. The guest house was very comfortable. From my experience working at many synchrotron radiation facilities, I can say this is a real asset to IMS and UVSOR.

During the short period I was at IMS, in addition to the discussion I had with you and your group about mutual research interests, I had very fruitful discussions with Dr. Mase and his student about their very interesting program of using Auger-ion coincidences to study mechanisms of ion desorption from surfaces. As you know this is an area where my group hopes to get involved in the near future so it was very helpful to discuss practical issues as well as see their recent results. In addition I had an interesting discussion - over a very pleasant breakfast in the facility - with Toshio Ibuki (Kyoto) concerning gas phase fragmentation of trifluoroacetonitrile. Another useful scientific exchange was with Professor Kinoshita and his group. It was good to see their photoelectron microscope and discuss mutual interests in that area.

Over all I was tremendously impressed with the number and vigour of the scientists working at UVSOR - especially since it was quite late in the evening when I was touring the beam lines. Clearly there is an exceptional cadre of dedicated and enthusiastic young scientists -both from IMS and from other institutions - using UVSOR. I was very interested in the organization of the synchrotron facility, in particular the existence of both in-house lines dedicated to a small number of experiments and mainly used by IMS staff, as well as more general beam lines with a wider range of experiments and greater outside access. The in-house lines appear to have significant advantages in terms of allowing more extensive experimentation than is typically possible on a more heavily multiplexed beam-line. The in-house lines and programs that I saw all seemed to be running very well, with adequate equipment and staffing to make proper use of the enhanced beam time access. This approach is one which the future Canadian Light source may wish to emulate.

UVSOR is a dynamic facility which is known world-wide for its exceptional contributions to applying synchrotron radiation to molecular and materials science. Ongoing development of new beam lines, end stations and new experiments, as well as planning for a new facility, are all necessary steps for UVSOR to maintain its high standing in the community of synchrotron research facilities. From my visit it is clear that these steps are all taking place. I wish you all the best in future activities at IMS and UVSOR.

Yours sincerely,

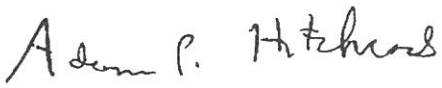

Adam P. Hitchcock
Professor of Chemistry
Brockhouse Institute for Materials Research
McMaster University
Hamilton, Ont. L8S 4Ml CANADA

ORGANIZATION

Director

Nobuhiro Kosugi	Professor	kosugi@ims.ac.jp

Light source division

Hiroyuki Hama	Associate Professor	hama@kekvax.kek.jp
Masahito Hosaka	Research associate	hosaka@ims.ac.jp
Toshio Kinoshita	Unit Chief Engineer	kinosita@ims.ac.jp
Jun-ichiro Yamazaki	Engineer	yamazaki@ims.ac.jp

Beam line division

Masao Kamada	Associate Professor	kamada@ims.ac.jp
Toyohiko Kinoshita	Associate Professor	toyohiko@ims.ac.jp
Shin-ichiro Tanaka	Research Associate	stanaka@ims.ac.jp
Shin-ichi Kimura	Research Associate	kimura@ims.ac.jp(-Mar. 98)
Tatsuo Gejo	Research Associate	gejo@ims.ac.jp
Osamu Matsudo	Section Chief Engineer	matsudo@ims.ac.jp
Masami Hasumoto	Unit Chief Engineer	hasumoto@ims.ac.jp
Eiken Nakamura	Engineer	eiken@ims.ac.jp (-May 97)
Tadanori Kondo	Engineer	kondo@ims.ac.jp
Kenji Hayashi	Engineer	h-kenji@ims.ac.jp(Jun. 97-)
Suekichi Matsuo	Supporting Engineer	matsuo@ims.ac.jp
Bunichi Kamimoto	Supporting Engineer	kamimoto@ims.ac.jp

Guest Scientists

Hitoshi Tanaka	Associate Professor	tanaka@spring8.or.jp
Michael Terekhin	Associate Professor	terekhin@ims.ac.jp (- Dec. 97)
Yuichi Haruyama	IMS fellow	haruyama@ims.ac.jp

Secretary

Hisayo Hagiwara		hagiwara@ims.ac.jp
Naoko Onitake		onitake@ims.ac.jp

Students

Krishna G. Nath		nath@ims.ac.jp
Shigeki Fujiwara	(Okayama Univ.)	fuziwara@ims.ac.jp (-Mar. 98)
Jun-ichi Murakami	(Shinshu Univ.)	murakami@ims.ac.jp(-Mar. 98)

STEERING COMMITTEE

(April 1997- March 1998)

Nobuhiro Kosugi	UVSOR IMS	Chairperson
Masao Kamada	UVSOR IMS	
Hiroyuki Hama	UVSOR IMS	
Toyohiko Kinoshita	UVSOR IMS	
Hitoshi Tanaka	UVSOR IMS (RIKEN)	
Shuji Saito	IMS	
Kyuya Yakushi	IMS	
Koichiro Mitsuke	IMS	
Toshinori Suzuki	IMS	
Toshiaki Ohta	Univ. of Tokyo	
Inosuke Koyano	Himeji Inst. of Tech.	
Makoto Waranabe	Tohoku Univ.	
Kazuhiko Seki	Nagoya Univ.	
Motohiro Kihara	KEK	
Yukihide Kamiya	Univ. of Tokyo	
Takatoshi Murata	Kyoto Univ. of Edu.	

JOINT STUDIES

(Financial Year 1997)

Special Projects	3
Cooperative Research Projects	22
Invited Research Projects	1
Use-of-UVSOR Projects	149
Workshop	1
Machine Time for Users	39 weeks

People of UVSOR

Location

Ultraviolet Synchrotron Orbital Radiation (UVSOR) is located at Okazaki.Okazaki (population 320,000) is 260km southwest of Tokyo, and can be reached within 3 hours from Tokyo via the Tokaido Shinkansen and the Meitetsu line.

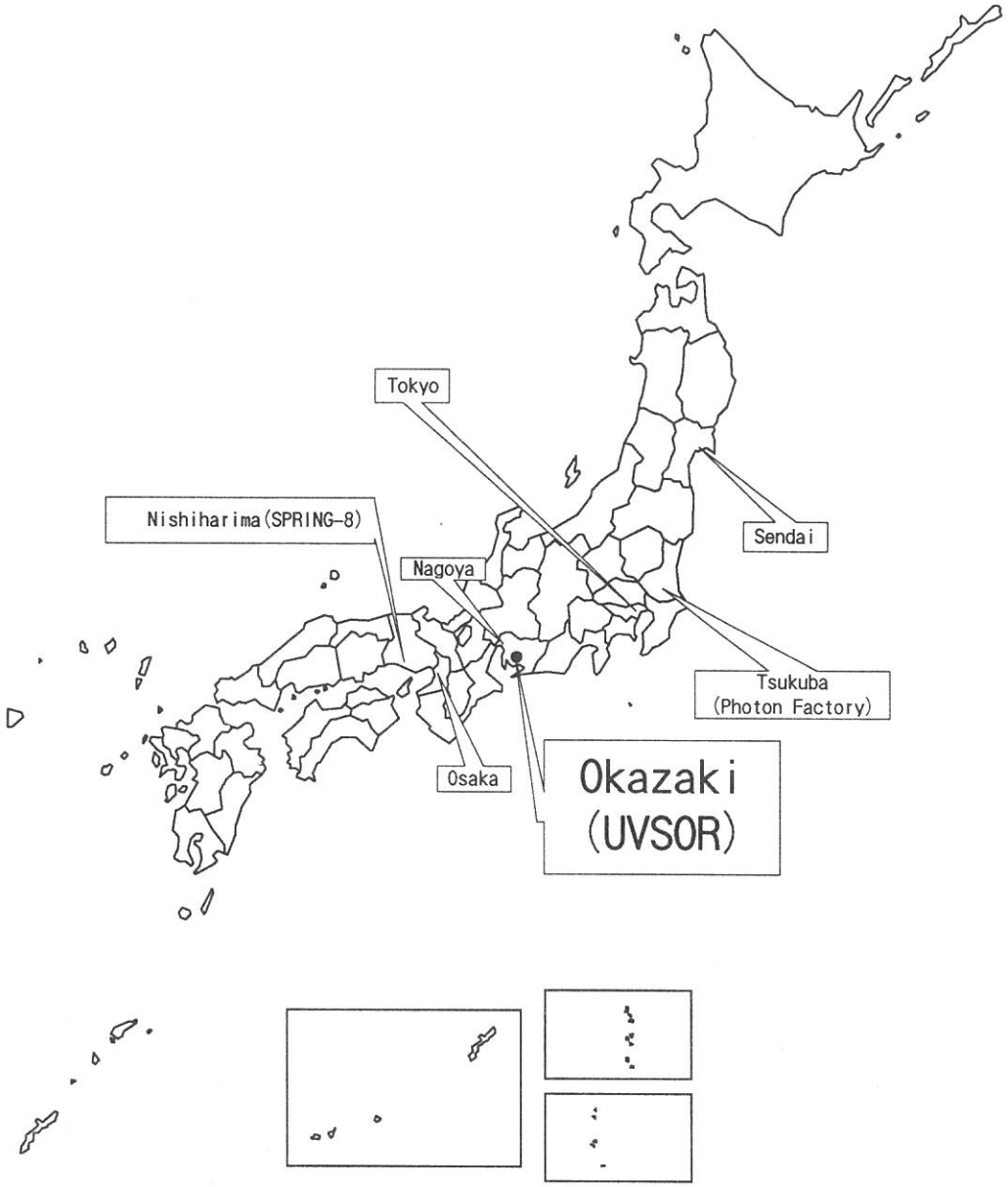

ADDRESS

UVSOR Facility
Institute for Molecular Science
Myodaiji, Okazaki, 444-8585, JAPAN

PHONE: +81-564-55-7402(Secretary)
+81-564-52-6101
FAX:+81-564-54-7079
Telex 4537475 KOKKEN J (IMS)
Homepage: http://www.uvsor.ims.ac.jp/

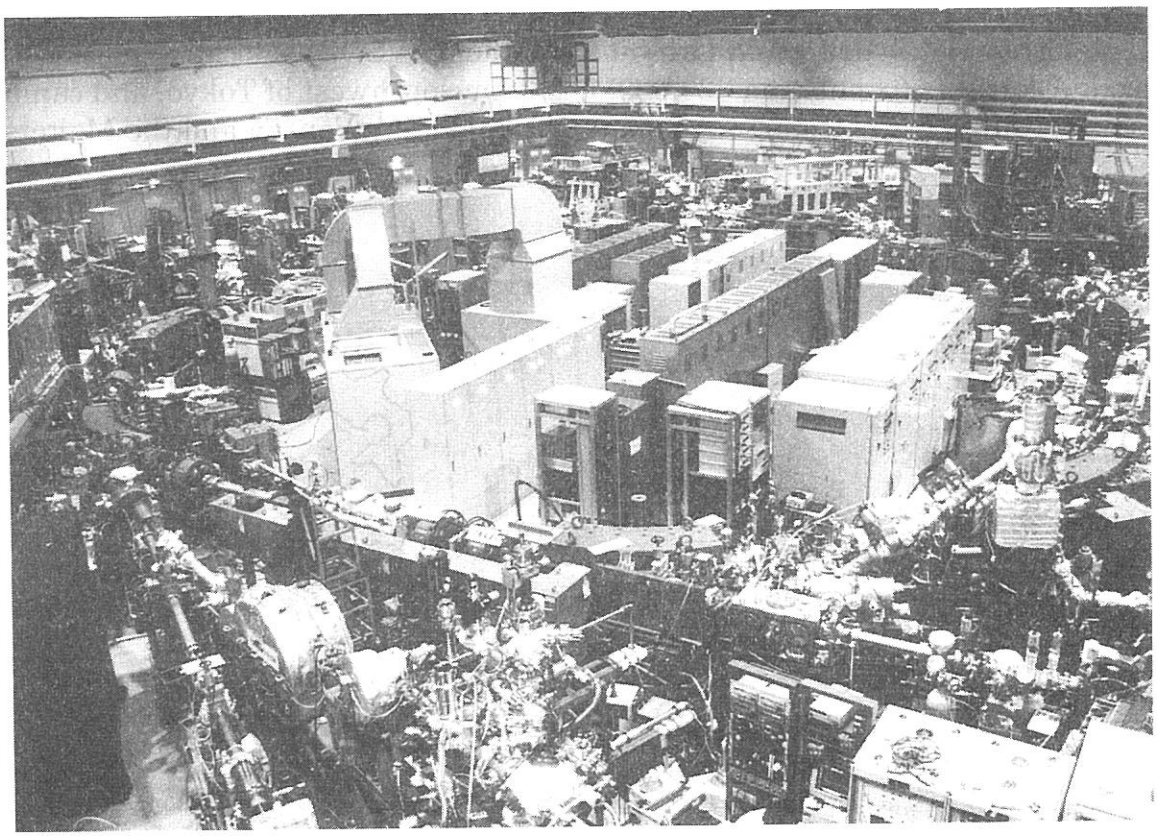

A picture of the experimental hall of the UVSOR facility.

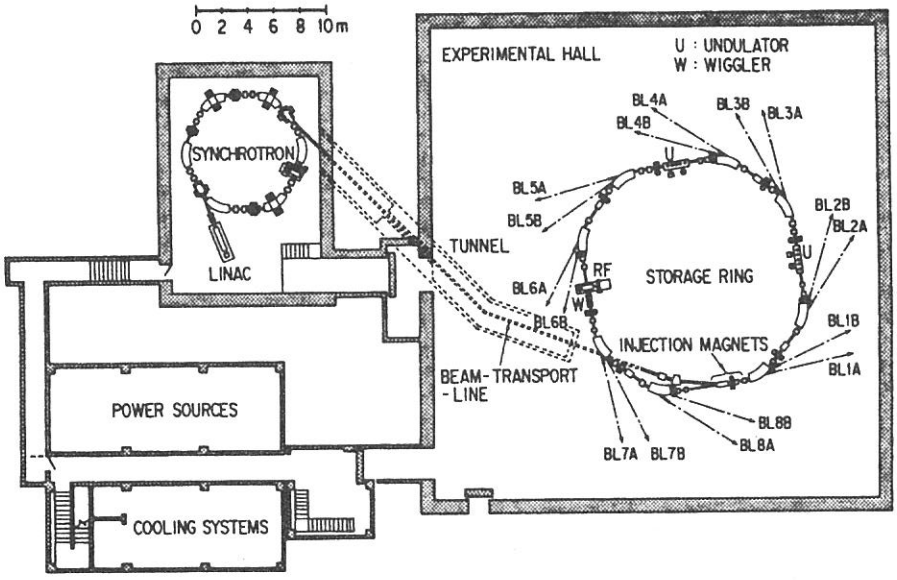

Ground plan of the basement of the UVSOR facility.